Defense Nuclear Agency
Alexandria, VA 22310-3398

DNA-TR-89-150

First-Order Intensity Statistics for Non-Rayleigh Fading

L. L. De Raad, Jr.
M. K. Grover
R&D Associates
P.O. Box 9695
Marina del Rey, CA 90295-2095

February 1990

Technical Report

CONTRACT No. DNA 001-88-C-0046

Approved for public release;
distribution is unlimited.

DISTRIBUTION LIST UPDATE

This mailer is provided to enable DNA to maintain current distribution lists for reports. We would appreciate your providing the requested information.

- ☐ Add the individual listed to your distribution list.
- ☐ Delete the cited organization/individual.
- ☐ Change of address.

NAME: ____________________

ORGANIZATION: ____________________

OLD ADDRESS	CURRENT ADDRESS
____________	____________
____________	____________
____________	____________

TELEPHONE NUMBER: (___) ____________

SUBJECT AREA(s) OF INTEREST:

____

____

____

DNA OR OTHER GOVERNMENT CONTRACT NUMBER: ____________

CERTIFICATION OF NEED-TO-KNOW BY GOVERNMENT SPONSOR (if other than DNA):

SPONSORING ORGANIZATION: ____________

CONTRACTING OFFICER OR REPRESENTATIVE: ____________

SIGNATURE: ____________

CUT HERE AND RETURN

Director
Defense Nuclear Agency
ATTN: TITL
Washington, DC 20305-1000

Director
Defense Nuclear Agency
ATTN: TITL
Washington, DC 20305-1000

REPORT DOCUMENTATION PAGE

Form Approved
OMB No. 0704-0188

1. AGENCY USE ONLY *(Leave blank)*	2. REPORT DATE	3. REPORT TYPE AND DATES COVERED
	900201	Technical 880101 to 881231

4. TITLE AND SUBTITLE
First-Order Intensity Statistics for Non-Rayleigh Fading

5. FUNDING NUMBERS
C-DNA-001-88-C-0046
PE-62715H
PR-P99GMXD
TA-B
WU-DH008670

6. AUTHOR(S)
DeRaad, Lester L., Jr. and Grover, Morgan K.

7. PERFORMING ORGANIZATION NAME(S) AND ADDRESS(ES)
R&D Associates
P.O. Box 9695
Marina del Rey, CA 90295-2095

8. PERFORMING ORGANIZATION REPORT NUMBER
RDA-TR-0226128902-002

9. SPONSORING/MONITORING AGENCY NAME(S) AND ADDRESS(ES)
Defense Nuclear Agency
6801 Telegraph Road
Alexandria, VA 22310-3398
RAAE/Wittwer

10. SPONSORING/MONITORING AGENCY REPORT NUMBER
DNA-TR-89-150

11. SUPPLEMENTARY NOTES
This work was sponsored by the Defense Nuclear Agency under RDT&E RMSS Code B310085466 P99QMXDB00099 H2590D.

12a. DISTRIBUTION/AVAILABILITY STATEMENT
Approved for public release; distribution is unlimited.

12b. DISTRIBUTION CODE

13. ABSTRACT *(Maximum 200 words)*

This report examines first-order intensity statistics under multipath scintillation conditions which are not sufficiently severe to lead to fully developed Rayleigh fading. It is shown that neither Rice nor Nakagami-m statistics are accurate in general. Actual signal intensity statistics can be systematically characterized in terms of the refractive index spatial power spectrum and the signal Fresnel length. Numerous calculated results are provided for signal intensity distributions and channel symbol bit error rates in non-Rayleigh fading. Keywords!)

14. SUBJECT TERMS		15. NUMBER OF PAGES
Scintillation Effects	Non-Rayleigh Fading	332
SATCOM	Propagation Effects	16. PRICE CODE

17. SECURITY CLASSIFICATION OF REPORT	18. SECURITY CLASSIFICATION OF THIS PAGE	19. SECURITY CLASSIFICATION OF ABSTRACT	20. LIMITATION OF ABSTRACT
UNCLASSIFIED	UNCLASSIFIED	UNCLASSIFIED	SAR

NSN 7540-01-280-5500

Standard Form 298 (Rev 2-89)
Prescribed by ANSI Std 239-18
298-102

Satellite Communications, Satellite links, Ionosphere Scattering. (KR)

TECHNICAL SUMMARY

In this report we describe the results from a large number of computations of signal intensity distributions and channel symbol bit error rates for satellite links under non-Rayleigh fading conditions. The computations are performed numerically using the Fresnel-Kirchhoff scattering equation. The computations address a broad range of parametric representations of the ionospheric scattering medium; where applicable, a broad range of Fresnel lengths (ℓ_F) is also considered. The intent has been to include at least some conditions which may not be predominant in the ambient environment but which might, perhaps, occur in the aftermath of one or more high altitude nuclear explosions.

The propagation medium is approximated as a thin, one-dimensional (anisotropic), spatially structured, phase-shifting screen. Phase screens are generated as numerical realizations of a stationary, spatially correlated Gaussian random process. The second-order statistics of the process are specified by the power spectral density (PSD), which is the Fourier transform of the spatial autocovariance of the phase screen phase. The PSD is parameterized versus k, the spatial wavevector, either as a "single power law" k^{1-n} form* or as a "double power law" form with an abrupt change in n at $k = k_B$. An outer scale size L_o is used to roll off the PSD at $k \lesssim L_o^{-1}$, and for $n \leq 3$ an inner scale size ℓ_i is also used to cut off the spectrum at large k.

*A k^{1-n} phase screen PSD corresponds to a k^{-n} three-dimensional refractive index (for electron density) spatial power spectrum.

The computed results are compared with the Rice and Nakagami-m models. Under certain conditions (mainly $n \lesssim 3.5$ and $\ell_F >> \ell_i$), the Rice model agrees fairly well with the computed results. More generally Rice tends to be a worst case. Under other specific conditions (mainly $n \cong 4$ and with $\ell_i << \ell_F << 2\pi L_o$), the Nakagami-m model agrees fairly well, but only at moderate signal intensity levels; Nakagami-m consistently underestimates the frequency of deep fades, which can often dominate communications performance. More generally, the computed results show that there are previously unrecognized, strong and systematic trends in signal intensity statistics as functions of the PSD parameterization and the Fresnel length. No existing simple model will reproduce these trends. Rice statistics offer an heuristic "worst case" specification for generally bounding the severity of the signal intensity effects.

We also briefly review the results from previous comparisons of ambient environment satellite link data versus Nakagami-m and other models. In these past studies, initially conflicting findings have apparently yielded to a consensus that Nakagami-m statistics seem to provide somewhat the better but imperfect fit (among those options considered) to the ambient environment data. We find this rough consensus to be consistent with our present results, since the conditions (e.g., $n \cong 4$ and $\ell_F << 2\pi L_o$) where Nakagami-m best approximates our computated results are also thought to nominally represent the most common features of the ambient ionosphere. Moreover, the data used in these past studies did not accurately sample deep fades, which are underestimated by Nakagami-m statistics.

CONVERSION TABLE

Conversion factors for U.S. Customary to metric (SI) units of measurement

MULTIPLY ——————→ BY ——————→ TO GET

TO GET ←—————— BY ←—————— DIVIDE

angstrom	1.000000 x E -10	meters (m)
atmosphere (normal)	1.01325 x E +2	kilo pascal (kPa)
bar	1.000000 x E +2	kilo pascal (kPa)
barn	1.000000 x E -28	meter² (m^2)
British thermal unit (thermochemical)	1.054350 x E +3	joule (J)
calorie (thermochemical)	4.184000	joule (J)
cal (thermochemical) / cm^2	4.184000 x E -2	mega joule/m^2 (MJ/m^2)
curie	3.700000 x E +1	*giga becquerel (GBq)
degree (angle)	1.745329 x E -2	radian (rad)
degree Farenheit	$t_K = (t_F + 459.67)/1.8$	degree kelvin (K)
electron volt	1.60219 x E -19	joule (J)
erg	1.000000 x E -7	joule (J)
erg/second	1.000000 x E -7	watt (W)
foot	3.048000 x E -1	meter (m)
foot-pound-force	1.355818	joule (J)
gallon (U.S. liquid)	3.785412 x E -3	meter³ (m^3)
inch	2.540000 x E -2	meter (m)
jerk	1.000000 x E +9	joule (J).
joule/kilogram (J/kg) (radiation dose absorbed)	1.000000	Gray (Gy)
kilotons	4.183	terajoules
kip (1000 lbf)	4.448222 x E +3	newton (N)
kip/inch² (ksi)	6.894757 x E +3	kilo pascal (kPa)
ktap	1.000000 x E +2	newton-second/m^2 ($N\text{-}s/m^2$)
micron	1.000000 x E -6	meter (m)
mil	2.540000 x E -5	meter (m)
mile (international)	1.609344 x E +3	meter (m)
ounce	2.834952 x E -2	kilogram (kg)
pound-force (lbs avoirdupois)	4.448222	newton (N)
pound-force inch	1.129848 x E -1	newton-meter (N m)
pound-force/inch	1.751268 x E +2	newton/meter (N/m)
pound-force/foot²	4.788026 x E -2	kilo pascal (kPa)
pound-force/inch² (psi)	6.894757	kilo pascal (kPa)
pound-mass (lbm avoirdupois)	4.535924 x E -1	kilogram (kg)
pound-mass-foot² (moment of inertia)	4.214011 x E -2	kilogram-meter² ($kg\,m^2$)
pound-mass/foot³	1.601846 x E +1	kilogram/meter³ (kg/m^3)
rad (radiation dose absorbed)	1.000000 x E -2	**Gray (Gy)
roentgen	2.579760 x E -4	coulomb/kilogram (C/kg)
shake	1.000000 x E -8	second (s)
slug	1.459390 x E +1	kilogram (kg)
torr (mm Hg, 0° C)	1.333220 x E -1	kilo pascal (kPa)

*The becquerel (Bq) is the SI unit of radioactivity; 1 Bq = 1 event/s.
**The Gray (Gy) is the SI unit of absorbed radiation.

TABLE OF CONTENTS

Section		Page
	Technical Summary	iii
	Conversion Table	v
	List of Illustrations	vii
	List of Tables	ix
1	Introduction	1
2	Mathematical Background and Approach	9
3	Single Power Law Results	21
4	Two Power Law Results	41
5	Discussion	50
6	List of References	57
Appendices		
A	Additional Mathematical Details	61
B	Numerical Considerations	67
C	Probability Distributions for Single Power Law PSD	75
D	Probability Distributions for Small Intensity for Single Power Law PSD	137
E	Calculated Bit Error Rates for Single Power Law PSD	151
F	Calculated Bit Error Rates for DBPSK Compared to Nakagami-m and Rice for Single Power Law PSD	183
G	Probability Distribution for Two Power Law PSD	211
H	Probability Distribution for Small Intensity Two Power Laws PSD	261
I	Calculated Bit Error Rates for Two Power Law PSD	271
J	Calculated Bit Error Rates for DBPSK Compared to Nakagami-m and Rice for Two Power PSD	297

LIST OF ILLUSTRATIONS

Figure		Page
1	Channel symbol bit error rates (BERs) versus signal-to-noise ratio (SNR (dB)) for DBPSK in Rayleigh fading (SRF curve and above) and in non-fading (AWGN) regimes........	3
2	Slow Rayleigh fading (SRF) and non-fading (AWGN) BER vs. SNR characteristics (from Figure 1), as compared with Rice (R) and Nakagami-m (N) statistics at S_4^2 = 0.378 -- all for DBPSK..................................	5
3	BER vs. SNR characteristics for DBPSK, as calculated from a k^{-n} refractive index PSD with n = 3.0, 3.5, 4.0, 4.5 and 5.0............	7
4	Scintillation index (S_4^2) versus the Rytov parameter ($\overline{X^2_{Ry}}$) for various single power law PSDs......................................	23
5	S_4^2 -versus- σ_{Ne} relationship (σ_{Ne} relative) for single power law PSDs with different spectral indexes..................................	25
6	Comparison of computed (C) results with Rice (R) and Nakagami-m (N) models at s = 1, $\overline{X^2_{Ry}}$ = 0.1, S_4^2 = 0.327..........................	27
7	Comparison of computed results (C) with Rice (R) and Nakagami-m (N) models at s = 1.5, $\overline{X^2_{Ry}}$ = 0.1, S_4^2 = 0.343..........................	28
8	Comparison of computed (C) results with Rice (R) and Nakagami-m (N) models at s = 2, $\overline{X^2_{Ry}}$ = 0.1, S_4^2 = 0.378..........................	29
9	Comparison of computed (C) results with Rice (R) and Nakagami-m (N) models at s = 2.5, $\overline{X^2_{Ry}}$ = 0.1, S_4^2 = 0.438..........................	31
10	Computed DBPSK channel symbol BERs versus SNR and $\overline{X^2_{Ry}}$ for single power law PSDs with: (a) s = 1 and (b) s = 3.........................	33

LIST OF ILLUSTRATIONS (CONTINUED)

Figure		Page
11	Computed DBPSK channel symbol BERs versus spectral index, either at fixed $S_4^2 = 0.378$ (Fig. 11a) or at fixed $\overline{X^2_{Ry}} = 0.1$ (Fig. 11b)....	34
12	Comparison of computed BER characteristics for DBPSK with Rice and Nakagami-m at $\overline{X^2_{Ry}} = 0.1$ for: (a) s = 1.5, (b) s = 2, (c) s = 2.5, (d) s = 3 -- S_4^2 values as indicated....................................	36
13	Comparison of computed signal intensity distributions for $S_4^2 > 1.0$ at s = 3 with Rayleigh statistics: (a) $\overline{X^2_{Ry}} = 0.4$, (b) $\overline{X^2_{Ry}} = 7.0$......	39
14	BER characteristics (for DBPSK) for single power law PSD with s = 3 in typical cases when $S_4^2 > 1.0$, compared with Rayleigh signal statistics............................	40
15	Two power law power spectral density; also indicated are the locations of k_α (α = 1-5)....	42
16	Scintillation index (S_4^2) versus the Rytov parameter ($\overline{X^2_{Ry}}$) for various Fresnel lengths...	45
17	Calculated signal intensity distribution for two power law striation PSD of Figure 15, at $\overline{X^2_{Ry}} = 0.05$ and ℓ_F = 1386 m and ℓ_F = 173 m, as compared to Rice and Nakagami-m.............	46
18	BER vs. SNR characteristics for DBPSK for various Fresnel lengths $\ell_F(\alpha)$ at $\overline{X^2_{Ry}} = 0.1$.....	48
19	Calculated channel symbol bit error rate vs. SNR at $\overline{X^2_{Ry}} = 0.1$ and ℓ_F = 1386 m and ℓ_F = 86 m, as compared to Rice and Nakagami-m.......................................	49
20	Sampled phase screen vs. position..............	68

LIST OF TABLES

Table		Page
1	S_4^2 vs. $\overline{X^2_{Ry}}$ and s	22
2	S_4^2 vs. $\overline{X^2_{Ry}}$ and k_α	44
3	Single Power Law Parameters	71
4	Two Power Law Parameters	71

SECTION 1
INTRODUCTION

This paper addresses signal intensity statistics for satellite communications links propagating through regions of ionospheric structure. Principal attention is given to conditions under which the propagation disturbances are not strong enough to cause fully developed Rayleigh fading. Also addressed is the systematic dependence of the intensity distribution and other signal characteristics upon certain detailed features of the ionospheric structure and the Fresnel length (ℓ_F).

It is well-known that under dynamic, nonequilibrium conditions the ionospheric F-region can become highly structured, in the form of elongated, geomagnetic-field-aligned "striations" of excess electron density (Refs. 1-4). Transmission of satellite signals through such striated regions can lead to multiple scattering and multipath propagation (Refs. 5-7). This multipath propagation can cause severe signal distortions, or "scintillations," in the form of intermittent fading, phase fluctuations, and signal angle and time of arrival spreads (Refs. 8-12) Because of the massive ionospheric disturbances that would be caused by high altitude nuclear explosions, these effects are of particular concern for military satellite communications (Refs. 13-17); however, they can also occur in the ambient environment under conditions of equatorial spread-F or severe auroral disturbances (Refs. 18-26).

Under sufficiently strong scattering and multipath conditions the signal scintillations can be accurately characterized in terms of Rayleigh distributed phase and amplitude (or intensity) statistics (Refs. 27-29). The convenient mathematical structure of Rayleigh signal statistics, and also the validity of such statistics over the broad range of strong scattering conditions, have had important benefits for the analysis, design, and testing of military satellite links.

Less severe scattering conditions are also important. Under these conditions, the signal phase fluctuations are typically rather slow, and angle or time of arrival spreads are generally negligible; but signal intensity fluctuations are still significant. The fades are less deep; but, because they are typically of longer duration, they can be very difficult to mitigate. For practical applications it is the intensity distribution (first-order statistics), and also the dynamics (second order statistics), of the intermittent signal fades and enhancements that is of greatest interest. This paper addresses only first-order intensity statistics and related properties.

Unfortunately, the proper description of signal intensity distributions under non-Rayleigh-fading conditions remains highly problematical. Several analytical forms have been considered, including the Rice, log-normal, and Nakagami-m distributions (Refs. 8, 30-33), and also a more pragmatic approach to be discussed below. It seems that the Rice distribution has been favored in some engineering applications while the Nakagami-m distribution is thought to provide a somewhat better but imperfect fit to certain satellite data taken in the ambient environment (Refs. 8, 31 and Section 5).

One of several methods which we will use for presentation and discussion of our computed results will be the channel symbol bit error rate characteristic as would be measured directly at the link demodulator output (see Section 2 and Appendix A for details). Figure 1 depicts predicted channel symbol bit error rates (BERs) for differential binary phase shift key (DBPSK) versus the average signal-to-noise ratio (SNR) for different extremes of the assumed signal intensity distribution. The region bounded by the "Slow Rayleigh Fading" (SRF) curve portrays the regime of Rayleigh statistics. The AWGN (additive white Gaussian noise) curve depicts normal link performance with no fading. There is obviously a large gap in between these two regimes. Signal intensity statistics within this "gap" region will be the subject of the present report.

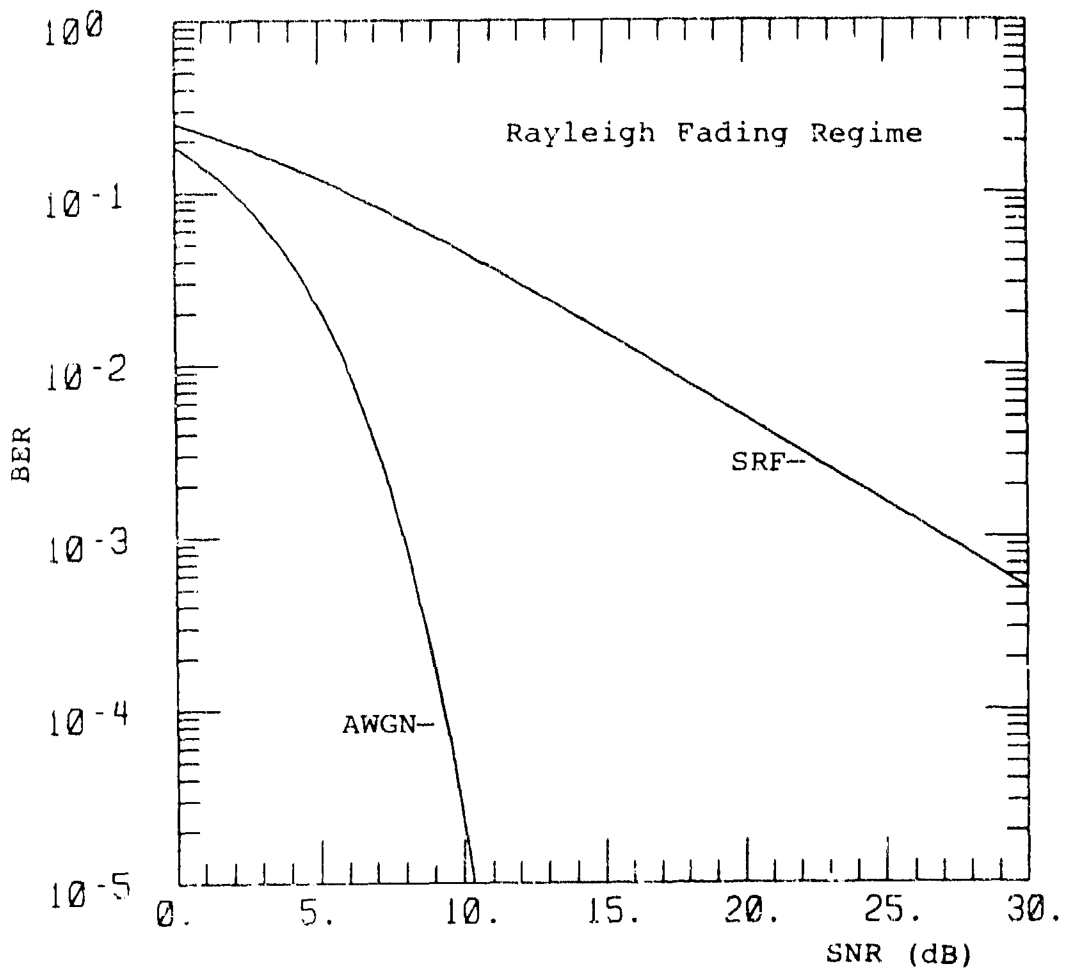

Figure 1. Channel symbol bit error rates (BERs) versus signal-to-noise ratio (SNR (dB)) for DBPSK in Rayleigh fading (SRF curve and above) and in non-fading (AWGN) regimes.

The most pragmatic approach for bridging this gap (Refs. 7,9,34) has been simply to assume Rayleigh statistics whenever the "Rytov parameter" (i.e., the Rytov approximation to the signal log-amplitude variance, herein denoted as $\overline{\chi^2_{Ry}}$--more fully defined later) exceeds the value $\overline{\chi^2_{Ry}} = 0.1$, and to assume negligible signal distortions whenever $\overline{\chi^2_{Ry}} < 0.1$. The rationale for this specific Rytov parameter criterion, within the overall approach, will be demonstrated below. An important practical advantage of this approach is its continuance of the mathematically convenient Rayleigh specifications into a broader regime of application. One disadvantage under weak scattering but for $\overline{\chi^2_{Ry}} \geq 0.1$, is that it provides an overly stressful specification under those slow fading conditions which are already quite difficult to mitigate, and which also persist over large areas and for long times in a nuclear environment. A further disadvantage is that it neglects link performance degradations altogether when $\overline{\chi^2_{Ry}} < 0.1$; these latter conditions can occur over even larger areas, and for even longer times.

Among other possibilities, the assumption of either Rice or Nakagami-m signal statistics offers a means to more continuously bridge the gap between AWGN (no fading) and SRF (strong scattering) conditions. By definition, both the Rice and Nakagami-m models are parameterized by the scintillation index S_4^2, which is the signal intensity variance. As $S_4^2 \rightarrow 1.0$, both Rice and Nakagami-m approach the SRF limit. As $S_4^2 \rightarrow 0$, both approach the AWGN, or no-fading limit. In between, however, the two models may differ appreciably.

For weak scattering, $S_4^2 \cong 4\overline{\chi^2_{Ry}}$. Included in Figure 2 are the BER vs. SNR characteristics (again DBPSK) predicted from both Rice and Nakagami-m statistics, and specifically at $S_4^2 = 0.378$, which also corresponds to $\overline{\chi^2_{Ry}} = 0.1$ for a particular scattering medium parameterization of common interest (see Table 1 of Section 3). It can be seen that either curve lies approximately midway between the SRF and AWGN extremes. Observations of this nature provide the rationale for selecting $\overline{X}^2_{Ry} = 0.1$ as a convenient dividing line between Rayleigh fading and no fading in the simpler pragmatic approach described above. However, it can also be seen from Figure 2 that even the BER vs. SNR characteristics of Rice versus Nakagami-m statistics may differ appreciably under conditions of practical interest. As described below, comparable

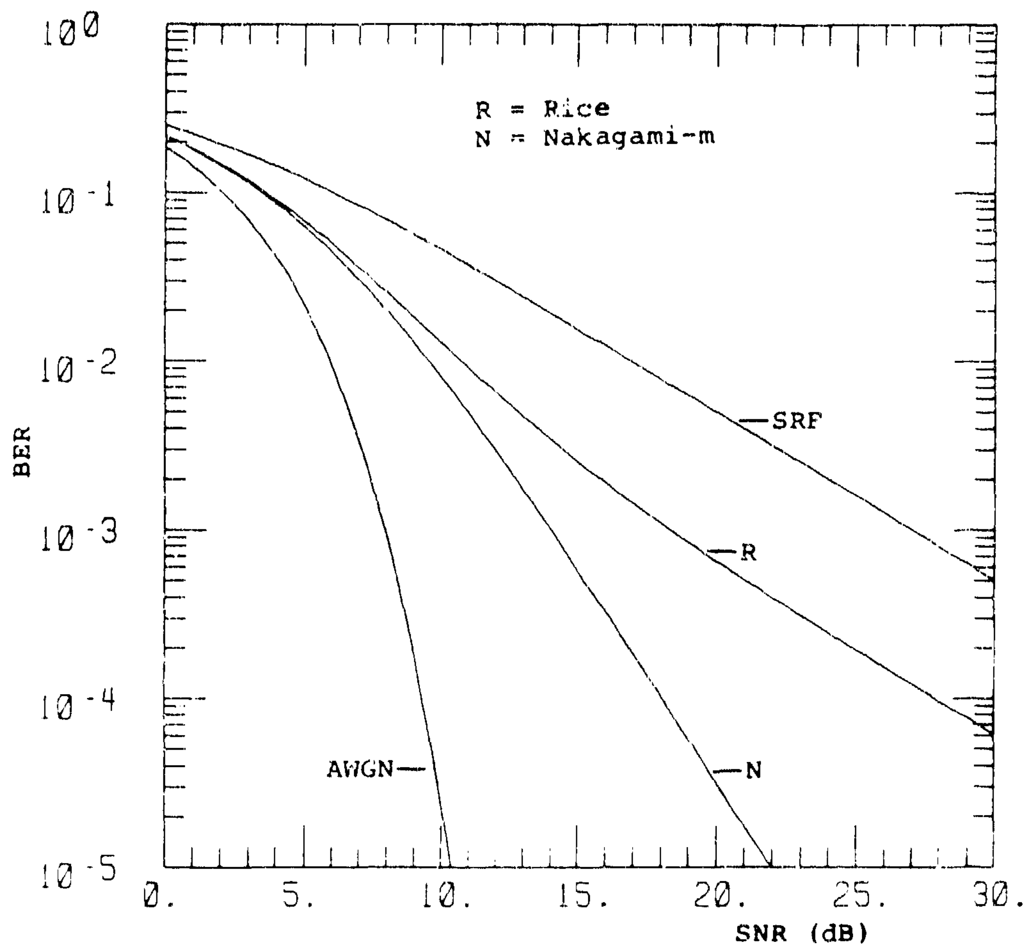

Figure 2. Slow Rayleigh fading (SRF) and non-fading (AWGN) BER vs. SNR characteristics (from Figure 1), as compared with Rice (R) and Nakagami-m (N) statistics at $S_4^2 = 0.378$ -- all for DBPSK.

or even larger differences can also occur when the models are compared with more detailed theoretical calculations. These differences further help to motivate the present investigation.

In this report, we will describe the results of a theoretical and computational investigation of signal intensity statistics under non-Rayleigh fading conditions. A large number of computations of received signal charactertics have been performed, using the Fresnel-Kirchhoff scattering equation, and encompassing a fairly broad range of parametric descriptions of the striated ionospheric propagation medium. Strong and systematic trends can be identified in the results, as summarized below.

We find that neither Nakagami-m nor Rice statistics are reliable in general. Within the parametric regimes of greatest present interest, the Rice distribution tends to provide an approximate upper bound on the frequency of deep fades, and on predicted channel symbol BERs, while the detailed BER vs. SNR curves may be either higher or lower than predicted by Nakagami-m statistics, depending both on the parametric model of the scattering medium and on the problem SNR and Fresnel length.

We consider situations in which the ionospheric electron density or refractive index structure can be parameterized in terms of a three-dimensional spatial power spectrum approximately of the form k^{-n}, where $k = 2\pi/\text{length}$ is the spatial wavevector. By definition, $s = n-2$ is then the "spectral index," and in the thin phase screen approximation (Section 2) the phase screen PSD varies as k^{1-n}. In the chosen parameterizations, the exponent n may be constant over a broad range of wave vectors, or it may be allowed to change discontinuously at $k = k_B$ (i.e., a k^{-n_1} form at $k < k_B$, and a k^{-n_2} form at $k > k_B$). In either case, we find that the signal intensity statistics, BER vs. SNR characteristics, and other results as well can be at least approximately characterized in terms of an "effective" value of n which provides a reasonable k^{-n} fit to the spectrum for wave vectors generally somewhat less than, and in the vicinity of, $k \cong 2\pi/\ell_F$. A more precise characterization is provided by the specific examples given later.

The findings are partially illustrated in Figure 3, which presents calculated BER vs. SNR characteristics (again for DBPSK) as a function of the exponent (n) of an approximately k^{1-n} phase

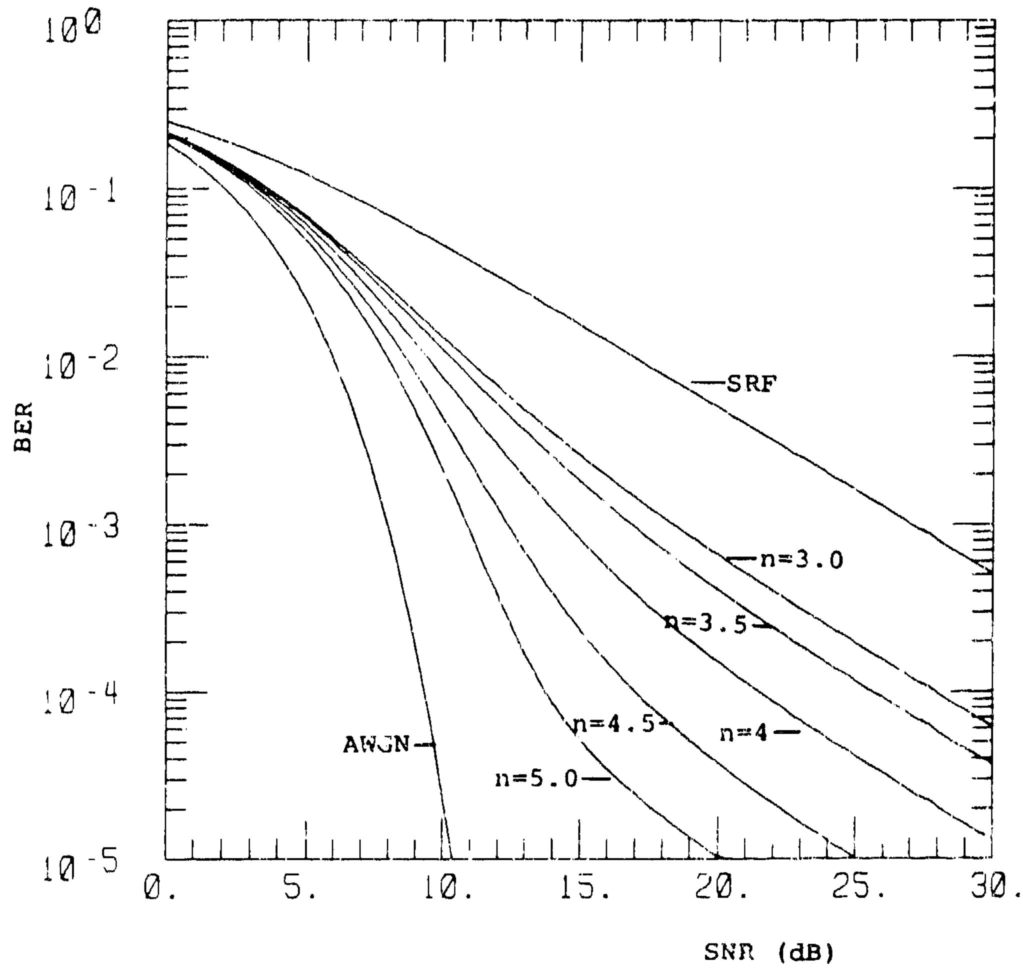

Figure 3. BER vs. SNR characteristics for DBPSK, as calculated from a k^{-n} refractive index PSD with n = 3.0, 3.5, 4.0, 4.5 and 5.0.

screen PSD all still at $S_4^2 = 0.378$. Also shown are the corresponding SRF and AWGN limits. For $n \lesssim 3.5$, the resulting BER vs. SNR characteristics fairly closely approximate those predicted by the Rice intensity distribution (compare Fig. 2). For $n \cong 4.0$ the BER versus SNR characteristics lie intermediate between those from Rice and Nakagami-m statistics, favoring Nakagami-m only at the lower SNR levels. For $n \gtrsim 4.5$, the BER characteristics lie below those from Nakagami-m statistics at lower SNR levels, but above Nakagami-m at higher SNR levels.

Related strong and systematic trends are found in the signal intensity distributions and in the $\overline{X^2_{Ry}}$ versus S_4^2 relationships as functions of the parameterization of the scattering medium and the Fresnel length, both for single and double power law phase screen PSDs. In addition to their relevance for the design and analysis of military satellite communications links, some of these results may also be applicable to the interpretation of satellite data taken in the ambient environment.

SECTION 2

MATHEMATICAL BACKGROUND AND APPROACH

In this section we describe the mathematical background and general parameterization schemes of interest for the present investigation. This will include: the mathematical description of the ionospheric scattering medium (subsection 2.1); the numerical generation of specific realizations of the medium (subsection 2.2); the Fresnel-Kirchhoff formalism for calculating the properties of received signals (subsection 2.3); and the definition of various measures of signal scattering intensity and other key parameters such as signal line-of-sight (LOS) phase variance (σ_ϕ^2), the scintillation index (S_4^2), the Rytov parameter approximation to the log-amplitude variance ($\overline{X}_{Ry}^2$), and the Fresnel length (ℓ_F)--all in subsection 2.4. In subsection 2.5 we describe the general properties of Rice, Nakagami-m, and Rayleigh intensity statistics. In subsection 2.6 we describe the general approach for representing slow fading effects in terms of BER vs. SNR characteristics for typical digital modems, with BERs as measured at the basic channel symbol level, without the benefits of error detection-correction coding and interleaving. Additional details are also provided in Appendixes A and B.

2.1 THE SCATTERING MEDIUM.

In the present investigation, the striated ionospheric scattering medium will be represented as a spatially thin, phase-shifting screen. The partial neglect of certain finite-medium-depth effects on signal propagation is an approximation, of course, but has been assessed for its reliability in Reference 34. Moreover, the overall findings from the subsequent analysis are clearly sufficiently robust as to be qualitatively unaffected by this approximation. The signal phase shift (more precisely, its deviation relative to the mean) is regarded as a Gaussian random variable in the (x, y) coordinates of the plane perpendicular to the signal line-of-sight (LOS). The phase statistics are therefore fully defined by the autocovariance,

$$\langle \phi(x,y)\phi(0,0) \rangle = B(x,y). \tag{1}$$

We effectively neglect the mean phase shift, phase advance, and group delay by setting $\langle \phi \rangle = 0$. In practice, we will also neglect the y-dependence of $\phi(x,y)$ and $B(x,y)$. This last assumption is expected to have very little qualitative effect on the signal scattering statistics; for a related discussion, see Reference 34.

The medium is specifically parameterized in terms of the phase screen power spectral density (PSD), defined as

$$\Phi(k) = \int_{-\infty}^{\infty} B(x) \exp(-ikx)\, dx. \tag{2}$$

Several different PSD parameterizations are addressed. The simplest is a "single power law" of the form (for $\nu > 1$)

$$\Phi(k) = 2\sqrt{\pi}\, \sigma_\phi^2 \frac{\Gamma(\nu)}{\Gamma(\nu-\frac{1}{2})} \frac{L_o}{[1+L_o^2k^2]^\nu}. \tag{3}$$

Here, σ_ϕ^2 is the phase screen phase variance (as sampled over an ensemble of LOS ray paths), and L_o is an "outer scale length" effectively defining the maximum striation scale size as measured perpendicular to the LOS. The exponent ν is related to the more conventional spectral index as $\nu = (s+1)/2$. This parameterization of the phase screen PSD, essentially as a $k^{-2\nu}$ power law (i.e., for $k >> L_o^{-1}$), also implies a parameterization of the underlying striation electron density three-dimensional PSD as a k^{-n} form, with

$$n = s + 2 = 2\nu + 1. \tag{4}$$

The special case $\nu = 1$ (also $s = 1$, $n = 3$) requires introduction of an additional "inner scale length" cutoff (ℓ_i) so that the underlying electron density variance will be finite. Therefore, for $\nu = 1$ we use

$$\Phi(k) = \frac{2\sigma_\phi^2 L_o}{1 + L_o^2 k^2} Z K_1(Z) \exp(\ell_i / L_o) \tag{5}$$

where $Z^2 L_o^2 = \ell_i^2 (1 + L_o^2 k^2)$, and $K_1(Z)$ is a Bessel function.

We will also address a more general "two power law" parameterization of the form

$$\Phi(k) = \begin{cases} c_1 \dfrac{L_o \sigma_\phi^2}{(1 + L_o^2 k^2)^{\nu_1}} & , k < k_B, \\[2ex] c_2 \dfrac{L_o \sigma_\phi^2}{(L_o^2 k^2)^{\nu_2}} & , k > k_B. \end{cases} \tag{6}$$

Conditions of continuity and normalization determine c_1 and c_2 as functions of ν_1, ν_2, and $L_o k_B$. These relations are detailed in Appendix A. Evidently, k_B defines a length scale ($2\pi/k_B$) at which there is a "break" in the spectral index. Under conditions of interest $L_o \sim 10$ km or so, while $2\pi/k_B$ is typically on the order of several hundreds of meters (Refs. 35-36). Thus, when $\nu_1 = \nu_2$ the two-power law PSD very closely approximates the one-power law form. As for the spectral index, many conditions of practical interest are presently thought to be encompassed by (Ref. 37)

$$1 \lesssim \nu_1 \lesssim 3/2 \lesssim \nu_2 \lesssim 5/2. \tag{7}$$

Even more complex "three power law" models are also under present consideration, based on recently acquired ambient ionosphere satellite data (Ref. 37); this report will emphasize effects which are largely invariant to such further details.

2.2 NUMERICAL REALIZATIONS.

Given these descriptions of the scattering medium in terms of a thin phase screen, with the LOS phase treated as a spatially stationary Gaussian random process having a specified PSD, representative phase screen realizations can then be numerically generated by standard statistical sampling methods. A representative sampling of such realizations can then be used to numerically calculate the statistical properties of the received signal.

For each defined phase screen PSD parameterization, a set of specific phase screen realizatons can be generated as

$$\phi(x_m) = \mathrm{Re}\left[\sqrt{\Delta k} \sum_{n=0}^{N-1} D_n r_n \exp(2\pi i n m/N)\right] \tag{8a}$$

where $\Delta k = 2\pi/N\Delta x = 2\pi/x_N$, (8b)

$D_0^2 = \Phi(k=0)/2\pi$, (8c)

$D_{n\neq 0}^2 = \Phi(n\Delta k)/\pi$. (8d)

The quantity $r_n = r_{1n}+ir_{2n}$ is a complex Gaussian random variable with $\langle r_1\rangle = \langle r_2\rangle = 0$, $\langle r_1^2\rangle = \langle r_2^2\rangle = 1$, and $\langle r_1 r_2\rangle = 0$. The numerical and implementational details are further defined in Appendix B.

2.3 FRESNEL-KIRCHHOFF SCATTERING FORMALISM.

With neglect of large angle scattering, geometric divergence, absorption, and antenna gain effects, the received signal can be determined from the Fresnel-Kirchhoff scattering equation as (Refs. 34,38)

$$h(x) = (\lambda Z^*)^{-1/2}\, e^{-i\pi/4} \int_{-\infty}^{\infty} dx'\; e^{i\phi(x')} \exp[2\pi i(x-x')^2/2\lambda Z^*]. \tag{9}$$

Here, $h(x)$ is a complex received signal amplitude modulation at position x in the receiver plane (y-dependent variations neglected). As usual, λ is the signal wavelength. The function $\phi(x')$ is a specific realization of the phase-shifting screen, determined as defined above. The parameter Z^* is an equivalent signal path length defined as

$$Z^* = \frac{Z_R Z_T}{Z_R + Z_T}, \tag{10}$$

where Z_R is the distance to the receiver from the center of the phase-shifting medium, and Z_T is the corresponding transmitter-to-medium distance. Notice the importance of the parameter combination λZ^*, which is one-half the square of the Fresnel length (ℓ_F). The role of the Fresnel length will further discussed in subsection 2.4.

Given a specific phase screen realization, as $\phi(x_\ell) = \phi(\ell\Delta x)$, we can numerically evaluate Equation 9 to determine the x-dependence of the received complex signal amplitude h(x). From sufficiently numerous calculations of this sort, and including a sufficiently numerous set of phase screen realizations, the statistics of the received signal intensity $I = |h|^2$ are ultimately determined. The numerical version of Equation 9 is written as

$$h(x_\ell) = \frac{\Delta x}{\sqrt{\lambda Z^*}} e^{-i\pi/4} \sum_{m=\ell-N/2}^{\ell+N/2-1} e^{i\phi(x_m)} \exp\left[2\pi i(\Delta x)^2(\ell-m)^2/2\lambda Z^*\right]. \tag{11}$$

Additional details are given in Appendixes A and B.

2.4 OTHER KEY PARAMETERS.

The total strength of the scattering medium can be characterized in terms of σ_ϕ^2, which is the signal phase variance as would be measured over an ensemble of LOS ray paths fully sampling the scattering medium. Under certain circumstances, the LOS signal phase variance, which normalizes the thin phase screen PSD (i.e., at k = 0), can be related to the non-thin striated medium's electron density variance as

$$\sigma_\phi^2 = 2\lambda^2 \, r_e^2 \, L L_o' \, \sqrt{\pi} \, \frac{\Gamma(\nu-1/2)}{\Gamma(\nu-1)} \, \sigma_{Ne}^2, \tag{12}$$

where σ_{Ne}^2 is the electron density variance, and L is the effective thickness of the scattering medium. L_o' is now the effective outer scale length specifically as measured along the signal LOS; $r_e = 2.82 \times 10^{-15}$ m is the classical electron radius. This simple relationship, which pertains only to the special case of a single-power law $k^{-2\nu}$ PSD (with $\nu > 1$), nonetheless helps to define the general nature of the relationship between the LOS signal variance of a thin phase screen model and the electron density variance of a finite-thickness striated ionospheric medium. Additional details are given in Appendix A.

The intensity of signal scattering effects can already be seen from Equation 9 to depend not only upon σ_ϕ^2 but also upon the correlation of these phase fluctuations over length scales measured relative to the wavelength-geometry-dependent Fresnel length. Because of this complication, other single-parameter measures of the strength of the signal perturbation effects have traditionally been introduced, as defined below.

The signal scintillation index, S_4^2, is defined as the variance of the signal intensity

$$S_4^2 = \frac{\langle I^2 \rangle - \langle I \rangle^2}{\langle I \rangle^2}. \tag{13}$$

Recall that the intensity is determined as $I = |h|^2$, where h(x) is the complex signal amplitude, as given in the Fresnel-Kirchhoff equation. Obviously, for no scattering $\langle I^2 \rangle = \langle I \rangle^2$, and $S_4^2 = 0$. Under fully developed strong scattering conditions, Rayleigh fading is rapidly approached, with $S_4^2 \cong 1.0$ (Refs. 27-29). Under less than fully saturated Rayleigh fading conditions, the scintillation index can also temporarily "overshoot" (i.e., $S_4^2 > 1.0$), to a degree which depends upon the specific parameterization of the scattering medium, and which also will be detailed by the present investigation.

A second commonly used measure of the strength of signal scattering is the Rytov approximation to the log-amplitude variance, herein defined as

$$\overline{\chi^2_{Ry}} = \int_0^{\infty} \frac{dk}{\pi} \Phi(k) \sin^2(Z^* \lambda k^2/4\pi). \qquad (14)$$

For weak scattering conditions it can be shown that $S_4^2 \cong 4\ \overline{\chi^2_{Ry}}$ (see Appendix A). However, for increasingly strong scattering conditions $\overline{\chi^2_{Ry}}$ increases without limit and ceases to be a physically meaningfully approximation to the true log-amplitude variance, while S_4^2 ultimately equilibrates at $S_4^2 = 1.0$. The detailed relationships between S_4^2 and $\overline{\chi^2_{Ry}}$ will be further discussed in the following sections.

Both Equations 9 and 14 demonstrate the critical role of the signal-geometry-dependent Fresnel length, defined as

$$\ell_F = [2\lambda Z^*]^{1/2}. \qquad (15)$$

The importance of the Fresnel length in these problems can be more fully appreciated by rewriting Equation 9 as

$$h(y\ell_F) = \sqrt{2}\, e^{-i\pi/4} \int_{-\infty}^{\infty} dy'\, e^{i\phi(y'\ell_F) + 2\pi i(y-y')^2}, \qquad (16)$$

where $y = x/\ell_F$ and $y' = x'/\ell_F$. Thus, the first order received signal statistics depend only upon the total strength of the phase screen fluctuations, as measured by σ_ϕ^2, and upon their variations upon length scales measured in terms of ℓ_F.

2.5 SIGNAL INTENSITY STATISTICS MODELS.

In lieu of detailed calculations of the types to be described in the present report, several different models have been proposed for signal intensity statistics under conditions of ionospheric scattering and multipath. Most extensively studied, by far, has been the Rayleigh distribution. It has been established that under sufficiently strong scattering conditions the signal intensity probability distribution will approach the Rayleigh limit, defined as (Ref. 39)

$$P(I) = e^{-I} \tag{17}$$

where I is the (normalized) signal intensity, and P(I) its probability distribution.

The Rice distribution assumes implicitly that the signal can be decomposed into the sum of a Rayleigh component and an unscattered component. Generalization to include superimposed uncorrelated phase effects is also fairly straightforward for both Rayleigh and Rice statistics. The Rice distribution is defined (Ref. 39) by

$$P(I) = \alpha e^{-\alpha(I+1)+1} \, I_0\left(2\sqrt{\alpha(\alpha-1)I}\right)$$

with $$\alpha = [1 - (1 - S_4^2)^{1/2}]^{-1}. \tag{18}$$

When $S_4^2 \to 0$, $\alpha \to \infty$, and $P(I) \to \delta(I - 1)$; with $\delta(x)$ being the Dirac delta function. When $S_4^2 \to 1$, $\alpha \to 1$, and $P(I)$ approaches the Rayleigh limit. Notice that for $S_4^2 > 1.0$ the entire prescription of Rice (and also Rayleigh) signal statistics is meaningless. Plausible conditions leading to $S_4^2 > 1.0$ will be described in this report; in practice however, these conditions do not appear to be appreciably more stressing for communications links than either Rice or Rayleigh statistics.

The Nakagami-m distribution is defined in terms of $m = S_4^{-2}$ as

$$P(I) = \frac{m^m}{\Gamma(m)} I^{m-1} e^{-mI}. \qquad (19)$$

Again, when $S_4^2 \to 0$, $m \to \infty$; and the distribution converges to $\delta(I-1)$. When $S_4^2 = 1.0$, $m = 1.0$; and Rayleigh statistics are regained. Unlike the Rice distribution, there seems to be no underlying physical model, valid or otherwise, for Nakagami-m statistics. Although approximate plausibility arguments have been presented (Ref. 40), the model is basically empirical; and, as we shall see, its erstwhile "success" in approximately fitting ambient environment satellite data seems to have been, at least in part, a coincidence of nature and of the limitations on the candidate models and data sets employed.

A further principal difference between Rice and Nakagami-m is that the Rice $P(I)$ versus I distribution is always finite at $I = 0$ (except, of course, in the $S_4^2 \to 0$ limit); whereas, the Nakagami-m distribution always vanishes at $I = 0$ (except in the limit when $S_4^2 \to 1.0$). Thus, Rice generally gives a higher probability of very deep fades than does Nakagami-m. In the opposite extreme, Rice also generally gives a higher probability of strong signal enhancements ($I \gg 1.0$) than Nakagami-m.

Because of the high instantaneous BERs encountered during deep fades, the Rice intensity distribution provides the more stressing specification of the two.

2.6 ERROR RATE CHARACTERISTICS.

Given a determination of the signal intensity distribution P(I), whether based on one of the above models or on the detailed Fresnel-Kirchhoff solutions, it is then straightforward to determine the channel-symbol-level BER versus SNR characteristics under the assumption that the fades (and the related signal phase distortions) are negligibly slow compared to the link modulation, and also as compared to the response rates of any receiver tracking loops.

This slow-fading channel symbol BER is simply the long-term average of the instantaneous demodulator output BER (i.e., without error correcting coding) versus the link's instantaneous, fluctuating SNR characteristics as averaged over the actual distribution of instantaneous signal intensities, and including both fades and also intermittent signal enhancements,

$$\langle P_e(\gamma) \rangle = \int_0^{\infty} dI \; P(I) \; P_e(\gamma I) . \qquad (20)$$

Here $\langle P_e(\gamma) \rangle$ is the average BER, and γ is the average SNR. P(I) is the signal intensity distribution for the fading channel, and $P_e(\gamma I)$ is the unperturbed BER versus SNR characteristic (i.e., for AWGN) at an instantaneous SNR = γI.

In this report, BER versus SNR characteristics are computed as a function of the specific scattering medium and Fresnel length parameterizations and for a variety of common binary digital modems. These include: coherent phase shift key (CPSK), differentially encoded but coherently demodulated phase shift key (ΔPSK), differentially encoded and demodulated phase shift key (DPSK), and frequency shift key (FSK). Results are also calculated for quaternary and 8-ary FSK. The qualitative results are understandably somewhat similar in all cases; therefore, in the main text, the special case of DBPSK will be used to illustrate the trends. A further discussion will be found in Appendix A, and a compilation concerning other modems will also be provided in Appendixes E and I. For now, we note that, for DBPSK,

$$P_e(\gamma I) = 1/2 \exp(-\gamma I). \tag{21}$$

SECTION 3
SINGLE POWER LAW RESULTS

The forms for the single power law PSD that we have employed in our calculations are given in Section 2 by Equation 3 for $\nu > 1$ and Equation 5 for $\nu = 1$. As already suggested, for $2\pi L_o \gg \ell_F \gg \ell_i$ (where $\ell_i \equiv 0$ unless $\nu = 1$) the results for single power laws are quite insensitive to the value of the Fresnel length and essentially depend only on the PSD exponent and the strength of the scattering. The bulk of calculations were performed for a Fresnel length of $\ell_F = 693$ m, and $L_o = 10$ km. Twelve values for $\overline{\chi^2_{Ry}}$ were selected in the range

$$0.01 \leqslant \overline{\chi^2_{Ry}} \leqslant 20.0.$$

These selected $\overline{\chi^2_{Ry}}$ values essentially span the range from negligible fading up through saturated Rayleigh fading.

Here we will discuss the general behavior of the S_4^2 -versus-$\overline{\chi^2_{Ry}}$ relationship, the intensity probability distributions, and the channel symbol bit error rates that result from single power law striation PSDs. The behavior will be illustrated with selected examples; numerous additional calculated results can be found in the Appendixes. Appendix C contains the intensity probability distributions compared either to Rice and Nakagami-m (for $S_4^2 < 1$) or to Rayleigh (for $S_4 \geqslant 1$). Appendix D contains deep fade behavior for selected distributions compared to Rice and Nakagami-m. Appendix E presents BER curves for the selected modems for $0.01 \leqslant \overline{\chi^2_{Ry}} \leq 0.4$. Finally, the comparison of the calculated BERs for DBPSK to the corresponding Rice and Nakagami-m behavior is given in Appendix F.

3.1 SIGNAL CHARACTERISTICS.

3.1.1 Scintillation Index.

The scintillation index S_4^2, Equation 13, has been calculated for all the selected values of $\overline{\chi^2_{Ry}}$ and $s = n-2 = 2\nu-1$. These results are given in Table 1 and presented graphically in Figure 4. Some well-known behavior is evident. For small values of $\overline{\chi^2_{Ry}}$ the results for all PSDs satisfy the approximate linear relationship $S_4^2 \cong 4\overline{\chi^2_{Ry}}$. For $s = 1$, S_4 monotonically increases and saturates at unity. For somewhat larger values of s, there is a modest overshoot and then a relaxation down to unity. For still larger values of s ($s > 2$), there can be a significant overshoot of unity, with the relaxation back to unity occurring only at quite large values of $\overline{\chi^2_{Ry}}$. This behavior is due to the relatively coherent signal focusing that can be caused by long wavelength ionospheric disturbances, which are statistically more prominent for steeper PSD distributions.

Table 1. S_4^2 vs $\overline{\chi^2_{Ry}}$ and s.

CASE	$\overline{\chi^2_{Ry}}$	s = 1	s = 1.5	s = 2	s = 2.5	s = 3
a	0.01	0.039	0.039	0.040	0.040	0.041
b	0.025	0.095	0.097	0.099	0.103	0.109
c	0.05	0.180	0.186	0.197	0.213	0.241
d	0.1	0.327	0.343	0.378	0.438	0.548
e	0.25	0.616	0.664	0.764	0.959	1.28
f	0.4	0.768	0.825	0.962	1.21	1.63
g	0.7	0.899	0.958	1.12	1.42	1.96
h	1.5	0.975	1.03	1.20	1.55	2.15
i	3.0	0.992	1.03	1.20	1.57	2.13
j	7.0	0.997	1.02	1.17	1.53	1.99
k	10.0	0.999	1.02	1.16	1.49	1.90
l	20.0	0.998	1.01	1.13	1.41	1.71

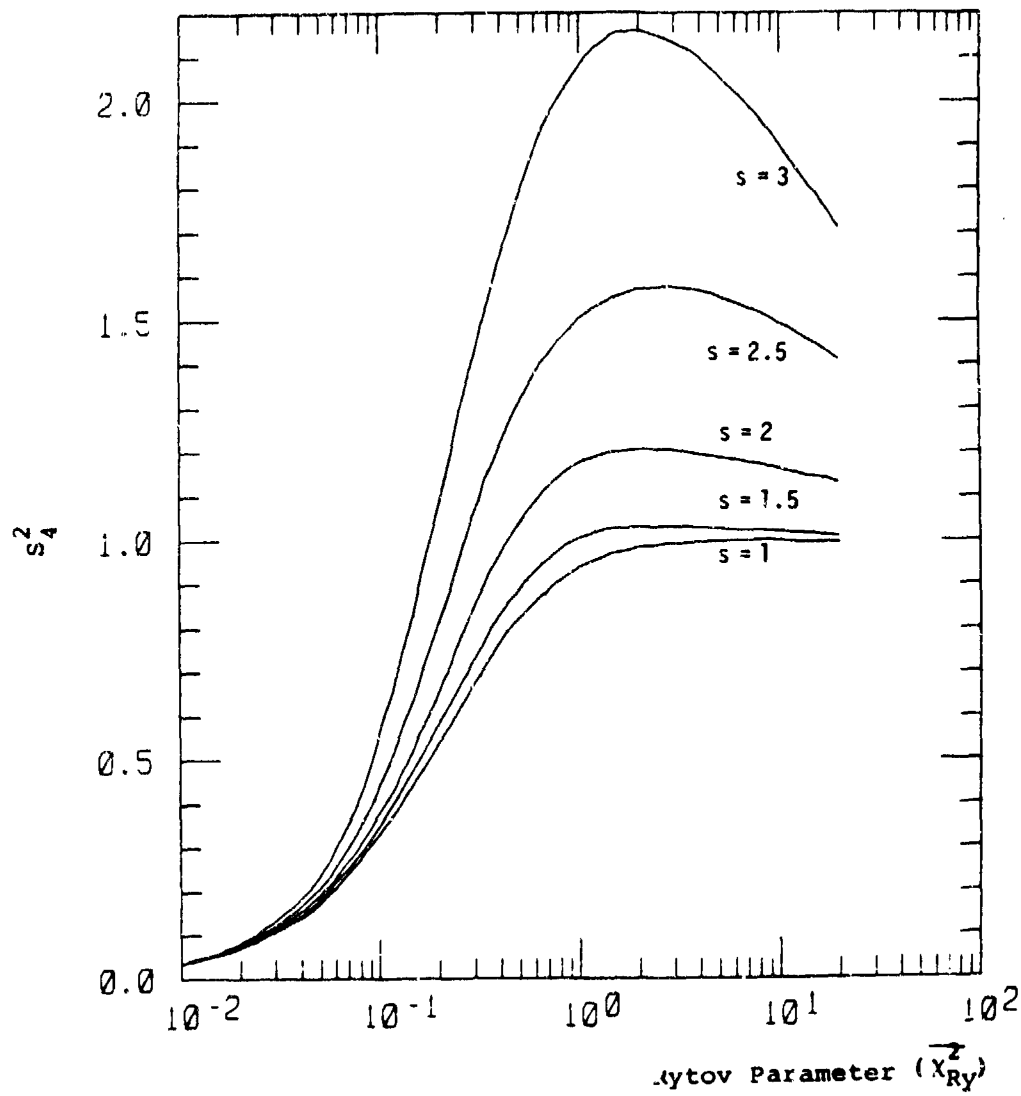

Figure 4. Scintillation index (S_4^2) versus the Rytov parameter ($\overline{\chi^2_{Ry}}$) for various single power law PSDs.

There has been some confusion in the research literature as to the behavior of S_4^2 at values greater than unity. Thus, for example, Rino and Owen (Ref. 10) state that for $s > 2$ and in the strong scatering limit S_4^2 will converge to a greater than unity value of $(6-s)/(4-s)$. However, the evidence to this effect presented by Reference 10 and others cited therein has not seemed persuasive; and our present results clearly show that the purported behavior does not occur. We have not carried the computations to sufficiently strong scattering to verify that S_4^2 always converges exactly to one, but we also can offer no reason to suppose otherwise.

The results in Table 1 and Figure 4 reveal a strong and systematic trend in the S_4^2 -versus- $\overline{X^2_{Ry}}$ relationship as a function of the single power law PSD spectral index. There is an even stronger and more basic trend which should also be noted, having to do with the effect of the spectral index on the relationship of S_4^2 to the standard deviation of the scattering medium's in-situ electron density or (equivalently) refractive index fluctuations. Unlike $\overline{X^2_{Ry}}$, which is a theoretically derived quantity, studies of the performance of military satellite links in nuclear-perturbed environments typically use the electron density standard deviation σ_{Ne} to characterize the basic environment. The electron density spatial power spectrum, which then essentially determines the PSD in the thin phase screen approximation, is separately specified as an overlay to the basic environment, with the assumed PSD details being subject to a range of parameterization uncertainties such as those addressed in this report.

For s > 1 the relationship between $\overline{X^2_{Ry}}$ and σ^2_{Ne} is formally defined by Equations 12 and 14 of Section 2. For the L_o and ℓ_F values used here, the $\overline{X^2_{Ry}}$ - to - σ^2_{ϕ} proportionality has been numerically evaluated and is given in Table B-1 of Appendix B. Using these results together with those of Table 1 or Figure 4 the corresponding S_4^2 -versus- σ_{Ne} relationship can be found. The result is depicted in Figure 5. There, σ_{Ne} is given in relative units, parametric in L_o, L_o', ℓ_F, L, and λ.

It can be seen from these calculated results that the range of σ_{Ne} values needed to drive the weak-to-strong scattering transition can be a very sensitive function of the PSD spectral index. The same, of course, is equally true of the regime of validity of strong scattering and Rayleigh signal statisties. This sensitivity to the assumed PSD spectral index can be a very important consideration of assessments of military satellite link performance in nuclear - perturbed environments.

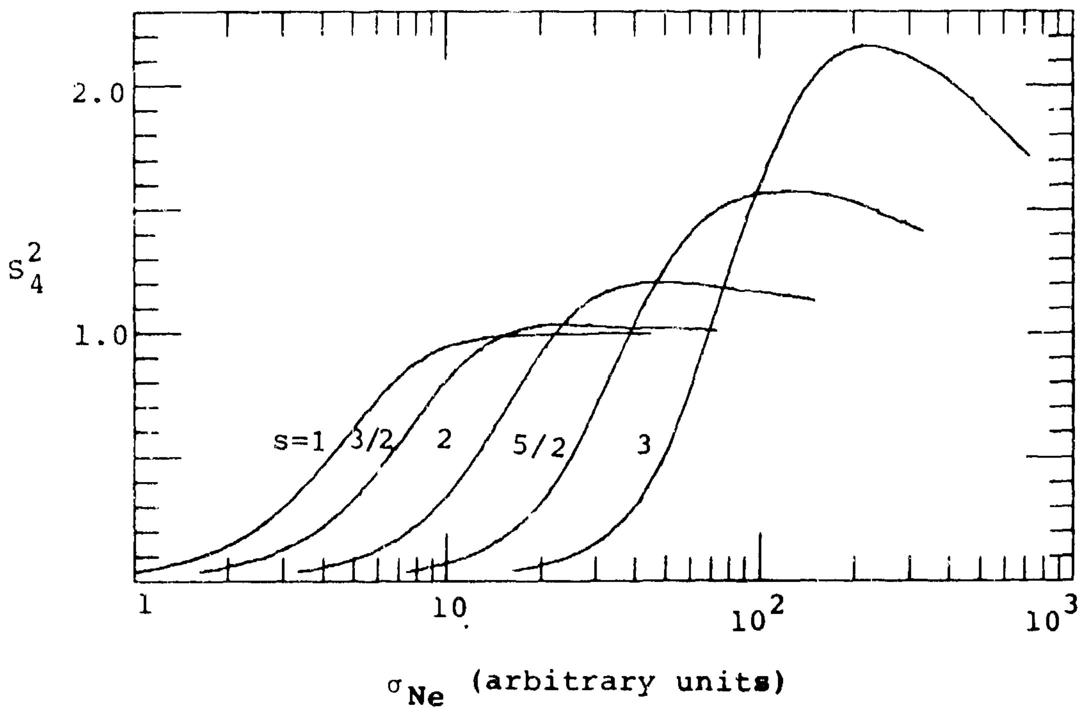

Figure 5. S_4^2 -versus- σ_{Ne} relationship (σ_{Ne} relative) for single power law PSDs with different spectral indexes.

With double power law PSD parameterizations (as discussed in Section 4) these dependences will be more complex, and the Fresnel length will also frequently be an important parameter.

Moreover, the sensitivity to either one of the two spectral indexes of a two power law PSD (i.e., with the other fixed) will typically be somewhat less than portrayed by Figure 5.

3.1.2 $S_4 < 1$ Intensity Distributions.

We will now present a representative set of calculated results for signal intensity distributions (i.e., P(I) versus I) and compare these results with the Rice and Nakagami-m models. Emphasis here will be on behavior for $S_4 < 1$. Specifically, we will look at $\overline{X^2_{Ry}} = 0.1$, which corresponds to S_4^2 in the range from 0.327 to 0.548 (see Table 1), depending on the value of the PSD exponent. This choice of $\overline{X^2_{Ry}}$ lies intermediate between the AWGN and SRF conditions, and therefore helps to bring out more clearly the various detailed differences between the models and computations. Of course, the model predictions change somewhat as S_4^2 changes, even though $\overline{X^2_{Ry}}$ is fixed. Numerous additional results at other $\overline{X^2_{Ry}}$ values (but still for $S_4 < 1$) can be found in Appendixes C and D, with Appendix D emphasizing the behavior at deep fades.

Figure 6 shows the computed and model predictions at $\overline{X^2_{Ry}} = 0.1$ for an s = 1 (also n = 3, ν = 1) PSD. Figure 6a gives the results at moderate intensity values, and Figure 6b gives the results for deep fades. Throughout this report the average (or unperturbed) signal intensity is $\langle I \rangle = 1$. It is immediately apparent that Rice statistics provide an excellent fit to the computed results in this case (s = 1). This is rather as expected, since an s = 1 PSD gives greater weight to shorter spatial wavelength ionospheric structures, which thus tends to put the receiver in the far zone from the scatterers. Under far zone conditions, Rice statistics are generally expected to be most accurate (Ref. 41).

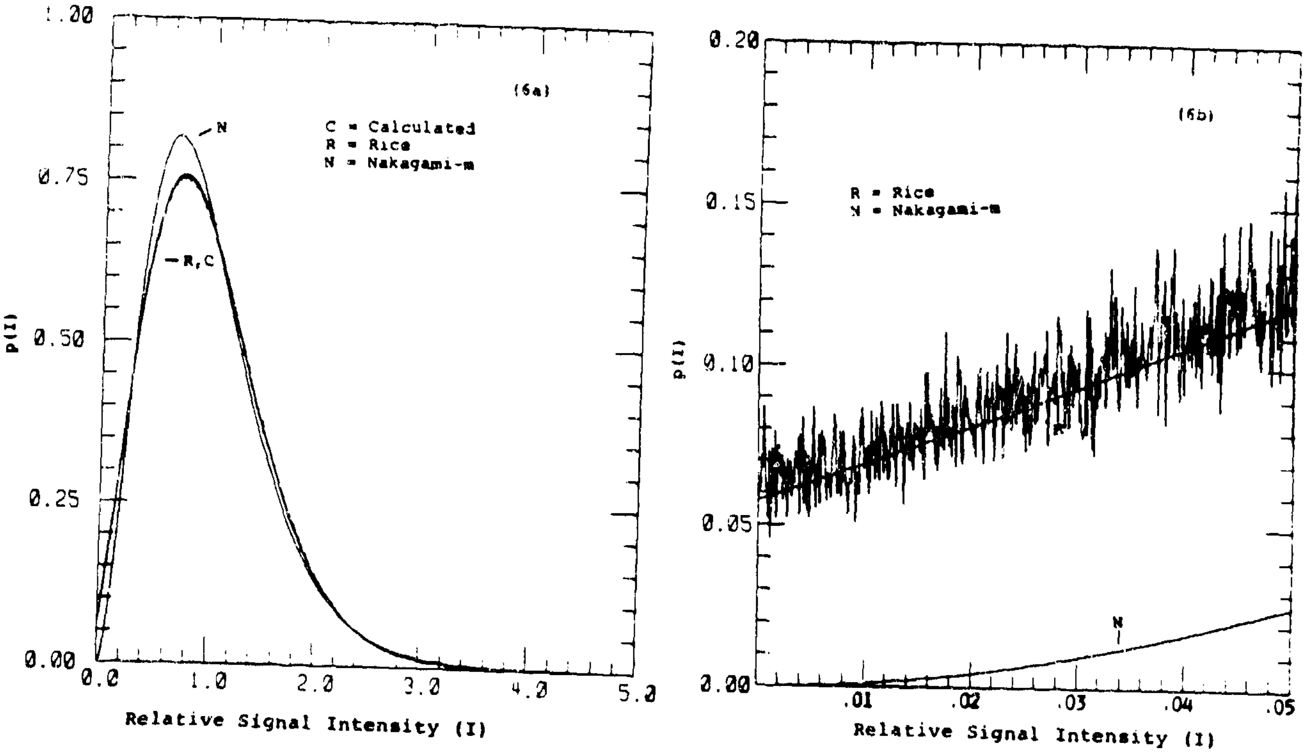

Figure 6. Comparison of computed (C) results with Rice (R) and Nakagami-m (N) models at s = 1, $\overline{\chi^2_{Ry}}$ = 0.1, S_4^2 = 0.327.

By comparison, we see that Nakagami-m provides a poor fit to the computed results under these conditions. It gives too high a probability of near-nominal (i.e., I $\cong$ 1.0) signal intensities, and too low a probability of deep fades.

Figure 7 compares the computations with the two models at $\overline{\chi^2_{Ry}}$ = 0.1 and s = 1.5 (n = 3.5, ν = 5/4). In this case, the computed results lie midway between the two models, with Rice underpredicting and Nakagami-m overpredicting the probability of near-nominal intensity levels, while Nakagami-m again underpredicts and Rice now somewhat overpredicts the probability of deep fades.

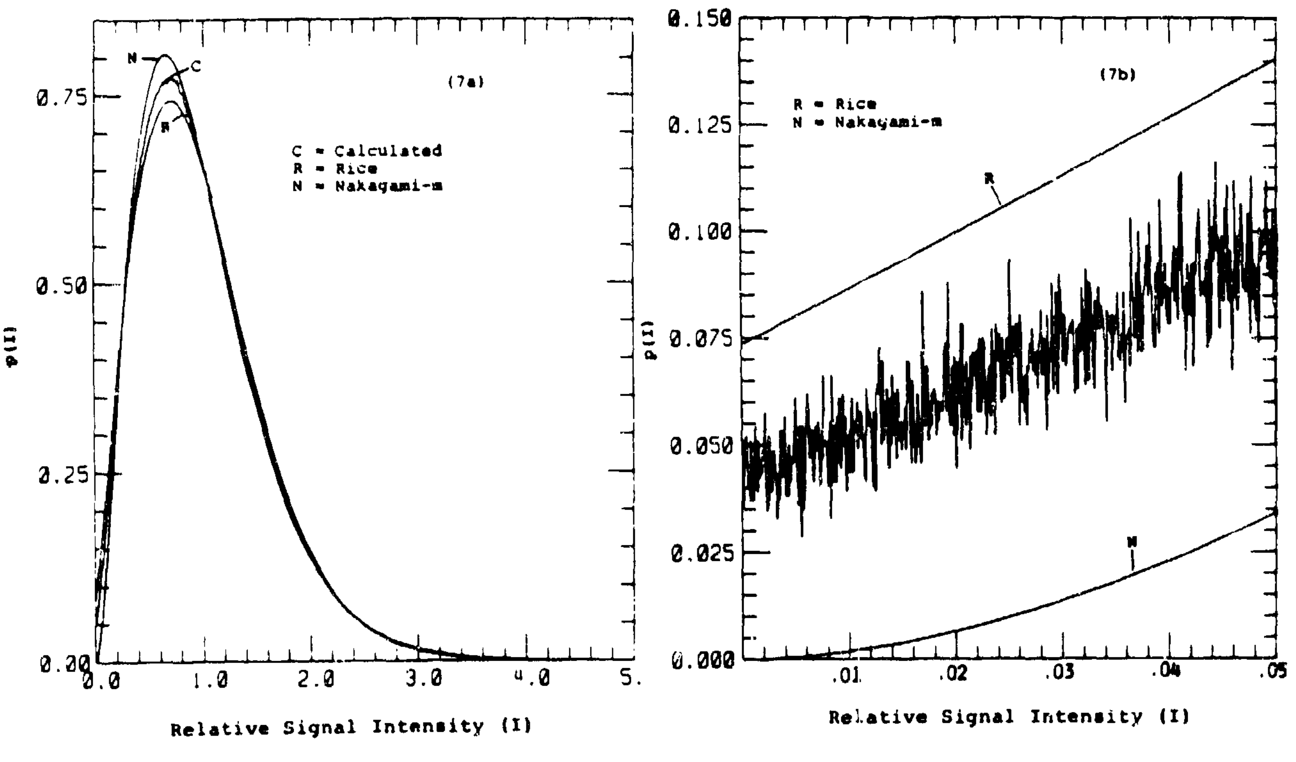

Figure 7. Comparison of computed results (C) with Rice (R) and Nakagami-m (N) models at s = 1.5, $\overline{X^2_{Ry}}$ = 0.1, S_4^2 = 0.343.

In Figure 8 we show the analogous results and comparisons at X^2_{Ry} = 0.1 for s = 2 (n = 4, ν = 3/2). This case is of particular interest because a single power law PSD with s = 2 is the simplest parameterization most commonly regarded as being a nominal overall representation of the ambient ionosphere. Of course, it must be recognized that no single PSD parameterization will be correct in general, that a single power law form may often be too simplistic, and also that conditions in nuclear-disturbed ionospheres may differ appreciably from the ambient.

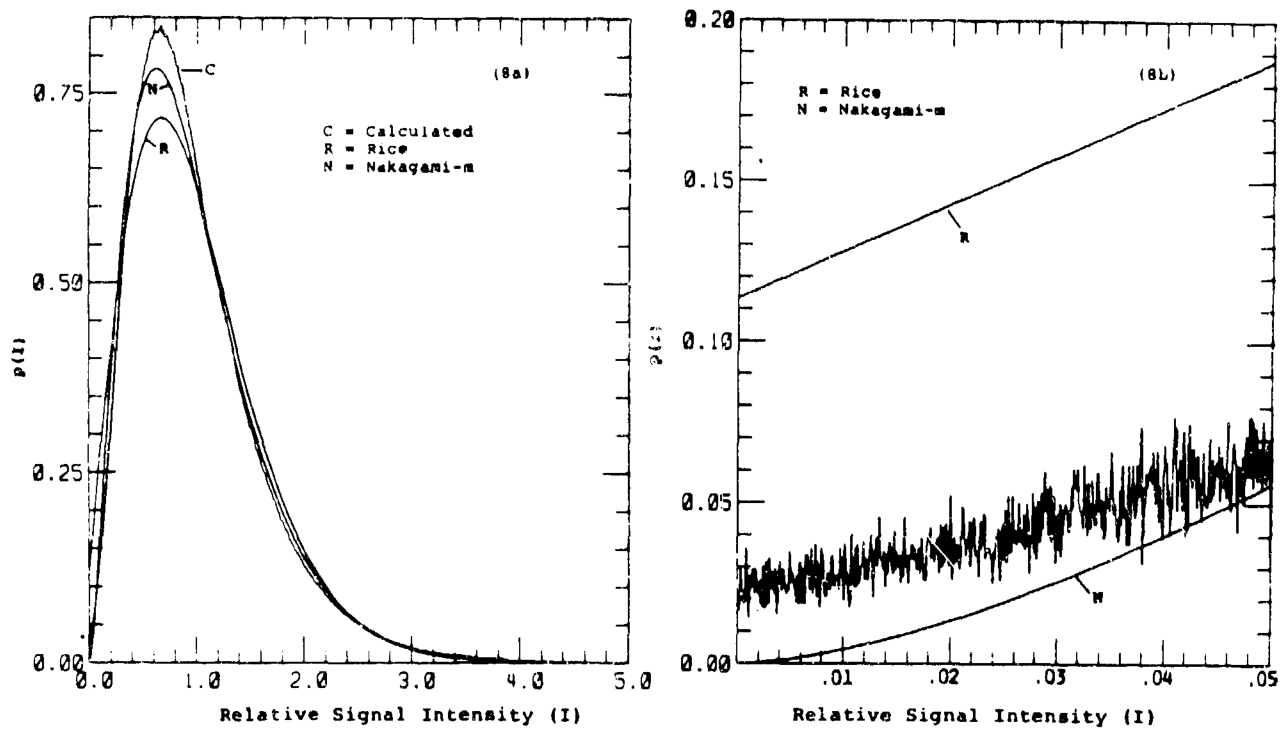

Figure 8. Comparison of computed (C) results with Rice (R) and Nakagami-m (N) models at s = 2, $\overline{\chi^2_{Ry}}$ = 0.1, S_4^2 = 0.378.

In Figure 8 it is seen that at s = 2 both Rice and Nakagami-m underpredict the probability of near-nominal signal intensity levels; but Rice continues to overpredict, and Nakagami-m to underpredict, the probability of deep fades. Comparison of Figures 7 and 8 suggests that Nakagami-m will provide a good fit to the computations at near-nominal intensity levels for a single power law PSD with an exponent $s \cong 1.75$ ($n \cong 3.75$, $\nu \cong 11/8$). However, the deeper fades (although relatively infrequent) are very important for satellite communications links; and even at s = 2 Nakagami-m continues to underpredict the probability of fades deeper than 12 dB or so (i.e., at $\overline{\chi^2_{Ry}} = 0.1$).

Lastly, Figure 9 shows the corresponding computed results versus model predictions at $\overline{\chi^2_{Ry}} = 0.1$ for s = 2.5. Here it is clear that both models tend to significantly underpredict the probability of near-nominal signal levels. They also overpredict the probability of above-nominal signal enhancements; a trend towards this effect can also be perceived in the previous figures. Both models now overpredict the occurrence of moderately deep fades, Rice much more so than Nakagami-m; but the Nakagami-m model continues to underpredict the likelihood of fades deeper than about 20 dB.

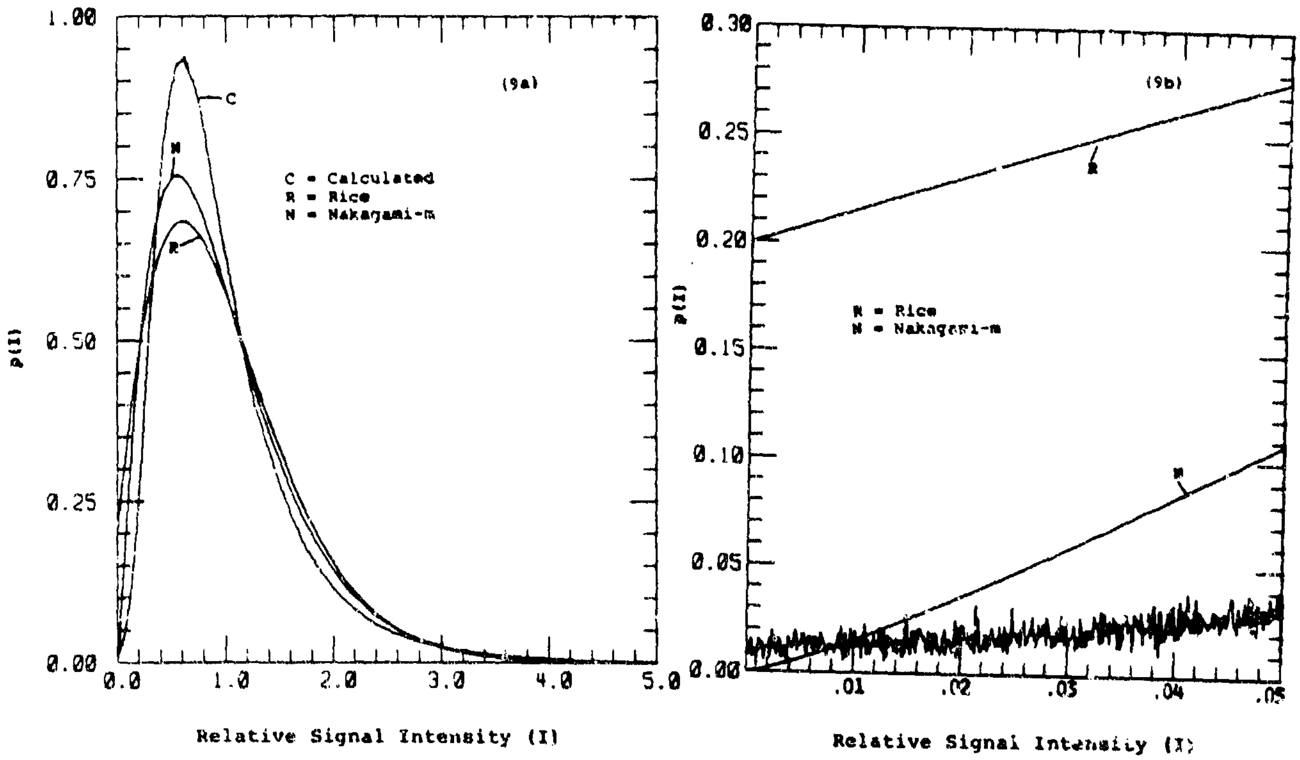

Figure 9. Comparison of computed (C) results with Rice (R) and Nakagami-m (N) models at $s = 2.5$, $\overline{\chi^2_{Ry}} = 0.1$, $S_4^2 = 0.438$.

At other values of $\overline{\chi^2_{Ry}}$, analogous systematic trends are observed in the computed signal intensity statistics versus the exponent of a single power law PSD, and also in the comparisons with the Rice or Nakagami-m models. The details of these trends and comparisons will differ as a function of $\overline{X^2_{Ry}}$ (see Appendixes D and E). The general inferences, however, remain as indicated. Rice is somewhat understandably a fair-to-excellent fit at $s \lesssim 3/2$ and generally bounds the severity of the intensity fluctuations under other conditions. Nakagami-m happens to be a useful fit near $s \cong 2$, but not for deep fades. Lastly, the strong and systematic trends in the computed results reveal the existence of signal effects that cannot be reproduced in general by any simple model which does not account for the details of the PSD parameterization (and also, as demonstrated shortly, the Fresnel length).

3.2 BER CHARACTERISTICS.

Analogous trends are seen in the computed channel symbol BER-versus-SNR characteristics. Selected examples will be presented and discussed here, using DBPSK as a point of reference. Numerous additional results, including other modulations, can be found in Appendixes E and F. Similar behavior is found for all modulations considered.

3.2.1 Variation with Spectral Index.

Figure 10 shows the computed DBPSK BER characteristics over a range of $\overline{X^2_{Ry}}$ values and for two extreme values of the PSD spectral index s. The $\overline{X^2_{Ry}}$ values are listed. Figure 10a is for $s = 1$ ($n = 3$, $\nu = 1$), and Figure 10b is for $s = 3$ ($n = 5$, $\nu = 2$). The overall trend is apparent. At any fixed values of SNR and $\overline{X^2_{Ry}}$, the BERs decrease with increasing spectral index. Similar behavior is found throughout the interval $1 \leq s \leq 3$ (see Appendix E).

Except perhaps at very low levels of scattering, these effects are manifested even more strongly when the BER characteristics

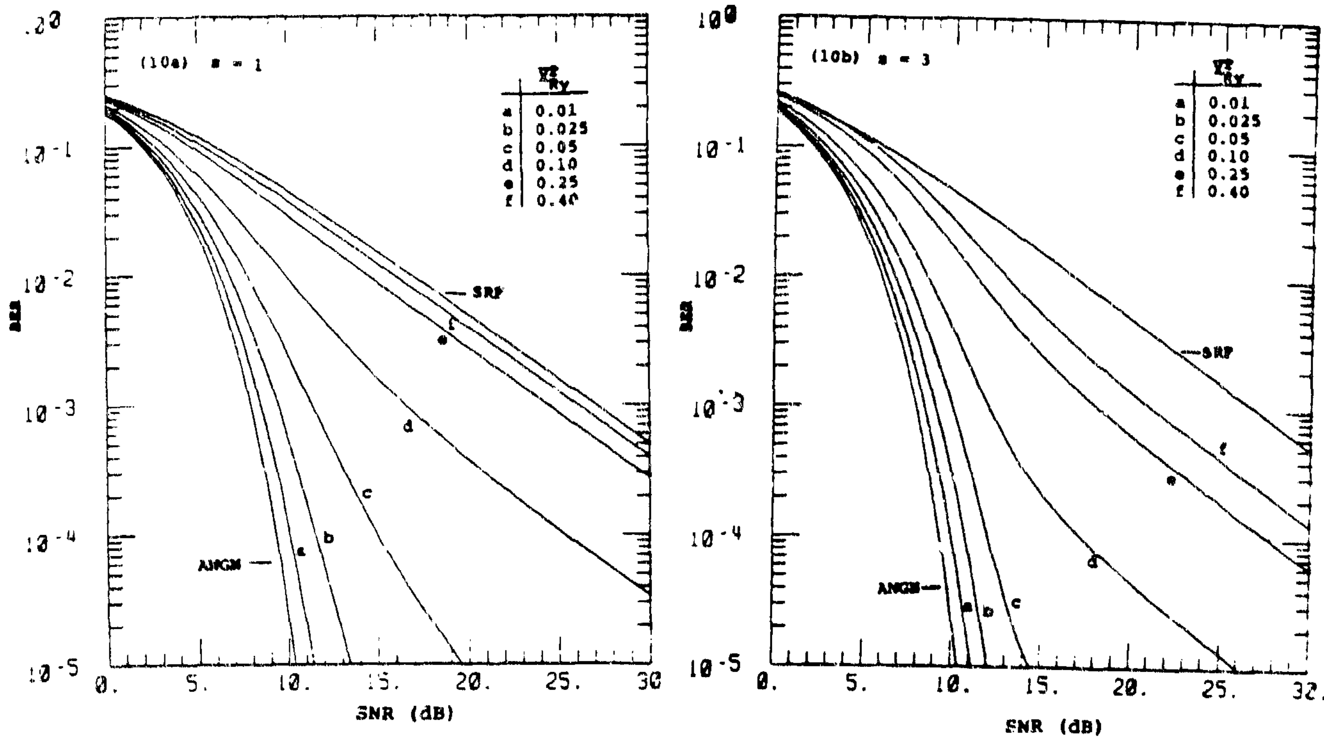

Figure 10. Computed DBPSK channel symbol BERs versus SNR and $\overline{X^2_{Ry}}$ for single power law PSDs with: (a) s = 1 and (b) s = 3.

are parameterized in terms of S_4^2 rather than $\overline{X^2_{Ry}}$. This is demonstrated in Figure 11. On the left, Figure 11a (taken from Fig. 3 of Section 1) has fixed S_4^2 = 0.378 throughout; the corresponding $\overline{X^2_{Ry}}$ values decrease with increasing spectral index with $\overline{X^2_{Ry}}$ = 0.1 at s = 2. On the right, Figure 11b has fixed $\overline{X^2_{Ry}}$ = 0.1 throughout. The corresponding S_4^2 values now increase with increasing spectral index; but despite the increasing value of S_4^2 the BERs at fixed $\overline{X^2_{Ry}}$ and SNR actually decrease with increasing s. Neither Nakagami-m nor Rice would allow such an effect (i.e., a decrease in BER as S_4^2 is increased). It is apparent that the reliability in detail of simple models such as Rice or Nakagami-m, which are specifically parameterized only in terms of S_4^2, can be very dependent upon the actual form of the underlying PSD.

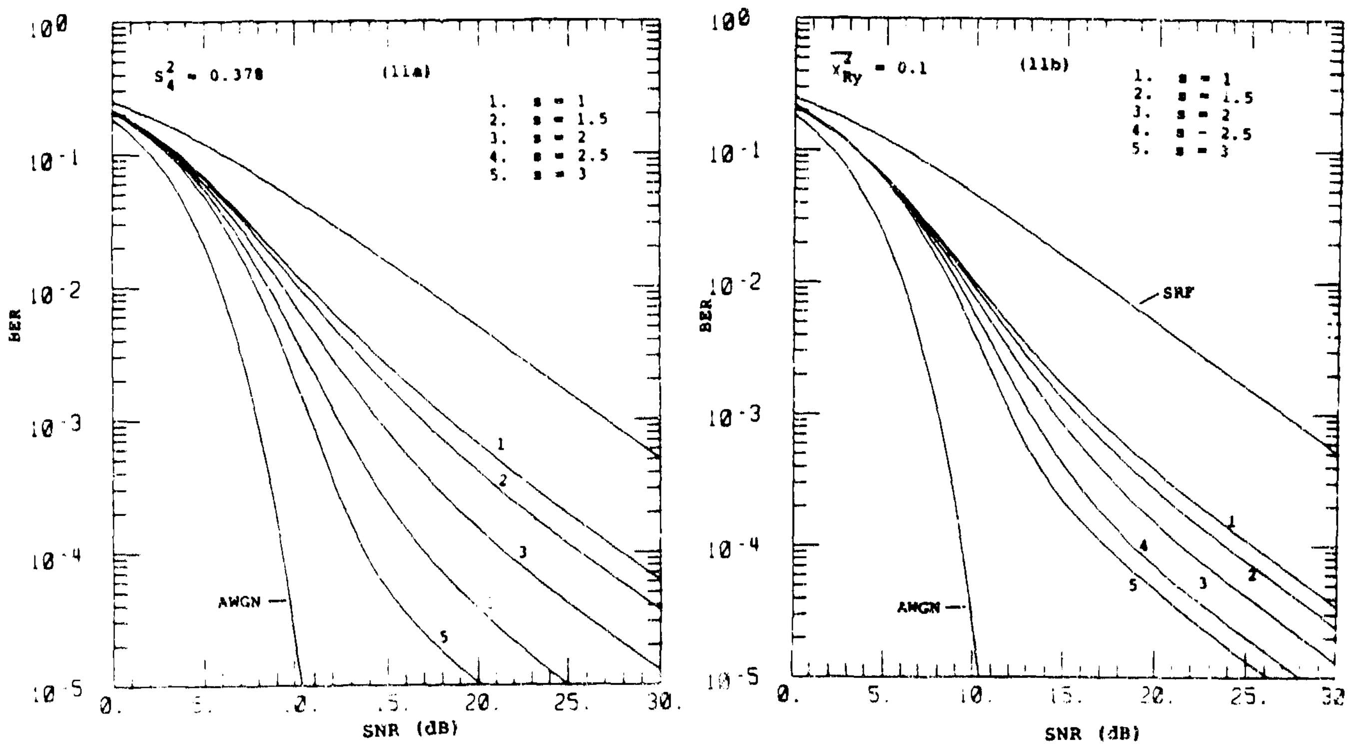

Figure 11. Computed DBPSK channel symbol BERs versus spectral index, either at fixed S_4^2 = 0.378 (Fig. 11a) or at fixed $\overline{X^2_{Ry}}$ = 0.1 (Fig. 11b).

3.2.2 Comparison to Rice and Nakagami-m.

Additional and more specific comparisons of the computed BER results with Rice and Nakagami-m statistics are presented and discussed here. Only four examples will be given; many more can be found in Appendix F. We will stress intermediate levels of scattering intensity, specifically $\overline{\chi^2_{Ry}} = 0.1$, in order to most clearly depict the differences which can occur between the calculated results and the model predictions. At much smaller values of $\overline{\chi^2_{Ry}}$ or S_4^2 all results, whether from the computations or from the models, merge together towards the AWGN limit; for larger $\overline{\chi^2_{Ry}}$ or $S_4^2 \to 1.0$, all results merge towards the SRF limit.

At $s \lesssim 1.5$ Rice statistics again provide a fairly good fit to the computed results (Figure 12a). At $s = 2$, Nakagami-m fits the computed results fairly well at SNR $\lesssim$ 15 dB (Figure 12b) but underpredicts the BERs at higher SNR levels. This is due to the tendency of Nakagami-m to consistently underestimate the frequency of deep fades. At $s = 2.5$, this particular deficiency in Nakagami-m statistics is compensated somewhat by an overprediction of the more shallow fades (see earlier Figure 9). Thus, as shown in Figure 12c, Nakagami-m now overpredicts the computed BERs up to SNR $\cong$ 21 dB, but still underpredicts the error rates at higher SNR levels. The trend continues, as shown in Figure 12d; here, at $s = 3$, the overprediction by Nakagami-m of the shallower fades causes a corresponding overprediction of the computed BERs up to SNR $\cong$ 30 dB. At higher SNR levels, Nakagami-m would again underpredict the computed BER levels.

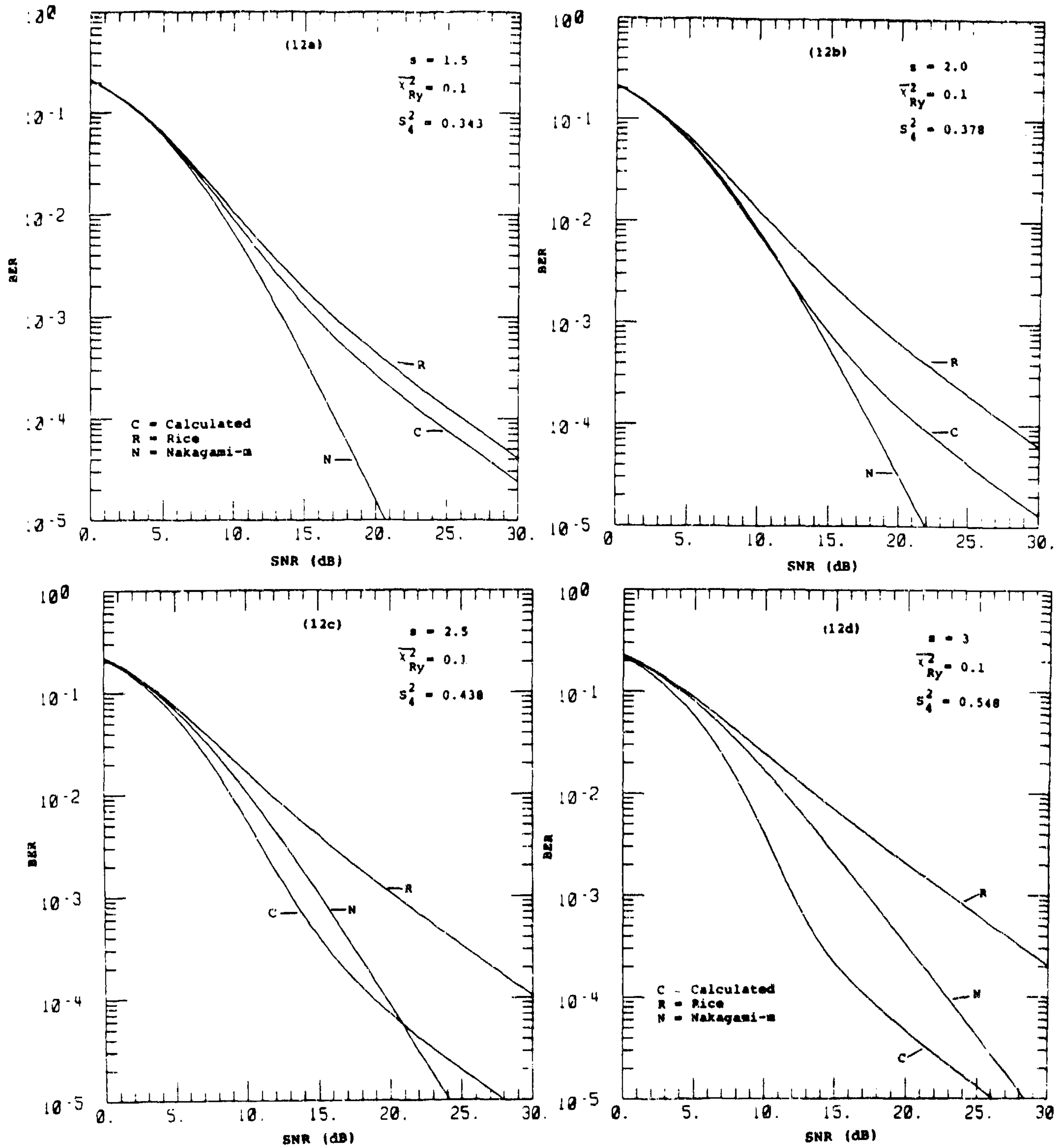

Figure 12. Comparison of computed BER characteristics for DBPSK with Rice and Nakagami-m at $\overline{X^2_{Ry}}$ = 0.1 for: (a) s = 1.5 (b) s = 2, (c) s = 2.5, (d) s = 3 -- S_4^2 values as indicated

It is clear that Rice is an excellent fit at $s = 1$, and remains a good approximation at $s \lesssim 1.5$. For higher values of the spectral index Rice provides an upper bound to the computed BERs. For reasons discussed above, Nakagami-m never reproduces the computed BER-versus-SNR characteristic in detail, but happens nonetheless to provide a good fit at $s = 2$ and SNR $\lesssim$ 15 dB, or an approximate fit at $s = 2.5$ and SNR $\lesssim$ 21 dB.

3.3 THE CASE $S_4^2 > 1.0$.

There is one special case which merits at least brief discussion in the context of single power law PSD parameterizations. This is the case $S_4^2 \geq 1.0$, which is not allowed by either Rice or Rayleigh statistics, nor (it would seem) purposefully accommodated in the design of the Nakagami-m model.

With signals of fluctuating intensity, $S_4^2 > 1.0$ merely implies that the standard deviation of the signal intensity is greater than its mean value. Such a thing is clearly possible, and our specific computations also show that conditions of $S_4^2 > 1.0$ can easily occur with PSD parameterizations encompassing those of current interest. There might be justifiable concern that $S_4^2 > 1.0$ could lead to BER levels which might greatly exceed the normally accepted "SRF limit" for slow fading effects. As a practical matter, however, our computations suggest that the resulting slow fading BER characteristics--over the range of PSD parameterizations investigated--always lie either below or within a few dB or less above the SRF limit.

To depict the general behavior encountered, we will first present two examples in Figure 13, below; many more can be found in Appendix C. As already shown in Table 1 and Figure 4, a significant tendency towards conditions with $S_4^2 > 1.0$ clearly exists at

$s \gtrsim 2$, but it is most pronounced at the higher values of spectral index. Therefore, we will concentrate here on the case $s = 3$.

Figure 13 depicts most of the features of the anomalous $S_4^2 > 1.0$ case as encountered in our computed results. The probability of very large signal intensity enhancements tends to significantly exceed that predicted by Rayleigh statistics. Yet, for more moderate levels of signal enhancement, the computed intensity distributions lie systematically below the SRF limit. Then, at slightly sub-nominal signal intensity levels (i.e., very weak fades), the computed intensity distributions again exceed the $S_4^2 \cong 1.0$ predictions of Rayleigh and other models.

The phenomena described above are observed consistently in all our computed results for $S_4^2 > 1.0$. At lower levels of signal intensity, however, a transition is observed. As shown in Figure 13a, at moderate levels of $\overline{X^2_{Ry}}$ the computed probability of deep fades is less than that predicted by Rayleigh statistics. At higher levels of $\overline{X^2_{Ry}}$, the computed results gradually merge toward the Rayleigh case. Throughout this interval, however, the computed channel symbol BERs continue to lie within a few dB or less of (but sometimes above) the "SRF limit."

Typical BER behavior at $S_4^2 > 1.0$ is illustrated in Figure 14, which contains the same two cases from Figure 13, plus a third example with $\overline{X^2_{Ry}} = 0.25$ and $S_4^2 = 1.28$. For $\overline{X^2_{Ry}} = 0.25$ to 0.40, and $S_4^2 = 1.28$ to 1.65, the BER characteristic still lies appreciably below the SRF limit, just as it does for other PSDs with $s > 1.5$ spectral indexes at these moderate or lower levels of $\overline{X^2_{Ry}}$. For $\overline{X^2_{Ry}} = 7.0$, the value of S_4^2 is 1.99: this is essentially twice the value ($S_4^2 = 1.0$) associated with Rayleigh statistics, and it is also nearly the largest value observed in

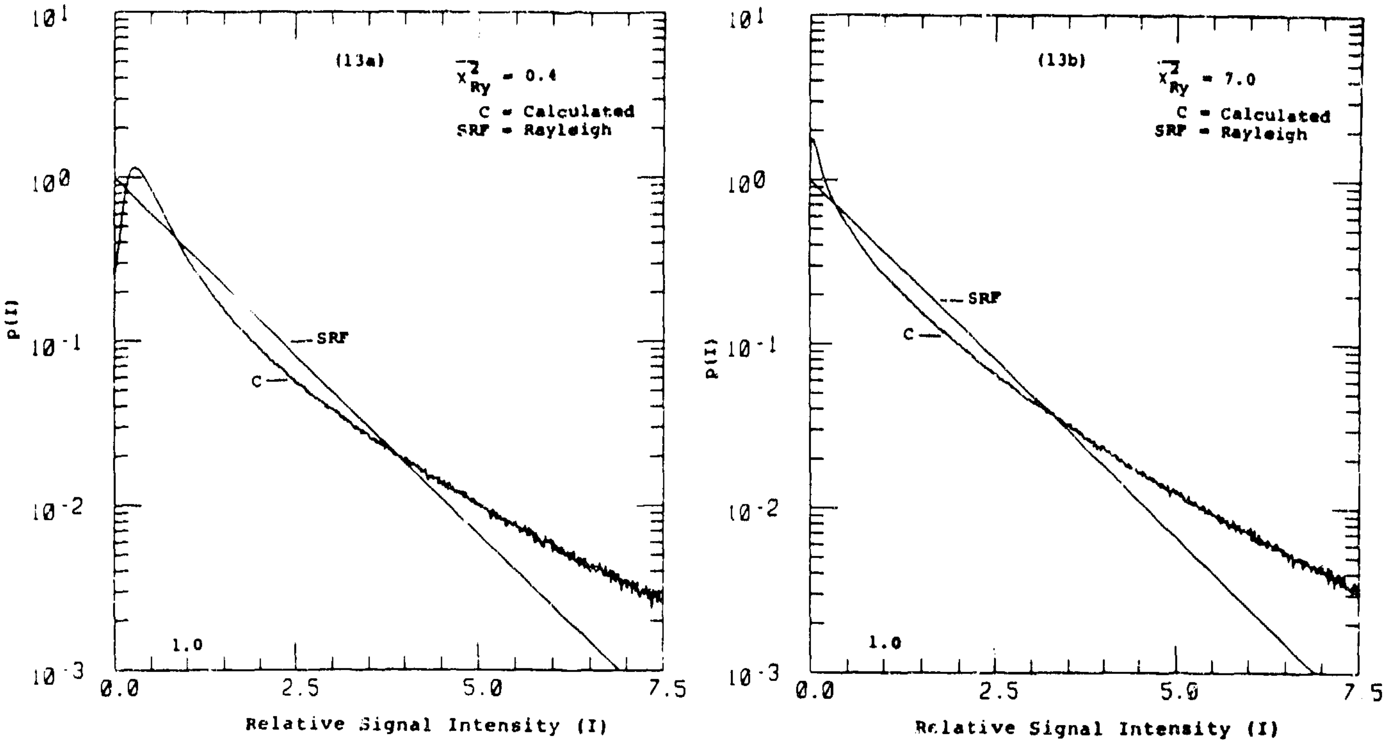

Figure 13. Comparison of computed signal intensity distributions for $S_4^2 > 1.0$ at $s = 3$ with Rayleigh statistics: (a) $\overline{X^2_{Ry}} = 0.4$, (b) $\overline{X^2_{Ry}} = 7.0$.

all of our computed results (see Table 1 or Figure 4). Nonetheless, the computed BER characteristic never exceeds the SRF limit by more than about 2 dB; and it will then move closer to SRF as $\overline{X^2_{Ry}}$ increases. Thus, despite the unusual and highly non-Rayleigh behavior of the computed intensity distributions at $S_4^2 >$ 1.0, the corresponding BER characteristics never substantially exceed those which would be predicted by Rayleigh statistics.

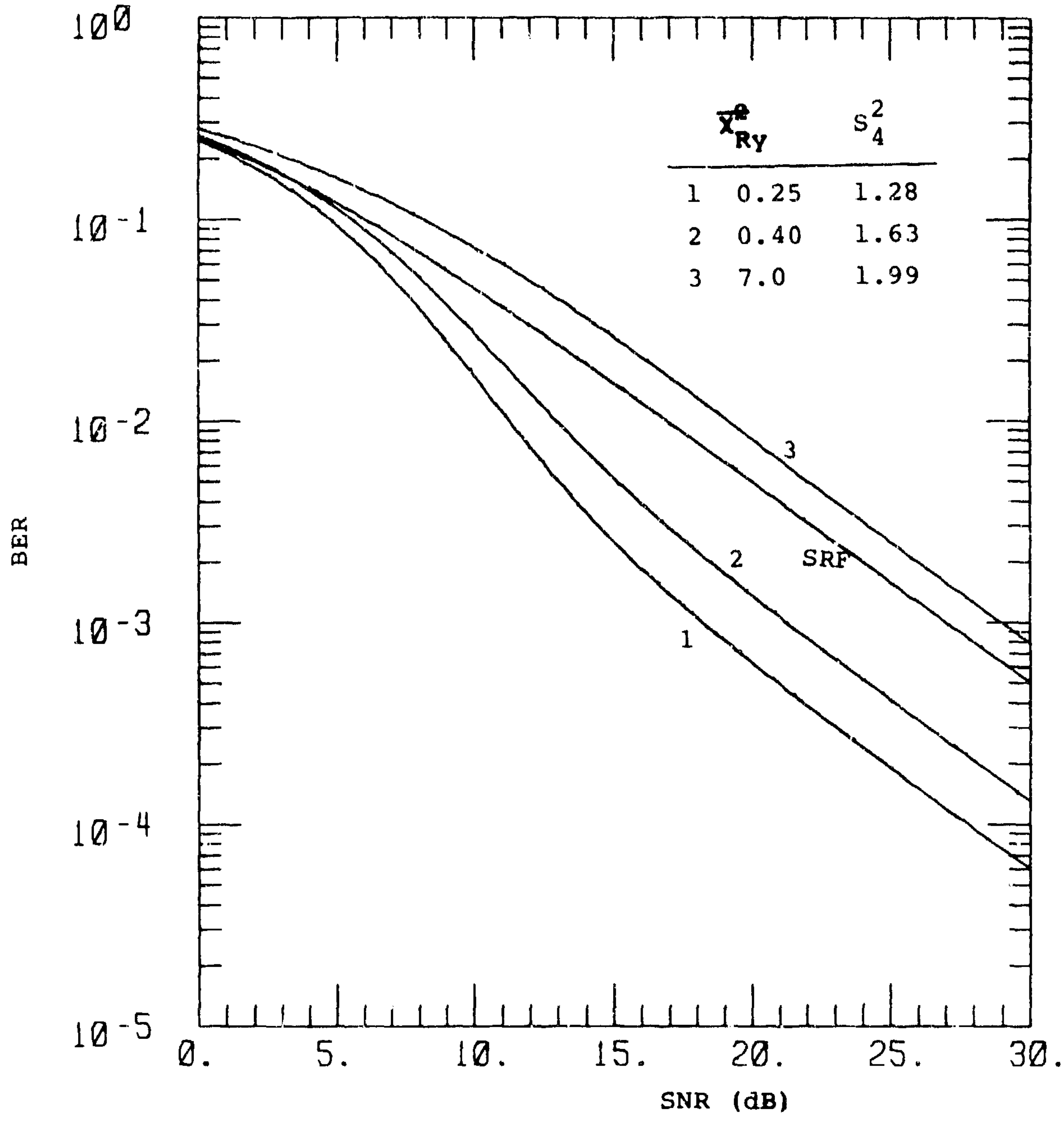

Figure 14: BER characteristics (for DBPSK) for single power law PSD with s = 3 in typical cases when $S_4^2 > 1.0$, compared with Rayleigh signal statistics.

SECTION 4
TWO POWER LAW RESULTS

Our computed results for first-order signal intensity statistics with a typical and realistically parameterized "two power law" PSD were found to be entirely analogous to, and qualitatively explainable by, the results from single power law PSDs of varying spectral index, as already presented in Section 3. Therefore, a smaller number of specific examples for two power law PSDs will be presented and discussed here. Additional examples can be found in the Appendixes.

The representative form of the two power law PSD that we employ is given in Equation 6 of Section 2, with the constants determined by Equation A-6 of Appendix A. The selected values for ν_1, ν_2 and k_B are:

$$\nu_1 = 5/4, \qquad (s_1 = 1.5),$$

$$\nu_2 = 2, \qquad (s_2 = 3),$$

$$k_B = 2\pi/700 \ m^{-1}.$$

These are representative of typical values determined from fitting a more complex, two power law, PSD to ambient environment data (Ref. 37). This PSD form is shown in Figure 15. The Fresnel lengths (Equation 13) which we will consider in greatest detail are (in meters)

$$\ell_F(\alpha) = 1386,\ 693,\ 346,\ 173, \quad \alpha = 1\text{-}4,$$

and their locations in k-space, k_α, are also shown in Figure 15 where $k_\alpha = 2\pi/\ell_F(\alpha)$.

We might anticipate on the basis of Figure 15 and earlier discussions that the k_1 results would be mainly characteristic of the s_1 slope and the k_4 results would be more nearly characteristic of the s_2 slope. The k_2 and k_3 results should be intermediate, although there will be a tendency toward the s_1 slope; this is expected since the results really depend on a region of k-space that includes small values of k up through and somewhat beyond the vicinity of k_α. Consequently, even the k_3 and k_4 results will still be influenced by the s_1 slope region. In Section 1, we very loosely summarized this complex behavior by indicating that the results are roughly equivalent to those of a single power law with an effective slope determined by the behavior at wave-vectors "generally less than and in the vicinity of" k_α.

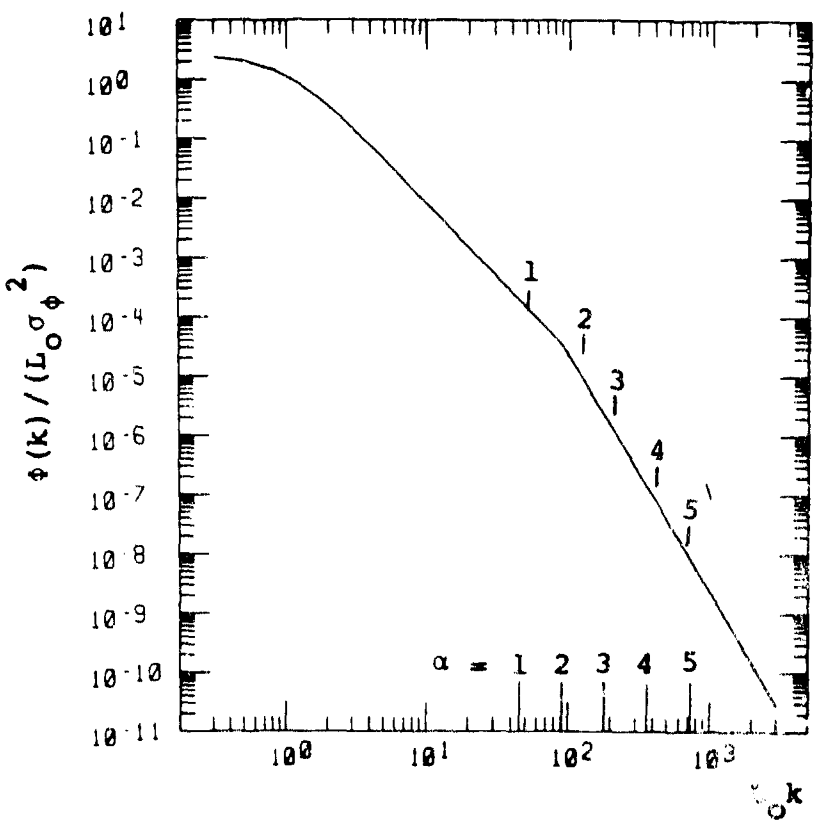

Figure 15. Two power law power spectral density; also indicated are the locations of k_α (α = 1-5).

In addition to the detailed results discussed below for α = 1-4, we will also present a few results for α = 5 with

$$\ell_F(5) = 87 \text{ m},$$

that is, a value of k_α twice as large as k_4, and thus further removed for the spectral break. As anticipated, this Fresnel length leads to behavior even more characteristic of s_2, but the influence of s_1 is still evident.

In this section, we will discuss the trends as the Fresnel length is changed. These trends will also be illustrated by a few examples. Additional results can be found in the Appendixes. Appendix G presents the calculated intensity probability distributions. The small intensity behavior is given in Appendix H. Since the main conclusions regarding small intensity behavior are essentially the same as for the corresponding single power law PSDs, we will not discuss them further in this section. The channel symbol BER curves are found in Appendix I, and the comparison with Rice and Nakagami-m for DBPSK is in Appendix J.

4.1 SIGNAL CHARACTERISTICS.

As with the single power law PSD, one of the parameters that characterize the probability distributions is the scintillation index S_4^2, Equation 13. Table 2 presents a complete list of the calculated values of S_4^2 for the selected values of $\overline{\chi^2_{Ry}}$ and k_α, including α = 5. This same information is presented graphically in Figure 16. For small values of $\overline{\chi^2_{Ry}}$(< 0.1), all S_4^2 versus $\overline{\chi^2_{Ry}}$ results continue to approximately satisfy the linear relationship, $S_4^2 \cong 4\overline{\chi^2_{Ry}}$. As $\overline{\chi^2_{Ry}}$ increases, and for the Fresnel lengths larger than or on the order of the freezing length (α = 1,2), S_4^2 overshoots and then returns towards unity. For the shorter Fresnel lengths, considerable transitory overshcot of

S_4^2 is possible. As we saw in the previous section, such overshoot of unity for S_4^2 is characteristic of steep ($s > 2$) PSDs. However, as also anticipated, the overshoot is somewhat moderated here by the influence of the $s = 1.5$ PSD behavior at small values of k.

The signal intensity distributions also show the trend from approximately $s = 1.5$ behavior toward approximately $s = 3$ behavior as k_α increases. For $S_4 < 1$, the distributions tend to be fairly close to Nakagami-m at moderate intensity levels and for the longer Fresnel lengths considered ($\alpha = 1, 2$). However, Nakagami-m continues to underestimate the probability of fades deeper than 10-to-20 dB (see deep fade results in Appendix H); and Rice continues to overestimate these fades.

Table 2. S_4^2 vs $\overline{X_{Ry}^2}$ and k_α.

CASE	$\overline{X_{Ry}^2}$	S_4^2 $\alpha = 1$	$\alpha = 2$	$\alpha = 3$	$\alpha = 4$	$\alpha = 5$
a	0.01	0.040	0.039	0.040	0.041	0.041
b	0.025	0.097	0.097	0.103	0.107	0.109
c	0.05	0.188	0.188	0.208	0.227	0.238
d	0.1	0.347	0.350	0.409	0.479	0.519
e	0.25	0.672	0.684	0.827	1.02	1.17
f	0.4	0.837	0.854	1.02	1.25	1.43
g	0.7	0.965	0.998	1.17	1.41	1.65
h	1.5	1.03	1.09	1.23	1.45	1.70
i	3.0	1.05	1.11	1.23	1.41	1.63
j	7.0	1.05	1.10	1.20	1.32	1.51
k	10.0	1.04	1.10	1.18	1.28	1.46
l	20.0	1.03	1.08	1.14	1.23	1.37

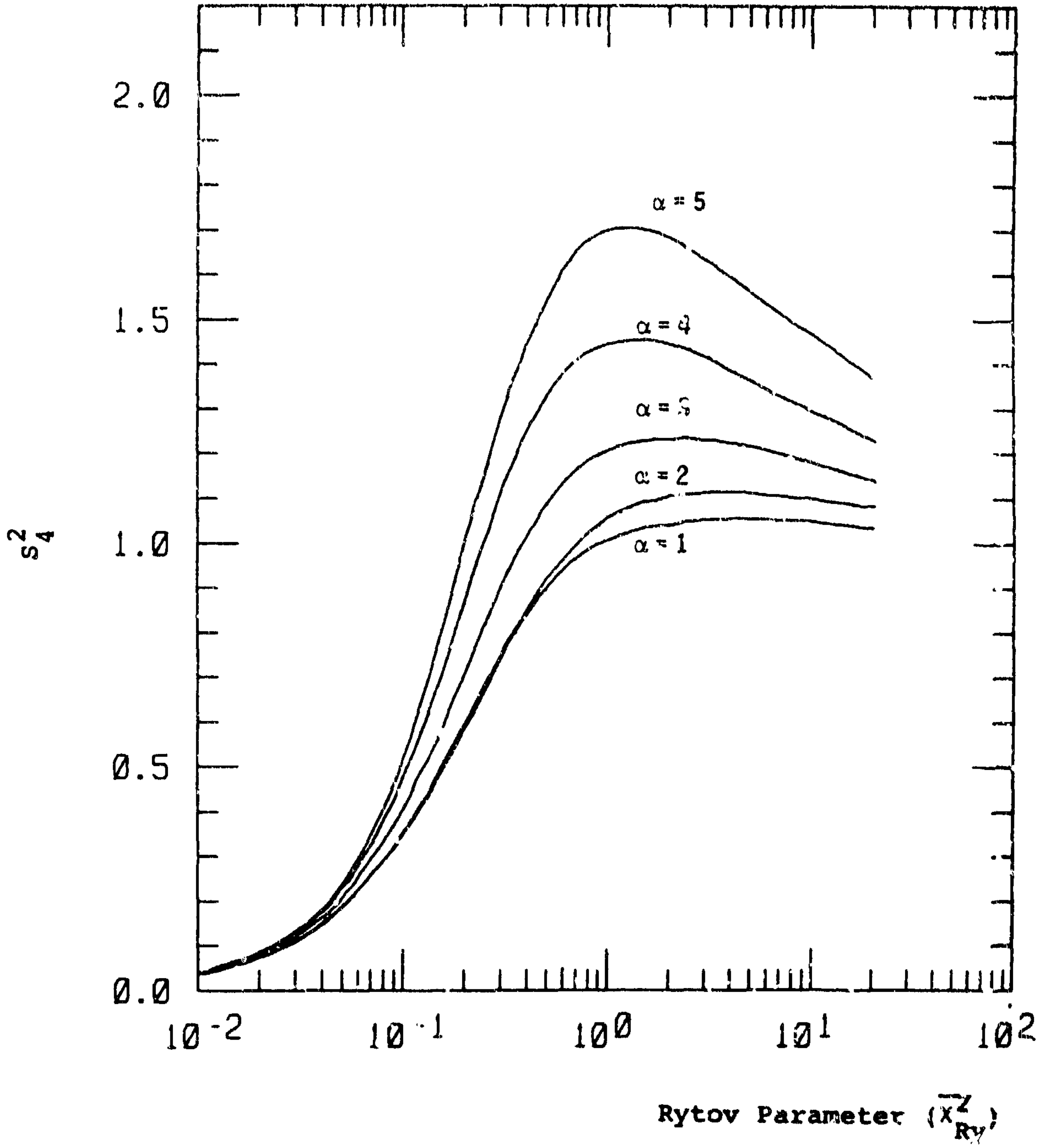

Figure 16. Scintillation index (S_4^2) versus the Rytov parameter ($\overline{\chi^2_{Ry}}$) for various Fresnel lengths.

As the Fresnel length becomes shorter than the freezing length (α = 3,4), even the limited agreement with Nakagomi-m at near-nominal signal levels disappears. As examples, Figure 17 shows the calculated distributions for $\overline{\chi^2_{Ry}}$ = 0.05, α = 1 and 4.

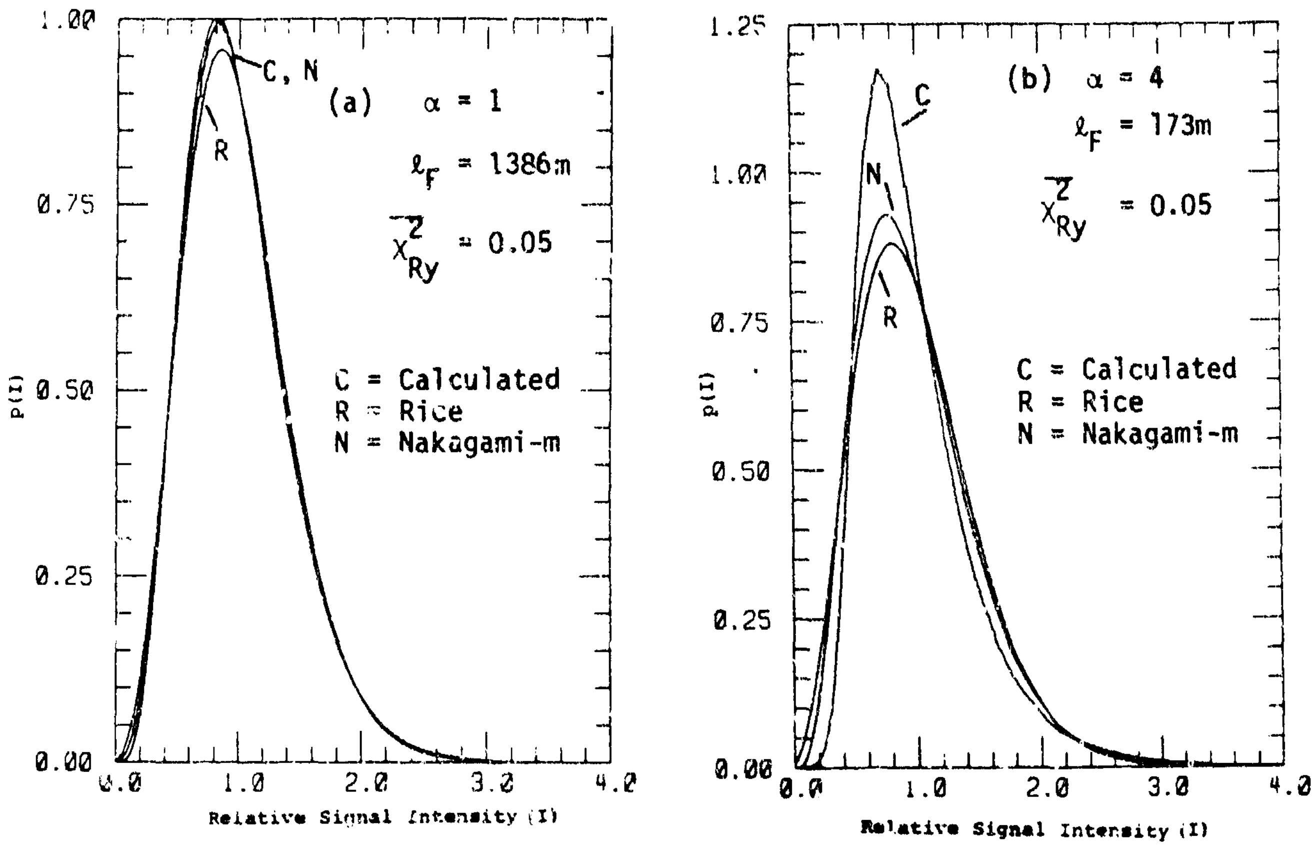

Figure 17. Calculated signal intensity distribution for two power law striation PSD of Figure 15, at $\overline{\chi^2_{Ry}}$ = 0.05 for ℓ_F = 1386 m and ℓ_F = 173 m, as compared to Rice and Nakagami-m.

The intensity distributions for $S_4 > 1$ also show the anticipated trends based upon the single power law PSD results. As the Fresnel length is decreased the expected progression from Rayleigh to distributions that are larger than Rayleigh for both small and large values of the intensity is observed. Detailed results are given in Appendix G.

4.2 CHANNEL SYMBOL BIT ERROR RATES.

As with the single power law results, $0.01 \leq \overline{\chi^2_{Ry}} \leq 0.4$ essentially spans the gap between the AWGN and SRF limits for the BER curves. Likewise, the results for $\overline{\chi^2_{Ry}} = 0.1$ are of particular interest and are shown in Figure 18 (including $\alpha = 5$) for DBPSK. This figure again illustrates that $\overline{\chi^2_{Ry}} = 0.1$ is a reasonable compromise between the AWGN and SRF limits. As would be anticipated from the single power law results, the BER improves as the Fresnel length decreases for this fixed value of $\overline{\chi^2_{Ry}}$. Figure 18 can be compared with Figure 11b of Section 3. Recall (Fig. 11a) that a larger spread in BER characteristics will be seen at fixed S_4^2 than at fixed $\overline{\chi^2_{Ry}}$.

The comparisons of the BER results with Rice and Nakagami-m are also as expected. For $\alpha = 1$ the calculated results agree reasonably well with Rice. At $\alpha = 2$, they may be compared with Nakagami-m except at large SNR where Nakagami-m again underestimates the BER. For $\alpha = 3, 4$, the BER curves behave quite differently from either Rice or Nakagami-m. Rice always overestimates the BER, and typically there is a range of lower SNR levels for which Nakagami-m also overestimates the BER. As illustrations, the comparisons at $\overline{\chi^2_{Ry}} = 0.1$ for $\alpha = 1, 5$ are shown in Figure 19. For larger values of $\overline{\chi^2_{Ry}}$ ($\overline{\chi^2_{Ry}} \geq 0.4$), the BERs are usually quite close to SRF. Small deviations are observed, which are very similar to those already discussed in

Section 3. As expected, the deviations are greatest for $k_\alpha \gg k_B$. Figure 19 may be compared with Figure 12 of Section 2. Thus, Figure 19a at $\alpha = 1$ shows behavior nearly identical to that of Figure 12a at $s = 1.5$; and Figure 19b at $\alpha = 5$ is most similar to Figure 12d at $s = 3$.

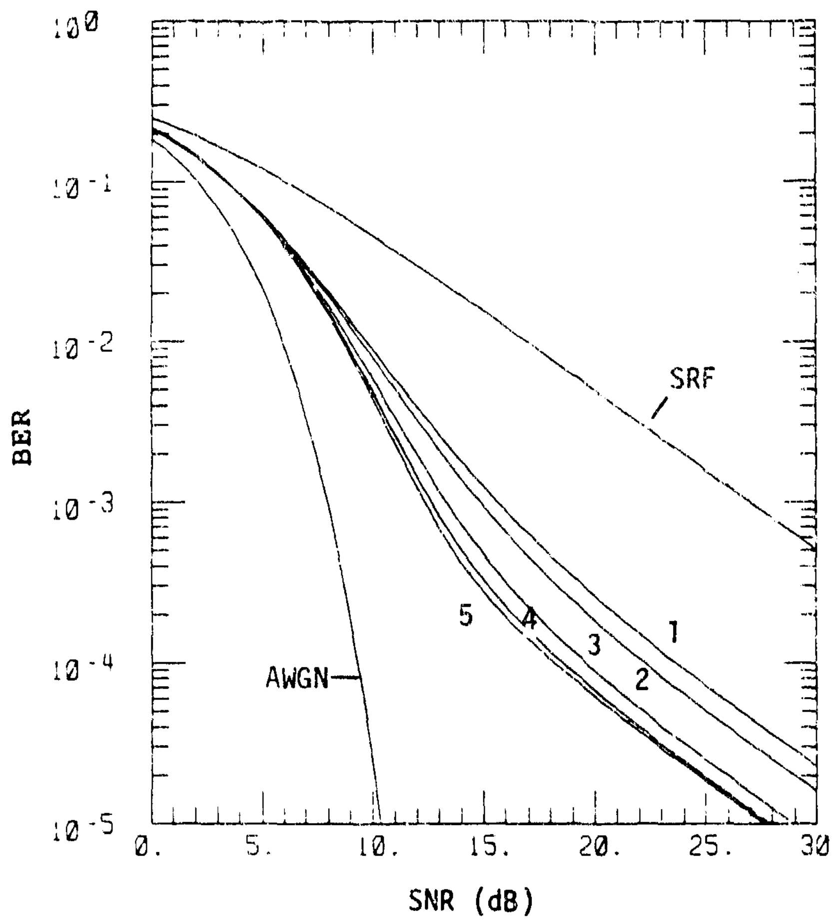

Figure 18. BER vs. SNR characteristics for DBPSK for various Fresnel lengths $\ell_F(\alpha)$ at $\overline{X^2_{Ry}} = 0.1$.

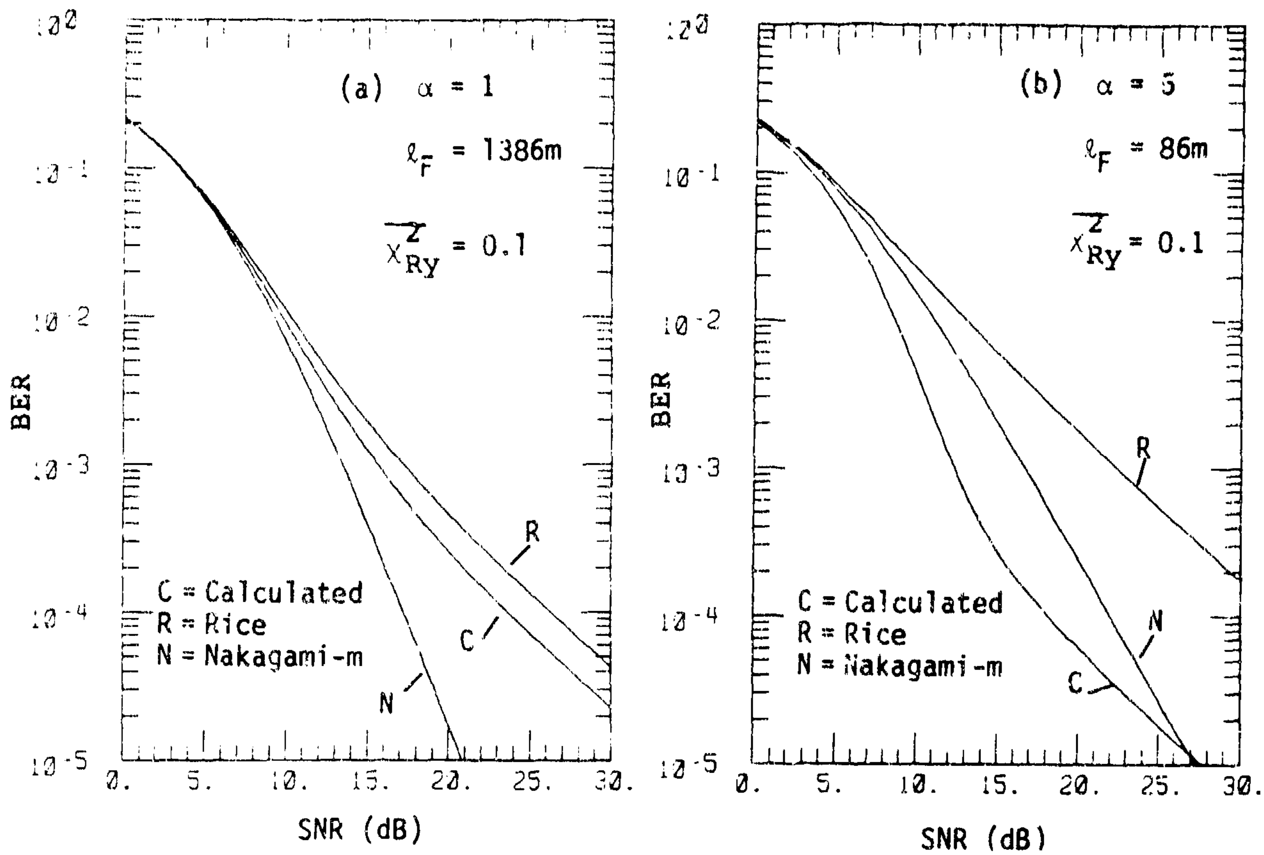

Figure 19. Calculated channel symbol bit error rate vs. SNR at $\overline{X^2_{Ry}} = 0.1$ and $\ell_F = 1386$ m and $\ell_F = 86$ m, as compared to Rice and Nakagami-m.

SECTION 5
DISCUSSION

The final discussion will consist of two parts. Firstly, we will supplement the preceding computational results with a review of past analyses and findings from the pertinent data on satellite link intensity distributions in the ambient environment. We will then conclude with a brief summary of what has been learned and its implications for further research and systems applications.

5.1 REVIEW OF AMBIENT ENVIRONMENT DATA.

Whitney, et al. (Ref. 32) published one of the earliest experimental studies of satellite link first-order intensity statistics. They compared their data only with Nakagami-m. The data were grouped together into five categories according to the value of

$$SI \equiv 100 \frac{I_{max} - I_{min}}{I_{max} + I_{min}} .$$

For each group, an overall median intensity distribution was determined from the data and then compared to Nakagami-m. From the comparison, a best-fit value for S_4^2 was determined. Thus, S_4^2 was actually treated as an adjustable parameter. With this degree of adjustment at their disposal, Whitney, et al were able to find five different S_4^2 values which would allow Nakagami-m to fit the overall median intensity distributions of each of their five different SI groups.

The fit to individual data sets from each SI group was poorer. The fit was also found to deteriorate noticeably at fade depths on the order of ~10 dB or greater; and very few data were available at fade depths beyond ~10-to-15 dB or so. Nonetheless, Whitney et al recommended that Nakagami-m could be used reliably to extrapolate from the data to greater depths of fade. Based upon our present computed results, it seems that this conclusion was not correct; even under conditions where Nakagami-m gives a good fit for shallow fades, it does not accurately match deep fade statistics.

In a subsequent study, Rino and Fremouw (Ref. 33) tested several hypothesized simple models against data. Considered were: Nakagami-m, Rice, Gaussian, and log-normal statistics. They concluded that equally good fits could be obtained from either the Gaussian or log-normal distribution, but that either Rice or Nakagami-m gave only a poor approximation to the data. The data used in this study were also of limited dynamic range, and therefore did not accurately sample deep fades. Nonetheless, the conclusions reached by Rino and Fremouw were clearly very different from those of Whitney, et al.

In yet a subsequent study, Rino, et al (Ref. 30) compared additional data sets with Rice statistics and with generalized Gaussian and log-normal models. According to a later report by Fremouw, et al (Ref. 31--see below), these authors did not separately consider Nakagami-m "because they viewed it as virtually identical to the Rice distribution," although it seems difficult at present to imagine that such a misperception could really have occurred. In any event, Rino, et al concluded that Rice gave a rather poor fit to their measured data, but that a generalized Gaussian (with two adjustable parameters) gave a somewhat better fit than the corresponding log-normal form (with no free parameters).

Lastly, Fremouw, et al (Ref. 31) performed what is apparently the most extensive model-data comparison of note, and reached yet a different set of conclusions. In this study, Nakagami-m, log-normal, and generalized Gaussian models were tested against the data, as well as a two-component model in which the signal is considered to be the product of a focused component with log-normal statistics and a scattered component with generalized Gaussian statistics. Except for Nakagami-m, the models were also tested for their ability to fit signal phase statistics, as well as intensity statistics.

The basic conclusion of Fremouw, et al was that Nakagami-m gave the better fit, in agreement with the original finding of Whitney, et al., but in contradiction to the more recent conclusions of Rino and Fremouw and (inferentially at least) of Rino, et al. More importantly, however, the fit of Nakagami-m to the data (which still did not accurately sample deep fades) was simply not very good. That is, Nakagami-m gave the best fit in only 32 out of 83 cases, while generalized Gaussian did nearly as well as best fit; and one or the other of the two remaining models also gave a best fit more that 27 percent of the time.

In hindsight, the proper conclusion to be drawn from all this is simply that <u>none</u> of these models are reliable in general, even for only the ambient environment, and even when deep fades are poorly sampled. The cause is evident in our computed results. The actual signal intensity distributions will have a strong and systematic dependence on the power spectrum of the scattering ionospheric structure as well as the Fresenl length in general; this structure (and the wavelength-dependent Fresnel length) is at least somewhat variable, even for the ambient environment; and none of the simple models put forth to date have been designed to accommodate these effects.

Moreover, the fact that Nakagami-m is not infrequently a good fit to the ambient environment data when deep fades are not included is entirely consistent with our computed results, since we also find Nakagami-m to be a useful heuristic fit at moderate intensity levels for the PSD conditions (i.e., $\sim k^{-3}$ form for $k \lesssim \ell_F$) thought to most nominally apply for the ambient environment.

5.2 CONCLUSIONS AND OUTLOOK.

The many computed results presented in this report and its Appendixes clearly reveal that signal intensity statistics in non-Rayleigh fading, as well as the basic regime of validity of the Rayleigh fading approximation, are strongly dependent upon the parametric representation of the scattering medium and the value of the Fresnel length. Although the specific dependencies that we have demonstrated have been based on the thin phase screen approximation and its details, it is clear that they are of more fundamental origin. Since none of the existing, simple models for non-Rayleigh fading have been designed with these effects in mind, it is not surprising that such models are not reliable in general.

The approximate agreement of Nakagami-m with either data or computations within certain ranges of PSD and Fresnel length parameterization, and also within certain regimes of signal intensity fluctuation, appears to be at least somewhat a coincidence, and of nonphysical origin. Nonetheless, Nakagami-m does happen to provide a useful fit for nominal ambient environment PSDs and for fade depths or average SNR levels which are not too large.

Rice intensity statistics are thought to be more physically based and they provide a very good fit at all levels of signal intensity or SNR for conditions which can be represented by a PSD with spectral index $s < 1.5$. However, these physically definable conditions are apparently more stressing than commonly encountered in the ambient ionosphere; and it appears, with some uncertainty, that they may also represent an extreme case for the nuclear-perturbed environment.

Thus, in general, it appears that Nakagami-m can continue to be used as a convenient but largely empirical curve fit for ambient environment conditions at link SNRs below 15 dB or so, while Rice can be used as a more fundamental approximate upper bound on the severity of the signal fading under all ambient or nuclear-perturbed conditions of probable interest. The usefulness of an empirical fit of limited validity (i.e., Nakagami-m) versus a potentially more rigorous upper bound (i.e., Rice) will depend upon the priorities of the application.

For more precise work, the alternative in principle is to use detailed computations such as those employed in the present study, or even as generalized to bypass the thin phase screen approximation. However, the credibility of this more laborious alternative depends entirely upon the ability to specify the phase screen PSD or its underlying refractive index power spectrum in an appropriate level of detail. The reliability with which this environment specification can now or eventually be provided is largely a matter of judgement and current research. In applications which require, and can afford the cost of insensitivity to such uncertainties, Rice statistics will continue to provide a useful "worst case" specification for the signal intensity statistics under all levels of scattering intensity, including the Rayleigh fading limit.

Our findings from this investigation indicate two priorities for further research. On the one hand, research aimed at better and more reliable characterization of the scattering medium must clearly seek to reduce the environment of uncertainties to the point that they no longer dominate the uncertainty in intensity statistics for non-Rayleigh fading, or the uncertainty in the value of the election density or refractive index variance needed to drive the weak-to-strong scattering transition (and, thus, the regime of validity of Rayleigh statistics).

On the other hand, the fact that the Rice distribution seems to offer a useful "worst case" specification for first-order intensity statistics suggests the possibility that a generalization of Rice intensity statistics to provide a reasonably worst-case specification for both amplitude and phase, as well as for second- and higher-order signal statistics, may also be achievable. This is an attractive concept, since: (1) Rice statistics merge to Rayleigh statistics in the strong scattering limit; (2) both Rice- and Rayleigh-type signal realizations are easily generated from sampling Gaussian statistics; and (3) the alternative of using Fresnel-Kirchhoff calculations is both difficult and subject to the reliability with which the underlying refractive index spectrum can be defined.

One problem to be met in pursuit of this last objective is the fact that Rice statistics will not be "accurate" in general.

Instead, they will presumably be an approximate worst case; but this means that the proper terms of reference for judging the utility of various alternate Rice model generalizations remains somewhat to be determined. A further problem to be met is the proper separation of diffractive and refractive signal effects in a Rice-type model. Although this issue most likely will not affect link performance assessments under those weak, slow fading conditions for which non-Rayleigh signal statistics will pertain, the proper specification of nondiffractive phase effects in general is an open issue which would inevitably merit further consideration during the development of a "worst case" signal structure specification encompassing both Rayleigh and non-Rayleigh fading.

In the final analysis, the need and utility of such further theoretical work towards signal structure specifications for non-Rayleigh fading will depend upon: (1) the reliability with which ionospheric structure power spectra can be specified, for both ambient and nuclear-perturbed environments (including multi-burst nuclear environments); (2) the assessed capability and readiness of communications system design, assessment, and test personnel to use detailed Fresnel-Kirchhoff calculations versus worst-case signal structure specifications; and (3) the probable sensitivity of DoD satellite communications systems and networks either to link conditions, including non-Rayleigh fading, or the reliable definition of the extent of the Rayleigh fading regime.

SECTION 6

LIST OF REFERENCES

1. Linson, L. M., and J. B. Workman, "Formation of Striations in Ionospheric Plasma Clouds," J. Geophys. Res., Vol. 75, No. 16, pp. 3211-3219, June 1970.

2. Basu, S., and M. C. Kelley, "A Review of Recent Studies of Equatorial F-Region Irregularities and Their Impact on Scintillation Modeling," Effect of the Ionosphere on Space and Terrestrial Systems, J. M. Goodman, Ed., U.S. Government Printing Office, pp. 90-106, 1978.

3. Ossakow, S. L., "Ionospheric Irregularities," Review of Geophysics and Space Physics, Vol. 17, No. 4, 1979.

4. Ossakow, S. L., Spread F Theories - A Review, Naval Research Laboratory, NRL-MR-4435, January 1981.

5. Ishimaru, A., Wave Propagation and Scattering in Random Media, Academic Press, 1978.

6. Fante, R. L., "Electromagnetic Beam Propagation in Turbulent Media," Proc. IEEE, Vol. 63, No. 12, pp. 1669-1692, 1975.

7. Wittwer, L. A., Radio Wave Propagation in Structured Ionization for Satellite Applications, Defense Nuclear Agency, DNA-5304D, December 1979.

8. Yeh, K. C., and C. H. Liu, "Radio Wave Scintillations in the Atmosphere," Proc. IEEE, Vol. 70, No. 4, April 1982, pp. 324-360.

9. Knepp, D. L., and L. A. Wittwer, "Simulation of Wide Bandwidth Signals that have Propagated Through Random Media," Rad. Sci, Vol. 19, No. 1, pp. 303-318, 1984.

10. Rino, C. L., and J. Owen, "Numerical Simulations of Intensity Scintillations Using the Power Law Phase Screen Model," Rad. Sci, Vol. 19, No. 3, pp. 891-908, 1984.

11. Yeh, K. C., C. H. Liu, and M.Y. Youakim, "Theoretical Study of Ionospheric Scintillation Behavior Caused by Multiple Scattering," Rad. Sci, Vol. 10, pp. 97-106, 1975.

12. Bogusch, R. L., F. W. Guigliano and D. L. Knepp, "Frequency-Selective Scintillation Effects and Decision Feedback Equalization in High-Rate Satellite Links," Proc. IEEE, Vol. 71, No. 6, pp. 754-767, June 1983.

13. Arendt, P. R., and H. Soicher, "Effects of Arctic Nuclear Explosions on Satellite Radio Communication," Proc. IEEE, Vol. 52, No. 6, pp. 672-676, June 1964.

14. King, M. A., and P. B. Fleming, "An Overview of the Effects of Nuclear Weapons on Communications Capabilities," Signal, pp. 59-66, January 1980.

15. Wittwer, L. A., A Tran-Ionospheric Signal Specification for Satellite C^3 Applications, Defense Nuclear Agency, DNA-5652D, December 1980.

16. Veseky, J. F., J. W. Chamberlain, J. M. Cornwall, D. A. Hammer, and F. W. Perkins, Irregularities in Ionospheric Plasma Clouds: Their Evolution and Effect on Radio Communication, JASON Technical Report, JSR-80-15, September 1980.

17. Rino, C. L., "Radiowave Propagation Disturbances--The Impact on Military Systems in Space," JED, pp. 53-54 May 1984.

18. Skinner, N. J., R. F. Kelleher, J. B. Hacking, and C. W. Benson, "Scintillation Fading of Signals in the SHF Band," Nature (Phys. Sci.), Vol. 232, pp. 19-21, 5 July 1971.

19. Pope, J. H., and R. B. Fritz, "High Latitude Scintillation Effects on Very High Frequency (VHF) and S-band Satellite Transmissions," Indian J. Pure App. Phys., Vol. 9, pp. 593-600, August 1971.

20. Taur, R. R., "Simultaneous 1.5- and 4-GHz Ionospheric Scintillation Measurements," Rad. Sci., Vol. 11, pp. 1029-1036, December 1976.

21. Fremouw, E. J., R. L. Leadabrand, R. C. Livingston, M. D. Cousins, C. L. Rino, B. C. Fair, and R. A. Long, "Early Results from the DNA Wideband Satellite Experiment-Complex Signal Scintillation," Rad. Sci., Vol. 13, No. 1, pp. 167-187, January-February, 1978.

22. Aarons, J., "Global Morphology of Ionospheric Scientillations," Proc. IEEE, Vol. 70, No. 4, pp. 360-378, April 1982.

23. Rino, C. L., "On the Application of Phase Screen Models to the Interpretation of Ionospheric Scintillation Data," Rad. Sci. Vol. 17, No. 4, pp. 855-867, 1982.

24. Rino, C. L., and R. C. Livingston, "On the Analysis and Interpretation of Spaced-Receiver Measurements of Trans-ionospheric Radio Waves," Rad. Sci, Vol. 17, No. 4, pp. 845-854, 1982.

25. Aarons, J., J. A. Klobuchar, H. E. Whitney, J. Austen, A. L. Johnson, and C. L. Rino, "Gigahertz Scintillations Associated with Equatorial Patches," Rad. Sci, Vol. 18, No. 3, pp. 421-434, 1983.

26. Basu, S., S. Basu, J. P. McClure, W. B. Hanson, and H. E. Whitney, "High Resolution Topside In Situ Data of Electron Densities and VHF/GHz Scintillations in the Equatorial Region," J. of Geo. Res., Vol. 88, No. A1, pp. 403-415, 1983.

27. Yeh, K. C. and G. W. Swenson, "Scintillations of Radio Signals from Satellites," J. of Geo. Res., Vol. 64, pp. 2281-2286, 1959.

28. Rumsey, V. H., "Scintillations Due to a Concentrated Layer with a Power-Law Turbulence Spectrum," Rad. Sci, Vol. 10, No. 1, pp. 107-114, 1975.

29. Rino, C. L., "A Power Law Phase Screen Model for Ionospheric Scintillation, 2. Strong Scatter," Rad. Sci Vol. 14, No. 6, pp. 1147-1155, 1979.

30. Rino, C. L., R. C. Livingston, and H. E. Whitney, "Some New Results on the Statistics of Radio Wave Scintillation, 1. Empirical Evidence for Gaussian Statistics," J. of Geo. Res., Vol. 81, No. 13, pp. 2051-2057, 1976.

31. Fremouw, E. J., R. C. Livingston, and D. A. Miller, "On the Statistics of Scintillating Signals," J. Atmos. Terr. Phys., Vol. 42, pp. 717-731, 1980.

32. Whitney, H. E., J. Arons, R. S. Allen, and D. R. Seeman, "Estimation of the Cumulative Amplitude Probability Distribution Function for Ionospheric Scintillations," Rad. Sci., Vol. 7, No. 12, pp. 1095-1104, 1972.

33. Rino, C. L. and E. J. Fremouw. "Statistics for Ionospherically Diffracted VHF/UHF Signals," Rad. Sci., Vol. 8, No. 3, pp. 223-233, 1973.

34. Knepp, D. L., Propagation of Wide Bandwidth Signals Through Strongly Turbulent Ionized Media, Defense Nuclear Agency, DNA-TR-81-78, March 1982.

35. Franke, S. J., and C. J. Liu, "Multifrequency Study of Ionospheric Scintillation at Ascension Island," Rad. Sci, Vol. 19, No. 3, pp. 695-706, 1984.

36. Livingston, R. C., and T. M. Dabbs, Phase Scintillation Under Weak and Strong Scatter Conditions, Defense Nuclear Agency, DNA-TR-86-333, September 1986.

37. Fremouw, E. J., Technical Discussions, 1988.

38. Ratcliffe, J. A., "Some Aspects of Diffraction Theory and Their Application to the Ionosphere," Reports on Progress in Physics, Vol. 19, pp. 188-267, The Physical Society, London, 1956.

39. Swartz, M., W. Bennet, and S. Stein, Communication Systems and Techniques, McGraw-Hill Book Company, 1966.

40. Nakagami-m., The M-Distribution, in Statistical Methods in Radio Propagation (W. C. Hoffman, ed.), pp 3-36, Pergamon, N.Y., 1960.

41. Mercier, R. P., "Diffraction by a Screen Causing Large Random Phase Fluctuations," Proc. Cambridge Phil. Soc., 52, pp. 382-400, 1962.

APPENDIX A
ADDITIONAL MATHEMATICAL DETAILS

Section 2 presented the physical and mathematical foundations of the calculations discussed in this report. We here extend and comment on some of the material given there.

A.1 SCINTILLATION INDEX AND RYTOV PARAMETER.

The relationship between S_4^2 and $\overline{X^2_{Ry}}$ for weak scattering ($S_4^2 \simeq 4\ \overline{X^2_{Ry}}$) can be derived as follows. From the expression for S_4^2, Equation 13, and scattered field, Equation 9, we have

$$S_4^2 + 1 = \frac{1}{(\lambda Z^*)^2} \int dx_1 dx_2 dx_3 dx_4 \exp\left[i \frac{\pi}{\lambda Z^*} (x_1^2 - x_2^2 + x_3^2 - x_4^2)\right]$$

$$\times \langle e^{i(\phi_1 - \phi_2 + \phi_3 - \phi_4)} \rangle . \qquad \text{(A-1)}$$

In the limit of weak scattering and employing various symmetry properties of the x_i under the sign of integration, we find, see Equation 1,

$$\langle e^{i(\phi_1 - \phi_2 + \phi_3 - \phi_4)} \rangle \rightarrow 1 - \frac{1}{2} \Big[4B(0) - 8B(x_1 - x_2)$$

$$+ 2B(x_1 - x_3) + 2B(x_2 - x_4) \Big] . \qquad \text{(A-2)}$$

Next, noting that

$$\int dx \exp\left[\pm i \frac{\pi}{\lambda Z^*} x^2\right] = \left[\lambda Z^*\right]^{1/2} e^{\pm i\pi/4} , \qquad \text{(A-3)}$$

we easily see that the terms independent of B cancel and

$$S_4^2 \simeq 4 \frac{1}{\lambda Z^*} \int dx_1 dx_2 \; B(x_1 - X_2) \left\{ \exp\left[i \frac{\pi}{\lambda Z^*} (x_1^2 - x_2^2)\right] \right.$$

$$+ \frac{1}{4} \exp\left[i \frac{\pi}{\lambda Z^*}(x_1^2 + x_2^2)\right] - \frac{1}{4} \exp\left[i \frac{\pi}{\lambda Z^*} (x_1^2 + x_2^2)\right] \left. \right\}$$

$$- 2B(0). \qquad \text{(A-4)}$$

Finally, introducing the PSD, Equation 2, and performing the coordinate integrations, we have

$$S_4^2 \simeq 4 \int \frac{dk}{2\pi} \Phi(k) \left[1 - \frac{1}{4} \exp\left(-i \frac{\lambda Z^*}{2\pi} k^2\right) - \frac{1}{4} \exp\left(i \frac{\lambda Z^*}{2\pi} k^2\right) - \frac{1}{2}\right]$$

$$= 4 \int_0^\infty \frac{dk}{\pi} \Phi(k) \sin^2 \frac{\lambda Z^*}{4\pi} k^2$$

$$= 4 \overline{\chi^2_{Ry}}. \qquad \text{(A-5)}$$

A.2 TWO POWER LAW COEFFICIENTS.

The form of the two power law spectrum that we have used is given in Equation 6. The coefficients are determined by continuity,

$$\delta^{2\nu_2} c_1 = c_2 (1+\delta^2)^{\nu_1}, \qquad \text{(A-6a)}$$

and normalization

$$\frac{\pi}{c_1} = \frac{\sqrt{\pi}}{2} \frac{\Gamma(\nu_1 - \frac{1}{2})}{\Gamma(\nu_1)} + \frac{1}{2\nu_2 - 1} \frac{\delta}{(1+\delta^2)^{\nu_1}} - \int_\delta^\infty \frac{dt}{(1+t^2)^{\nu_1}} \qquad \text{(A-6b)}$$

Here we have defined $\mathcal{S}$ as

$$\mathcal{S} = L_o \; k_B \tag{A-7}$$

and is typically much larger than unity.

A.3 RYTOV PARAMETER EVALUATION.

The Rytov parameter was defined in Equation 14. In the limit of ζ,

$$\zeta = \frac{\lambda Z^*}{4\pi L_o^2}, \tag{A-8}$$

being small, which is the typical case, we have for the single power law spectrum ($1/2 < \nu < 5/2$)

$$\overline{\chi^2_{Ry}} = \frac{1}{2} \, (\pi/2)^{1/2} \, \frac{\Gamma(\nu)}{\Gamma(\nu-1/2)\Gamma(\nu+1/2)} \, (2 \; \zeta)^{\nu-1/2} \, \frac{\sigma_\phi{}^2}{\sin \frac{\pi}{2}\nu \; - \; \cos \frac{\pi}{2}\nu} \tag{A-9}$$

Of course, the $\nu = 1$ spectrum that we used was not exactly a strict power law, Equation 5, but Equation A-9 is still reasonably accurate. However, in the numerical calculations, we actually integrated Equation 14 for the $\nu = 1$ case. In addition, this integration was, of necessity, required as well for the two power law PSD.

A.4 RELATIONSHIP TO ELECTRON DENSITY VARIANCE.

It was noted in Section 2 that there is a connection between σ_ϕ^2, the variance of the LOS phase change, and the variance of the electron density fluctuations, σ_{Ne}^2. That connection, for a single power law PSD with $\nu > 1$, is given in Equation 12.

The corresponding connection for $\nu = 1$ is

$$\sigma_\phi^2 = \pi\lambda^2 \, r_e^2 \, L \, L_o' \, \sigma_{Ne}^2 \frac{1}{K_o(\ell_i/L_o')} \exp(-\ell_i/L_o')$$

$$\sim \pi\lambda^2 \, r_e^2 \, L \, L_o' \, \sigma_{Ne}^2/\ln(L_o'/\ell_i) \qquad \text{(A-10)}$$

and for the two power law spectrum, Equation 6, is

$$\sigma_\phi^2 = 2\pi \, \lambda^2 \, r_e^2 \, L \, L_o' \, \sigma_{Ne}^2/c_3, \qquad \text{(A-11a)}$$

$$c_3 = \frac{1}{2} \frac{1}{\nu_1 - 1} \left[1-(1+\delta^2)^{1-\nu_1}\right] c_1 + \frac{1}{2} \frac{1}{\nu_2 - 1} \delta^{2(1-\nu_2)} c_2. \qquad \text{(A-11b)}$$

A.5 BER FOR AWGN.

In the text, DBPSK was the modem selected to illustrate the effects of various levels of fading. In all, we have considered the behavior of six modems. The BER's for AWGN are (Ref. 39)

CPSK: $$P_e = \frac{1}{2} \operatorname{erfc} \sqrt{\gamma} \qquad \text{(A-12a)}$$

ΔPSK: $$P_e = \operatorname{erfc} \sqrt{\gamma} \left(1 - \frac{1}{2} \operatorname{erfc} \sqrt{\gamma}\right), \qquad \text{(A-12b)}$$

DBPSK: $$P_e = \frac{1}{2} e^{-\gamma}, \qquad \text{(A-12c)}$$

BFSK: $$P_e = \frac{1}{2} e^{-\gamma/2}, \quad \text{(A-12d)}$$

QFSK: $$P_e = 1 - [1 - \frac{1}{2} e^{-\gamma}]^{3/2}, \quad \text{(A-12e)}$$

8-ARYFSK: $$P_e = 1 - [1 - \frac{1}{2} e^{-3\gamma/2}]^{7/3}, \quad \text{(A-12f)}$$

where γ is the bit energy-to-noise ratio (SNR). The BER in a fading environment is given in Equation 20

$$\langle P_e(\gamma) \rangle = \int_0^\infty dI \; P(I) \; P_e \; (\gamma I). \quad \text{(A-13)}$$

It can be seen that P_e drops off very rapidly so that for large values of γ in Equation A-13, only small values of I contribute. Consequently, the small intensity (deep fades) behavior of the probability distributions control the BER's for large SNR. If the fading statistics is Rayleigh, the corresponding BER is the slow Rayleigh fading limit (SRF).

APPENDIX B
NUMERICAL CONSIDERATIONS

B.1 PHASE SCREEN.

The realization of the phase screen is given as a FFT in Equation 8. It is clear from its creation that if we extend the phase screen beyond the range $0 \leq \ell \leq N-1$, it is periodic,

$$\phi_{\ell+N} = \phi_{\ell}, \tag{B-1}$$

and continuous. As an illustration of this last point, Figure 20 shows a section of a representative normalized phase screen, ϕ/σ_{ϕ}, generated using Equation 8 with $\nu = 3/2$ and $N = 16384$. We here plot the region

$$\ell = 15500 - 17500 \text{ (Mod } N) \tag{B-2}$$

to emphasize that there is no discontinuity at $\ell = N$. Such a discontinuity would have lead to edge diffraction when the scattered field was calculated.

B.2 SAMPLED FRESNEL-KIRCHHOFF.

The sampled version of the Fresnel-Kirchhoff integral was given in Equation 11. This result depended on the fact that the main contribution to $h(x)$, Equation 9, comes from the region of x' near x and we have sampled x and x' as

$$x = m\Delta x,$$

$$x' = \ell\Delta x.$$

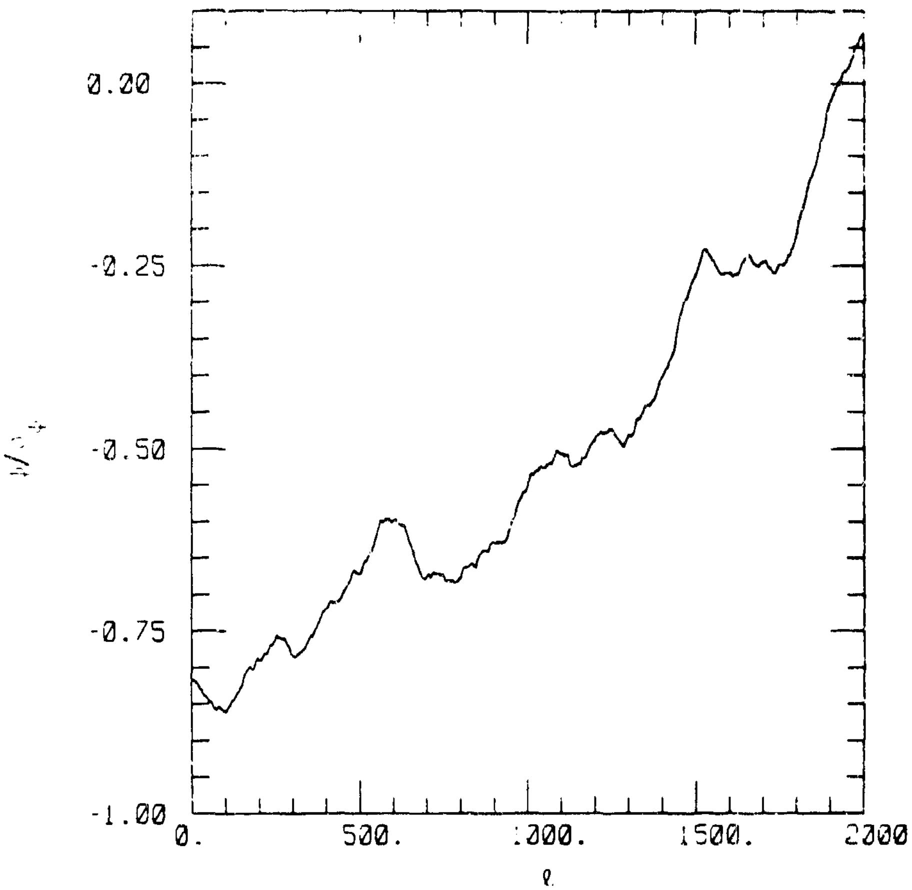

Figure 20. Sampled phase screen vs. position.

To employ FFT techniques, we require

$$\Delta x = \left[\lambda Z^* / N\right]^{1/2} \qquad \text{(B-3)}$$

where N is the number of points in the FFT. Then noting the periodicity of ϕ_ℓ, we can write h_m as a common sum from 0 to N - 1,

$$h_m = \frac{1}{\sqrt{N}} e^{-i\pi/4} e^{i\pi m^2/N} \sum_{\ell=0}^{N-1} e^{i\pi\ell^2/N} e^{i\phi_\ell} e^{-i2\pi m\ell/N} \qquad \text{(B-4)}$$

which is in the standard format of a FFT.

B.3 SAMPLING CRITERIA.

In order to accurately calculate the scattered field by means of the discrete sum, Equation B-4, we have to adequately sample the phase screen, that is, the phase cannot change by more than π from one sample point to the next,

$$|\phi(x+\Delta x)-\phi(x)| < \pi. \tag{B-5}$$

An average on this requirement leads to a bound on σ_ϕ given by

$$\sigma_{MAX} \equiv \frac{1}{\sqrt{2}}\,\pi\,\frac{L_o}{\Delta x}\,F^{-1}\left(\frac{\Delta x}{L_o}\right) \tag{B-6}$$

where the function F is defined as

$$F^2(a) = \frac{1}{a^2}\int \frac{dk}{2\pi}\,\frac{\Phi(k)}{\sigma_\phi^2}\,(1-\cos a\,L_o k). \tag{B-7}$$

For the power law spectrum, Equation 3, this becomes

$$F^2\,(a,\nu) = \left[1 - \frac{2}{\Gamma(\nu-\frac{1}{2})}\,\left(\frac{a}{2}\right)^{\nu-\frac{1}{2}}\,K_{\nu-\frac{1}{2}}(a)\right]/a^2. \tag{B-8}$$

The other necessary condition for the finite sum, Equation B-4, to represent the scattered field is that little energy is scattered from the neglected parts of the phase screen, that is, we can ignore edge effects. Since the angle of scatter is approximately

$$\theta \sim \frac{1}{k}\frac{d\phi}{dx}, \tag{B-9}$$

we require

$$\frac{1}{k}\,\frac{|\phi(x+\Delta x) - \phi(x)|}{\Delta x} < \frac{1}{2}\,\frac{L}{z^*} \tag{B-10}$$

or, in an averaged sense, a bound on σ_ϕ identical to Equation B-6.

The degree to which our calculations satisfy the bound Equation B-6 is shown in Table 2 for the single power law cases and in Table 2 for the two power law cases. Shown there is the relationship between $\overline{X^2_{Ry}}$ and σ^2_ϕ, determined either by Equation A-9 or by numerically integrating Equation 14. The maximum $\overline{X^2_{Ry}}$ we considered was $\overline{X^2_{Ry}} = 20$ with the corresponding σ_ϕ given in the Tables. The bound determined from Equation B-6 is given in the Tables as σ_{MAX}. As can be seen, all the values of σ_ϕ of interest to us are comfortably small compared to the maximum values so the conditions on sampling and edge effects are well satisfied.

Finally, there is the requirement that the PSD is adequately sampled. This is accomplished if the sampled spatial extent, L, satisfies

$$L \sim 5\ L_o \tag{B-11a}$$

or

$$\Delta k \sim 1/L_o. \tag{B-11b}$$

TABLE 3. SINGLE POWER LAW PARAMETERS.

s	$\frac{\sigma_\phi}{\left[\overline{X^2_{Ry}}\right]^{1/2}}$	σ_ϕ ($\overline{X^2_{Ry}}$ = 20)	σ_{MAX}
1	11.7	52	264
3/2	30.8	138	687
2	81.6	365	2818
5/2	208.9	934	5804
3	501.8	2244	8208

TABLE 4. TWO POWER LAW PARAMETERS.

ℓ_F (in m)	$\frac{\sigma_\phi}{\left[\overline{X^2_{Ry}}\right]^{1/2}}$	σ_ϕ ($\overline{X^2_{Ry}}$ = 20)	σ_{MAX}
1386	18.8	84.3	886
693	33.4	149.5	1766
346	72.6	324.5	3543
173	185.2	828.4	7150

This requirement is met for all the single power law PSD considerations. For a few of the cases considered for the two power law PSD, the requirement is violated by at most a few factors of two. However, the very small k portion of the spectrum contributes little to the results so that the sampling is adequate even for these cases. We did perform a few calculations at larger values of N and confirmed that we obtained similar results to those presented.

B.4 NUMERICAL VALUES OF PARAMETERS.

For our calculations, we assumed

$$L_o = 10 \text{ km},$$

$$\ell_i = 10 \text{ m},$$

$$N = 2^{14}.$$

The probability distributions were calculated by partitioning the intensity range 0 to 15 into bins of ΔI with

$$\Delta I = 10^{-2}.$$

For every combination of PSD, Fresnel length and $\overline{\chi^2_{Ry}}$, 640 phase screen realizations were created, each supplying 14384 intensity samples. Consequently, the total number of numbers that contributed to a given probability density curve was about 9.2 million and the minimum probability density measurable is about

$$P_{MIN} \sim 10^{-5}.$$

Of particular concern for moderate values of S_4 was the behavior of the probability distribution for small values of the intensity. The behavior here determines the communication channel behavior for large values of SNR. We investigated the small I behavior in order to verify that P(~0) was indeed non-zero and, in particular, that it is typically significantly different than the result for the Rice distribution,

$$P_{RICE}(0) = \frac{1}{1-\sqrt{1-S_4^2}} \exp\left[\sqrt{1-S_4^2}\ /(1-\sqrt{1-S_4^2})\right]. \qquad \text{(B-12)}$$

Of course, Nakagami-m goes to zero in this limit. The procedure was to consider the interval $0 \leq I \leq 0.05$ in bins of ΔI with

$$\Delta I = 10^{-4}.$$

APPENDIX C

PROBABILITY DISTRIBUTIONS FOR SINGLE POWER LAW PSD

This Appendix contains calculated probability distributions for single power law PSDs under conditions where $2\pi L_O >> \ell_F >> \ell_i$. These distributions are compared to Nakagami-m (labeled as N) and Rice (labeled as R) if S_4 is less than unity and to Rayleigh (labeled as SRF) if S_4 is greater than or equal to unity. Throughout, the calculated are labeled C.

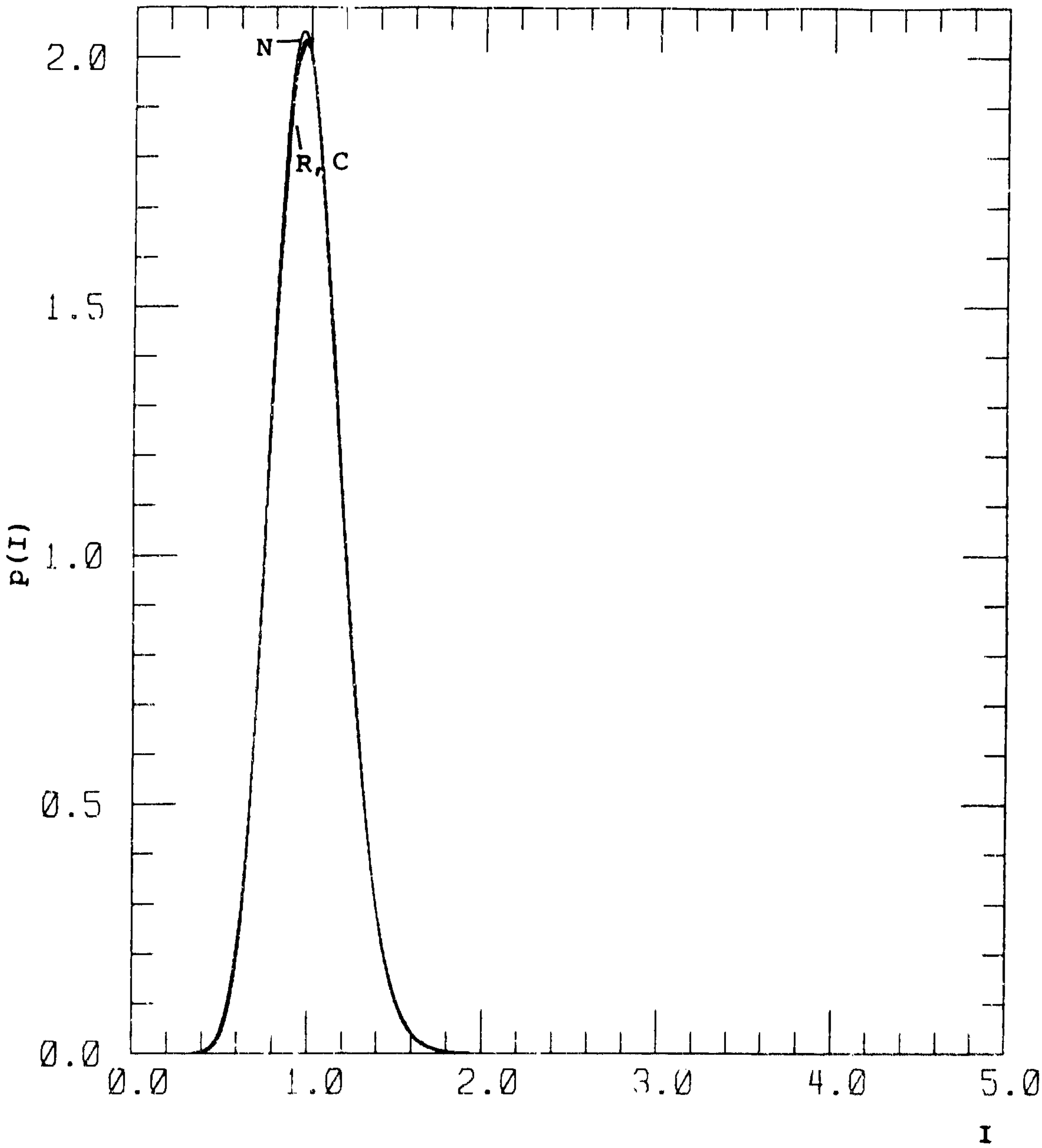

Figure C-1. Probability Distribution for
$s = 1$, $\chi^2 = 0.01$, $S_4^{\,2} = 0.039$.

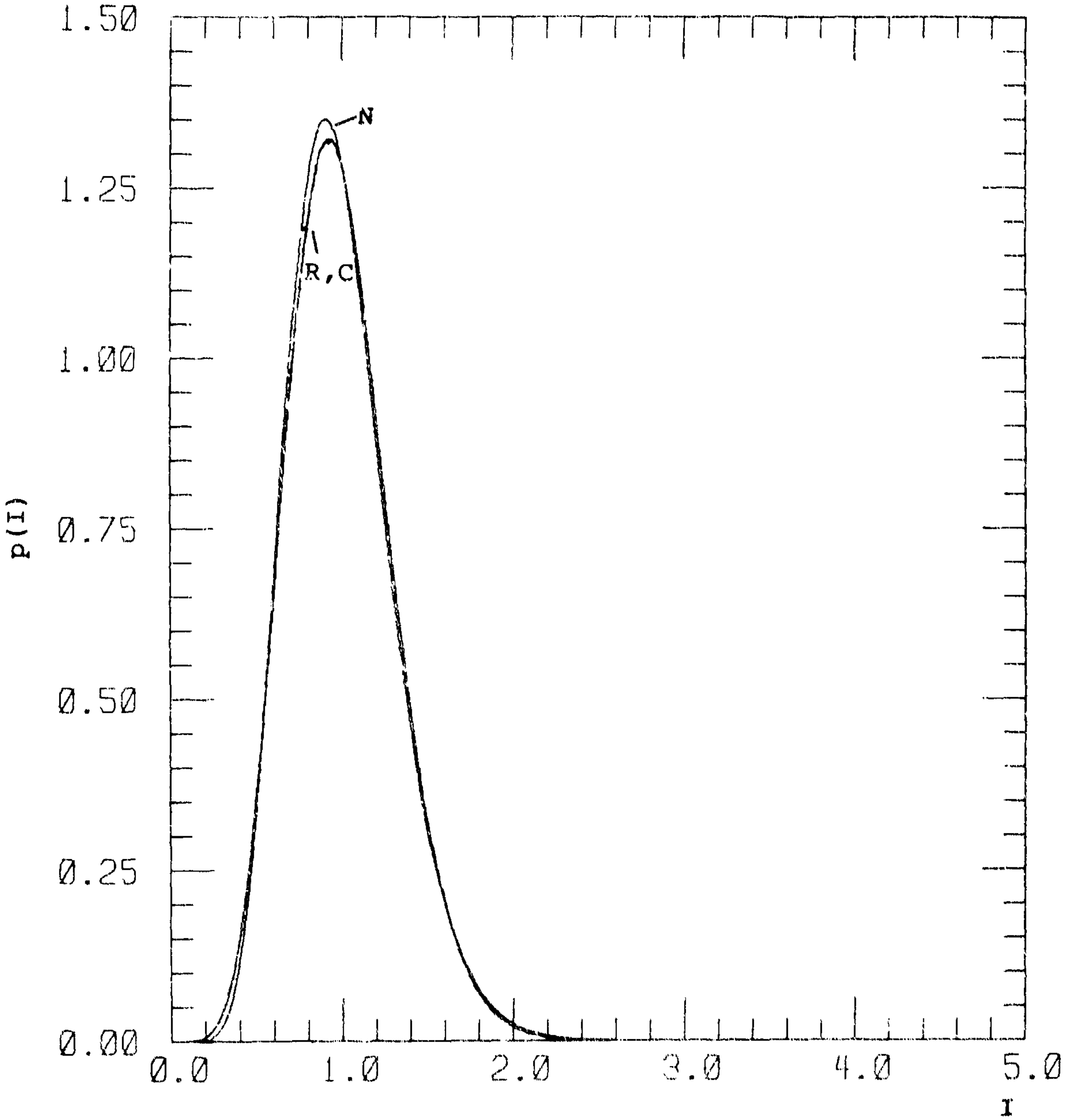

Figure C-2. Probability Distribution for
$s = 1,\ \gamma^2 = 0.025,\ S_4{}^2 = 0.095.$

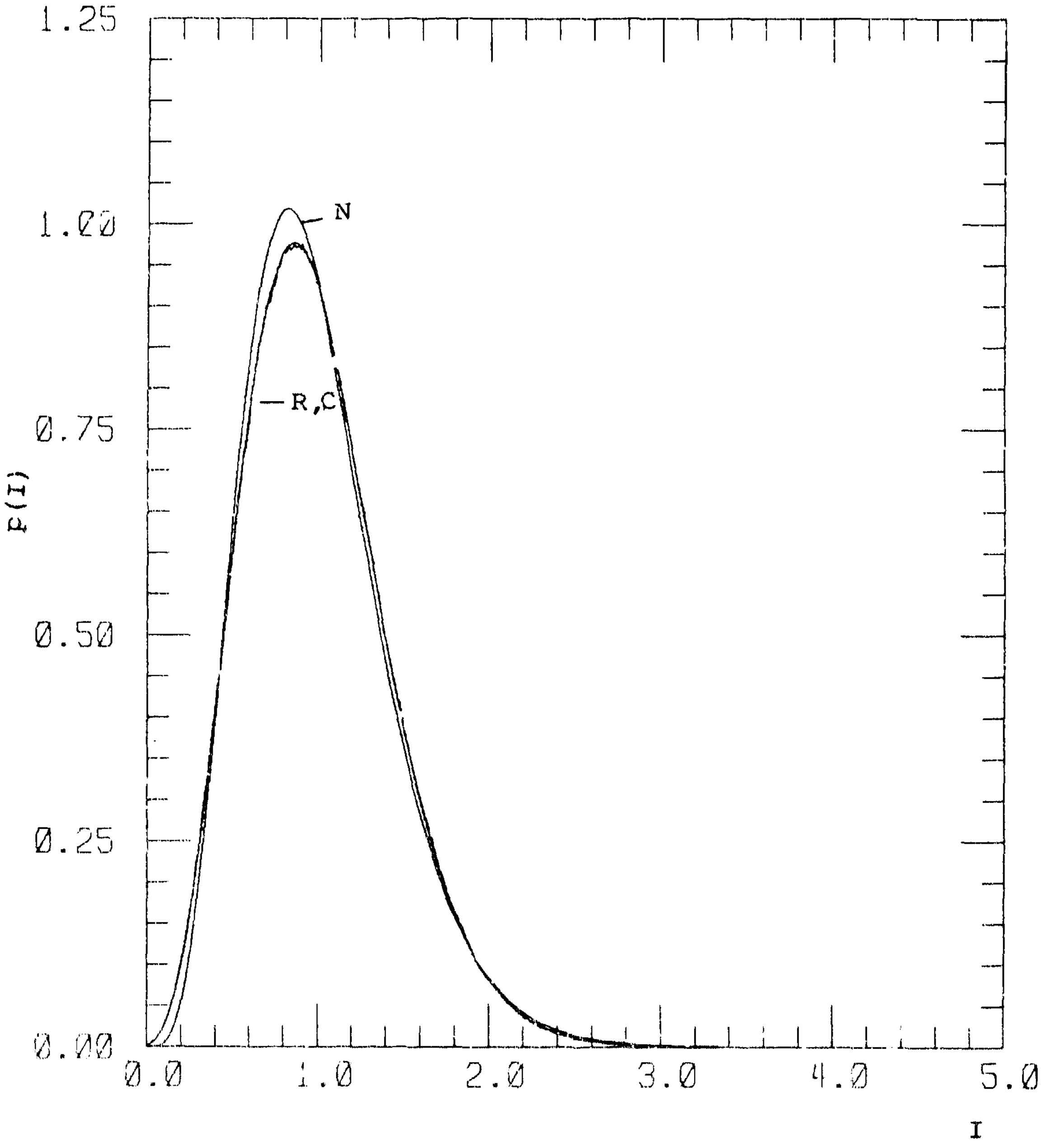

Figure C-3. Probability Distribution for
$s = 1$, $\chi^2 = 0.05$, $S_4{}^2 = 0.180$.

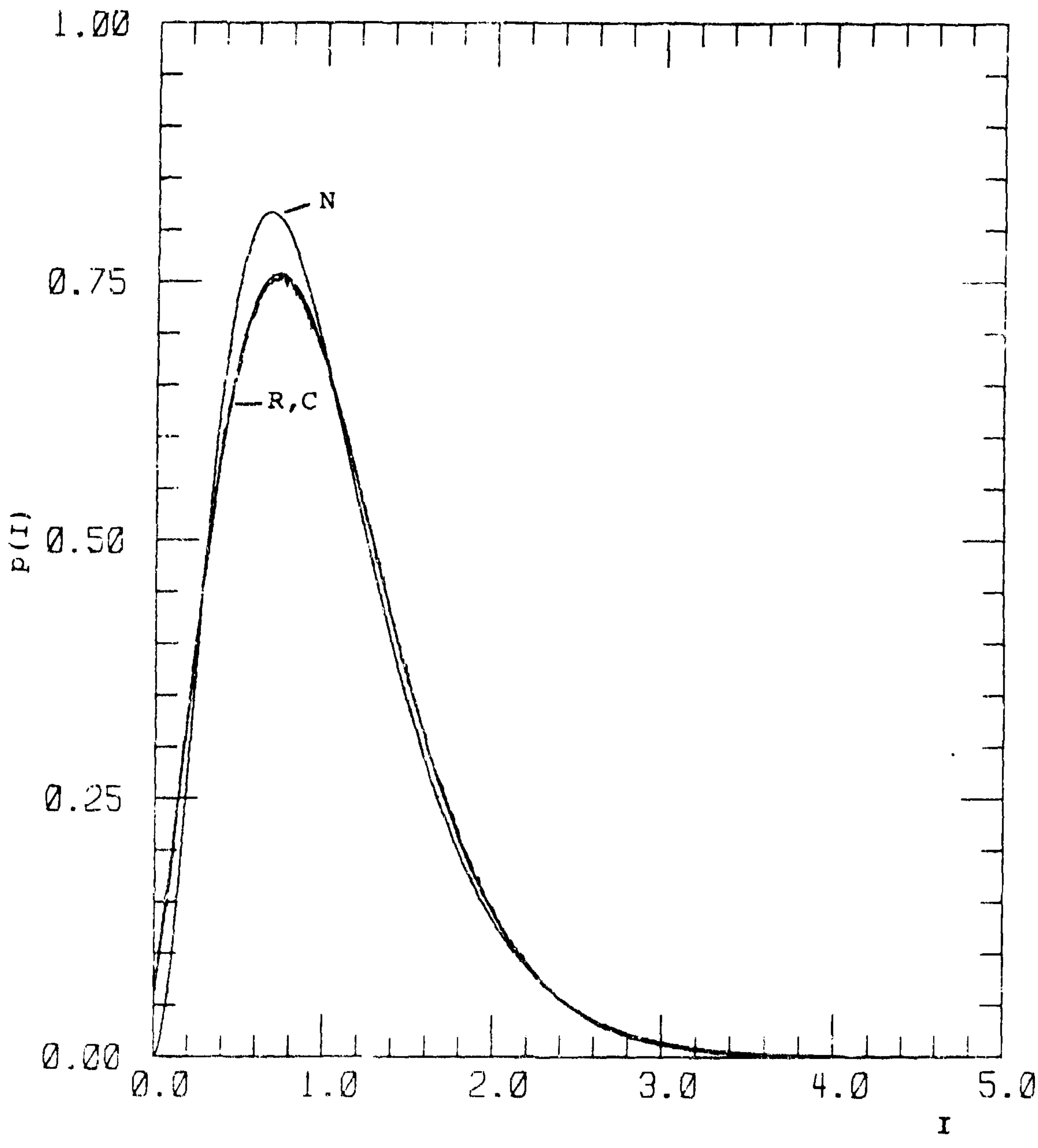

Figure C-4. Probability Distribution for
$s = 1$, $\chi^2 = 0.1$, $S_4^2 = 0.[illegible]27$.

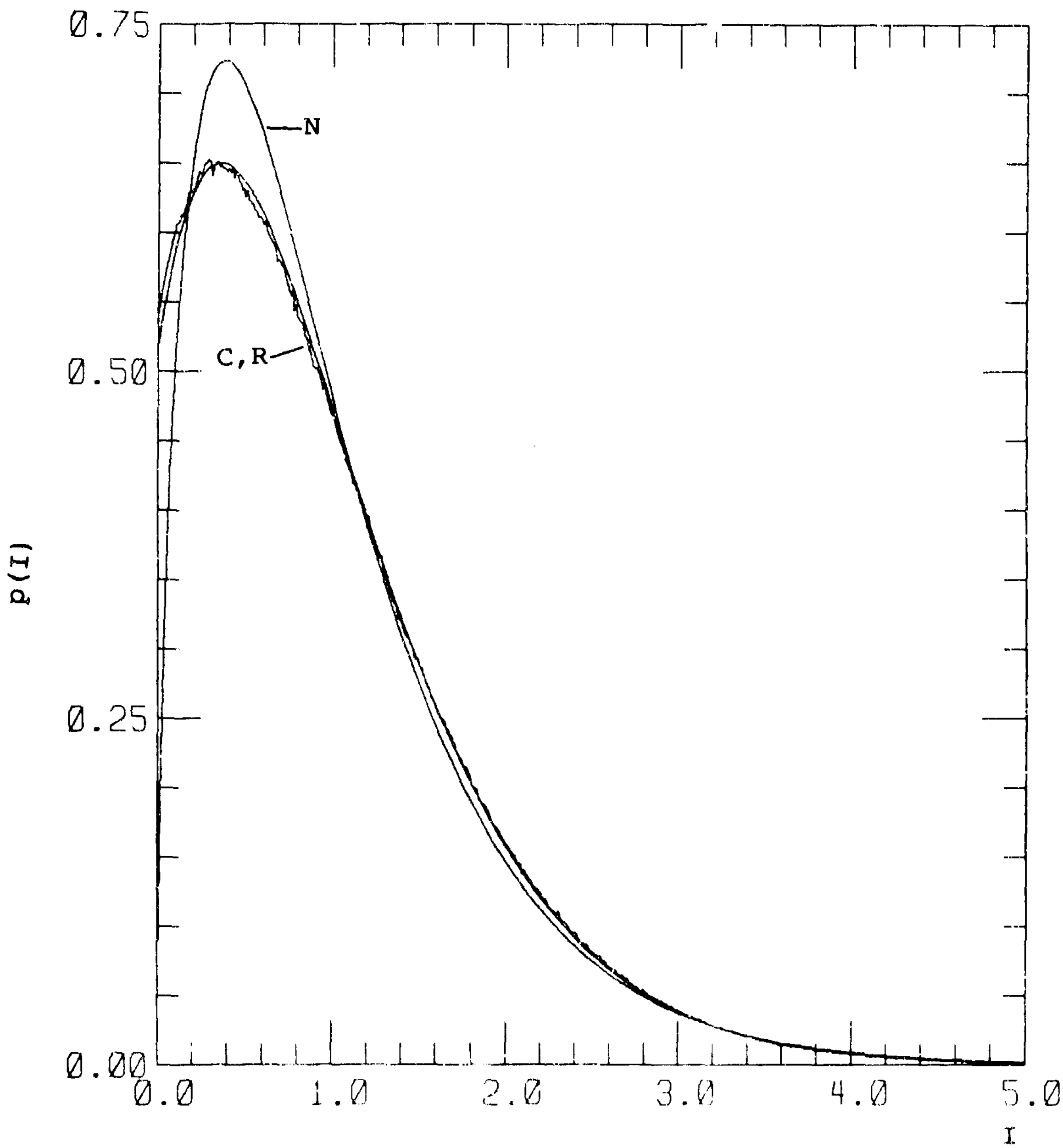

Figure C-5. Probability Distribution for $s = 1$, $\chi^2 = 0.25$, $S_4^{\ 2} = 0.616$.

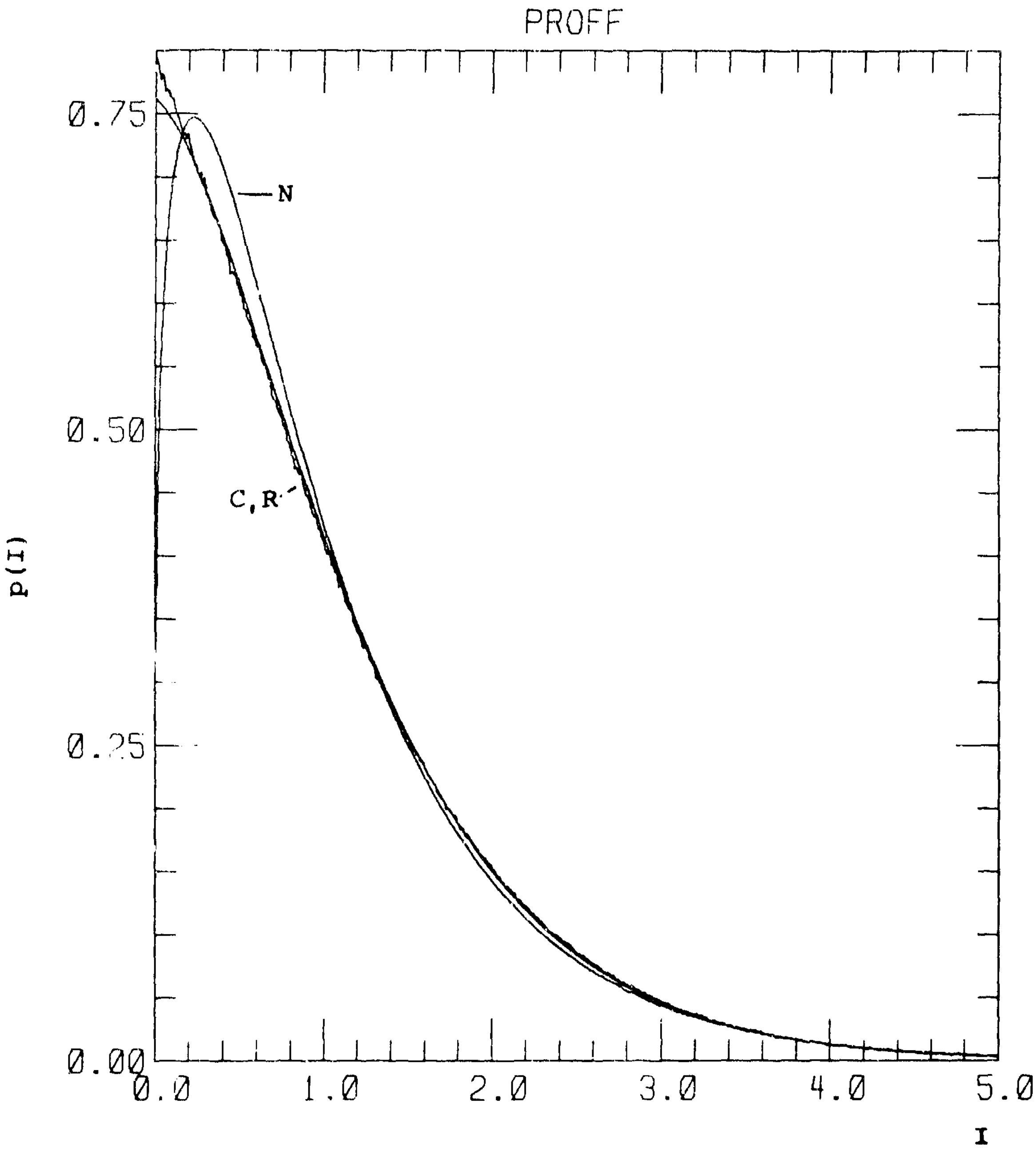

Figure C-6. Probability Distribution for

$s = 1,\ \chi^2 = 0.4,\ S_4{}^2 = 0.768.$

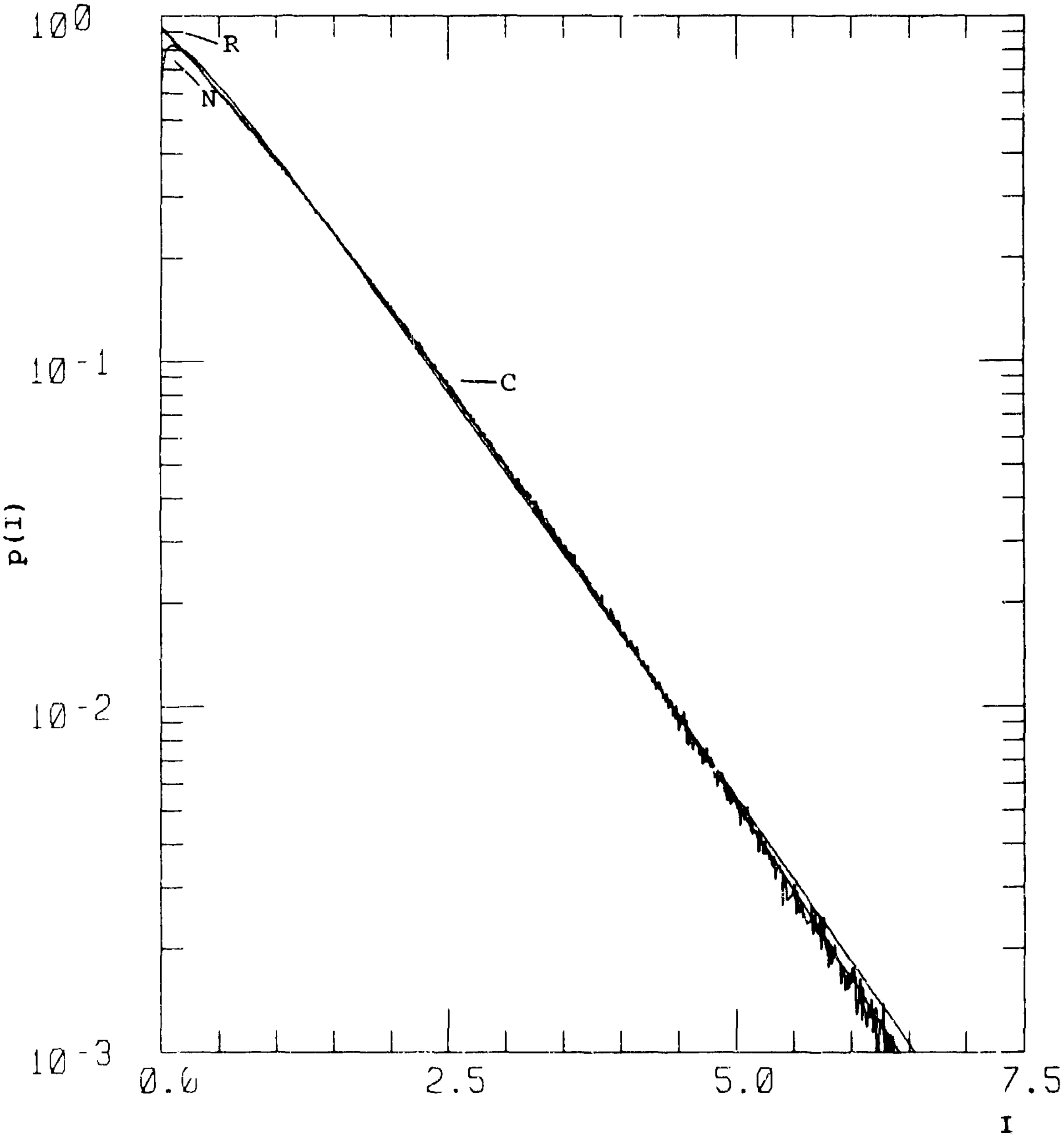

Figure C-7. Probability Distribution for $s = 1$, $\chi^2 = 0.7$, $S_4{}^2 = 0.899$.

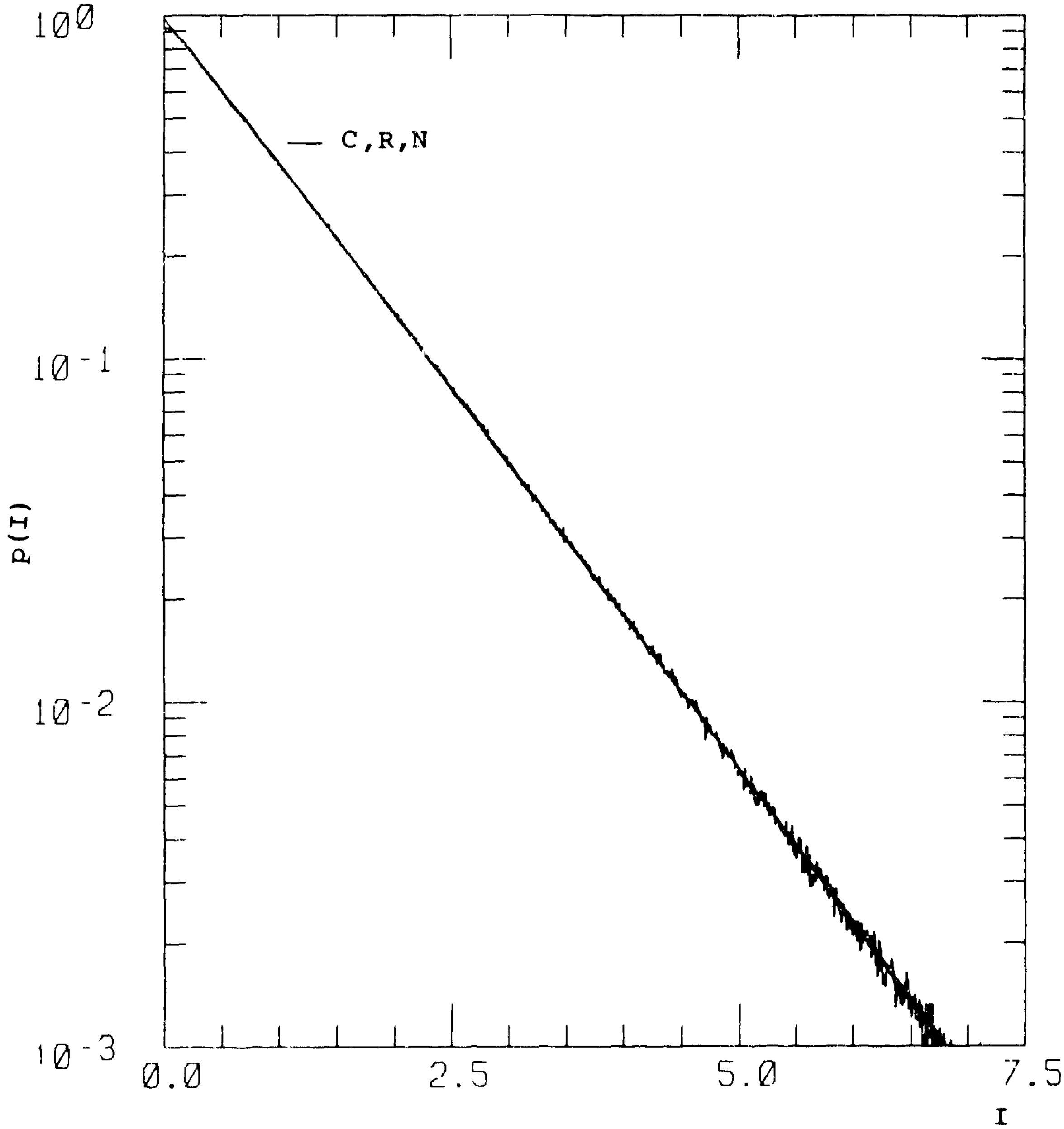

Figure C-8. Probability Distribution for $s = 1$, $\chi^2 = 1.5$, $S_4{}^2 = 0.975$.

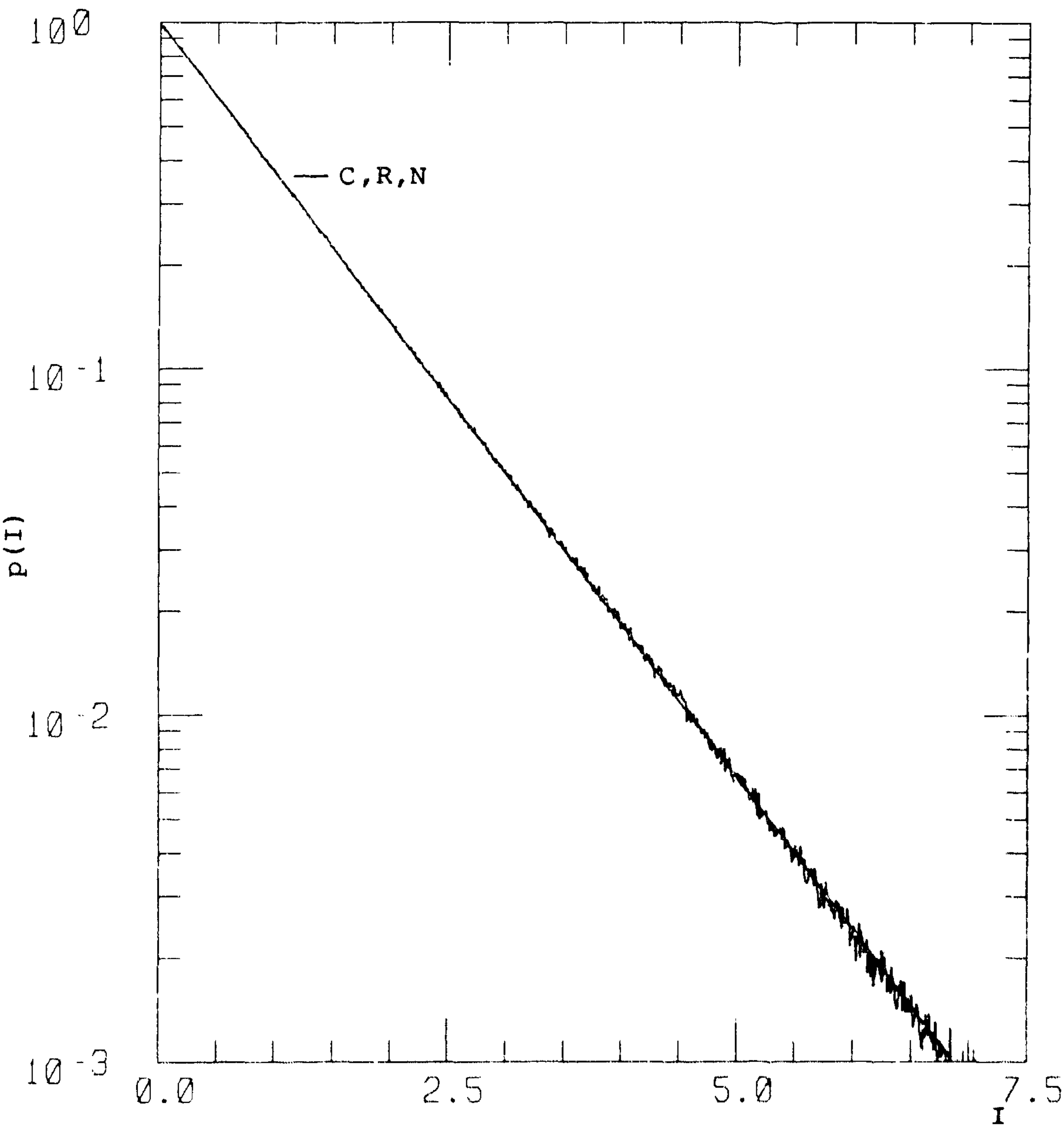

Figure C-9. Probability Distribution for $s = 1$, $\chi^2 = 3.0$, $S_4^{\,2} = 0.992$.

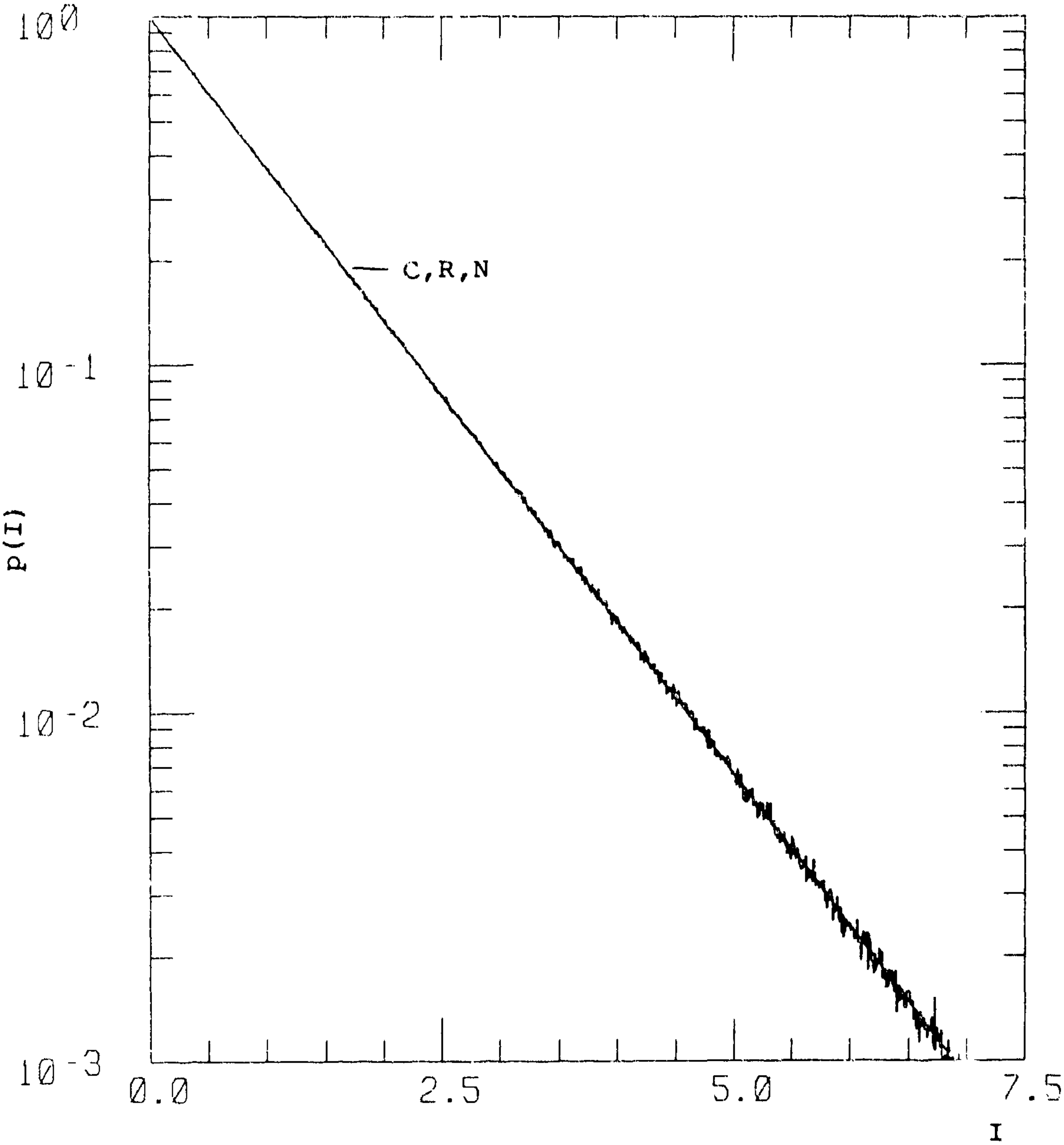

Figure C-10. Probability Distribution for

$s = 1,\ \chi^2 = 7.0,\ S_4^{\ 2} = 0.997.$

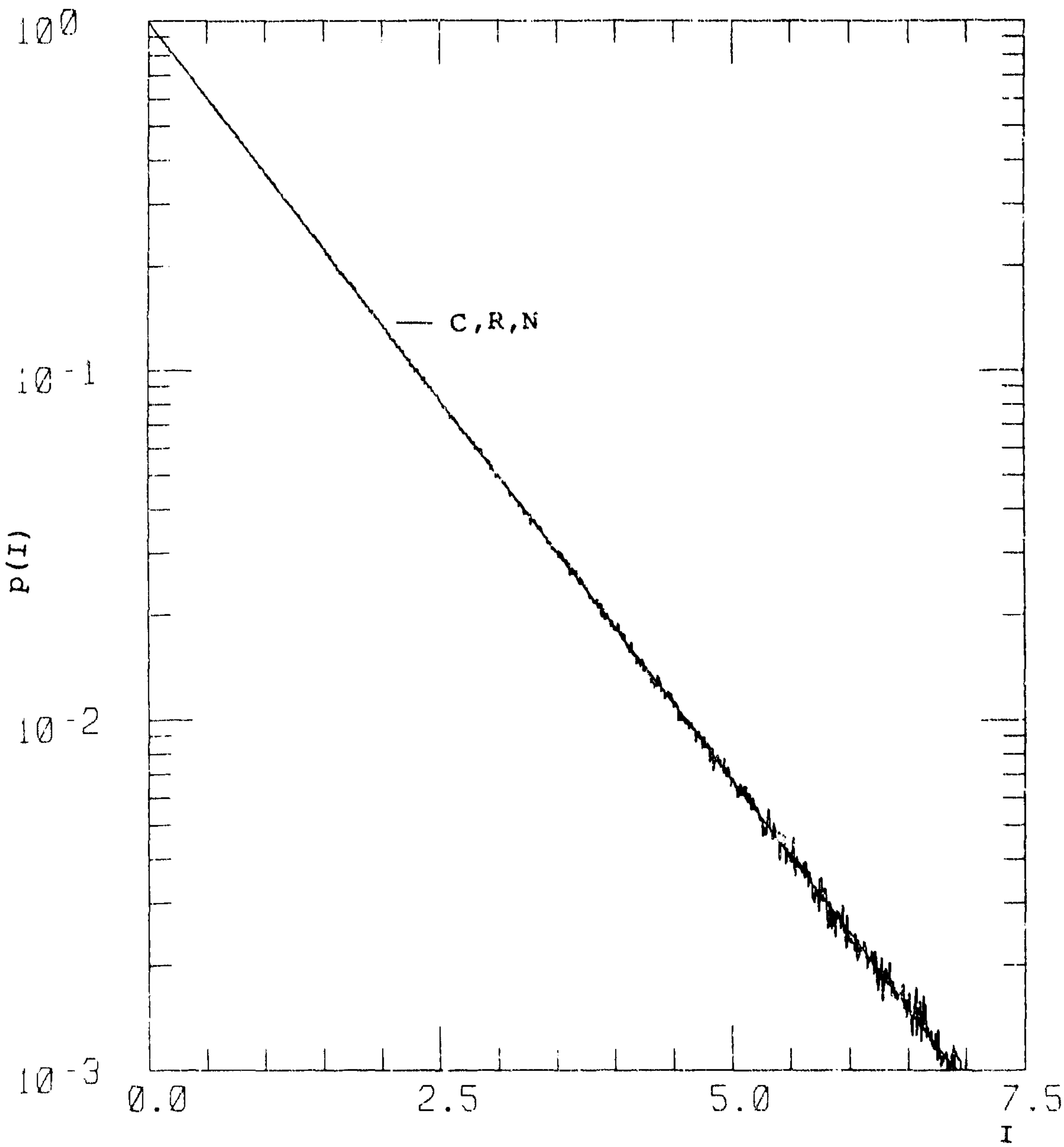

Figure C-11. Probability Distribution for

$s = 1$, $\chi^2 = 20.0$, $S_4{}^2 = 0.999$.

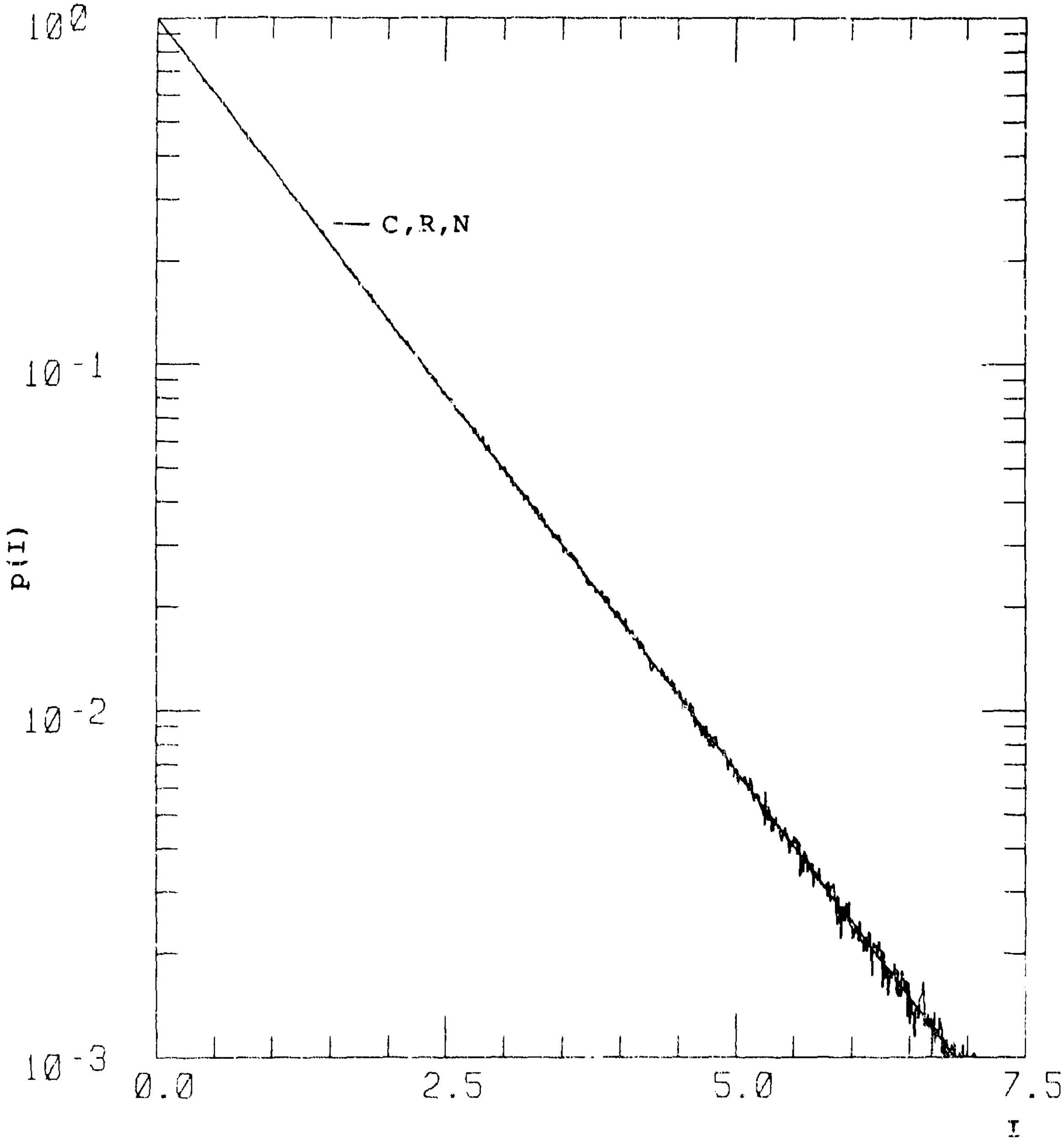

Figure C-12. Probability Distribution for $s = 1$, $\chi^2 = 20.0$, $S_4^{\ 2} = 0.998$.

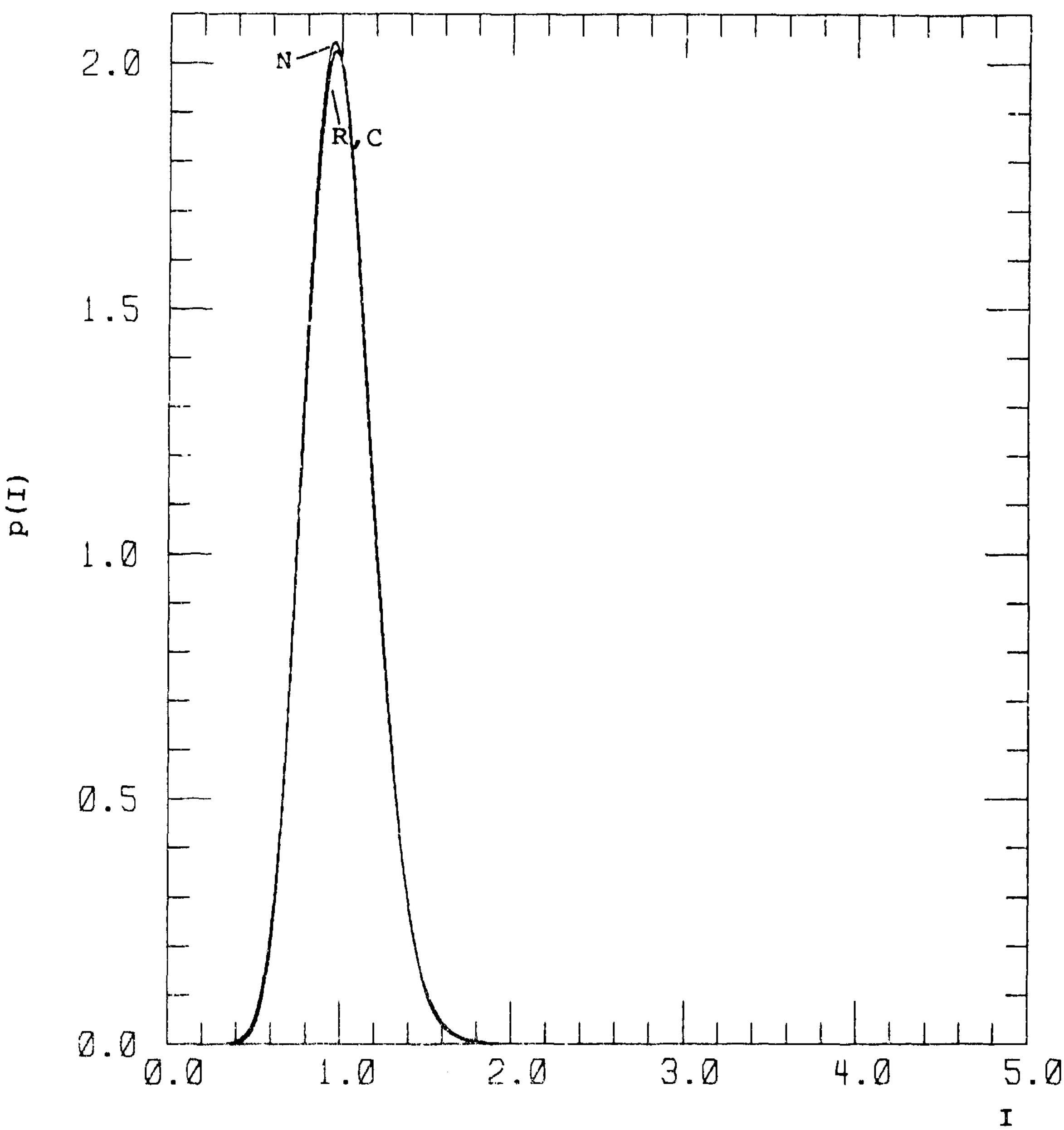

Figure C-13. Probability Distribution for $s = 1.5$, $\chi^2 = 0.01$, $S_4^2 = 0.039$.

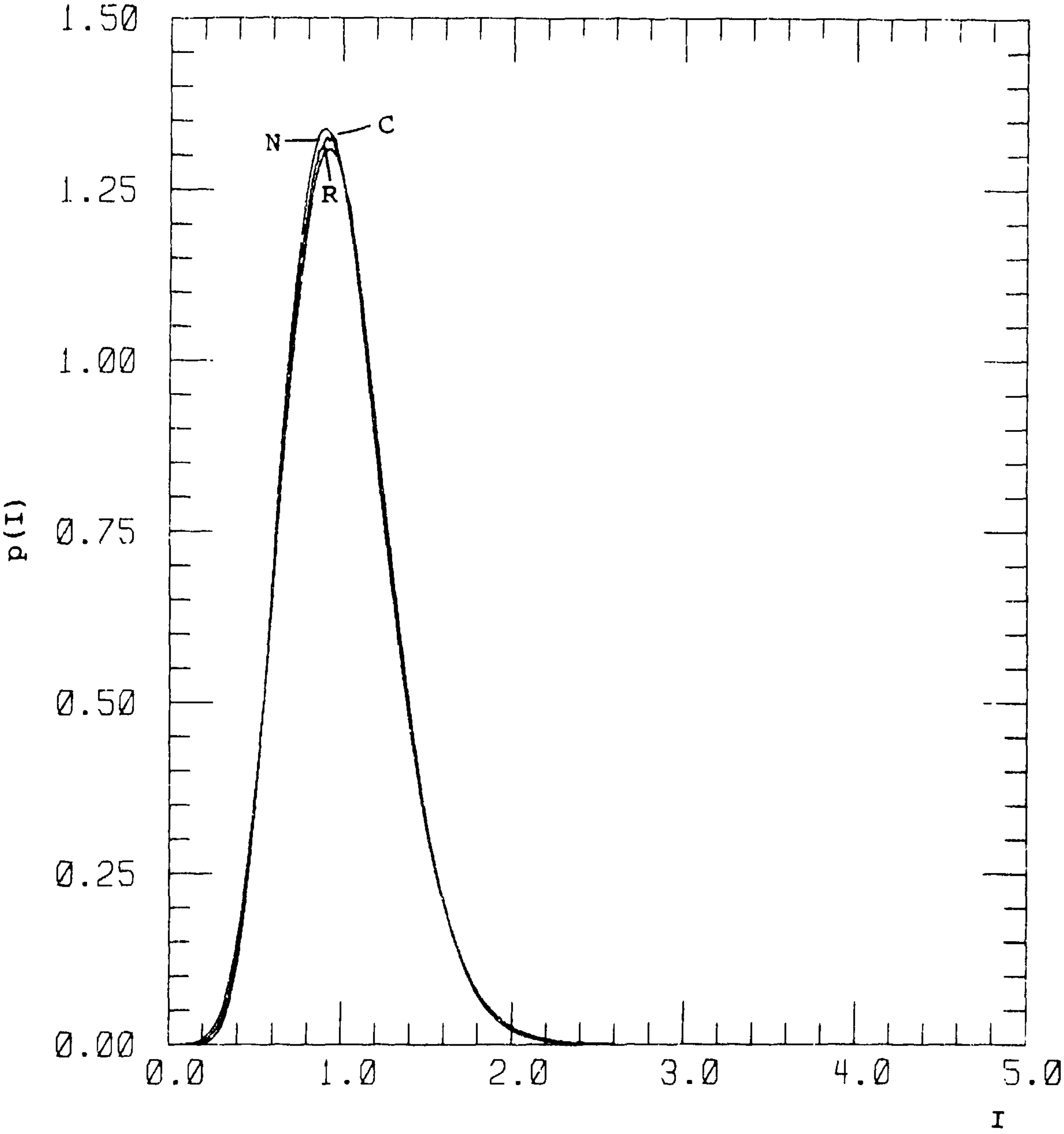

Figure C-14. Probability Distribution for $s = 1.5$, $\chi^2 = 0.025$, $S_4^2 = 0.097$.

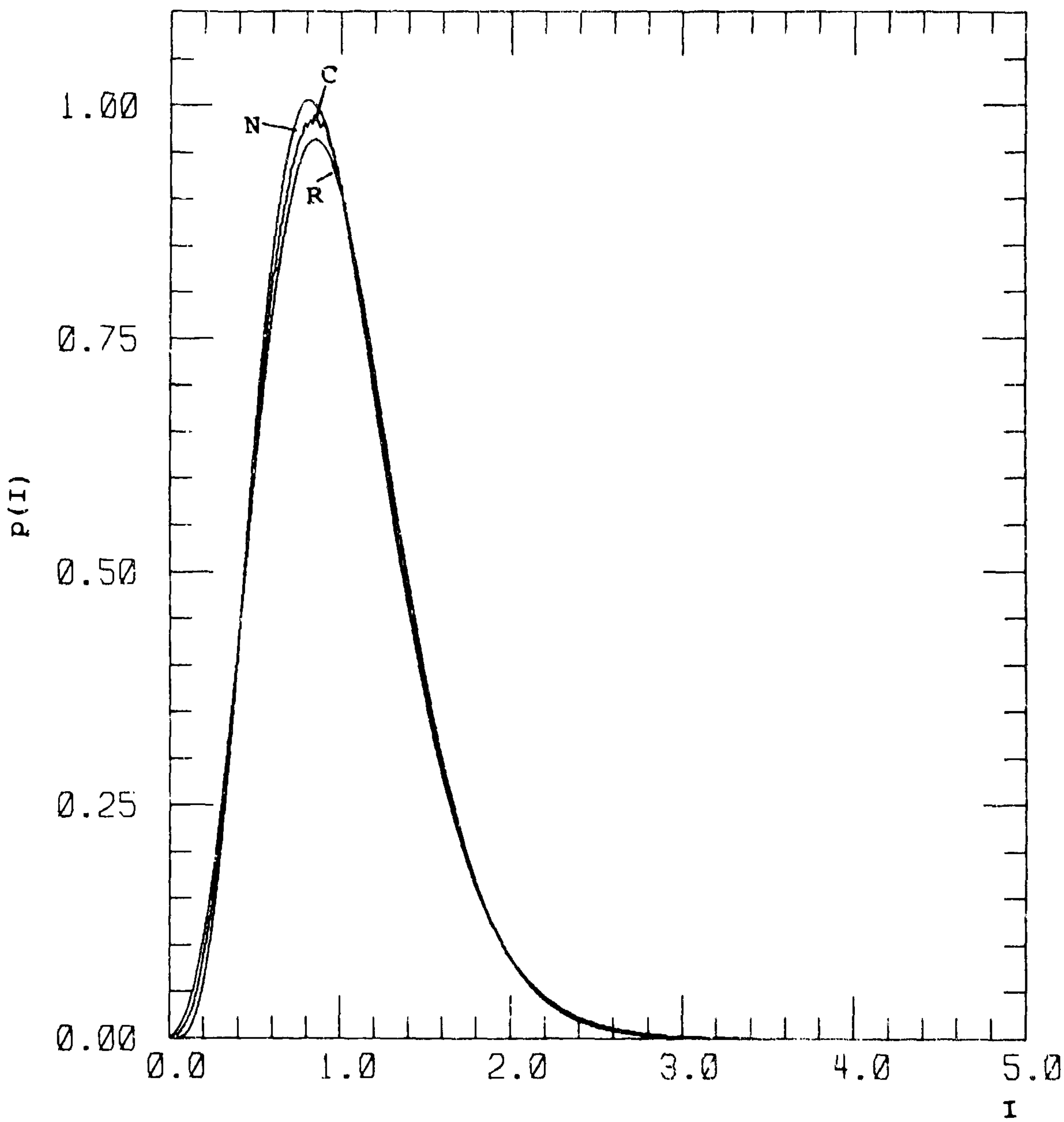

Figure C-15. Probability Distribution for
$s = 1.5$, $\chi^2 = 0.05$, $S_4^{\ 2} = 0.186$.

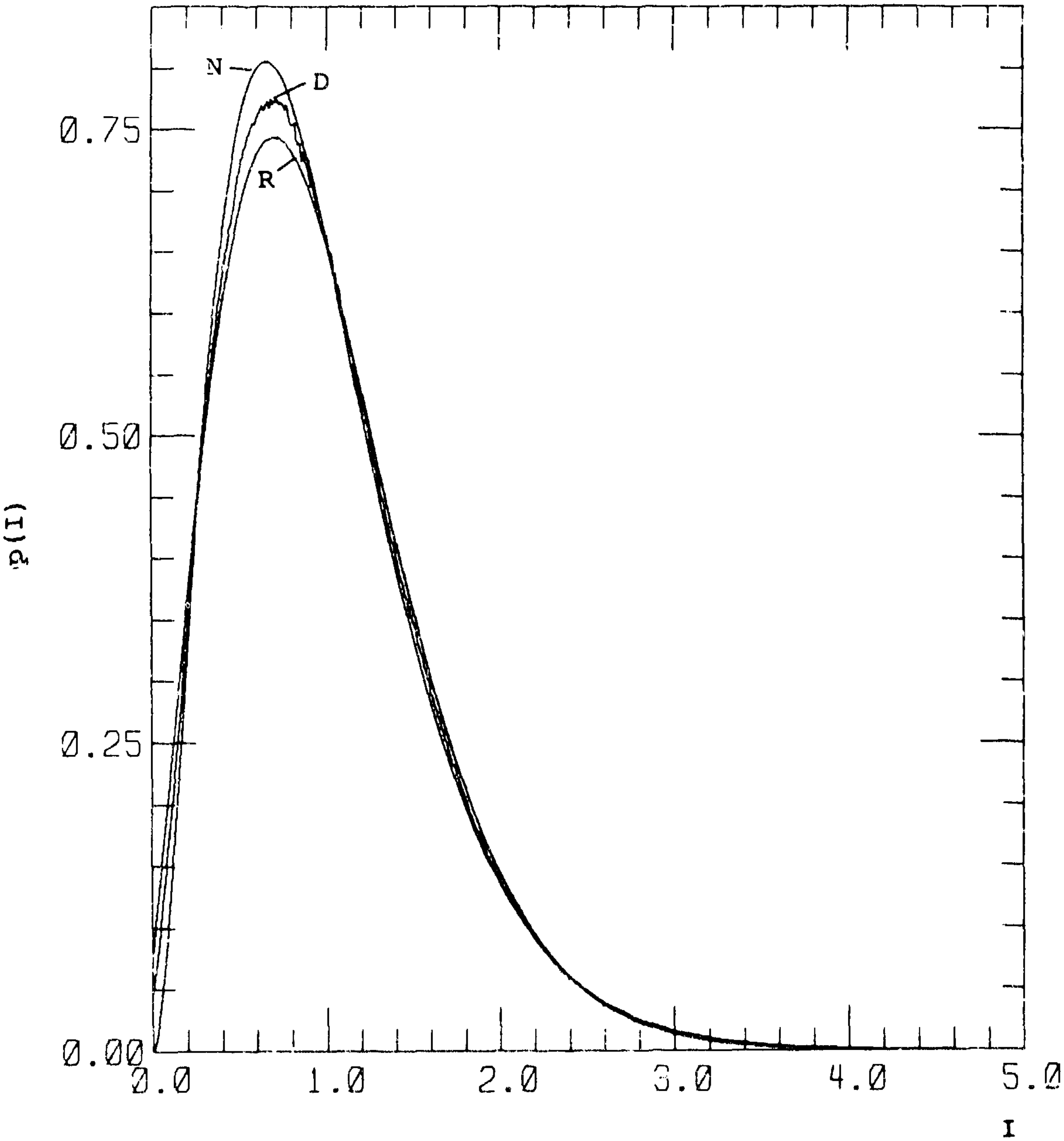

Figure C-16. Probability Distribution for $s = 1.5$, $\chi^2 = 0.1$, $S_4{}^2 = 0.343$.

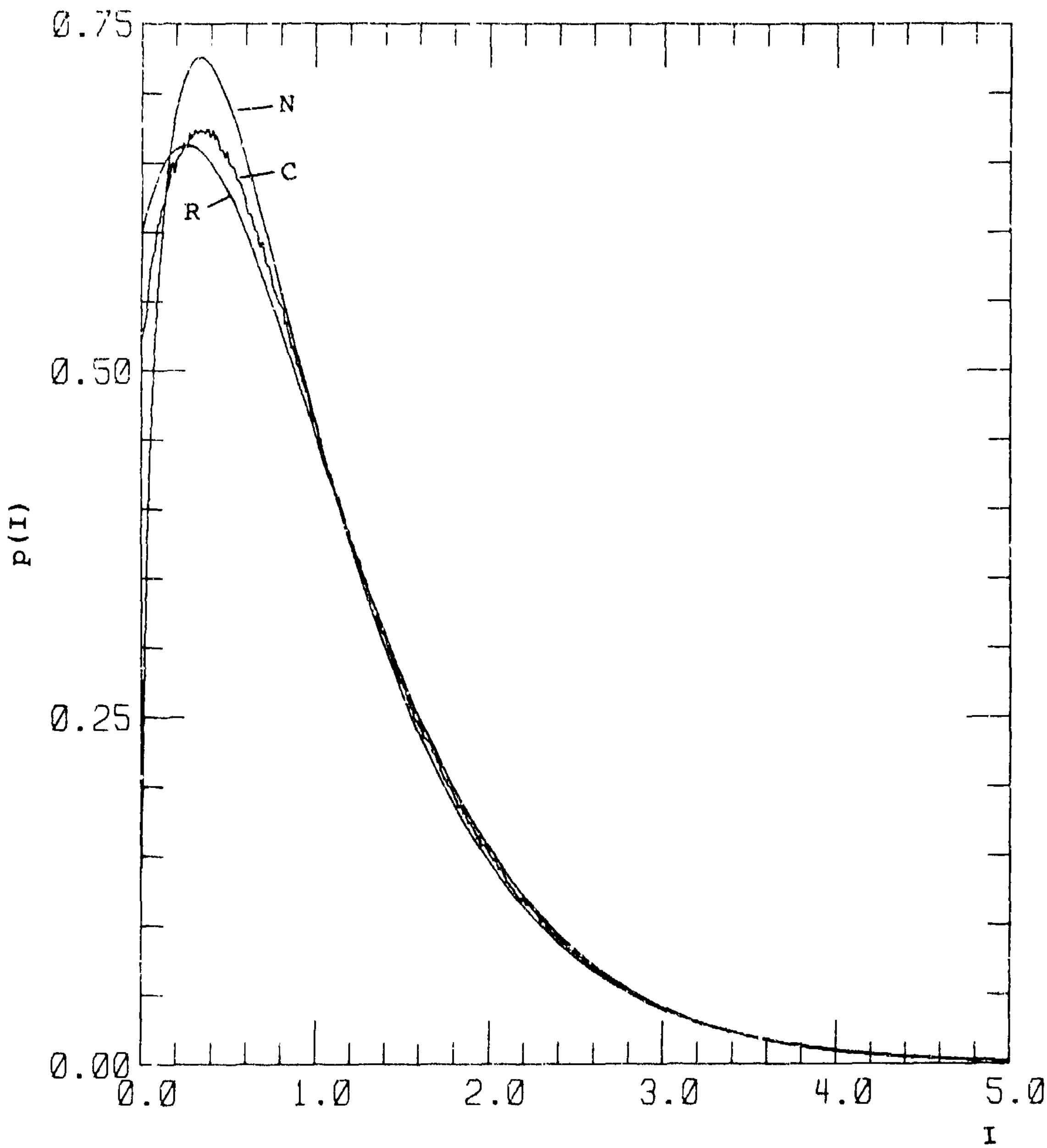

Figure C-17. Probability Distribution for $s = 1.5$, $\chi^2 = 0.25$, $S_4^2 = 0.664$.

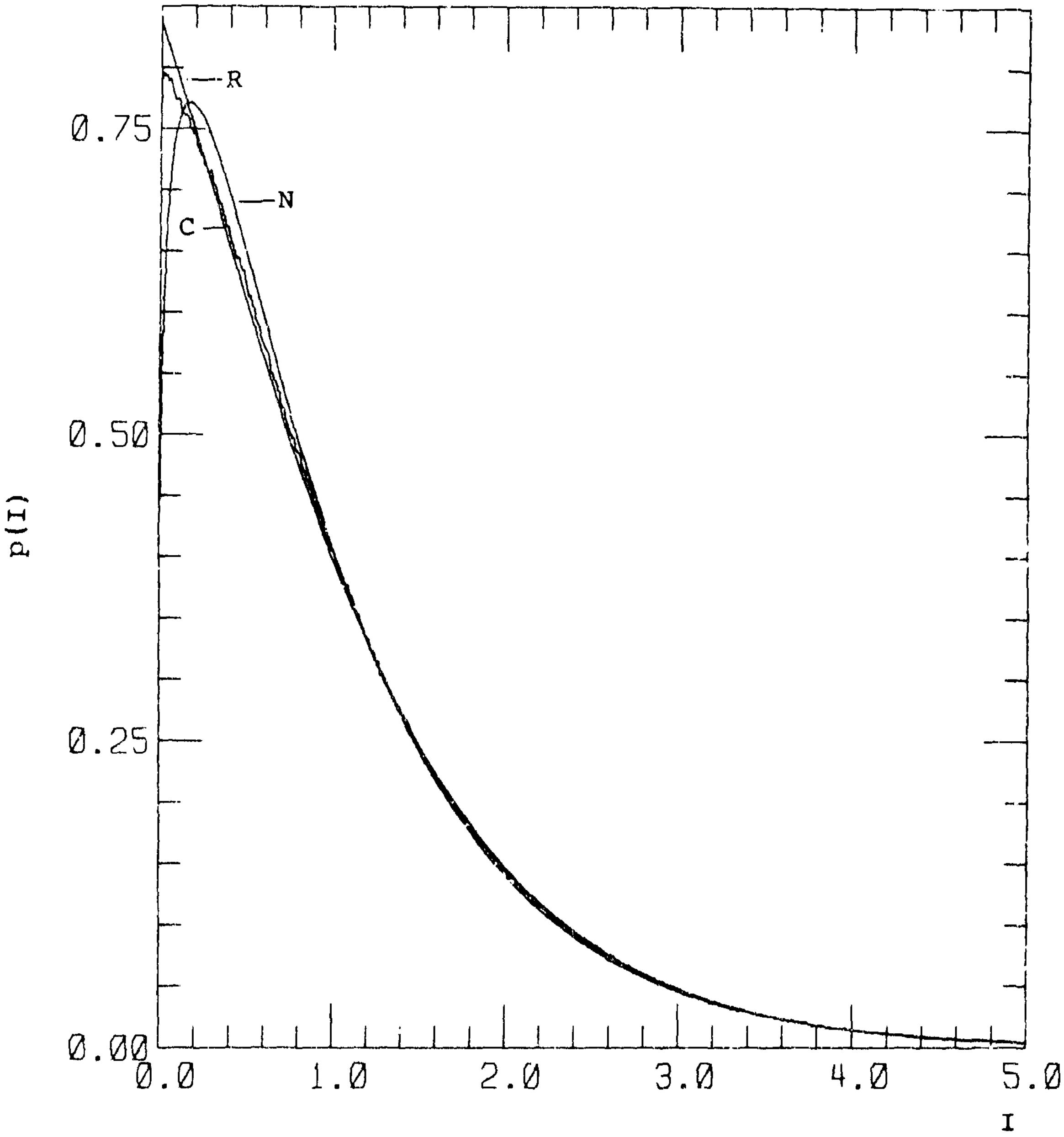

Figure C-18. Probability Distribution for
$s = 1.5$, $\chi^2 = 0.4$, $S_4{}^2 = 0.825$.

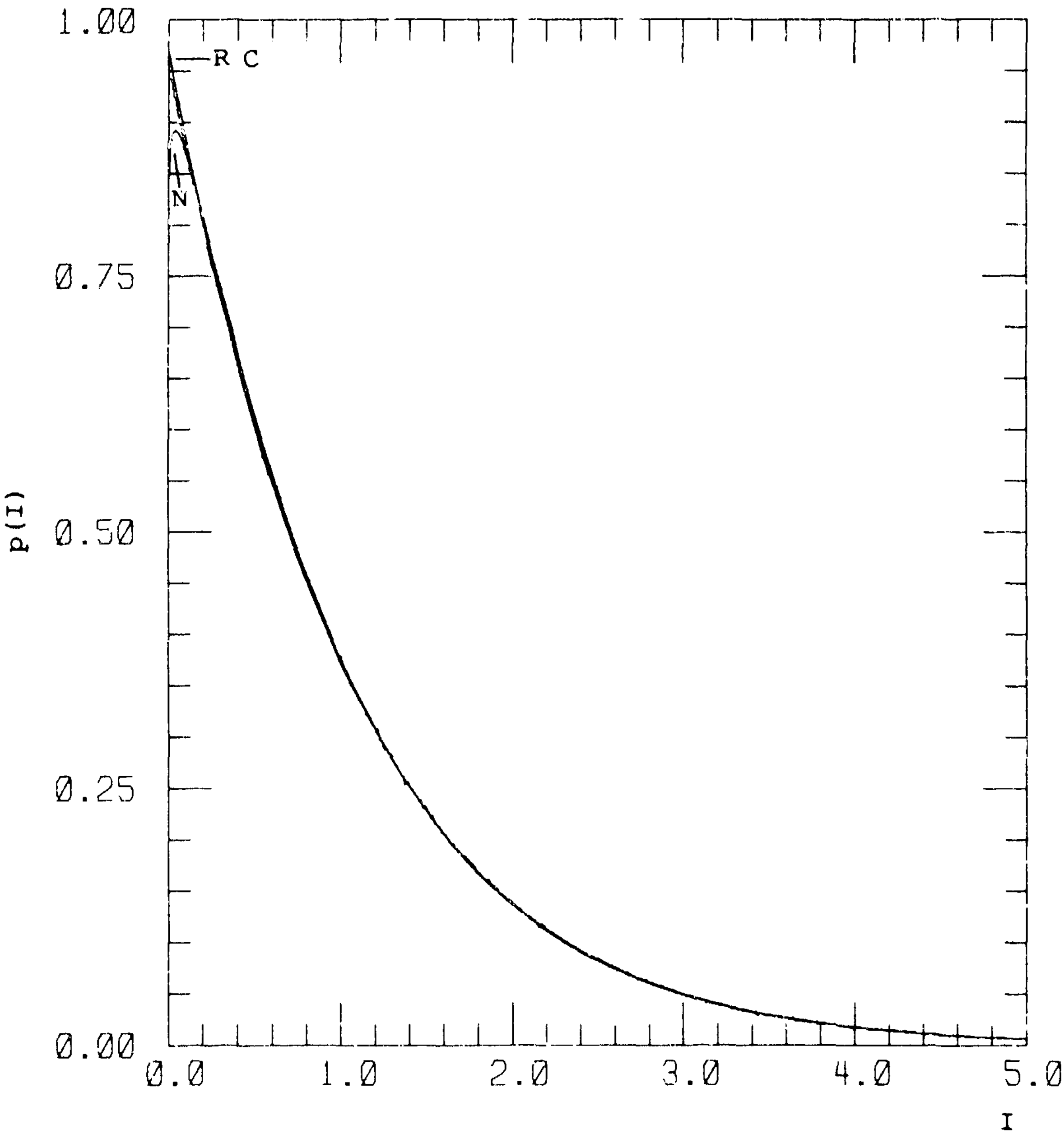

Figure C-19. Probability Distribution for $s = 1.5$, $\chi^2 = 0.7$, $S_4{}^2 = 0.958$.

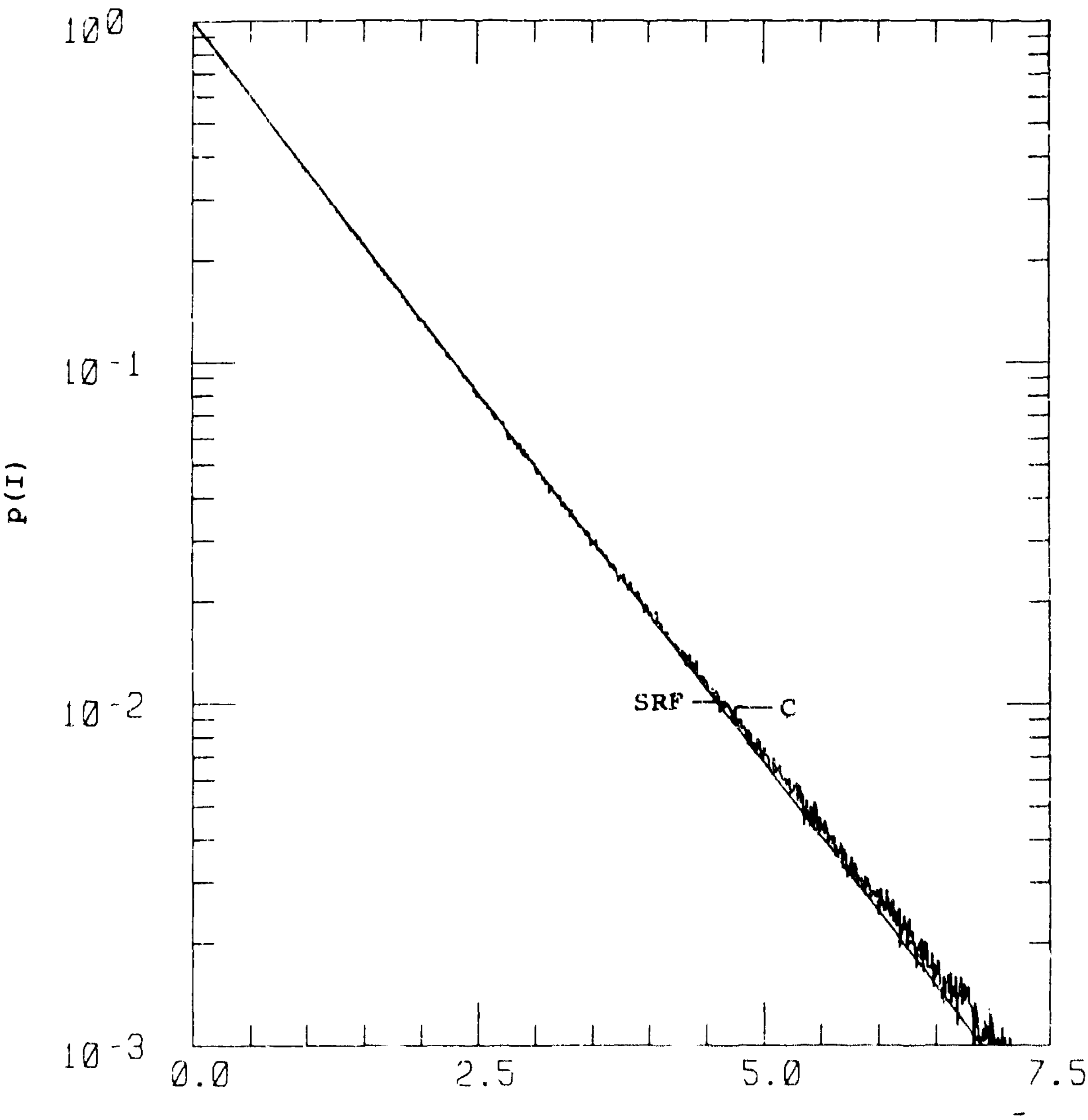

Figure C-20. Probability Distribution for $s = 1.$, $\chi^2 = 1.5$, $S_4^{\,2} = 1.03$.

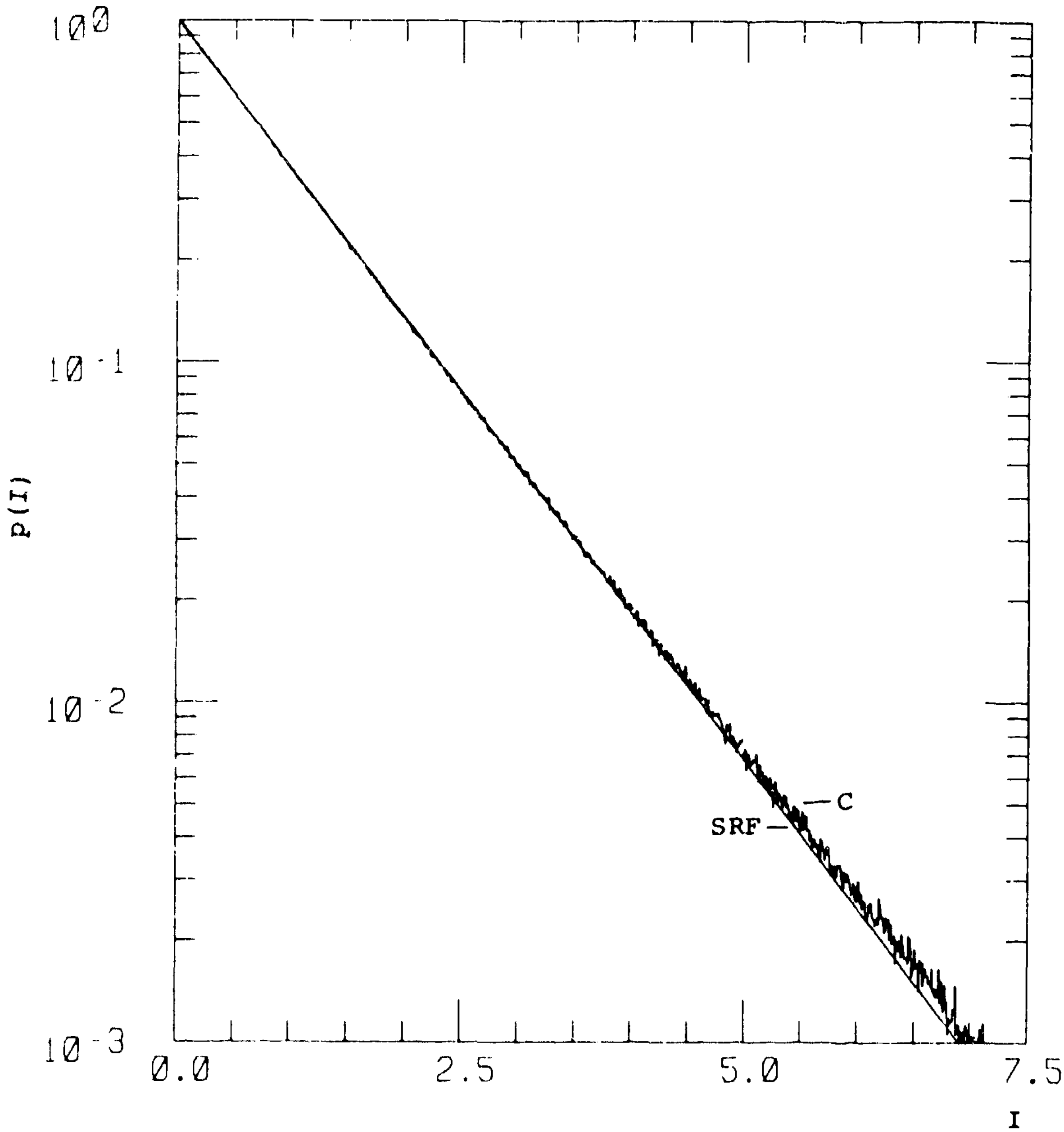

Figure C-21. Probability Distribution for $s = 1.5$, $\chi^2 = 3.0$, $S_4^2 = 1.03$.

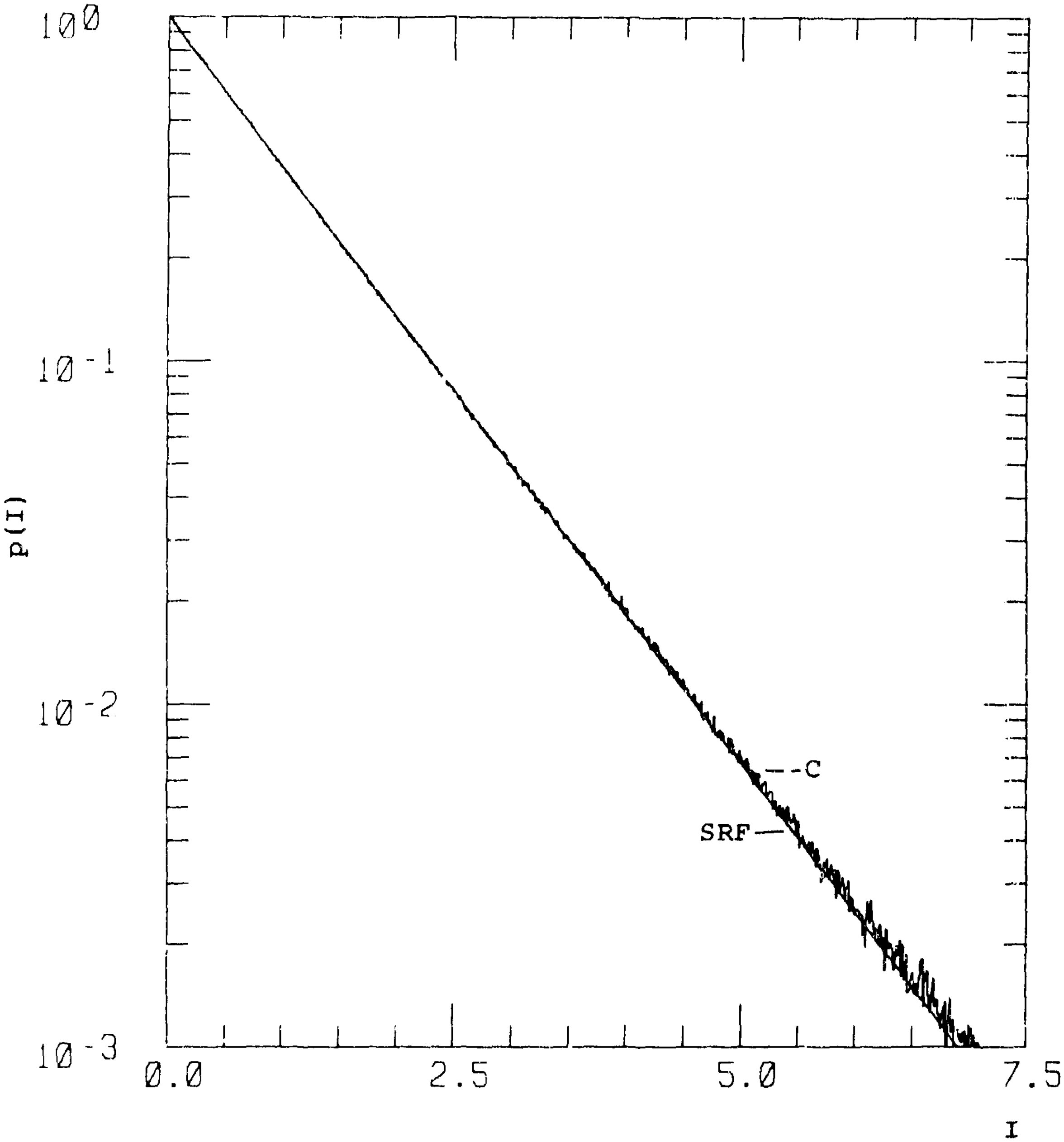

Figure C-22. Probability Distribution for $s = 1.5$, $\chi^2 = 7.0$, $S_4^{\ 2} = 1.02$.

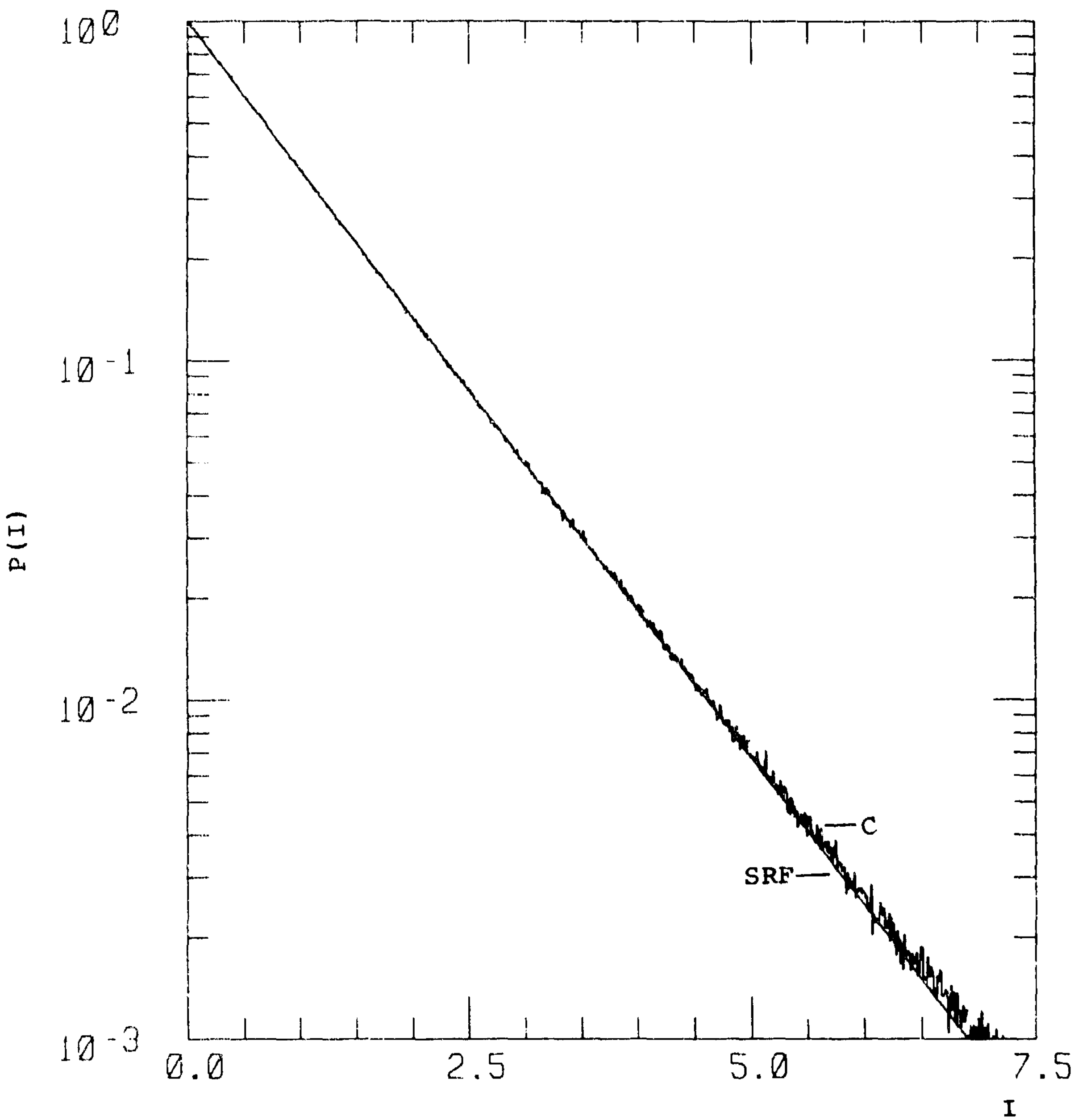

Figure C-23. Probability Distribution for $s = 1.5$, $\chi^2 = 10.0$, $S_4^{\ 2} = 1.02$.

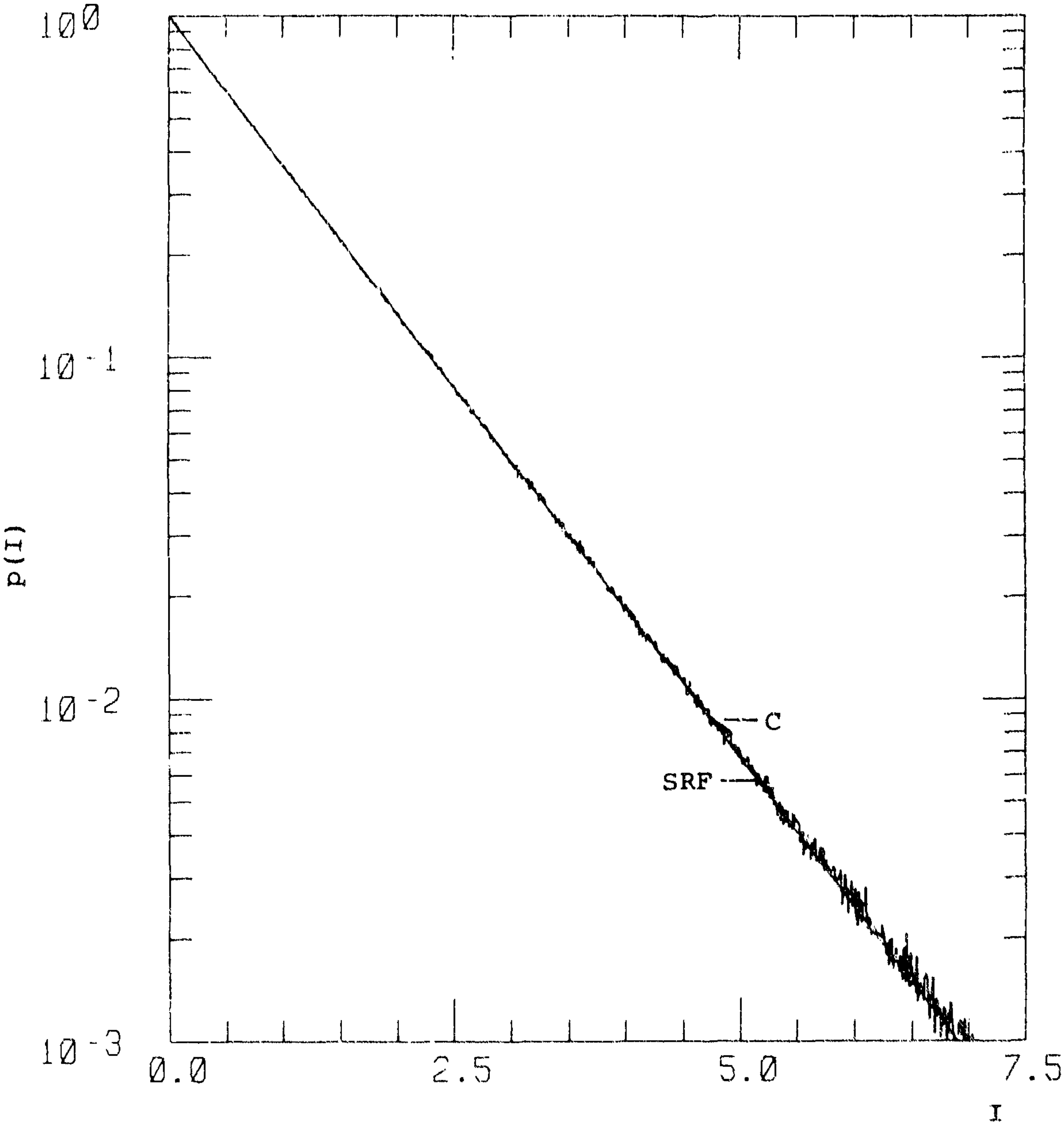

Figure C-24. Probability Distribution for $s = 1.5$, $\chi^2 = 20.0$, $S_4^{\ 2} = 1.01$.

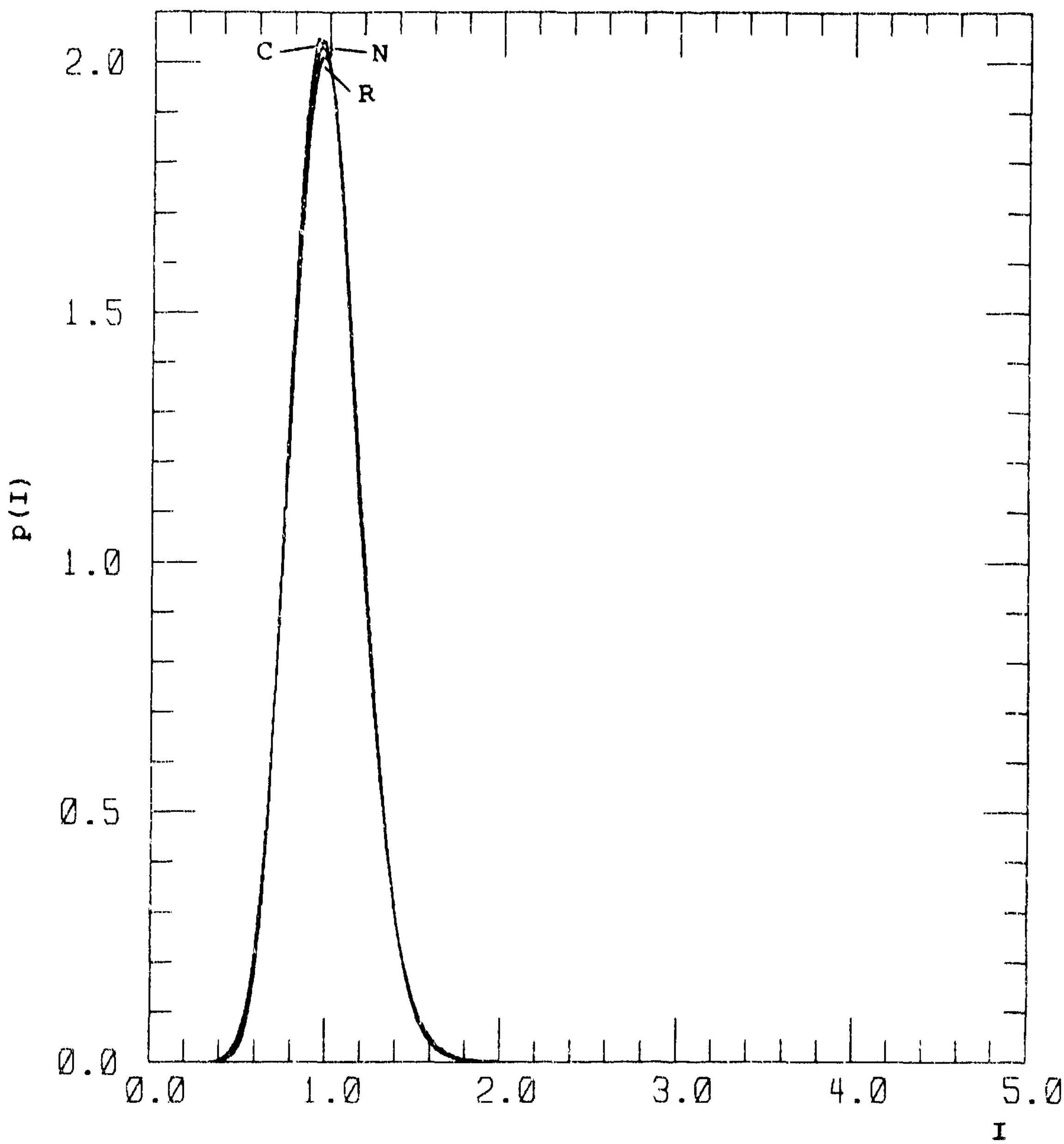

Figure C-25. Probability Distribution for $s = 2$, $\chi^2 = 0.01$, $S_4^{\,2} = 0.040$.

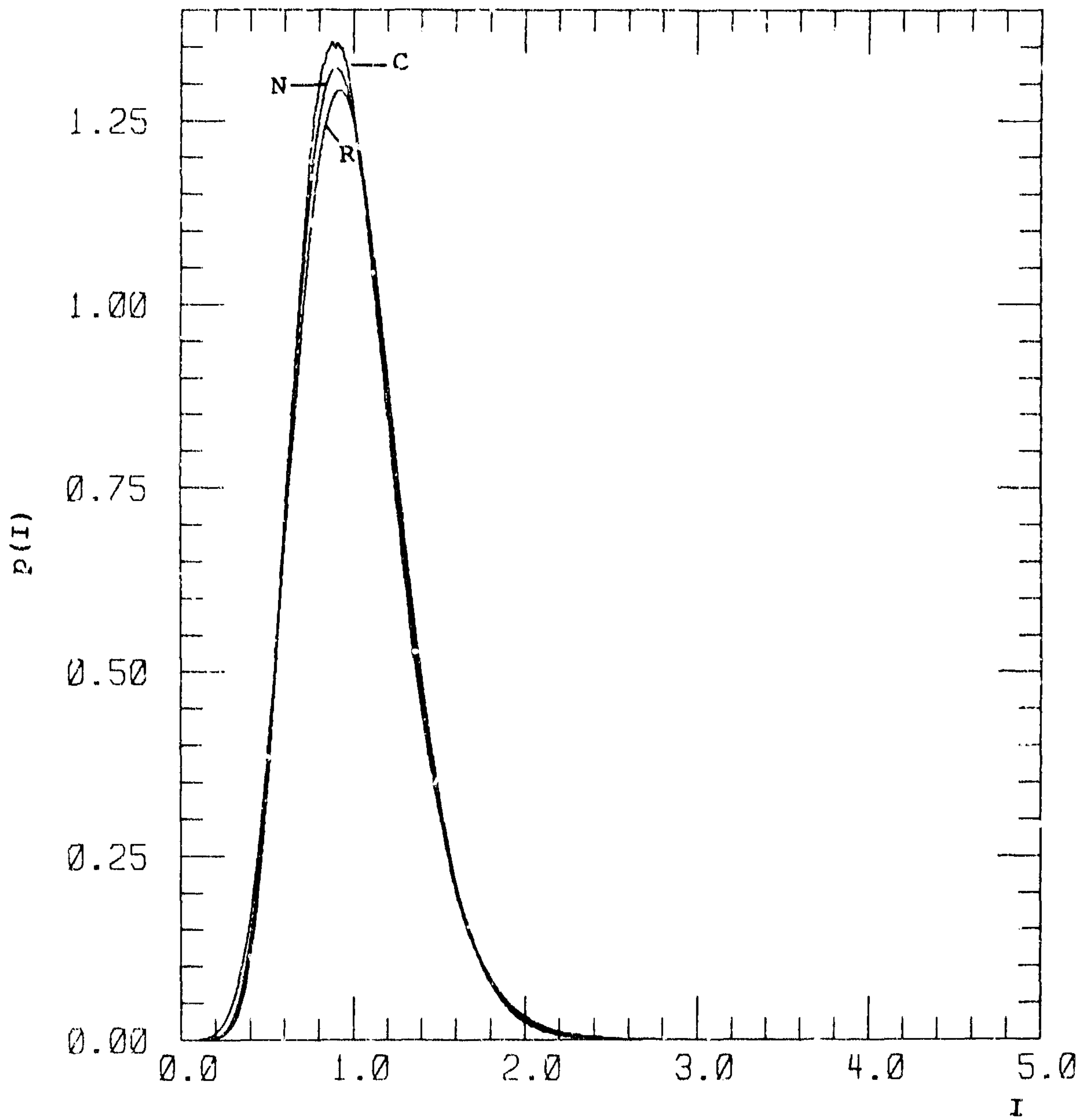

Figure C-26. Probability Distribution for
$s = 2$, $\chi^2 = 0.025$, $S_4{}^2 = 0.099$.

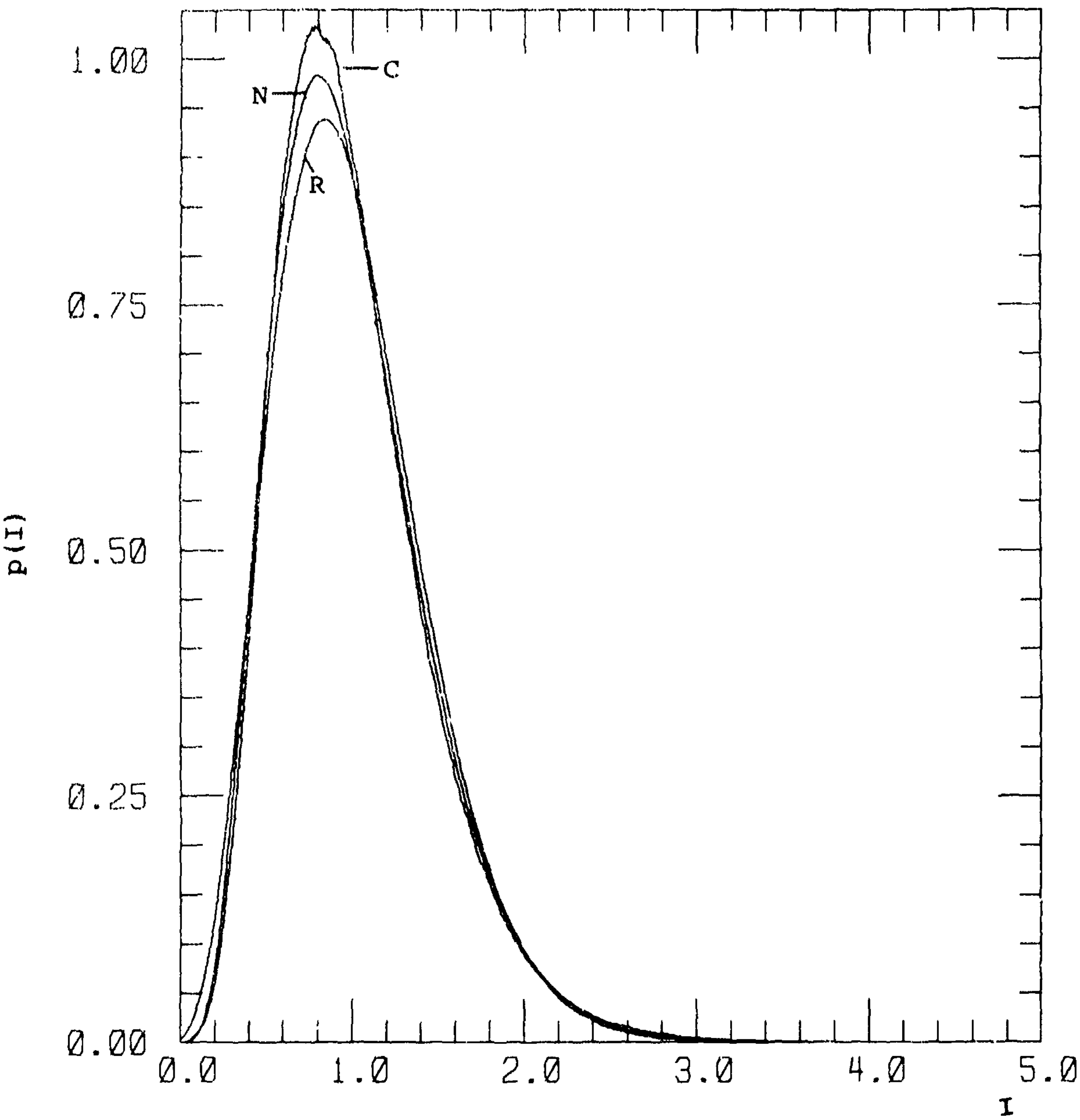

Figure C-27. Probability Distribution for $s = 2$, $\chi^2 = 0.05$, $S_4^{\,2} = 0.197$.

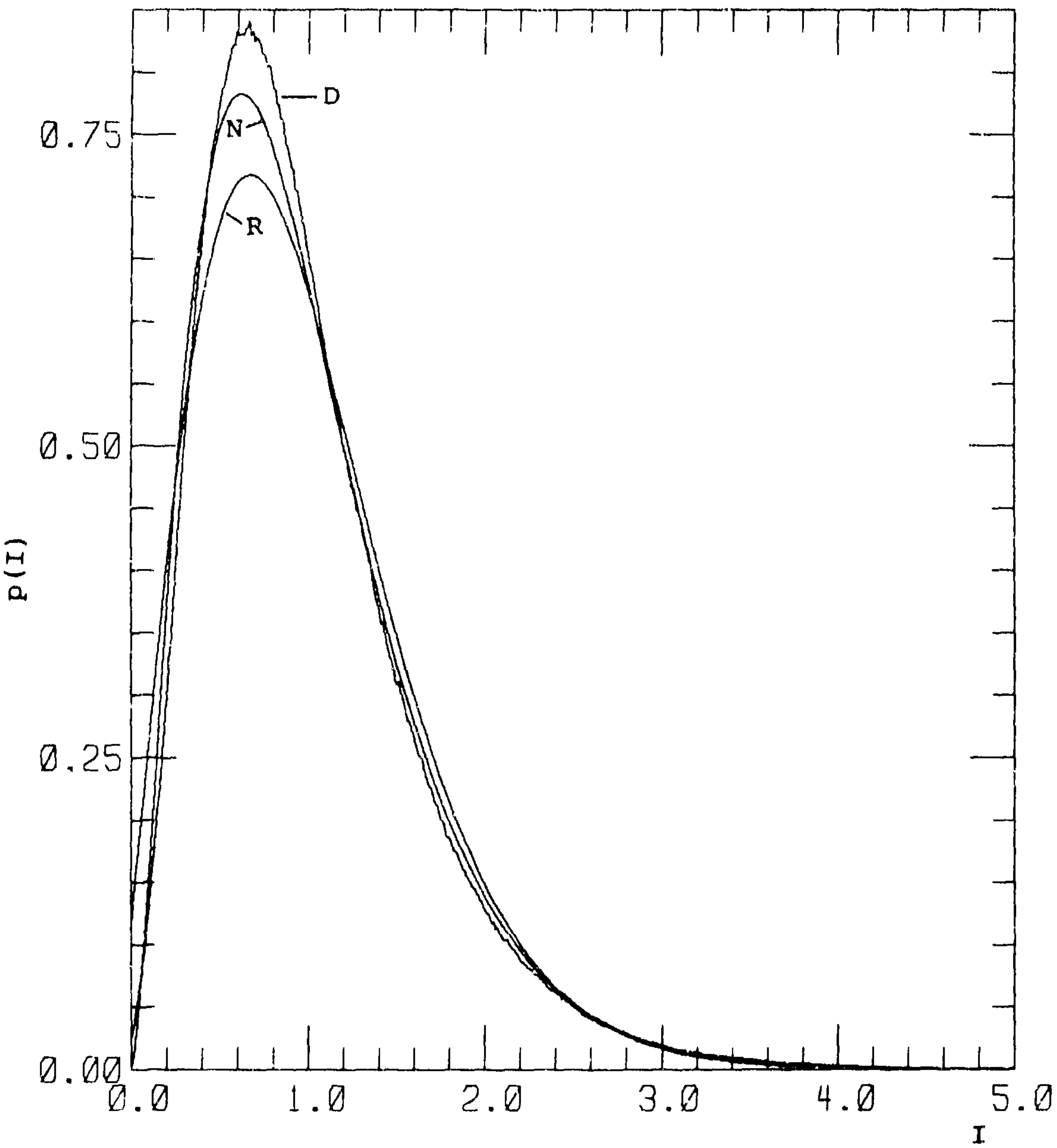

Figure C-28. Probability Distribution for $s = 2$, $\chi^2 = 0.1$, $S_4{}^2 = 0.378$.

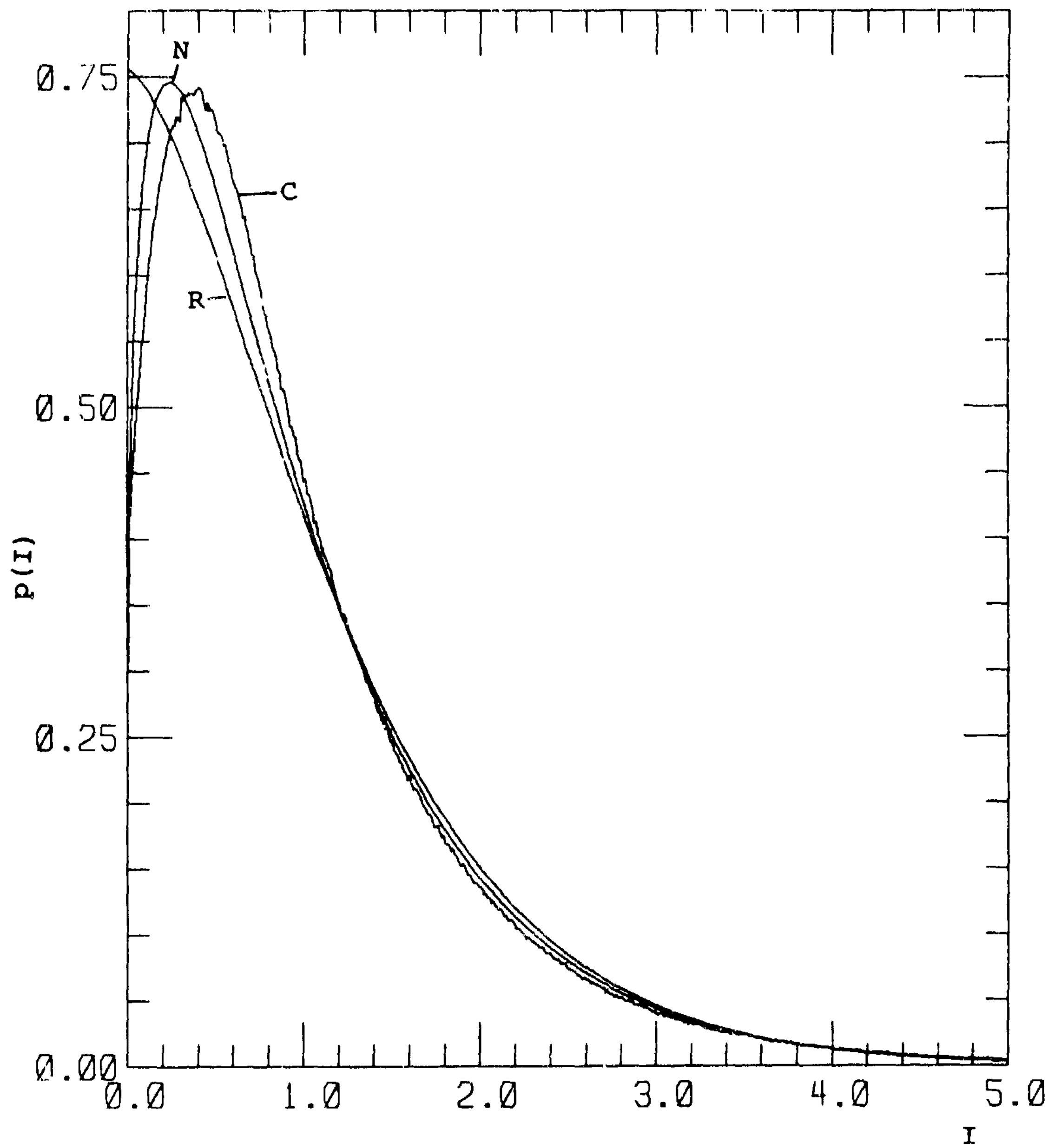

Figure C-29. Probability Distribution for
$s = 2$, $\chi^2 = 0.25$, $S_4^2 = 0.764$.

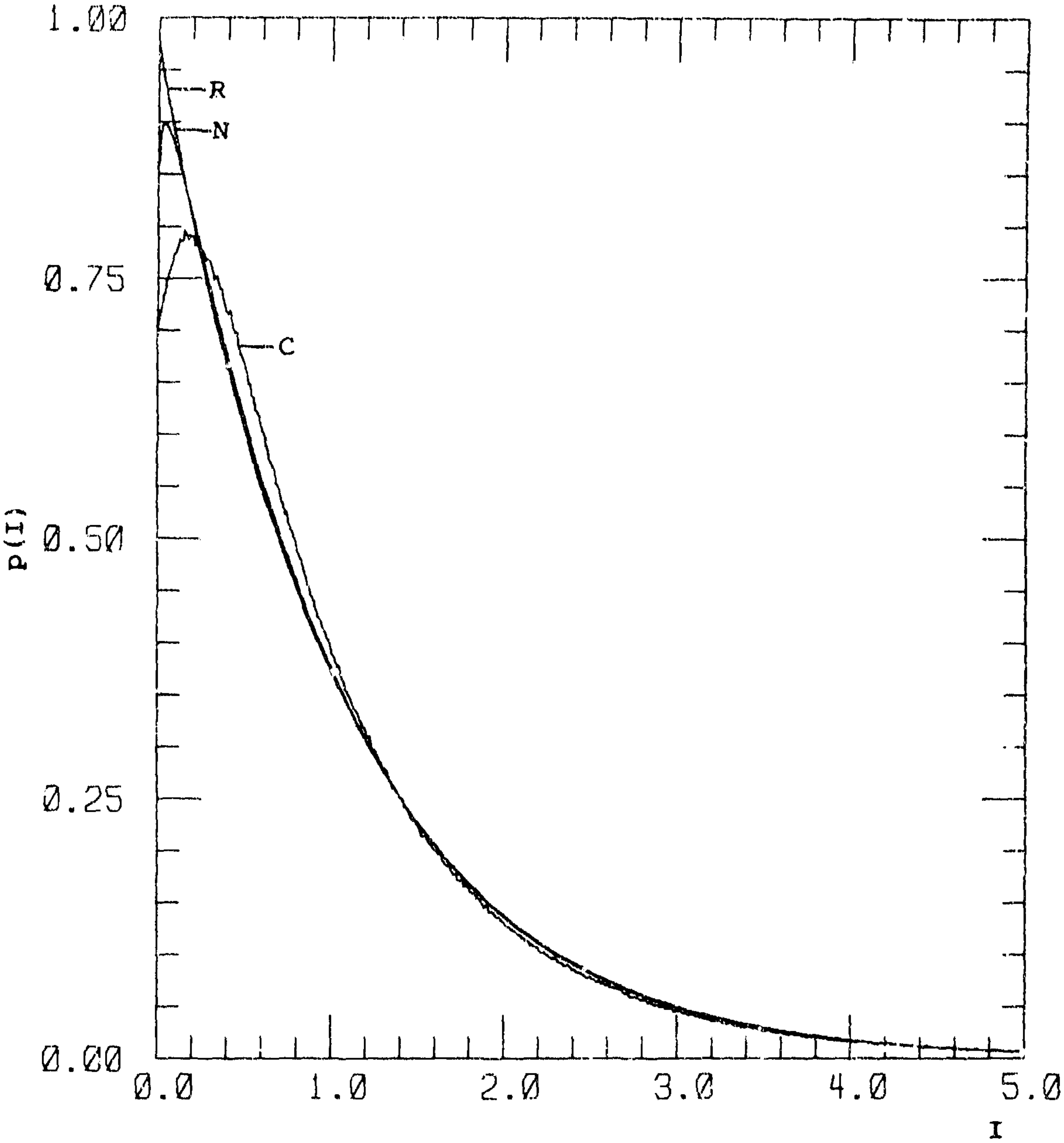

Figure C-30. Probability Distribution for
$s = 2$, $\chi^2 = 0.4$, $S_4{}^2 = 0.962$.

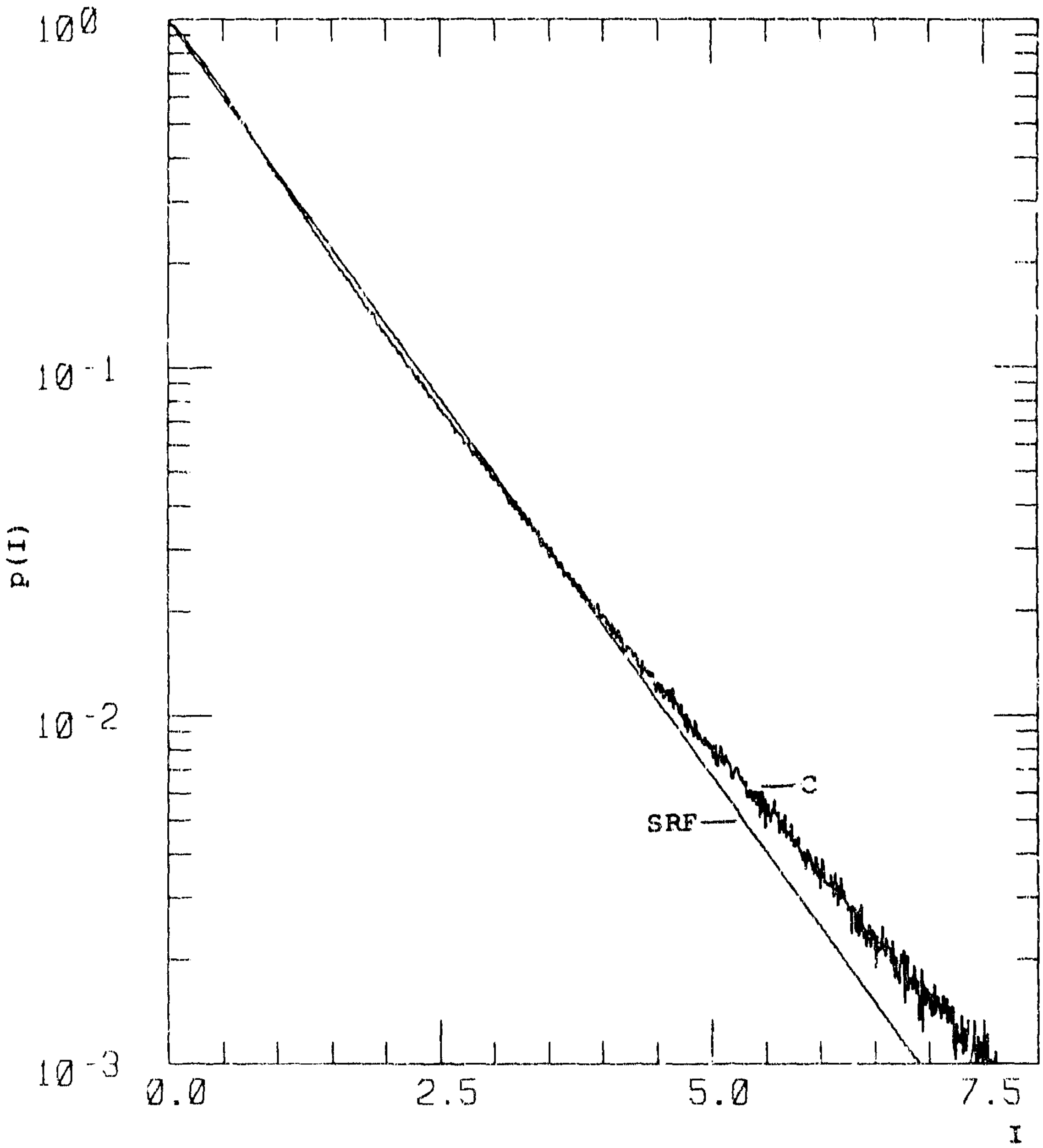

Figure C-31. Probability Distribution for $s = 2$, $\chi^2 = 0.7$, $S_4^{\ 2} = 1.12$.

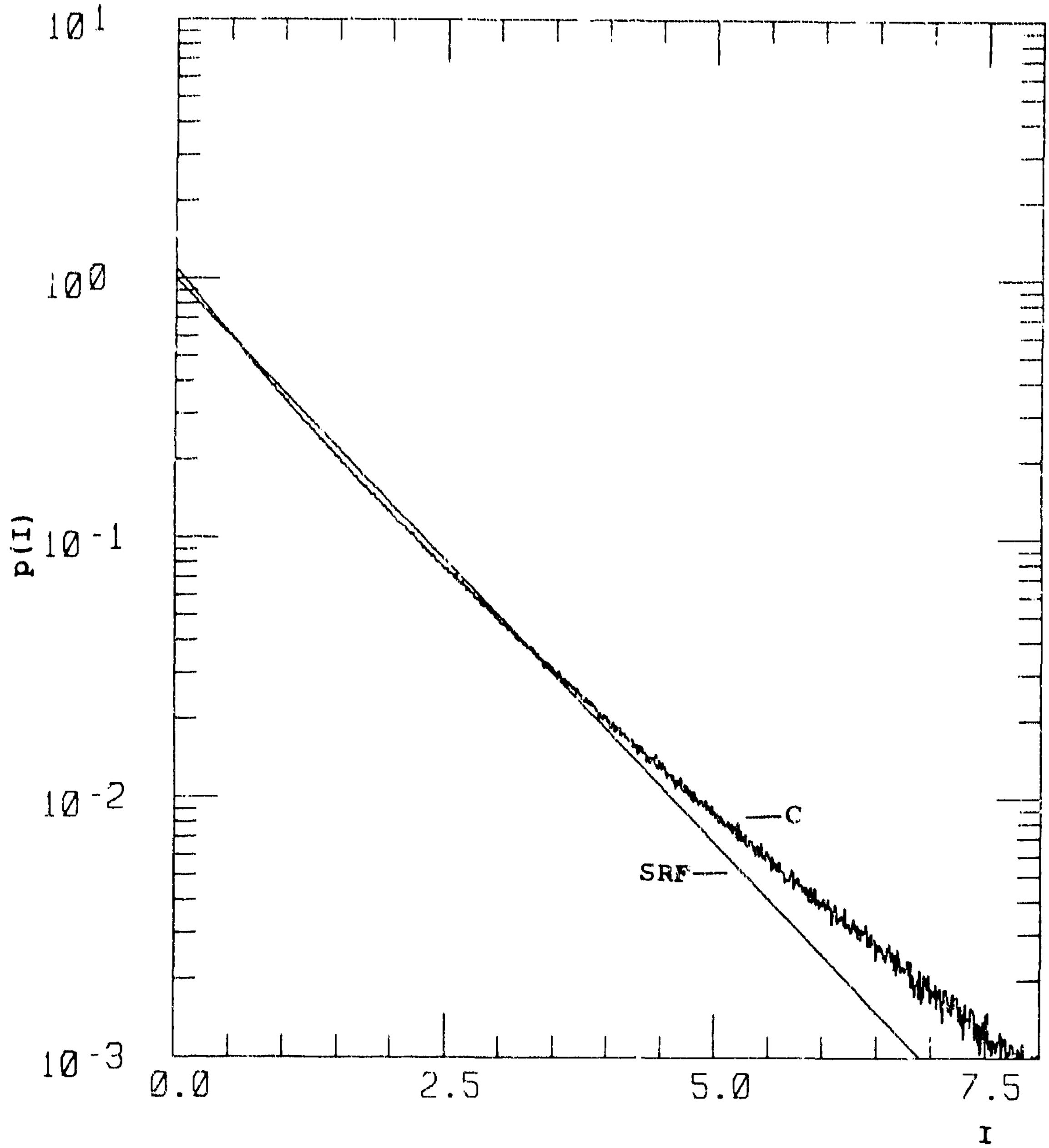

Figure C-32. Probability Distribution for $s = 2$, $\chi^2 = 1.5$, $S_4{}^2 = 1.20$.

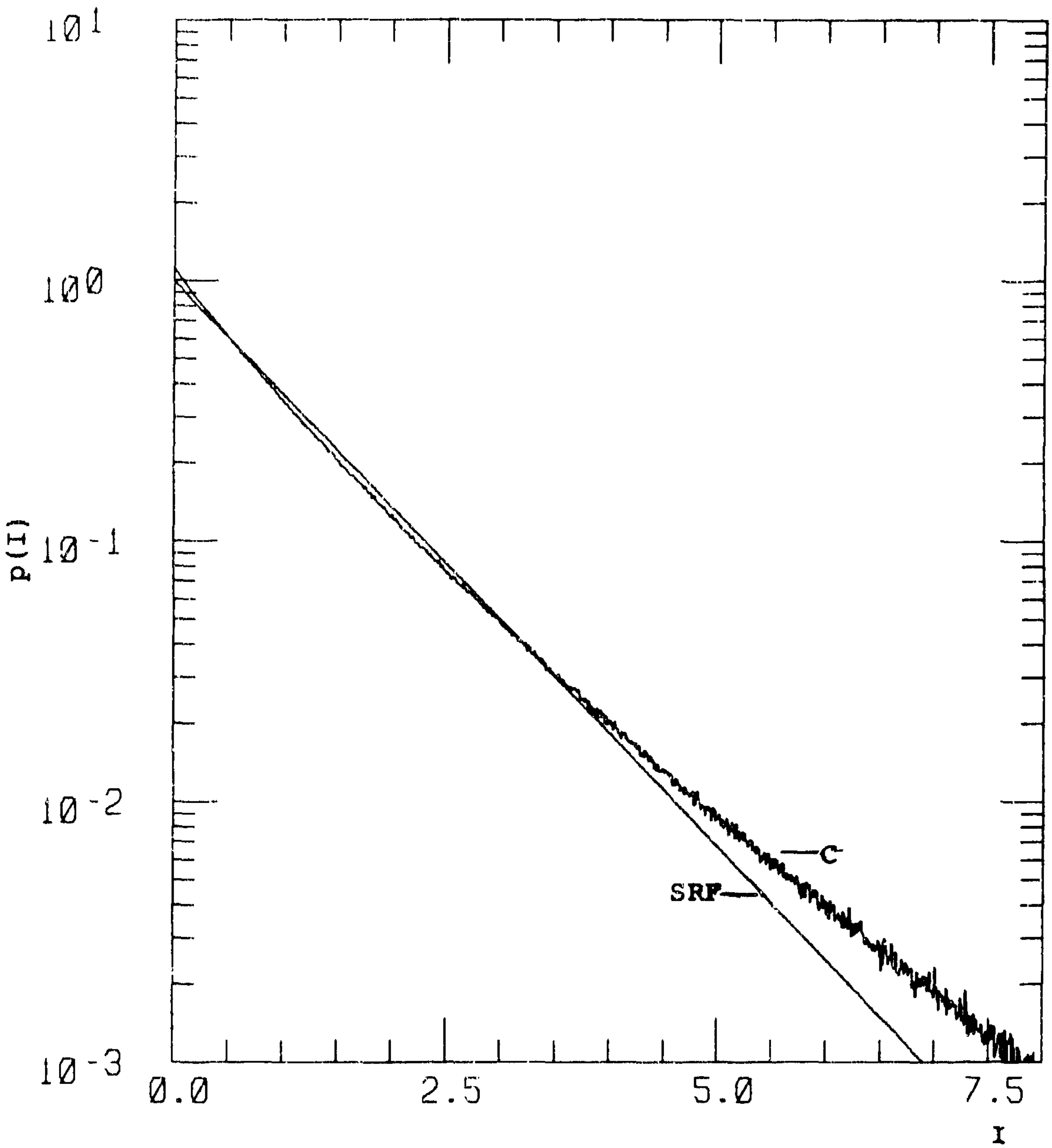

Figure C-33. Probability Distribution for
$s = 2$, $\chi^2 = 3.0$, $S_4{}^2 = 1.20$.

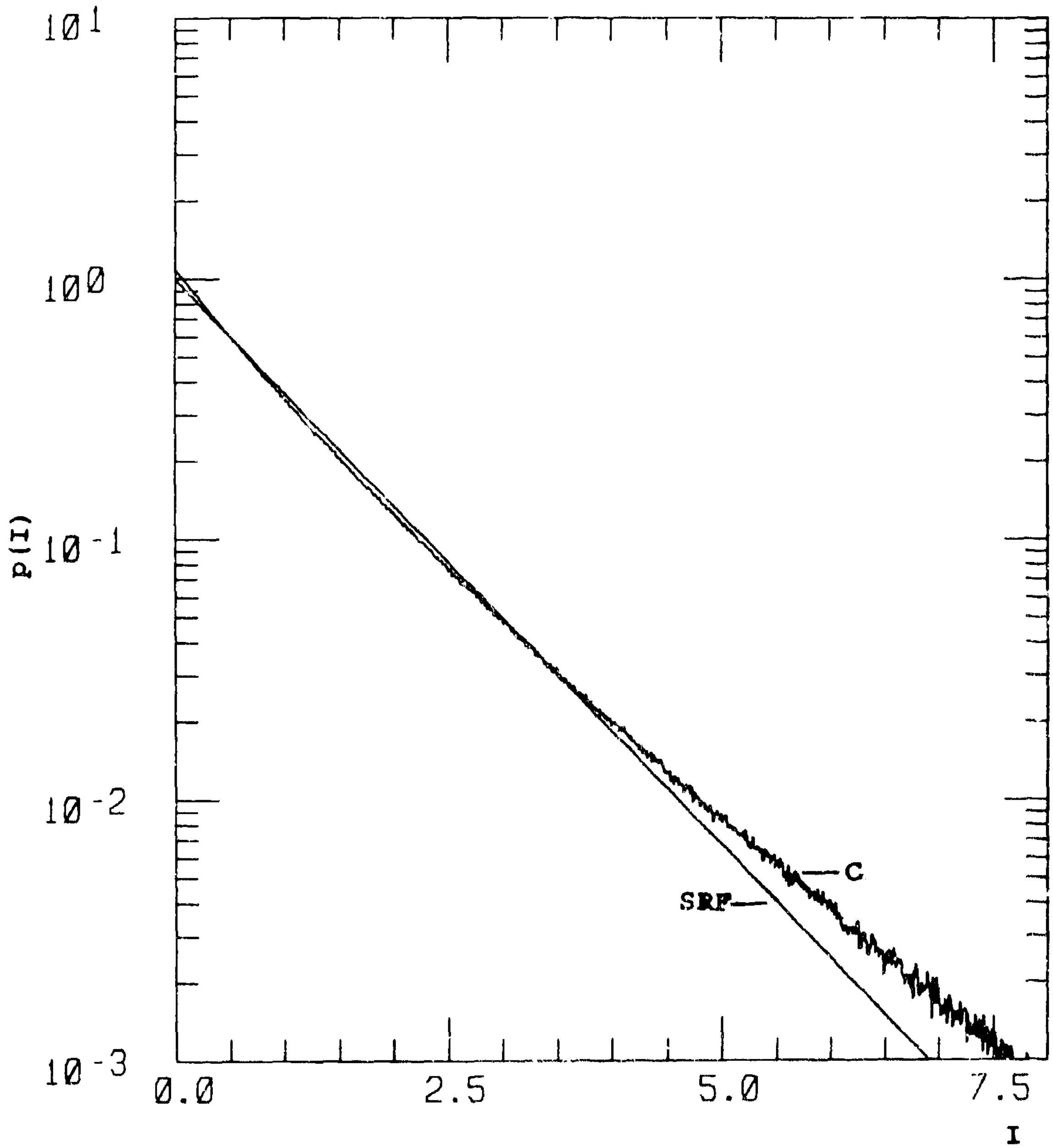

Figure C-34. Probability Distribution for
$s = 2$, $\sigma^2 = 7.0$, $S_4^{\ 2} = 1.17$.

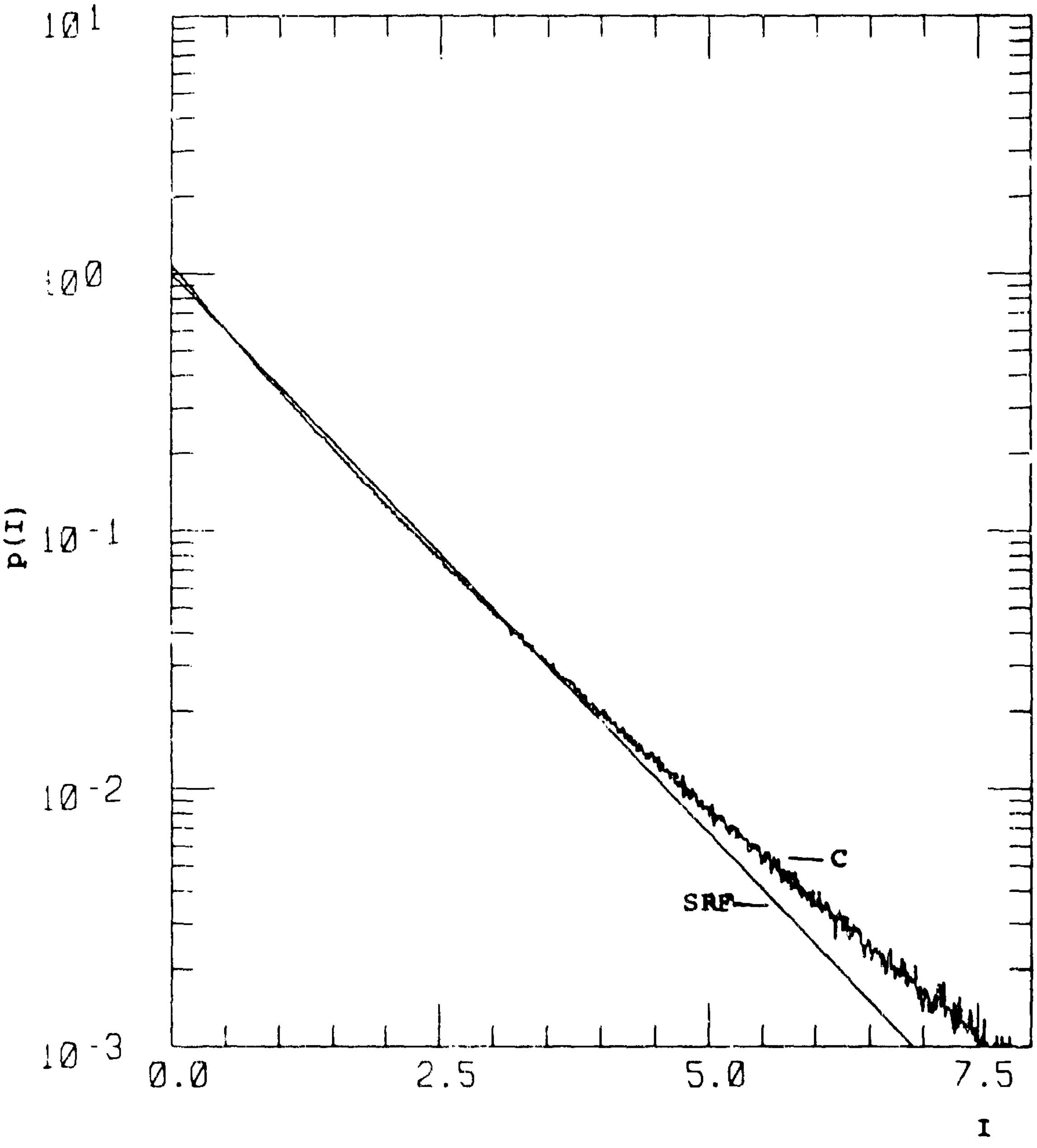

Figure C-35. Probability Distribution for $s = 2$, $\chi^2 = 10.0$, $S_4^2 = 1.16$.

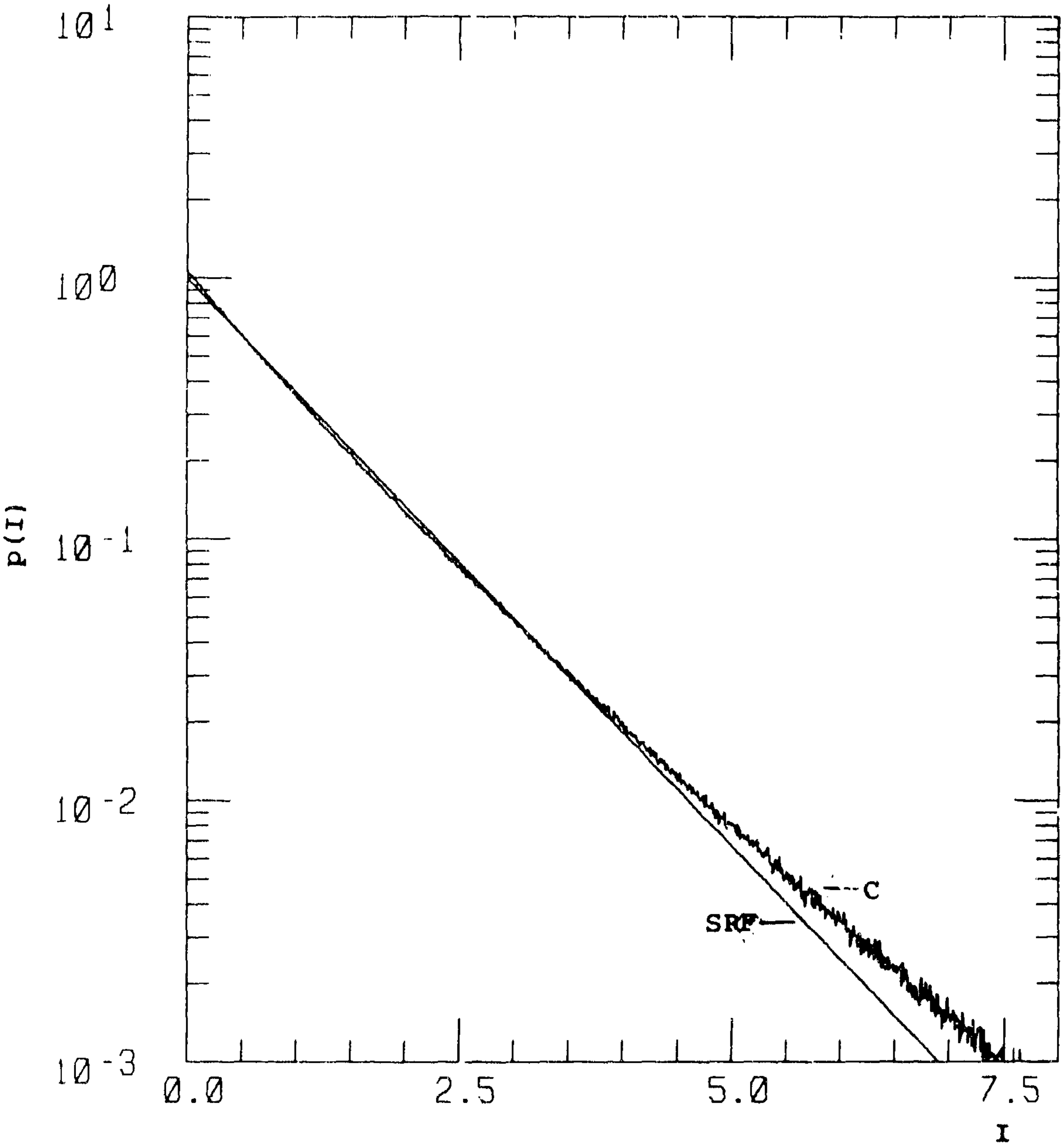

Figure C-36. Probability Distribution for $s = 2$, $\chi^2 = 20.0$, $S_4^{\ 2} = 1.13$.

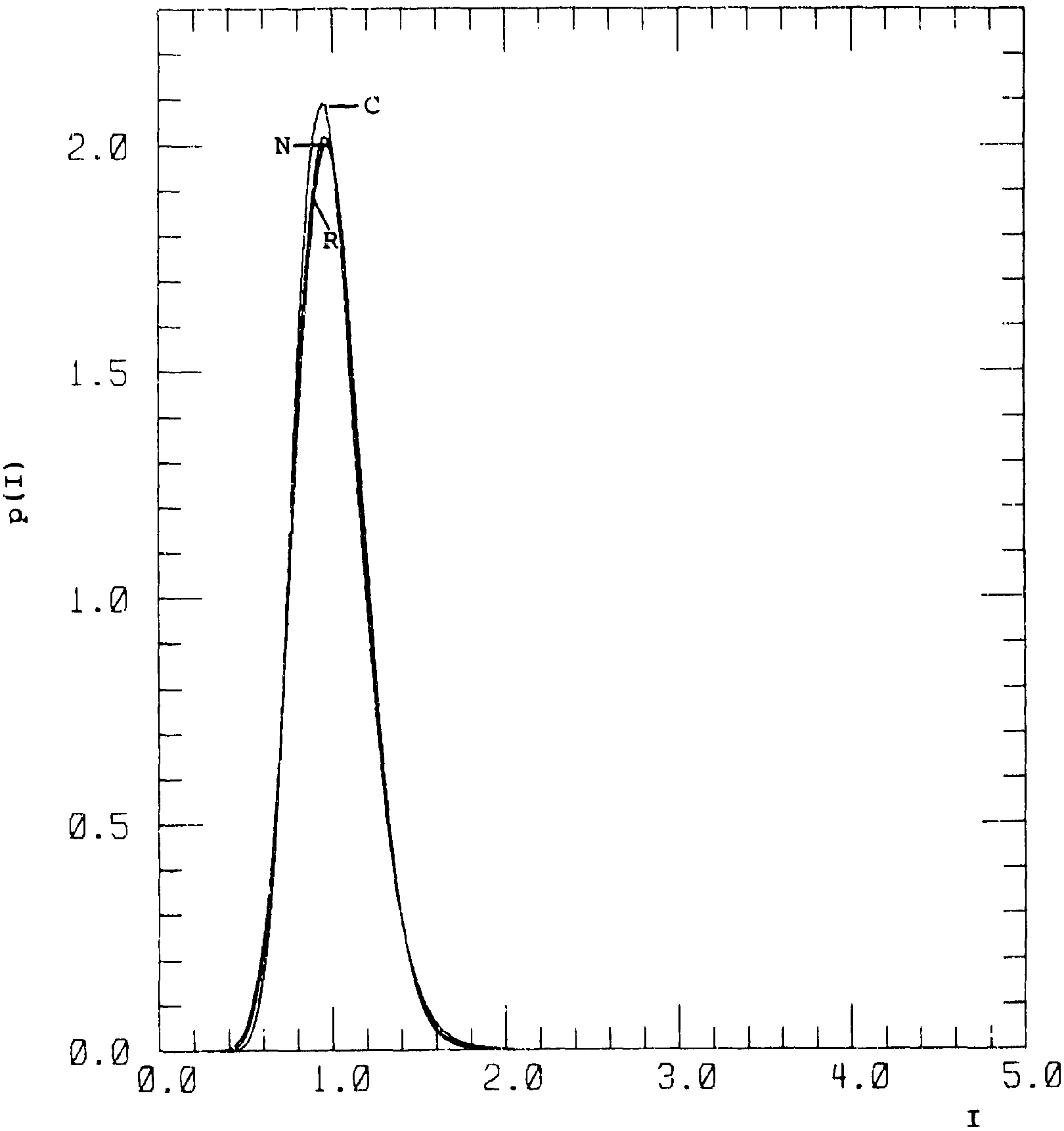

Figure C-37. Probability Distribution for
$s = 2.5$, $\chi^2 = 0.01$, $S_4{}^2 = 0.40$.

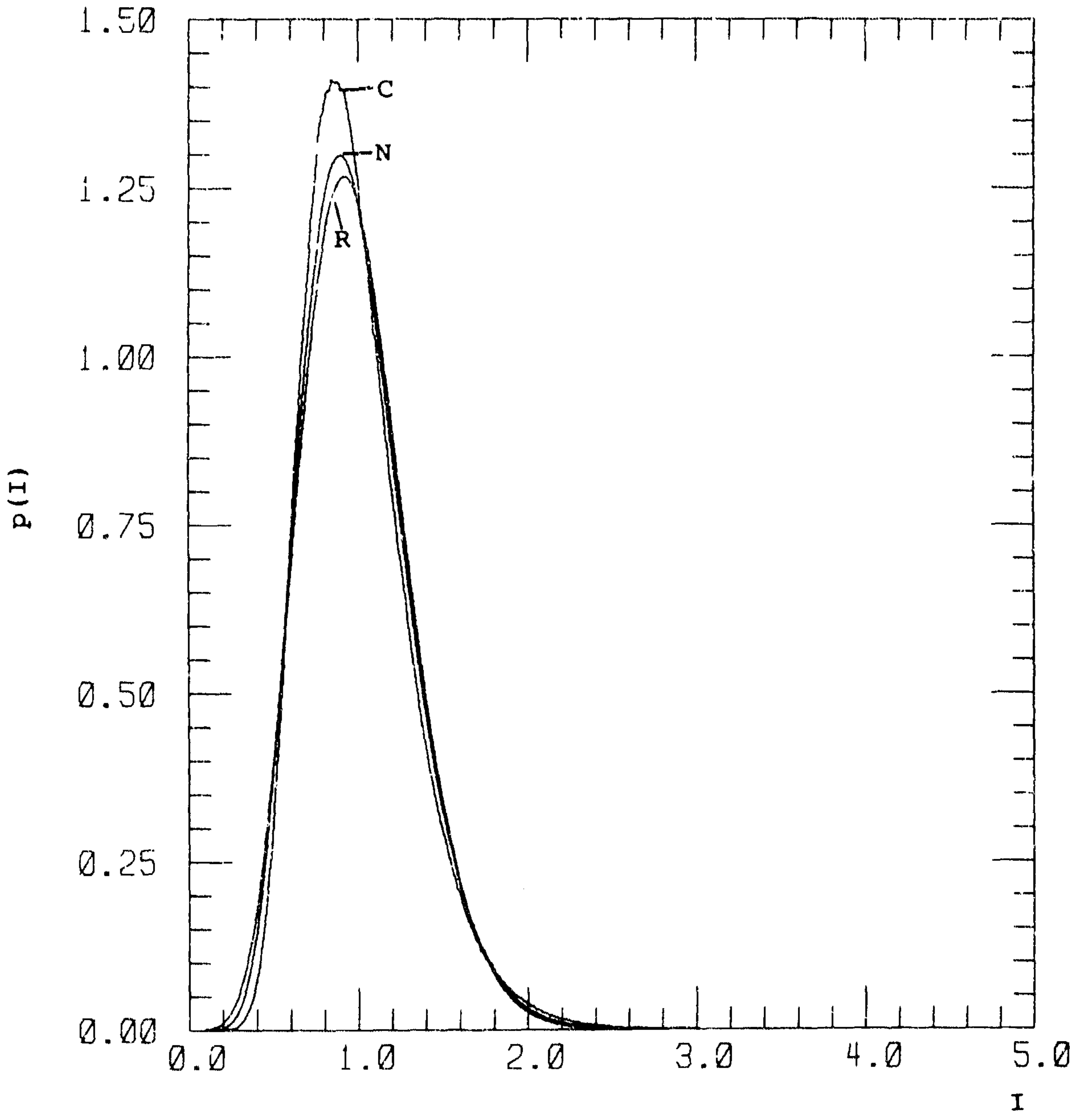

Figure C-38. Probability Distribution for $s = 2.5$, $\chi^2 = 0.025$, $S_4^{\ 2} = 0.103$.

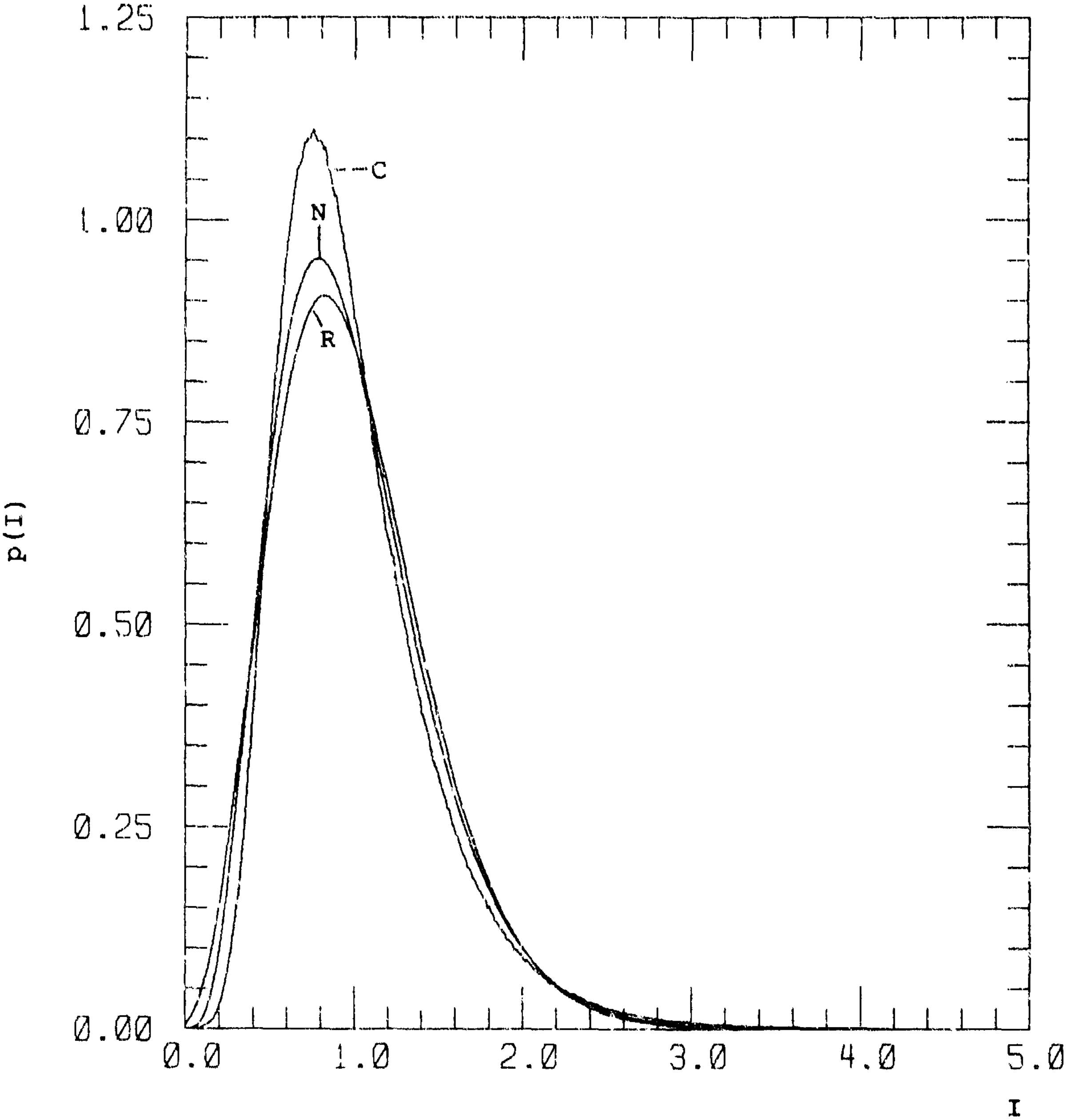

Figure C-39. Probability Distribution for $s = 2.5$, $\chi^2 = 0.05$, $S_4^{\,2} = 0.213$.

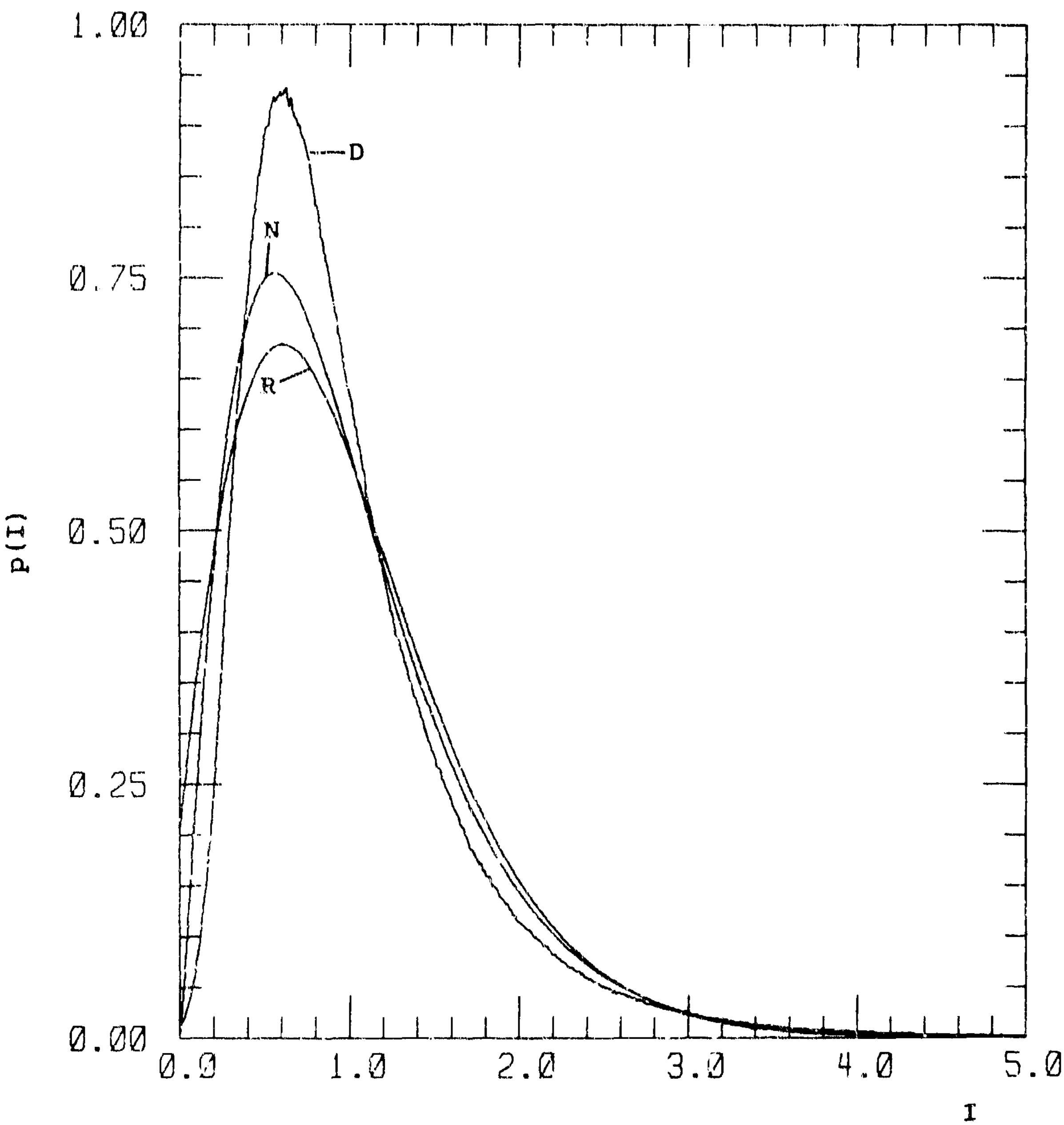

Figure C-40. Probability Distribution for $s = 2.5$, $\chi^2 = 0.1$, $S_4^2 = 0.438$.

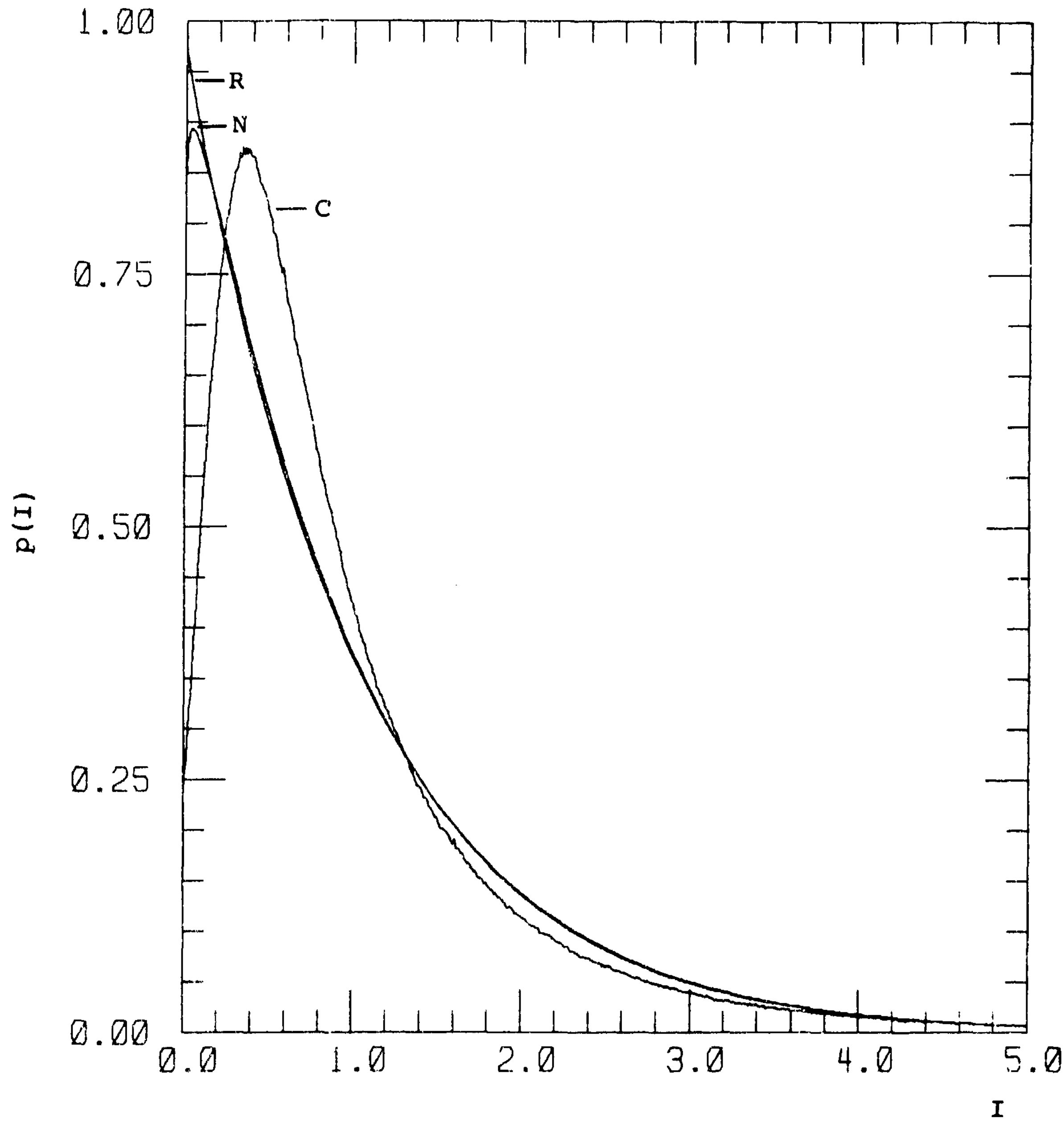

Figure C-41. Probability Distribution for $s = 2.5$, $\chi^2 = 0.25$, $S_4^{\;2} = 0.959$.

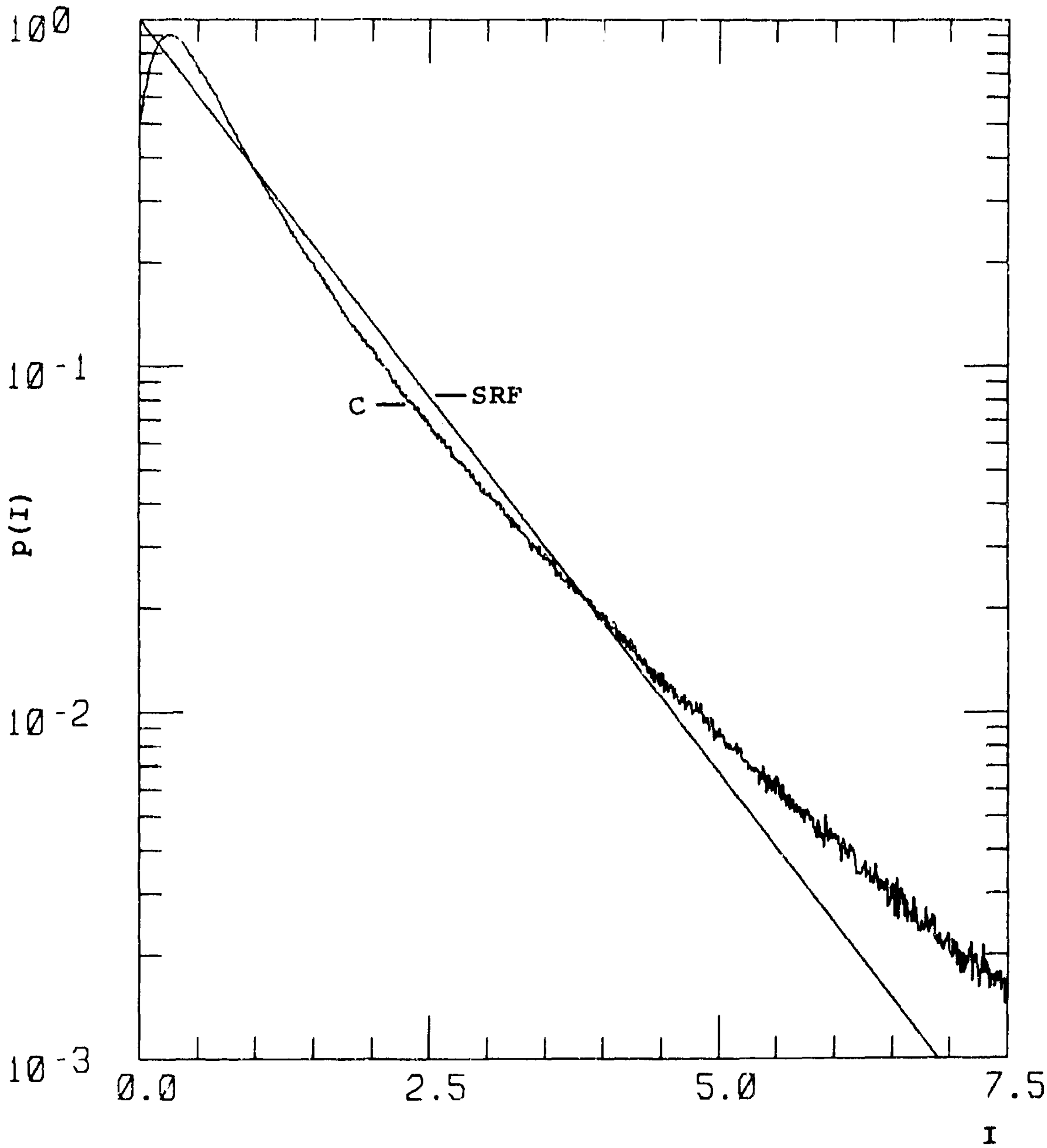

Figure C-42. Probability Distribution for
$s = 2.5$, $\chi^2 = 0.4$, $S_4{}^2 = 1.21$.

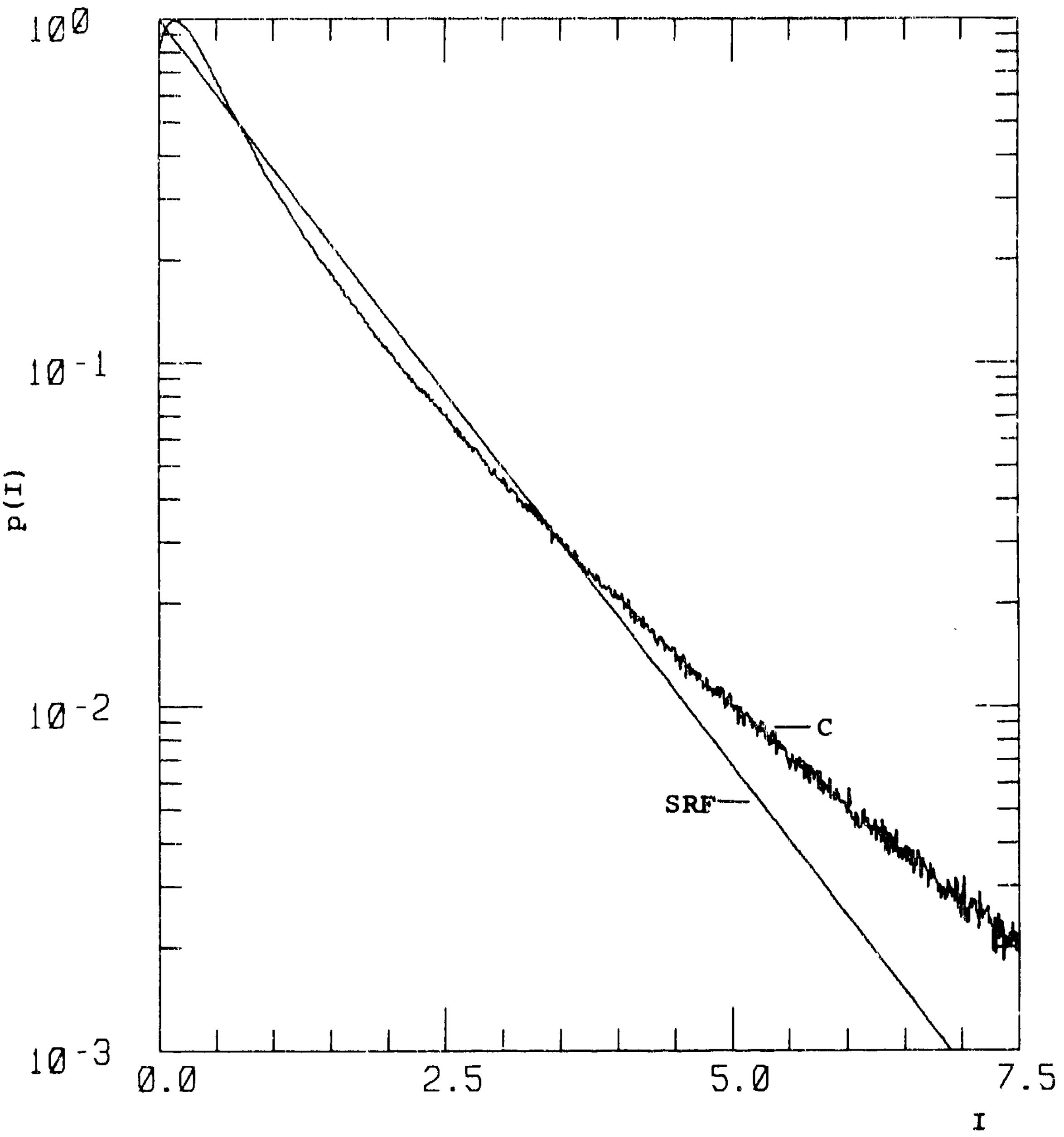

Figure C-43. Probability Distribution for $s = 2.5$, $\chi^2 = 0.7$, $S_4^2 = 1.42$.

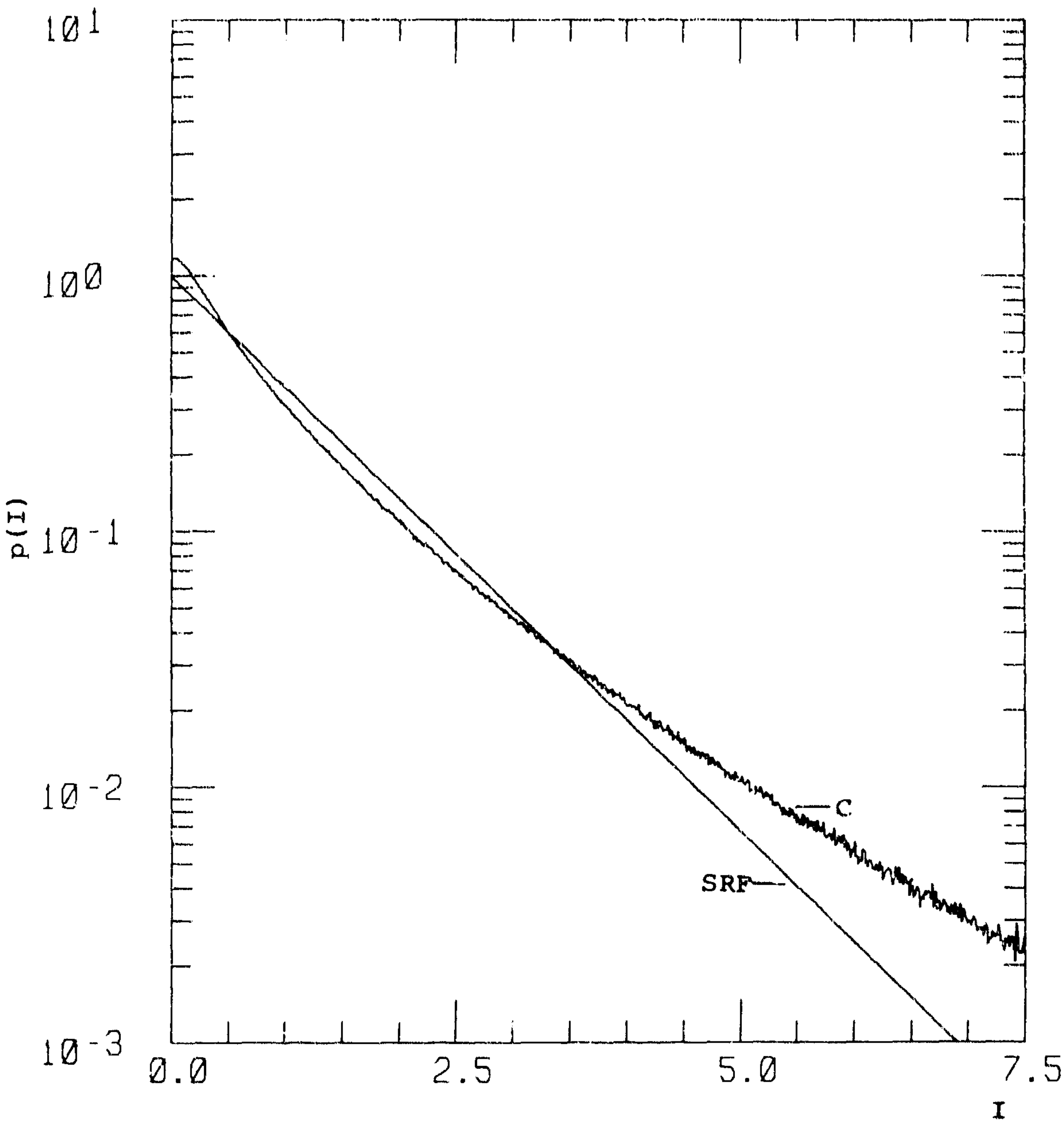

Figure C-44. Probability Distribution for $s = 2.5$, $\chi^2 = 1.5$, $S_4{}^2 = 1.55$.

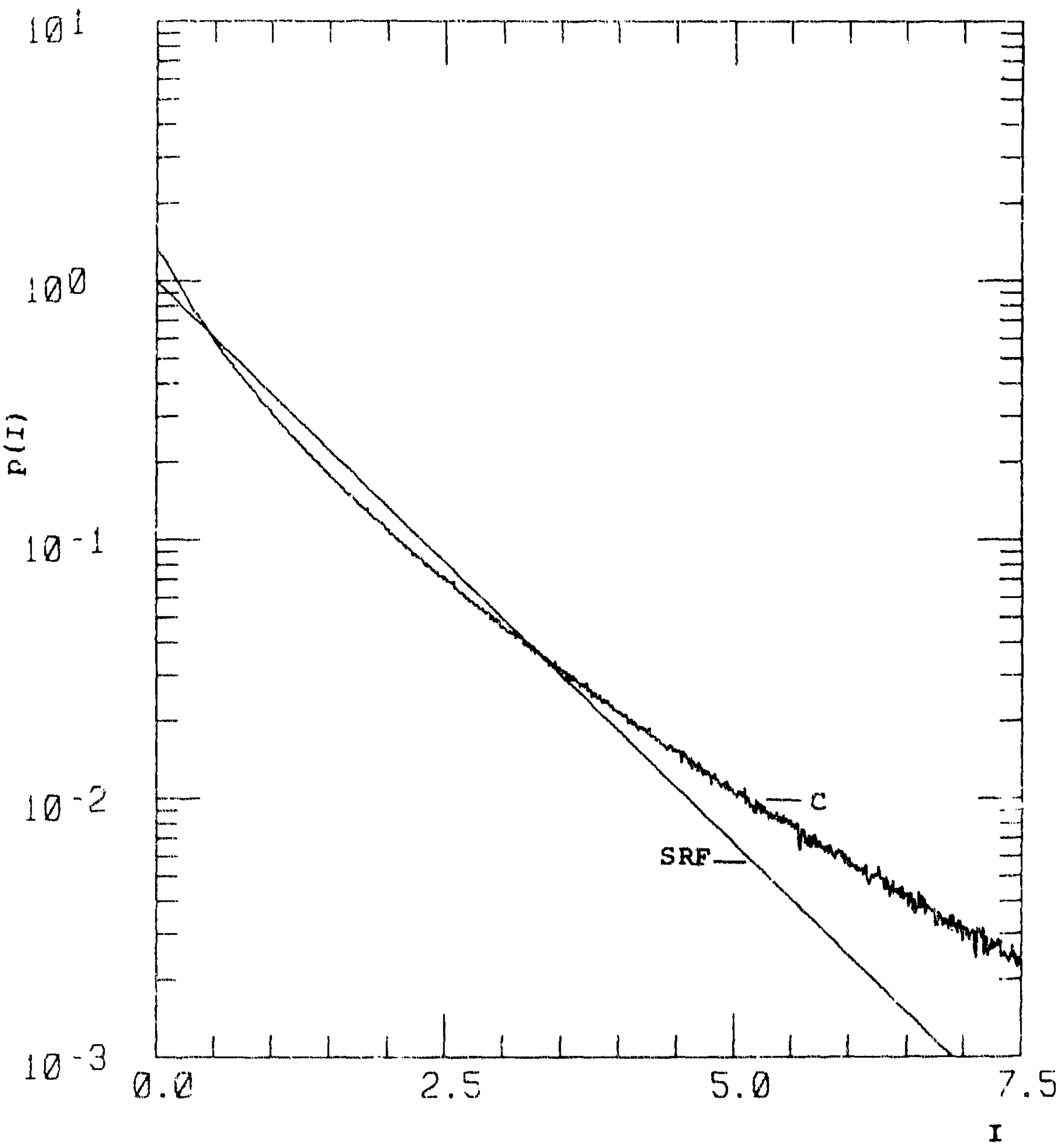

Figure C-45. Probability Distribution for $s = 2.5$, $\chi^2 = 3.0$, $S_4^2 = 1.57$.

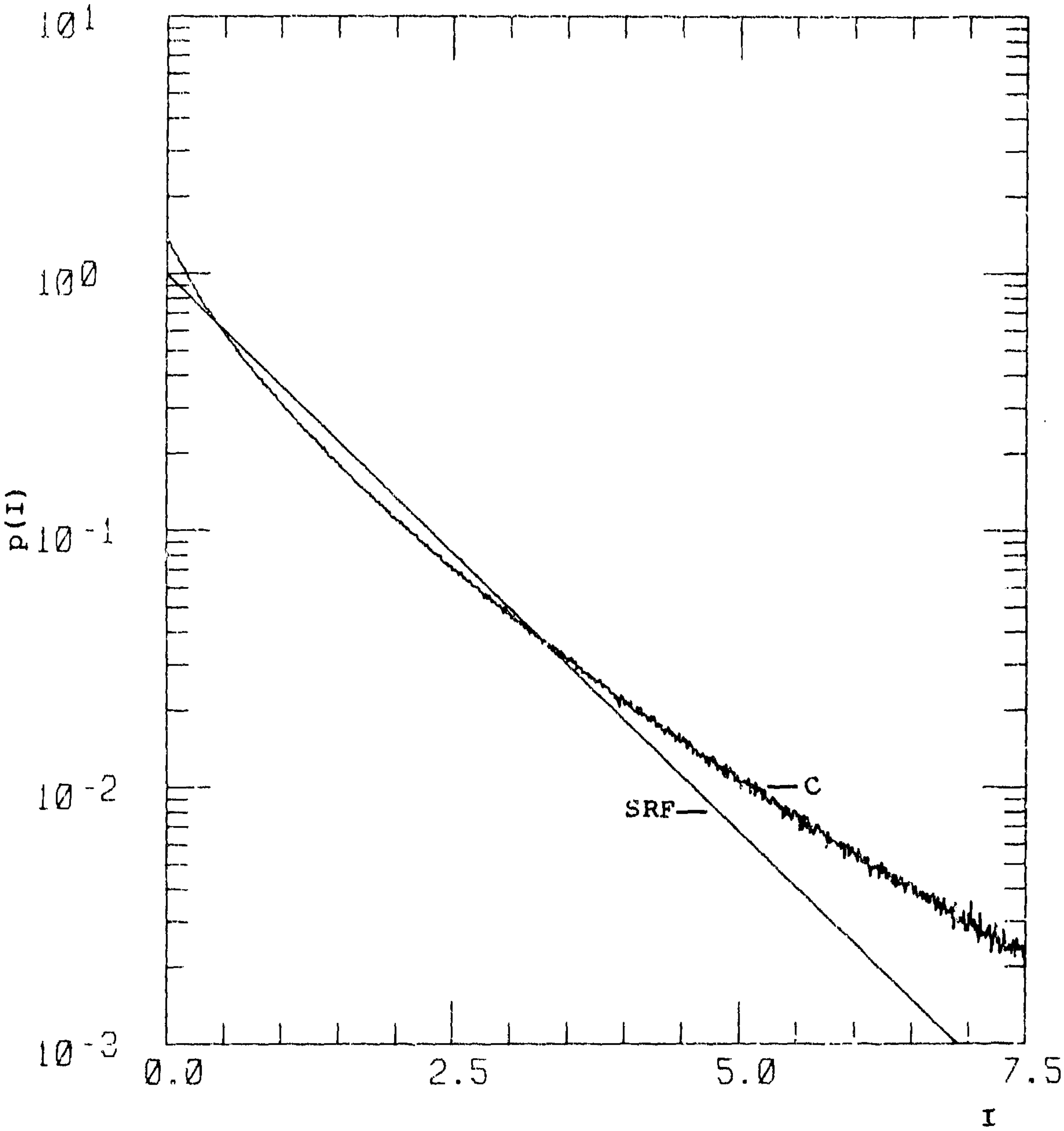

Figure C-46. Probability Distribution for
$s = 2.5$, $\chi^2 = 7.0$, $S_4{}^2 = 1.53$.

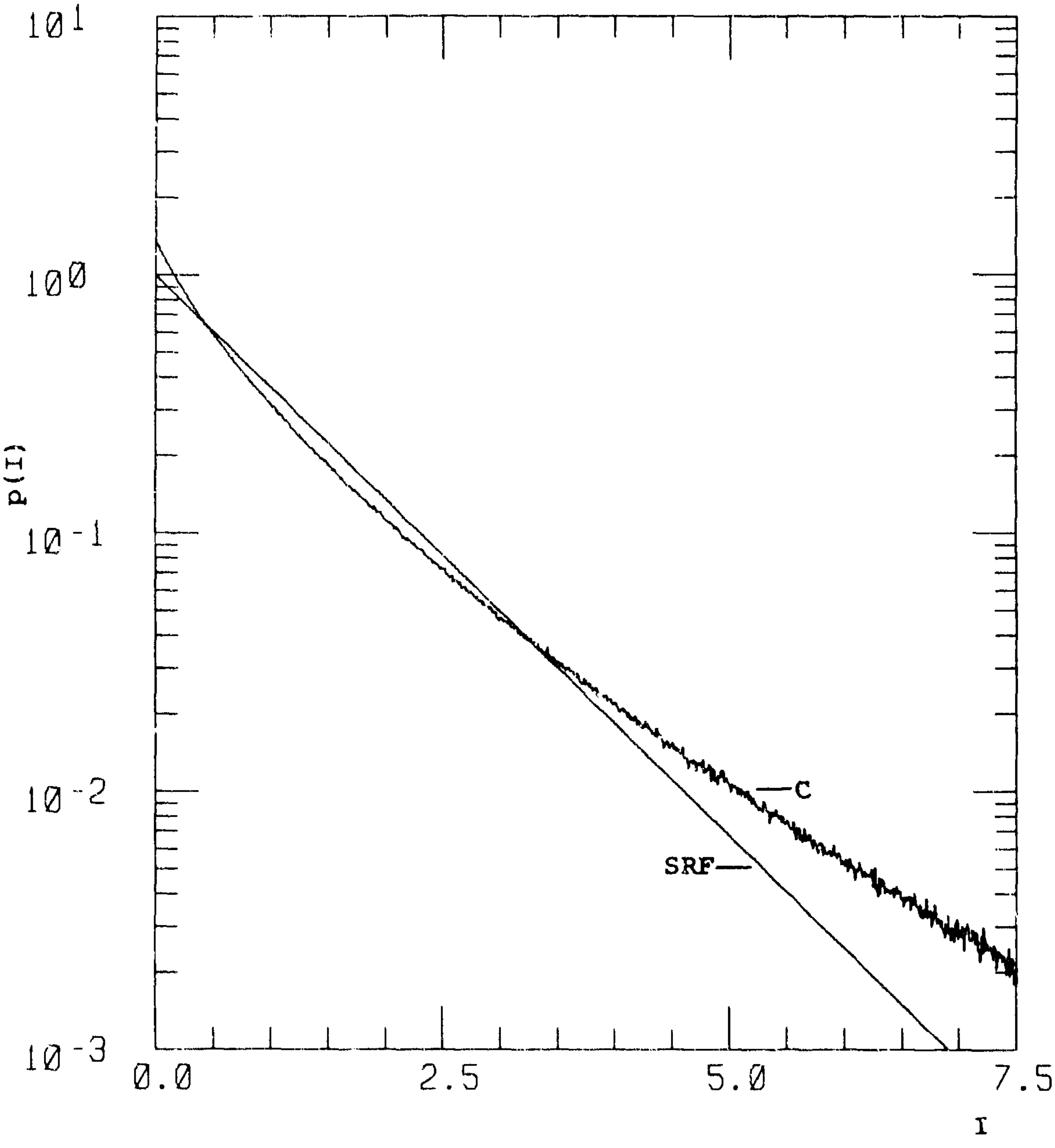

Figure C-47. Probability Distribution for $s = 2.5$, $\chi^2 = 10.0$, $S_4{}^2 = 1.49$.

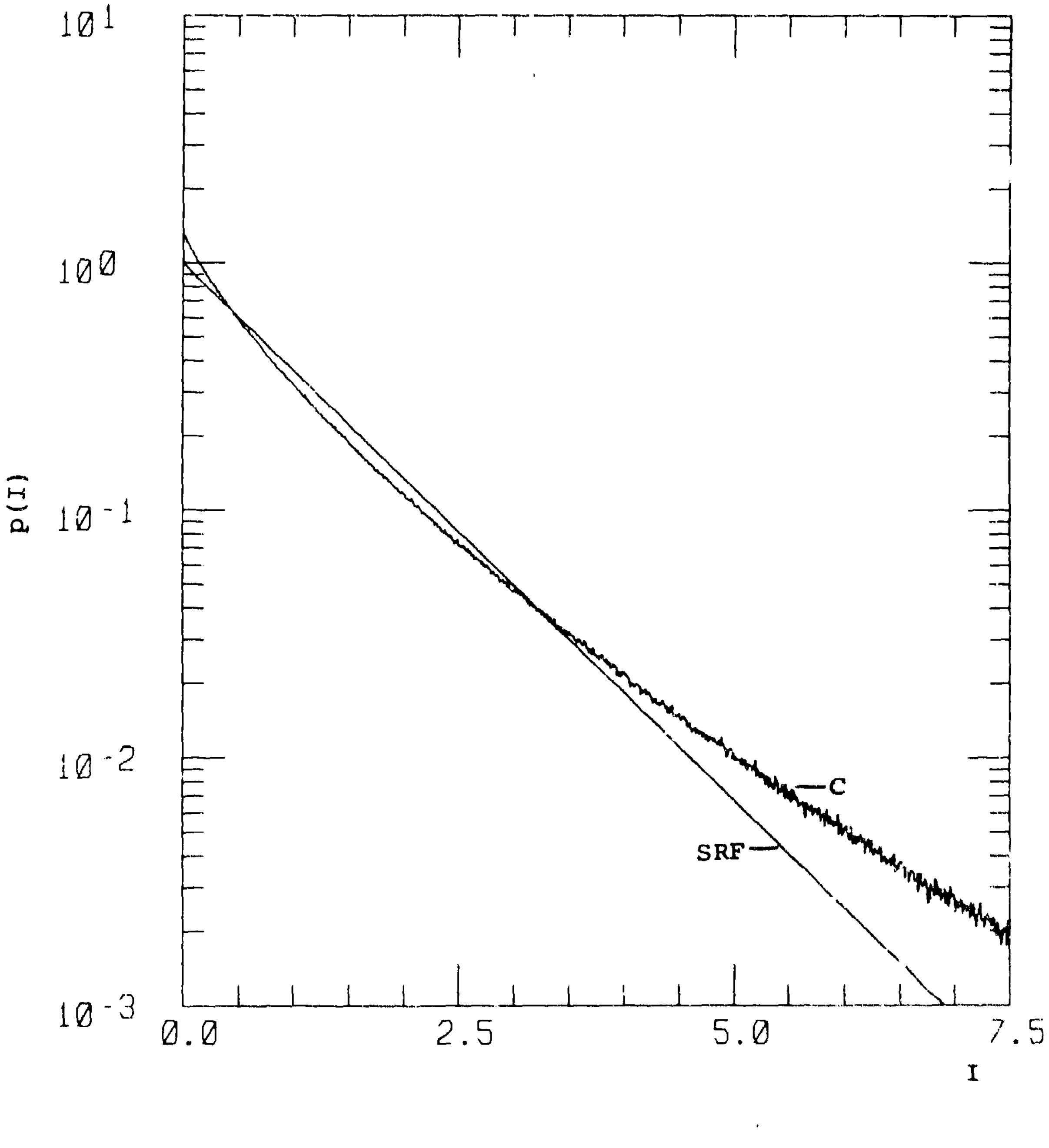

Figure C-48. Probability Distribution for $s = 2.5$, $\chi^2 = 20.0$, $S_4{}^2 = 1.41$.

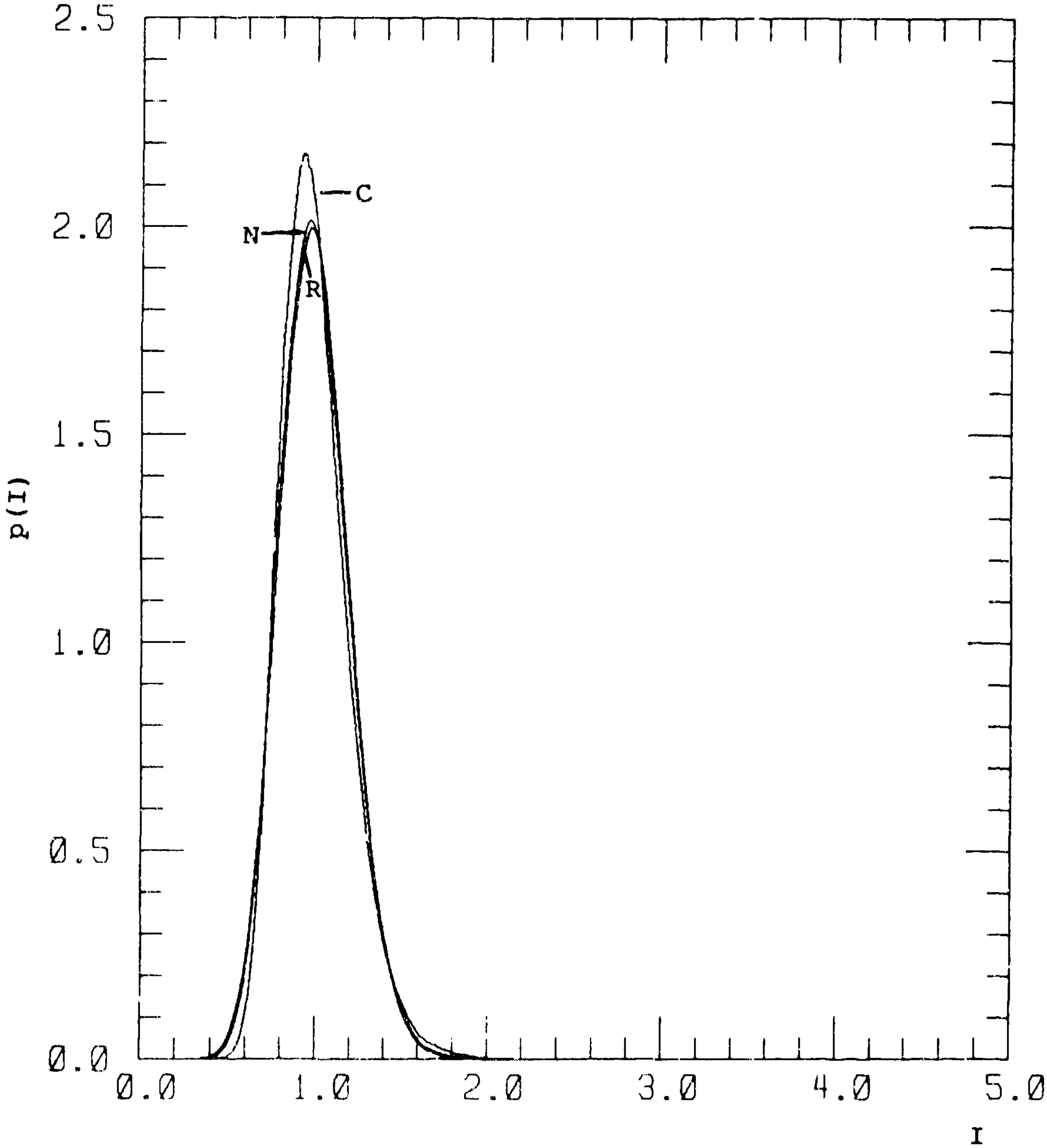

Figure C-49. Probability Distribution for $s = 3$, $\chi^2 = 0.01$, $S_4^2 = 0.041$.

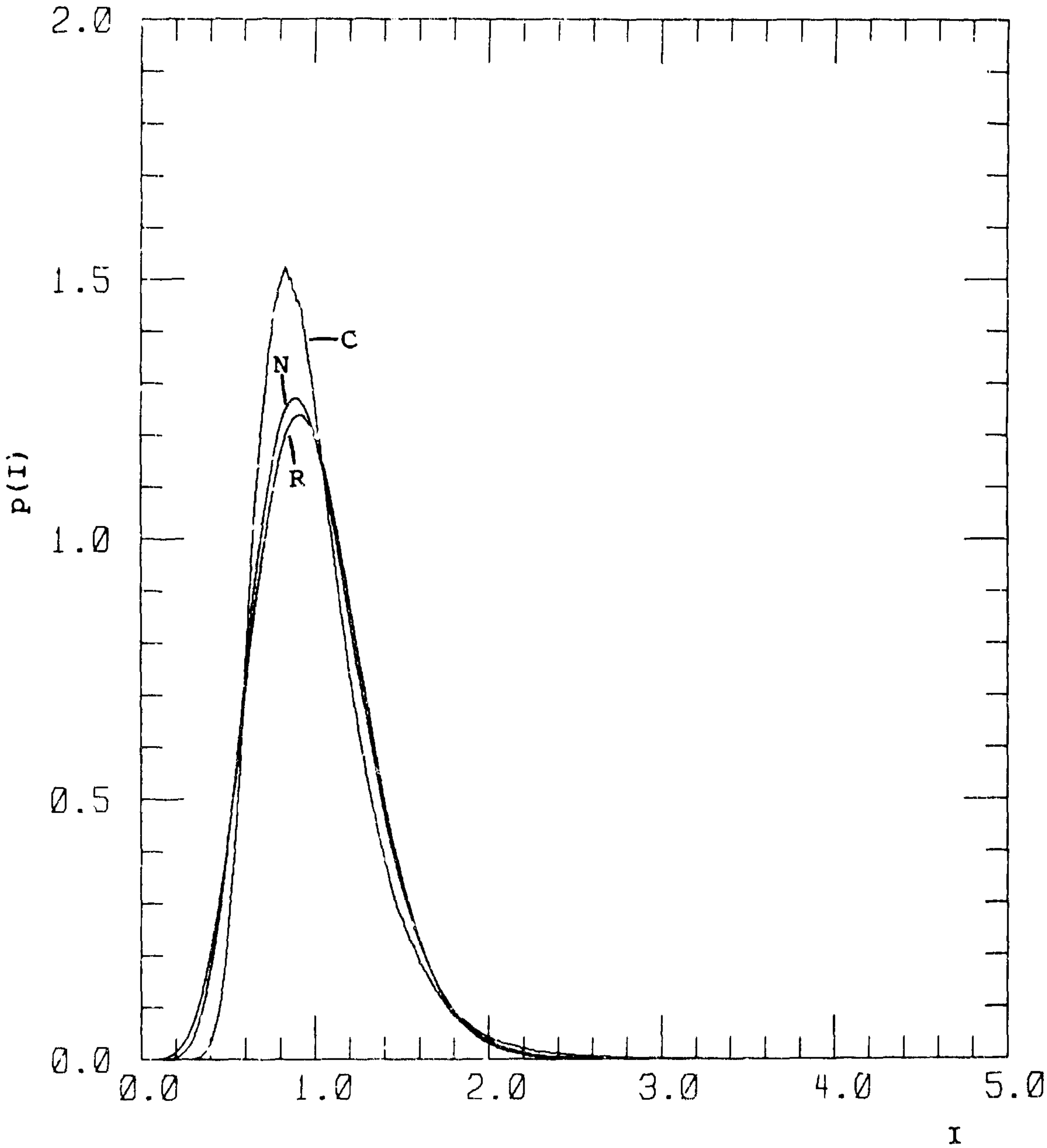

Figure C-50. Probability Distribution for $s = 3$, $X^2 = 0.025$, $S_4{}^2 = 0.109$.

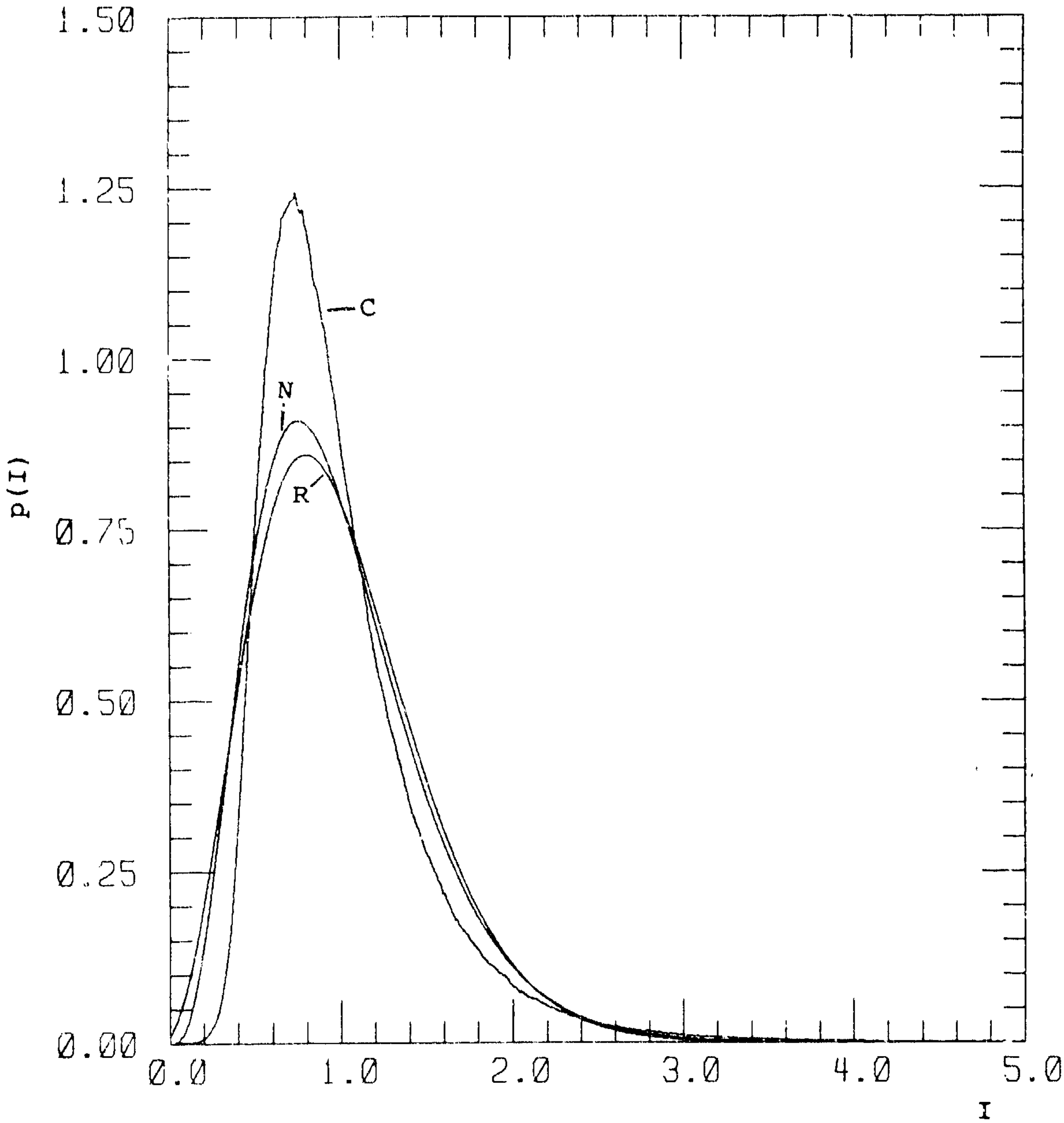

Figure C-51. Probability Distribution for
$s = 3, \chi^2 = 0.05, S_4{}^2 = 0.241$.

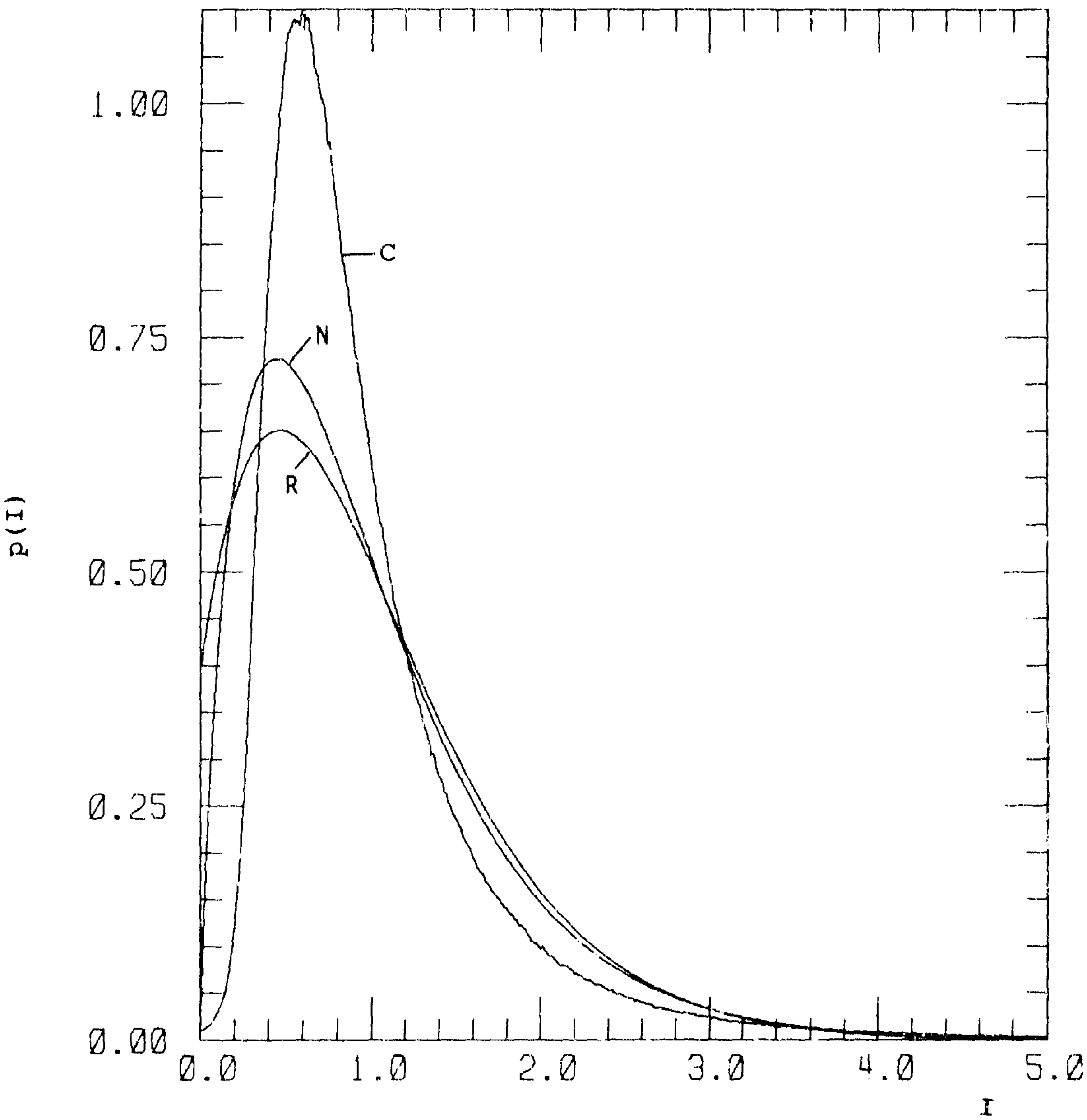

Figure C-52. Probability Distribution for $s = 3, X^2 = 0.1, S_4^2 = 0.548$.

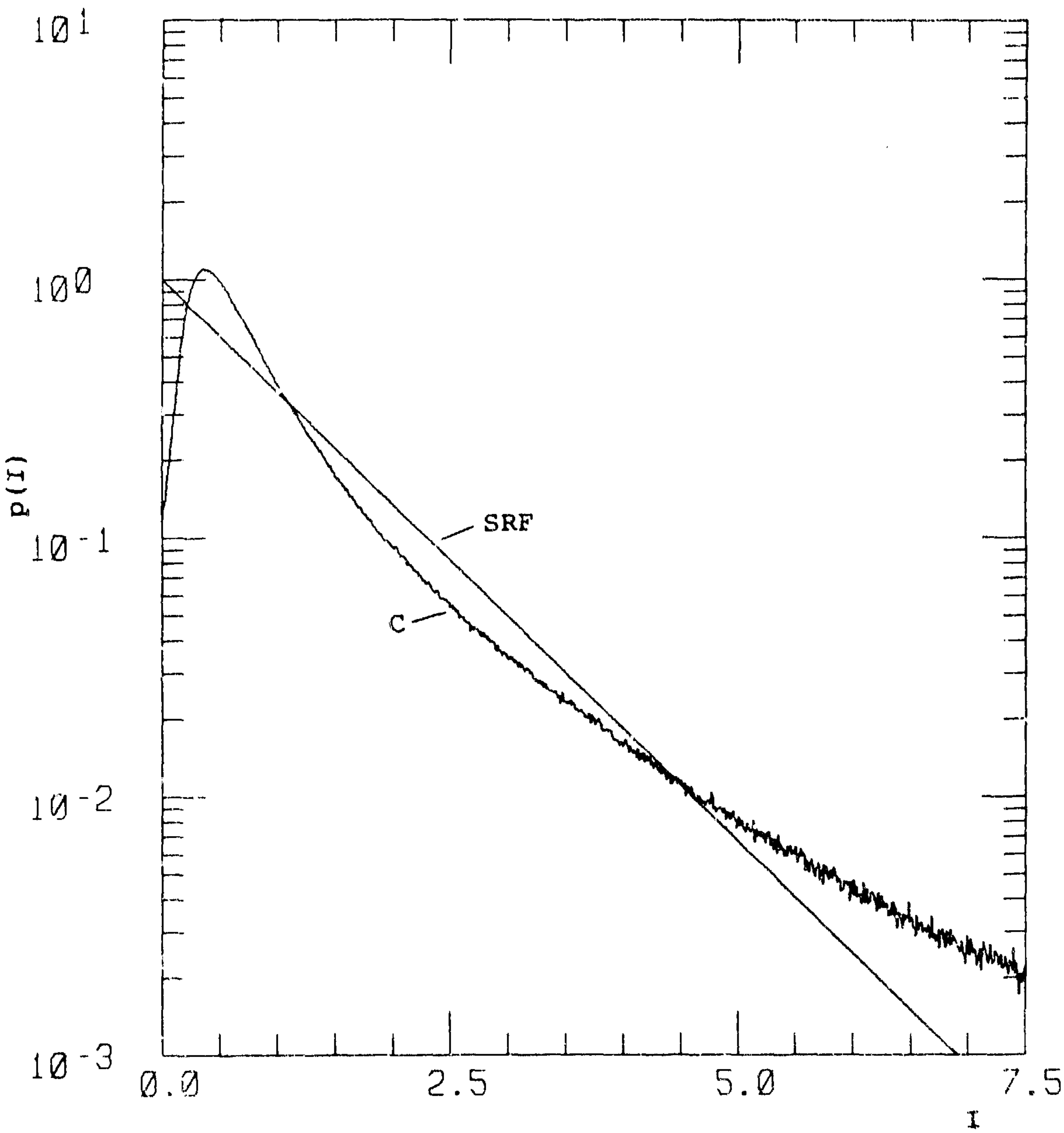

Figure C-53. Probability Distribution for $s = 3$, $\chi^2 = 0.25$, $S_4{}^2 = 1.28$.

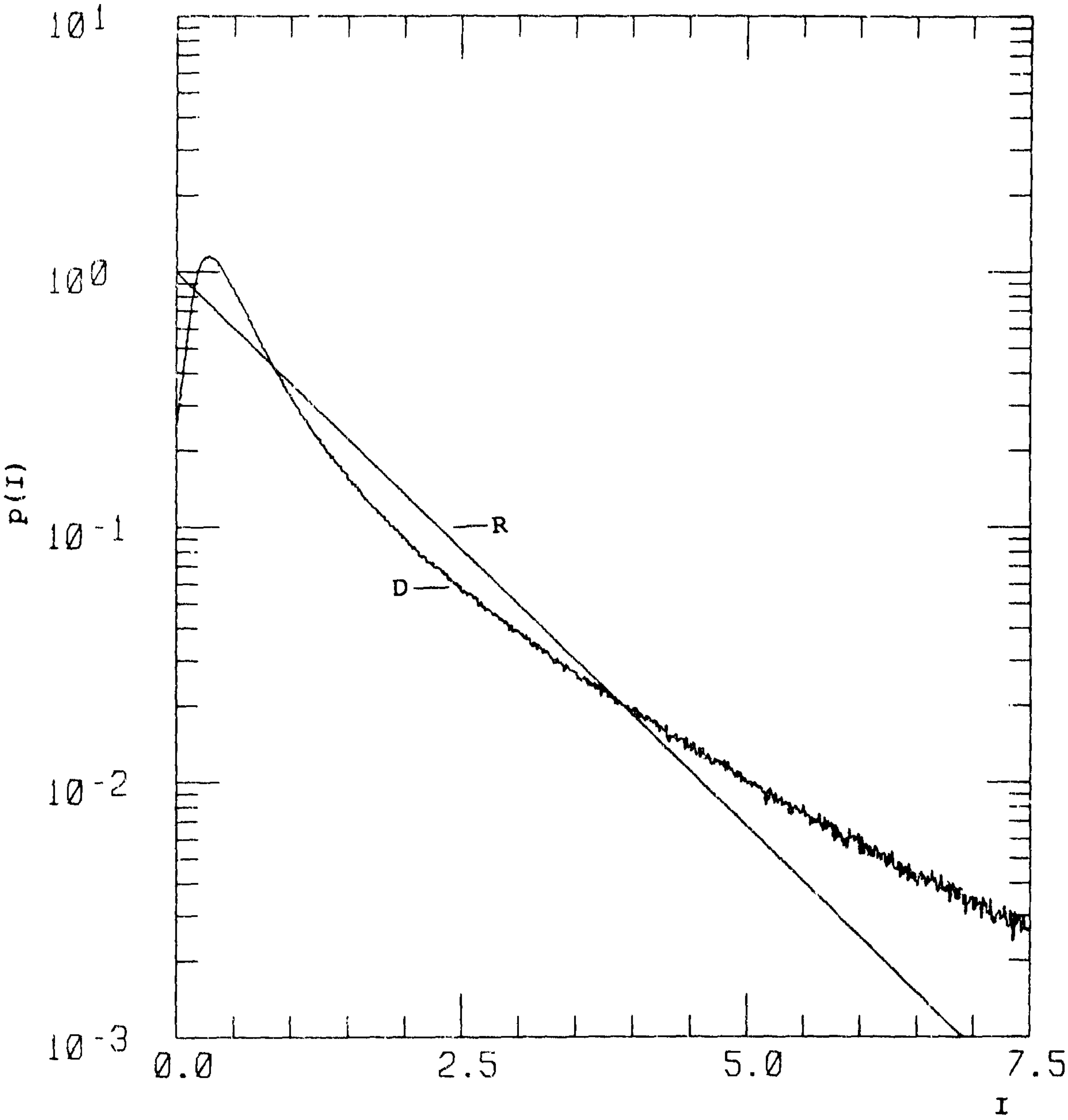

Figure C-54. Probability Distribution for $s = 3$, $\chi^2 = 0.4$, $S_4{}^2 = 1.63$.

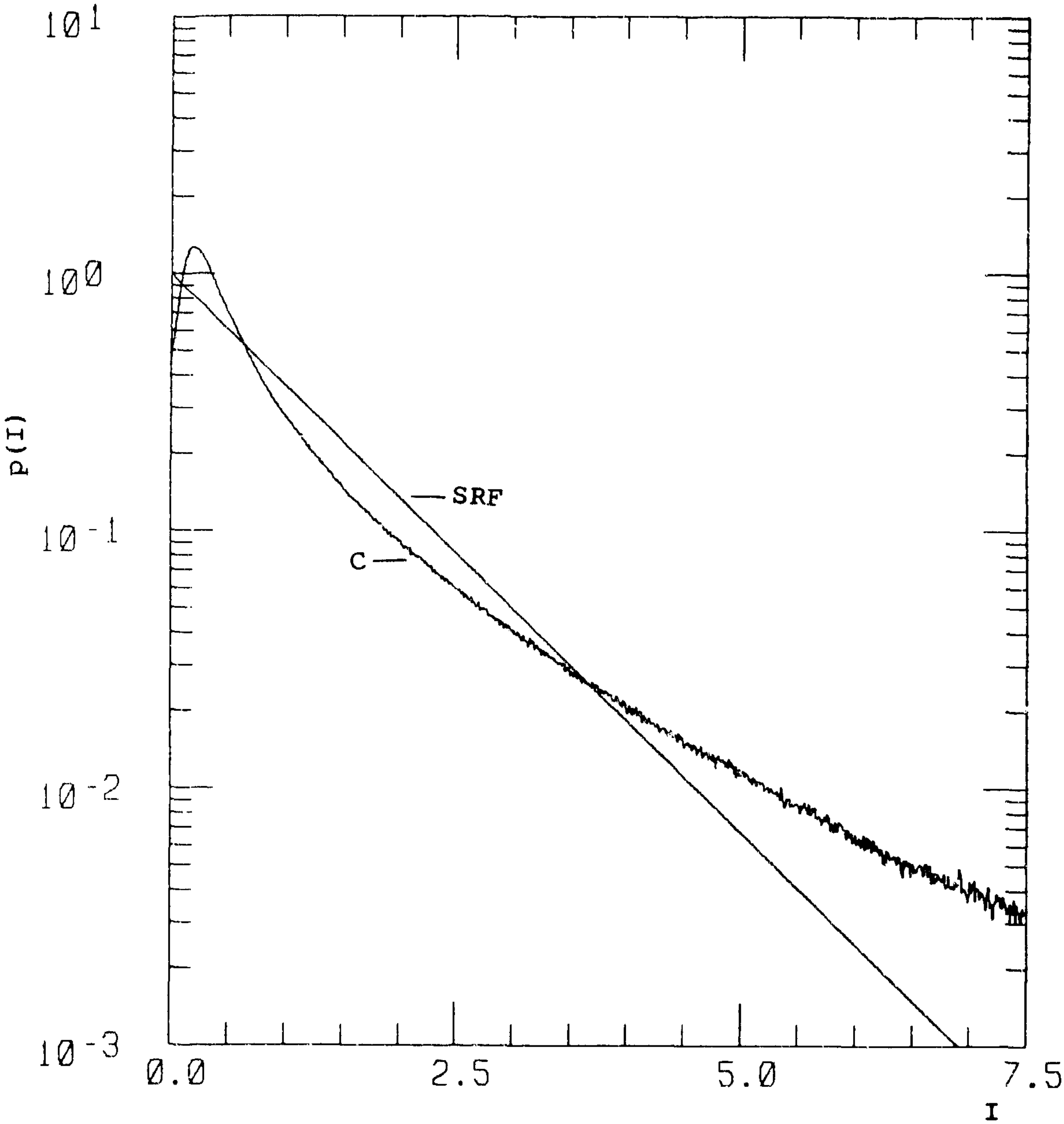

Figure C-55. Probability Distribution for $s = 3$, $\chi^2 = 0.7$, $S_4^{\ 2} = 1.96$.

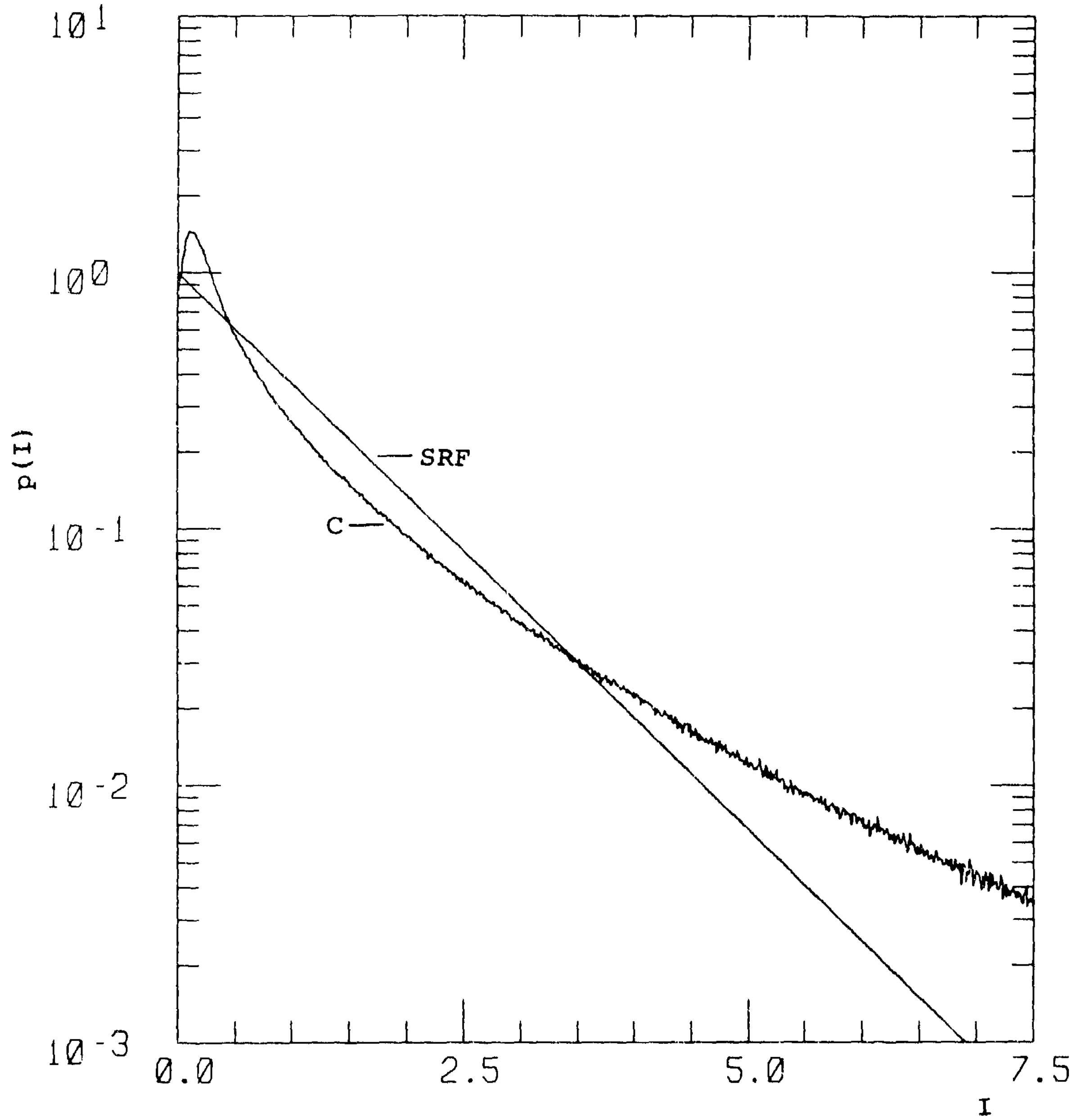

Figure C-56. Probability Distribution for $s = 3$, $\chi^2 = 1.5$, $S_4^2 = 2.15$.

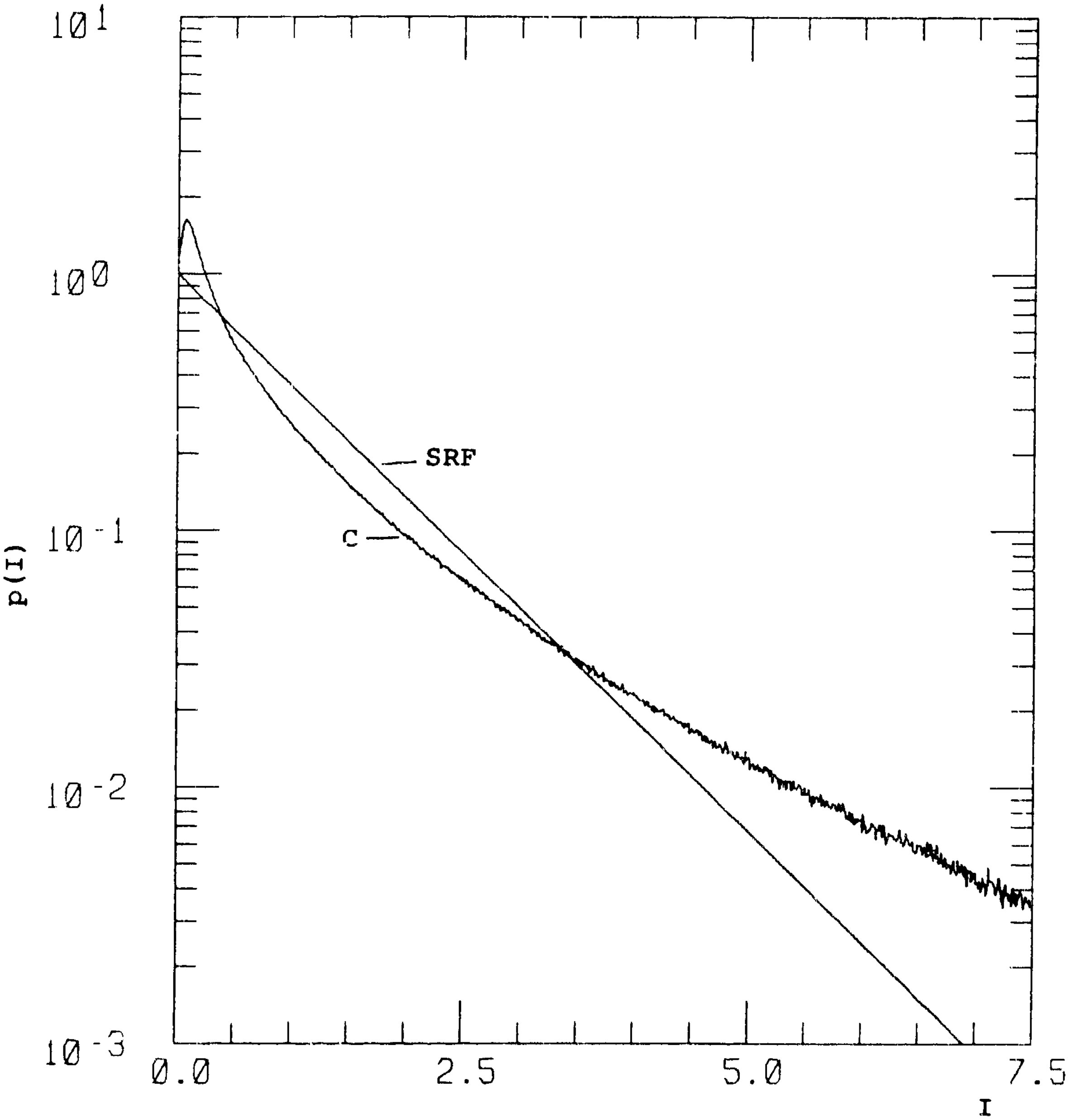

Figure C-57. Probability Distribution for
$s = 3$, $\chi^2 = 3.0$, $S_4{}^2 = 2.13$.

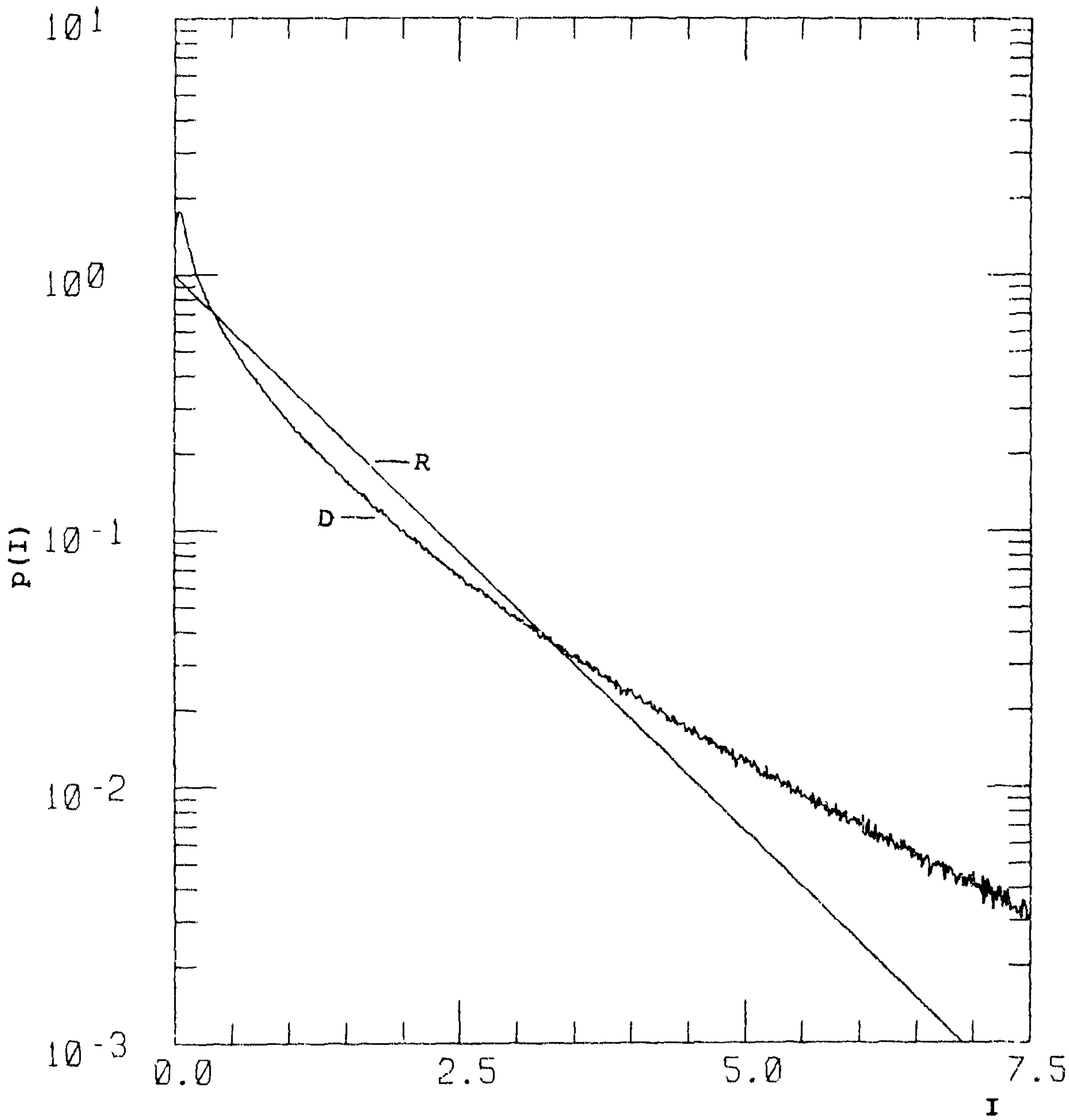

Figure C-58. Probability Distribution for $s = 3$, $\chi^2 = 7.0$, $S_4{}^2 = 1.99$.

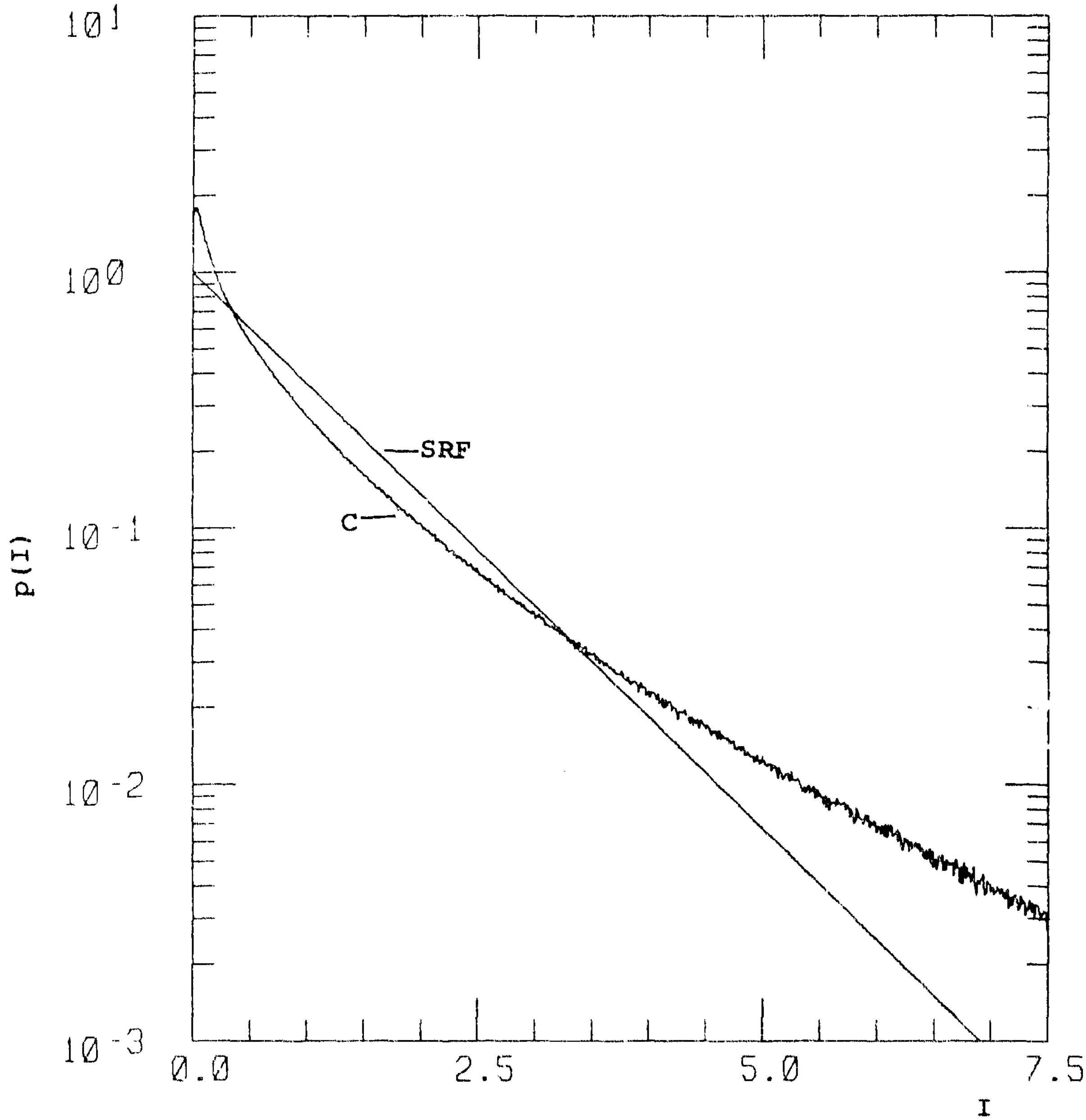

Figure C-59. Probability Distribution for $s = 3$, $\chi^2 = 10.0$, $S_4^{\ 2} = 1.90$.

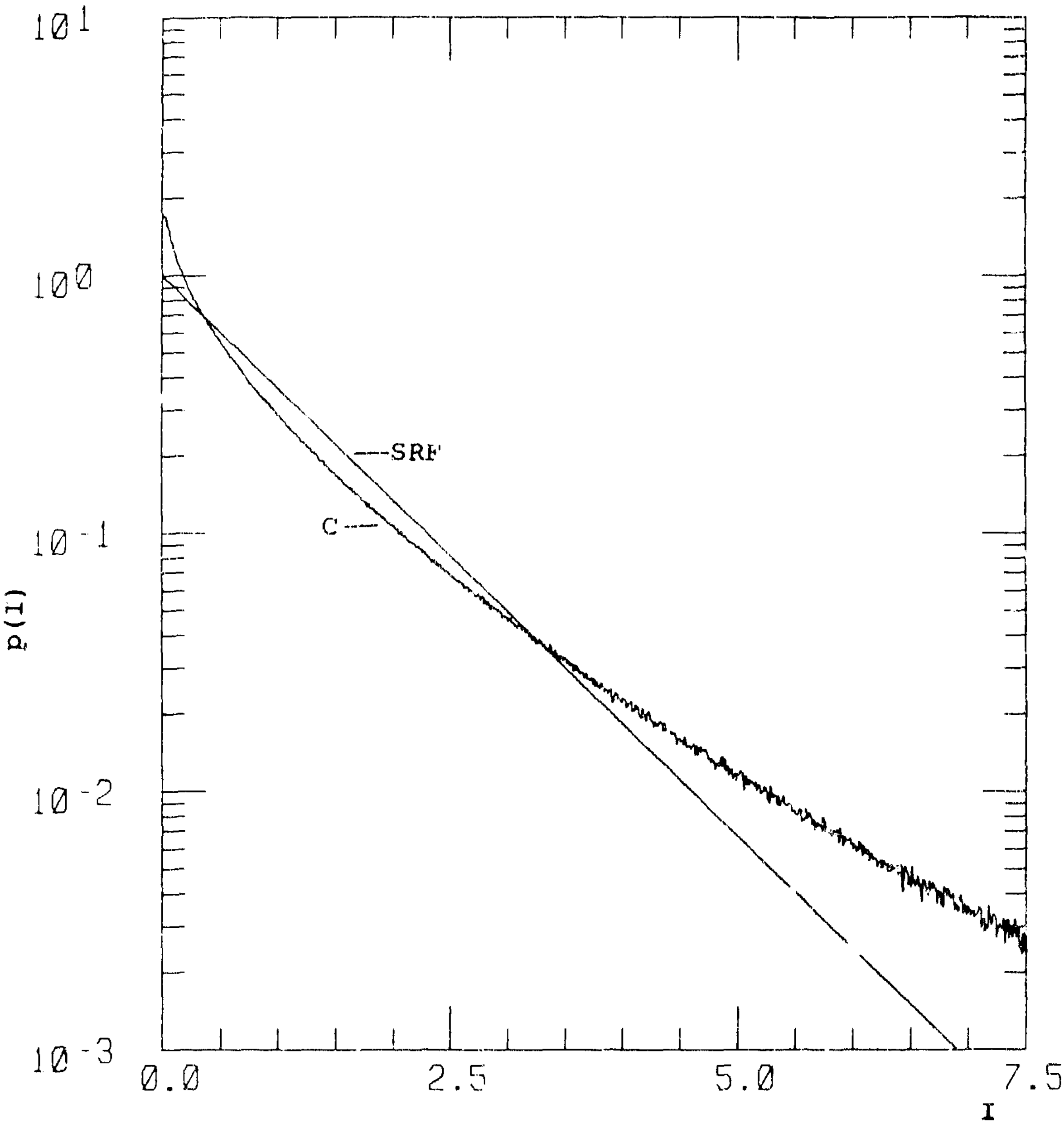

Figure C-60. Probability Distribution for $s = 3$, $\chi^2 = 20.0$, $S_4^{\;2} = 1.71$.

APPENDIX D

PROBABILITY DISTRIBUTIONS FOR SMALL INTENSITY FOR SINGLE POWER LAW PSD

This Appendix contains all the calculated small intensity behavior for single power law PSD. These distributions are compared to Nakagami-m (labeled as N) and Rice (labeled as R).

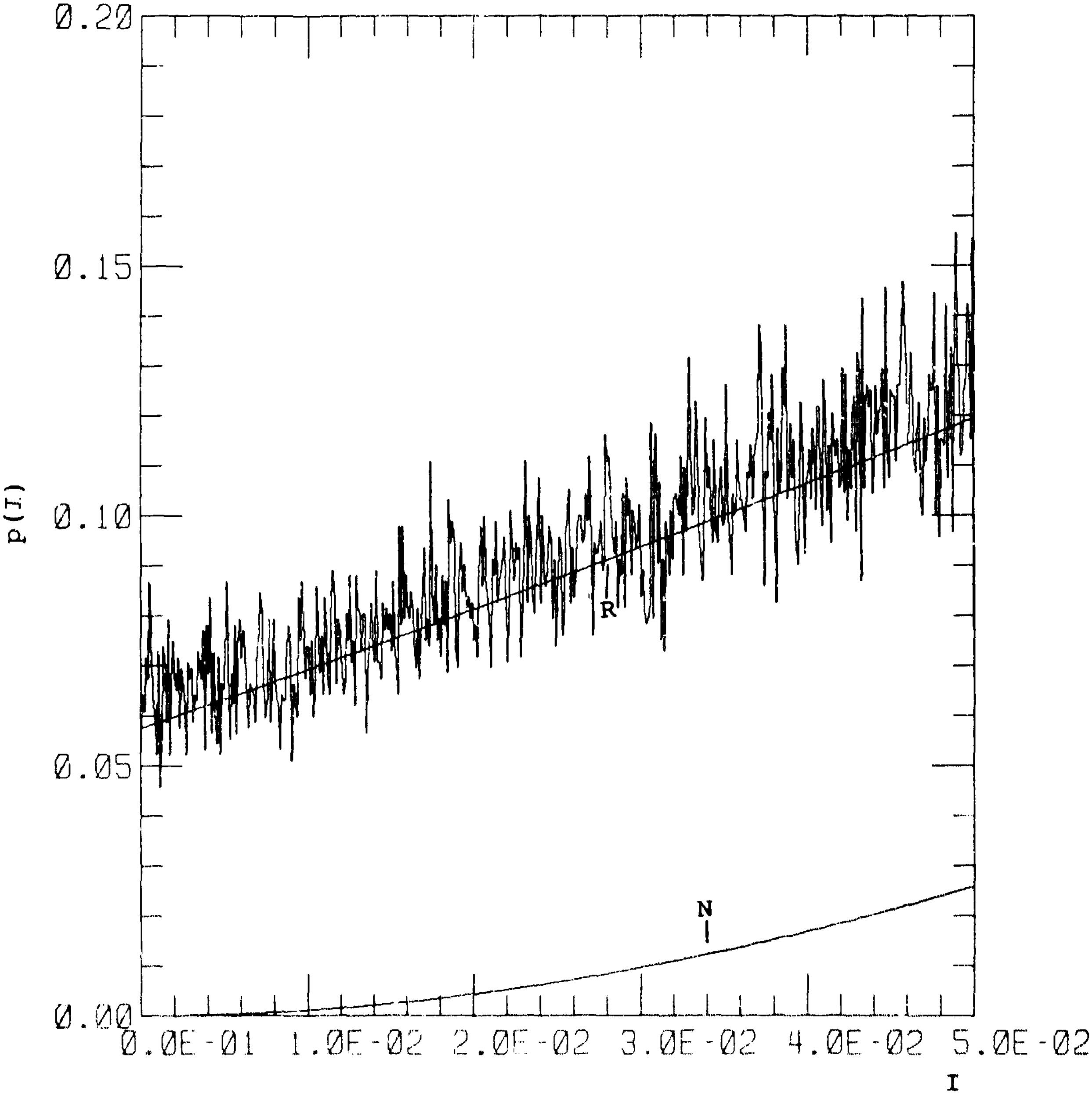

Figure D-1. Probability Distributions for Small I for $s = 1$, $\chi^2 = 0.1$, $S_4^2 = 0.327$.

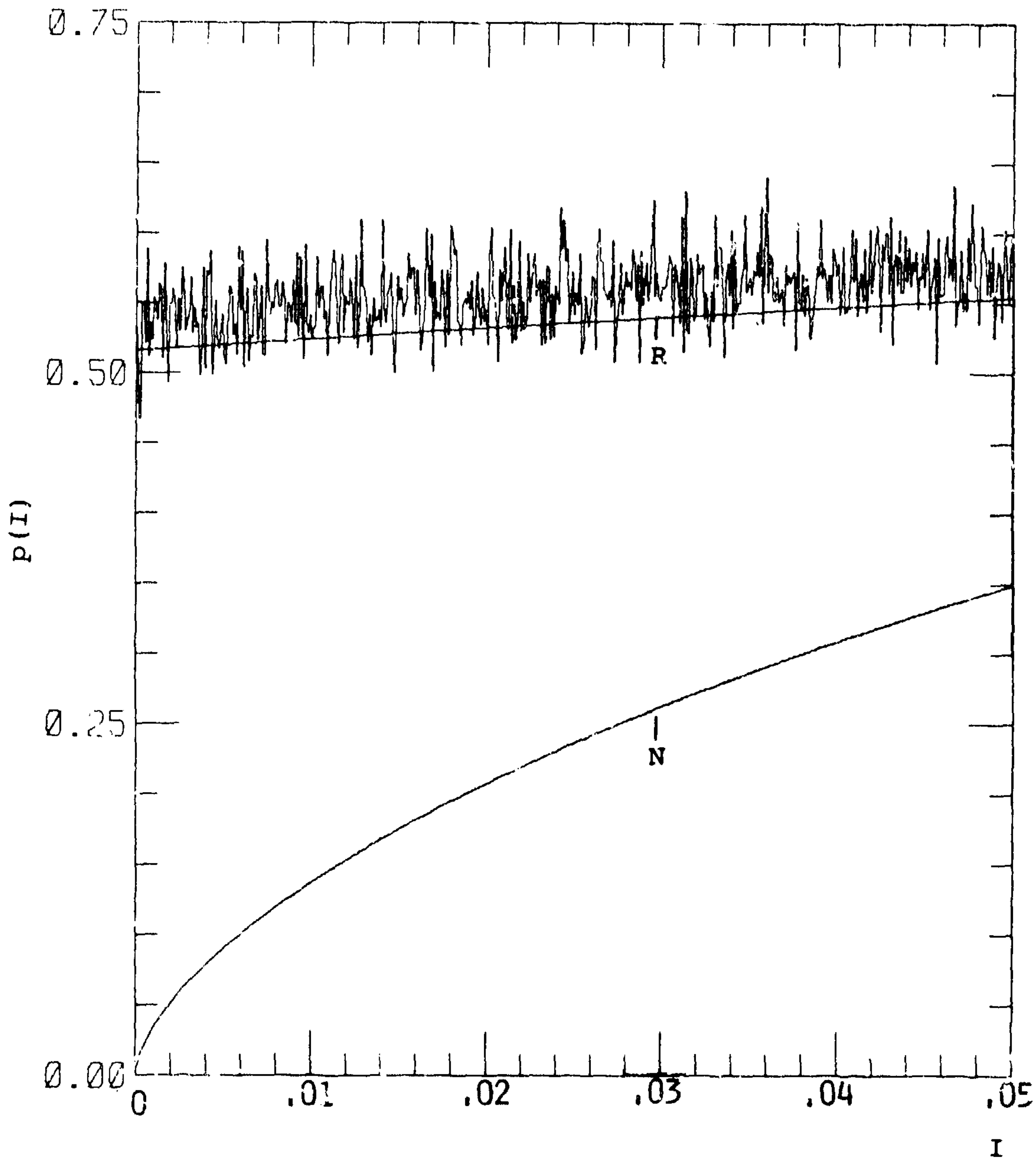

Figure D-2. Probability Distributions for Small I for $s = 1$, $\chi^2 = 0.25$, $S_4^2 = 0.616$.

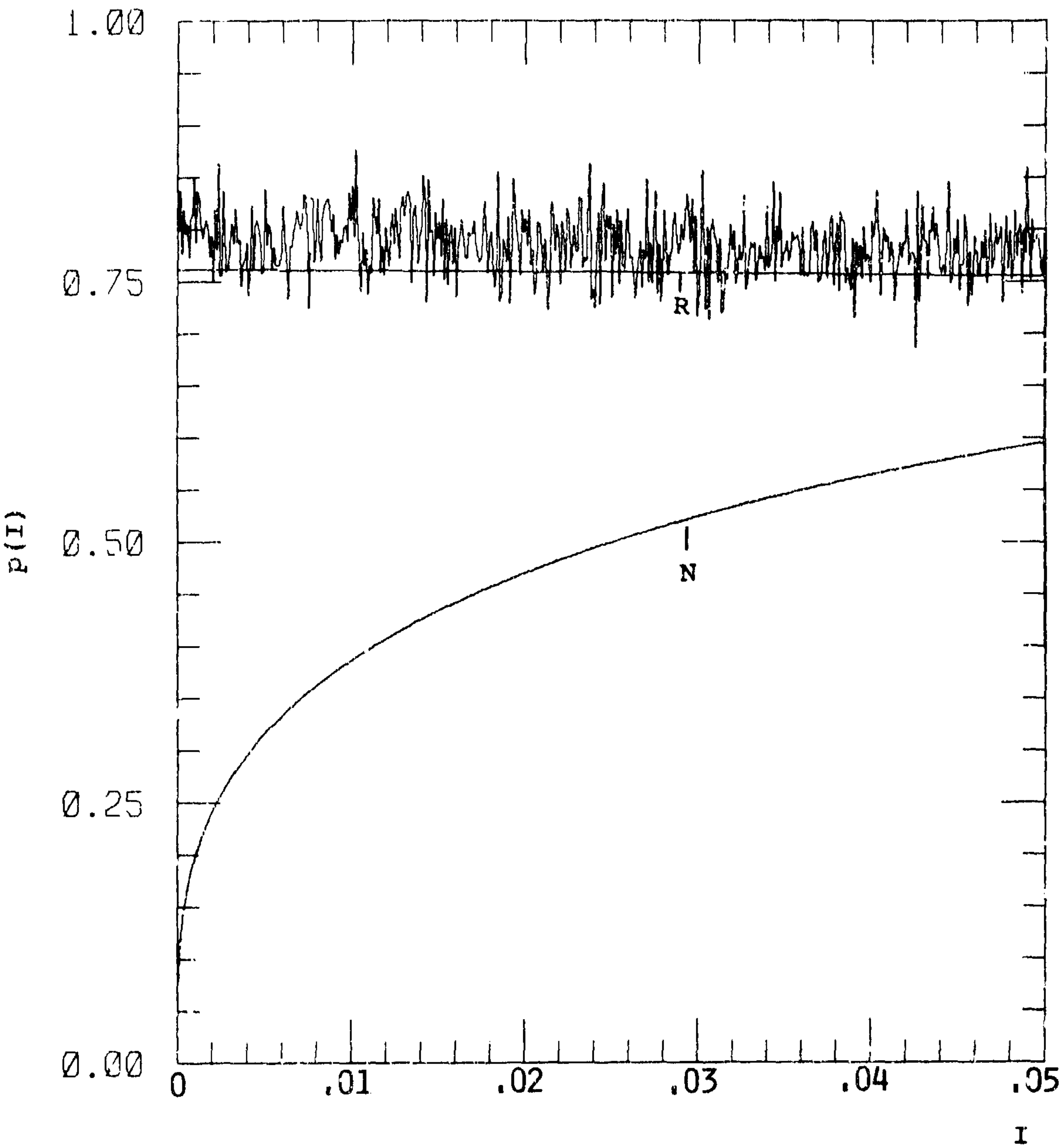

Figure D-3. Probability Distributions for Small I for $s = 1$, $\chi^2 = 0.4$, $S_4^{\ 2} = 3.768$.

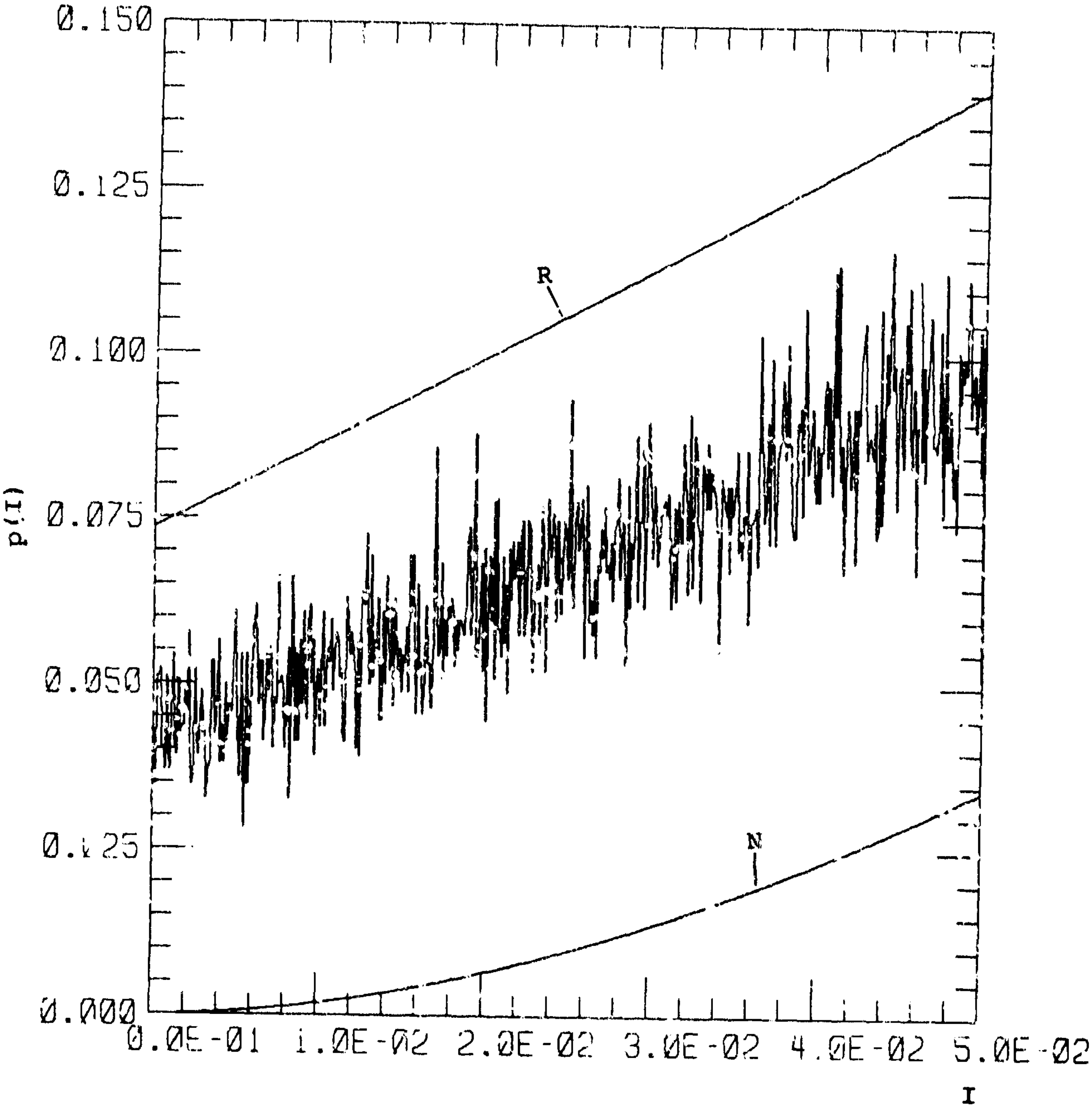

Figure D-4. Probability Distribution for Small I for $s = 1.5$, $\chi^2 = 0.1$, $S_4{}^2 = 0.343$.

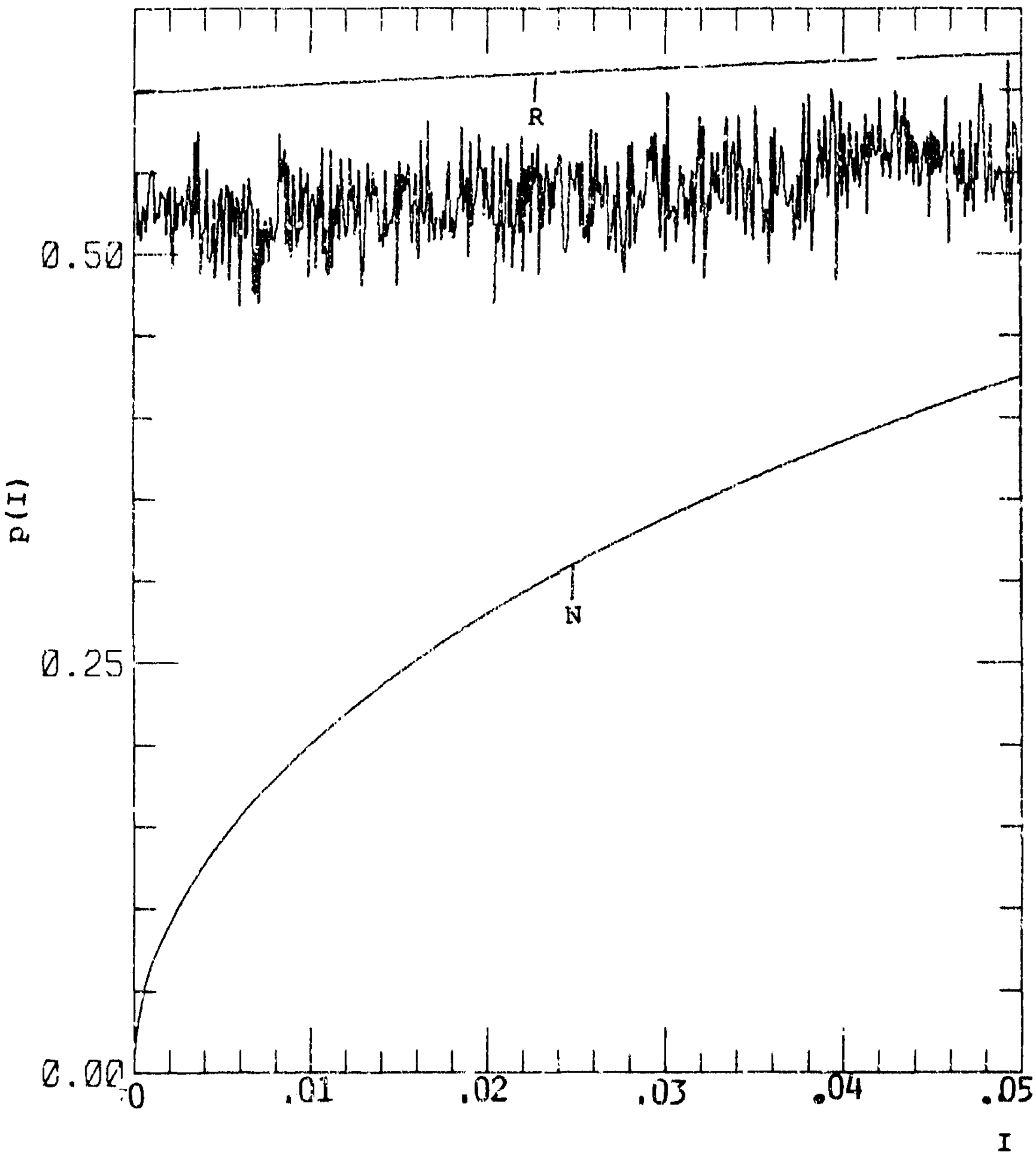

Figure D-5. Probability Distributions for Small I for
$s = 1.5$, $\chi^2 = 0.25$, $S_4^{\,2} = 0.664$.

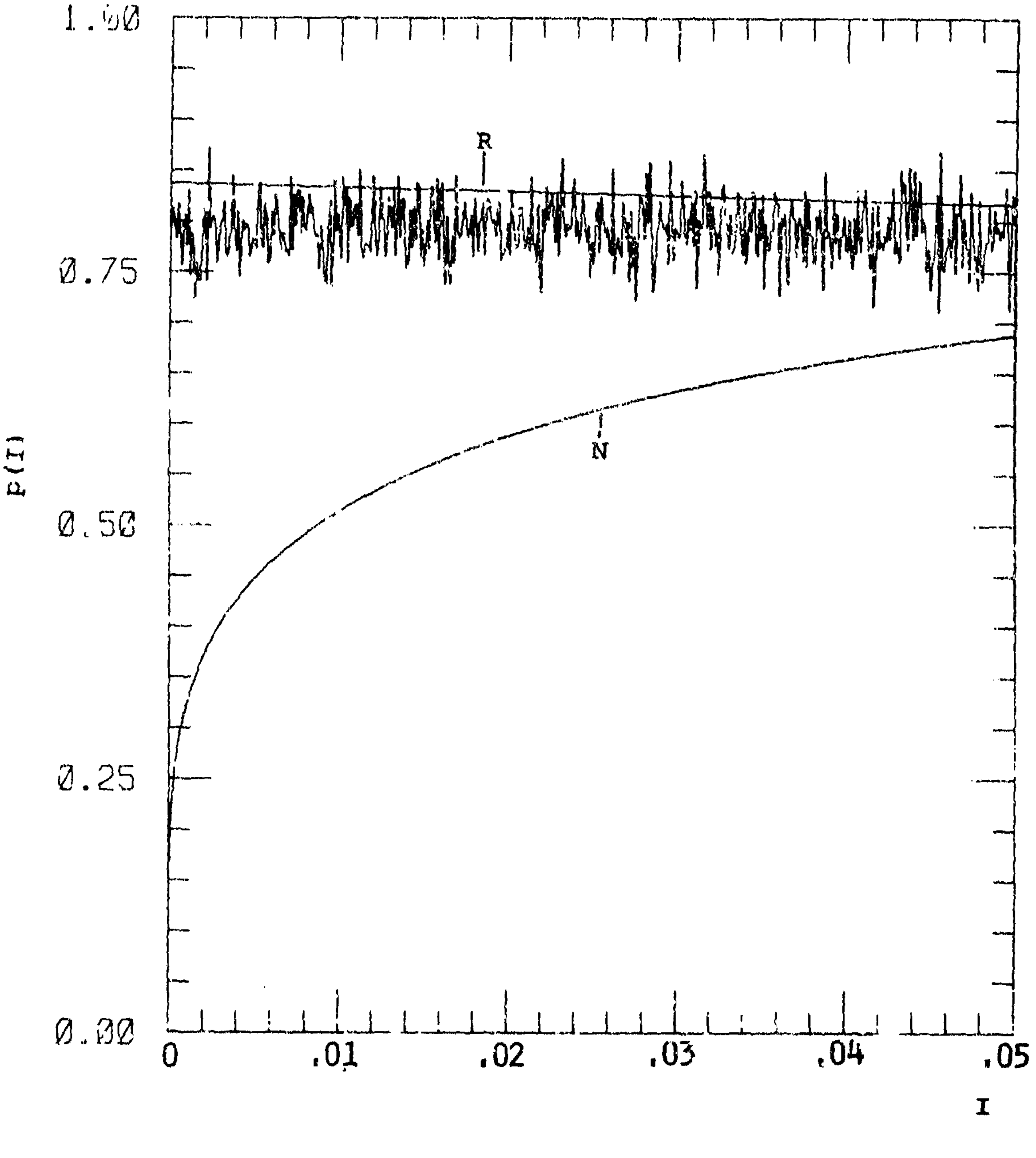

Figure D-6. Probability Distributions for Small I for $s = 1.5$, $X^2 = 0.4$, $S_4{}^2 = 0.825$.

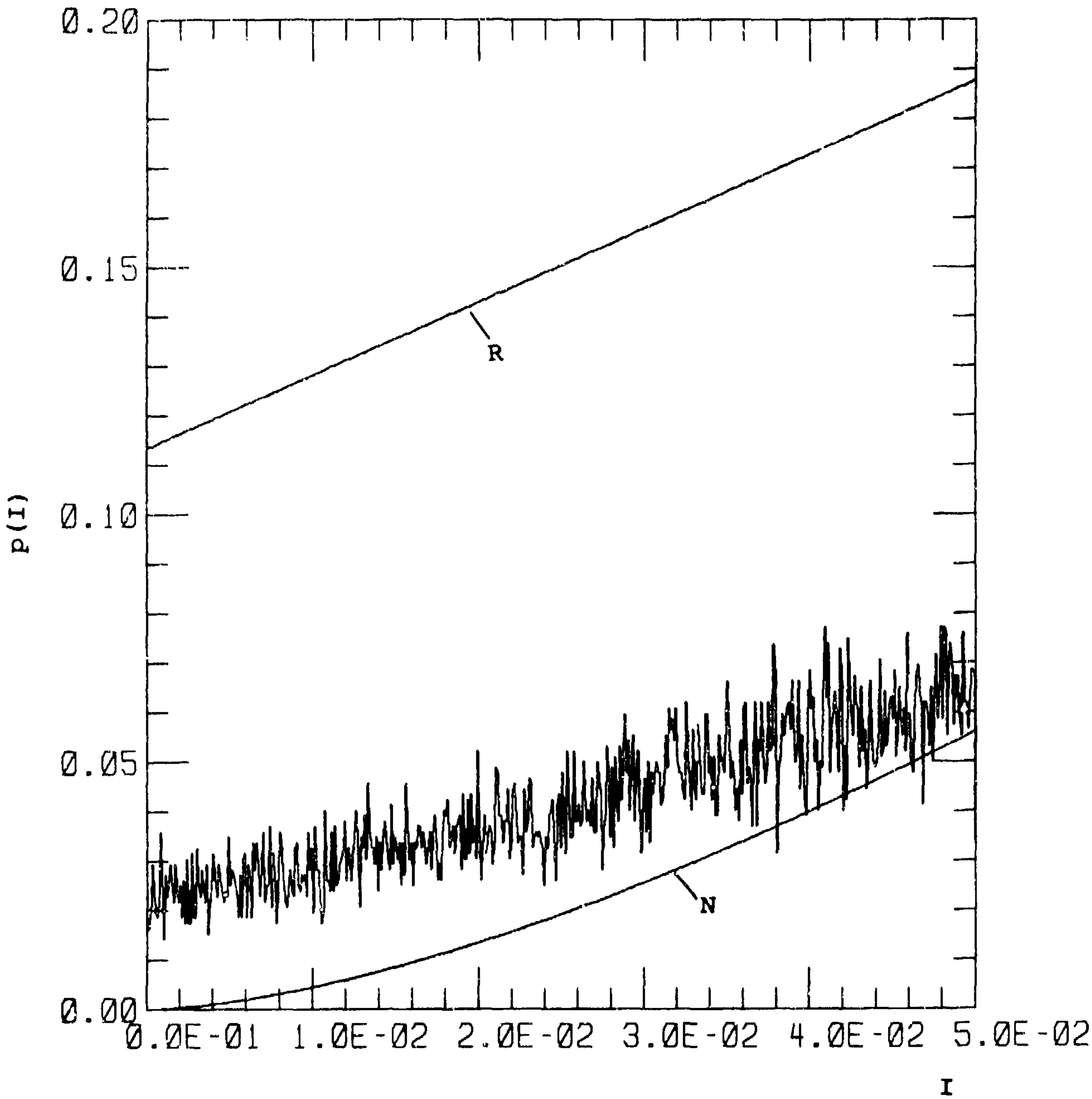

Figure D-7. Probability Distribution for Small I for $s = 2$, $\chi^2 = 0.1$, $S_4^2 = 0.378$.

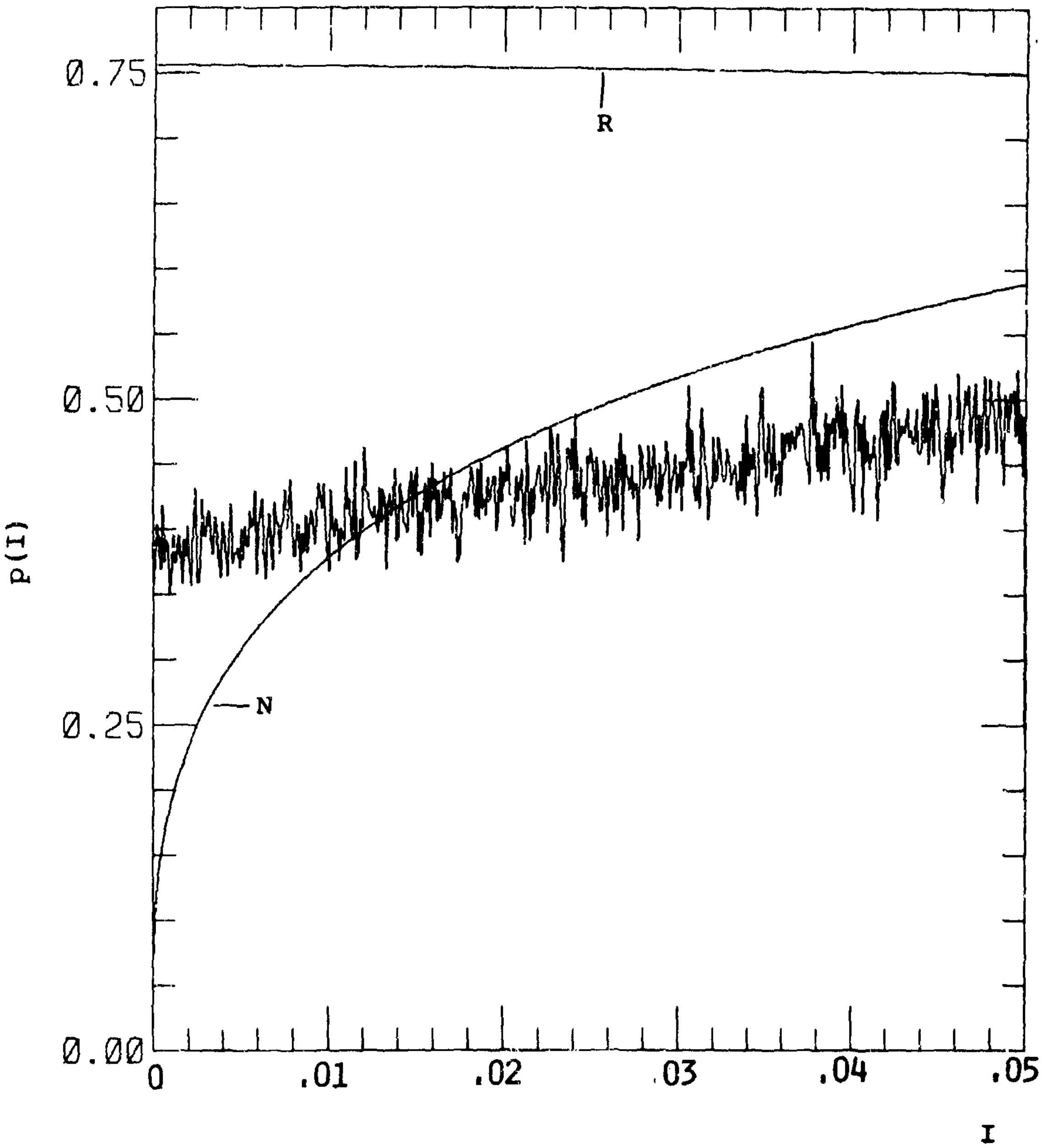

Figure D-8. Probability Distribution for small I for $s = 2$, $\chi^2 = 0.25$, $S_4^{\,2} = 0.764$.

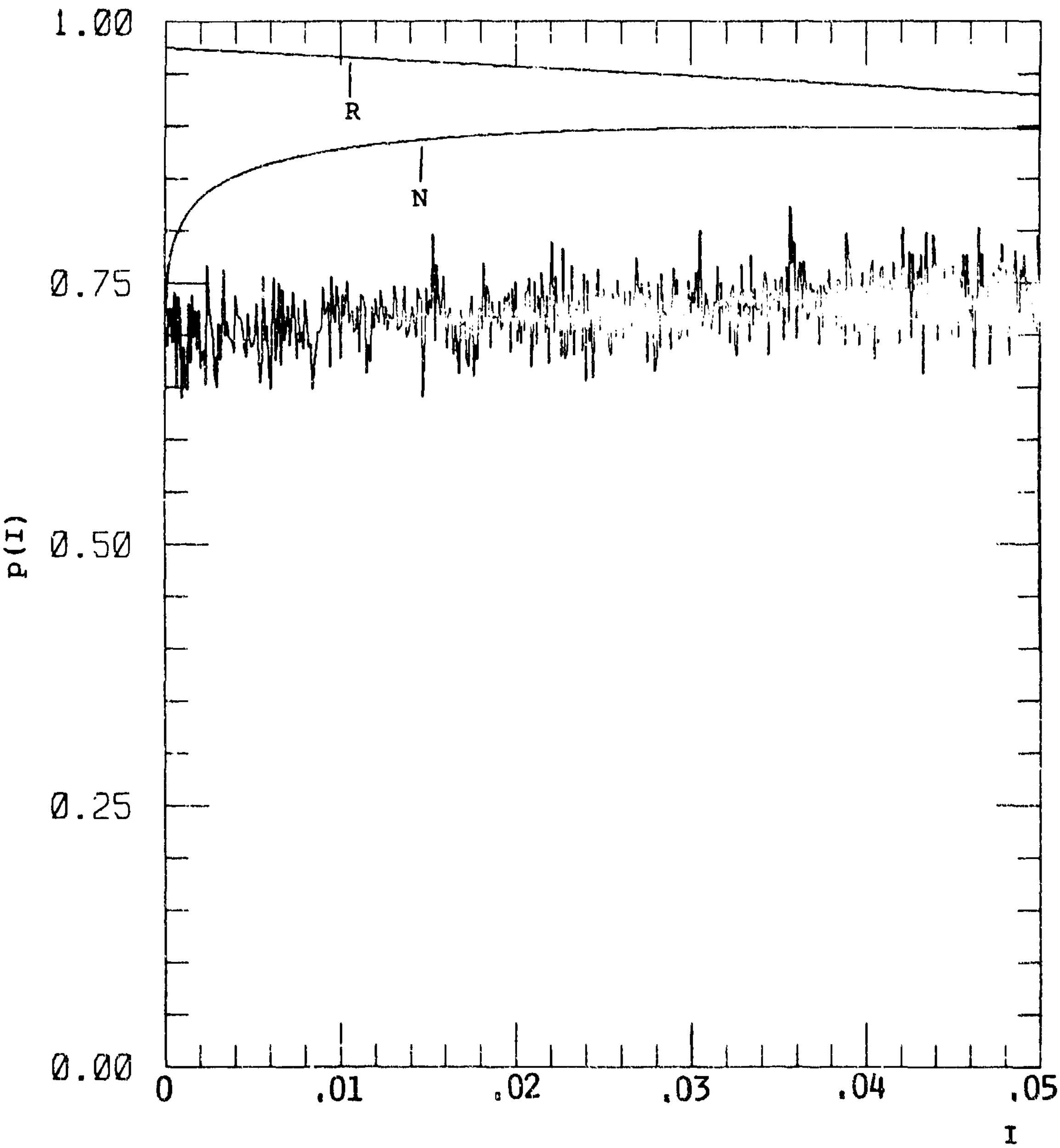

Figure D-9. Probability Distribution for Small I for
$s = 2$, $\chi^2 = 0.4$, $S_4{}^2 = 0.962$.

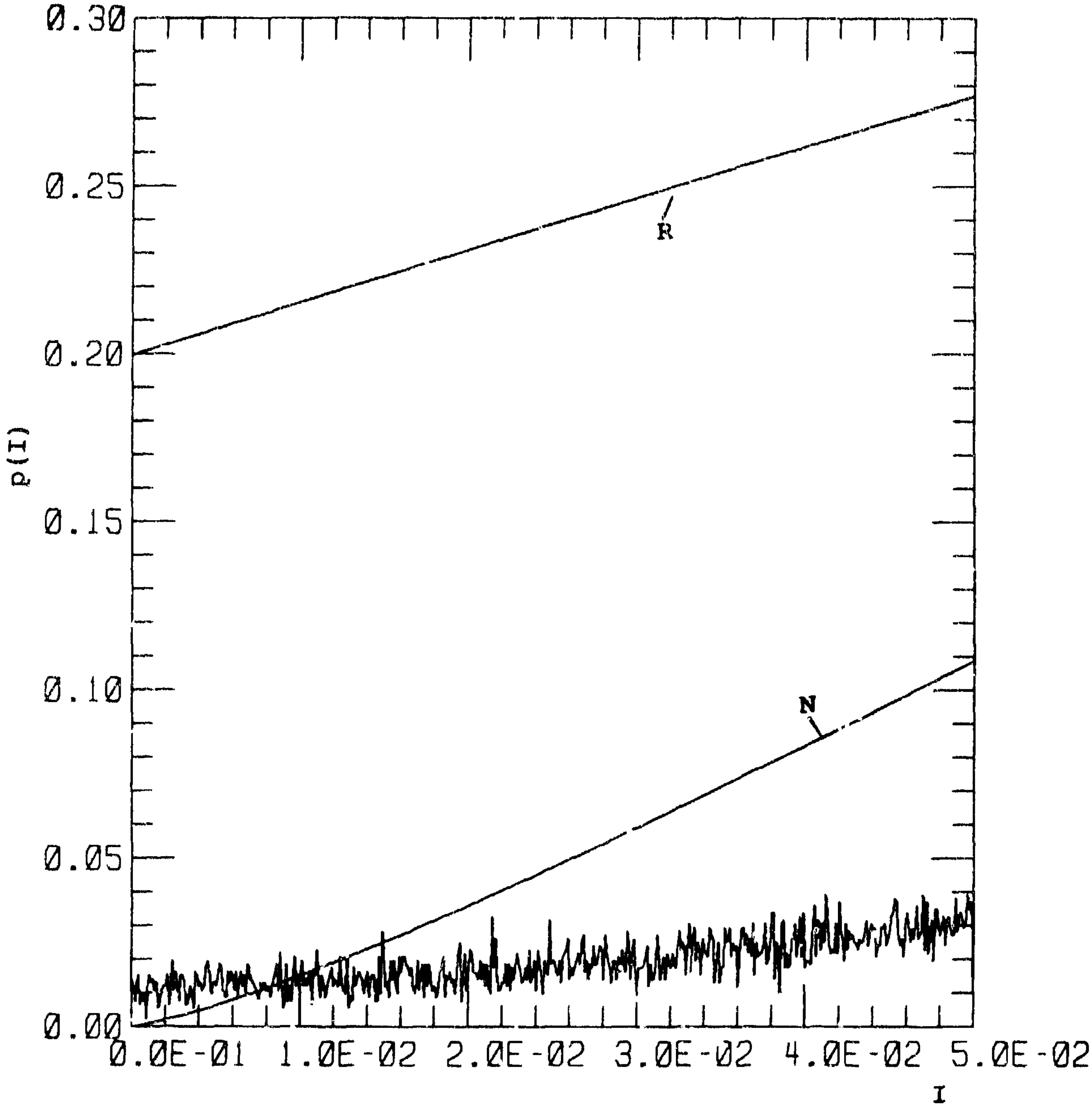

Figure D-10. Probability Distributions for Small I for $s = 2.5$, $\chi^2 = 0.1$, $S_4{}^2 = 0.438$.

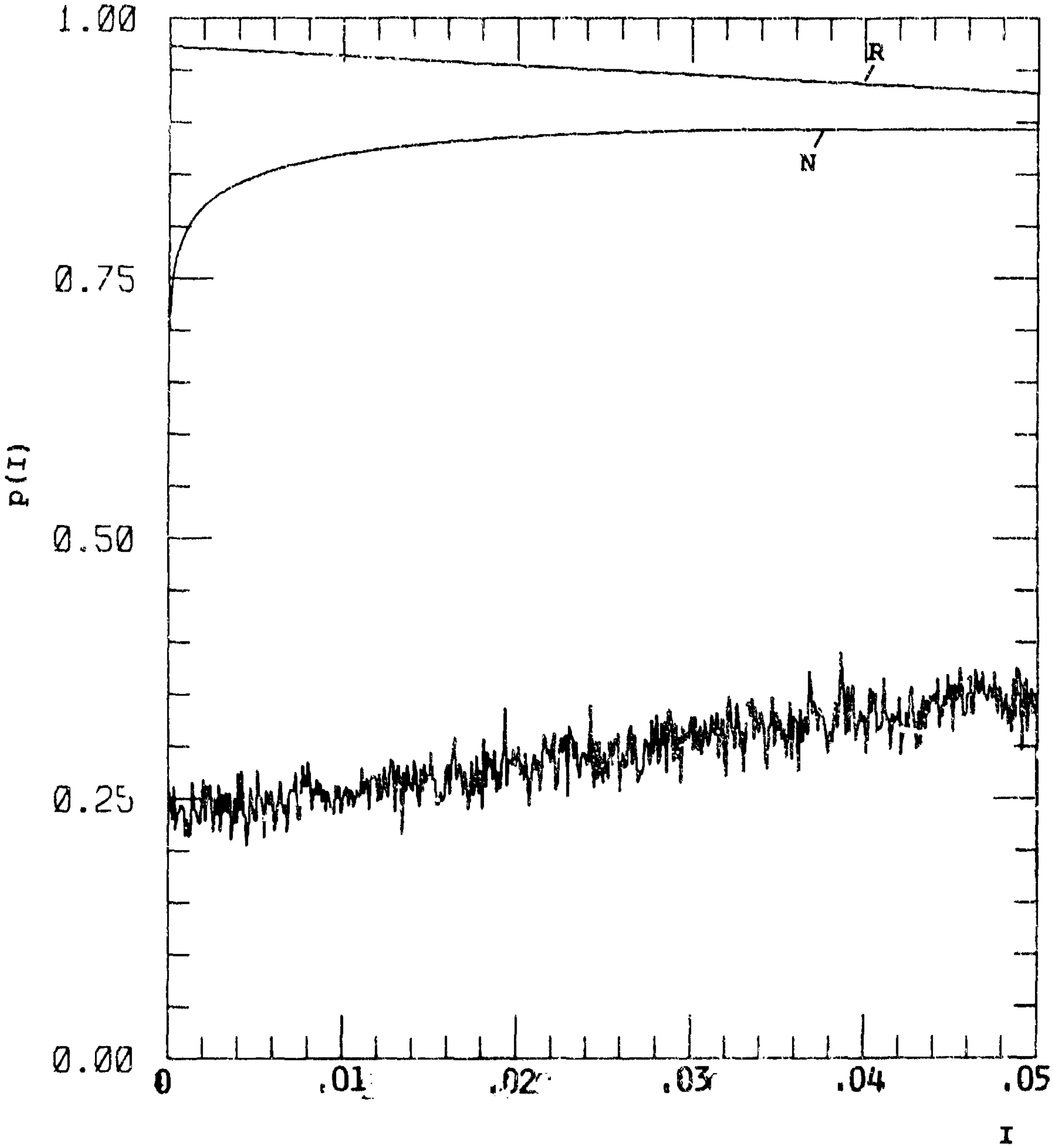

Figure D-11. Probability Distribution for Small I for $s = 2.5$, $\chi^2 = 0.25$, $S_4^{\,2} = 0.959$.

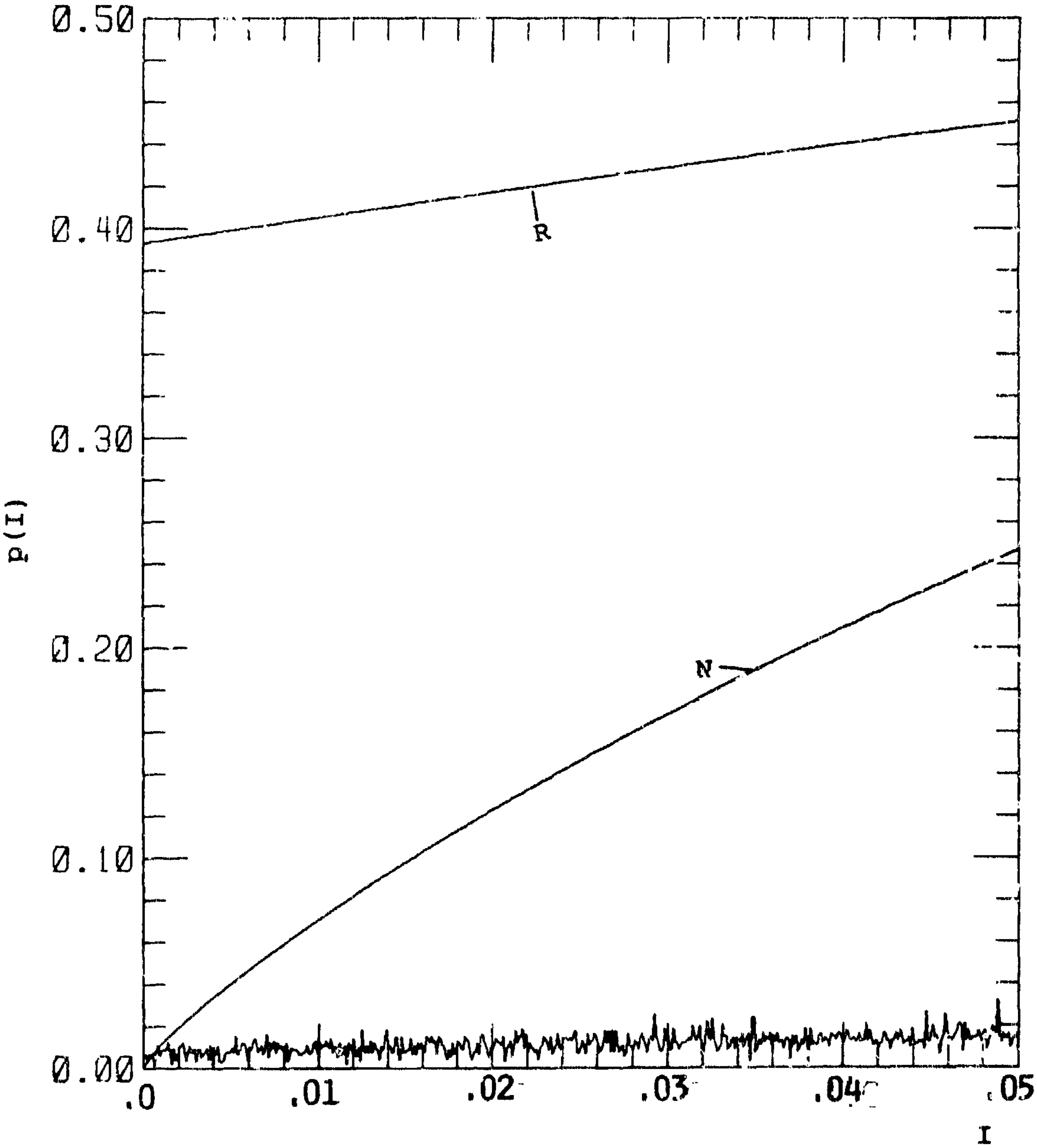

Figure D-12. Probability Distributions for Small I for $s = 3$, $X^2 = 0.1$, $S_4^{\ 2} = 0.548$.

APPENDIX E

CALCULATED BIT ERROR RATES FOR SINGLE POWER LAW PSD

This Appendix contains all the calculated bit error rates for single power law PSD. The six modems considered are: CPSK, ΔPSK, DBPSK, BFSK, QFSK and 8-ARYFSK. The curves are labeled as follows:

AWGN	Additive white Gaussian noise
a	$\overline{X^2_{Ry}} = 0.01$
b	$= 0.025$
c	$= 0.05$
d	$= 0.1$
e	$= 0.25$
f	$= 0.4$
SRF	Slow Rayleigh Fading

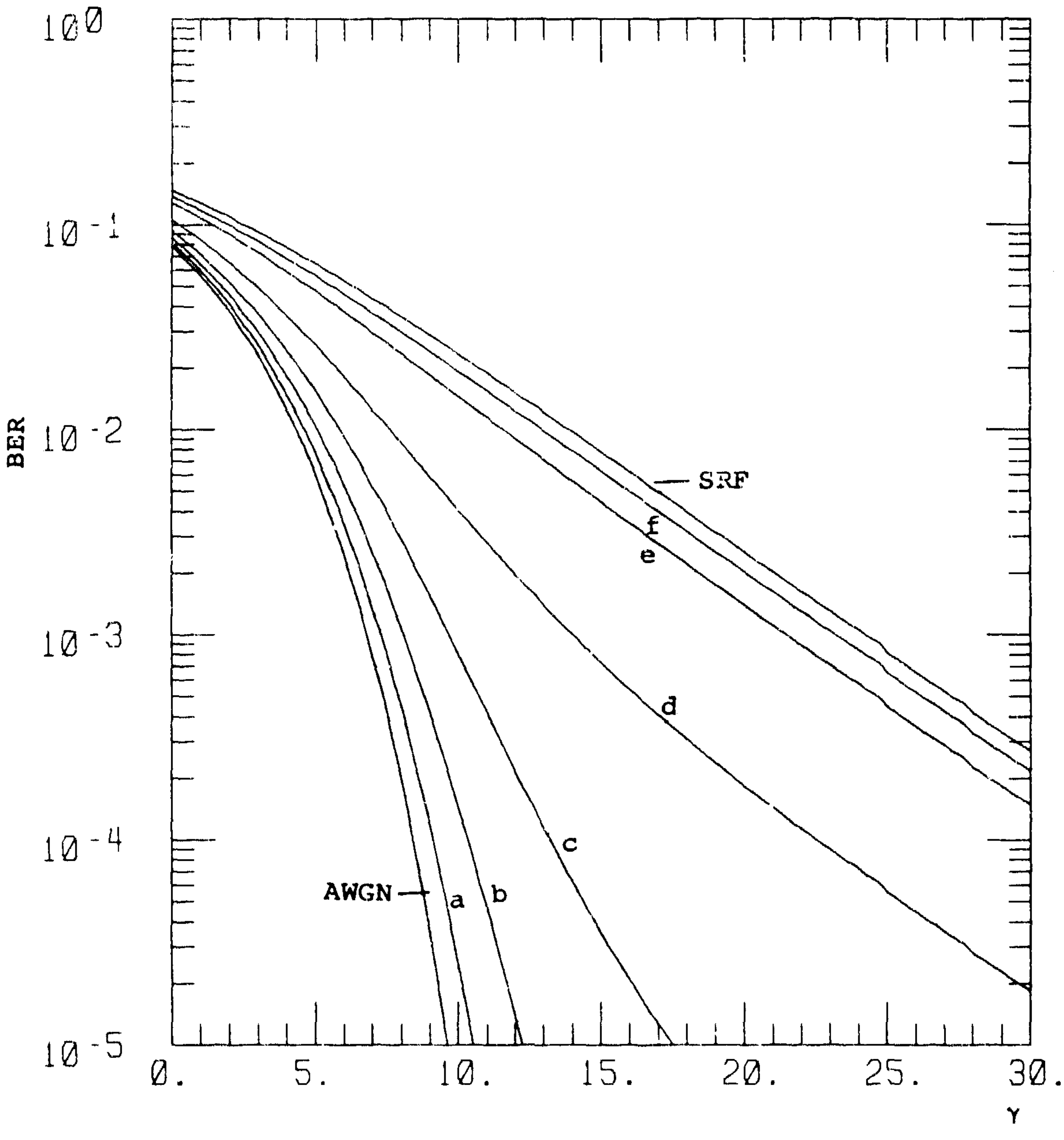

Figure E-1. BER for CPSK, s = 1

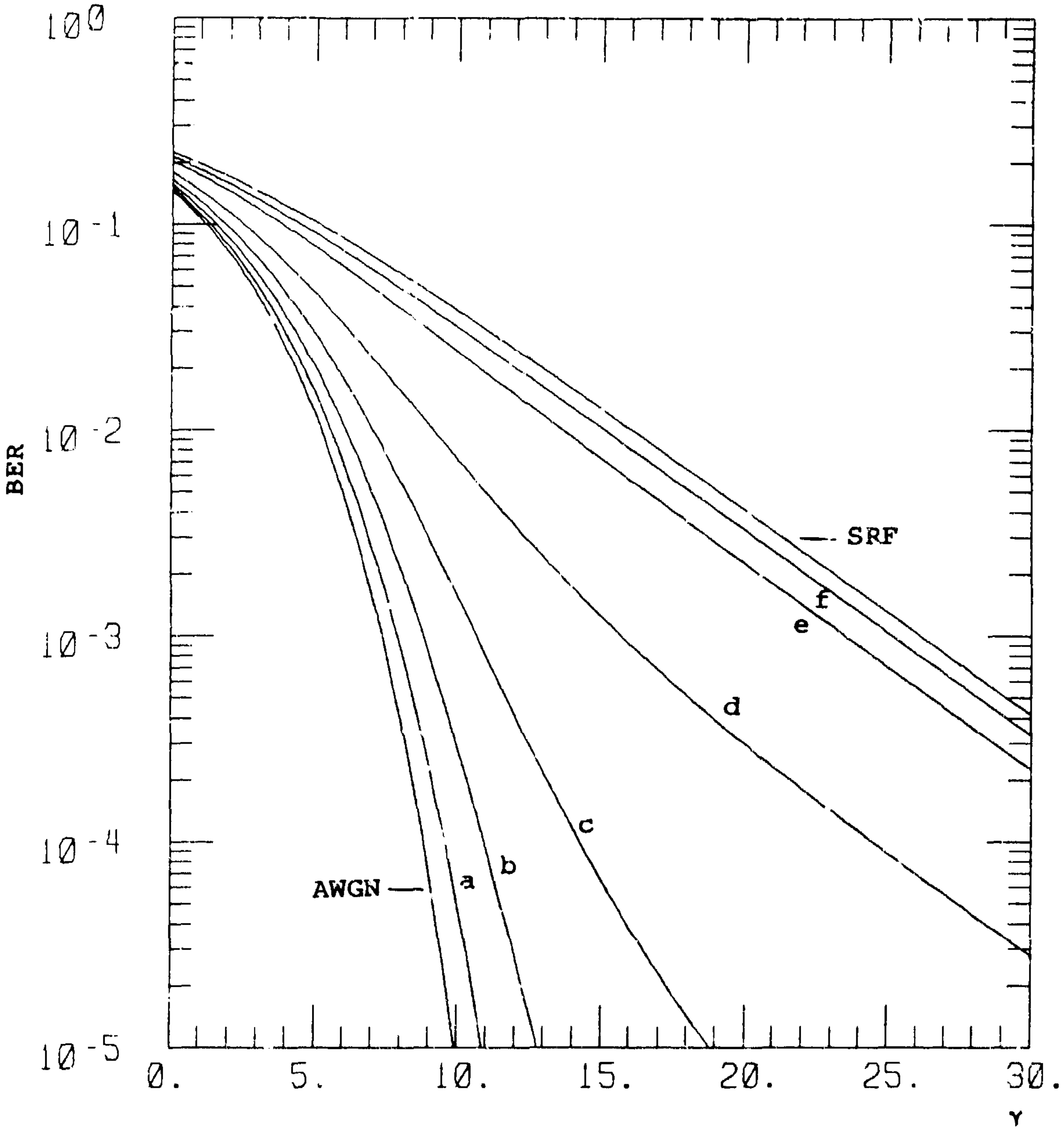

Figure E-2. BER for ΔPSK, s = 1.

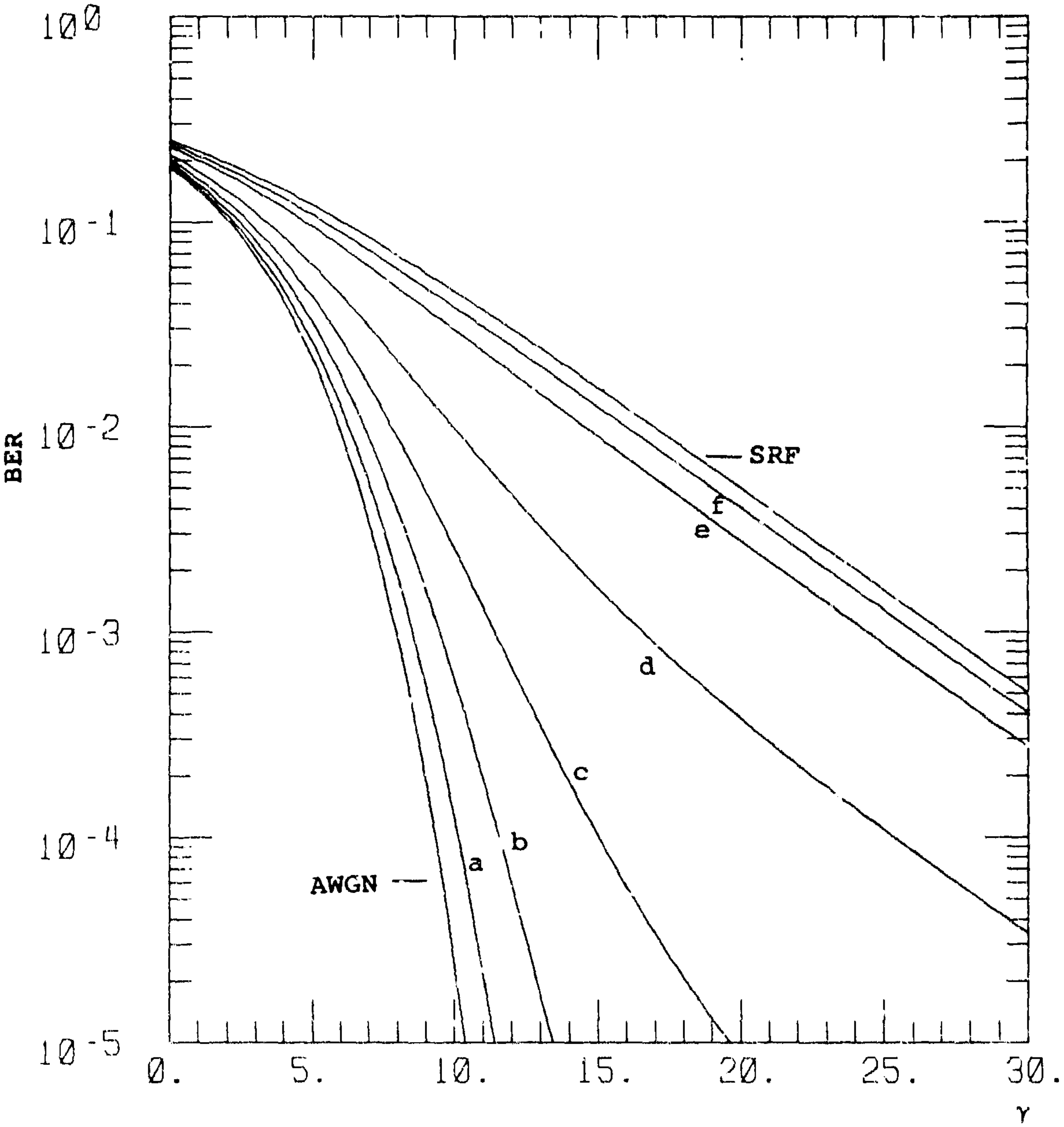

Figure E-3. BER for BDPSK, s = 1.

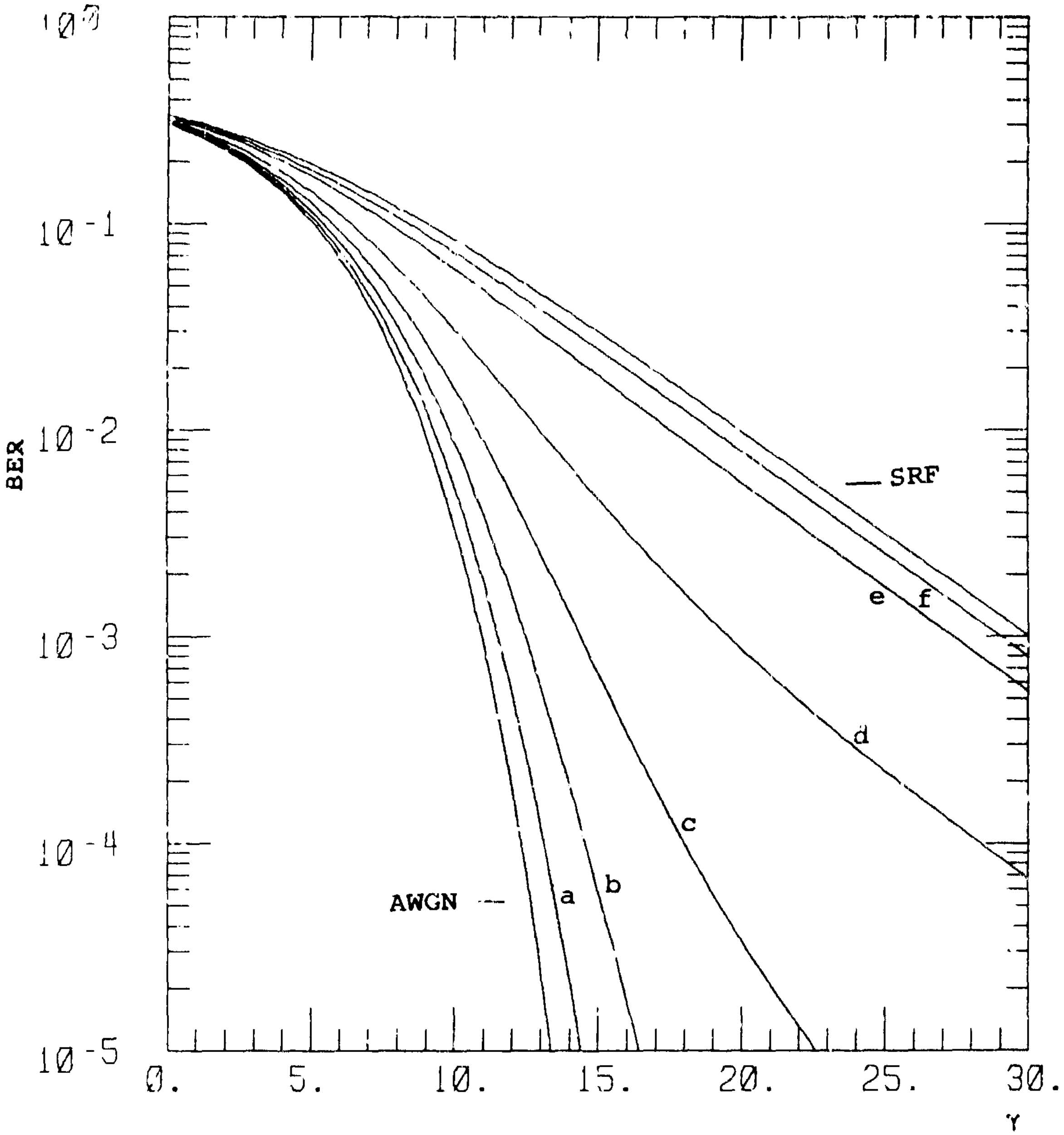

Figure E-4. BER for BFSK, s = 1.

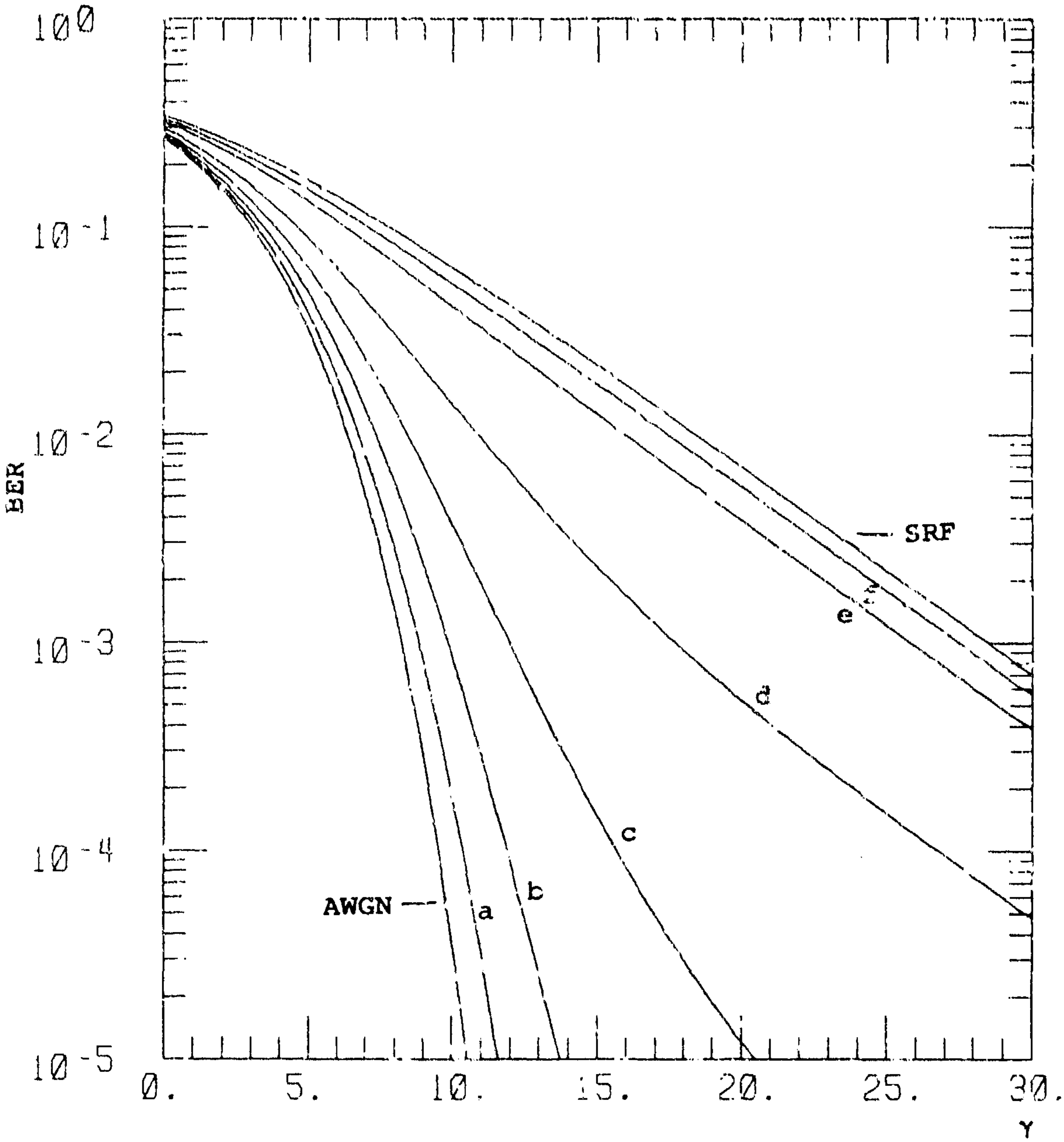

Figure E-5. BER for QFSK.

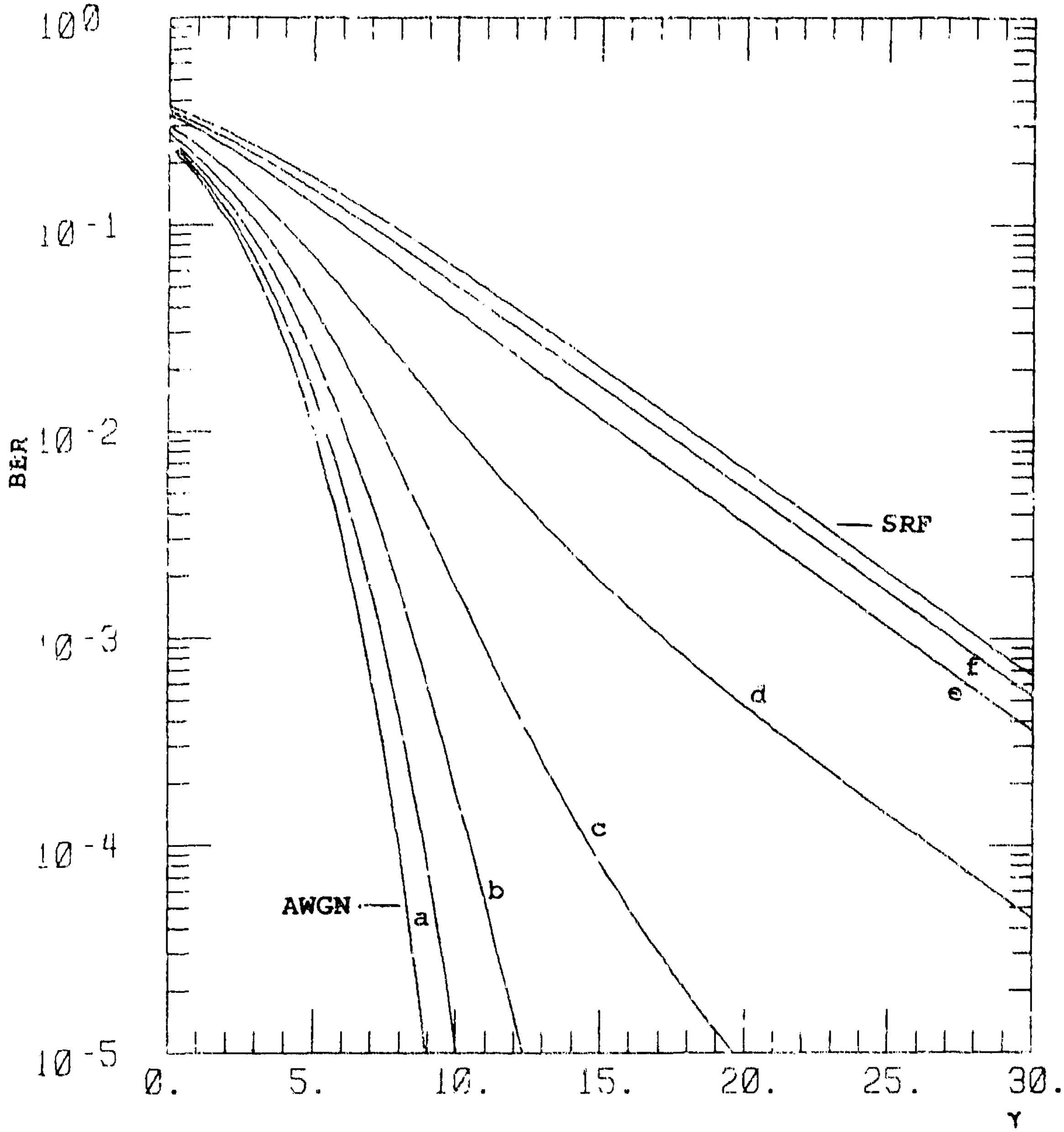

Figure E-6. BER for 8-ARYFSK.

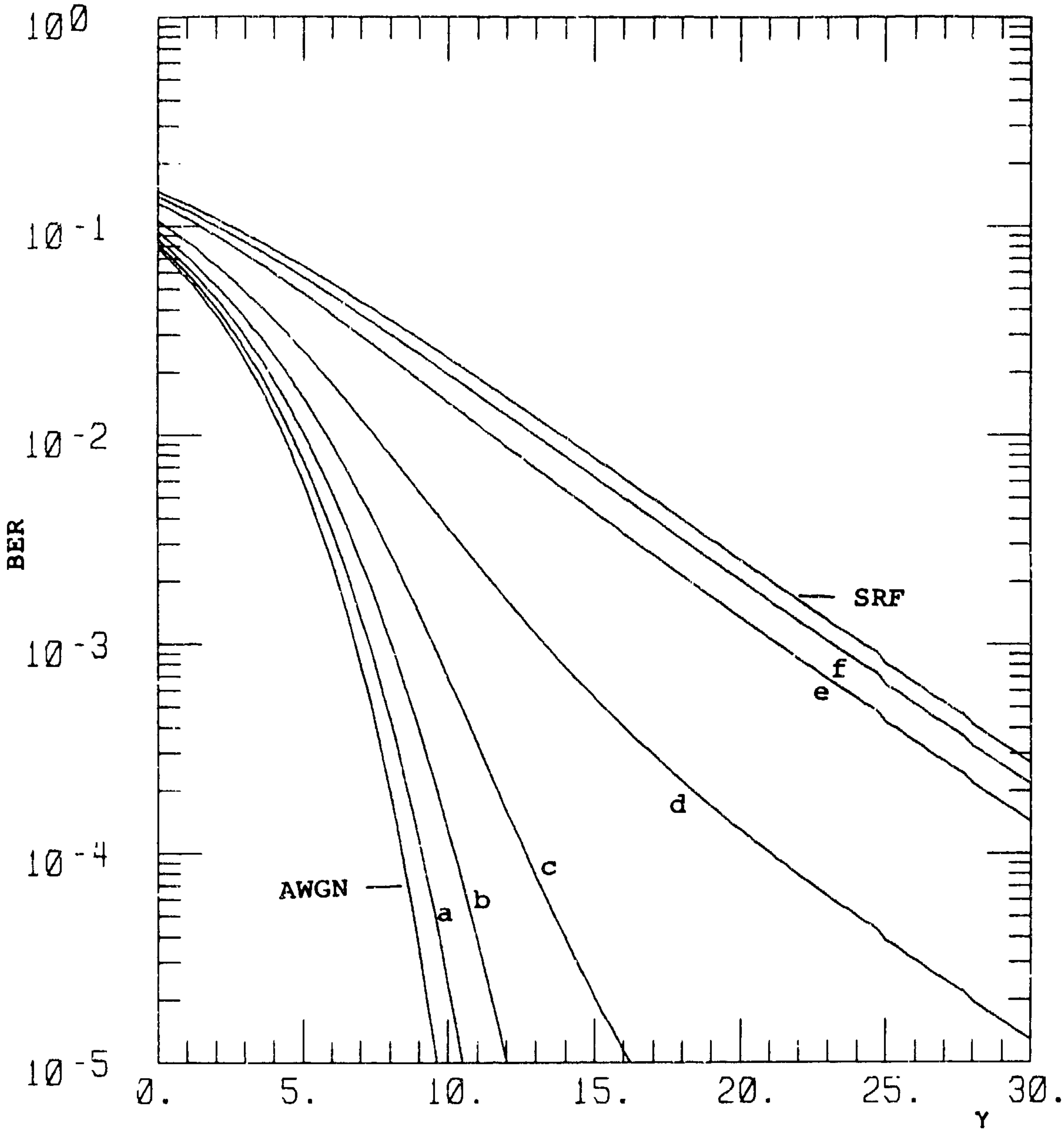

Figure E-7. BER for CPSK s = 1.5.

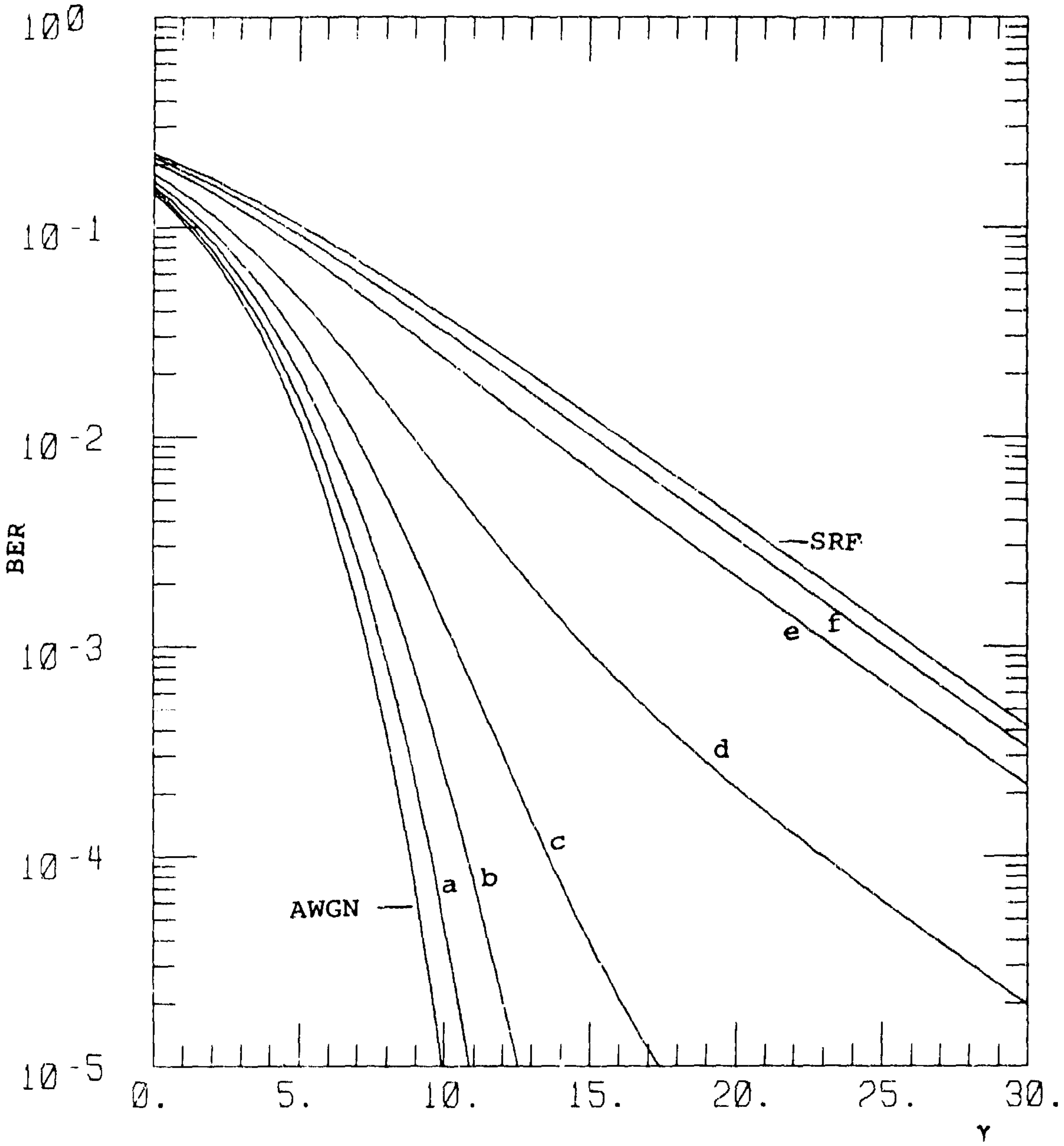

Figure E-8. BER for ΔPSK s = 1.5

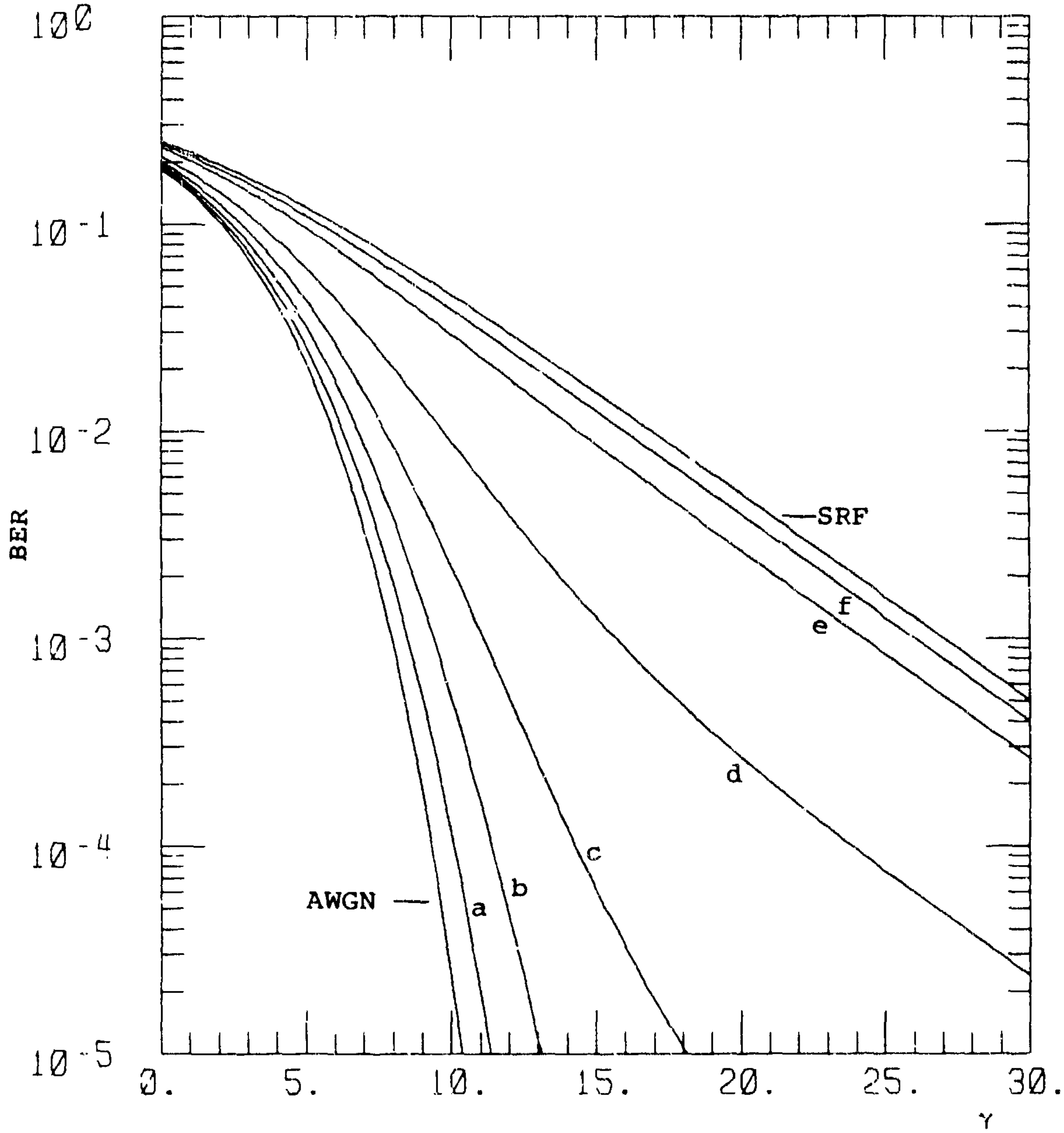

Figure E-9. BER for DBPSK s = 1.5.

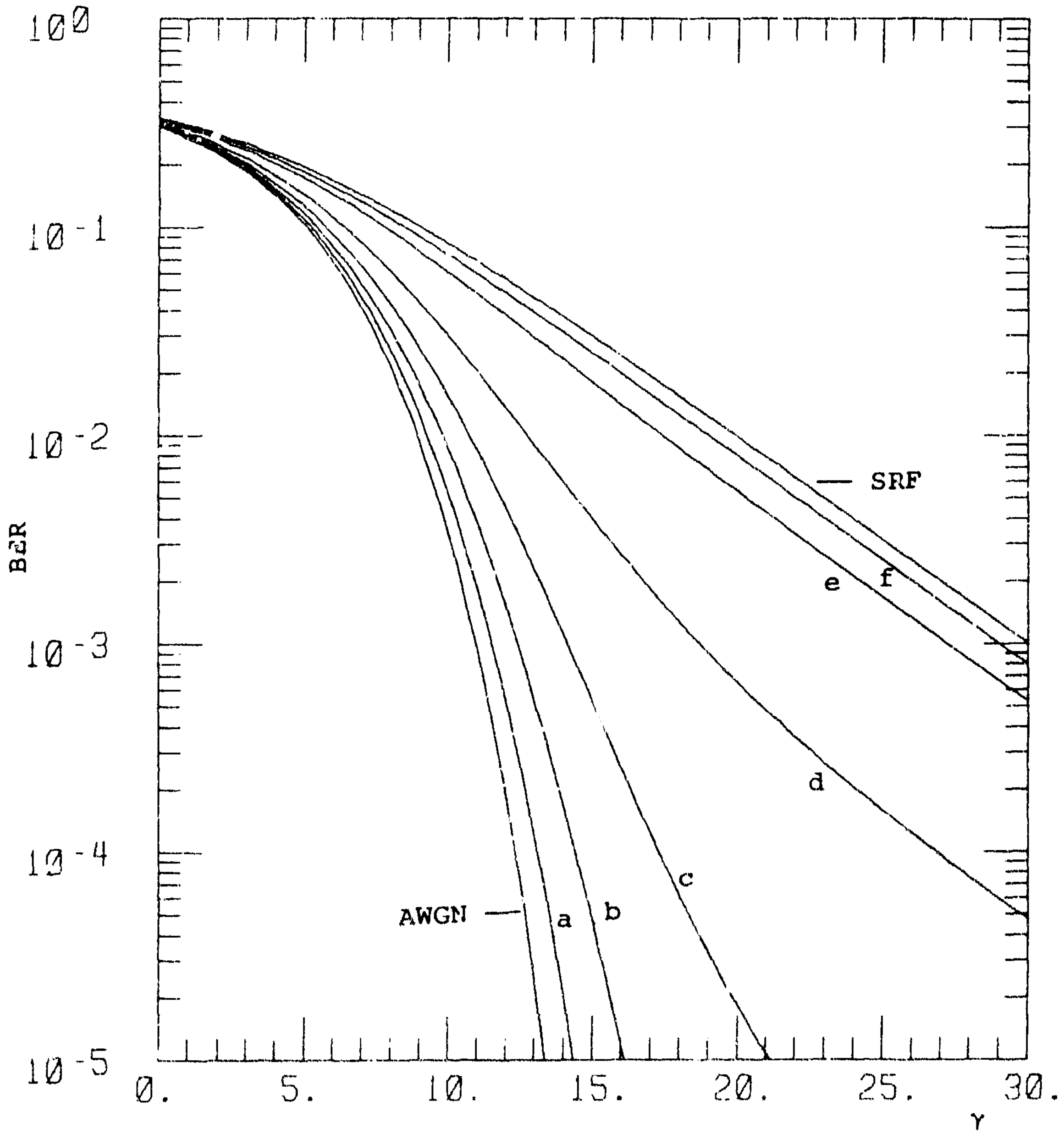

Figure E-10. BER for BFSK s = 1.5.

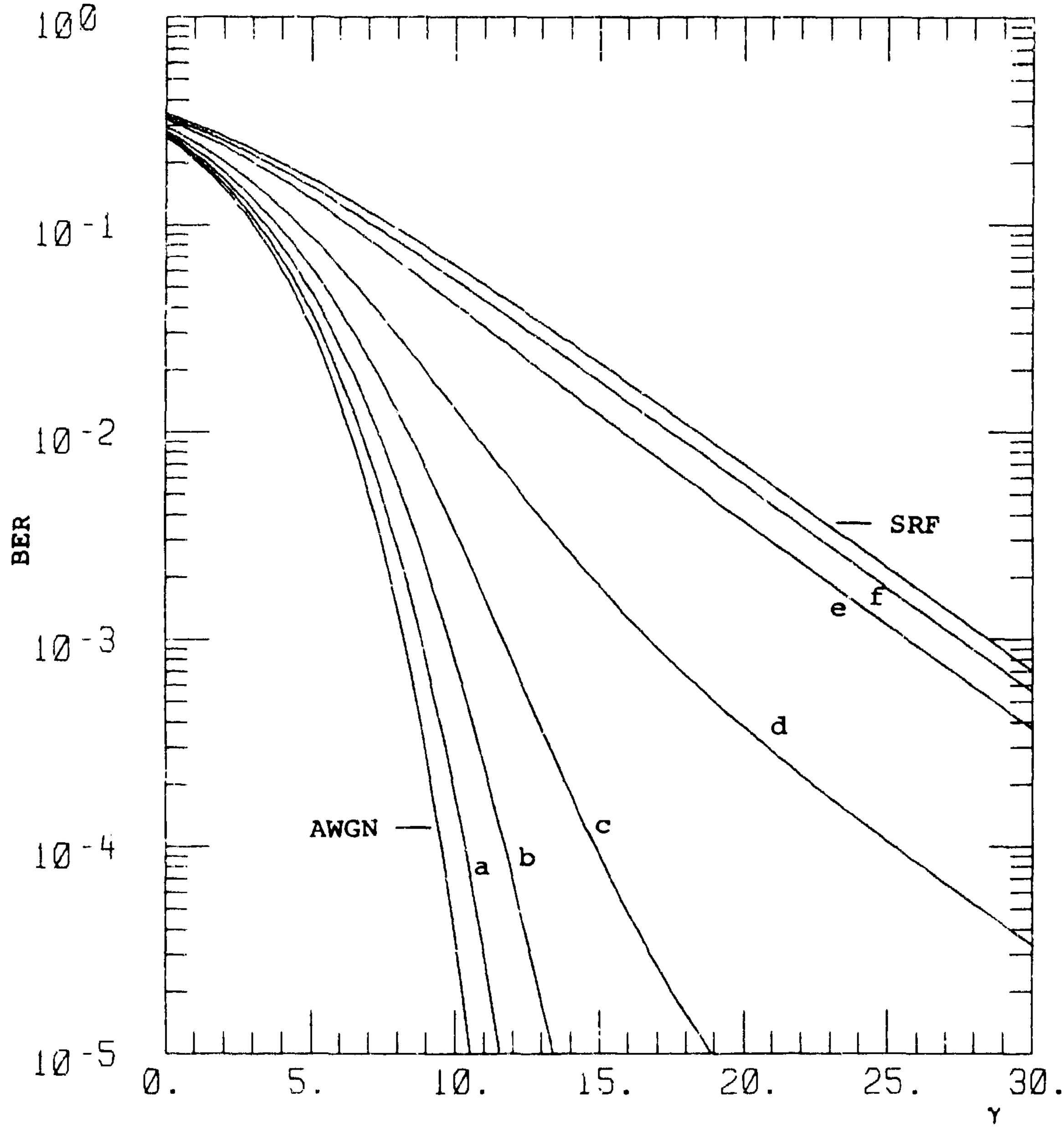

Figure E-11. BER for QFSK s = 1.5.

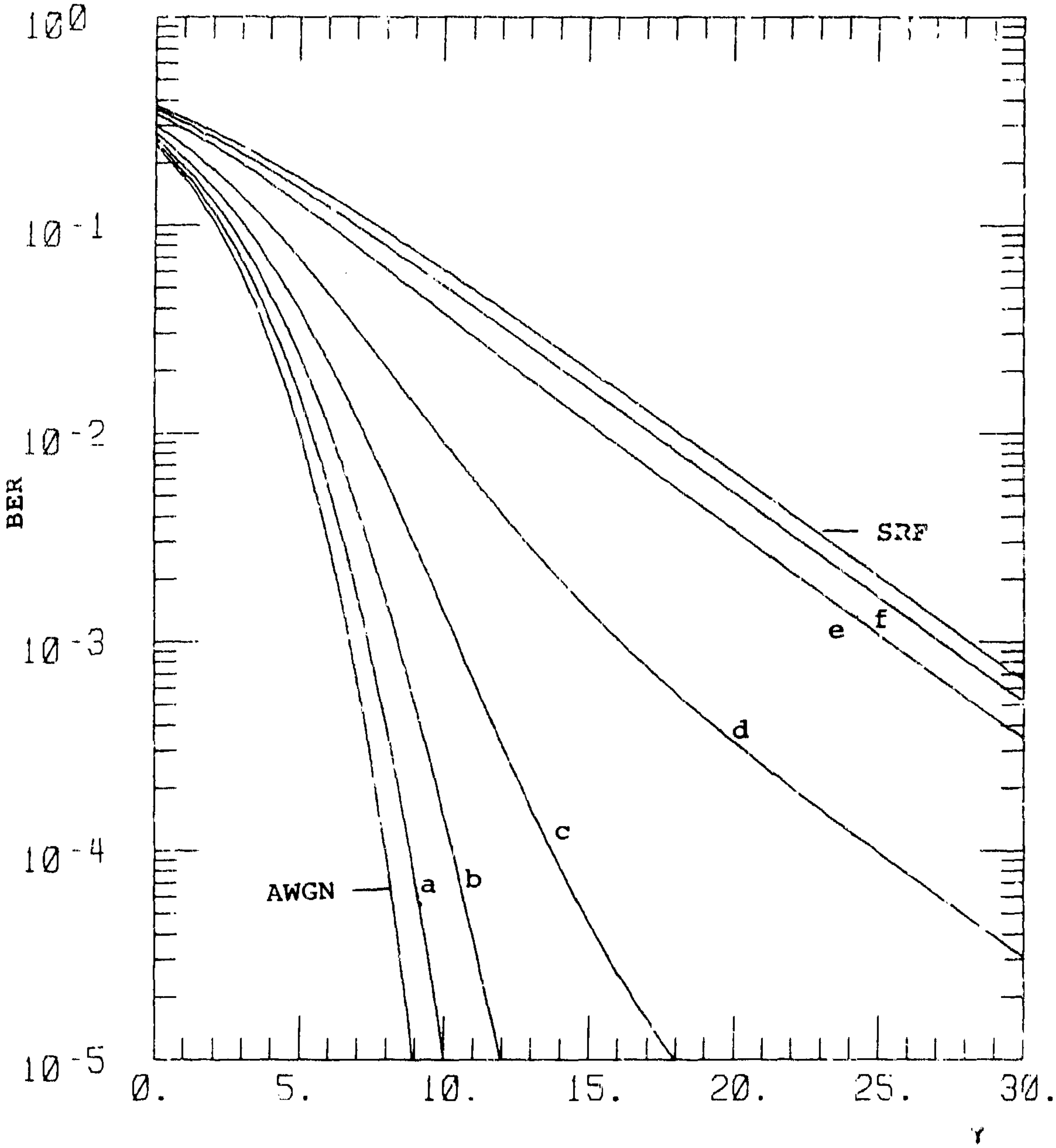

Figure E-12. 8-ARYFSK s = 1.5.

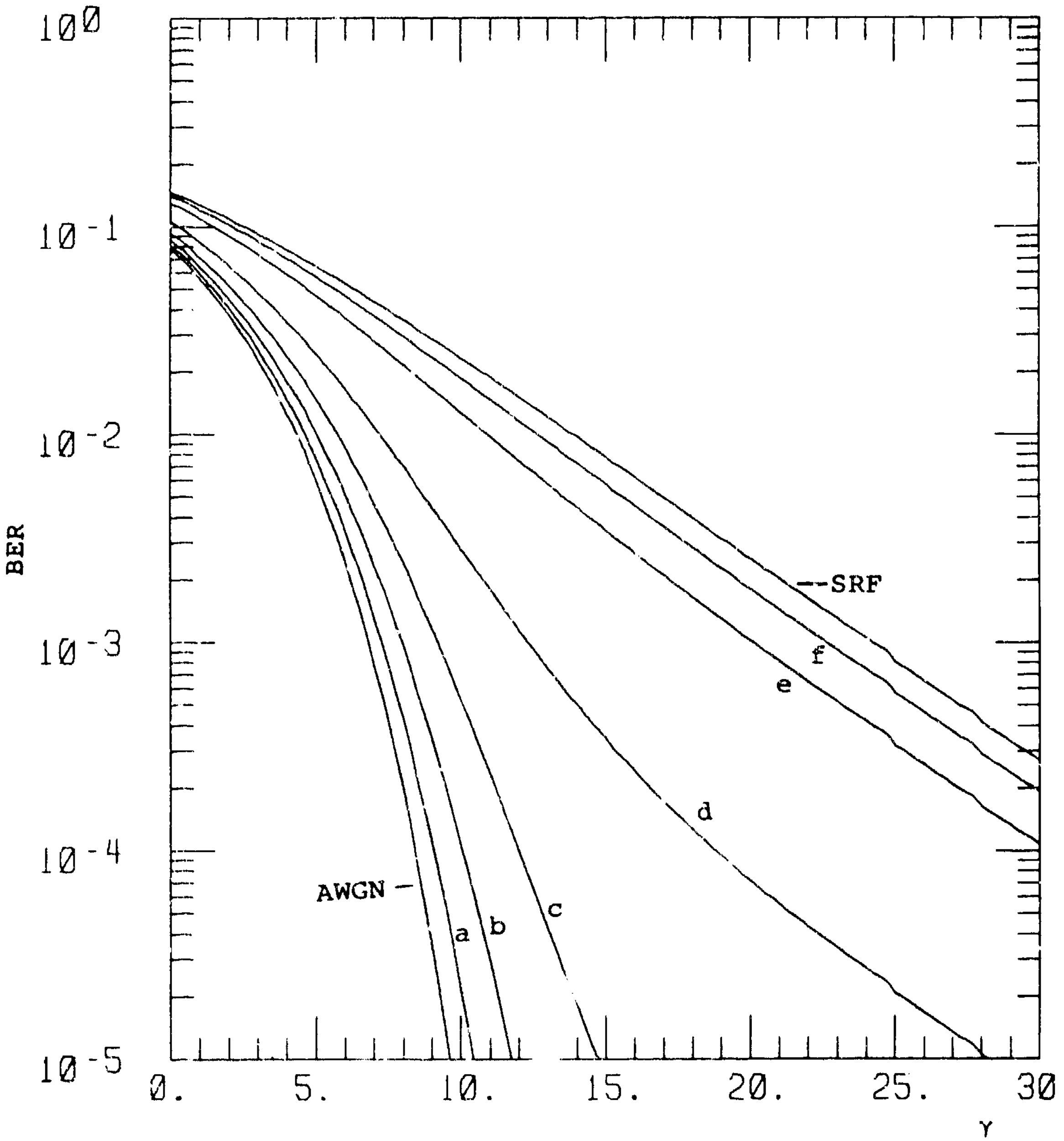

Figure E-13. BER for CPSK, s = 2.

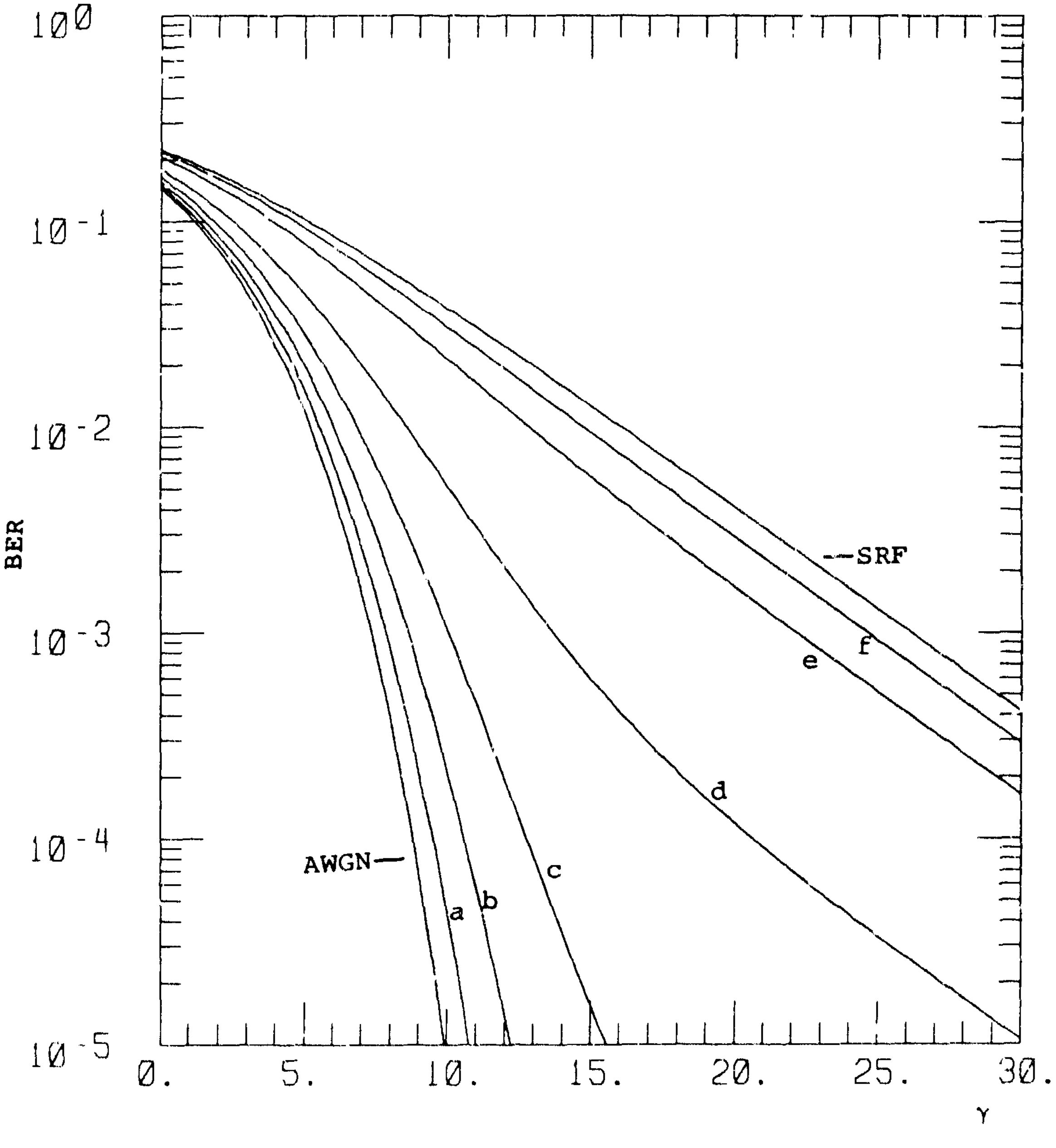

Figure E-14. BER for ΔPSK, s = 2.

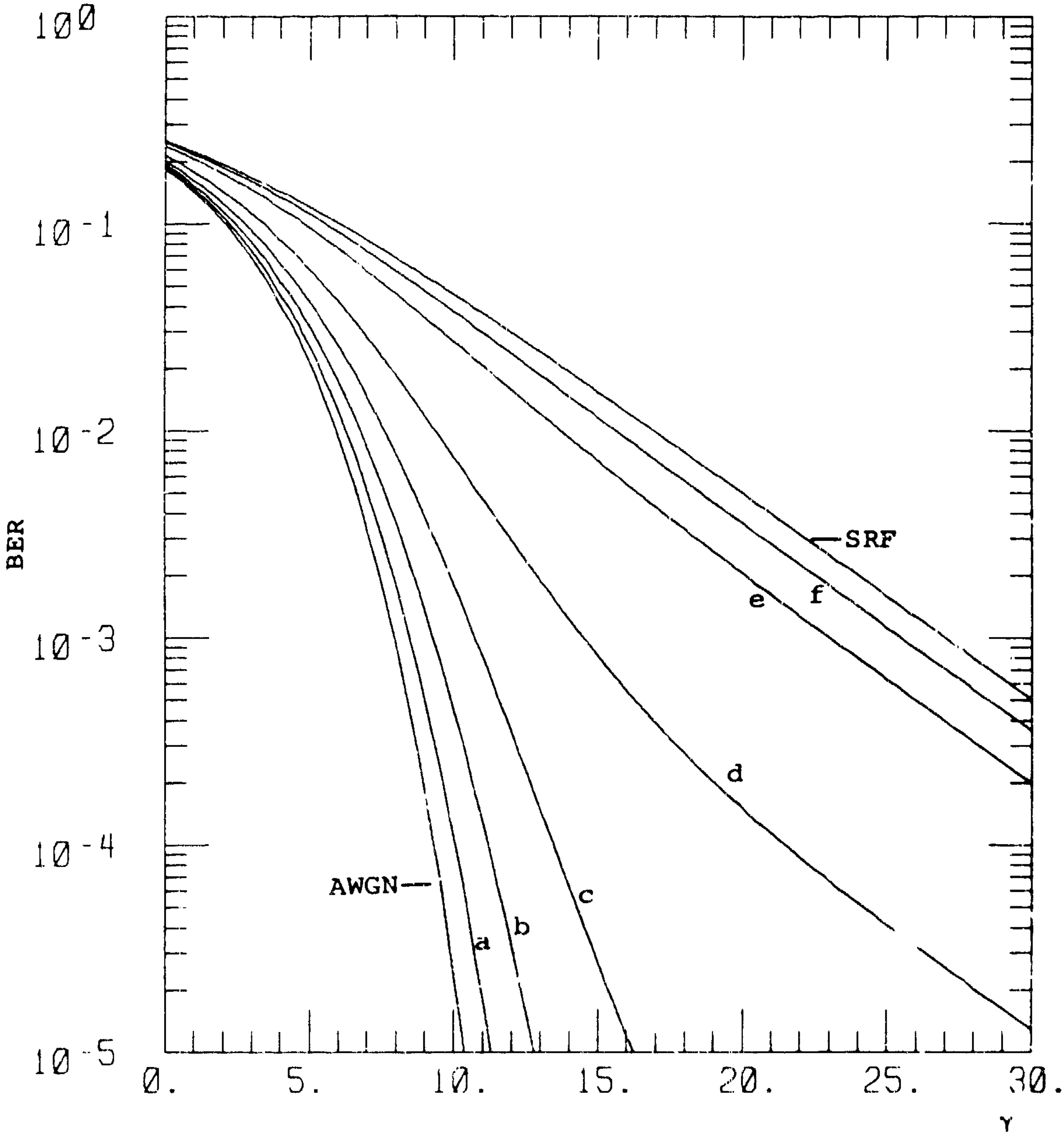

Figure E-15. BER for DBPSK, s = 2.

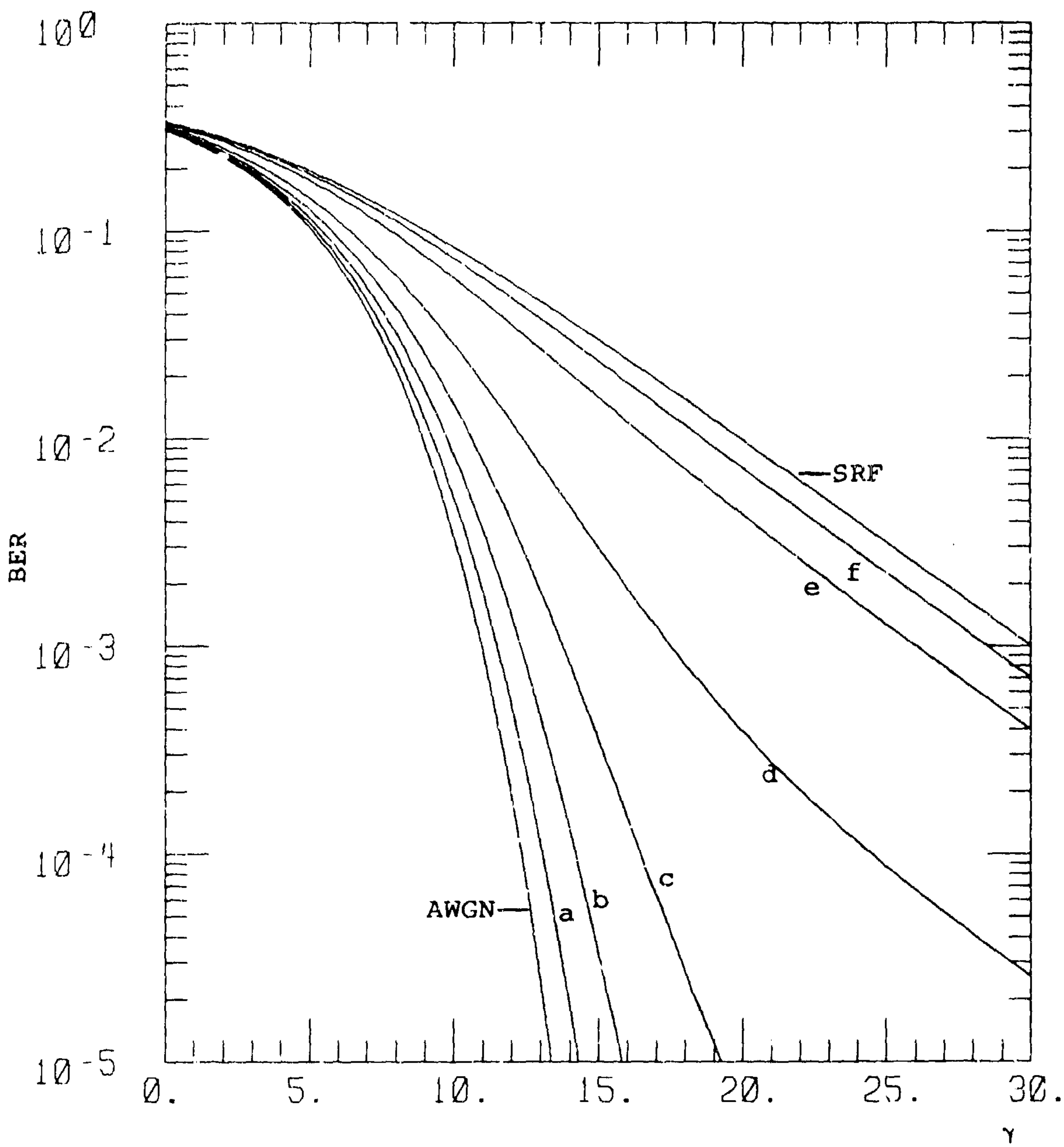

Figure E-16. BER for BFSK, s = 2.

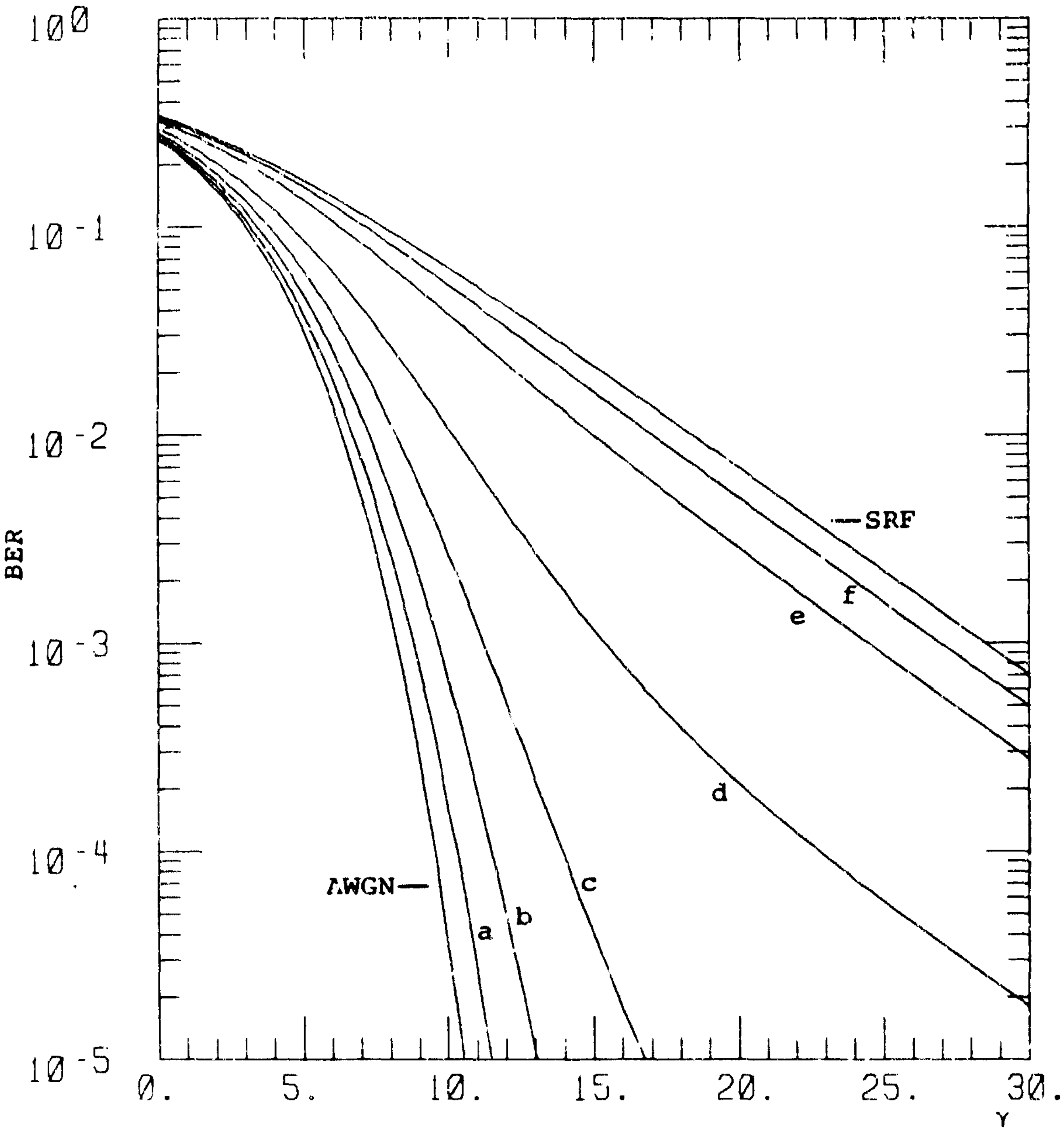

Figure E-17. BER for QFSK, s = 2.

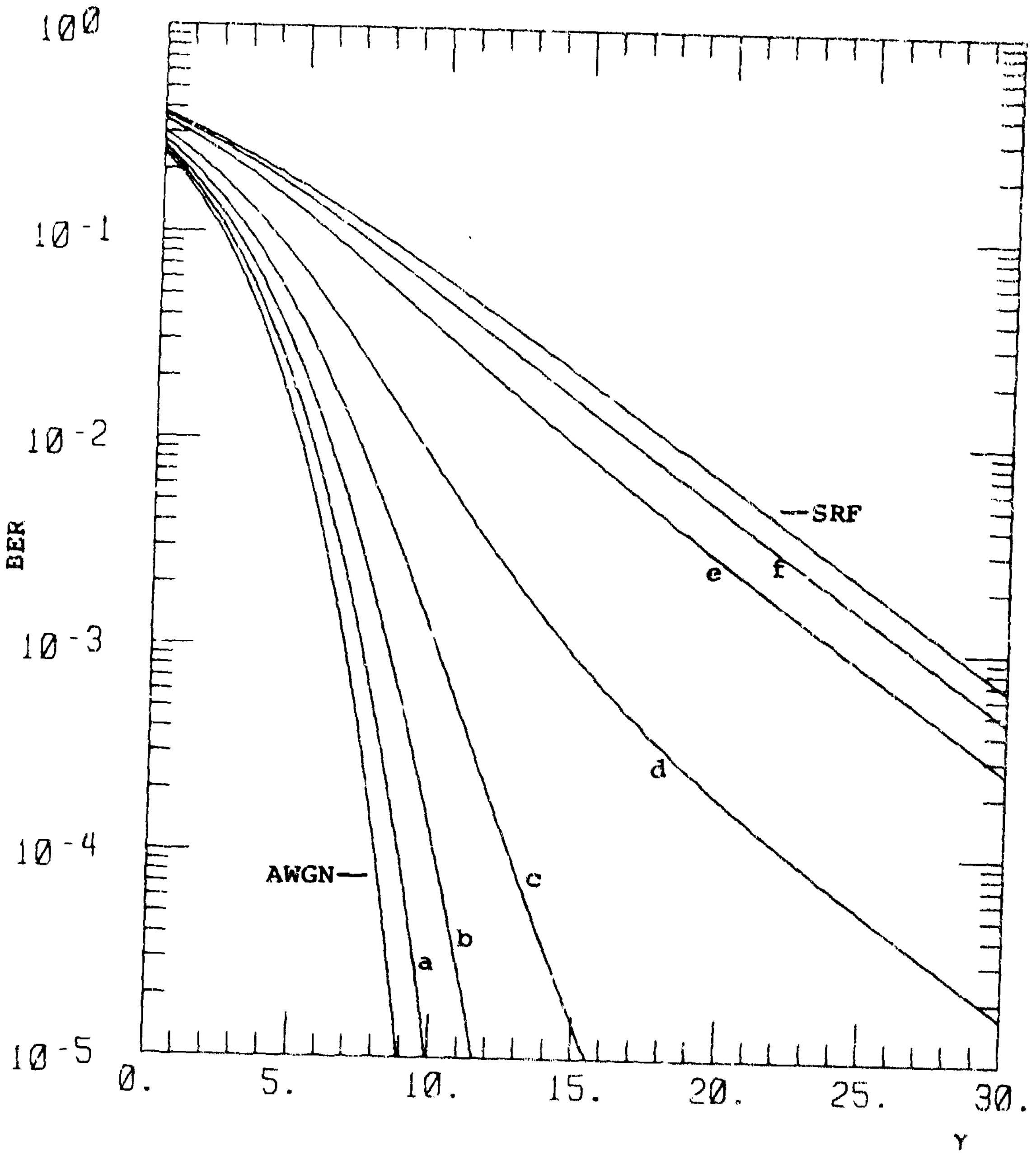

Figure E-18. BER for 8-ARYFSK, s = 2.

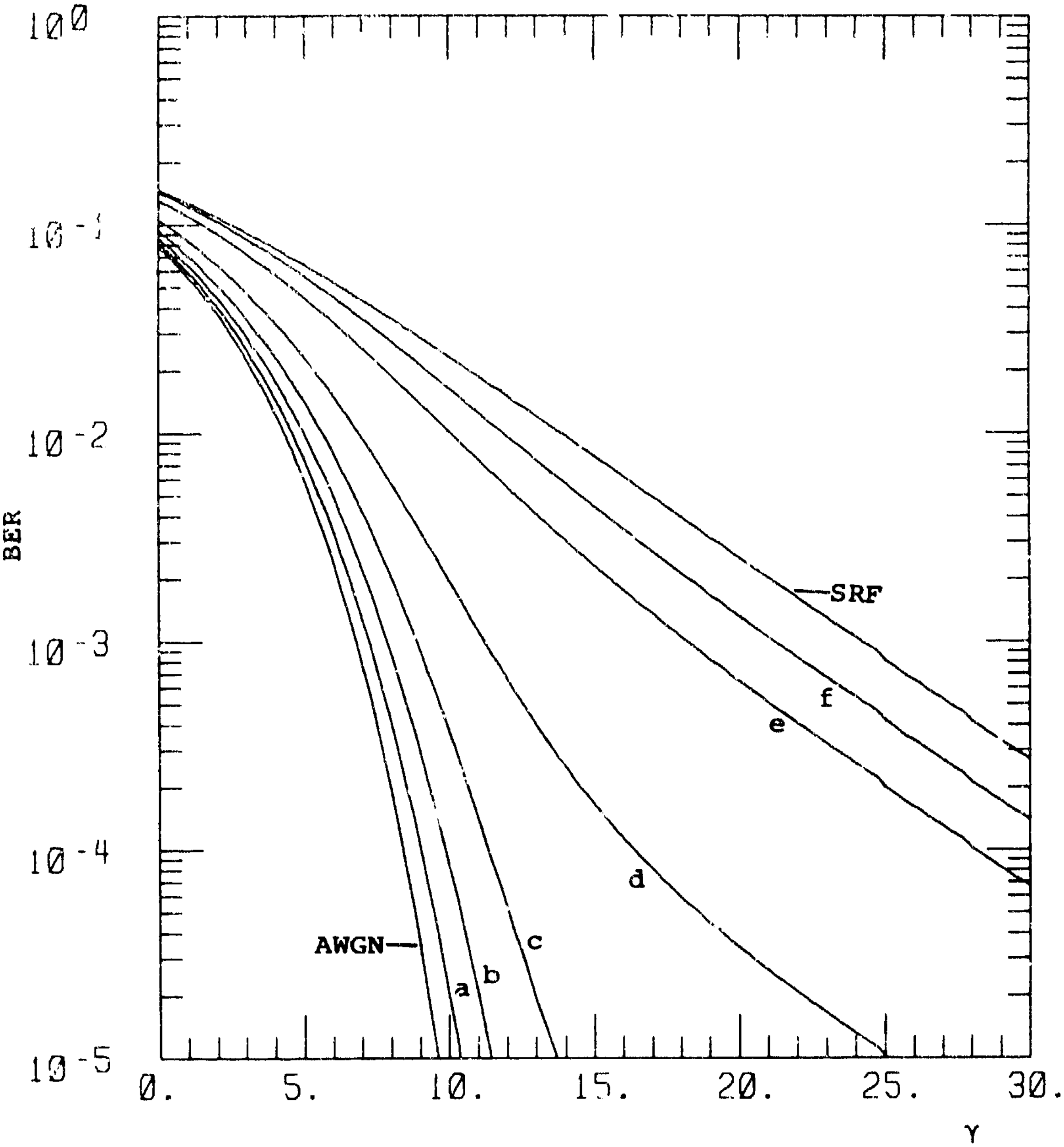

Figure E-19. BER for CPSK s = 2.5.

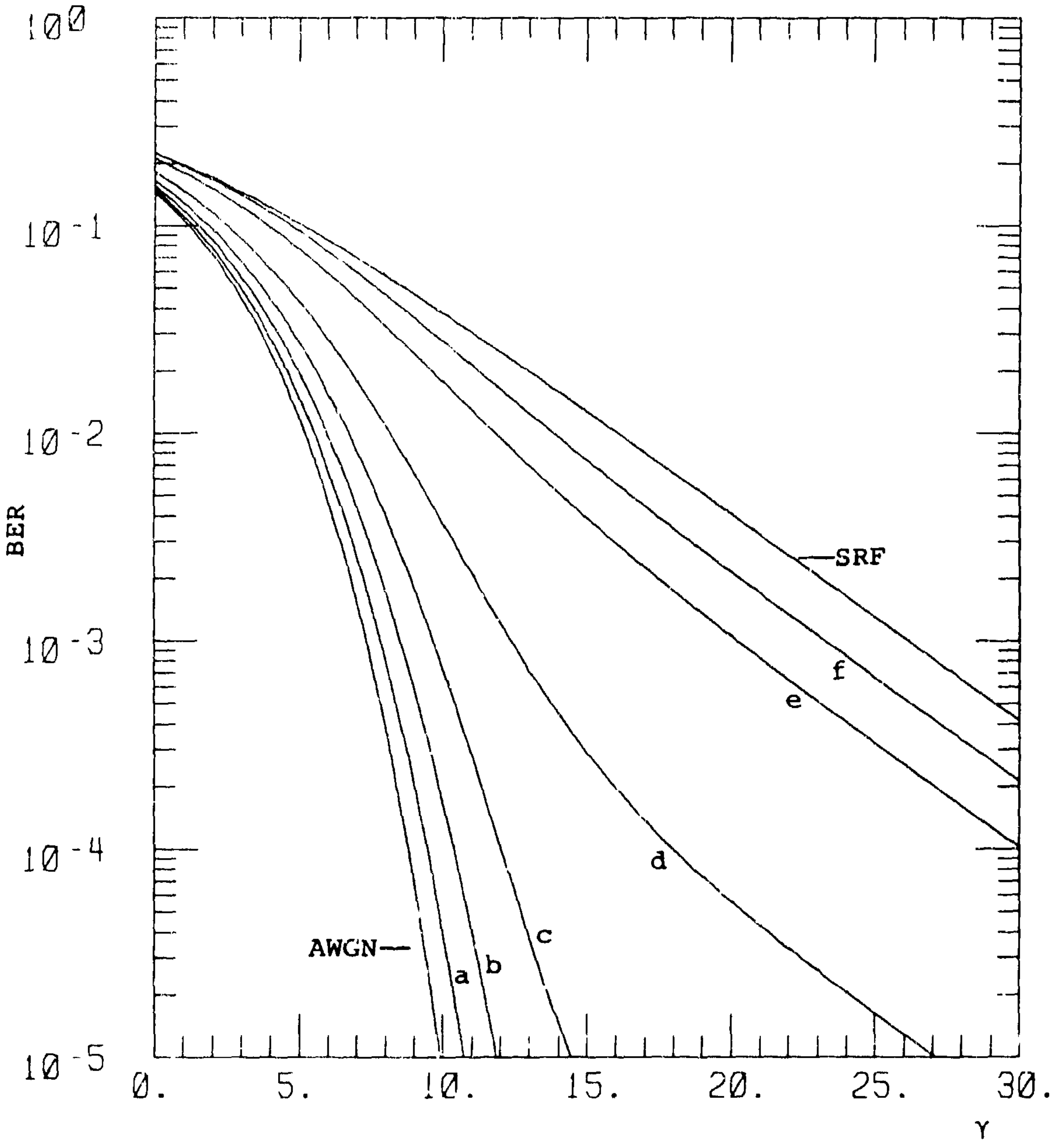

Figure E-20. BER for ΔPSK ς = 2.5.

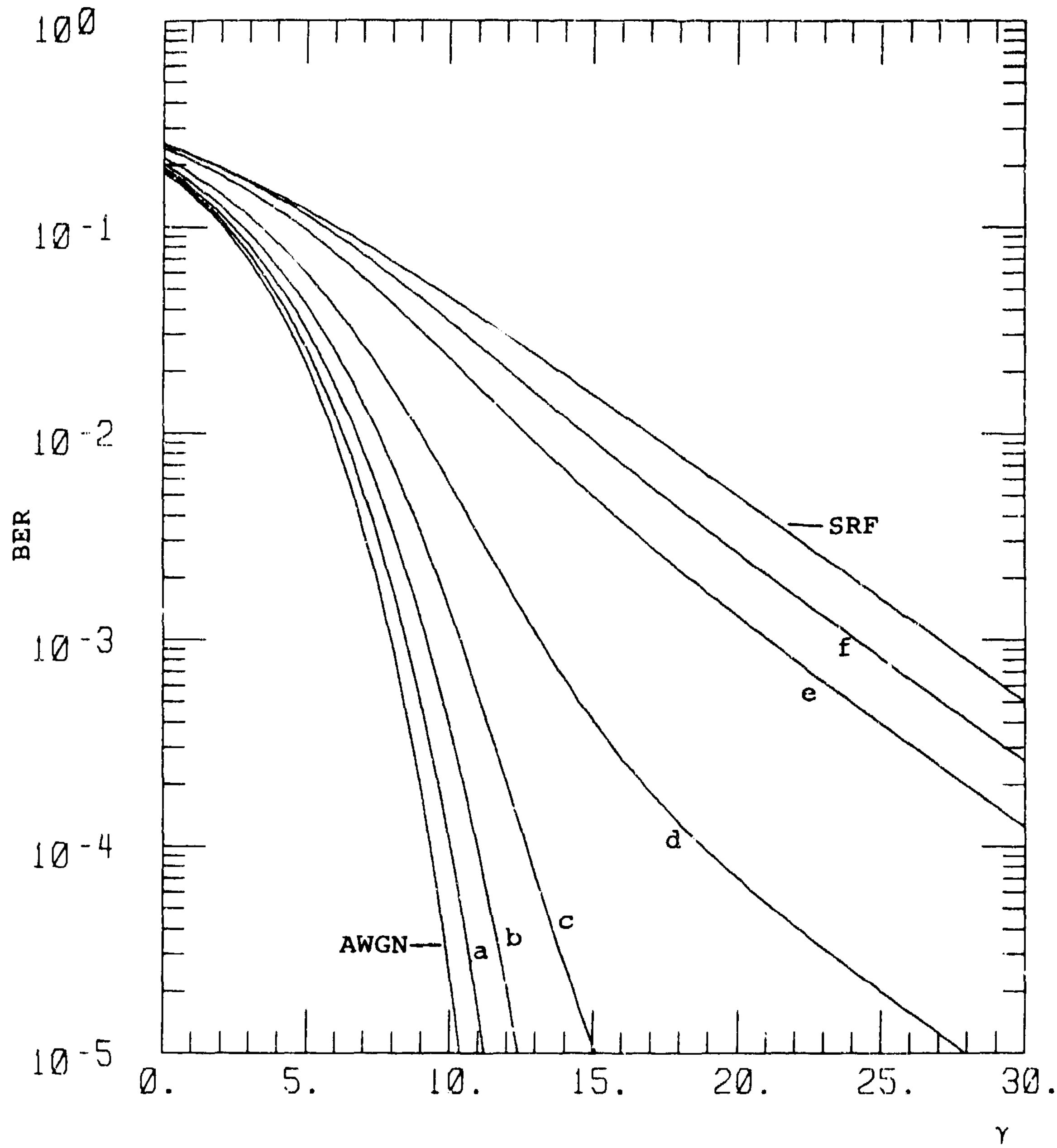

Figure B-21. BER for DBPSK s = 2.5.

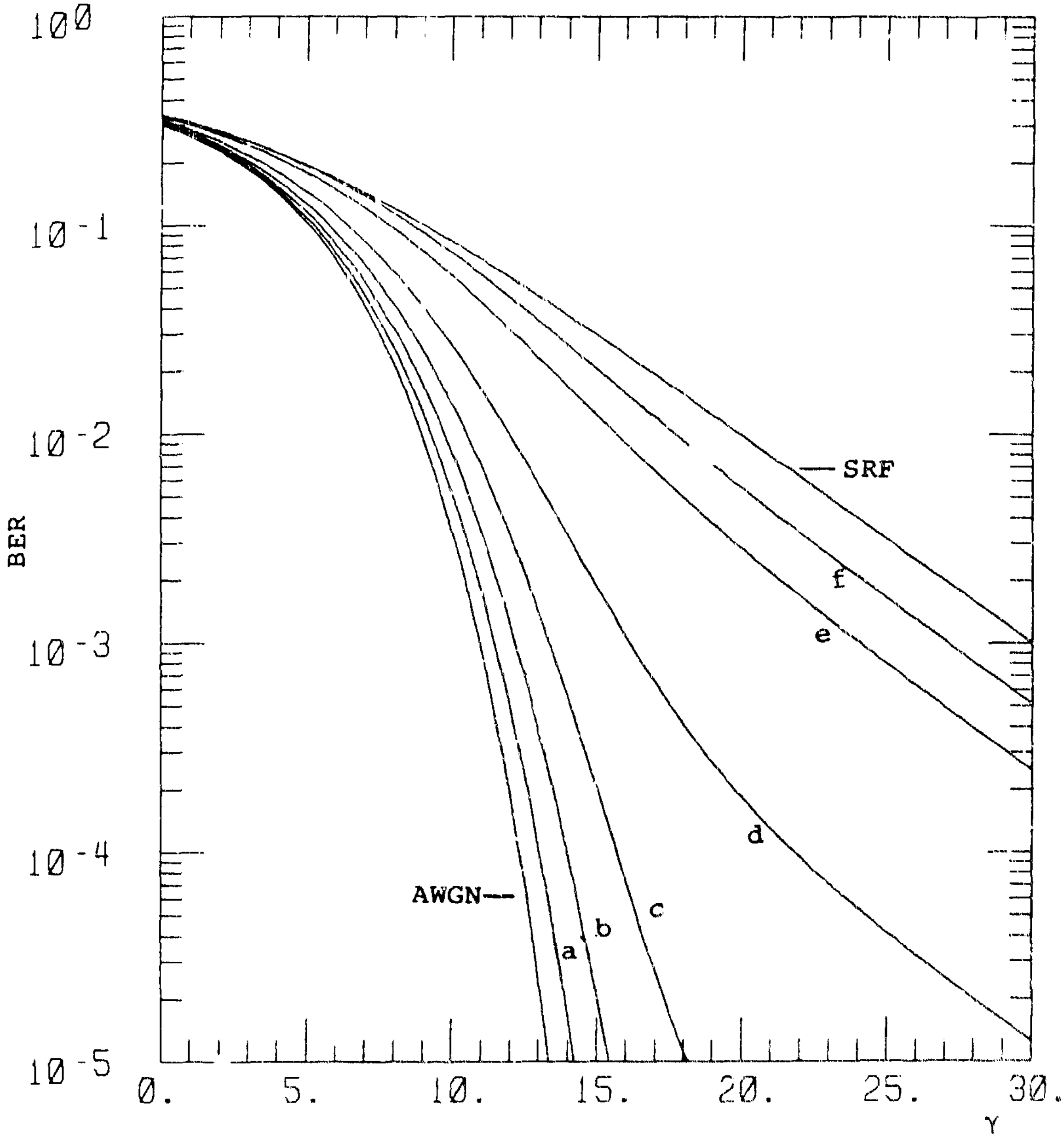

Figure E-22. BER for BFSK s = 2.5.

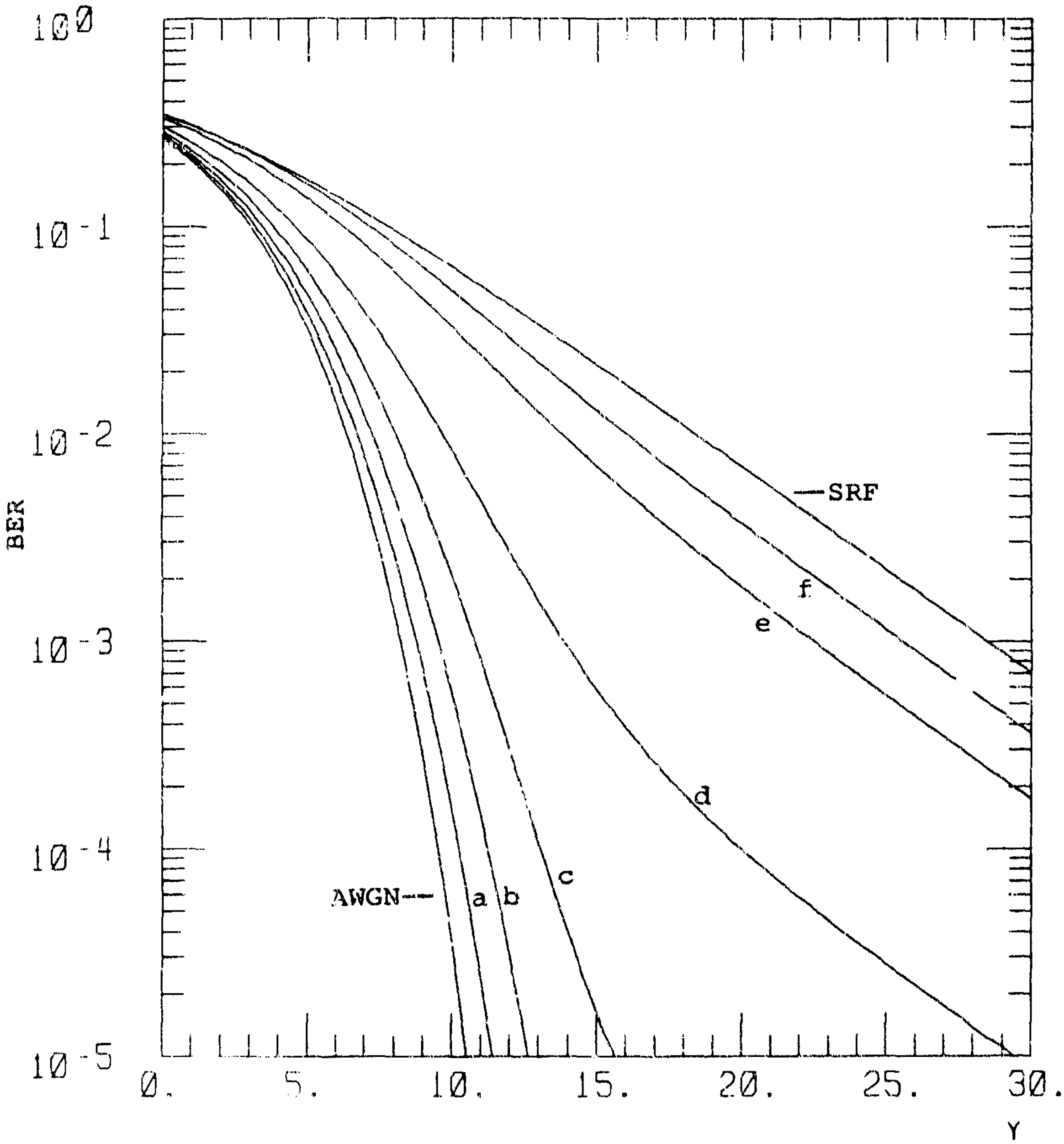

Figure E-23. BER for QFSK s = 2.5.

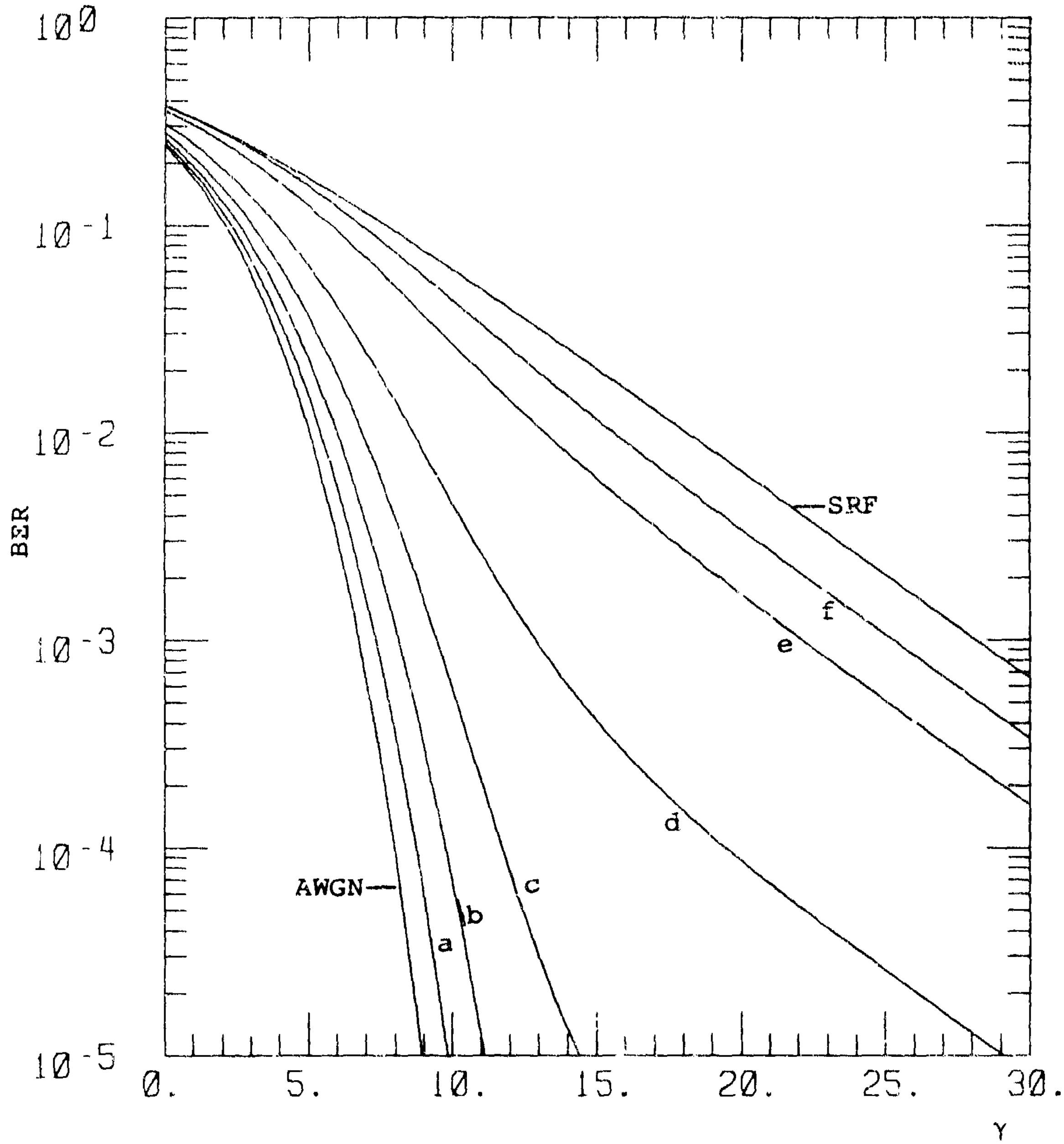

Figure E-24. BER for 8-ARYFSK s = 2.5.

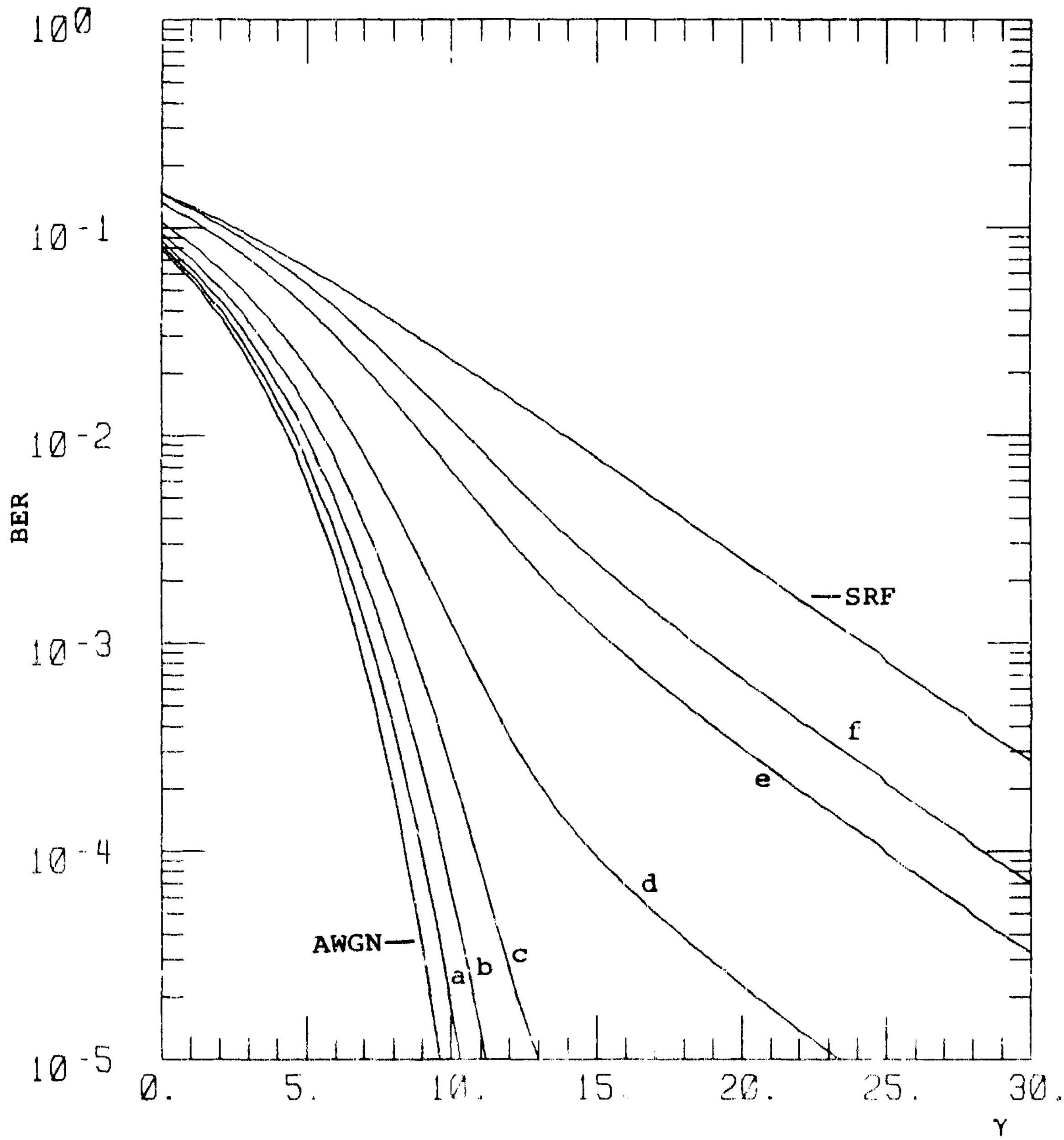

Figure E-25. BER for CPSK s = 3.

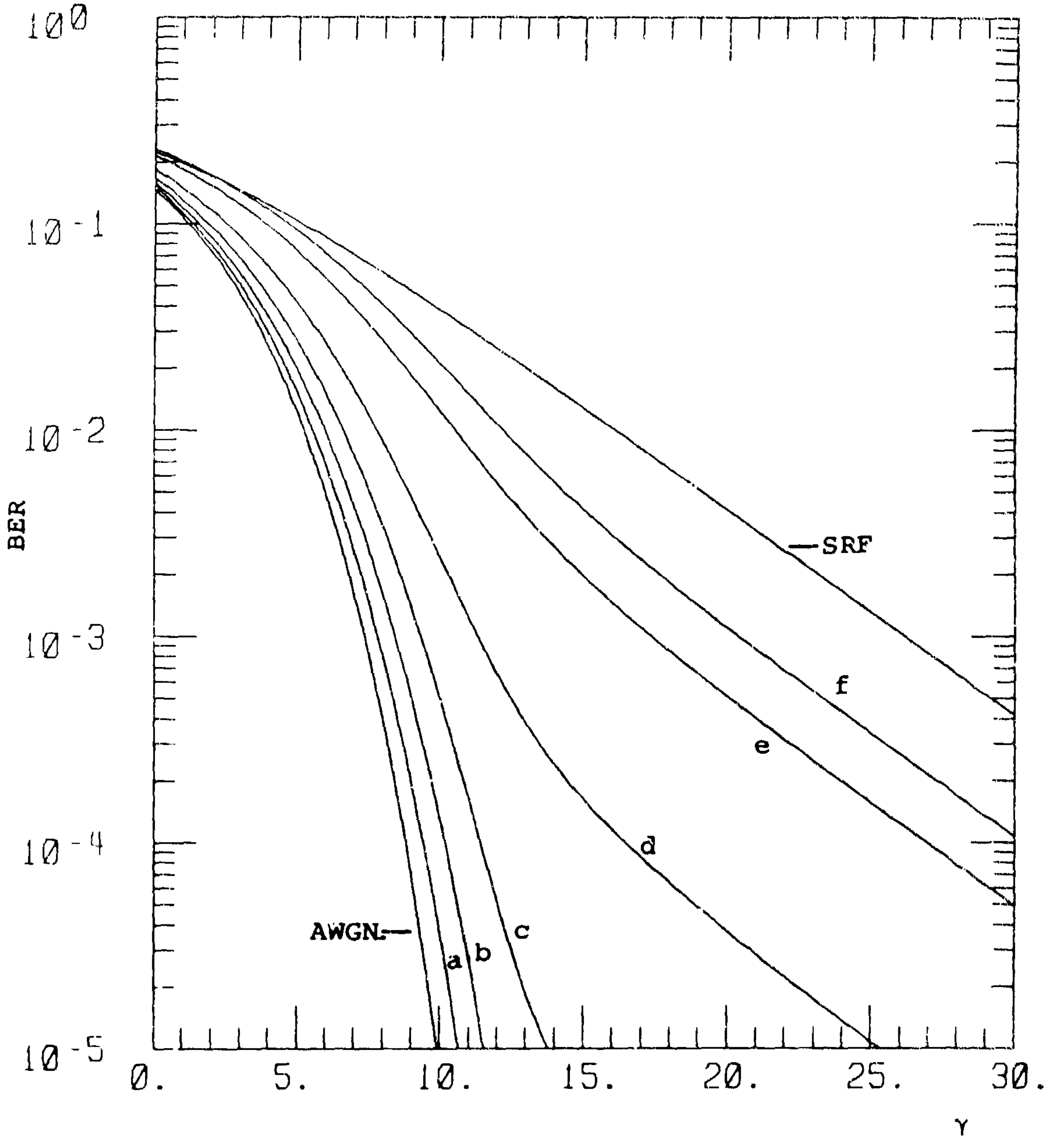

Figure E-26. BER for ΔPSK s = 3.

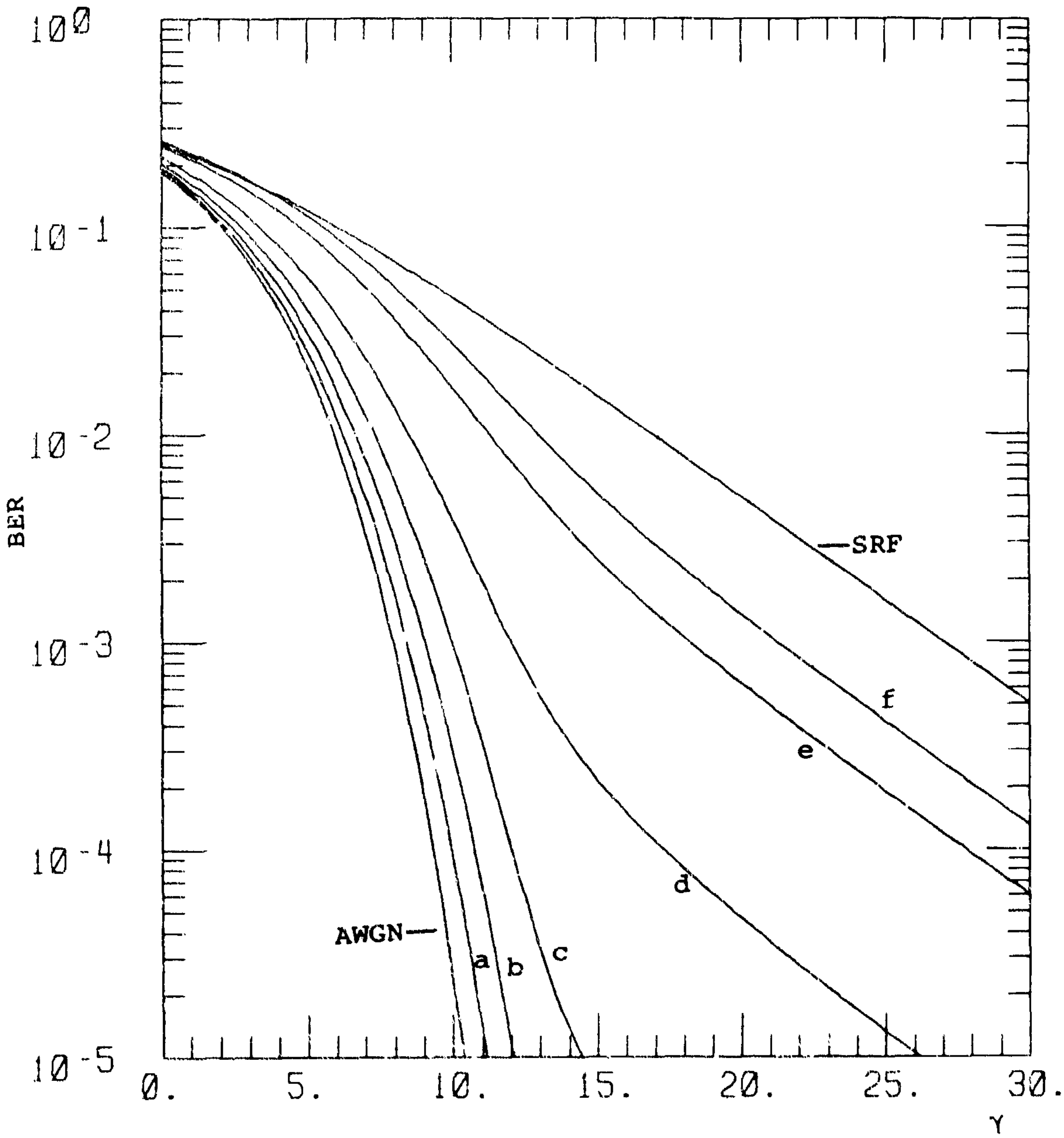

Figure E-27. BER for DBPSK s = 3.

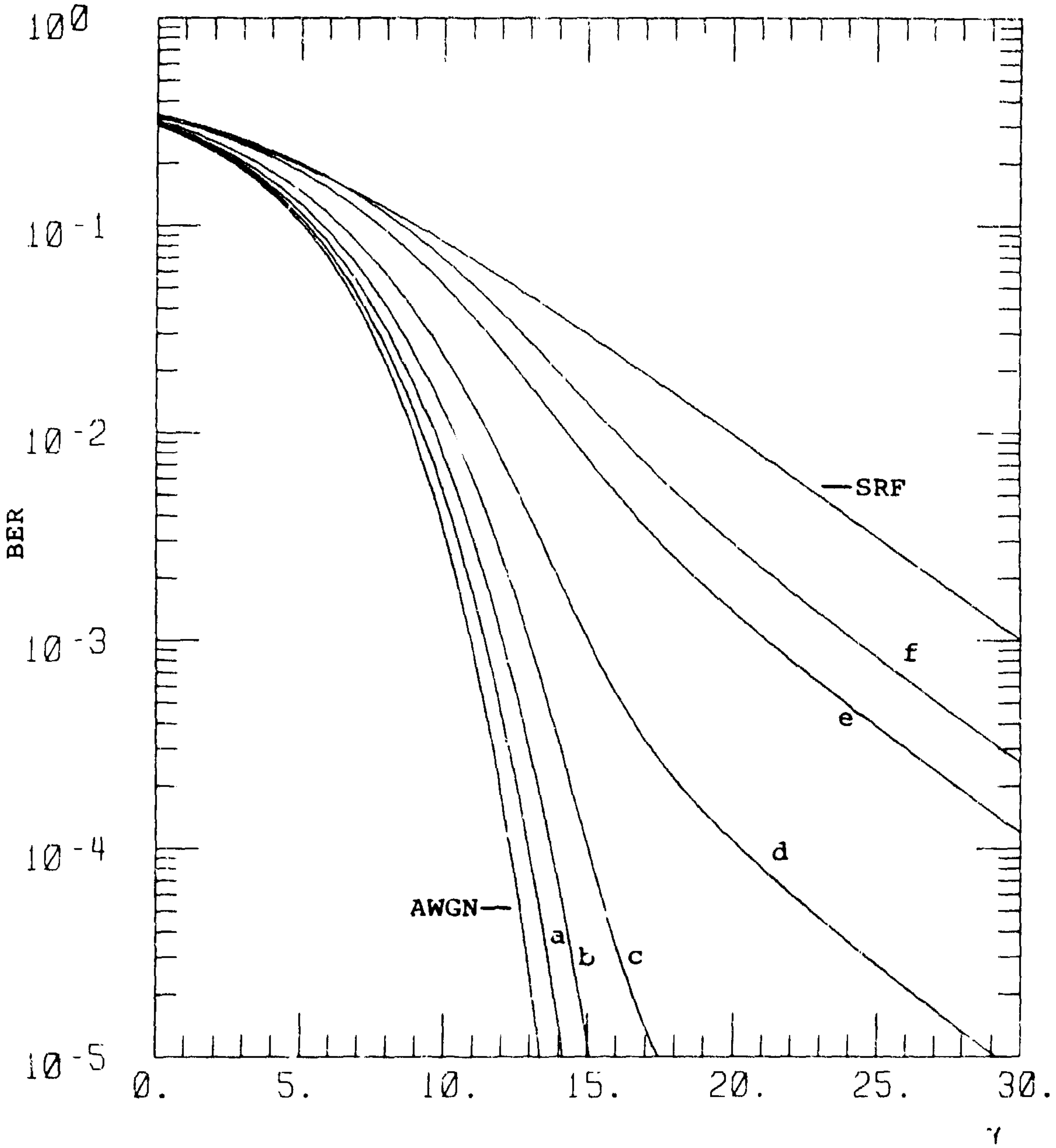

Figure E-28. BER for BFSK s = 3.

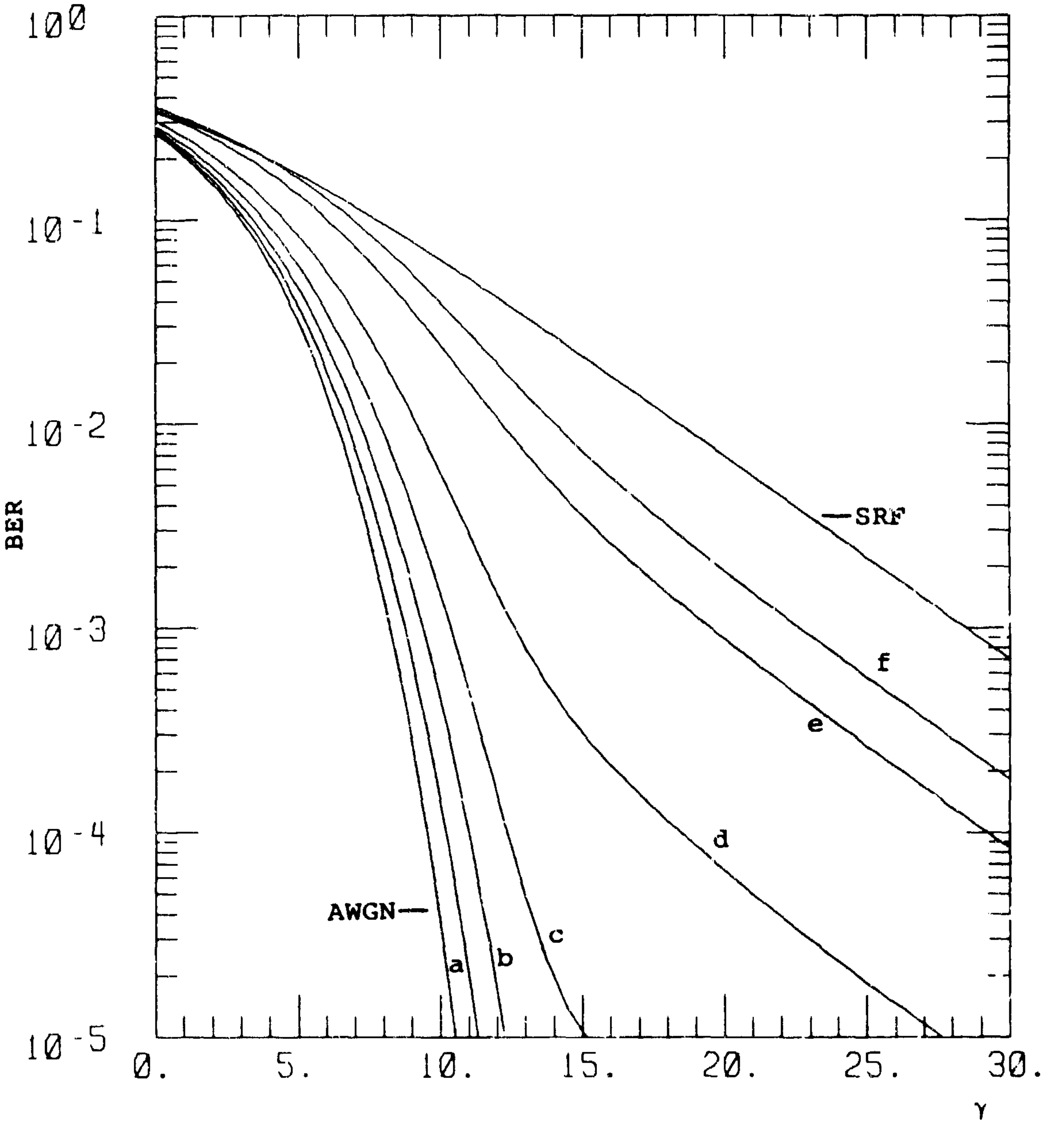

Figure E-29. BER for QFSK s = 3.

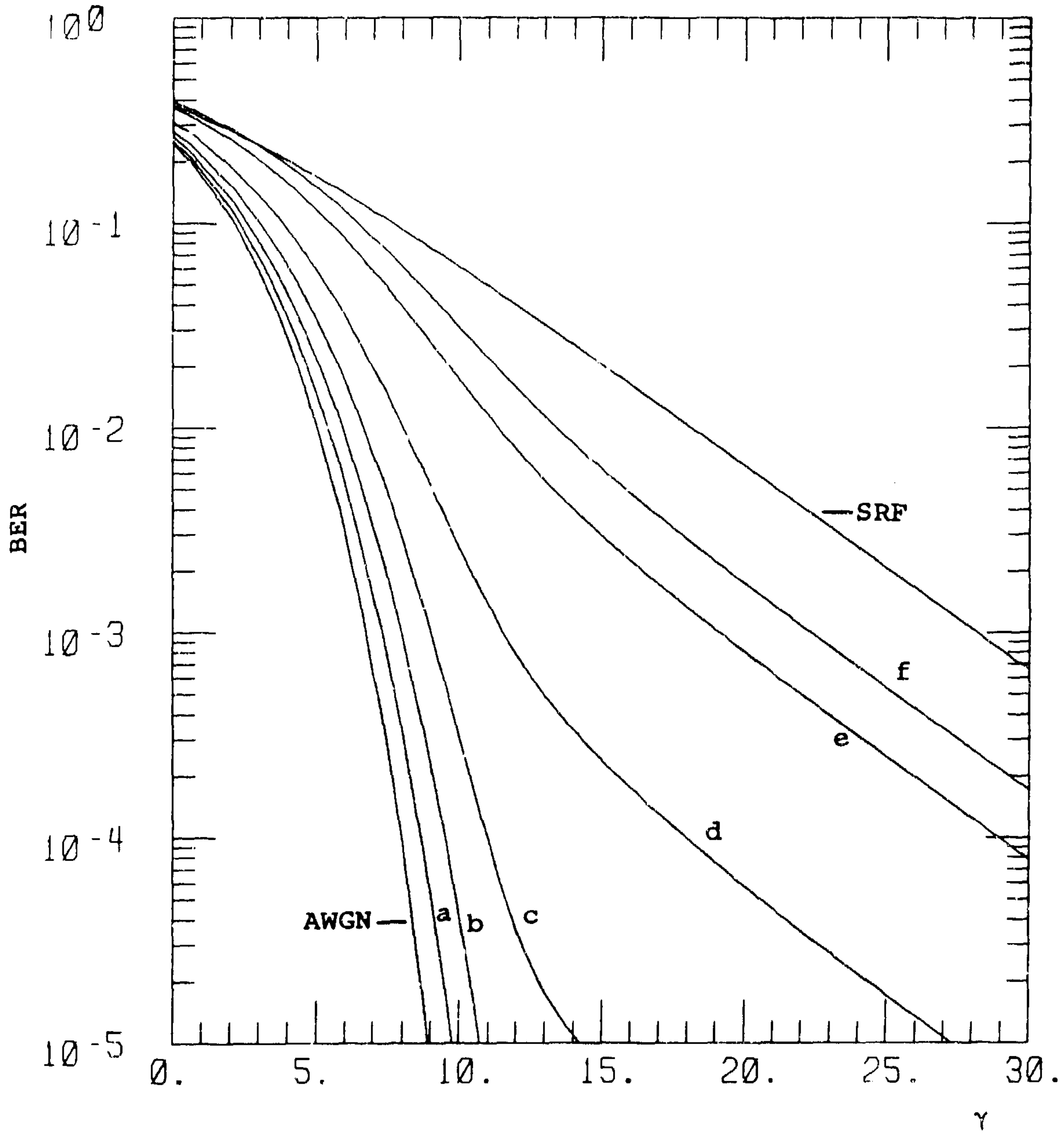

Figure E-30. BER for 8-ARYFSK s = 3.

APPENDIX F

CALCULATED BIT ERROR RATES FOR DBPSK COMPARED TO NAKAGAMI-M AND RICE FOR SINGLE POWER LAW PSD

This Appendix contains the calculated bit error rate for DBPSK compared to Nakagami-m (labeled as N) and Rice (labeled as R) for single power law PSD. Throughout, the calculated results are labeled C.

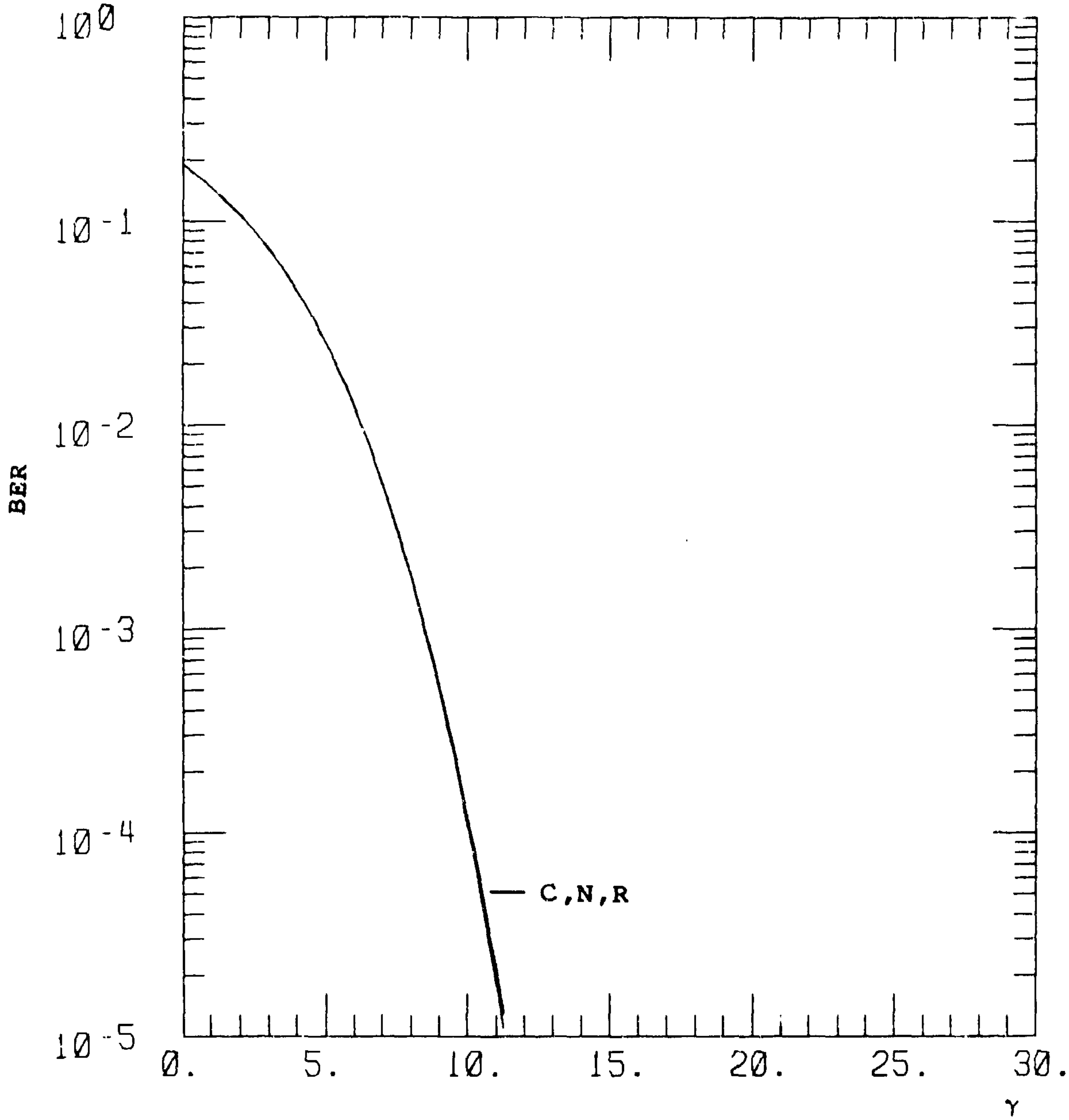

Figure F-1. BER for DBPSK s = 1, χ^2 = 0.01, $S_4^{\ 2}$ = 0.039.

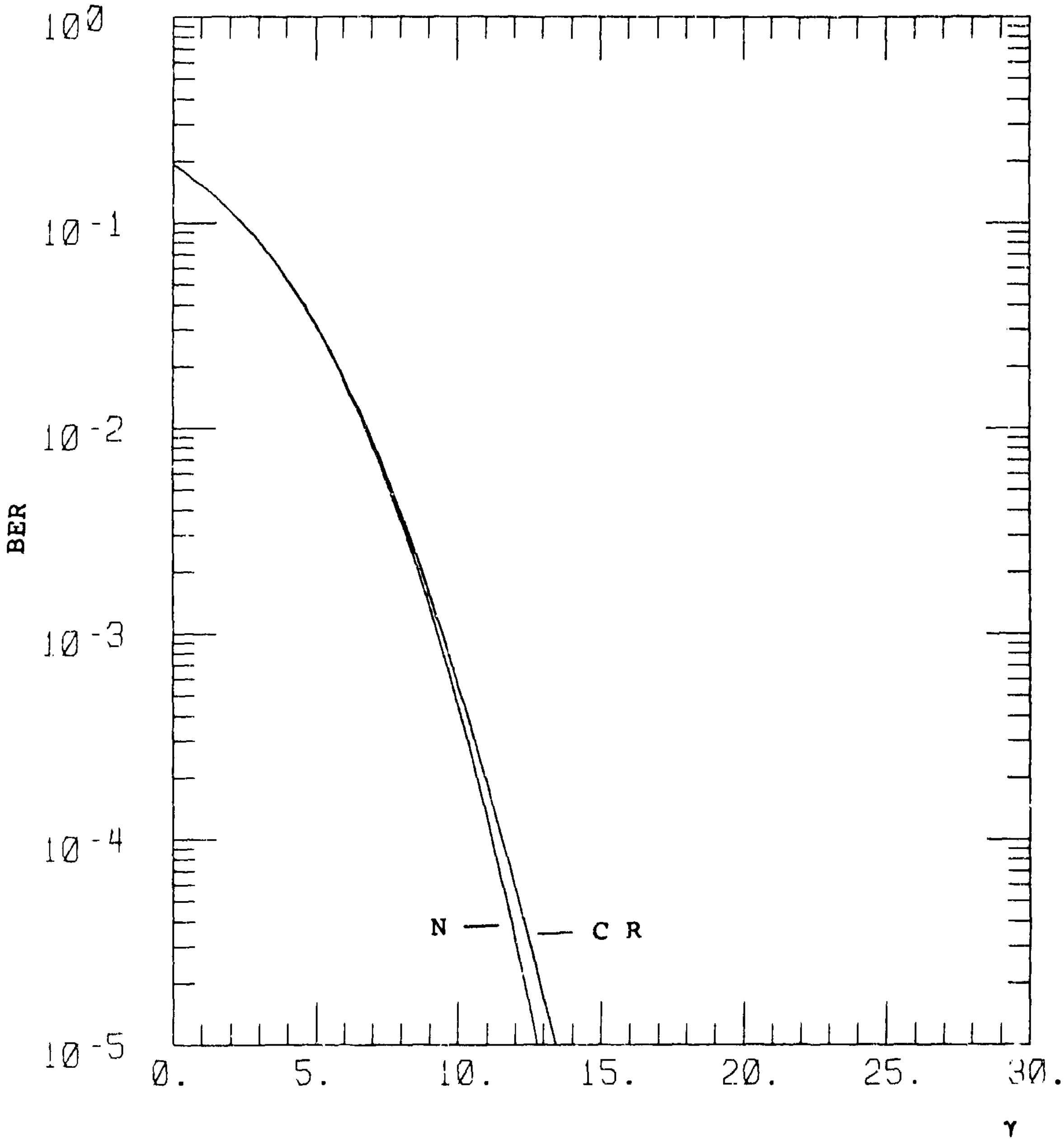

Figure F-2. BER for DPPSK s = 1, χ^2 = 0.025, S_4^2 = 0.095.

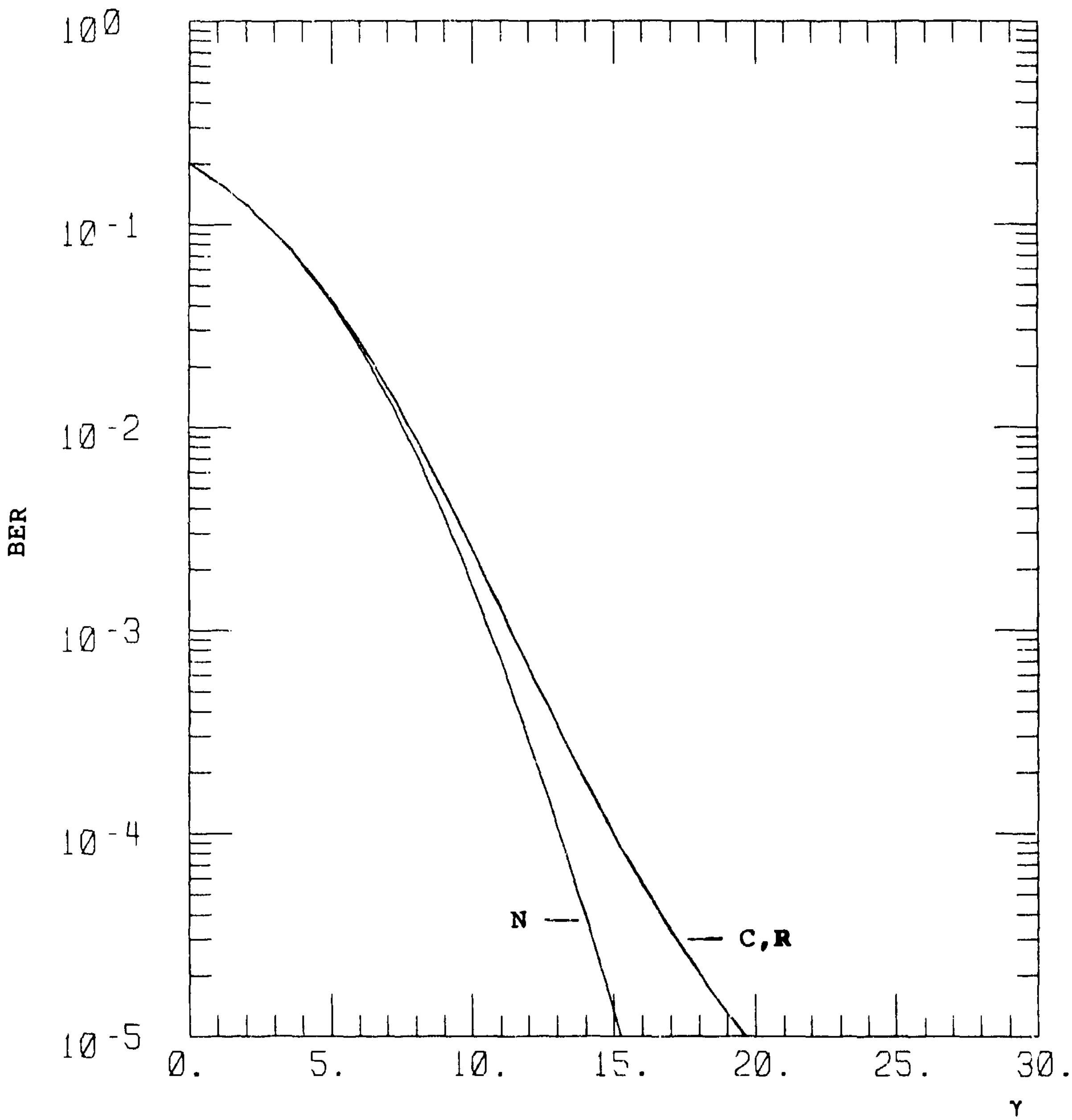

Figure F-3. BER for DBPSK s = 1, χ^2 = 0.05, $S_4{}^2$ = 0.180.

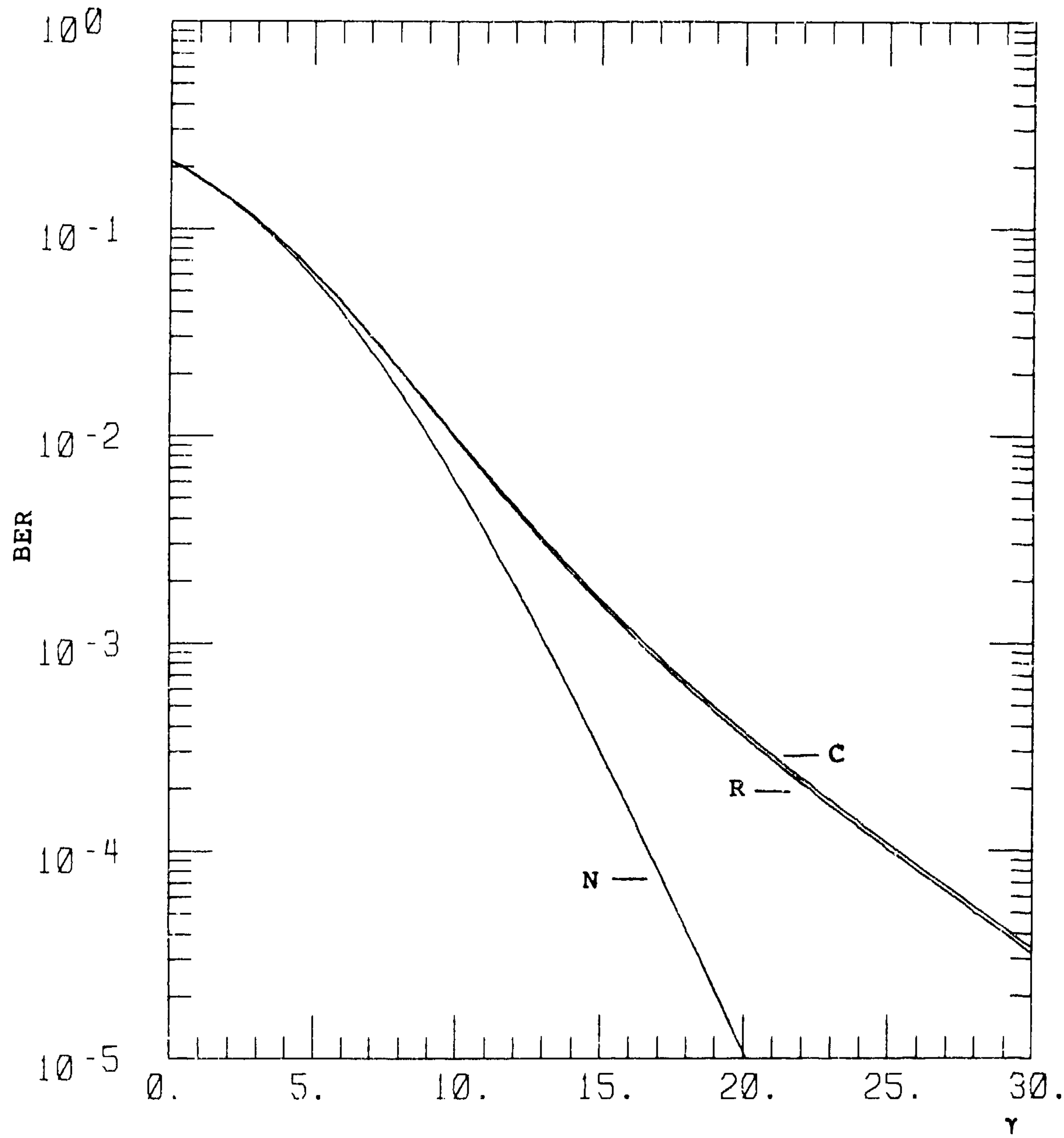

Figure F-4. BER for DBPSK s = 1, χ^2 = 0.1, $S_4{}^2$ = 0.327.

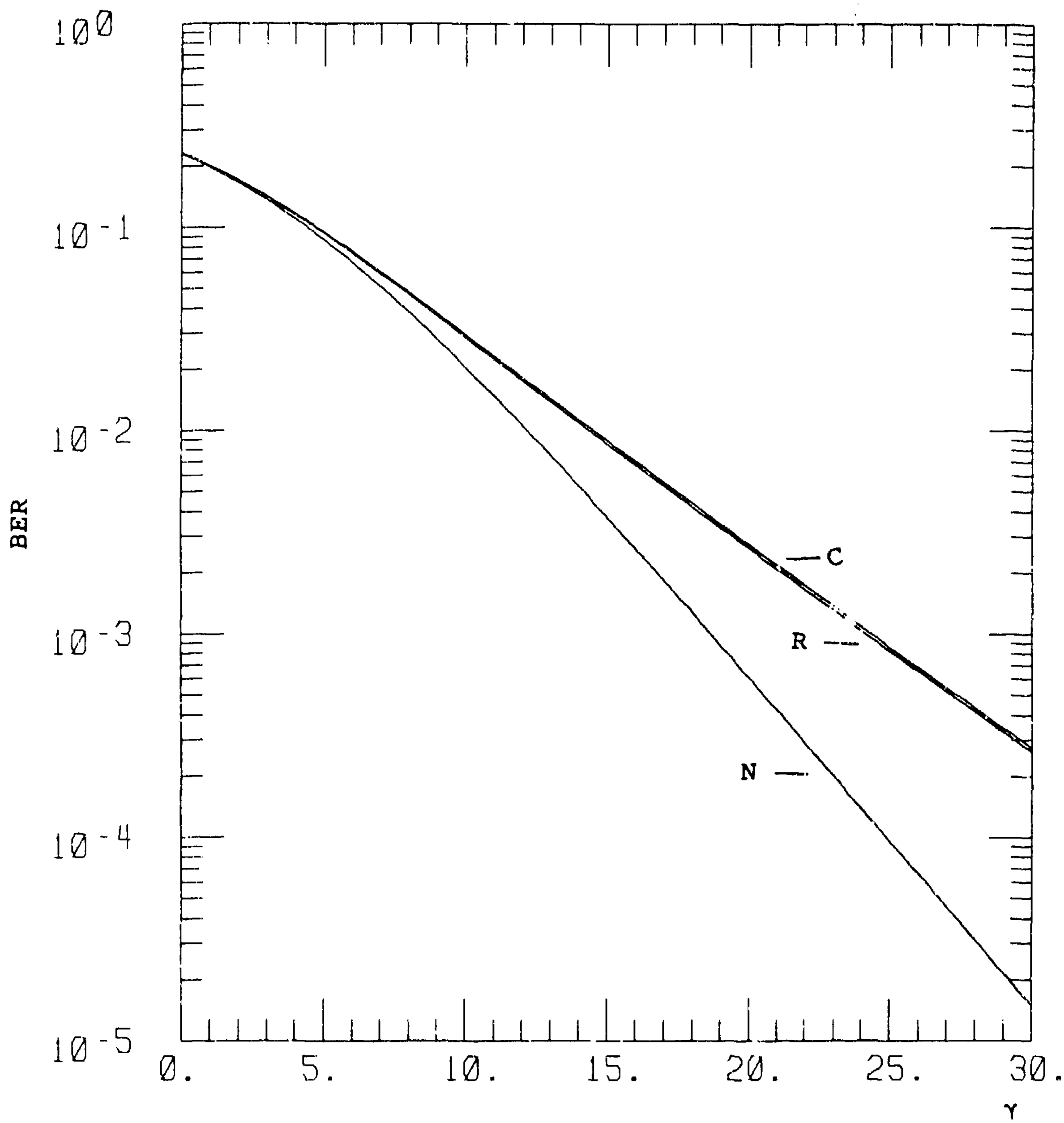

Figure F-5. BER for DBPSK s = 1, χ^2 = 0.25, S_4^2 = 0.616.

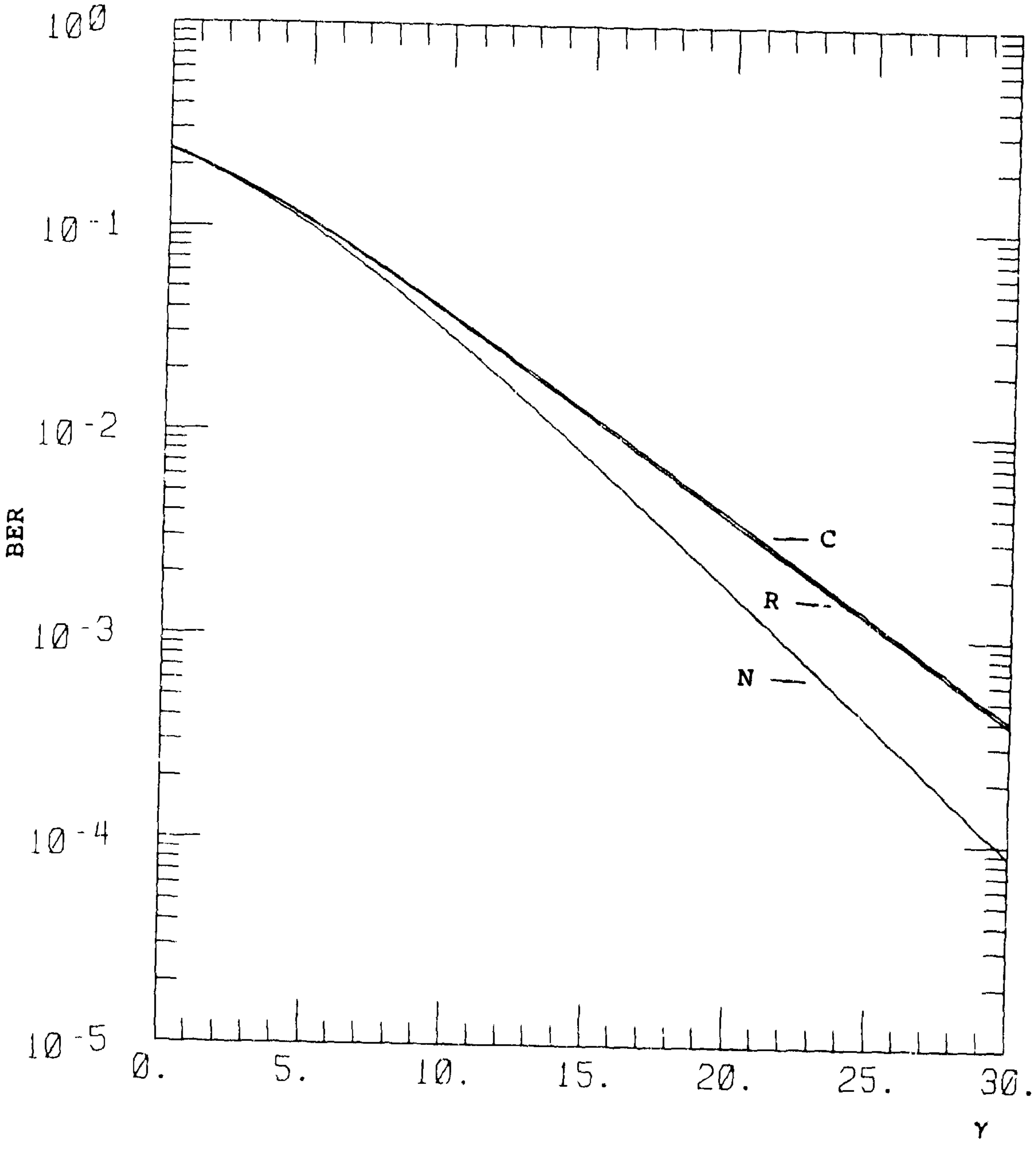

Figure F-6. BER for DBPSK s = 1, $\chi^2 = 0.4$, $S_4{}^2 = 0.768$.

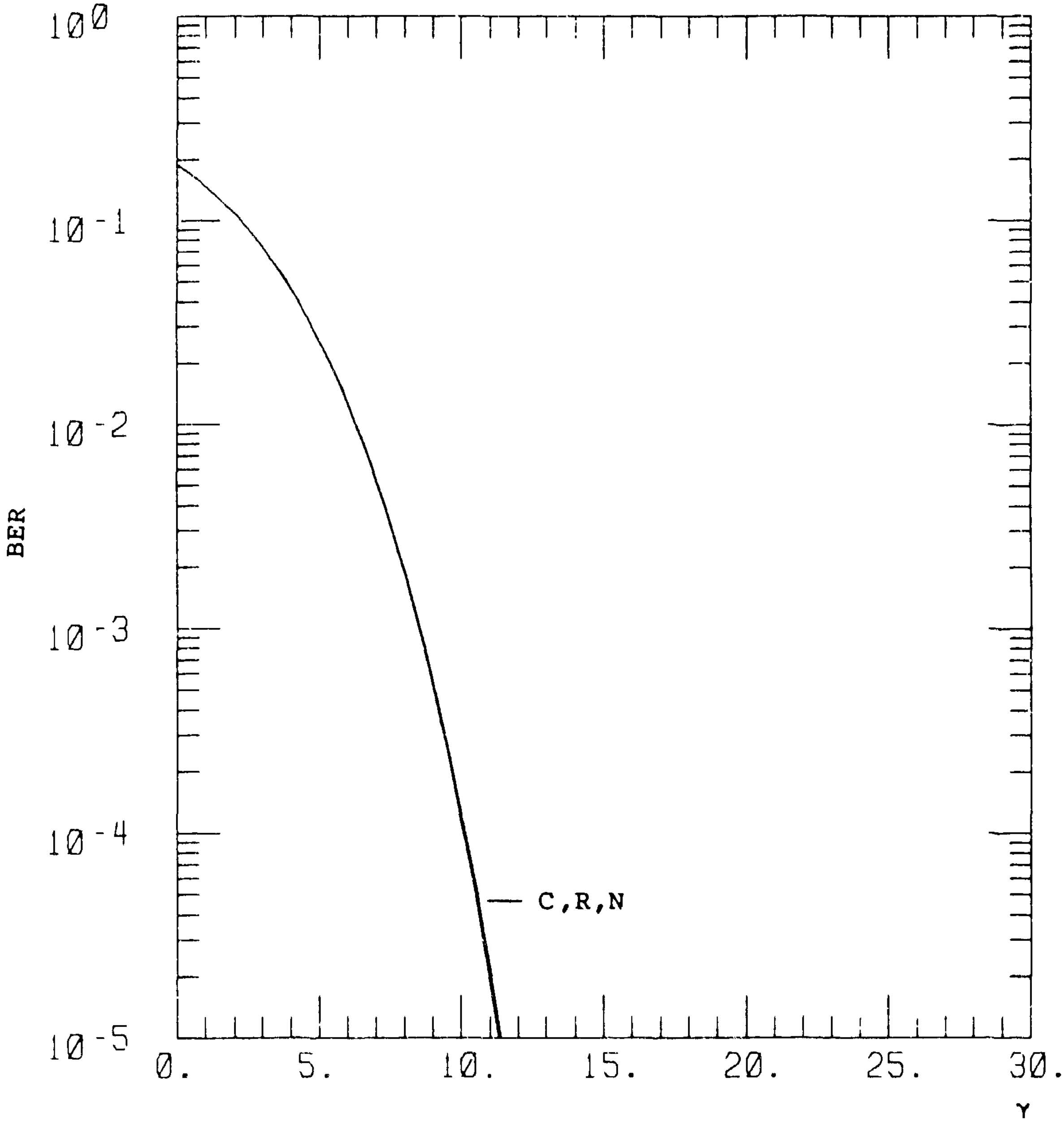

Figure F-7. BER for DBPSK s = 1.5, χ^2 = 0.01, $S_4{}^2$ = 0.039.

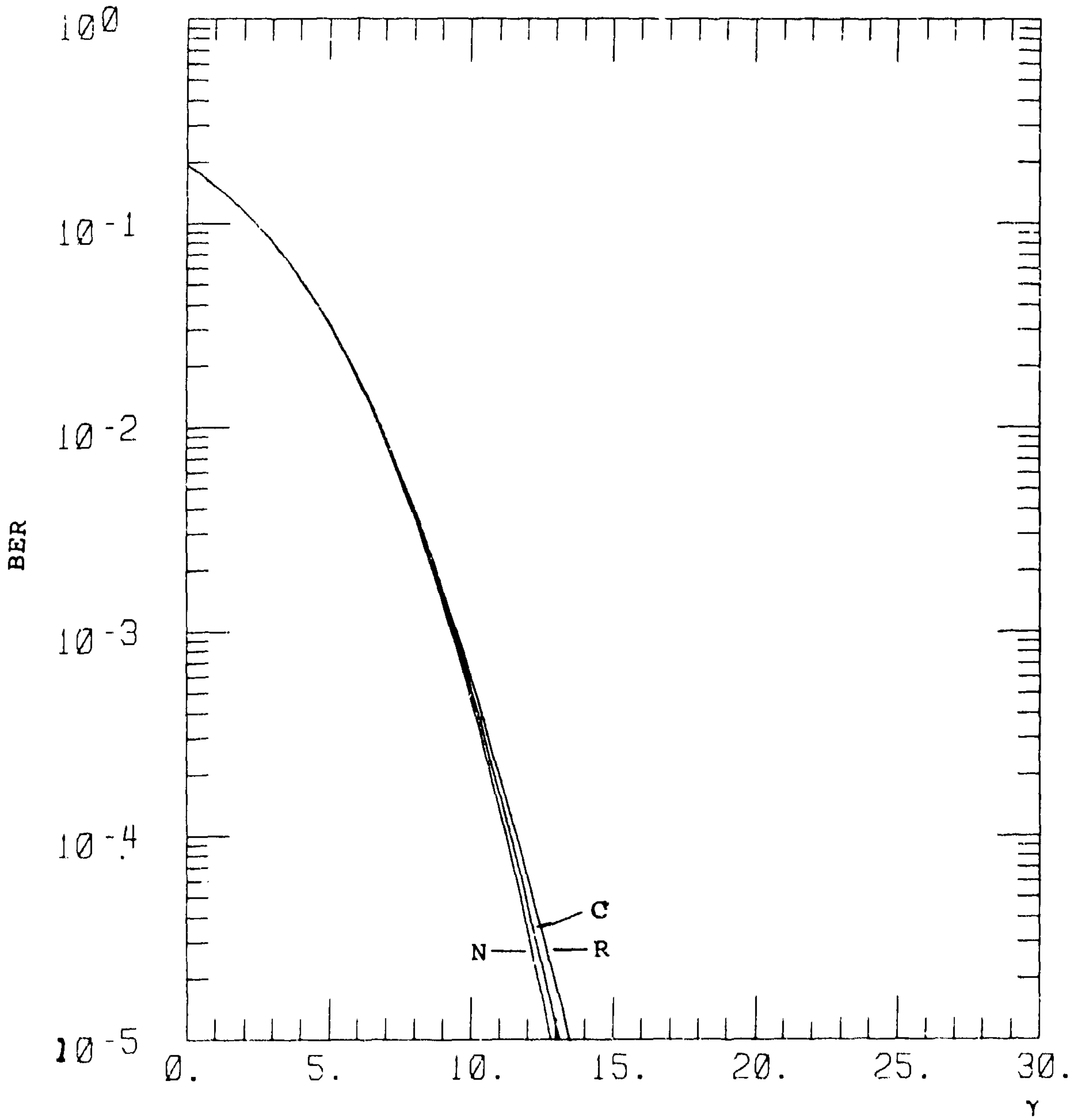

Figure F-8. BER for DBPSK s = 1.5, χ^2 = 0.025, $S_4{}^2$ = 0.097.

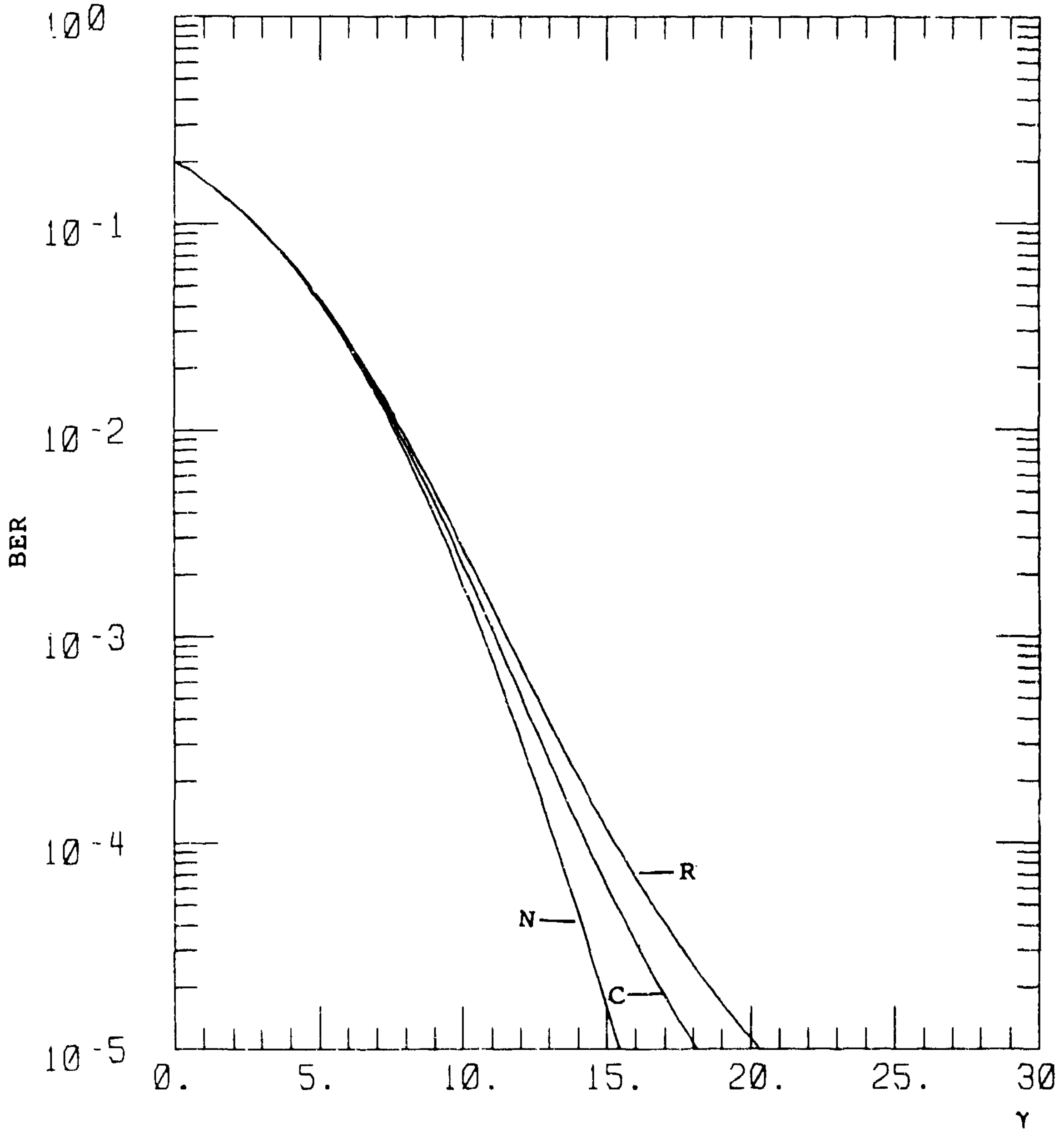

Figure F-9. BER for DBPSK s = 1.5, χ^2 = 0.05, $S_4{}^2$ = 0.186.

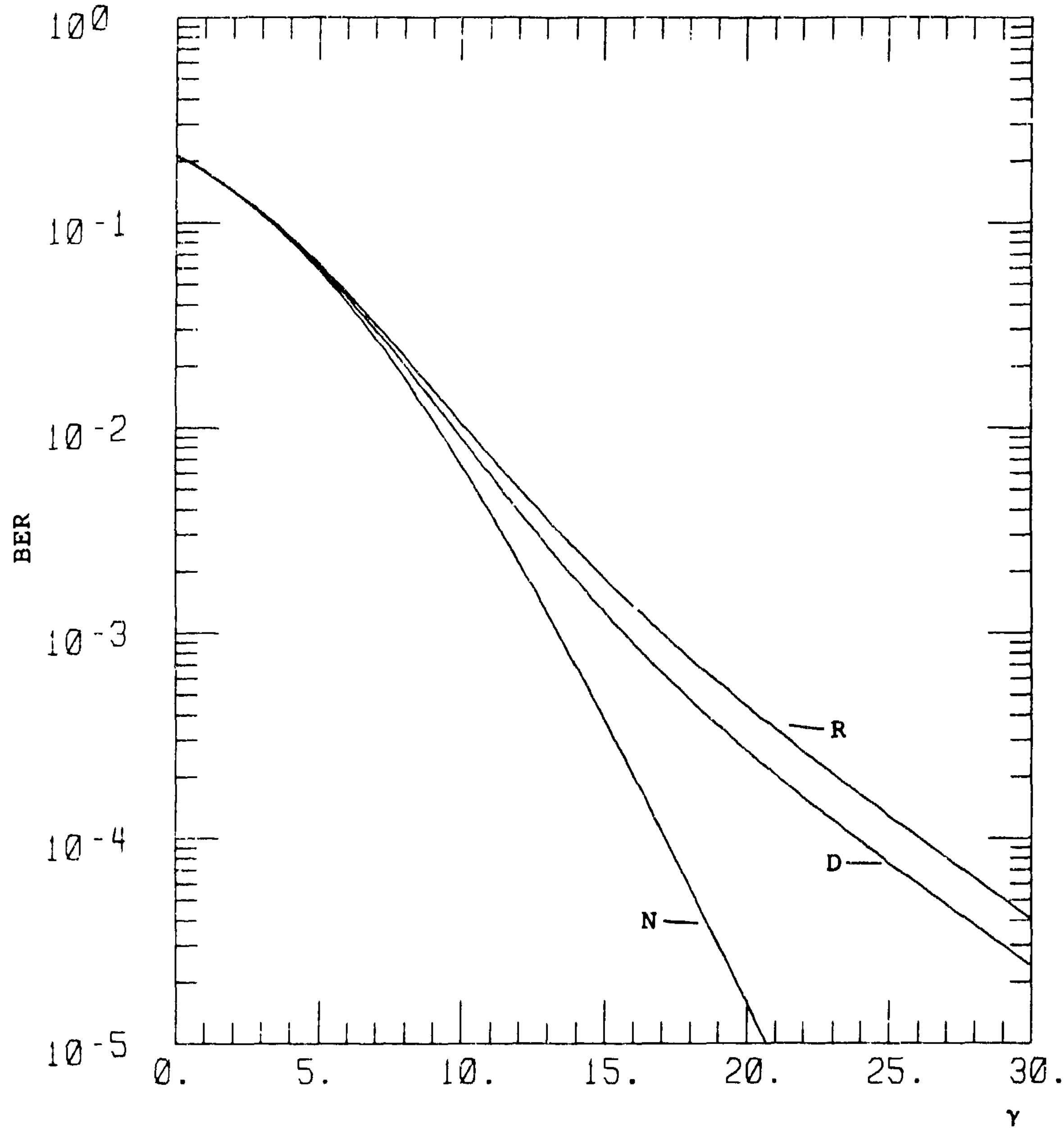

Figure F-10. BER for DBPSK s = 1.5, χ^2 = 0.1, $S_4{}^2$ = 0.343.

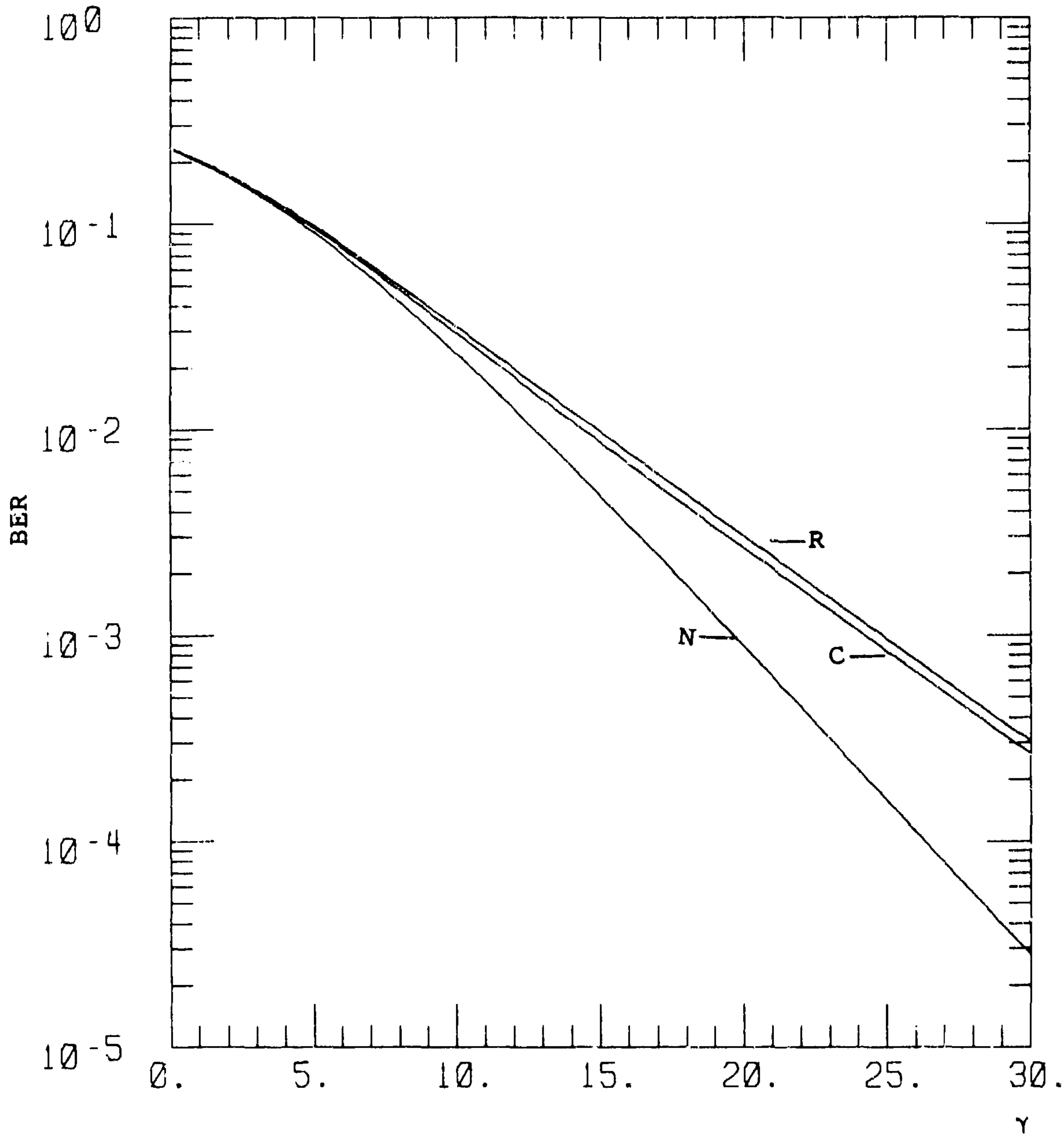

Figure F-11. BER for DBPSK s = 1.5, χ^2 = 0.25, $S_4{}^2$ = 0.664.

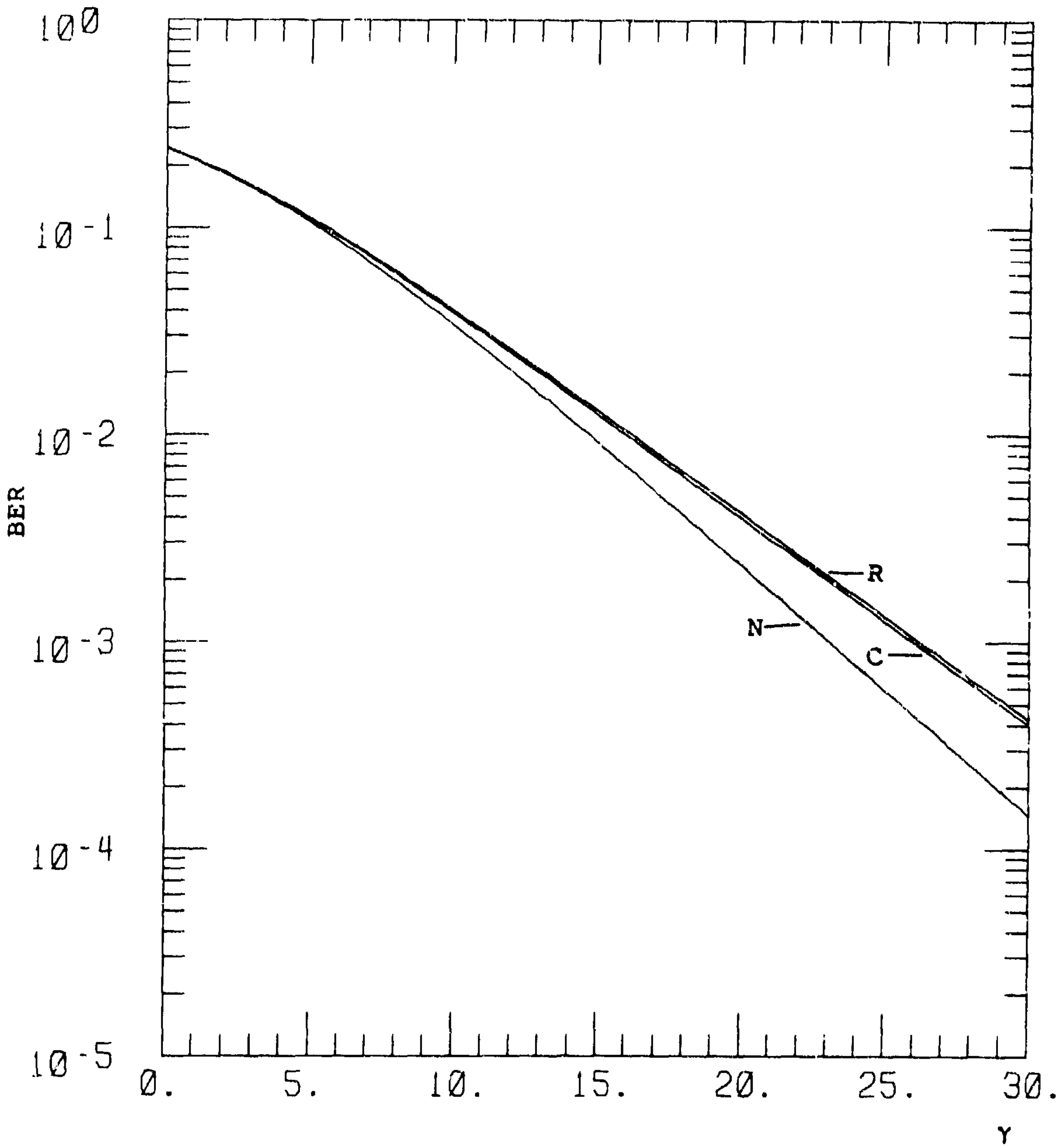

Figure F-12. BER for DBPSK s = 1.5, χ^2 = 0.4, $S_4{}^2$ = 0.825.

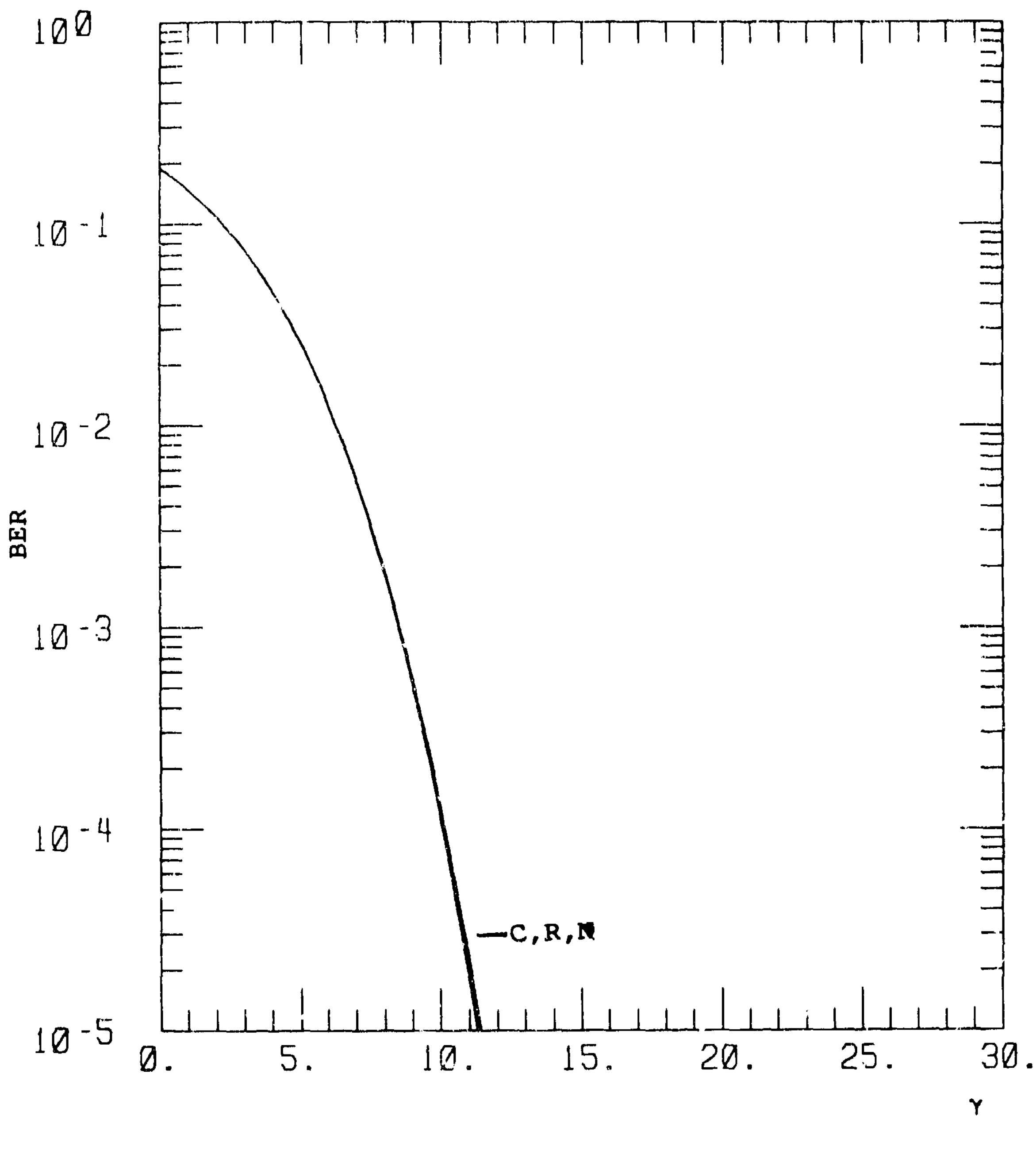

Figure F-13. BER for DBPSK, s = 2, $\chi^2 = 0.01$, $S_4{}^2 = 0.040$.

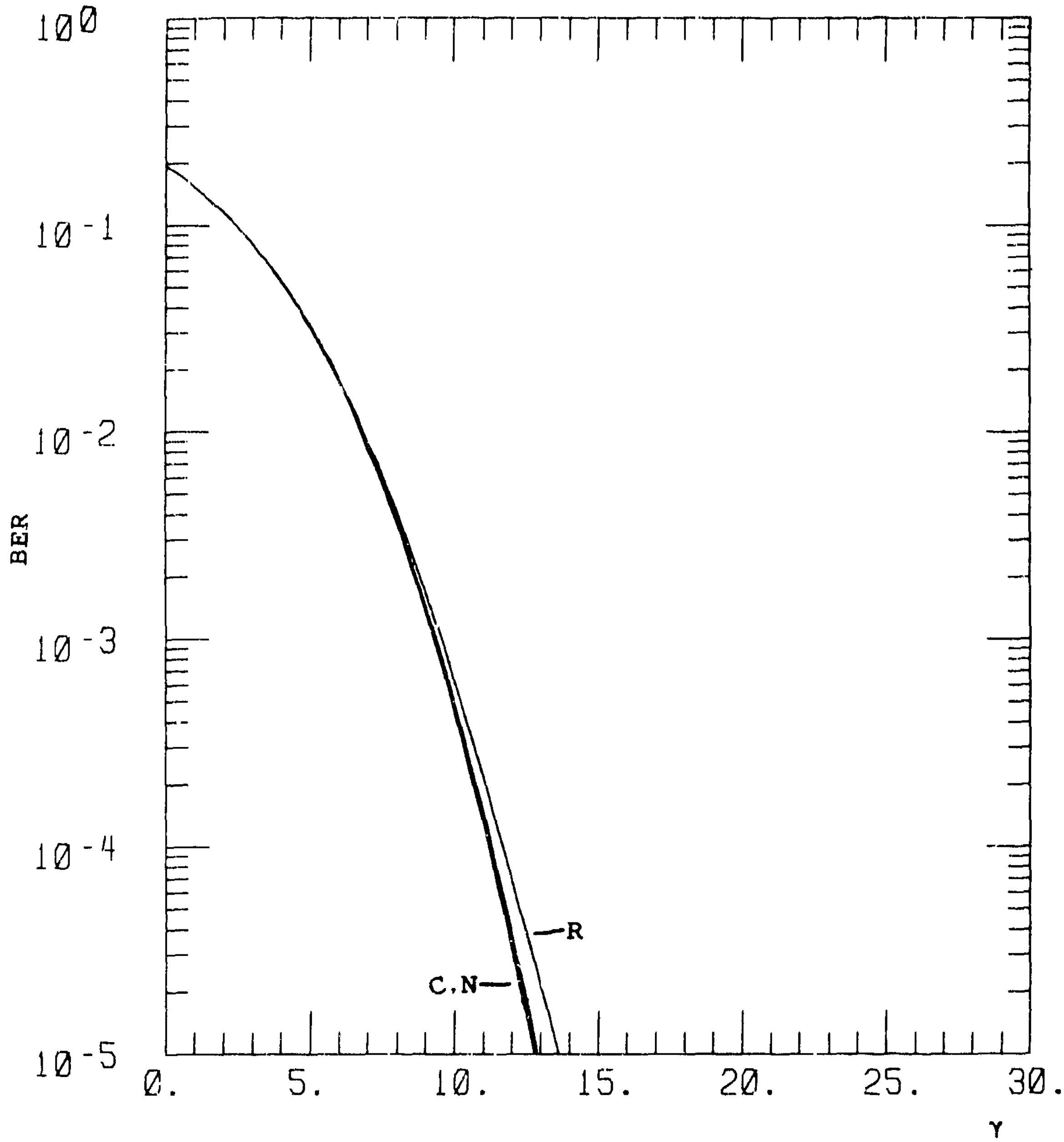

Figure F-14. BER for DBPSK, s = 2, χ^2 = 0.025, $S_4{}^2$ = 0.099.

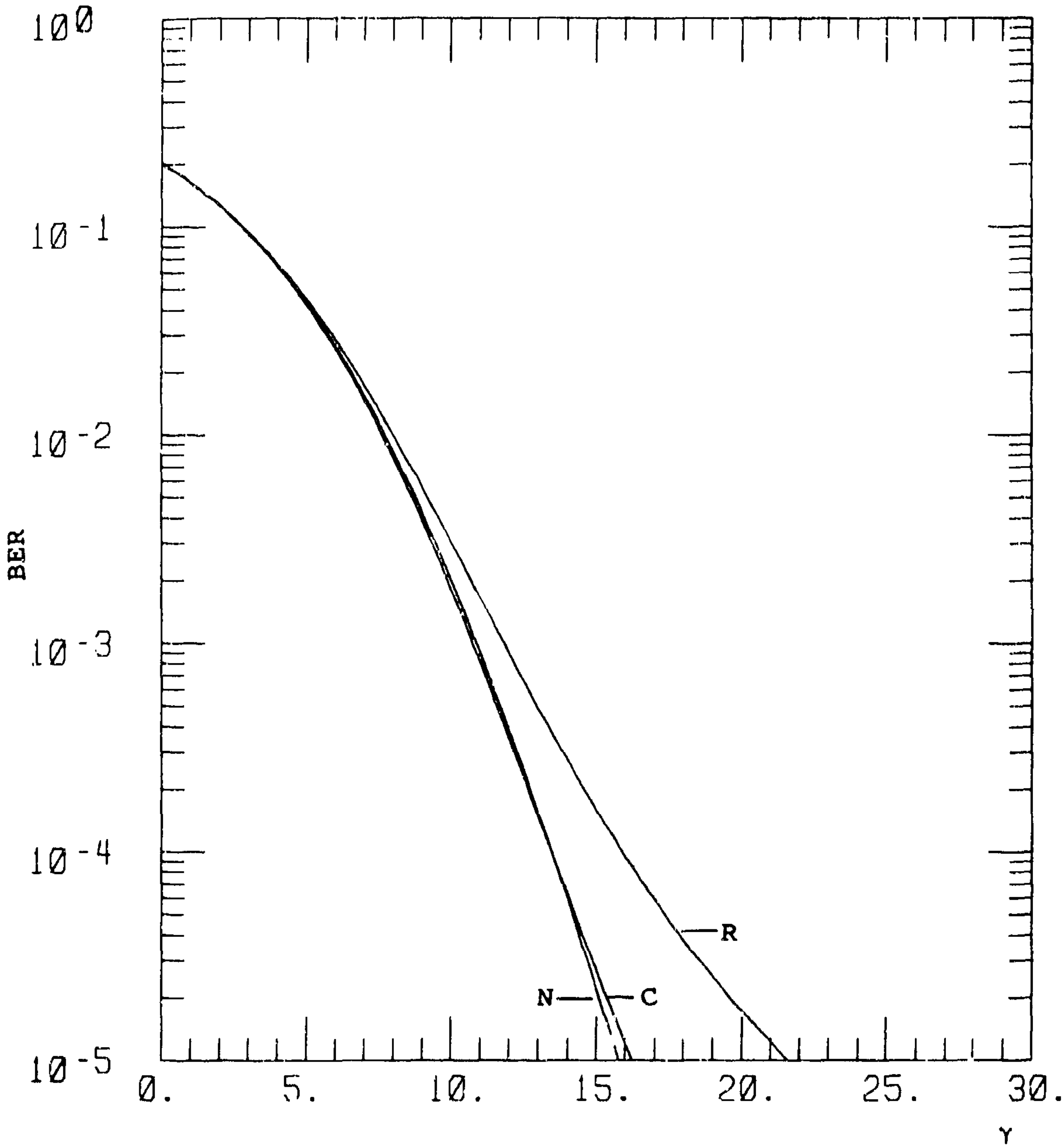

Figure F-15. BER for DBPSK, $s = 2$, $\chi^2 = 0.05$, $S_4^{\ 2} = 0.197$.

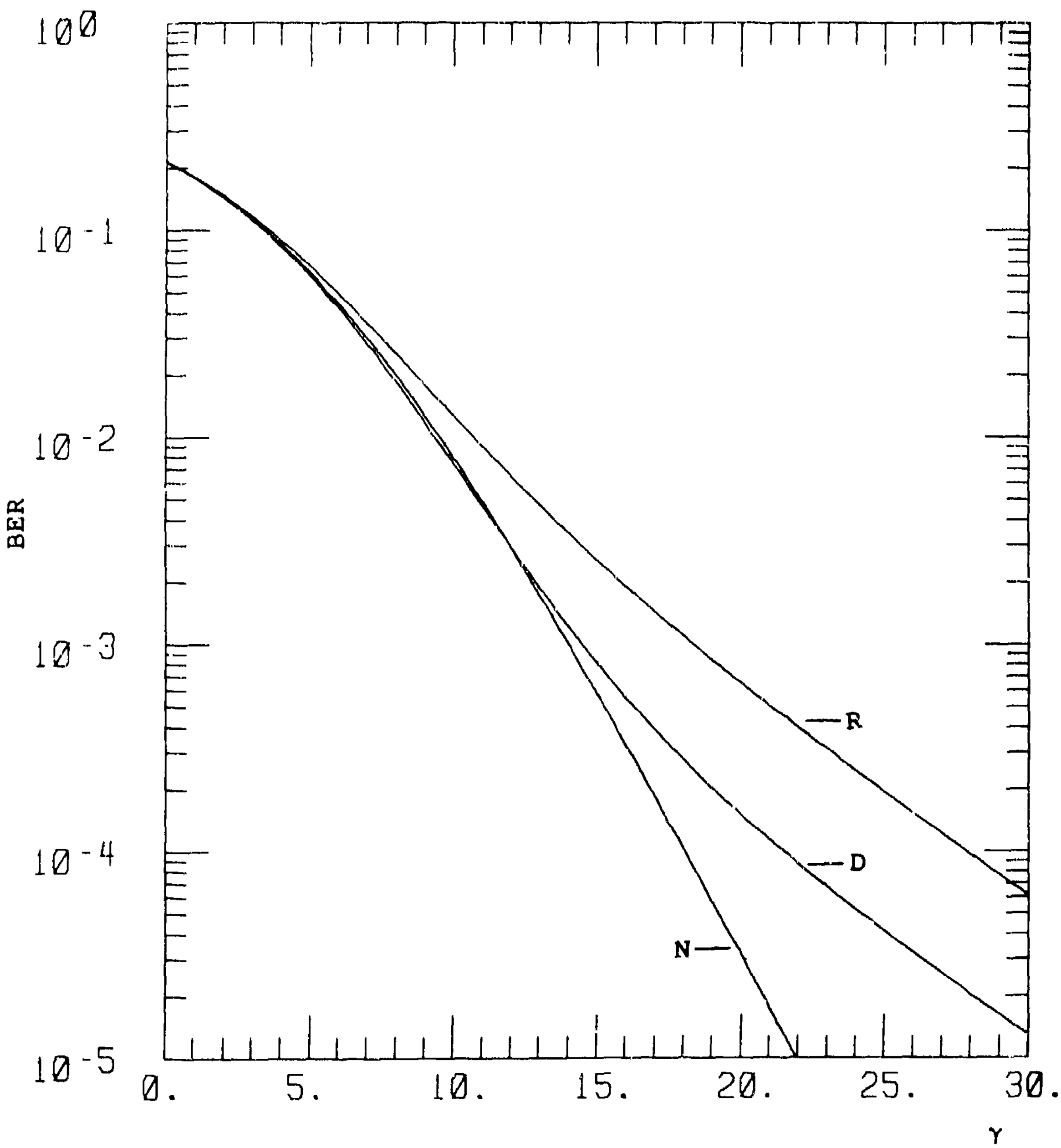

Figure F-16. BER for DBPSK, $s = 2$, $\chi^2 = 0.1$, $S_4^{\ 2} = 0.378$.

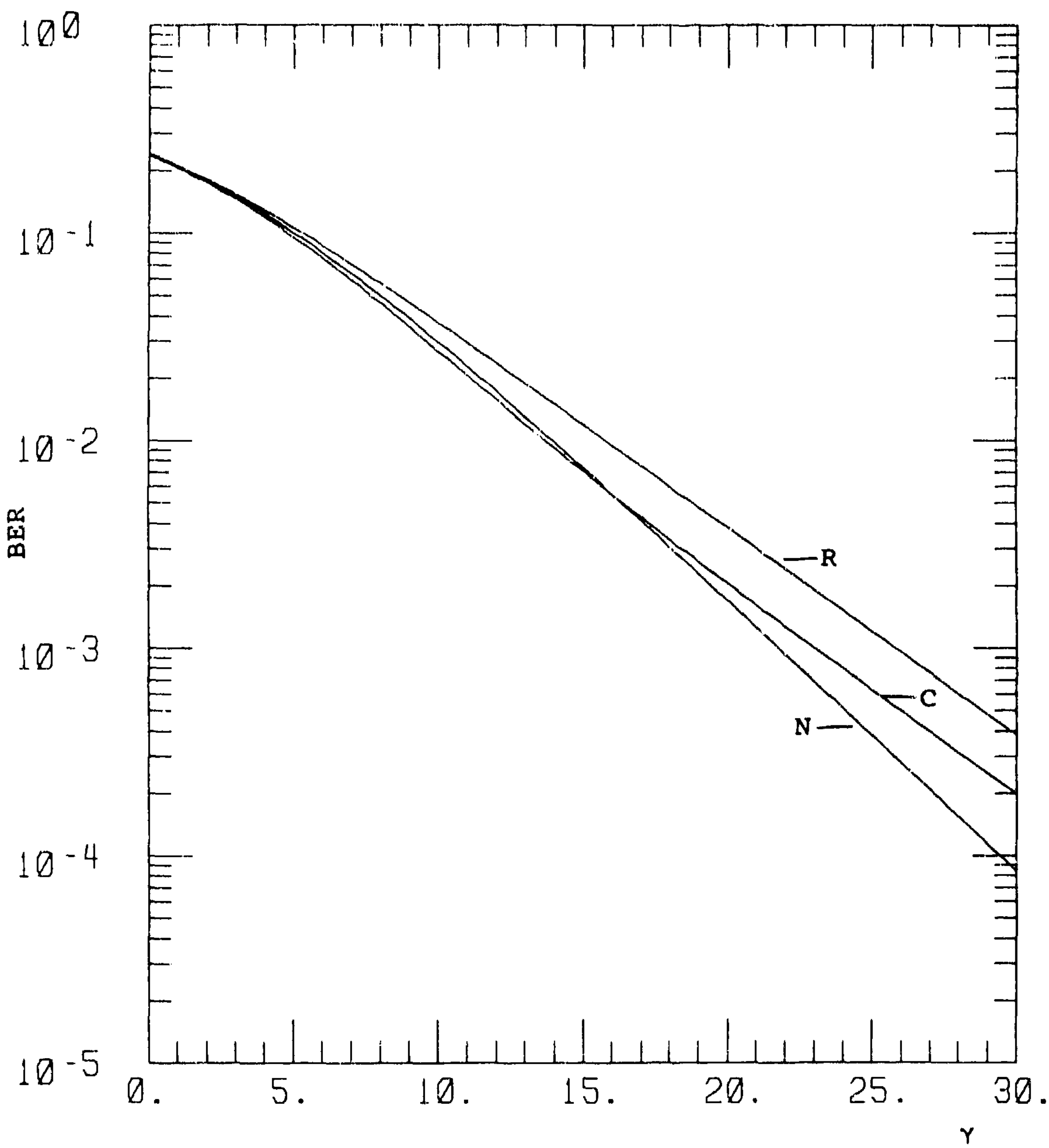

Figure F-17. BER for DBPSK, $s = 2$, $\chi^2 = 0.25$, $S_4^2 = 0.764$.

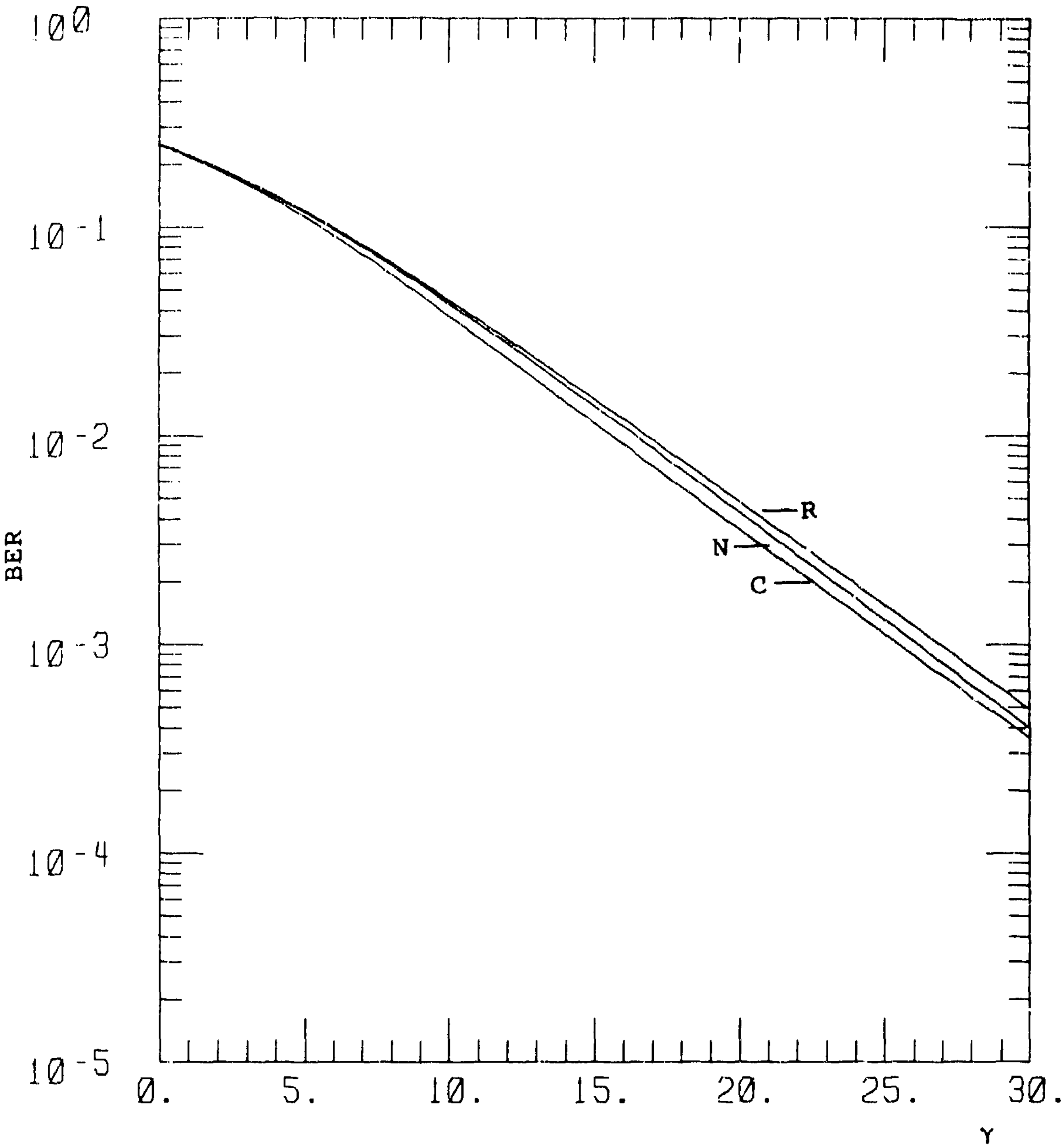

Figure F-18. BER for DBPSK, $s = 2$, $\chi^2 = 0.4$, $S_4{}^2 = 0.962$.

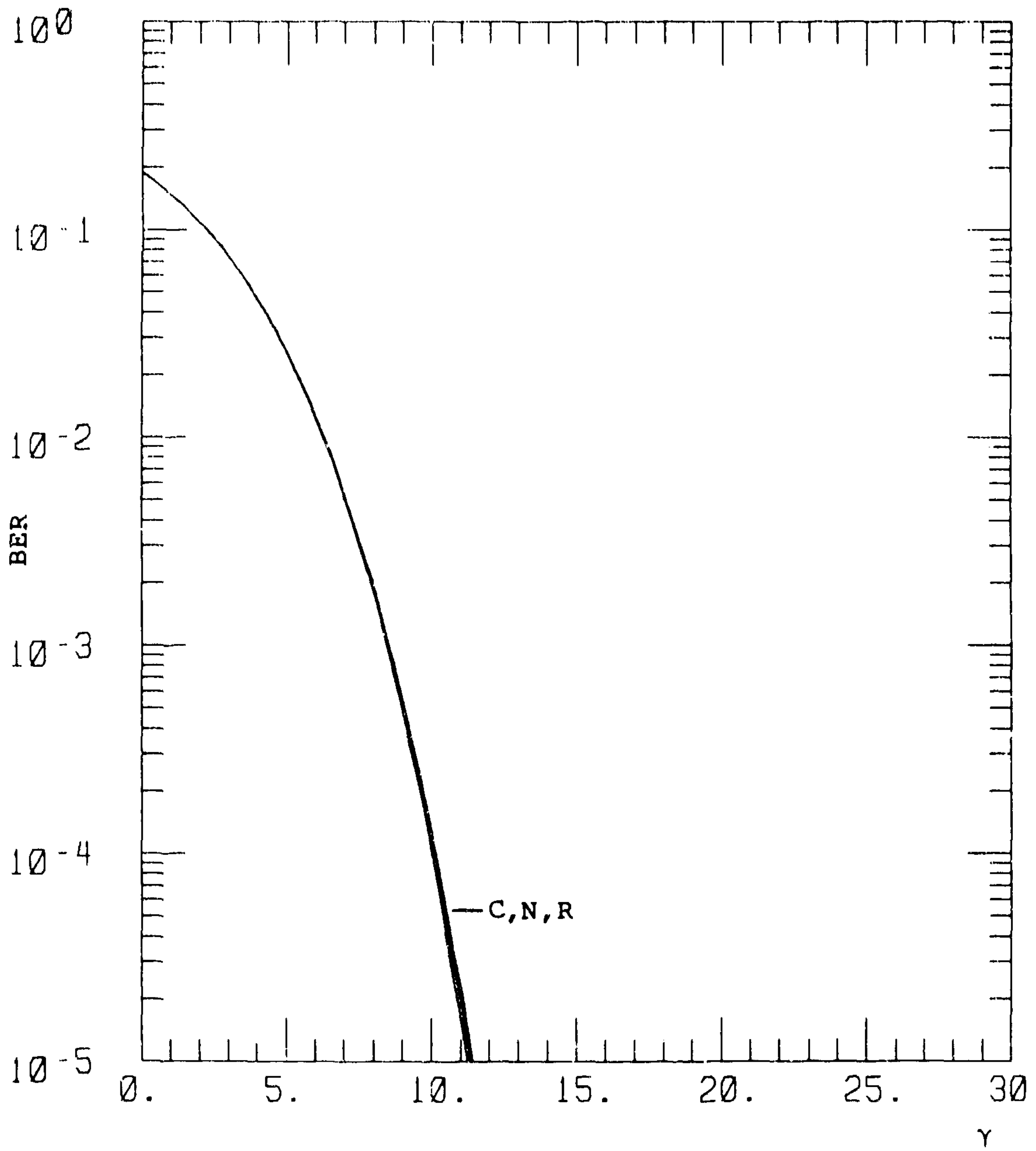

Figure F-19. BER for DBPSK s = 2.5,
$\chi^2 = 0.01$, $S_4^{\,2} = 0.040$.

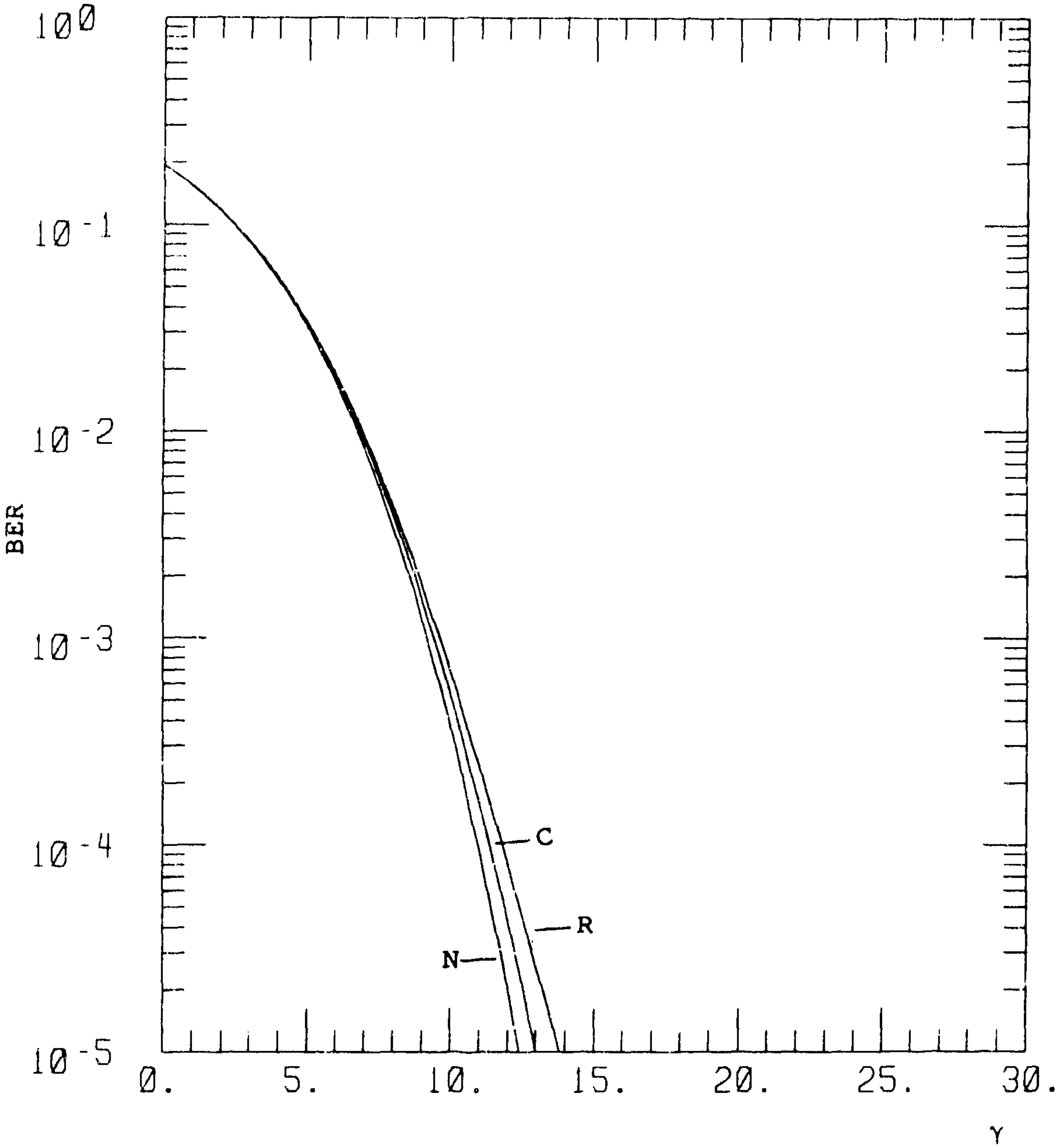

Figure F-20. BER for DBPSK s = 2.5, $\chi^2 = 0.025$, $S_4{}^2 = 0.103$.

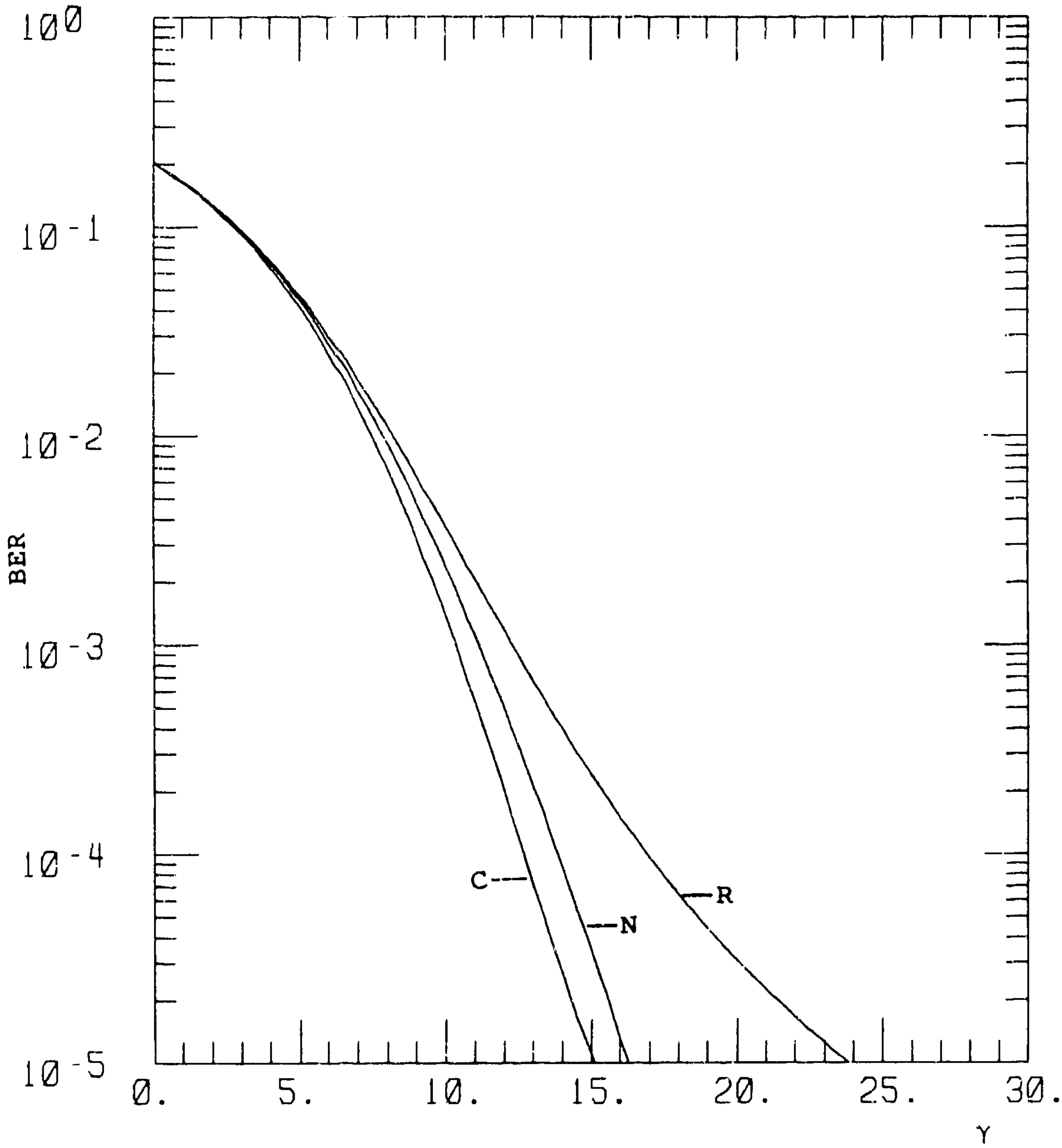

Figure F-21. BER for DBPSK s = 2.5, $\chi^2 = 0.05$, $S_4{}^2 = 0.213$.

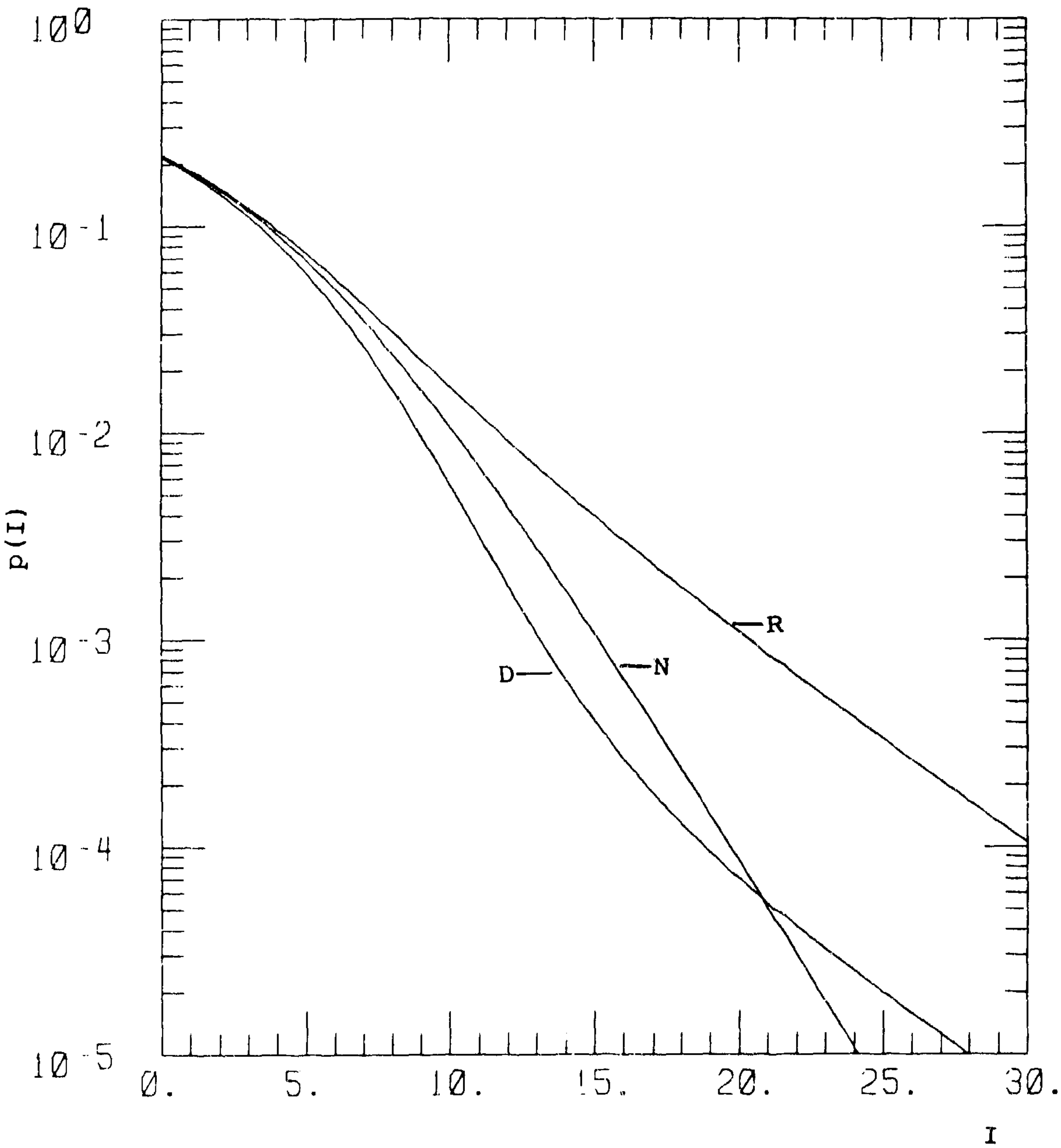

Figure F-22. BER for DBPSK s = 2.5,
$\chi^2 = 0.1$, $S_4^{\ 2} = 0.438$.

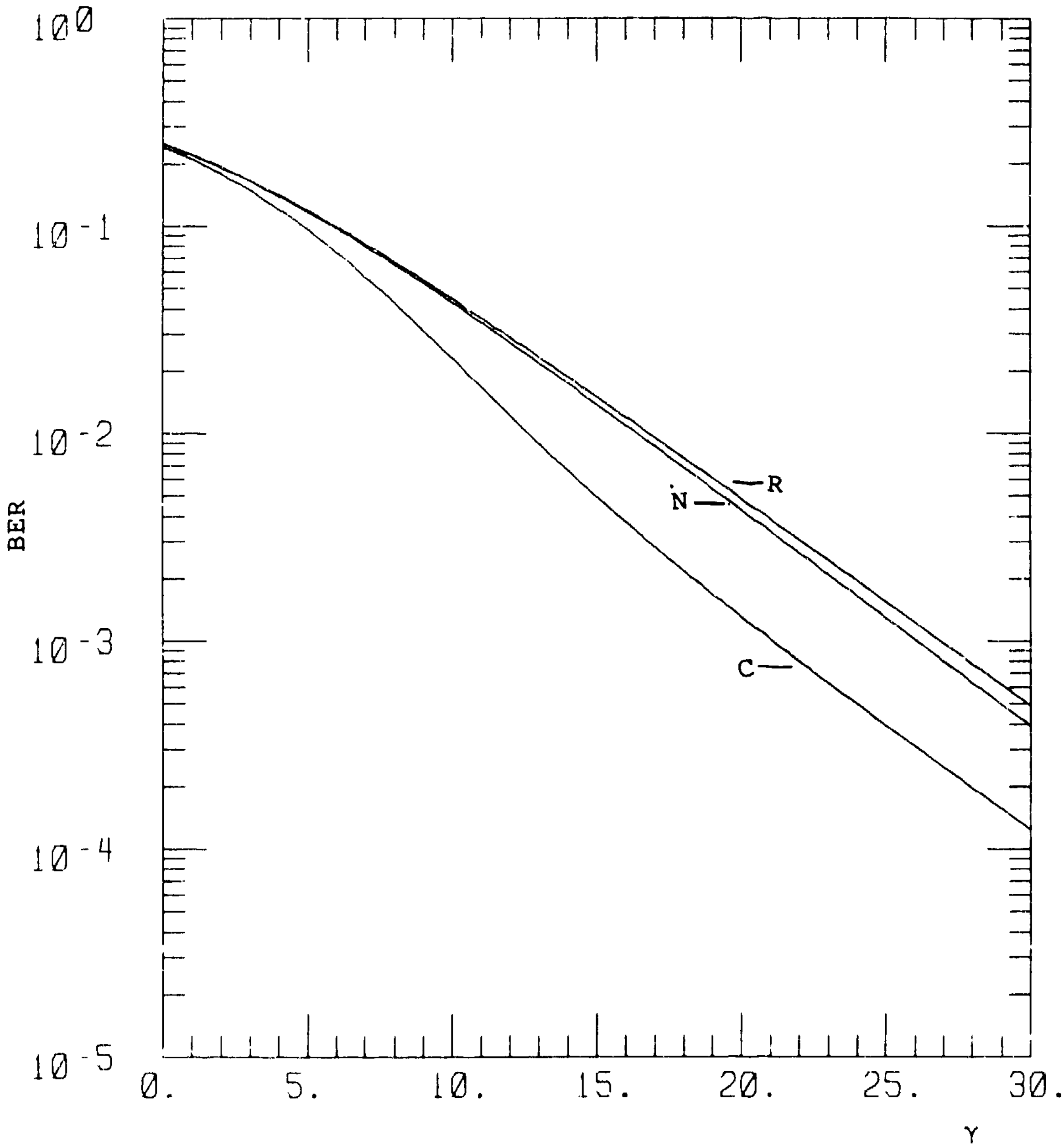

Figure F-23. BER for DBPSK s = 2.5, $\chi^2 = 0.25$, $S_4^{\ 2} = 0.959$.

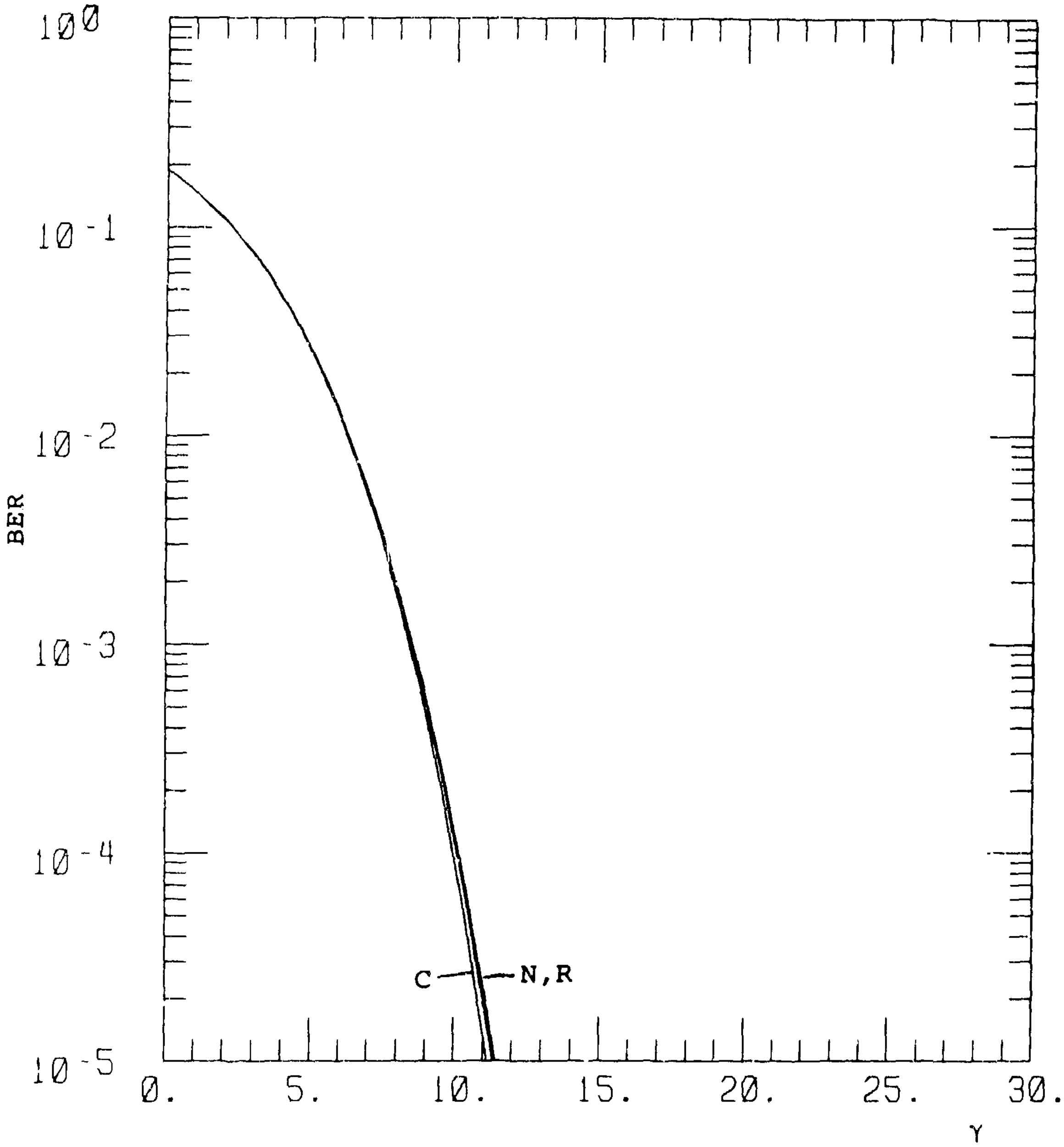

Figure F-24. BER for DBPSK s = 3, χ^2 = 0.01, $S_4{}^2$ = 0.041.

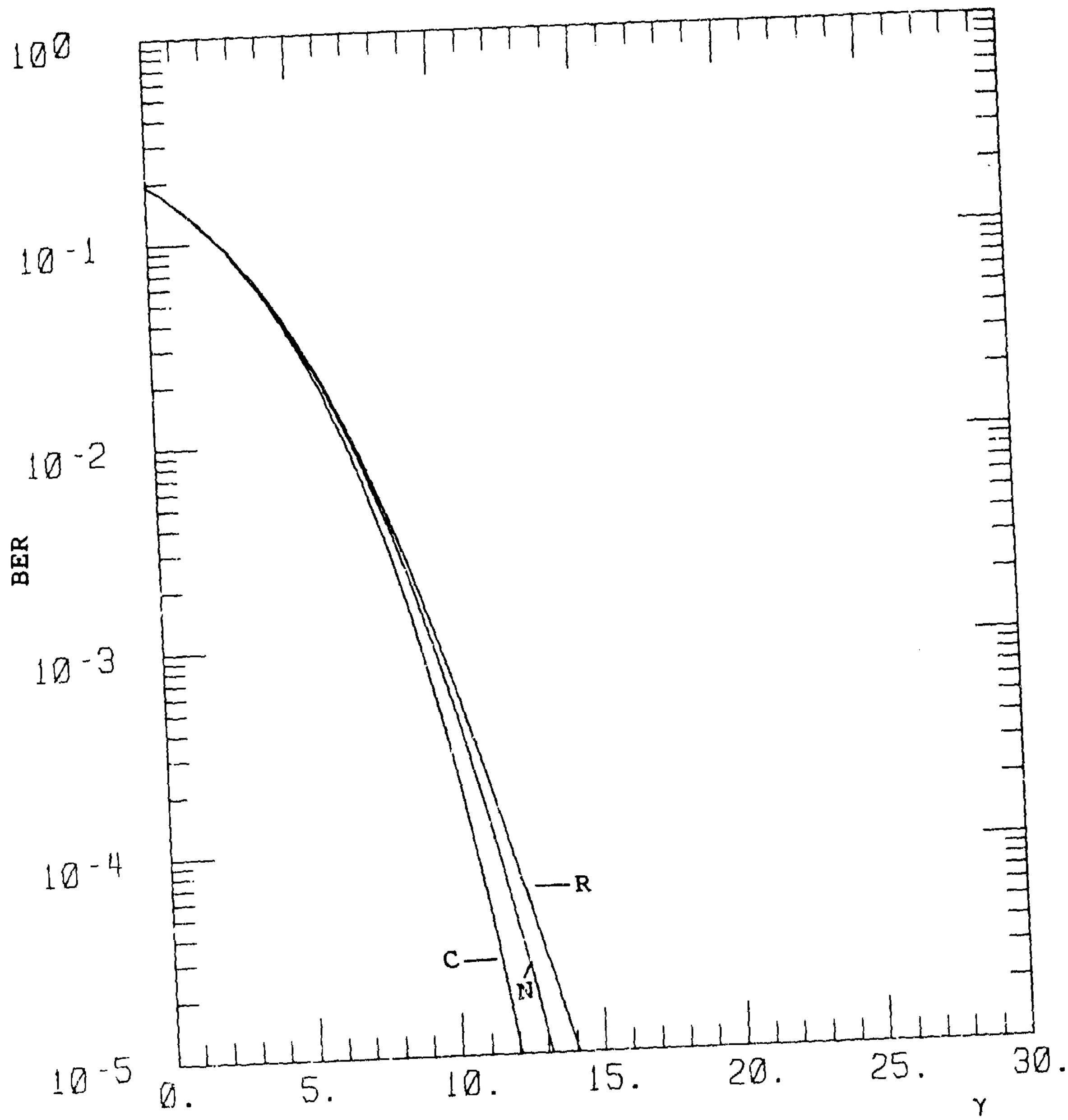

Figure F-25. BER for DBPSK s = 3, χ^2 = 0.025, $S_4{}^2$ = 0.109.

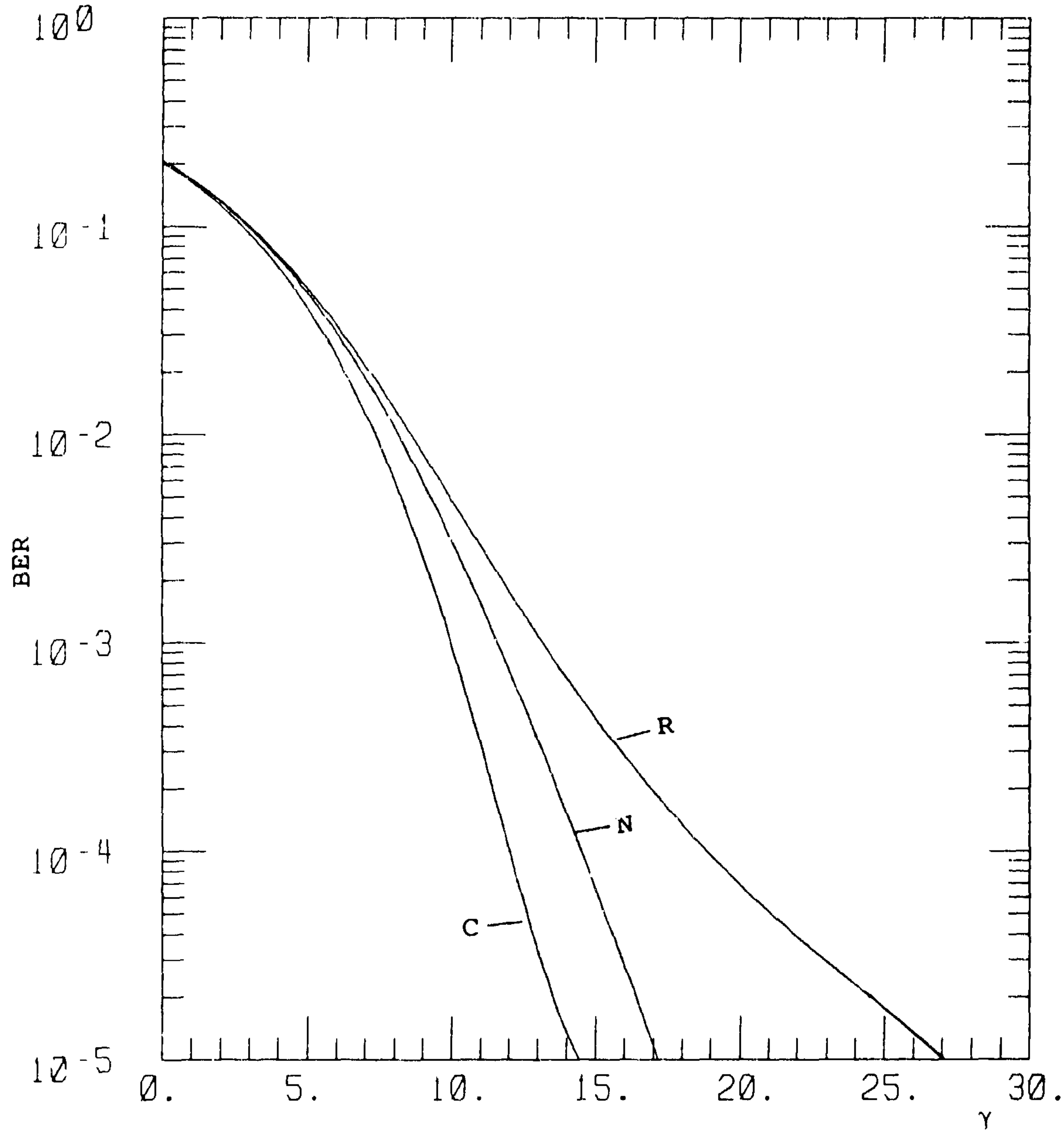

Figure F-26. BER for DBPSK s = 3, $\chi^2 = 0.05$, $S_4^{\,2} = 0.241$.

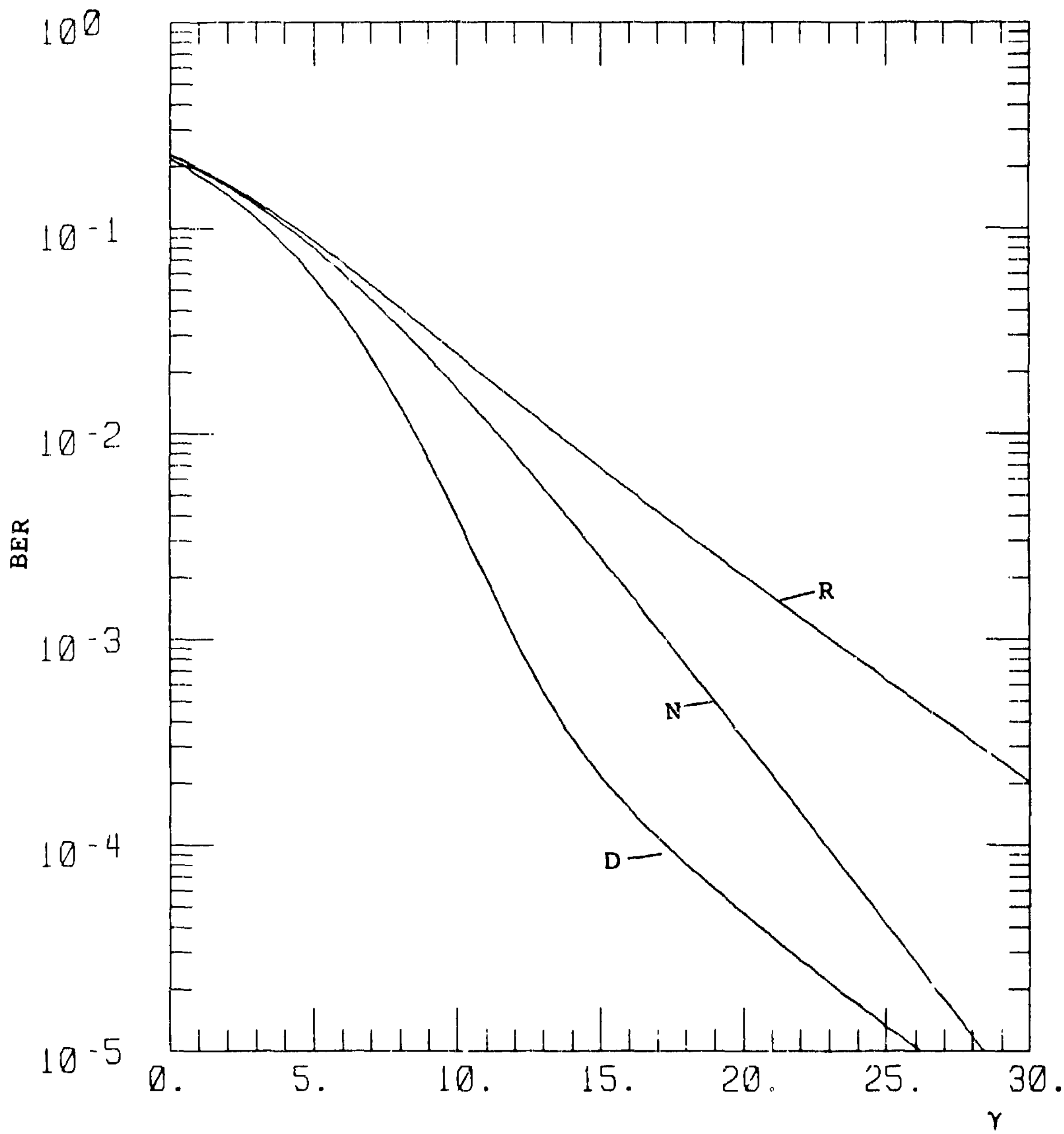

Figure F-27. BER for DBPSK s = 3, $\chi^2 = 0.1$, $S_4{}^2 = 0.548$.

APPENDIX G

PROBABILITY DISTRIBUTIONS FOR TWO POWER LAW PSD

This Appendix contains all the calculated probability distributions for two power law PSD. These distributions are compared to Nakagami-m (labeled as N) and Rice (labeled as R) if S_4 is less than unity and to Rayleigh (labeled as SRF) if S_4 is greater than or equal to unity. Throughout, the calculated results are labeled C.

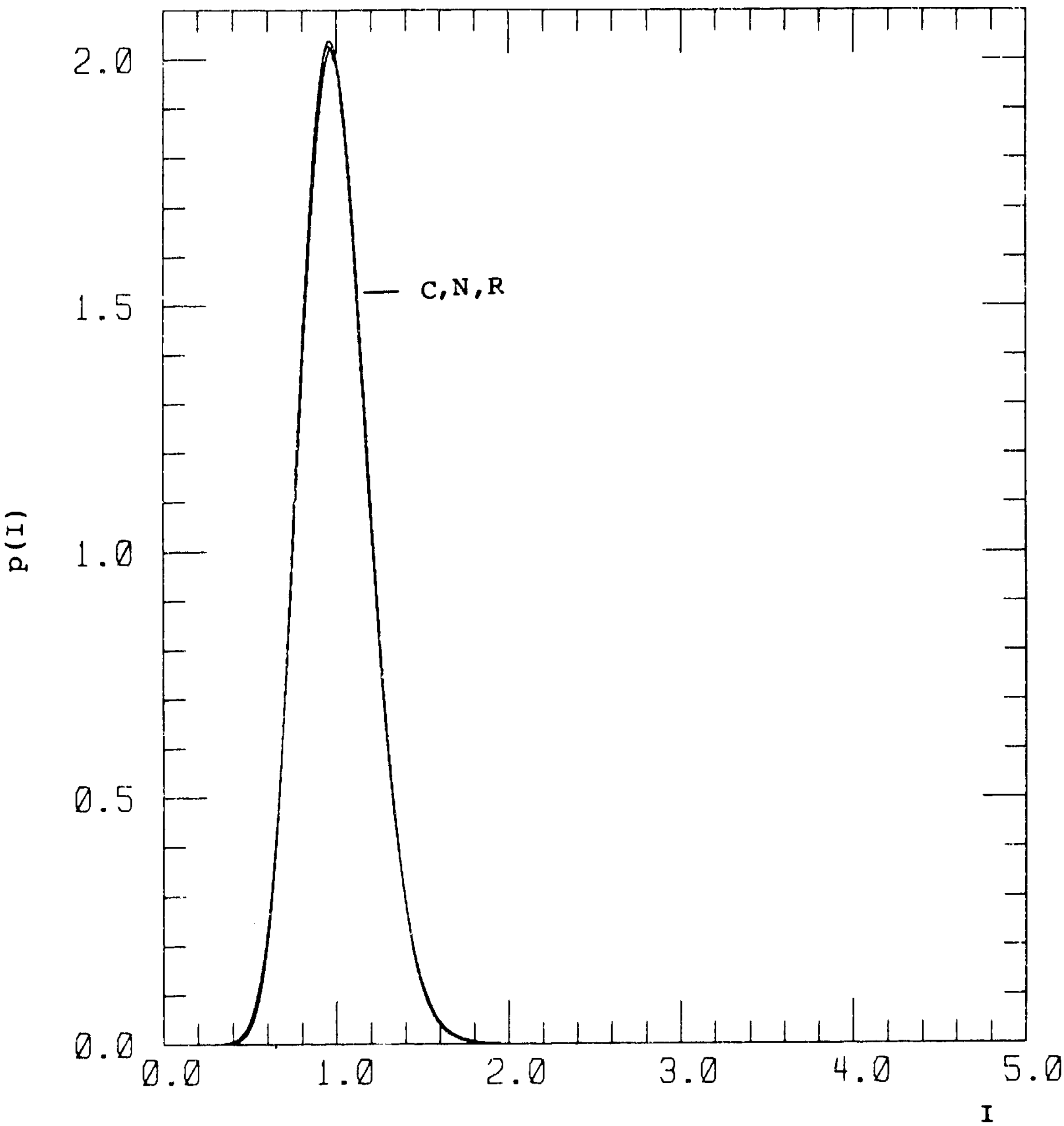

Figure G-1. Probability Distribution for
$\alpha = 1$, $\chi^2 = 0.01$, $S_4{}^2 = 0.040$.

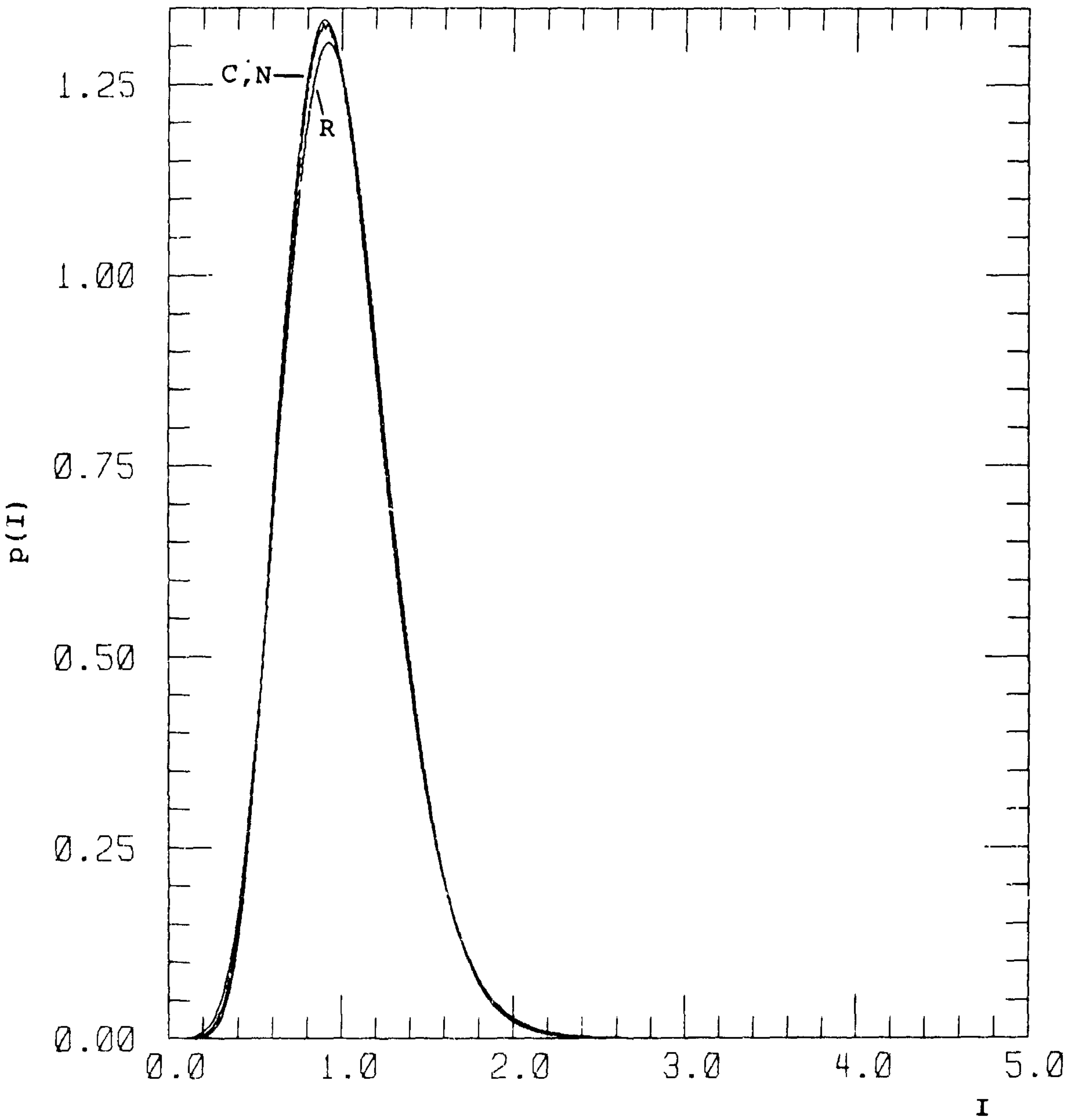

Figure G-2. Probability Distribution for $\alpha = 1$, $\chi^2 = 0.025$, $S_4^{\ 2} = 0.097$.

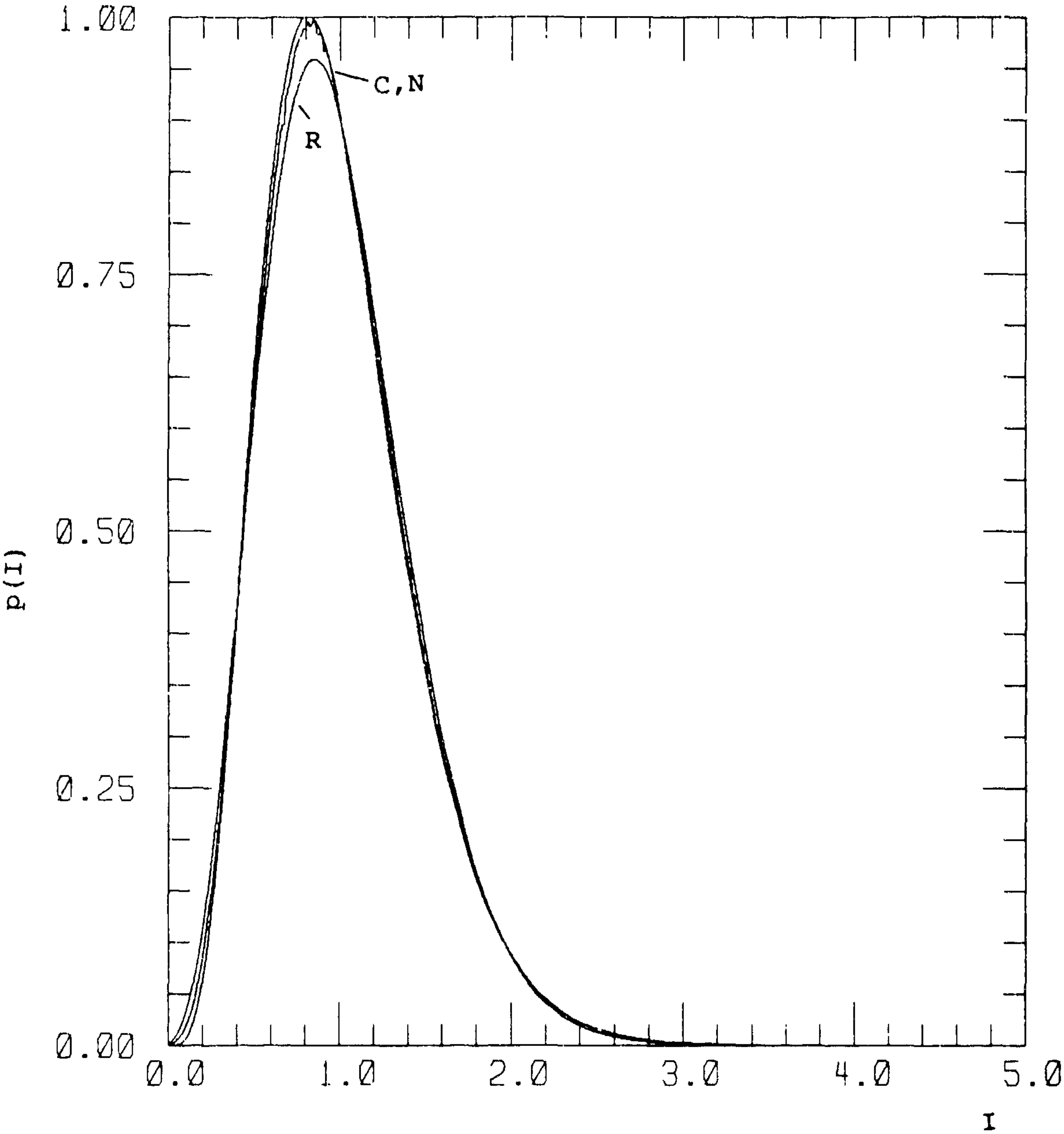

Figure G-3. Probability Distribution for $\alpha = 1$, $\chi^2 = 0.05$, $S_4{}^2 = 0.188$.

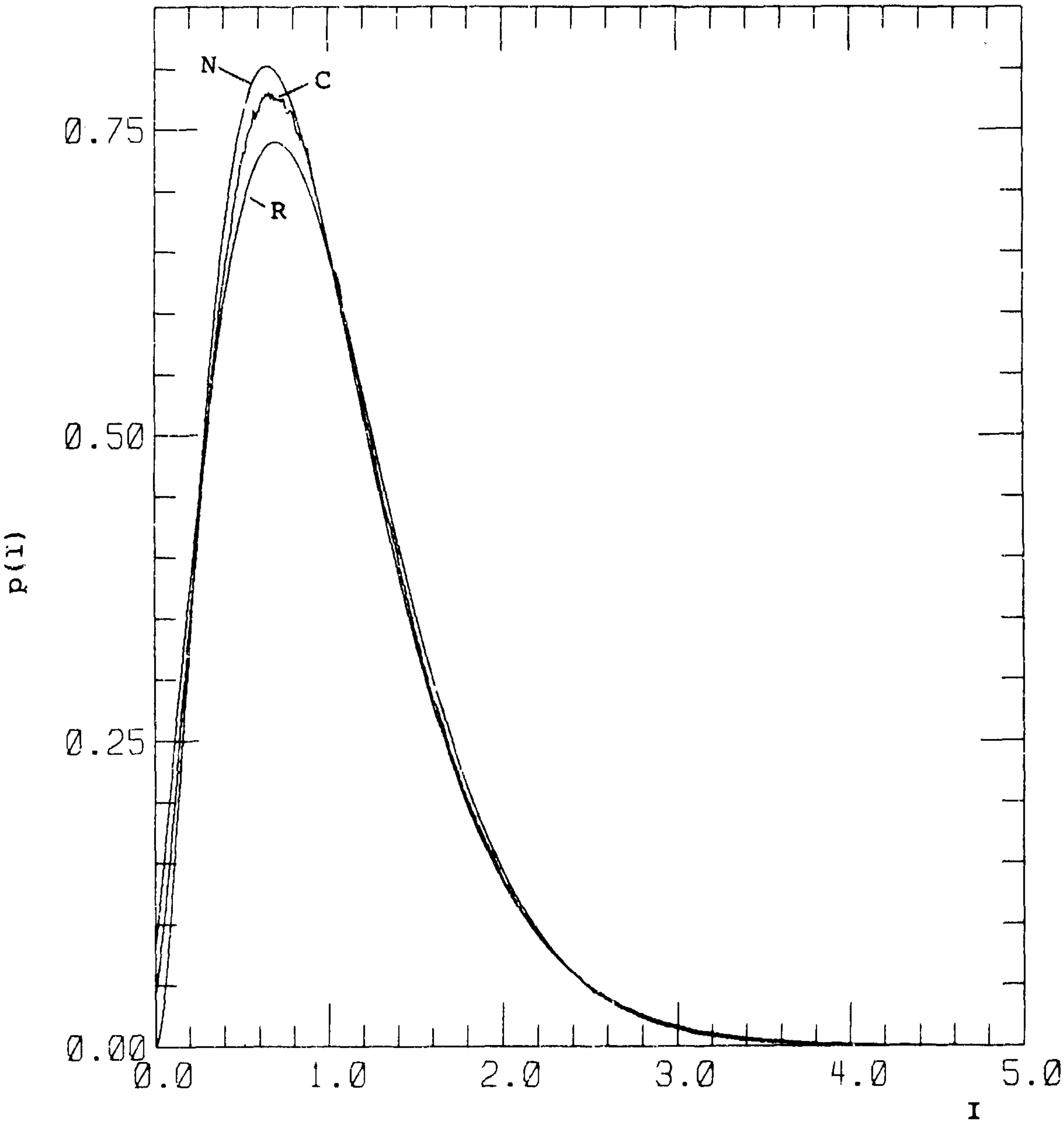

Figure G-4. Probability Distribution for
$\alpha = 1$, $\chi^2 = 0.1$, $S_4{}^2 = 0.347$.

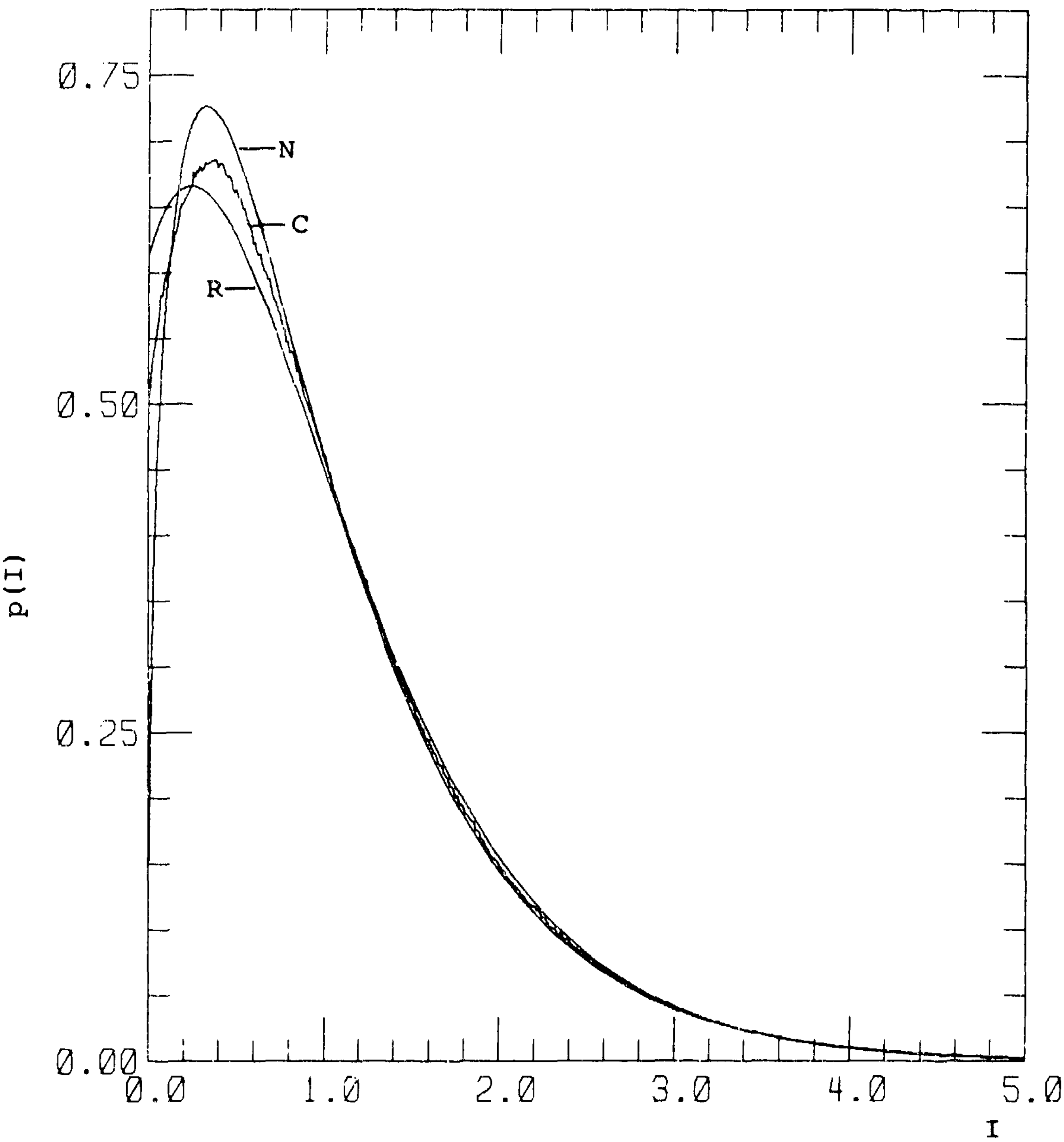

Figure G-5. Probability Distribution for
$\alpha = 1$, $\chi^2 = 0.25$, $S_4^{\ 2} = 0.672$.

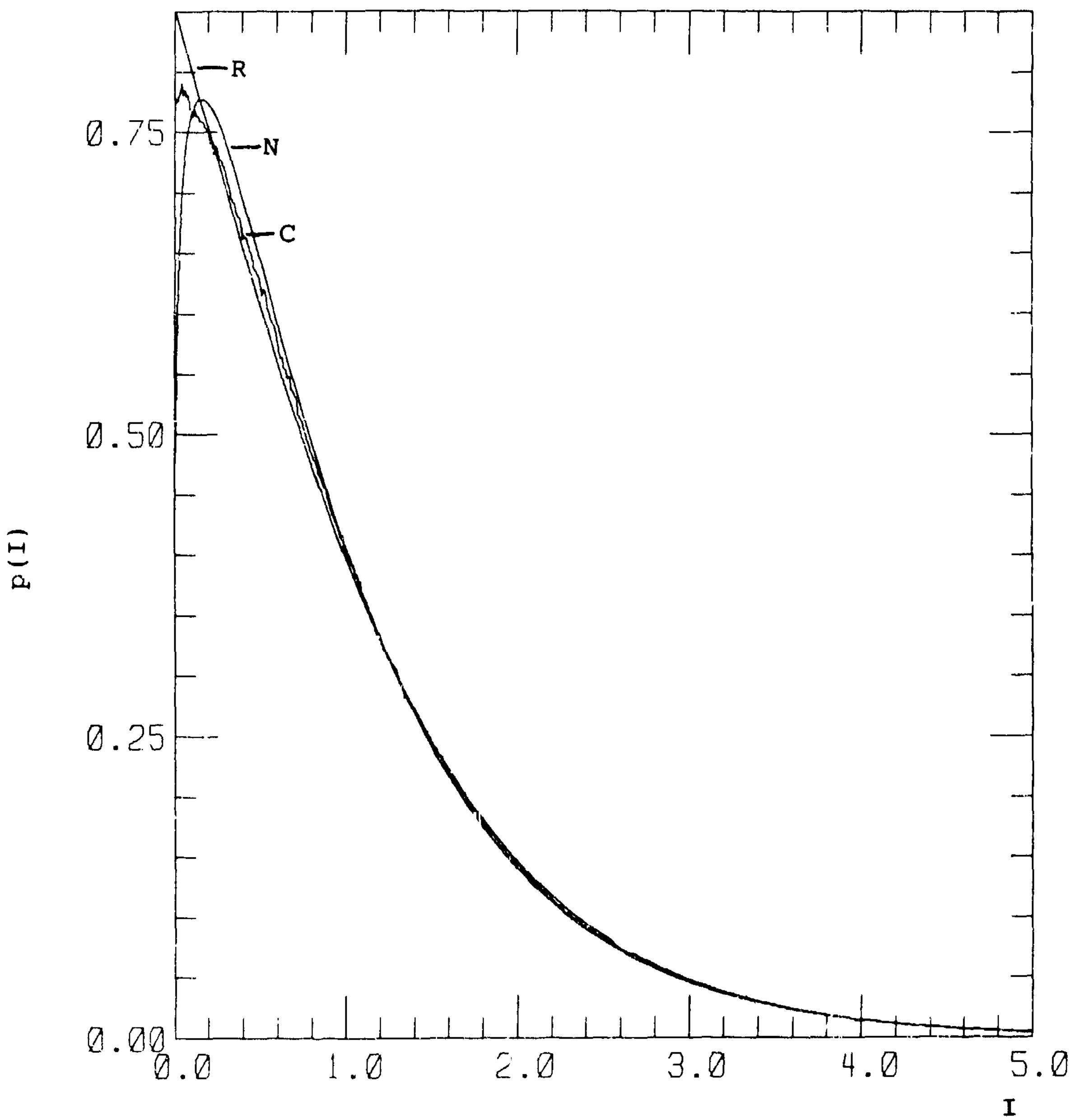

Figure G-6. Probability Distribution for $\alpha = 1$, $\chi^2 = 0.4$, $S_4^{\,2} = 0.837$.

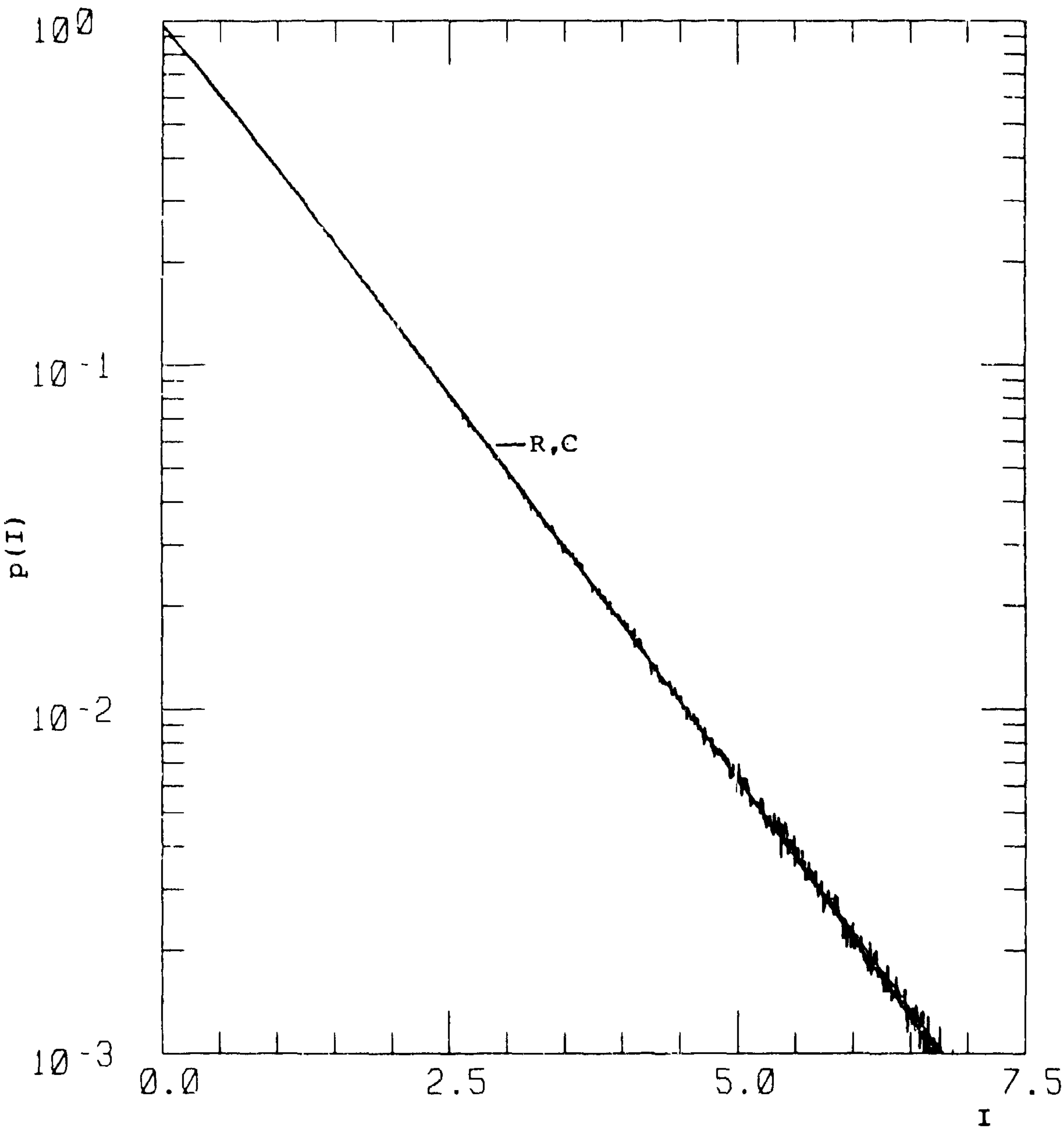

Figure G-7. Probability Distribution for $\alpha = 1$, $\chi^2 = 0.7$, $S_4^{\,2} = 0.965$.

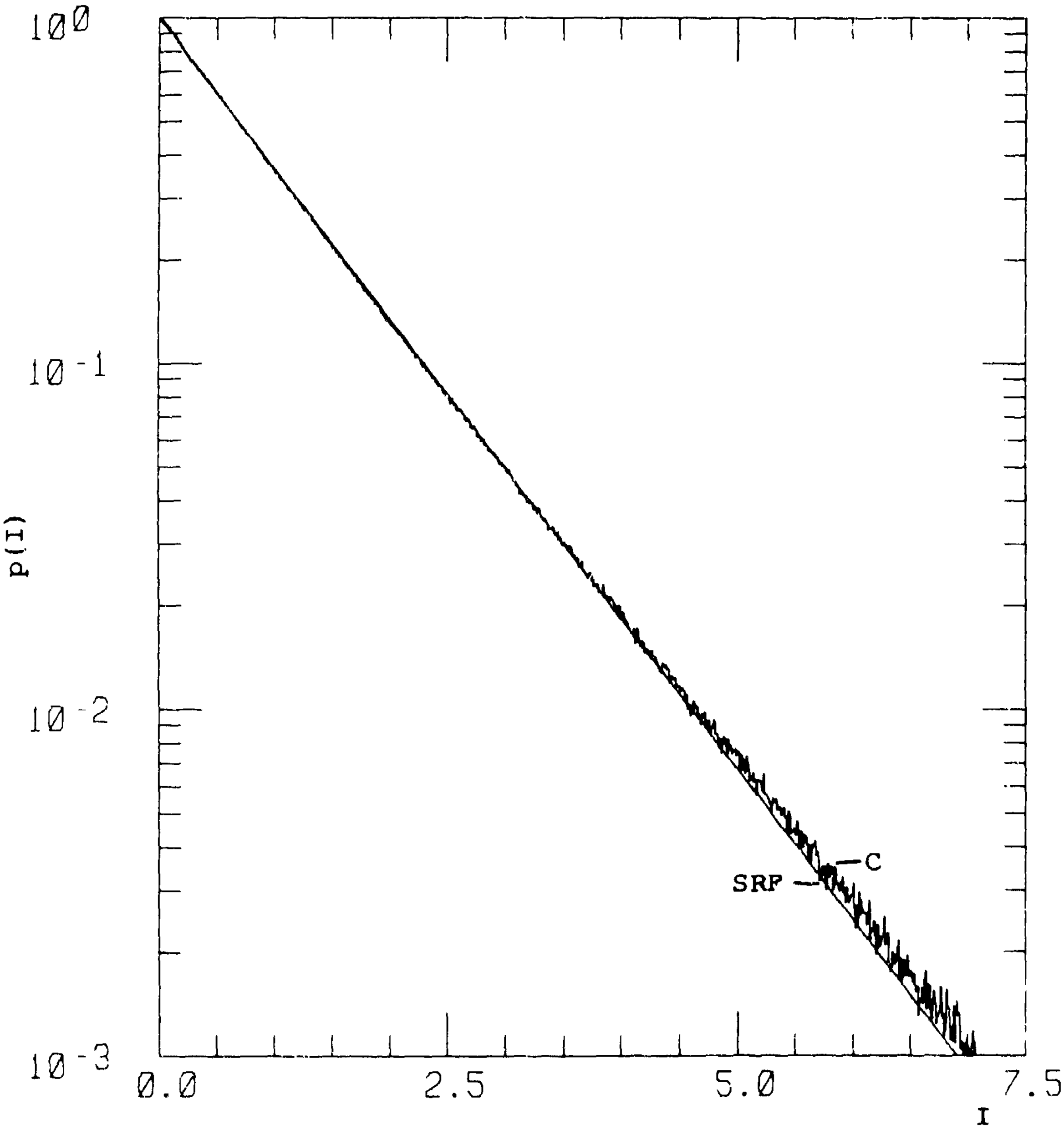

Figure G-8. Probability Distribution for $\alpha = 1$, $\chi^2 = 1.5$, $S_4^2 = 1.03$.

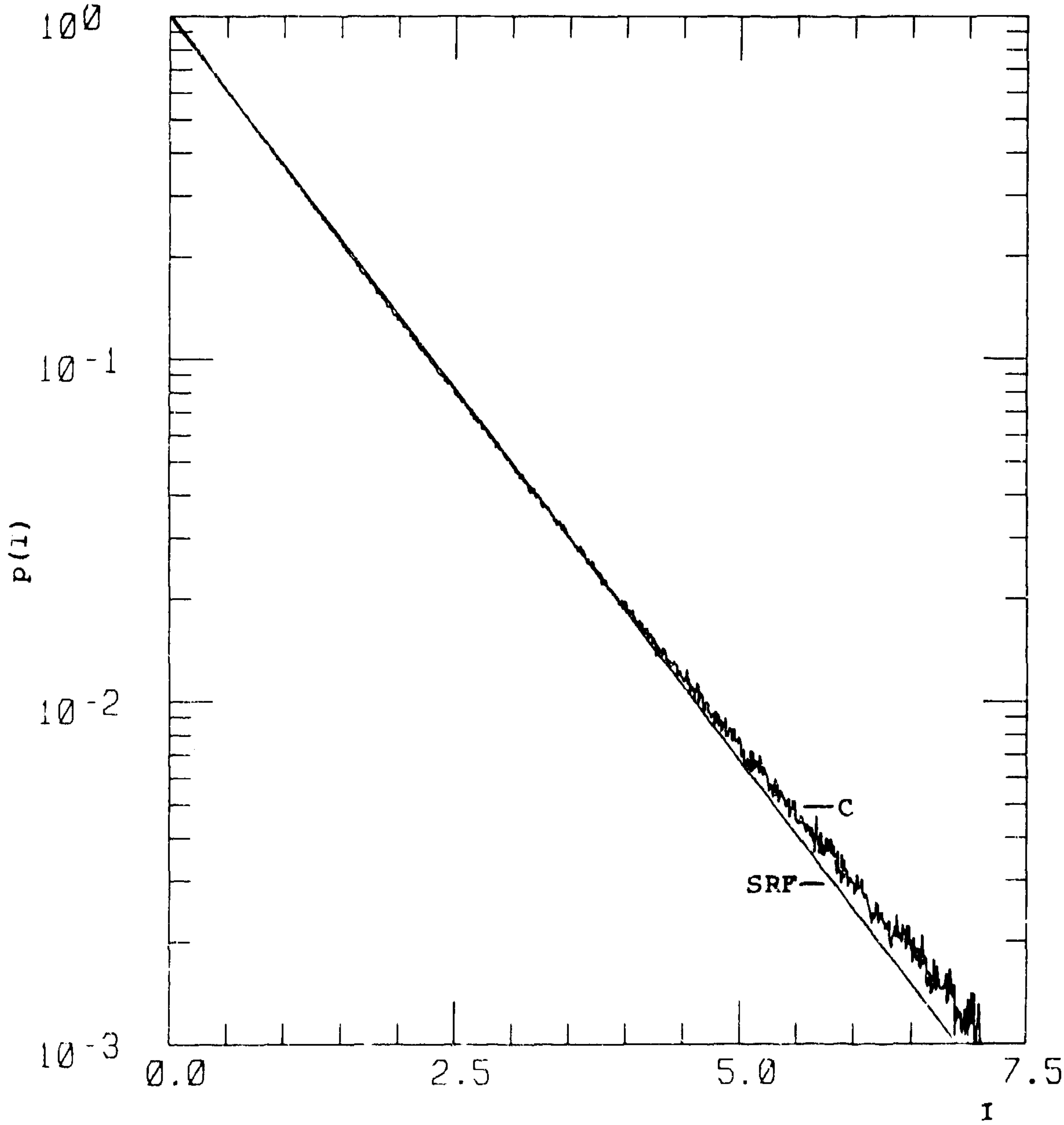

Figure G-9. Probability Distribution for $\alpha = 1, \chi^2 = 3.0$, $S_4{}^2 = 1.05$.

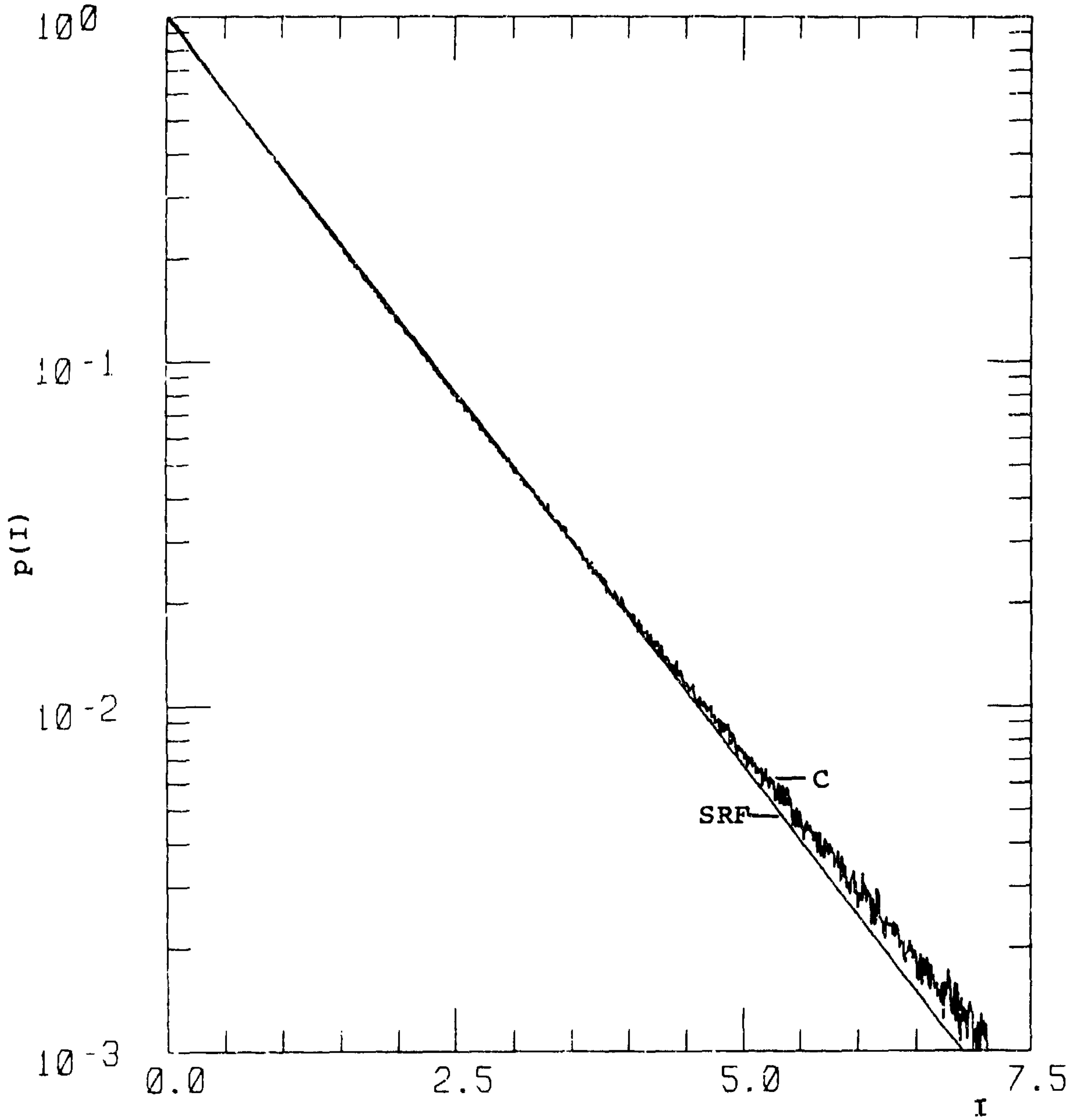

Figure G-10. Probability Distribution for $\alpha = 1$, $\chi^2 = 7.0$, $S_4{}^2 = 1.05$.

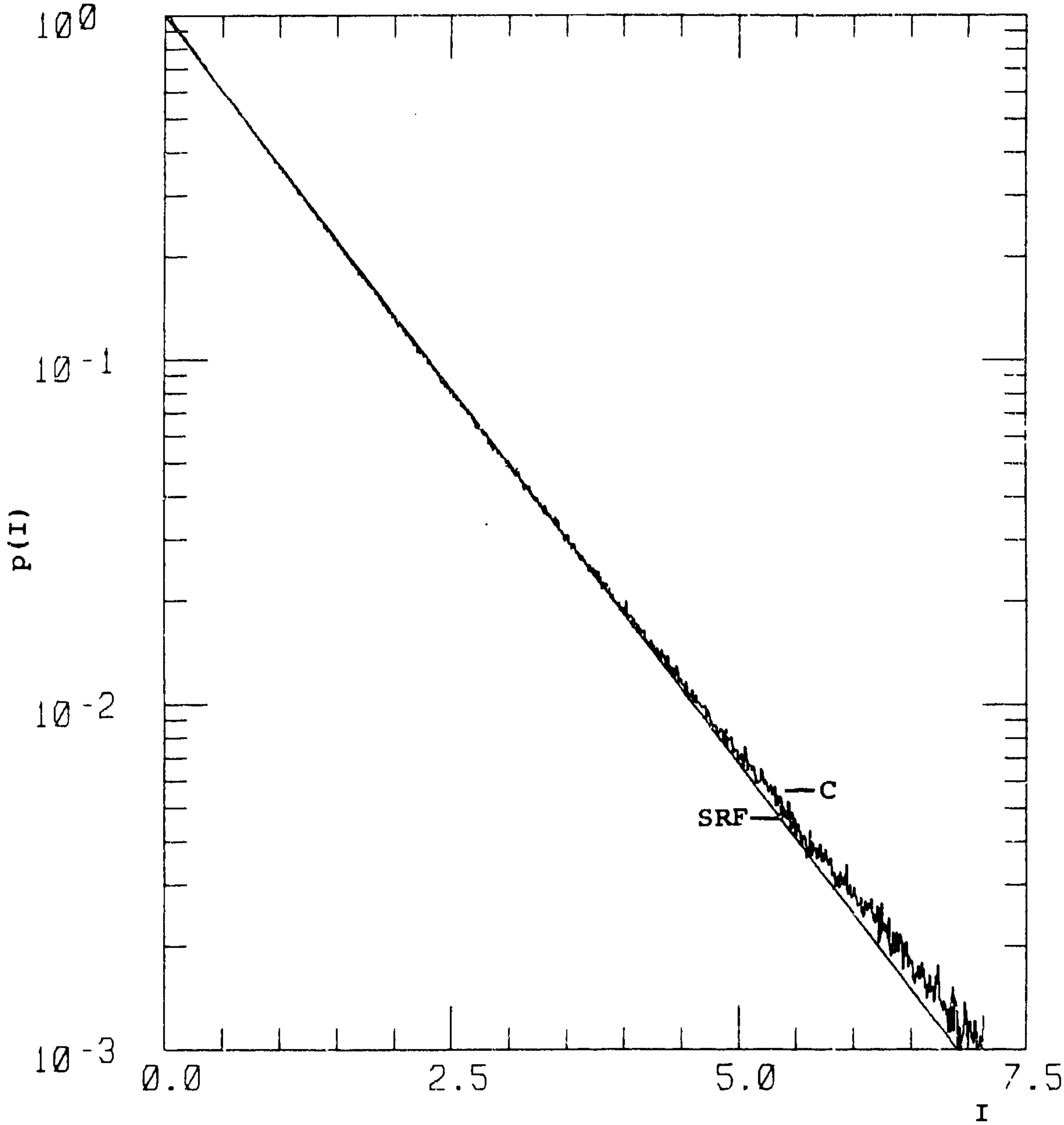

Figure G-11. Probability Distribution for $\alpha = 1$, $\chi^2 = 10.0$, $S_4^{\,2} = 1.04$.

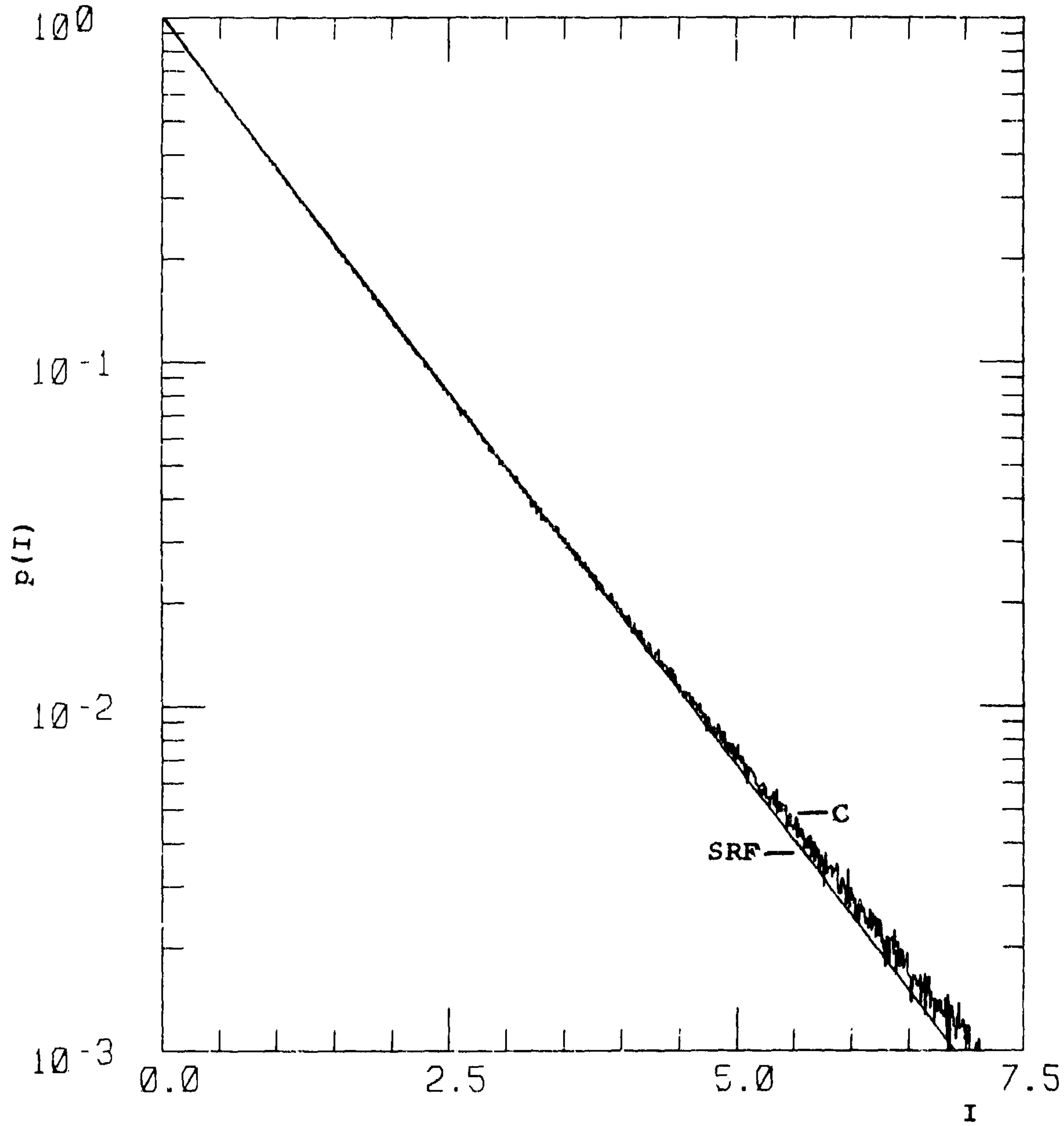

Figure G-12. Probability Distribution for $\alpha = 1$, $\chi^2 = 20.0$, $S_4^{\ 2} = 1.03$.

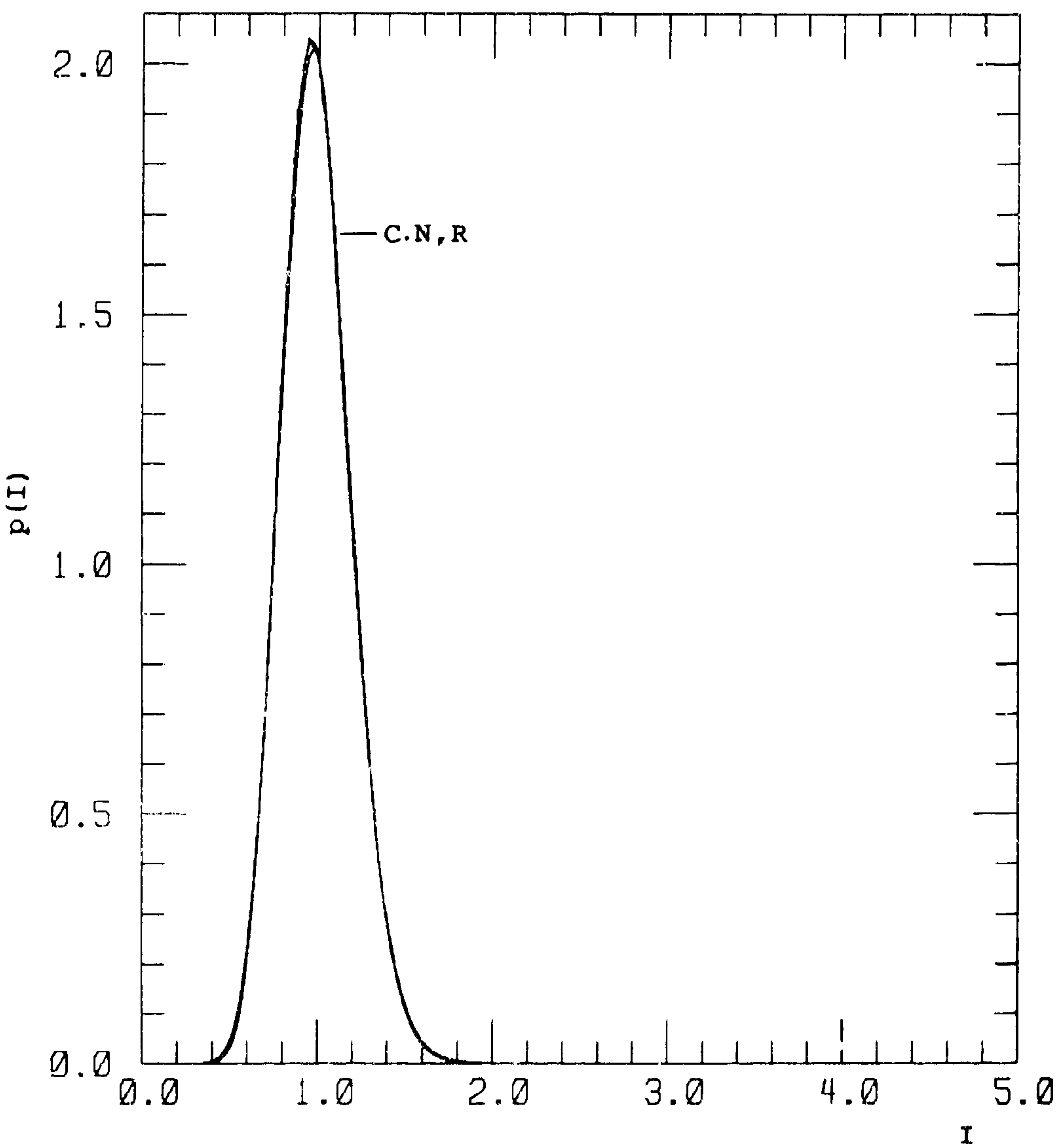

Figure G-13. Probability Distribution for $\alpha = 2$, $\chi^2 = 0.01$, $S_4^{\,2} = 0.039$.

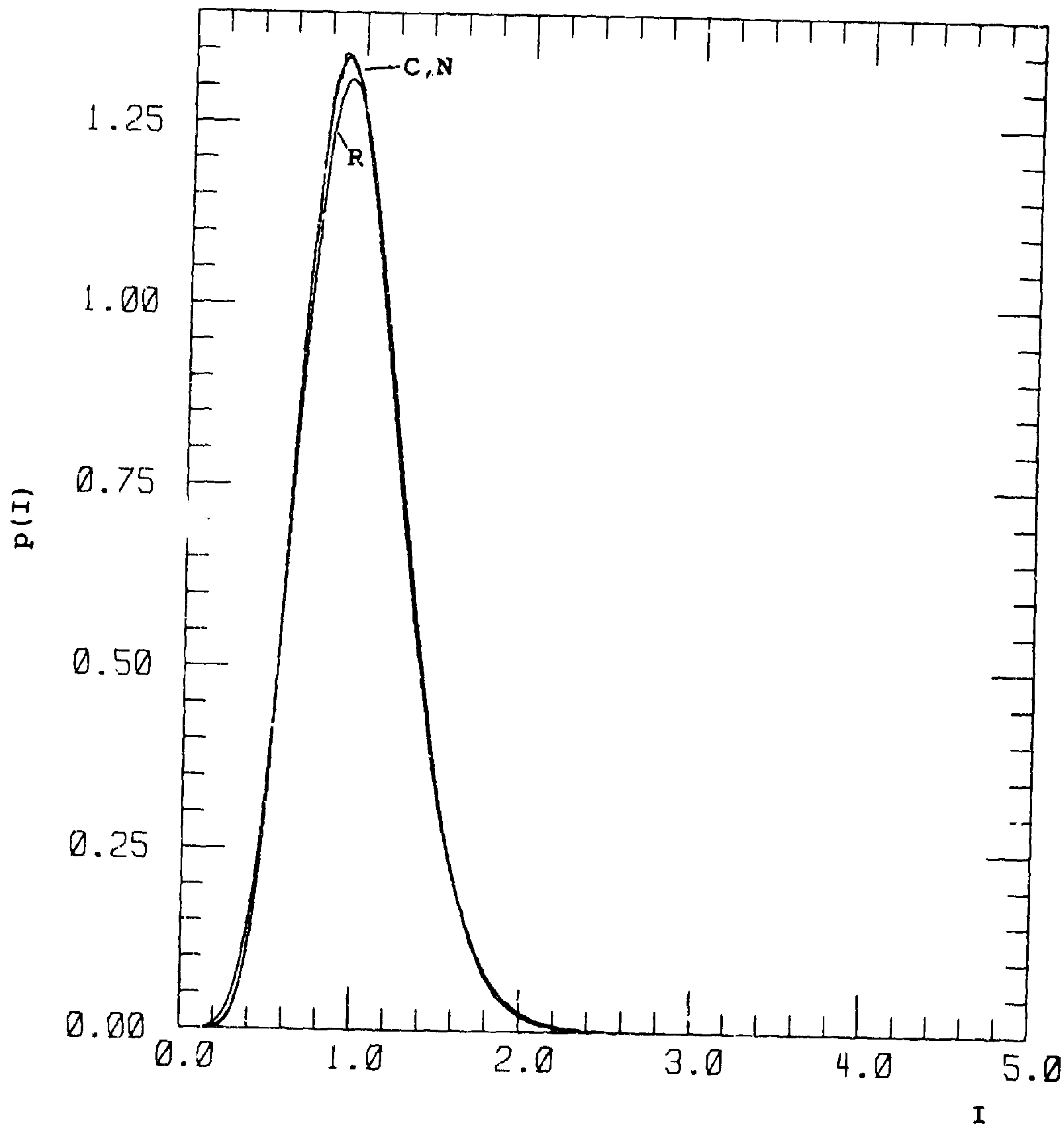

Figure G-14. Probability Distribution for $\alpha = 2$, $\chi^2 = 0.025$, $S_4{}^2 = 0.097$.

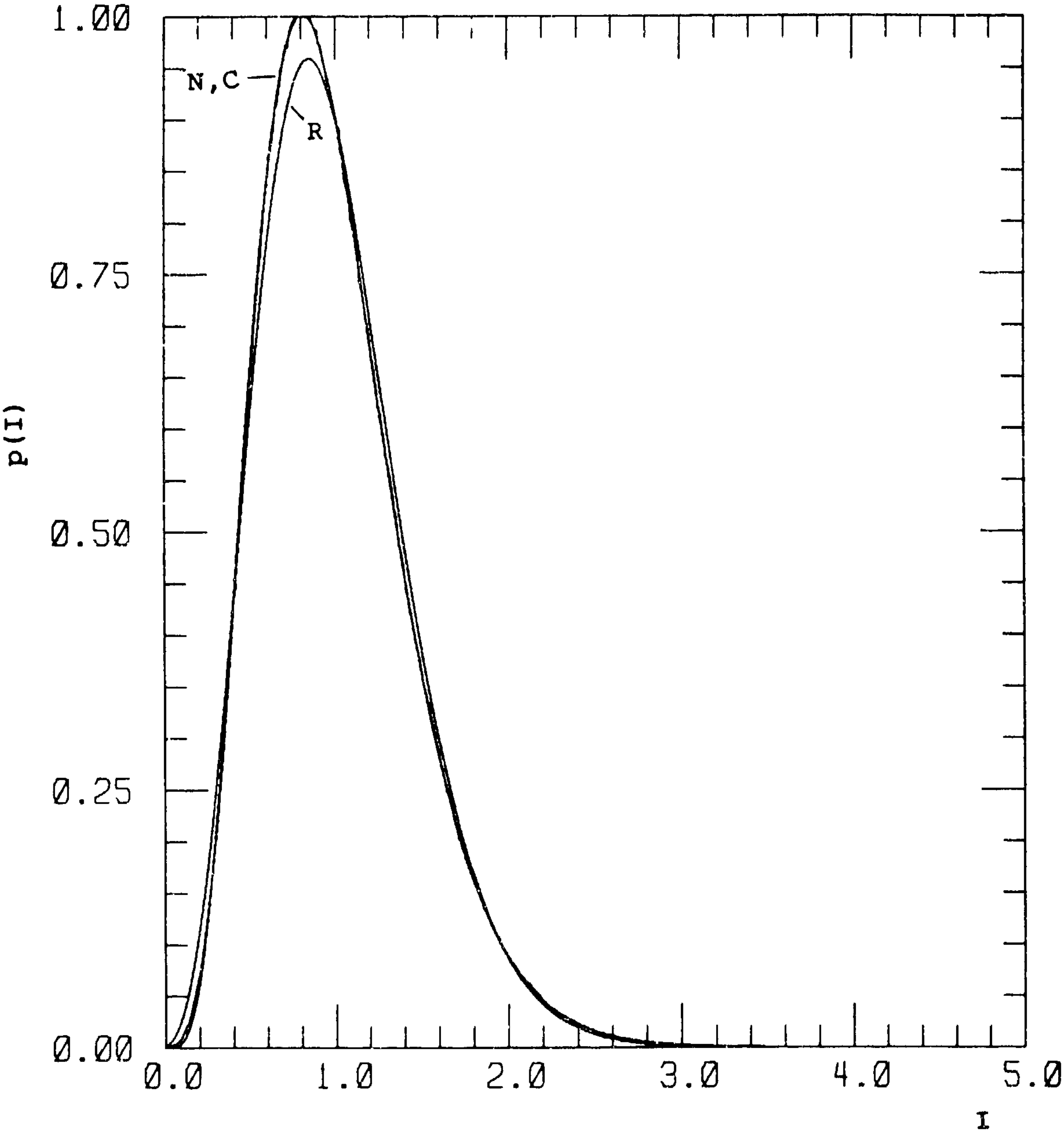

Figure G-15. Probability Distribution for $\alpha = 2$, $\chi^2 = 0.05$, $S_4{}^2 = 0.188$.

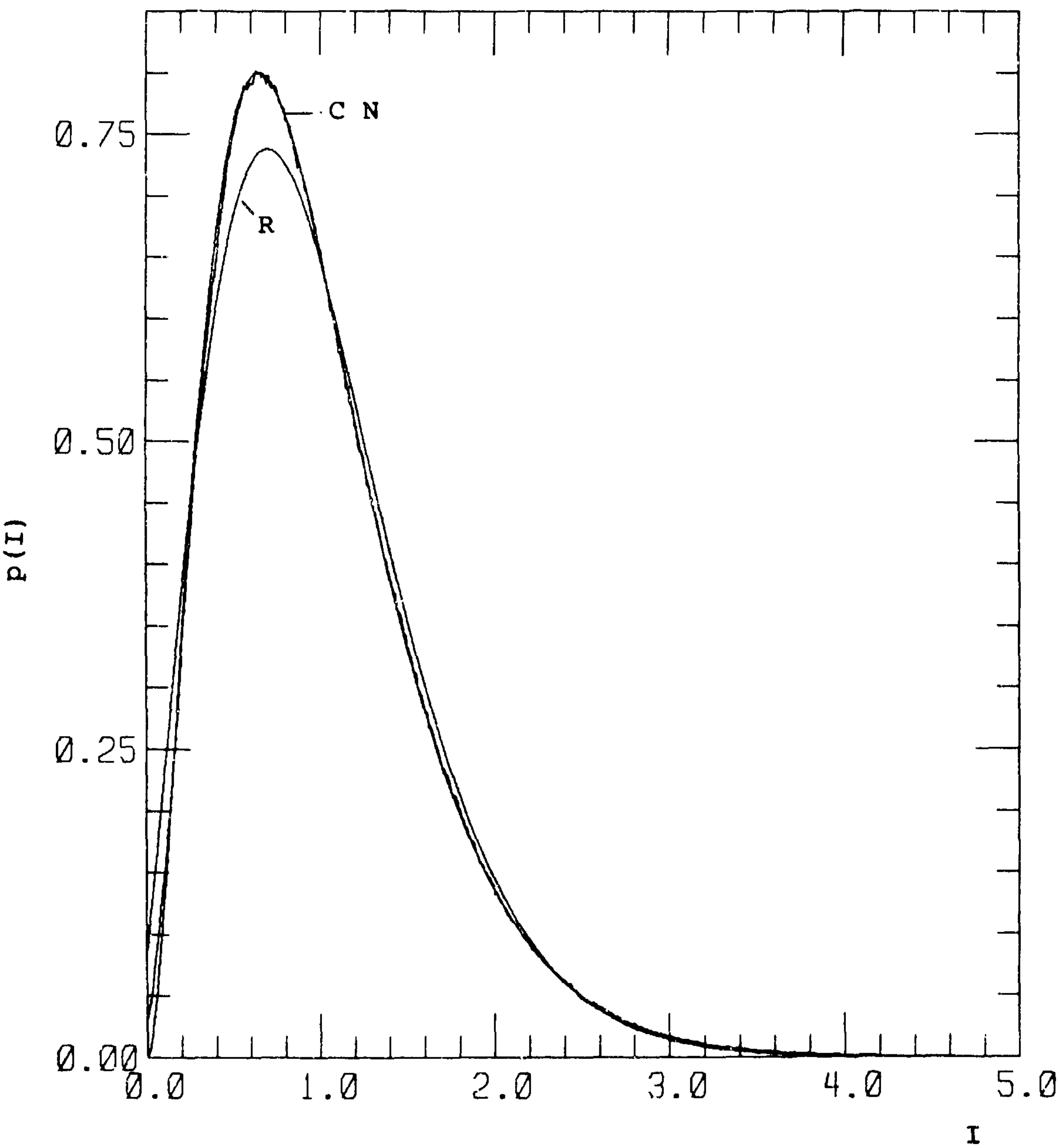

Figure G-16. Probability Distribution for $\alpha = 2$, $\chi^2 = 0.1$, $S_4{}^2 = 0.350$.

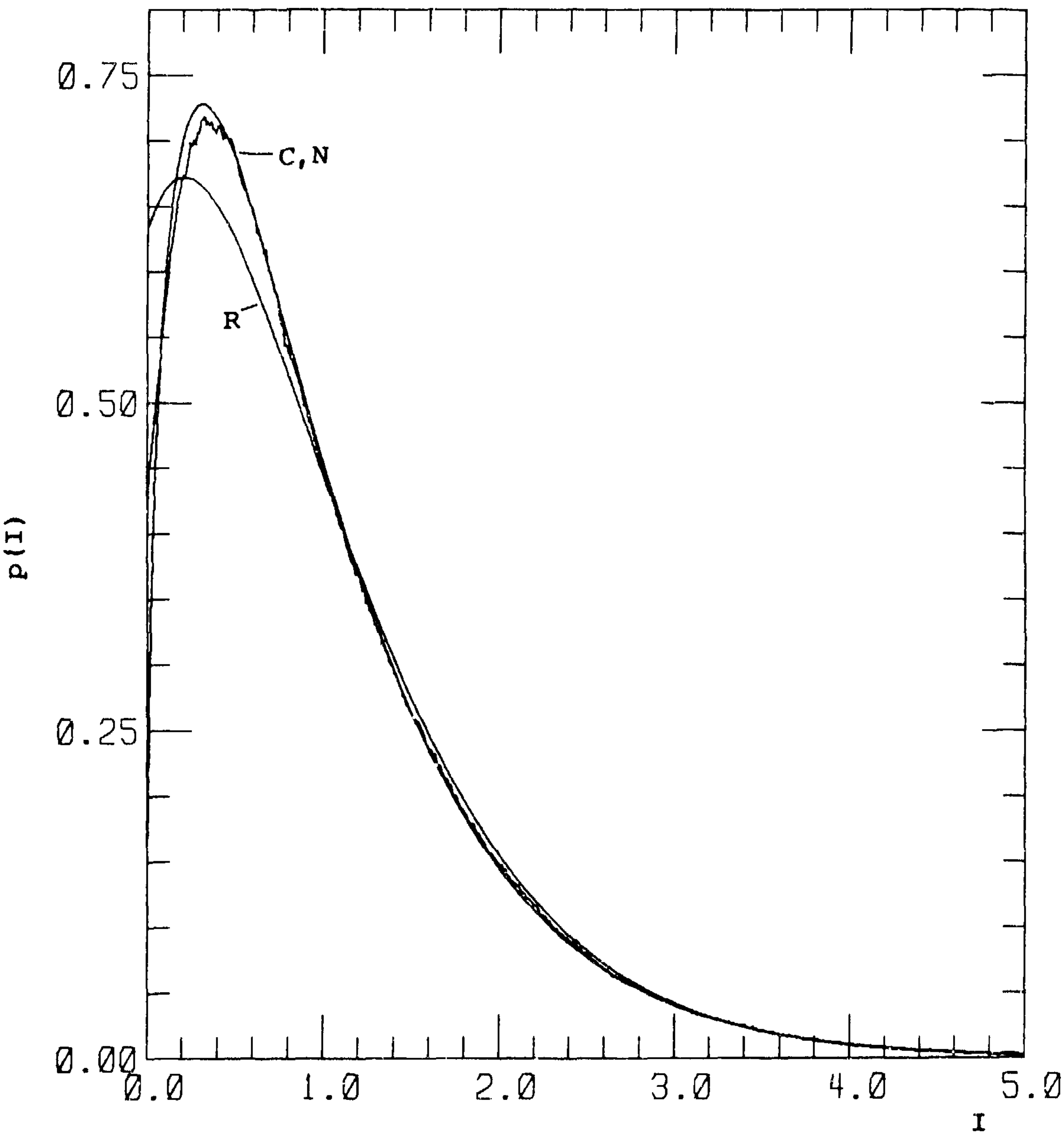

Figure G-17. Probability Distribution for $\alpha = 2$, $\chi^2 = 0.25$, $S_4{}^2 = 0.634$.

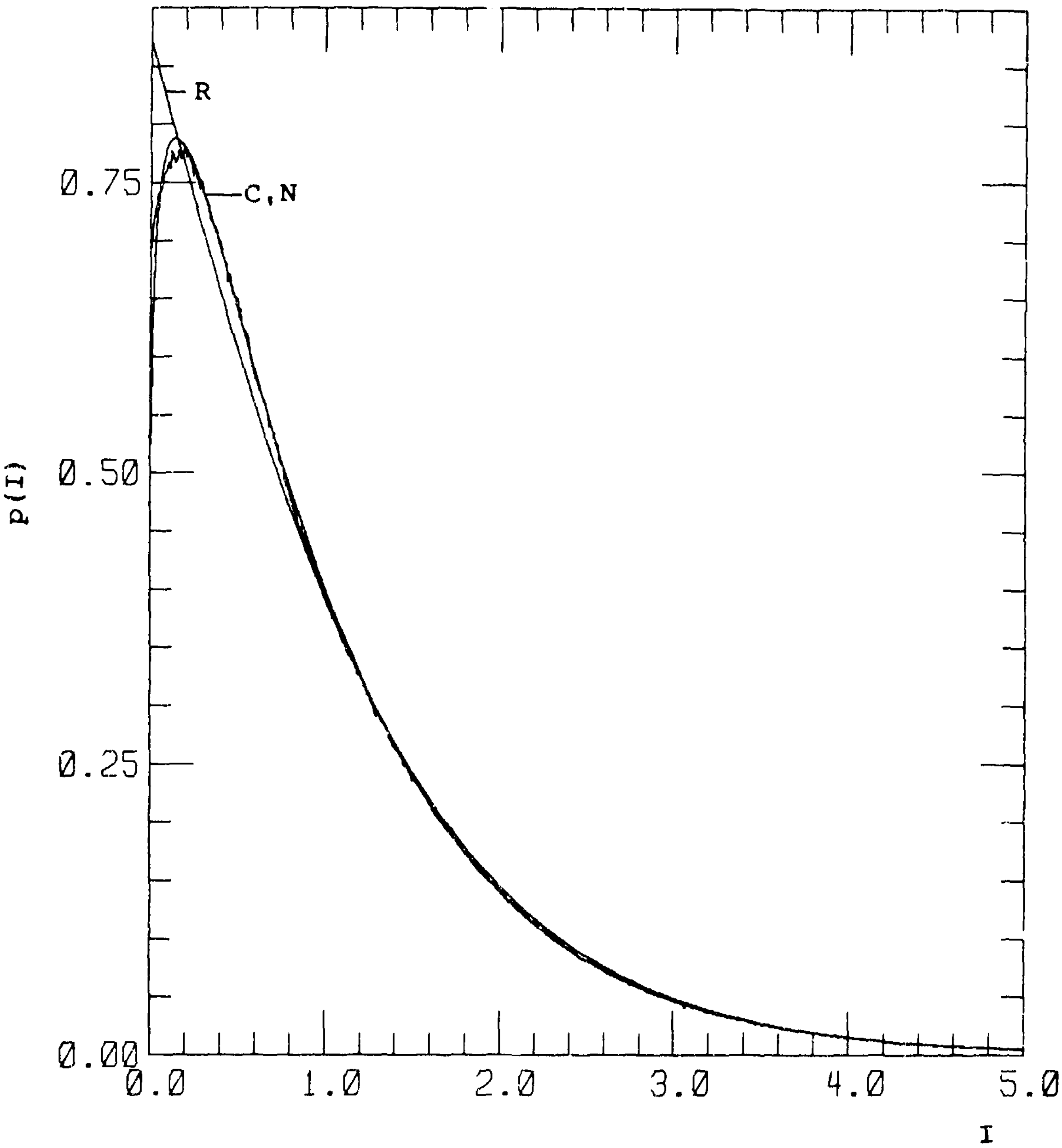

Figure G-18. Probability Distribution for $\alpha = 2$, $\chi^2 = 0.4$, $S_4{}^2 = 0.854$.

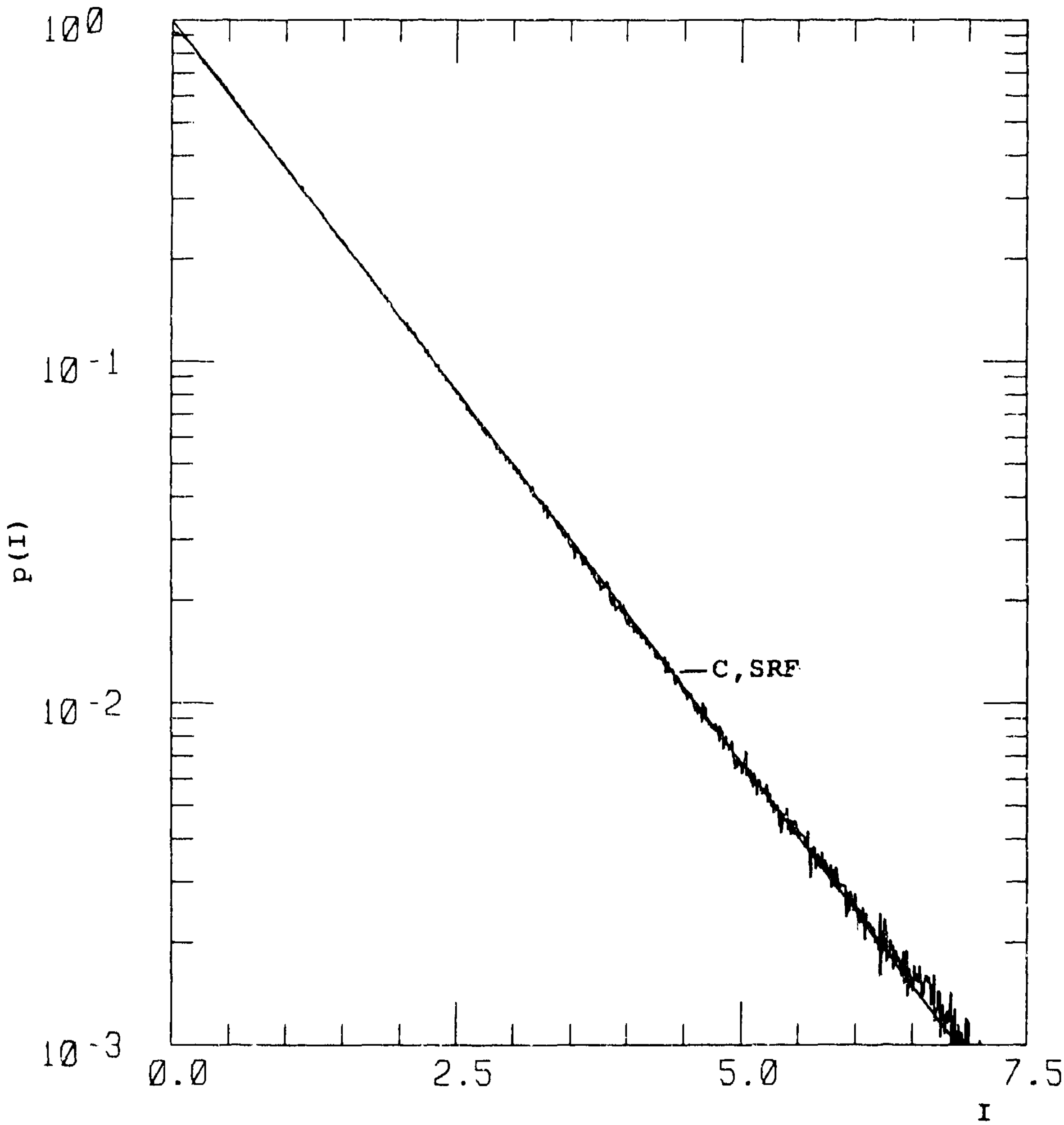

Figure G-19. Probability Distribution for $\alpha = 2$, $\chi^2 = 0.7$, $S_4^{\ 2} = 0.998$.

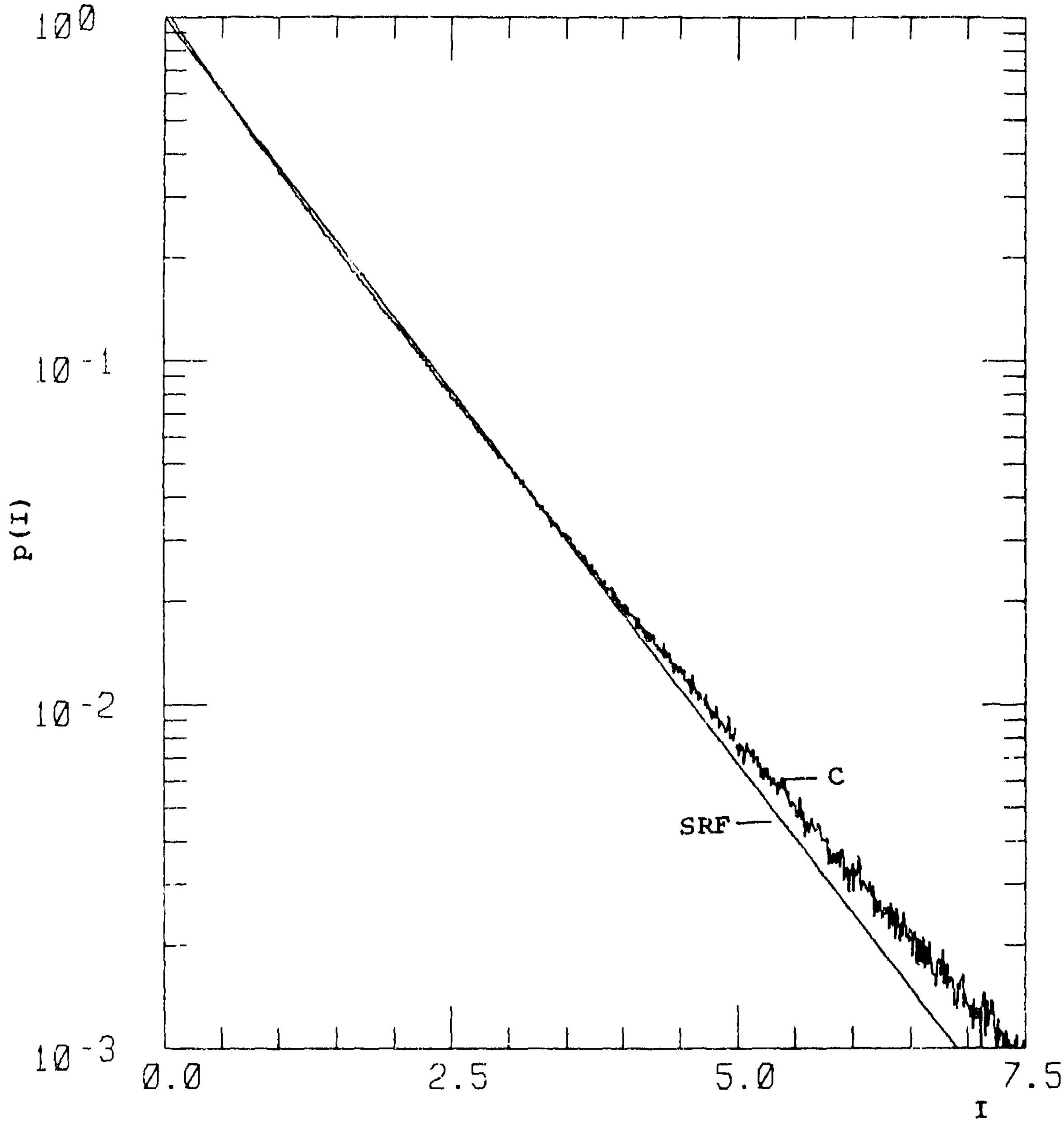

Figure G-20. Probability Distribution for $\alpha = 2$, $\chi^2 = 1.5$, $S_4{}^2 = 1.09$.

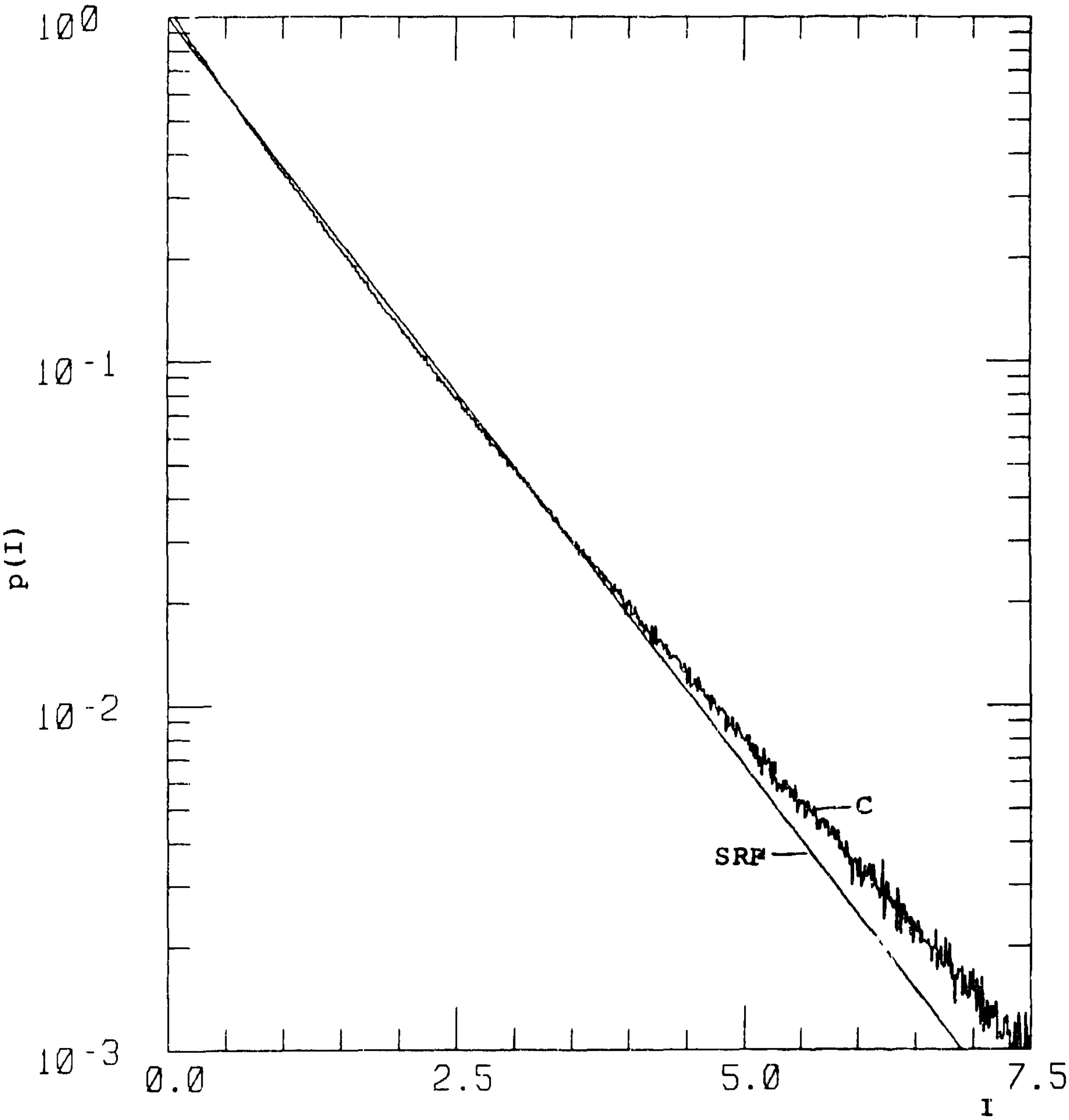

Figure G-21. Probability Distribution for $\alpha = 2,\ \chi^2 = 3.0,\ S_4{}^2 = 1.11$.

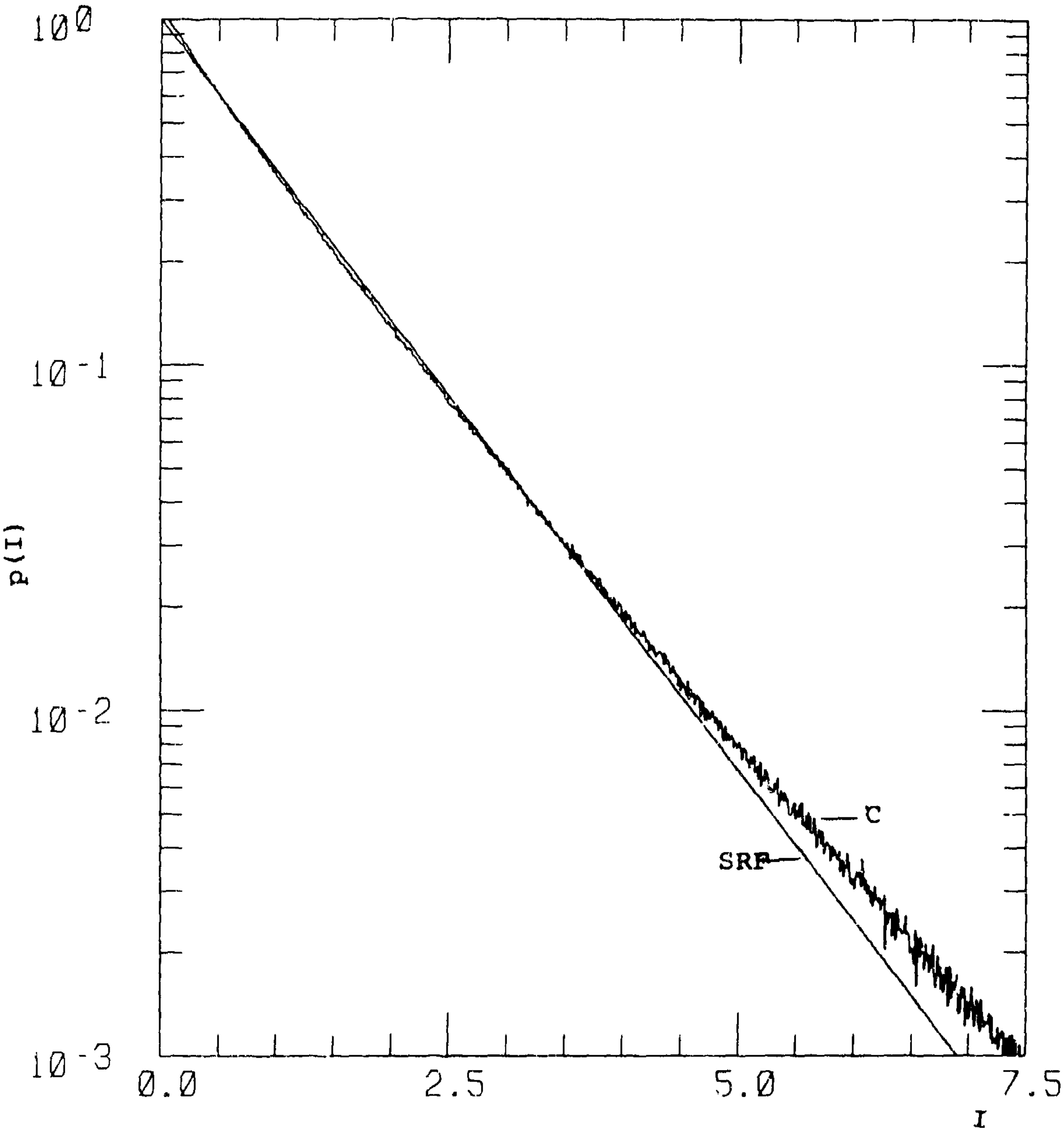

Figure G-22. Probability Distribution for $\alpha = 2$, $\chi^2 = 7.0$, $S_4^{\,2} = 1.10$.

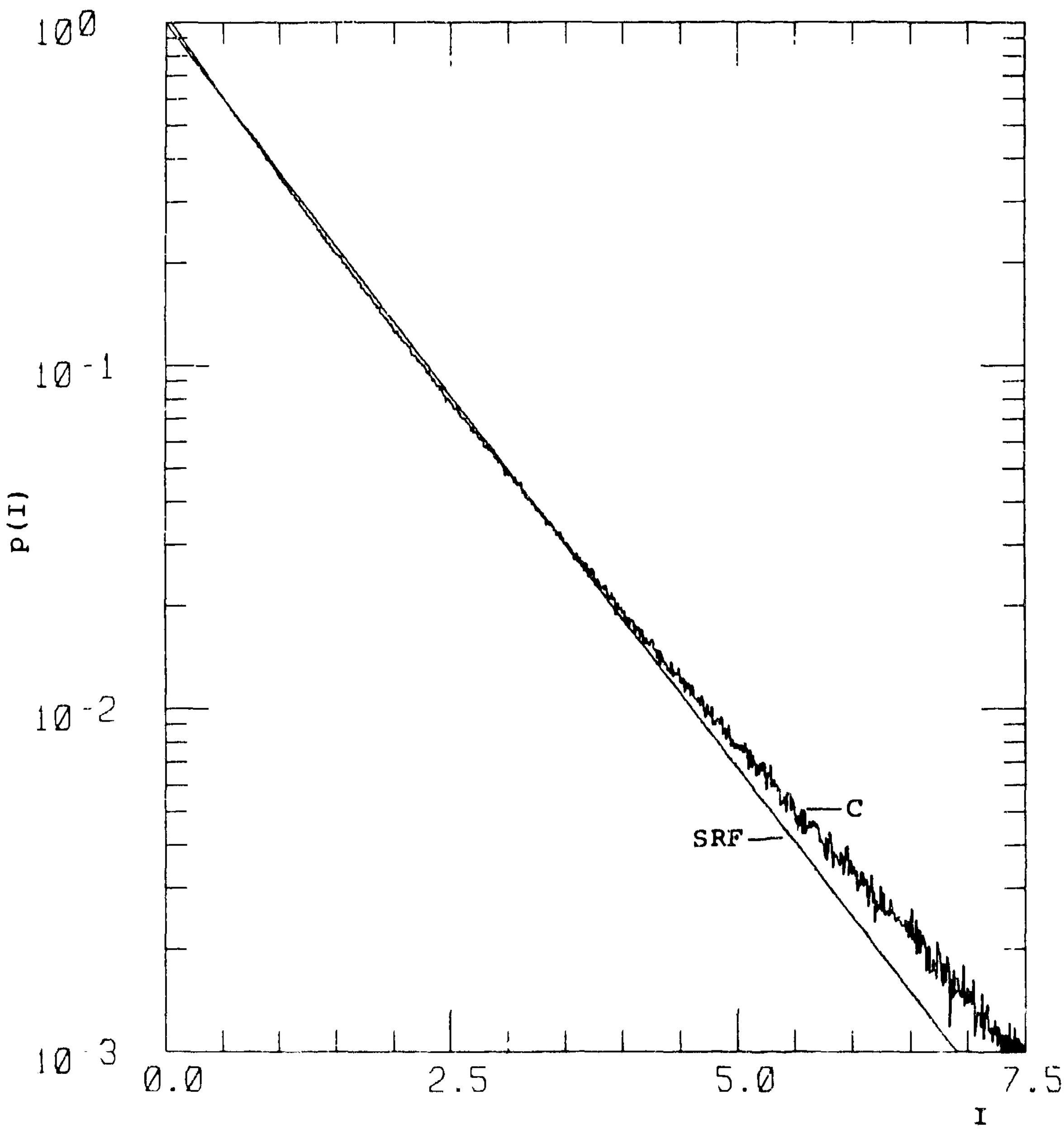

Figure G-23. Probability Distributicn for
α = 2, χ^2 = 10.C, $S_4^{\ 2}$ = 1.10.

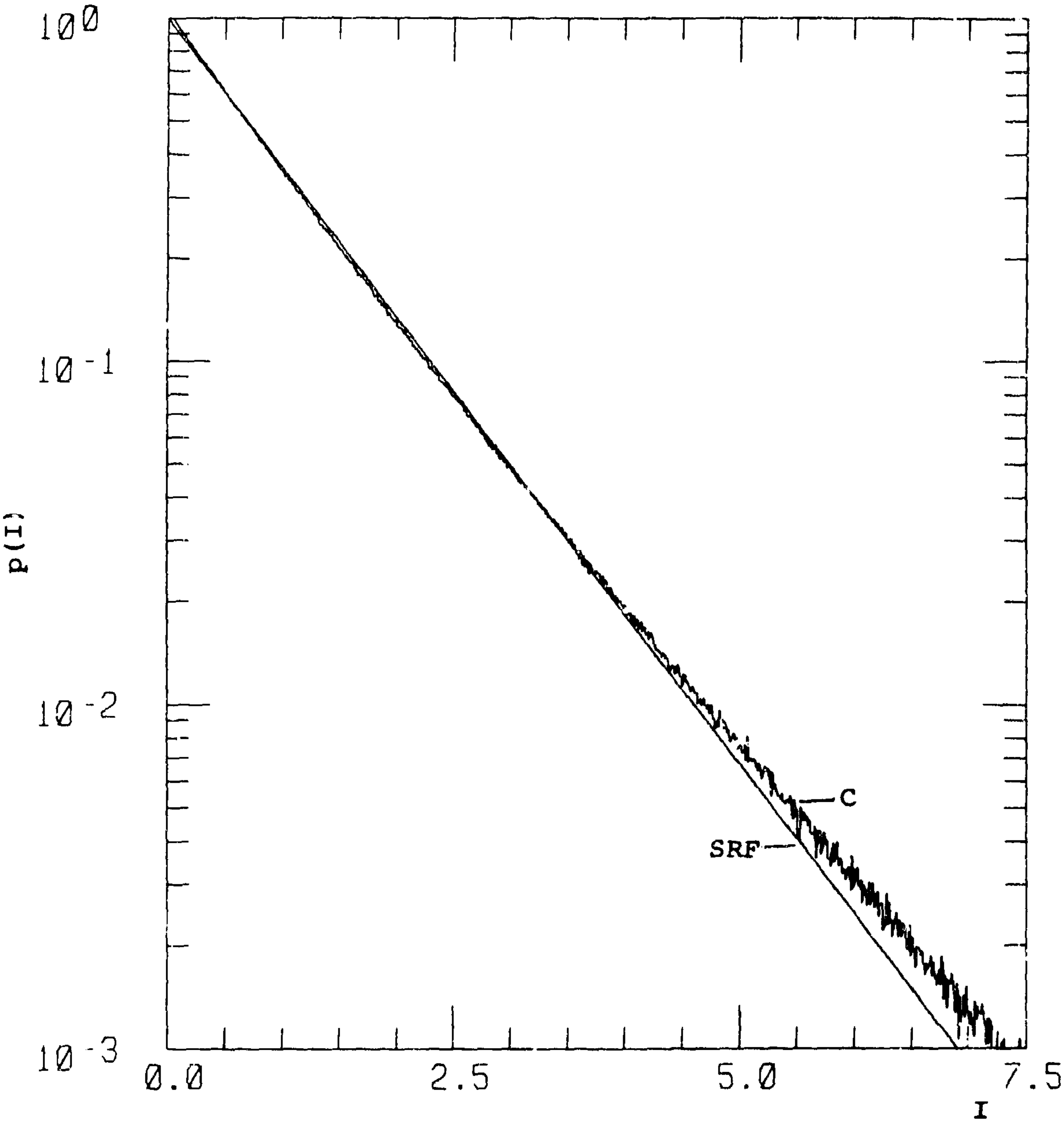

Figure G-24. Probability Distribution for $\alpha = 2$, $\chi^2 = 20.0$, $S_4{}^2 = 1.08$.

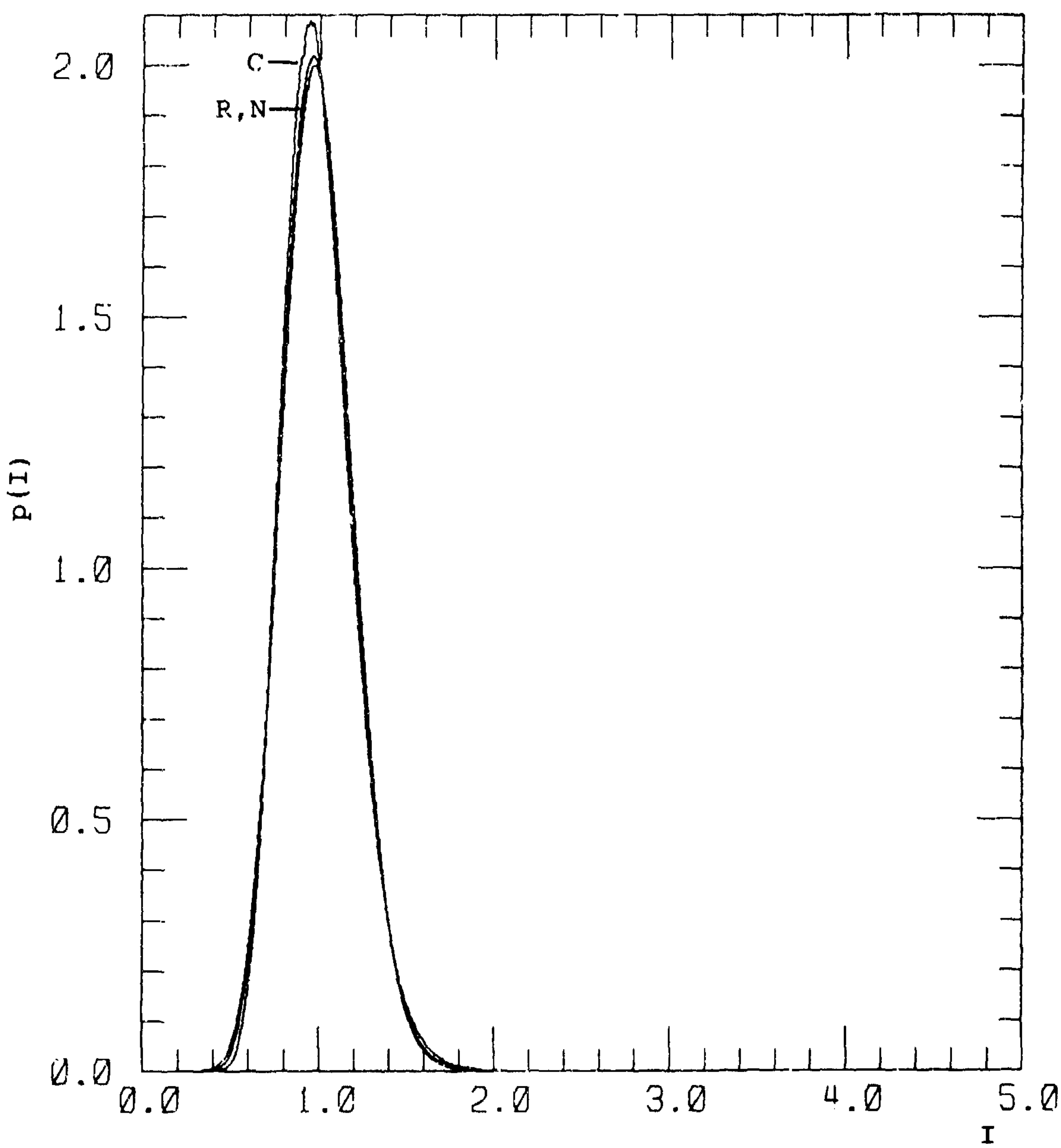

Figure G-25. Probability Distribution for $\alpha = 3$, $\chi^2 = 0.01$, $S_4{}^2 = 0.040$.

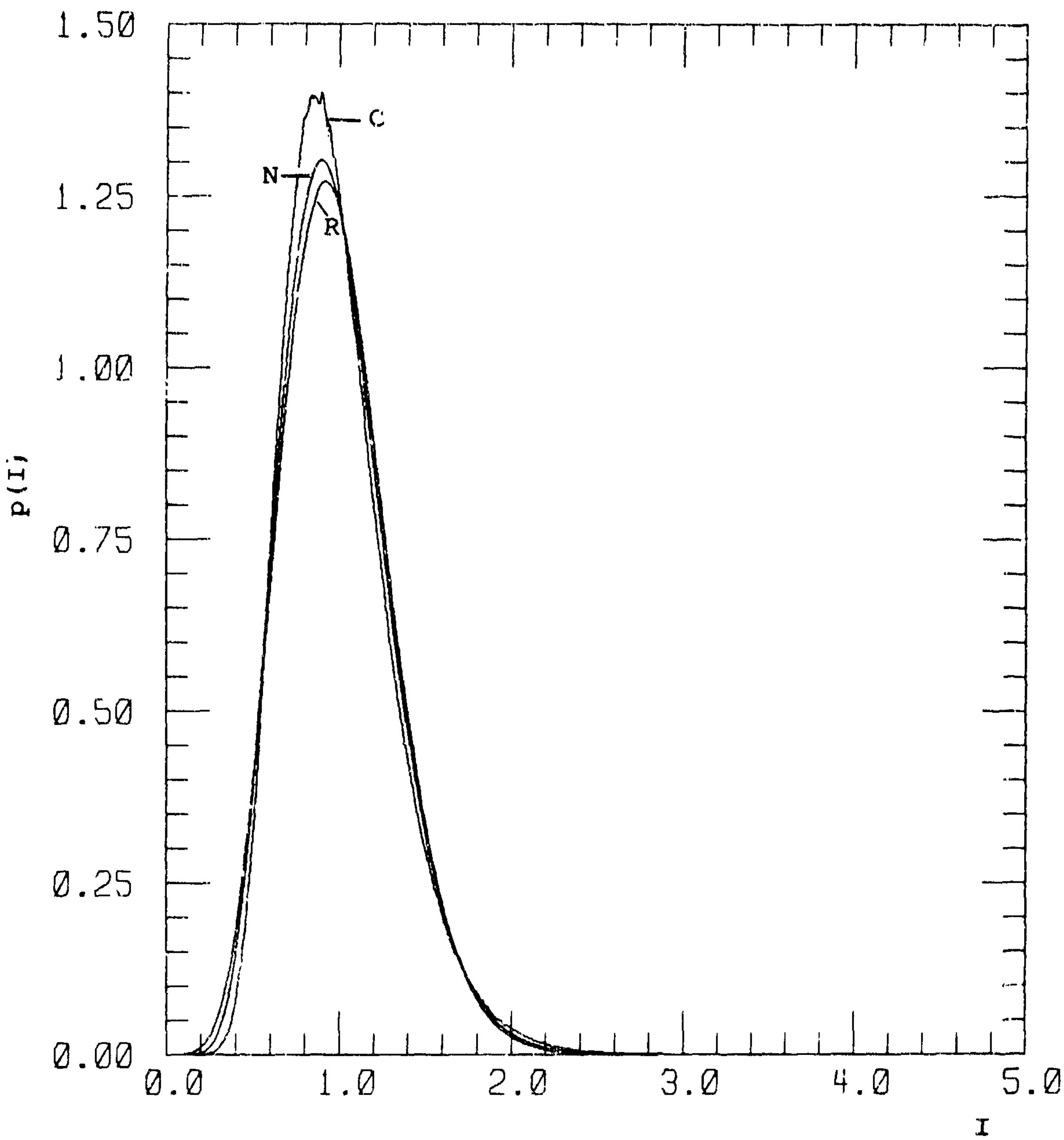

Figure G-26. Probability Distribution for $\alpha = 3$, $\chi^2 = 0.025$, $S_4^2 = 0.103$.

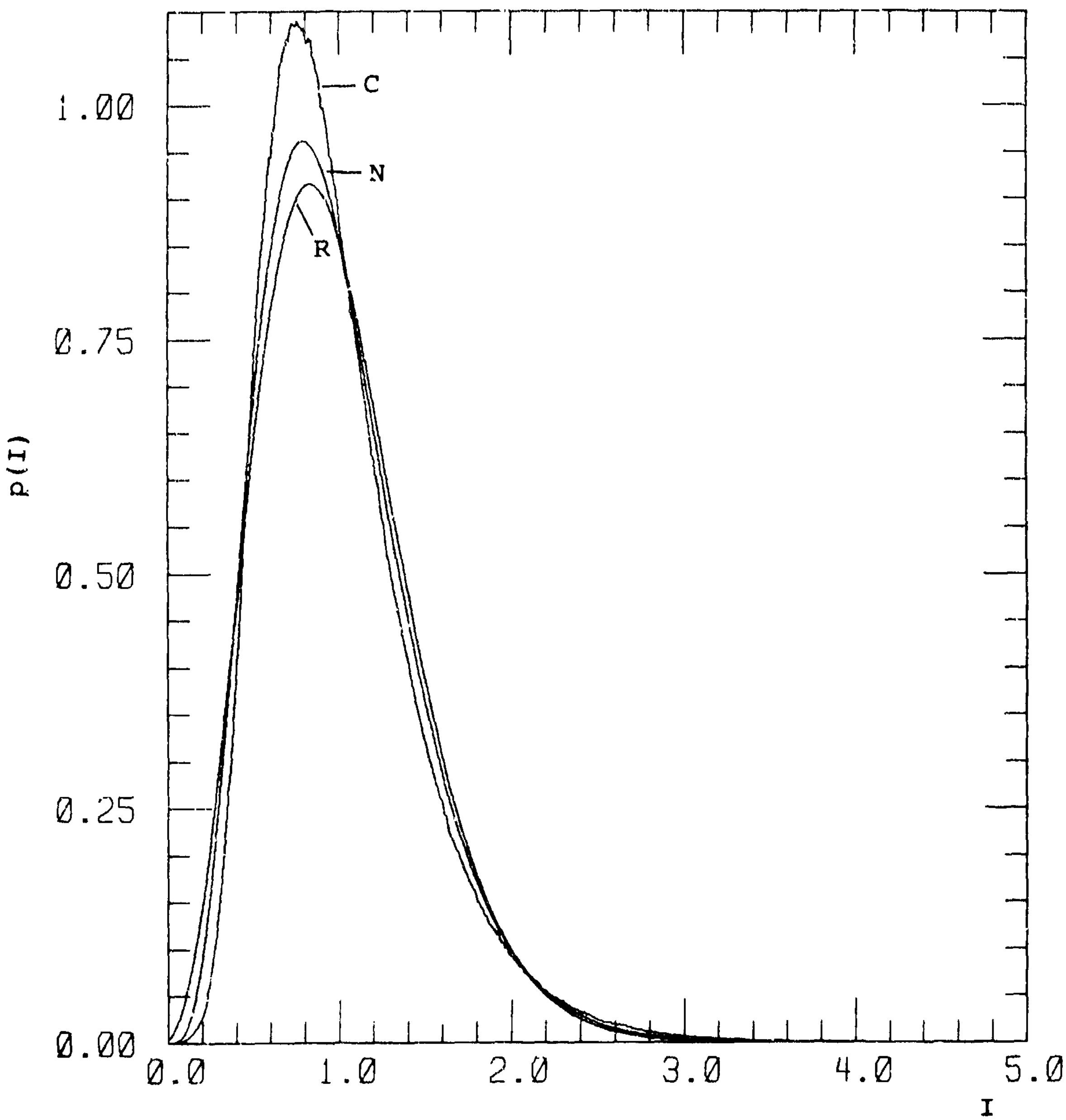

Figure G-27. Probability Distribution for $\alpha = 3$, $\chi^2 = 0.05$, $S_4{}^2 = 0.208$.

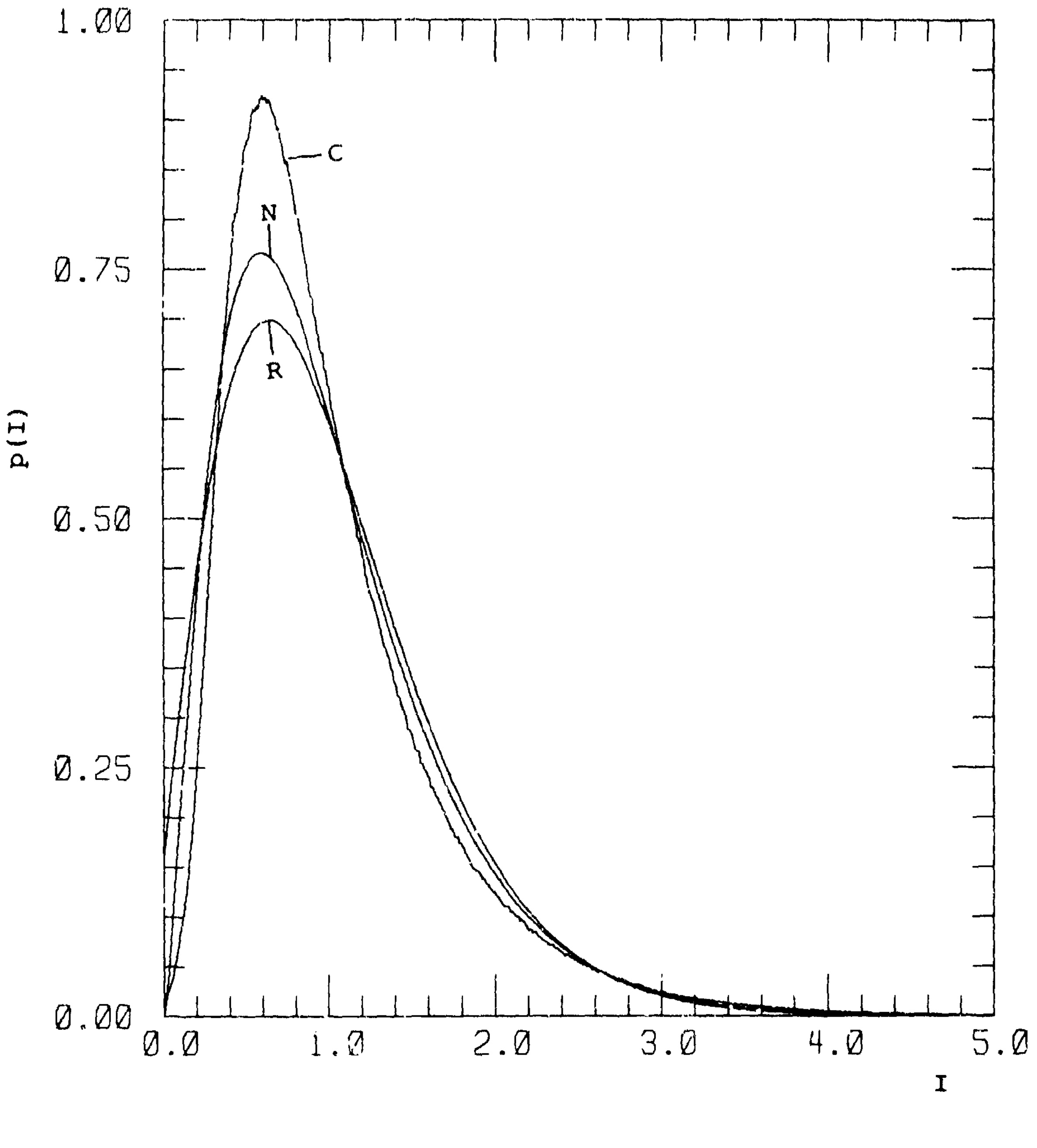

Figure G-28. Probability Distribution for
$\alpha = 3$, $\chi^2 = 0.1$, $S_4{}^2 = 0.409$.

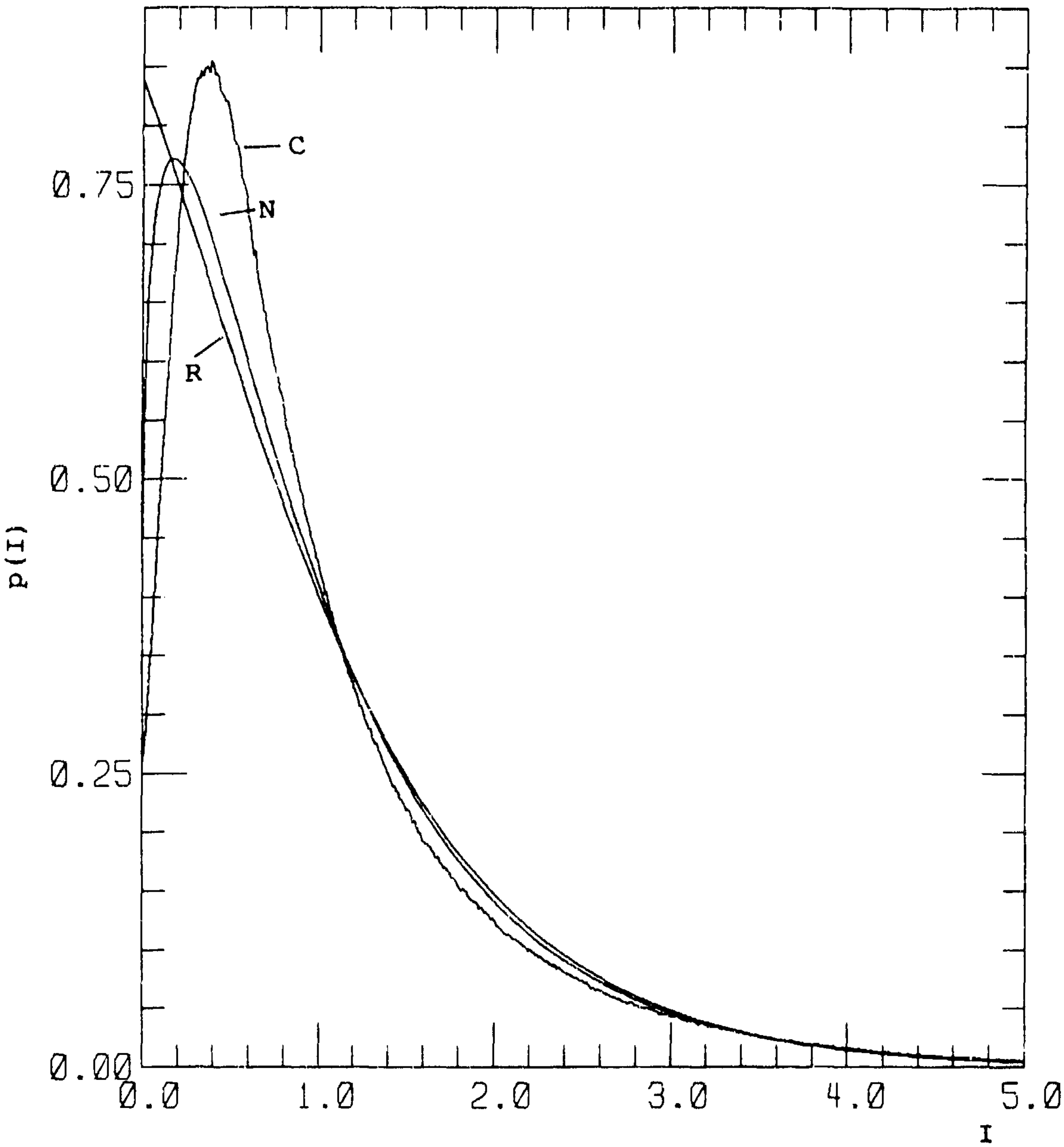

Figure G-29. Probability Distribution for $\alpha = 3$, $\chi^2 = 0.25$, $S_4^{\ 2} = 0.827$.

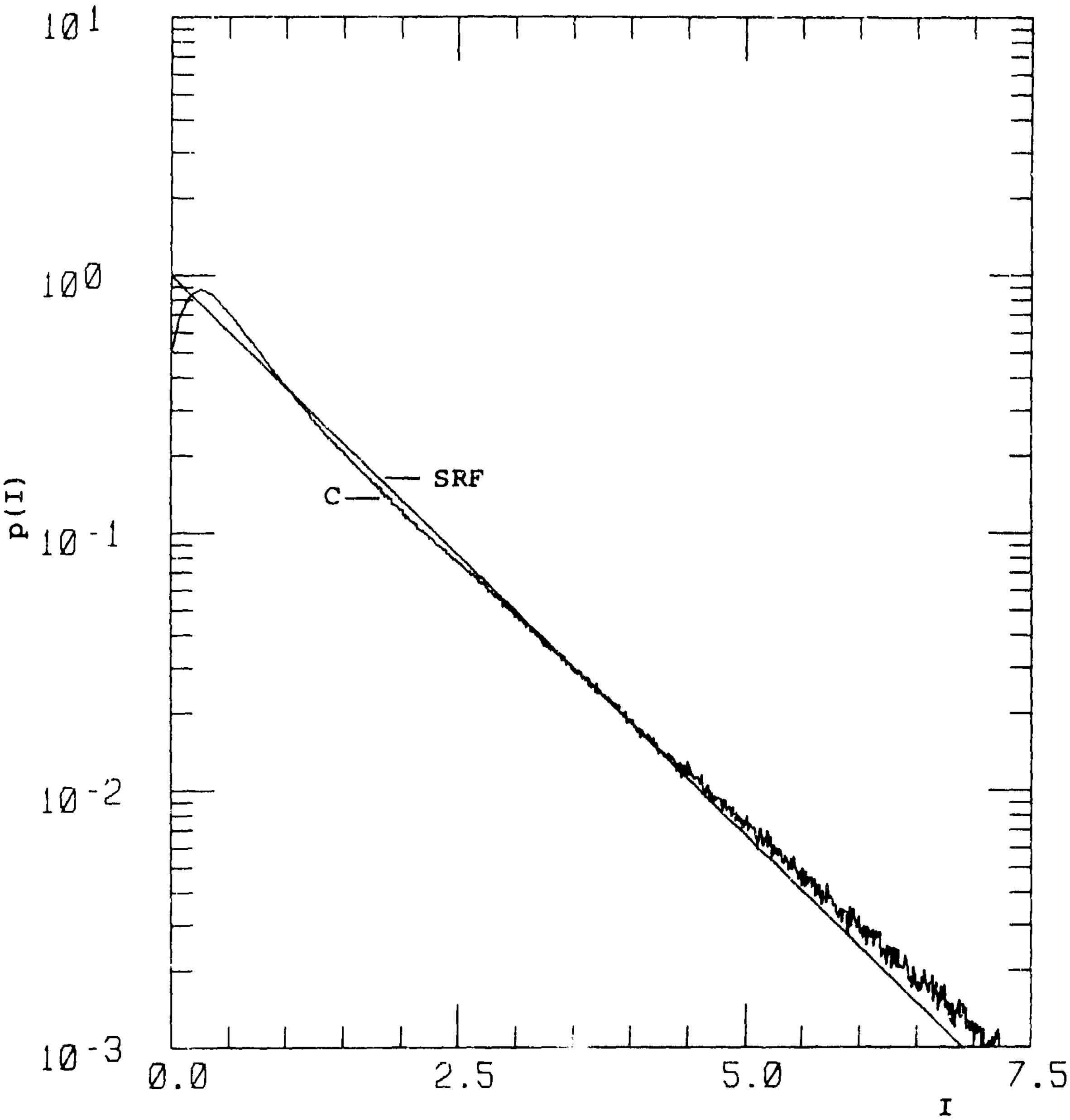

Figure G-30. Probability Distribution for $\alpha = 3$, $\chi^2 = 0.4$, $S_4^{\;2} = 1.02$.

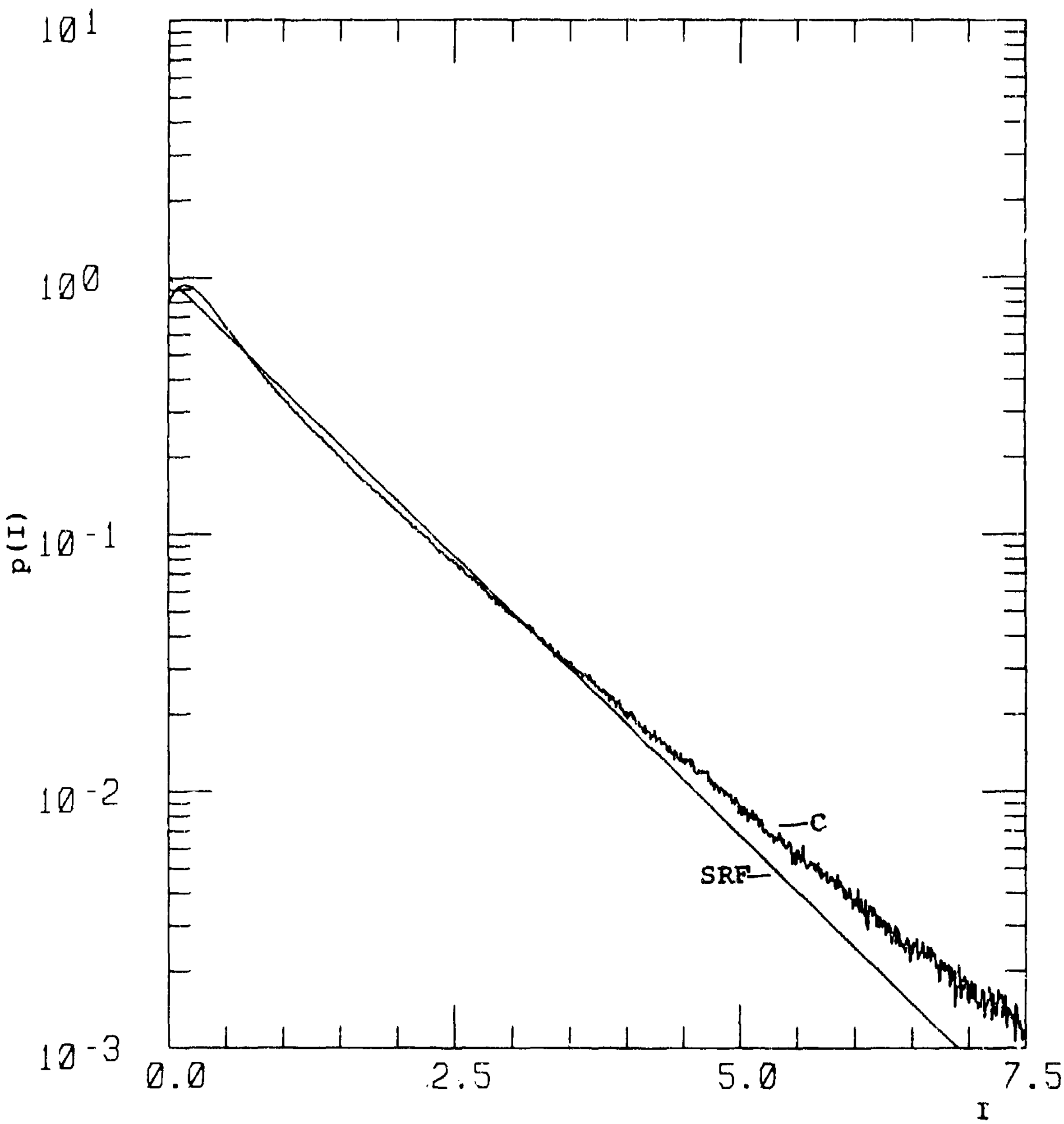

Figure G-31. Probability Distribution for $\alpha = 3$, $\chi^2 = 0.7$, $S_4^{\ 2} = 1.17$.

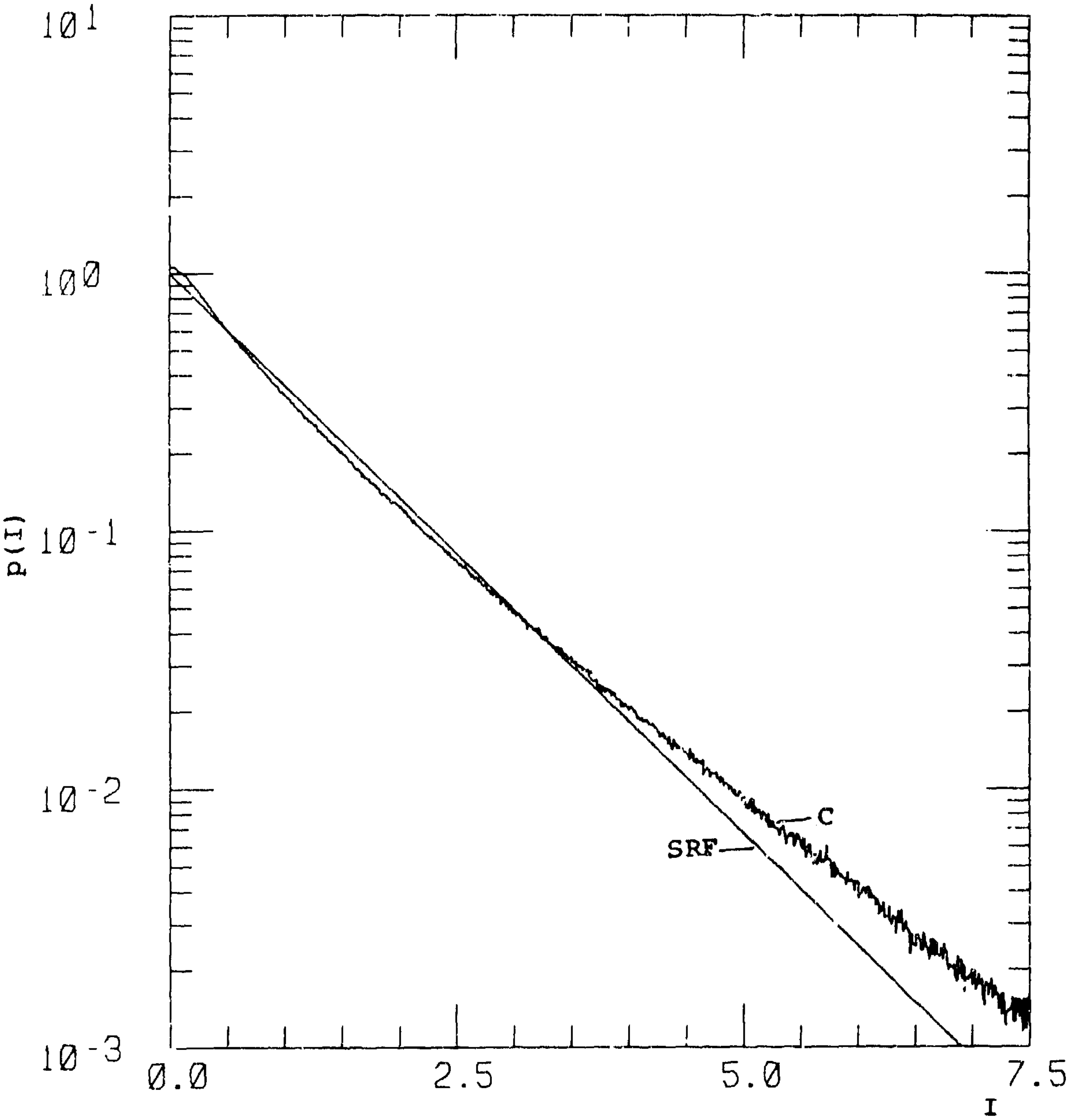

Figure G-32. Probability Distribution for $\alpha = 3$, $\chi^2 = 1.5$, $S_4^{\ 2} = 1.23$.

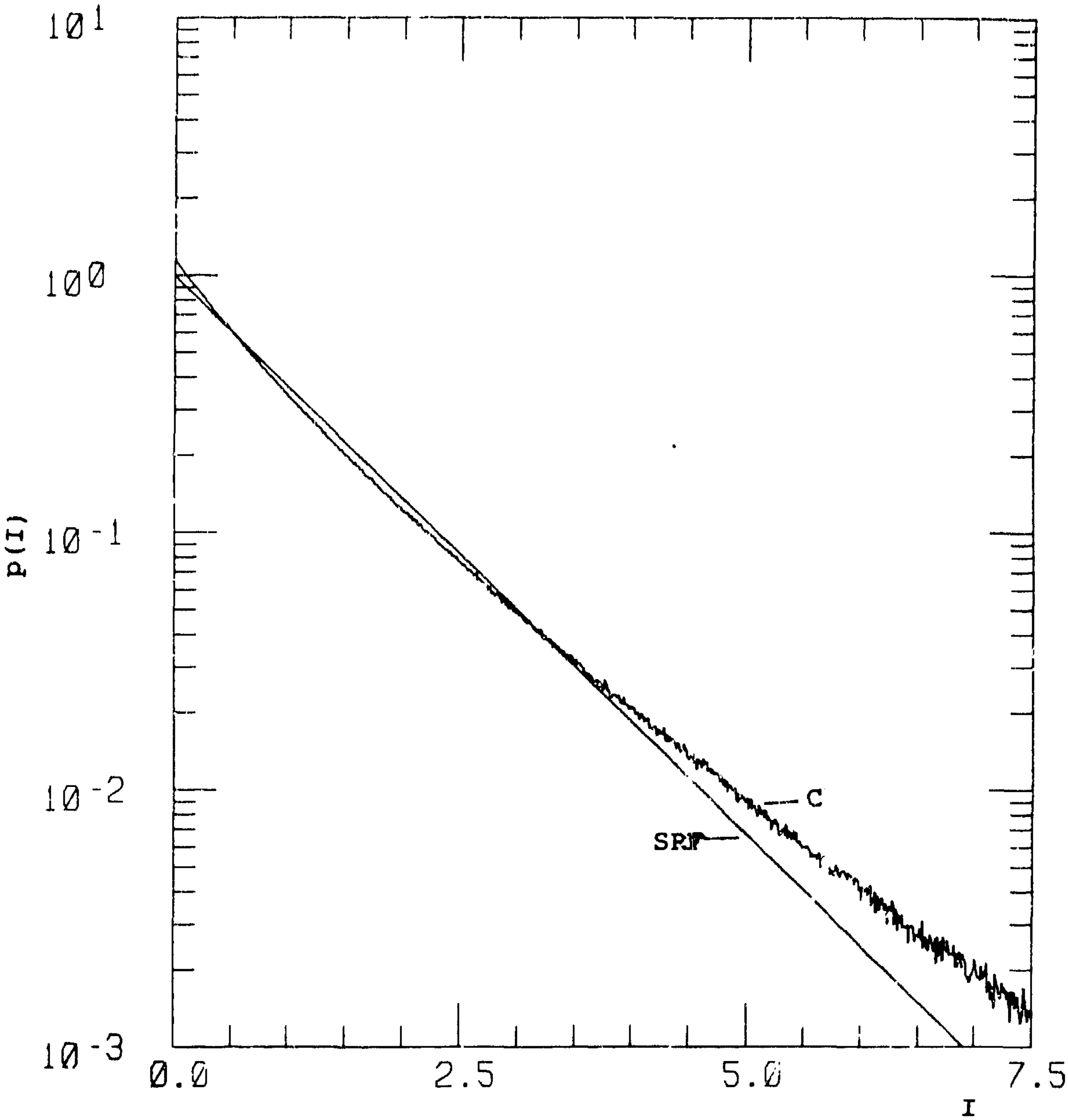

Figure C-33. Probability Distribution for $\alpha = 3$, $\chi^2 = 3.0$, $S_4{}^2 = 1.23$.

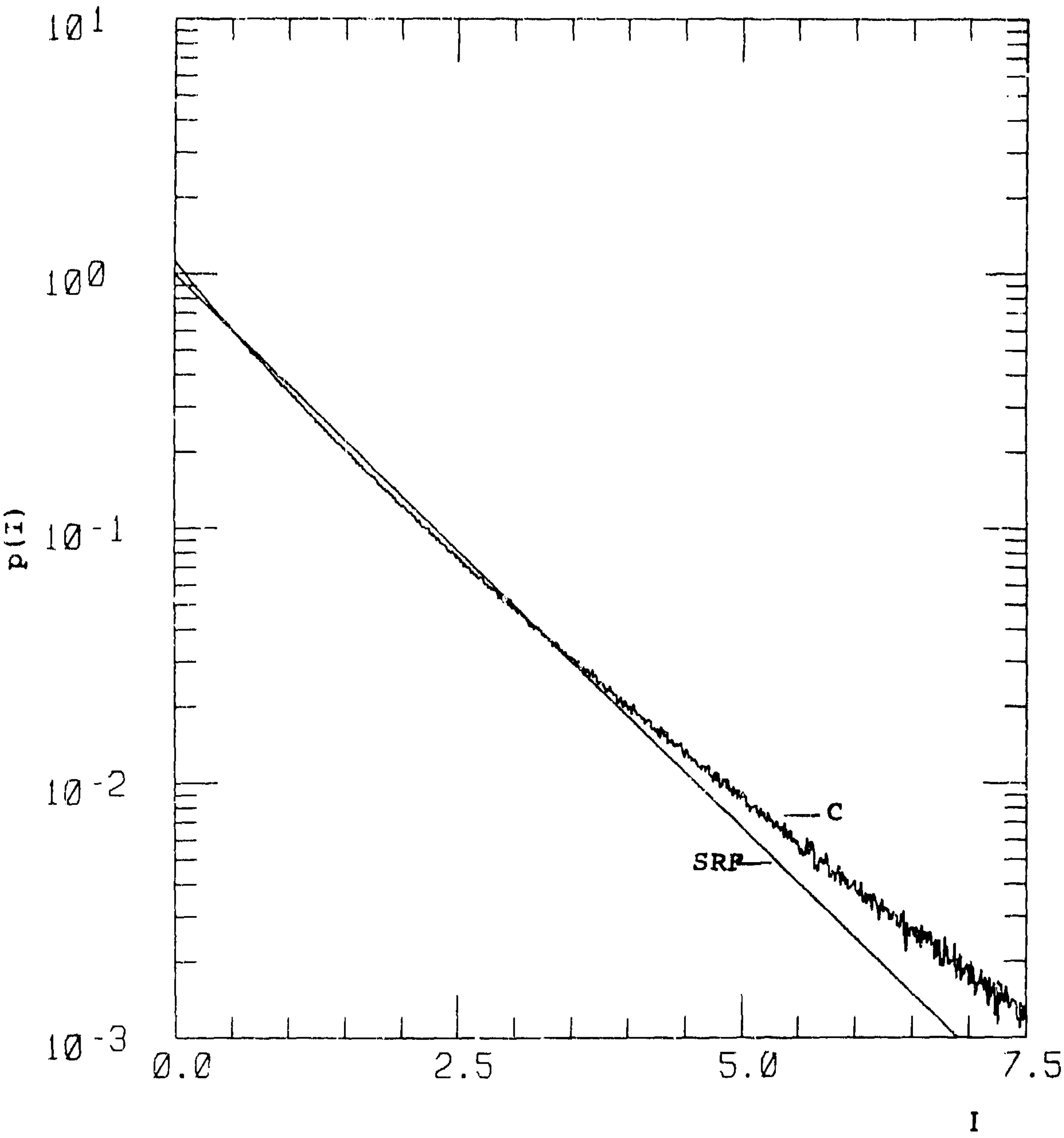

Figure G-34. Probability Distribution for $\alpha = 3$, $\chi^2 = 7.0$, $S_4^{\ 2} = 1.20$.

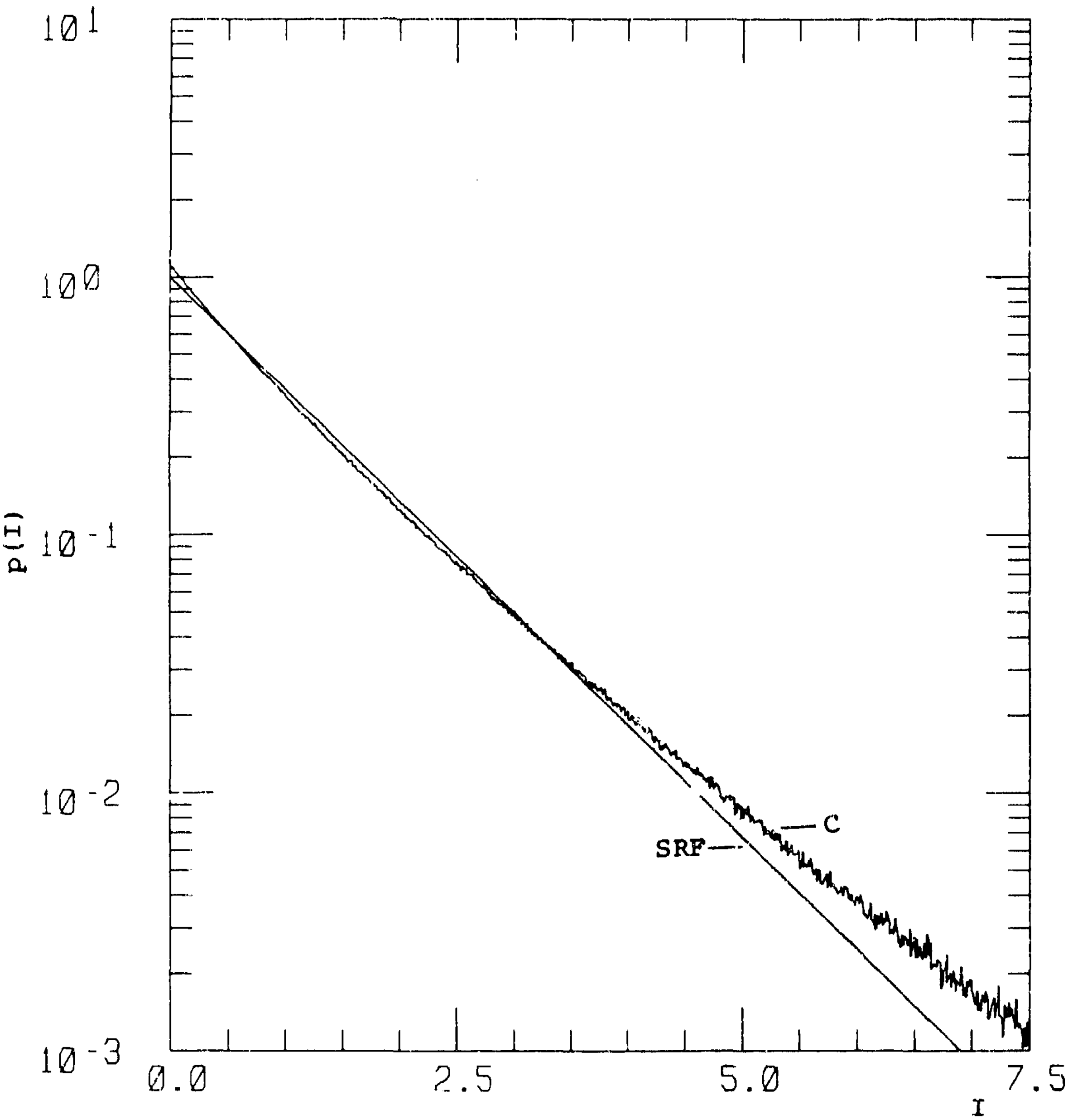

Figure G-35. Probability Distribution for $\alpha = 3$, $\chi^2 = 10.0$, $S_4{}^2 = 1.18$.

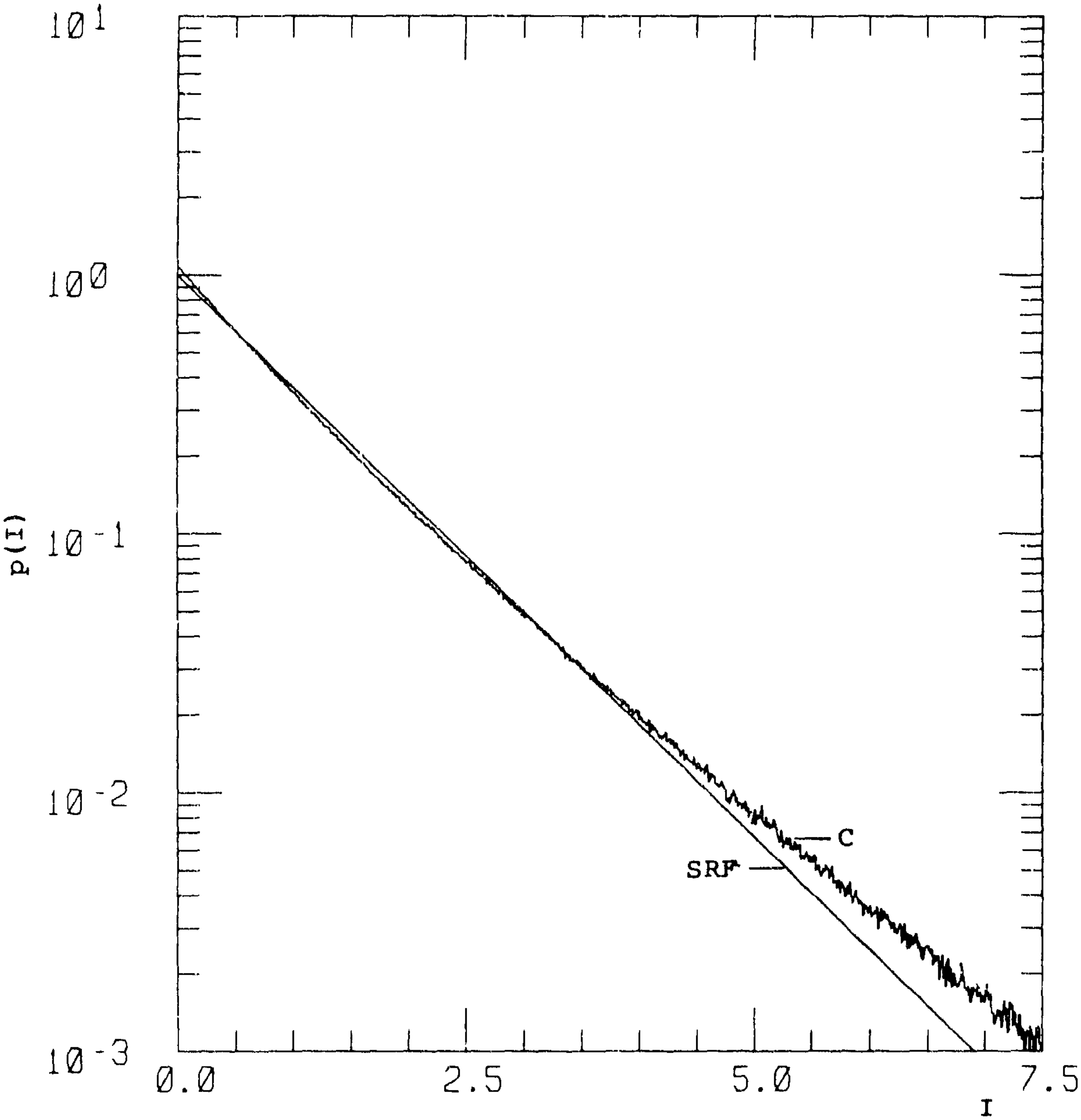

Figure G-36. Probability Distribution for $\alpha = 3$, $\chi^2 = 20.0$, $S_4^{\,2} = 1.14$.

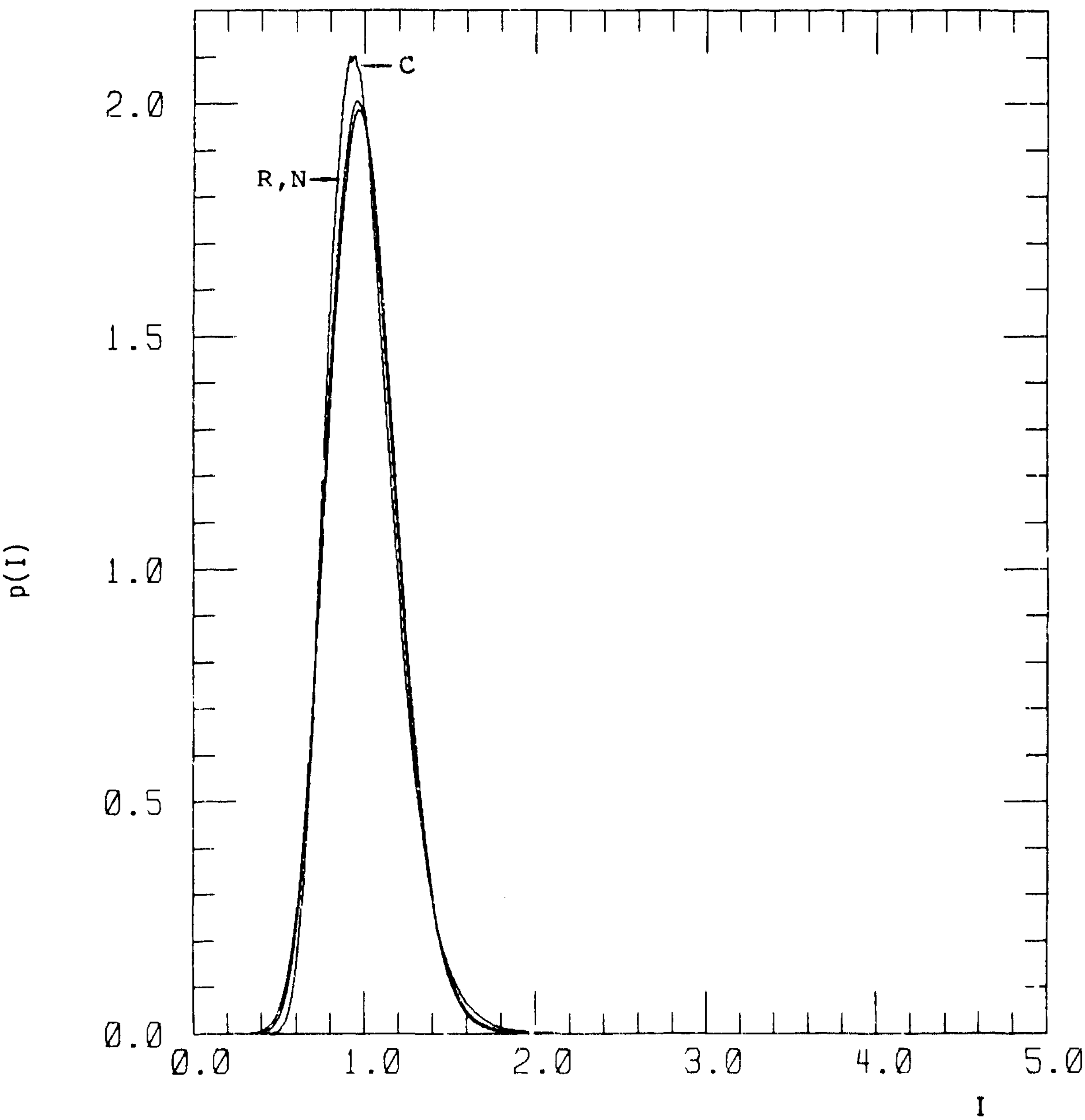

Figure G-37. Probability Distribution for $\alpha = 4$, $\chi^2 = 0.01$, $S_4{}^2 = 0.041$.

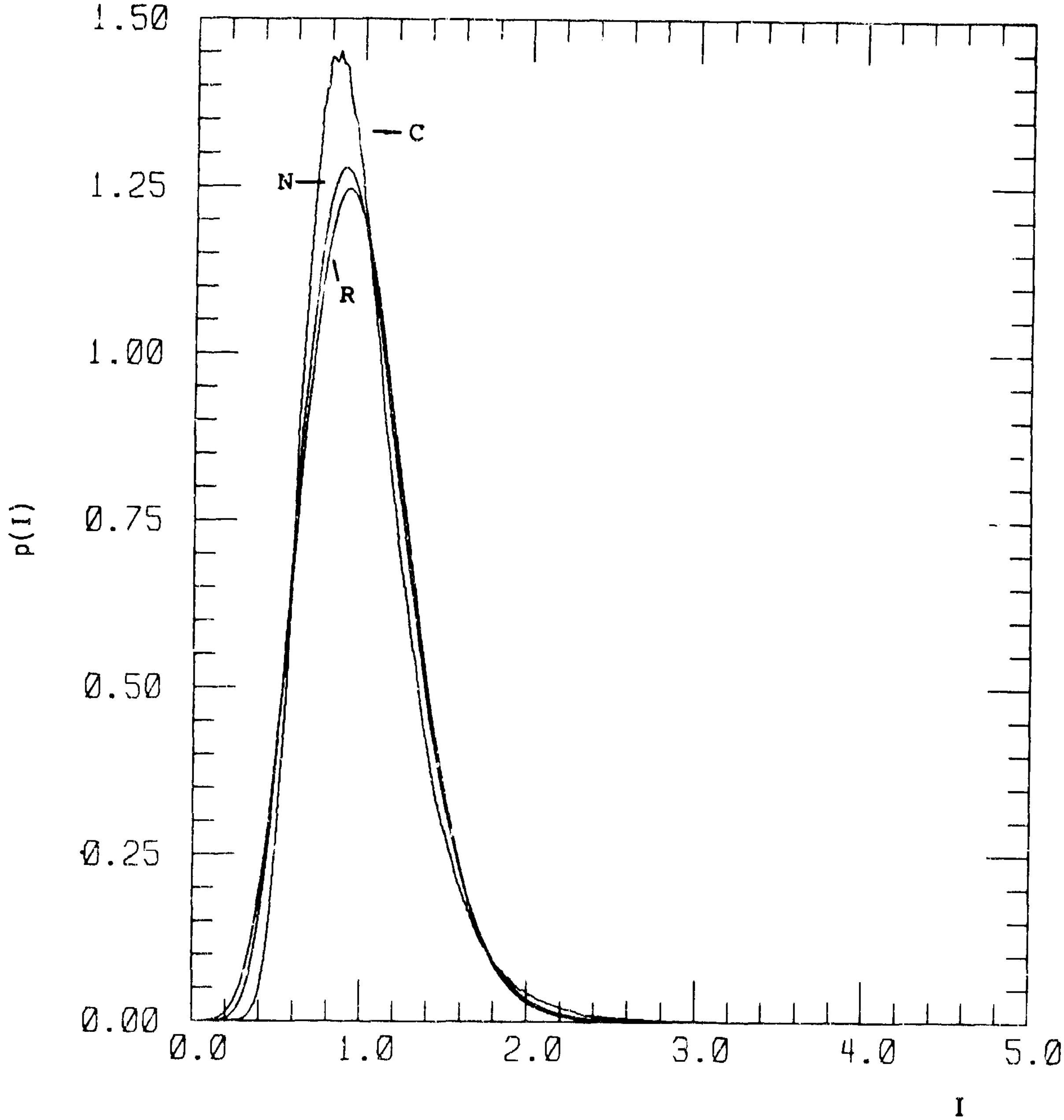

Figure G-38. Probability Distribution for $\alpha = 4$, $\chi^2 = 0.025$, $S_4{}^2 = 0.107$.

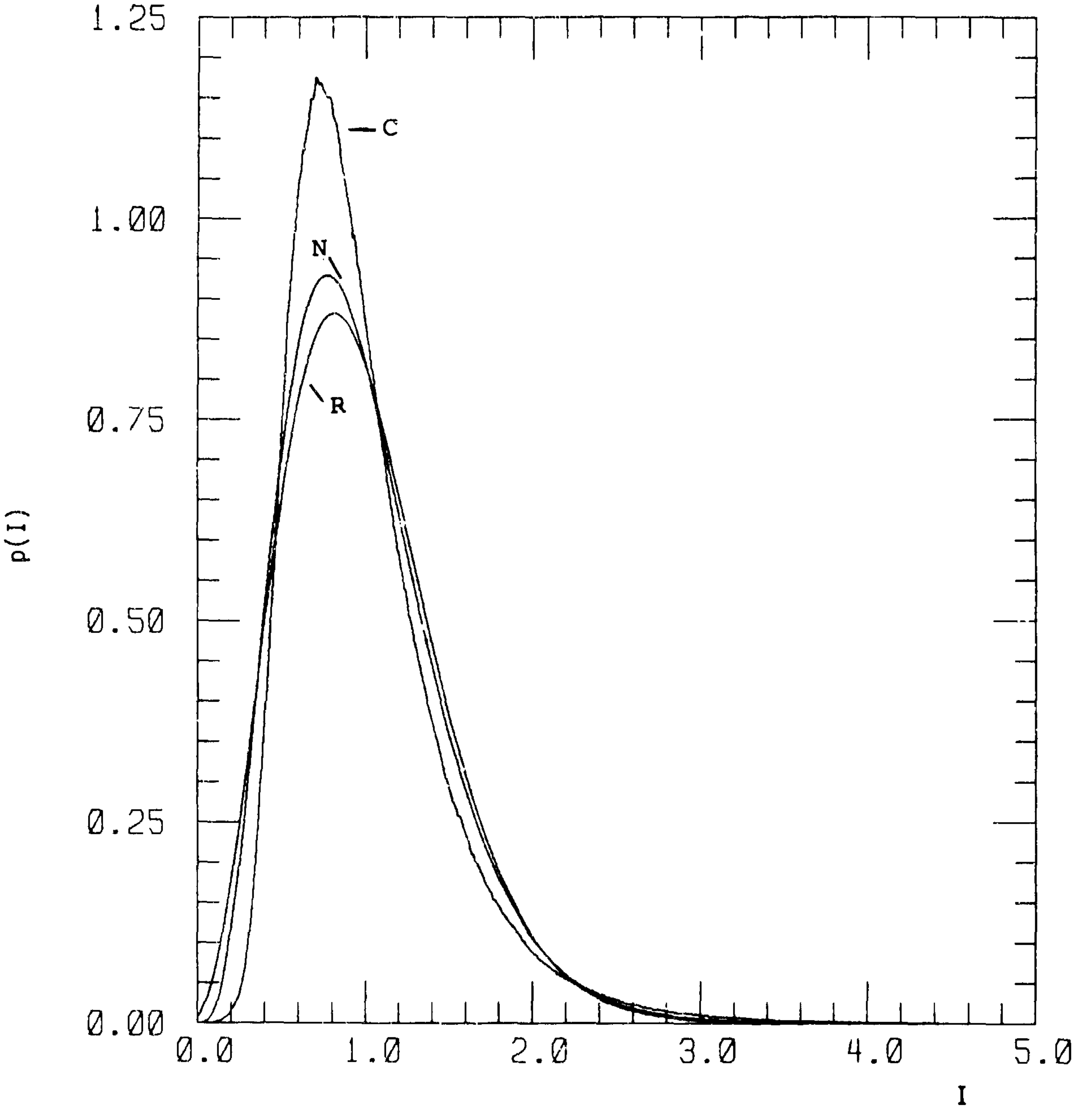

Figure G-39. Probability Distribution for $\alpha = 4$, $\chi^2 = 0.05$, $S_I^2 = 0.227$.

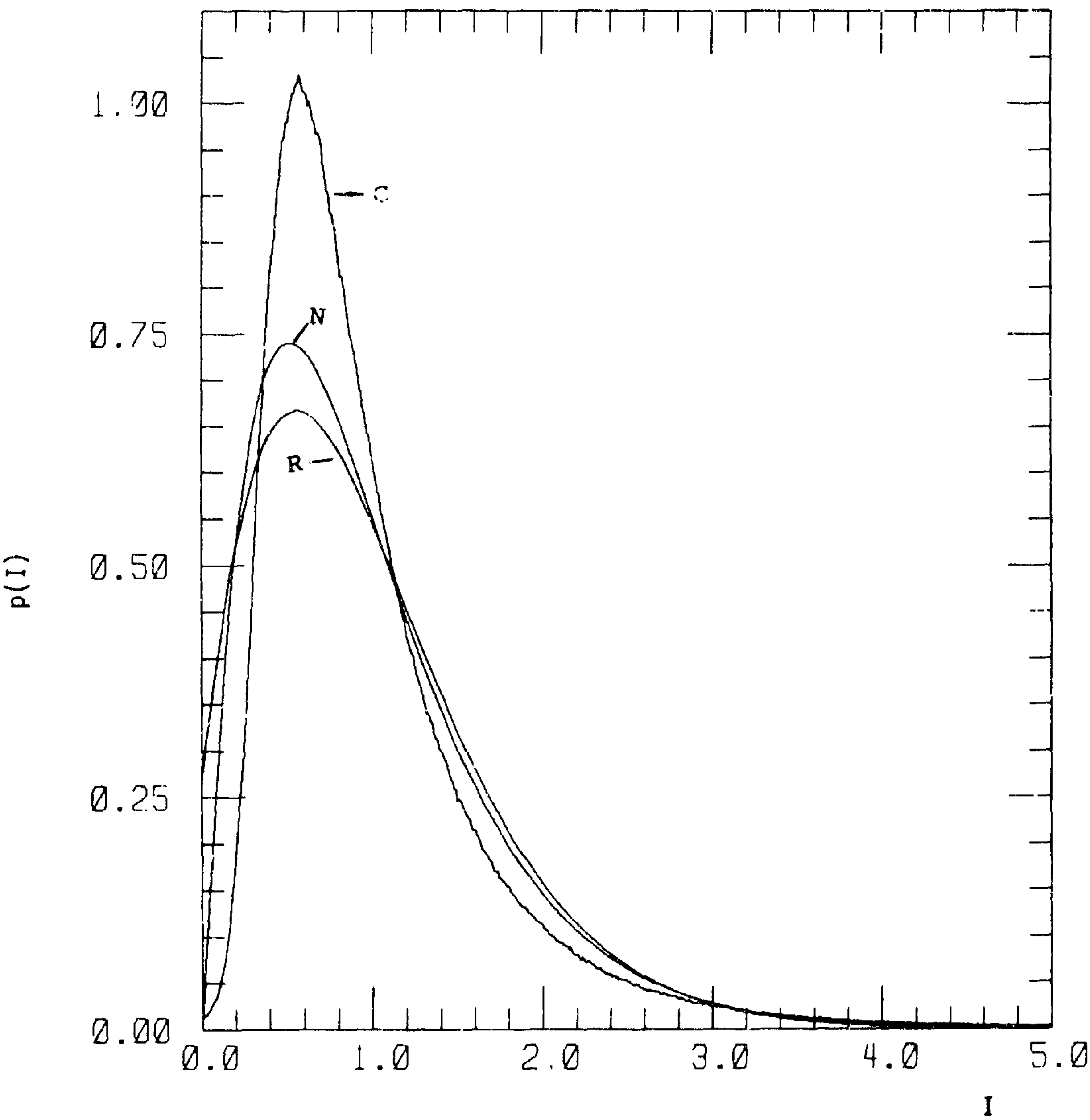

Figure G-40. Probability Distribution for $\alpha = 4$, $\chi^2 = 0.1$, $S_4^{\ 2} = 0.479$.

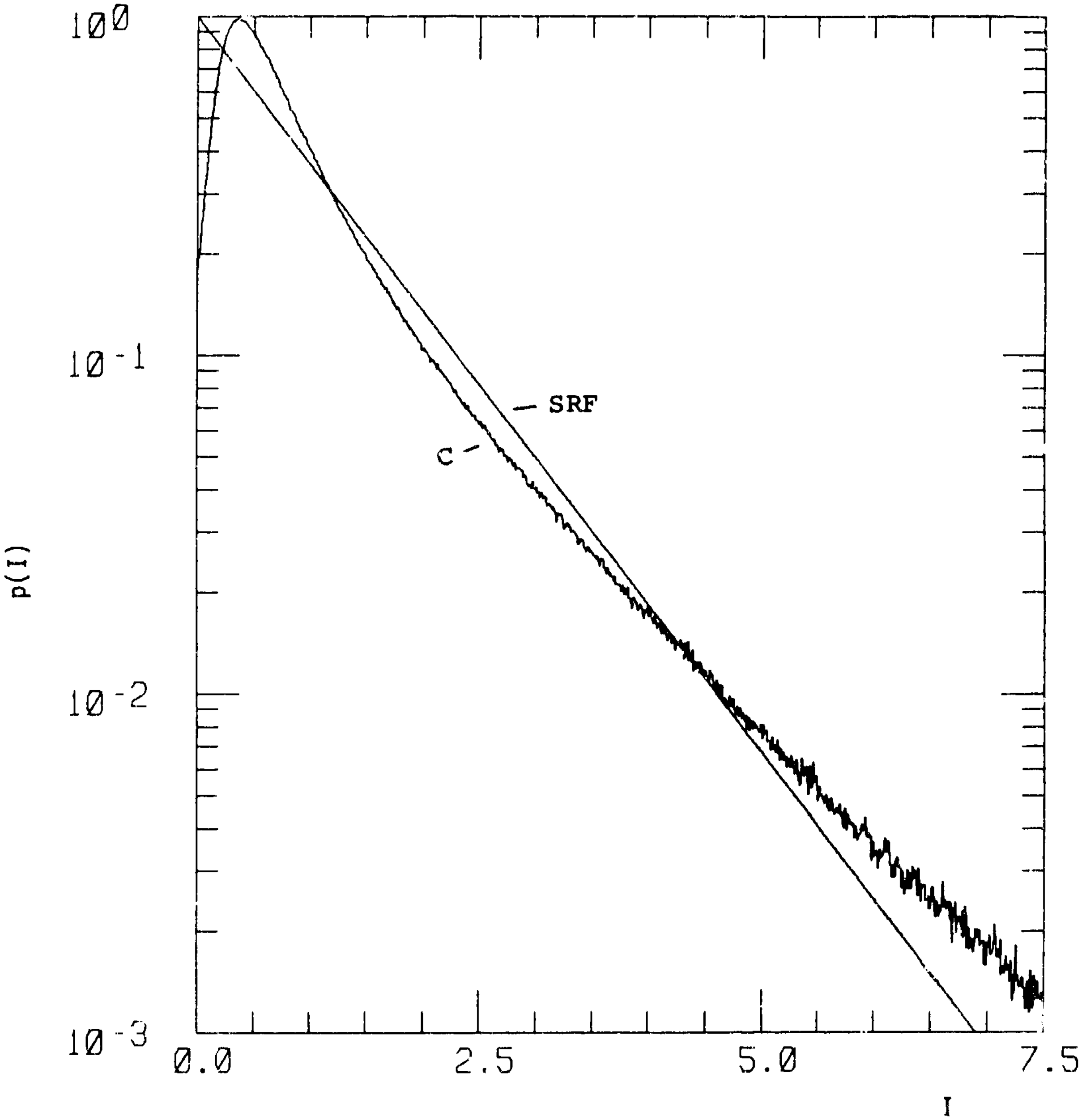

Figure G-41. Probability Distribution for
$\alpha = 4,\ \chi^2 = 0.25,\ S_4^{\ 2} = 1.02.$

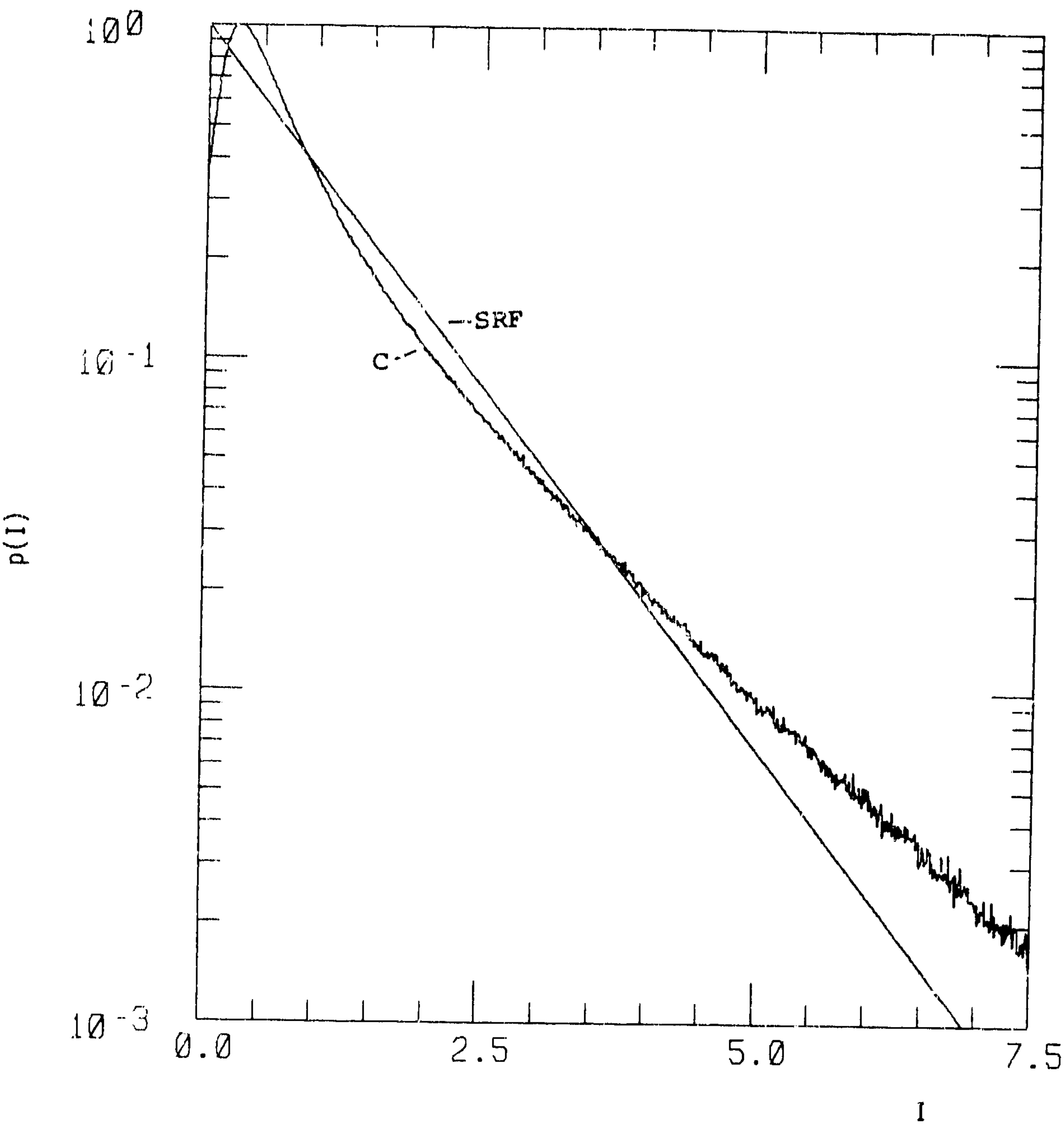

Figure G-42. Probability Distribution for $\alpha = 4$, $\gamma^2 = 0.4$, $S_4{}^2 = 1.25$.

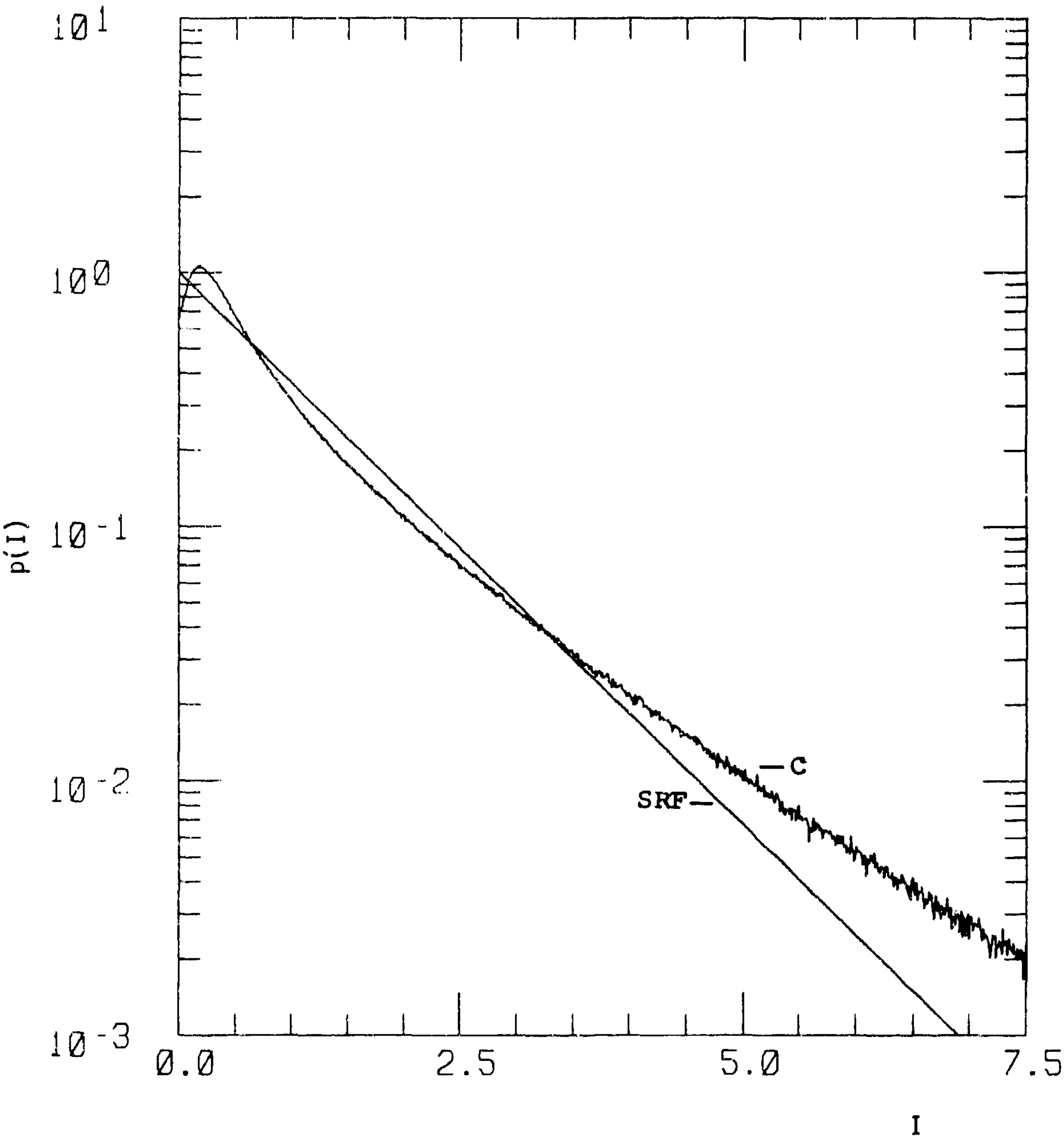

Figure G-43. Probability Distribution for $\alpha = 4$, $\chi^2 = 0.7$, $S_4^2 = 1.41$.

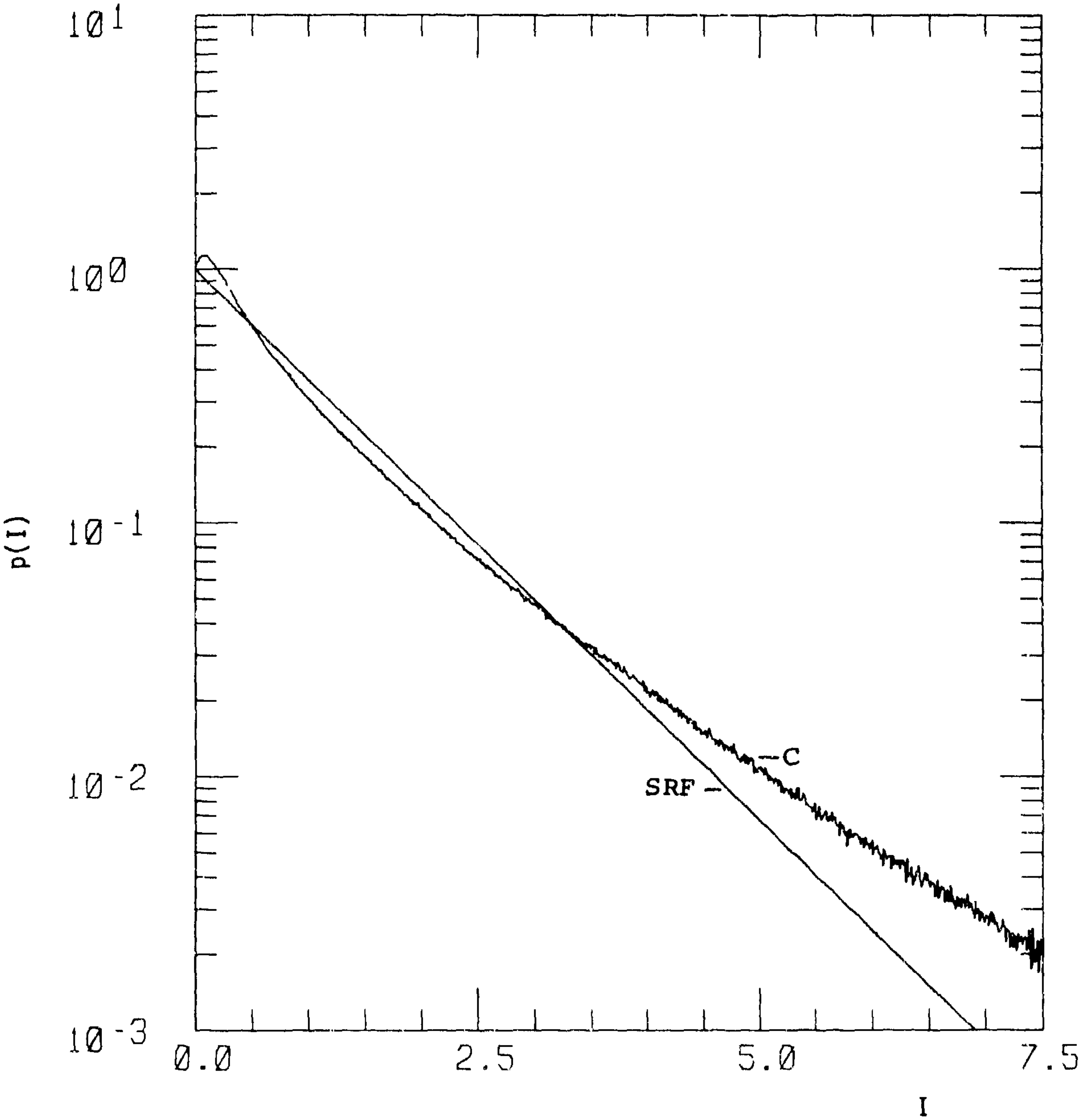

Figure G-44. Probability Distribution for $\alpha = 4$, $\chi^2 = 1.5$, $S_4^{\,2} = 1.45$.

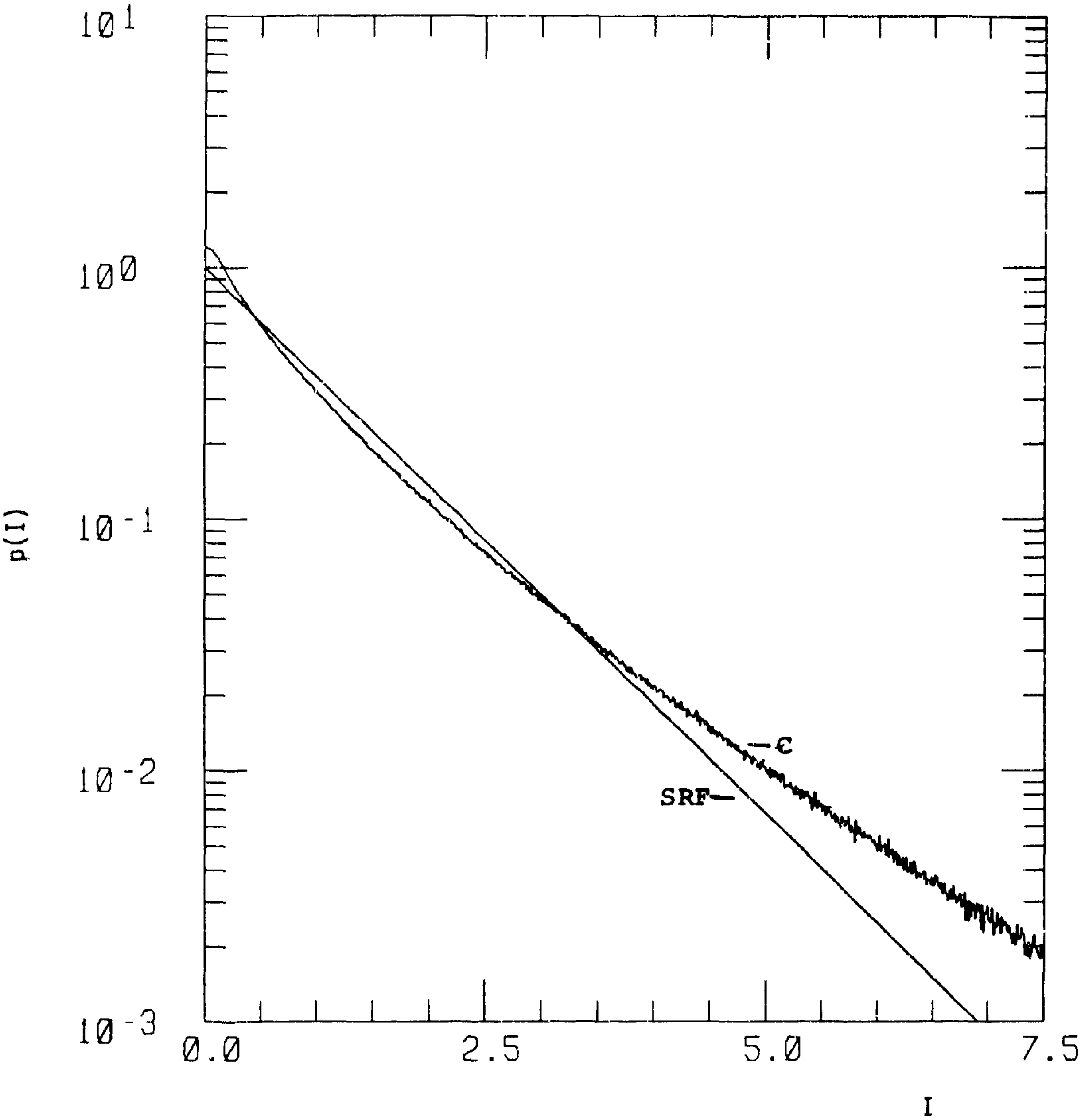

Figure G-45. Probability Distribution for $\alpha = 4$, $\chi^2 = 3.0$, $S_4{}^2 = 1.41$.

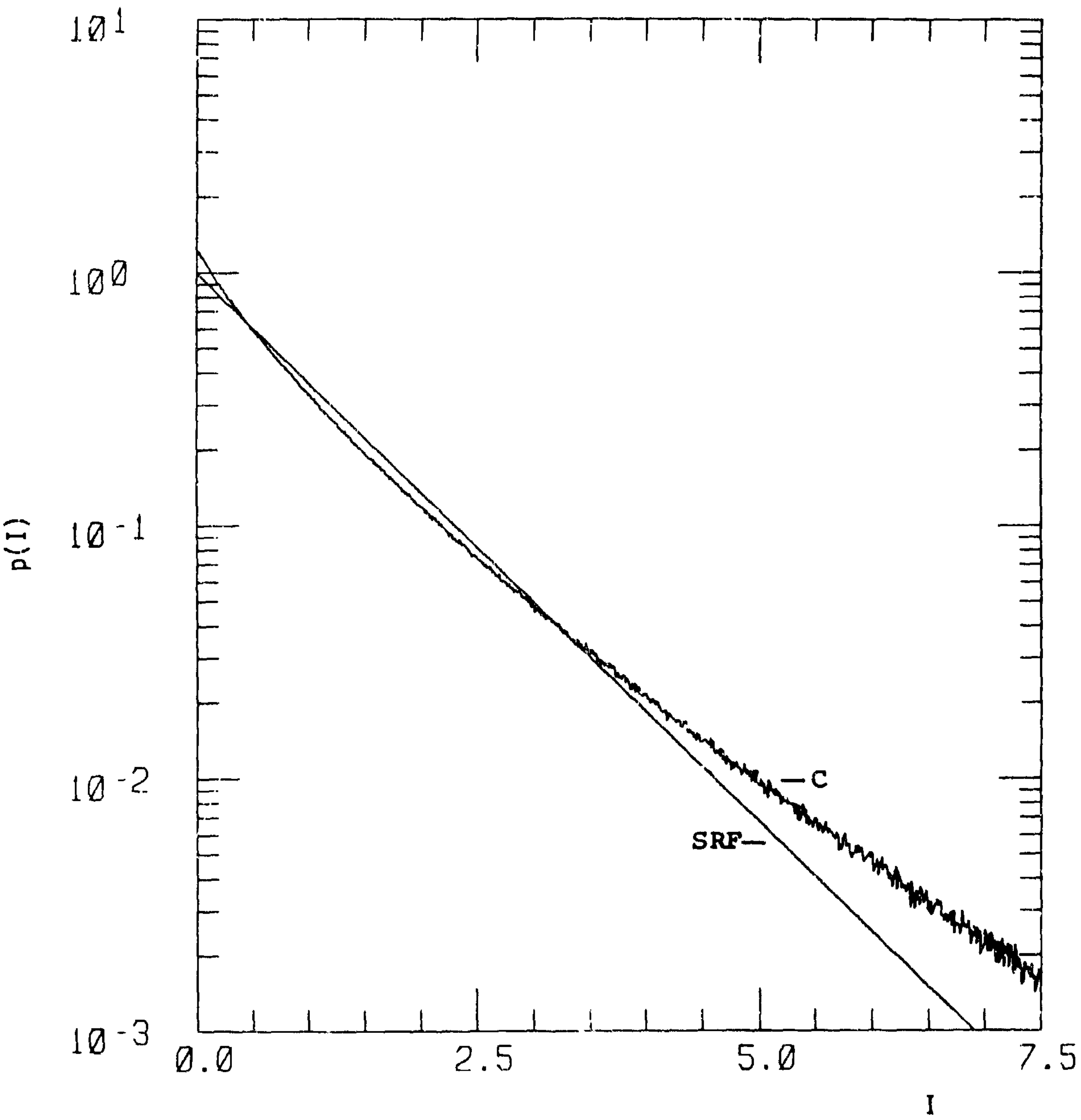

Figure G-46. Probability Distribution for $\alpha = 4$, $\chi^2 = 7.0$, $S_4^2 = 1.32$.

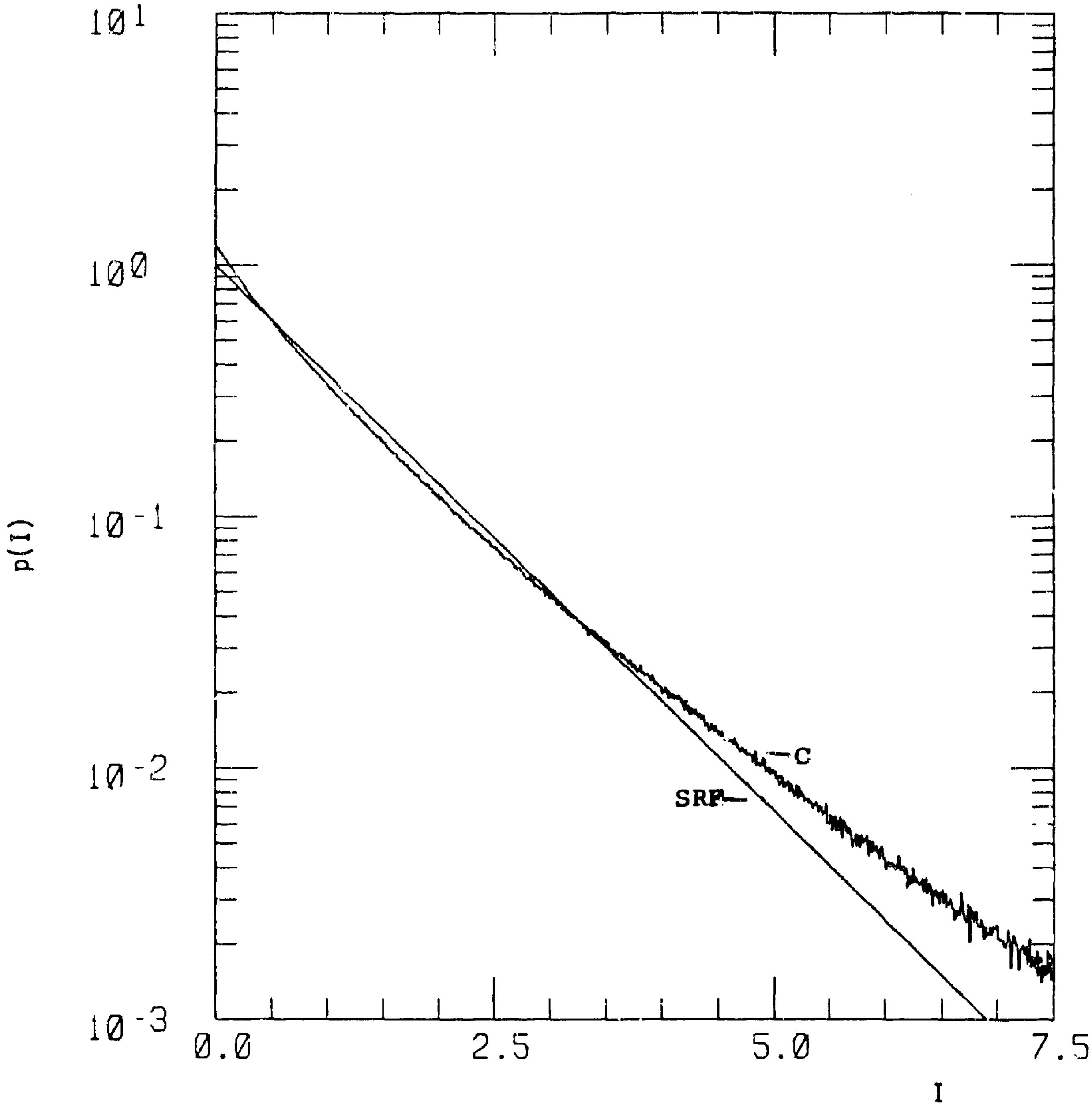

Figure G-47. Probability Distribution for $\alpha = 4$, $\chi^2 = 10.0$, $S_4{}^2 = 1.28$.

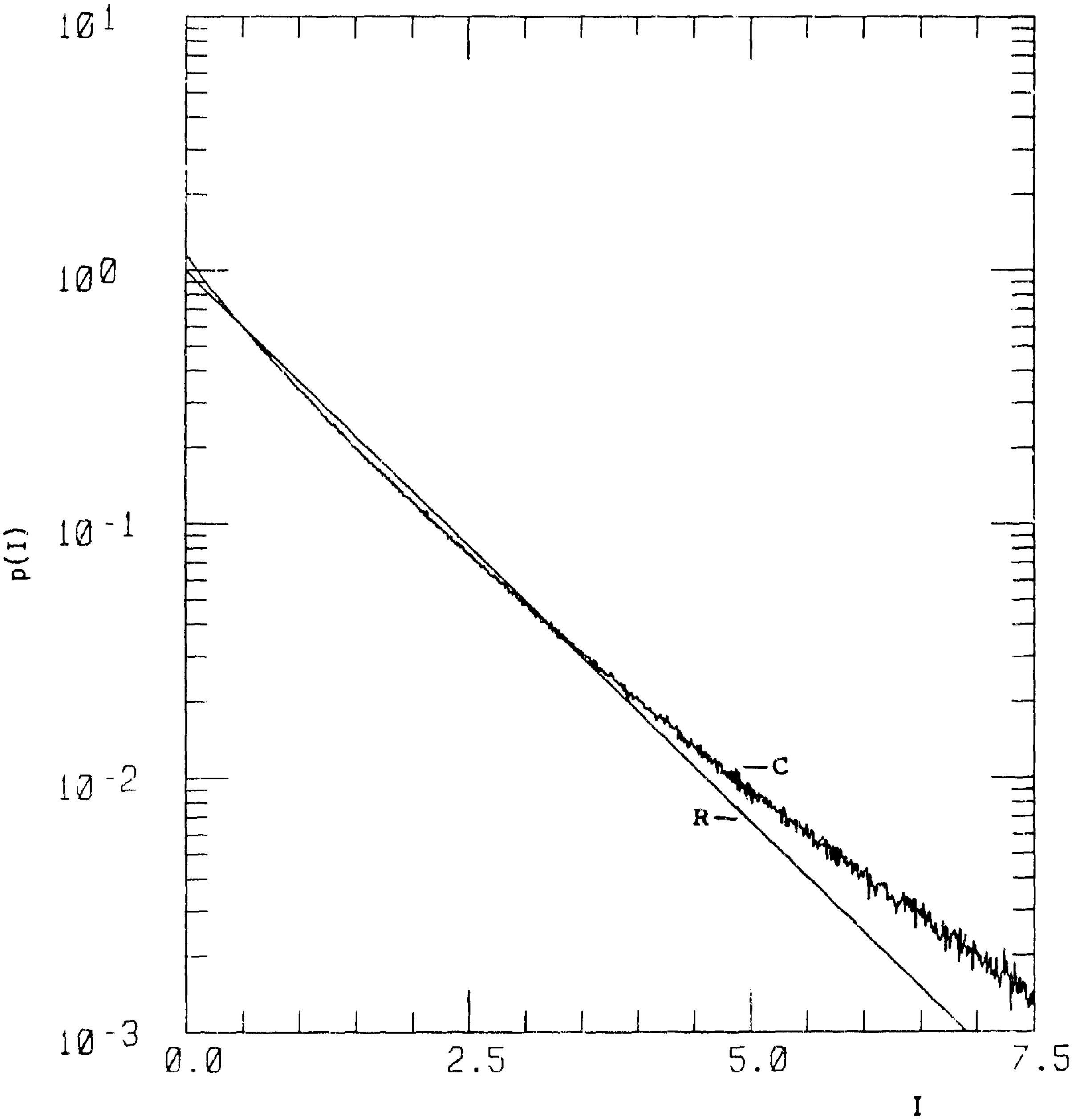

Figure G-48. Probability Distribution for $\alpha = 4$, $\chi^2 = 20.0$, $S_4^2 = 1.23$.

APPENDIX H

PROBABILITY DISTRIBUTIONS FOR SMALL INTENSITY FOR TWO POWER LAW PSD

This Appendix contains all the calculated small intensity behavior for two power law PSD. These distributions are compared to Nakagami-m (labeled as N) and Rice (labeled as R).

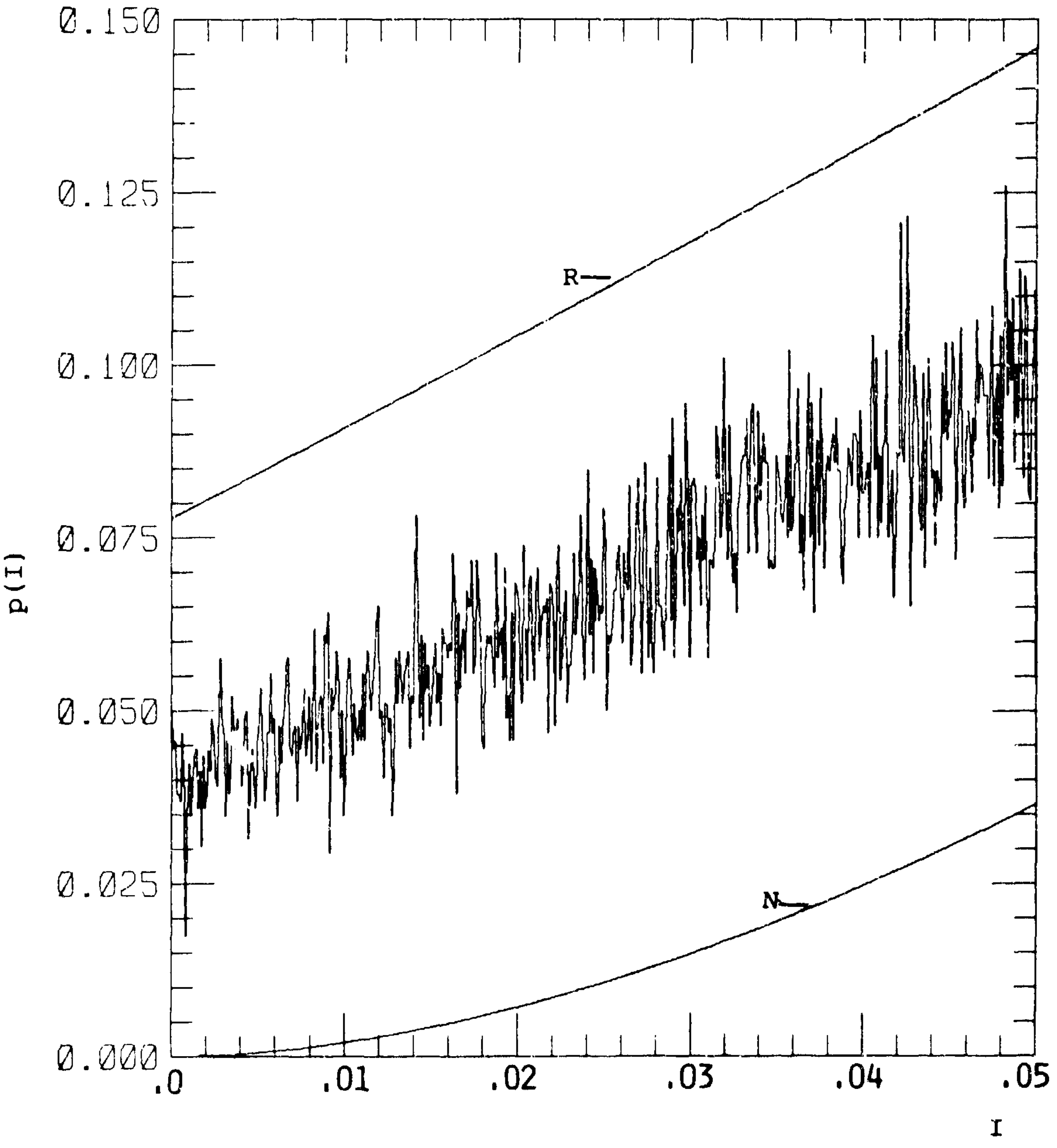

Figure H-1. Probability Distribution for Small I for $\alpha = 1$, $\chi^2 = 0.1$, $S_4^{\,2} = 0.347$.

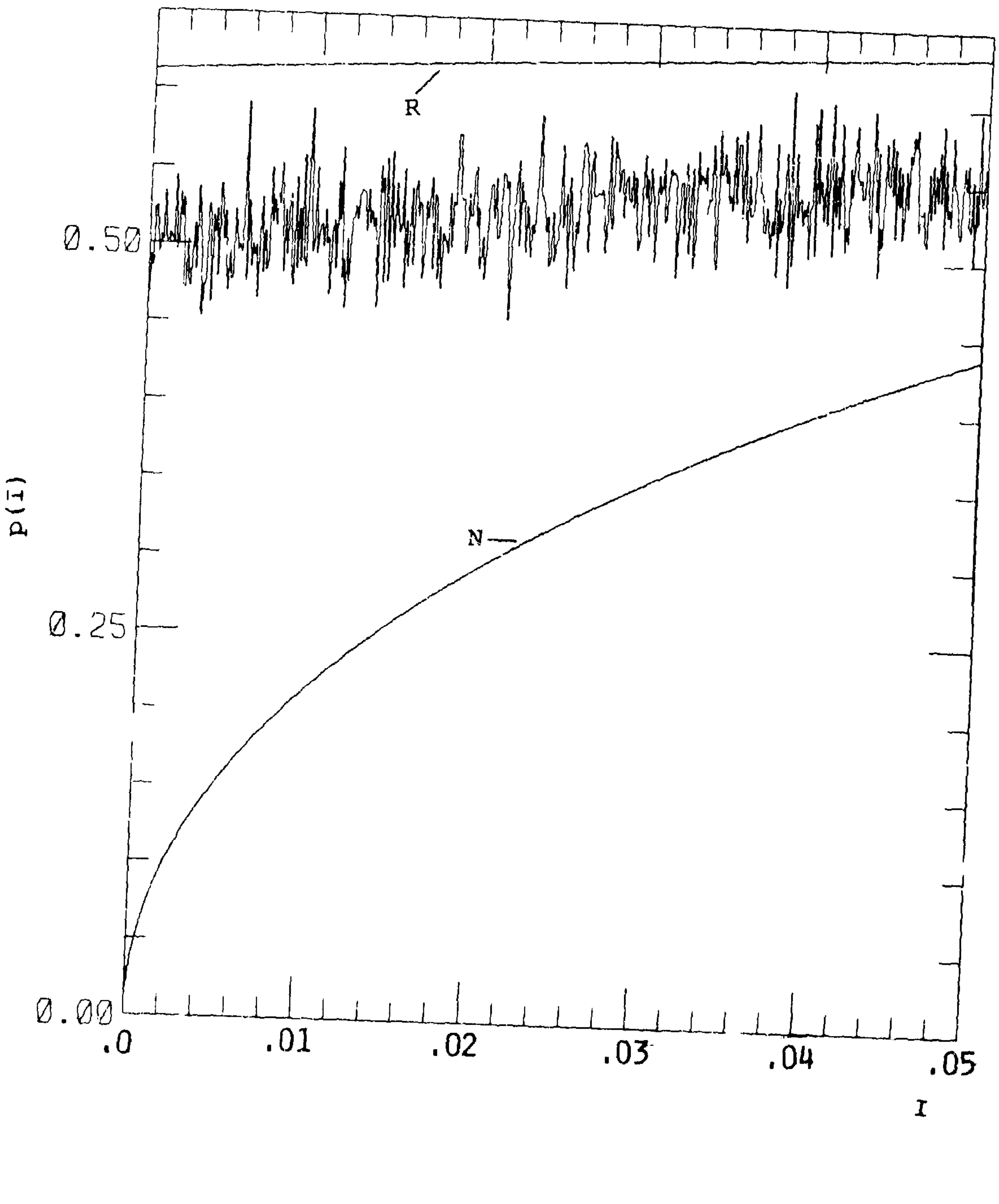

Figure H-2. Probability Distribution for Small I for $\alpha = 1$, $\chi^2 = 0.25$, $S_4^2 = 0.672$.

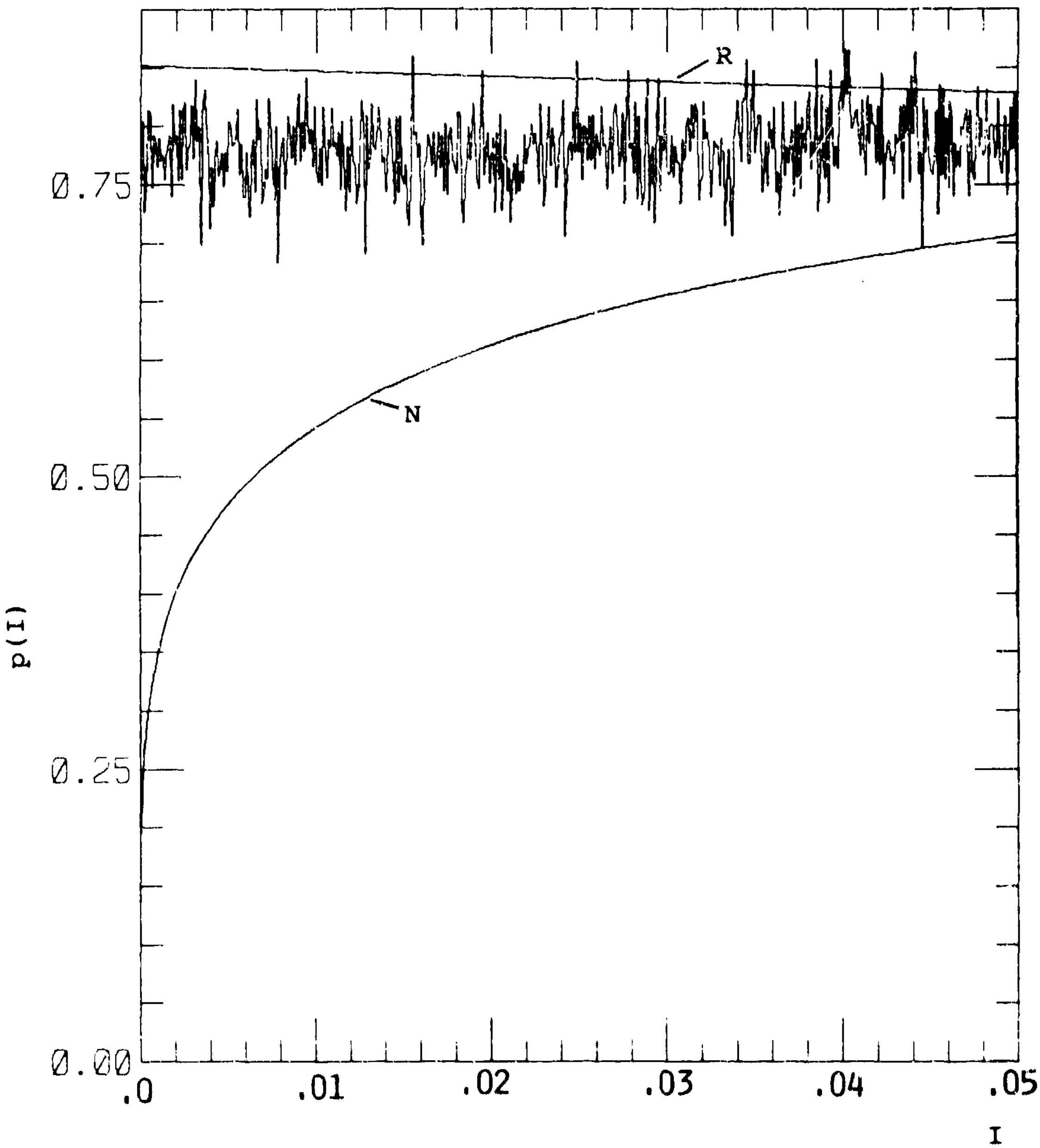

Figure H-3. Probability Distribution for Small I for $\alpha = 1$, $\chi^2 = 0.4$, $S_4^2 = 0.837$.

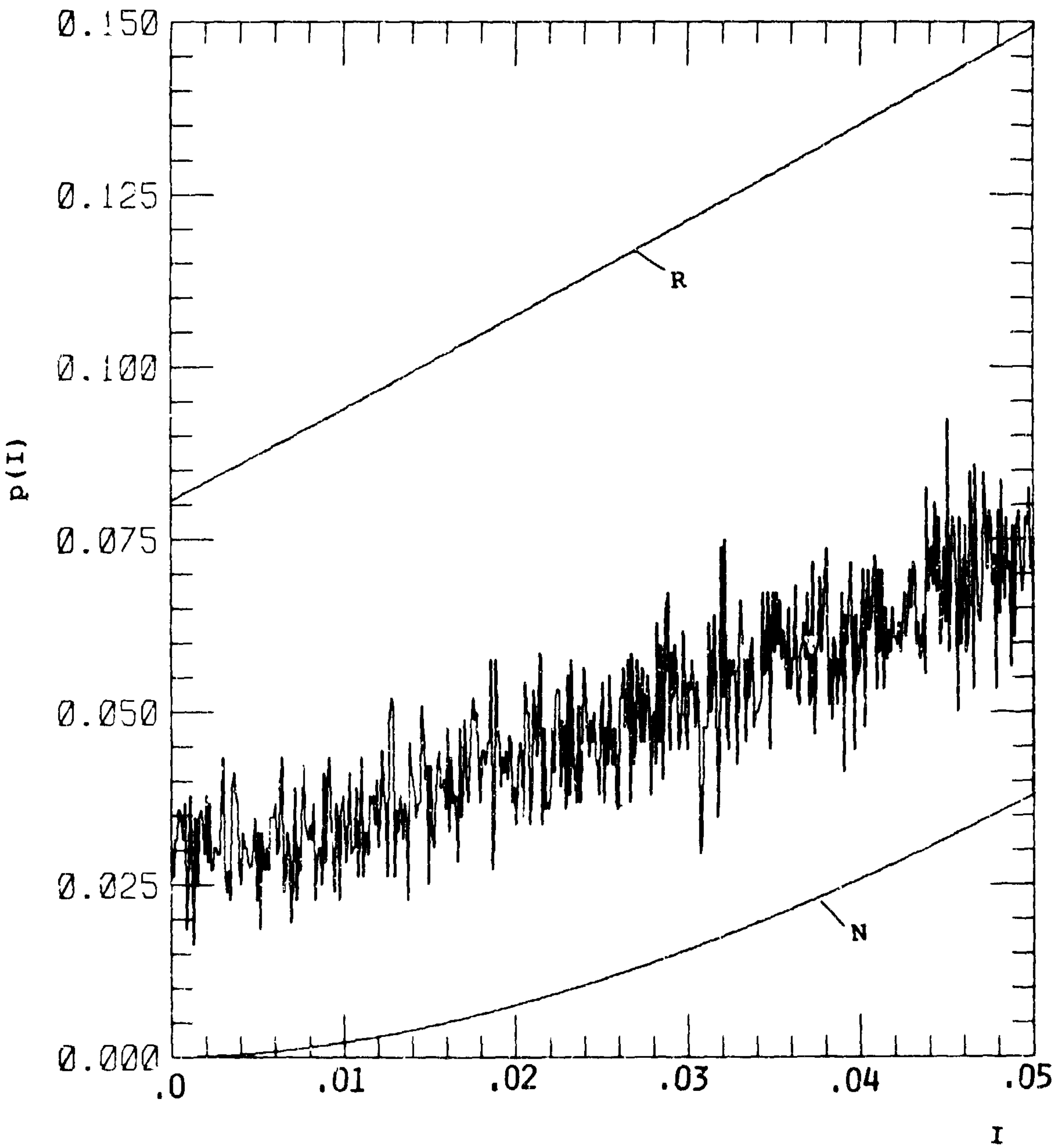

Figure H-4. Probability Distribution for Small I for $\alpha = 2$, $\chi^2 = 0.1$, $S_4{}^2 = 0.350$.

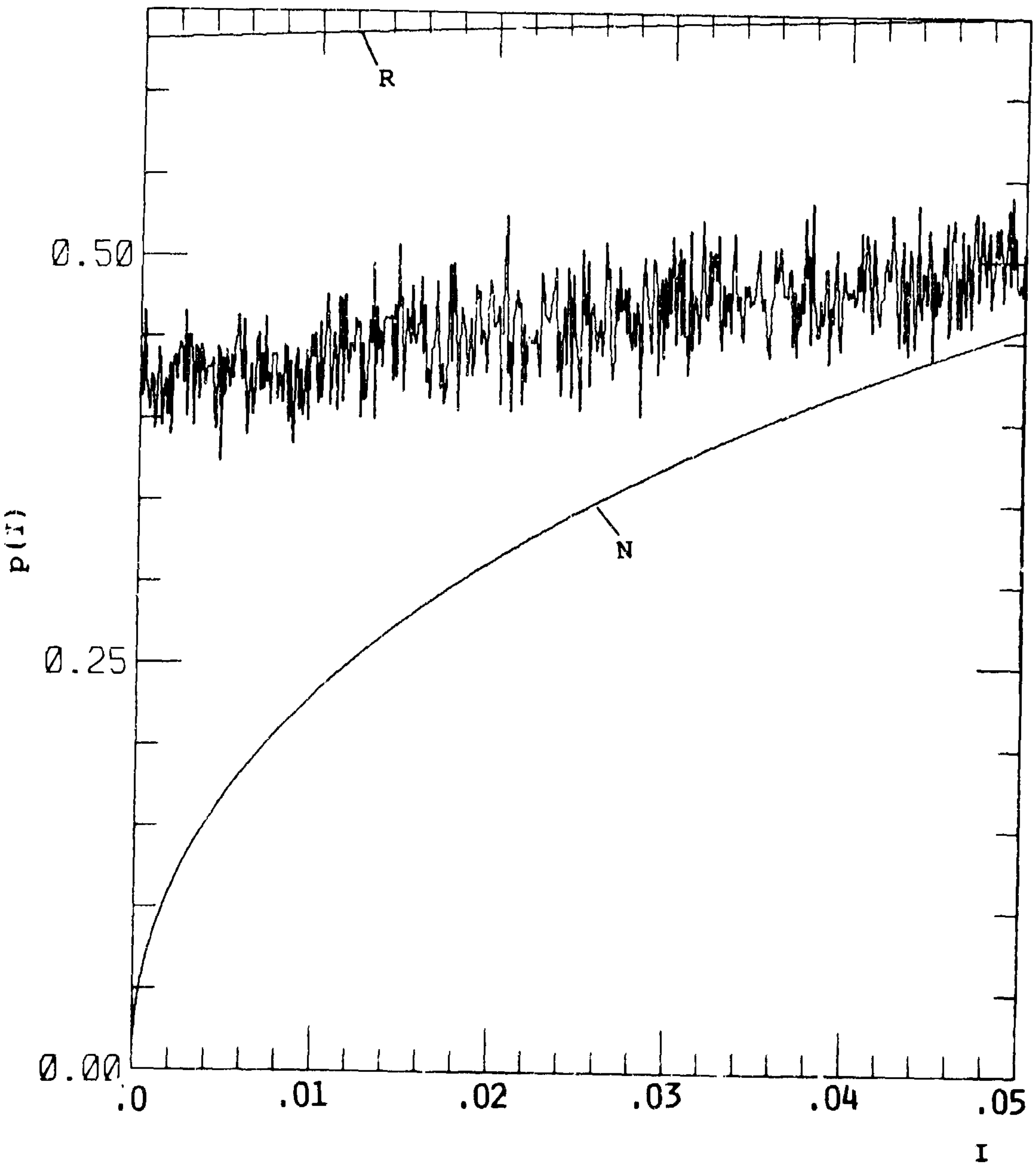

Figure H-5. Probability Distribution for Small I for $\alpha = 2$, $\chi^2 = 0.25$, $S_4^2 = 0.684$.

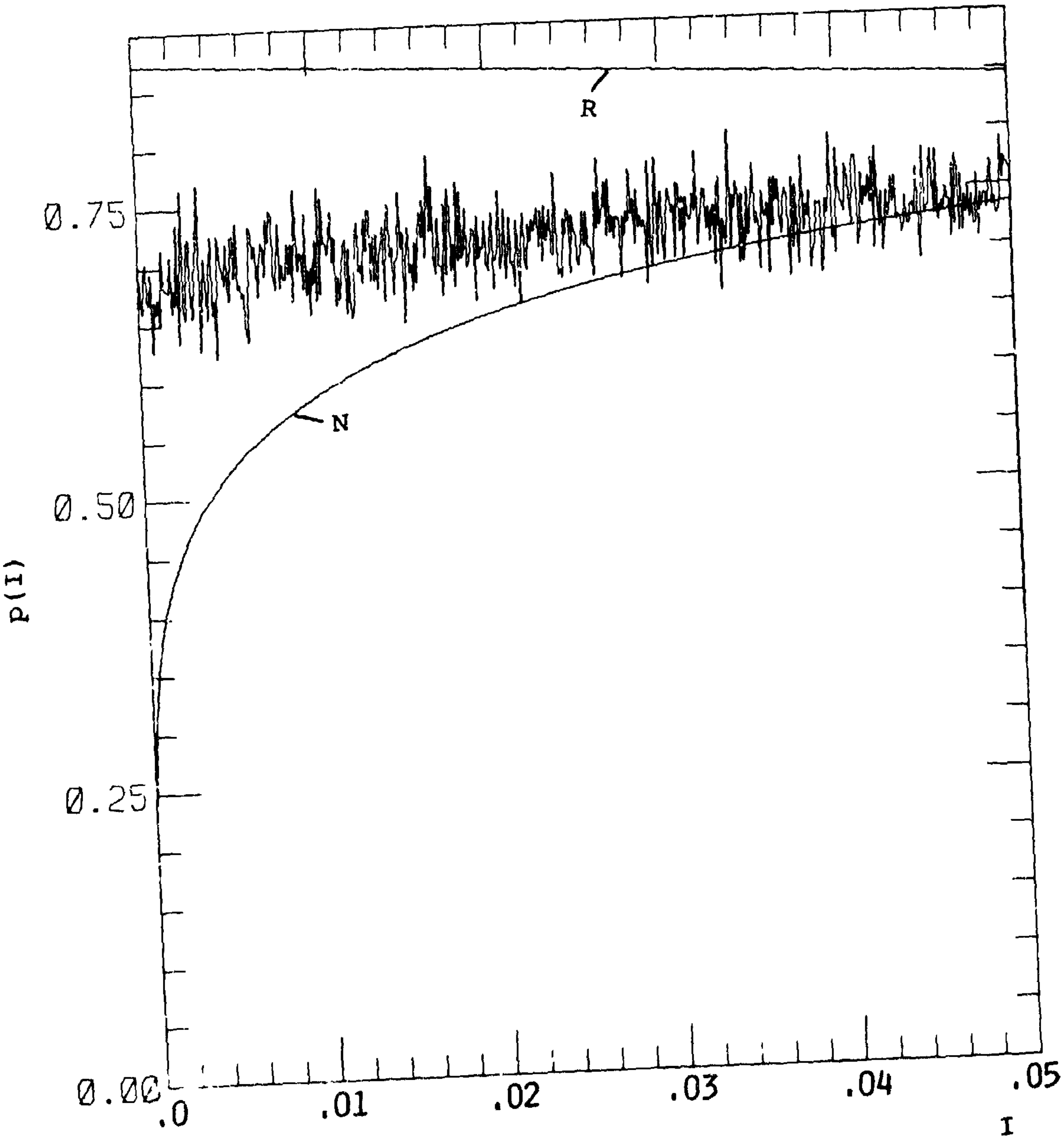

Figure H-6. Probability Distribution for Small I for $\alpha = 2$, $\chi^2 = 0.4$, $S_4{}^2 = 0.854$.

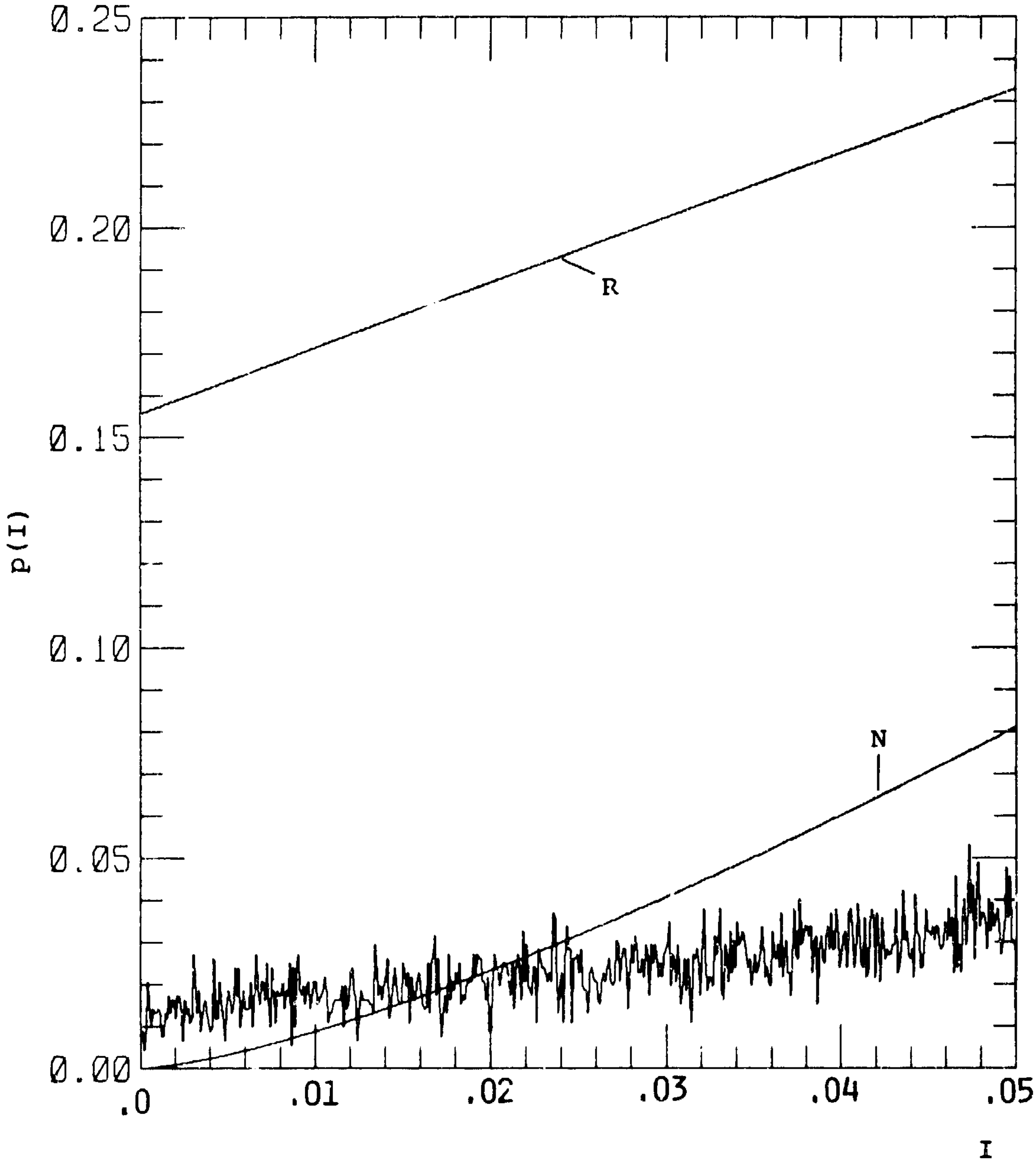

Figure H-7. Probability Distribution for Small I for $\alpha = 3$, $\chi^2 = 0.1$, $S_4^{\ 2} = 0.409$.

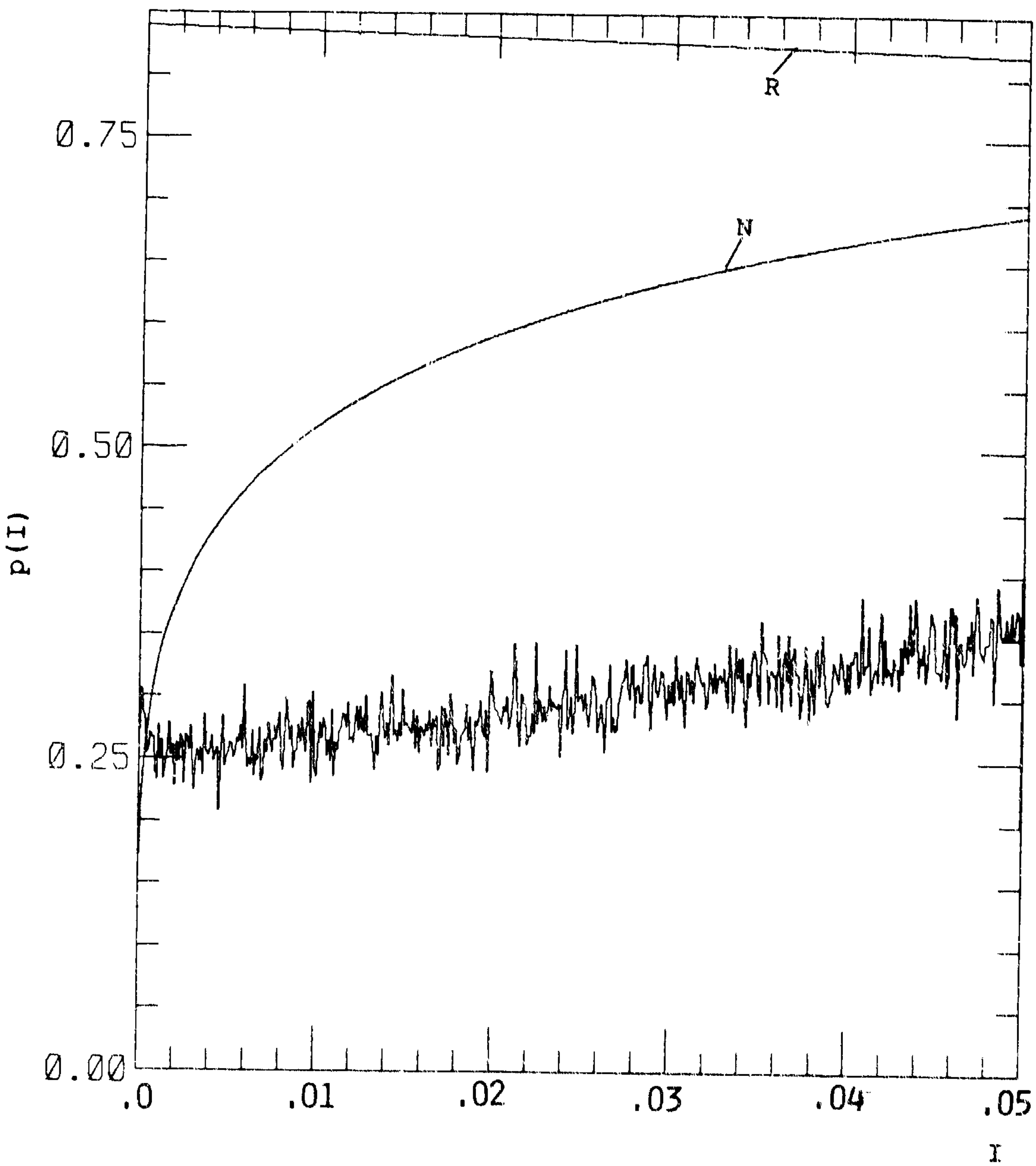

Figure H-8. Probability Distribution for Small I for $\alpha = 3$, $\chi^2 = 0.25$, $S_4^{\,2} = 0.827$.

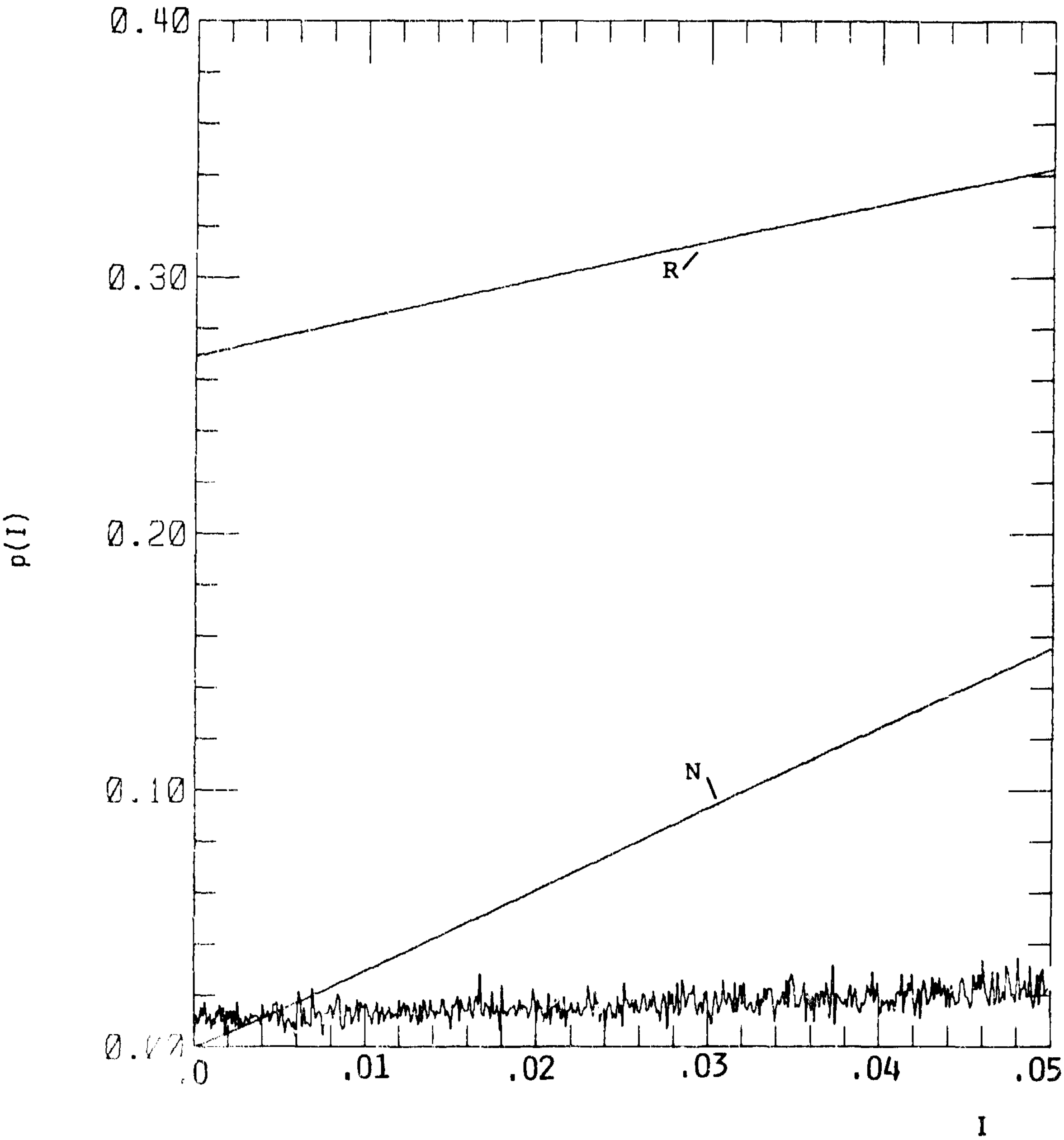

Figure H-9. Probability Distribution for small I for $\alpha = 4$, $\chi^2 = 0.1$, $S_4^2 = 0.479$.

APPENDIX I

CALCULATED BIT ERROR RATES FOR TWO POWER LAW PSD

This Appendix contains all the calculated bit error rates for two power law PSD. The six modems considered are: CPSK, ΔPSK, DBPSK, BFSK, QFSK and 8-ARYFSK. The curves are labeled as follows:

AWGN	Additive white Gaussian noise
a	$\overline{\chi^2_{Ry}} = 0.01$
b	$= 0.025$
c	$= 0.05$
d	$= 0.1$
e	$= 0.25$
f	$= 0.4$
SRF	Slow Rayleigh Fading

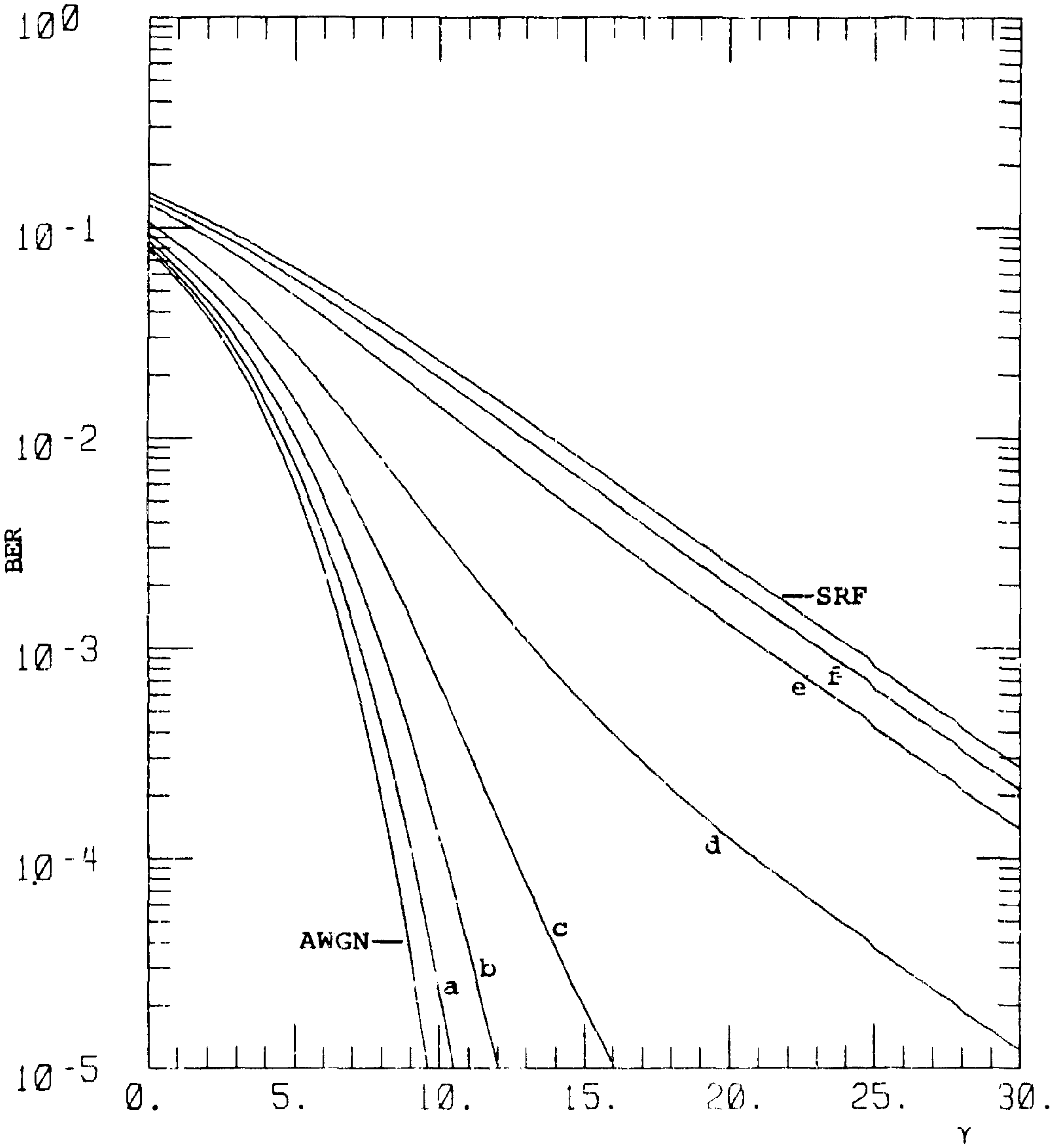

Figure I-1. BER for CPSK, $\alpha = 1$.

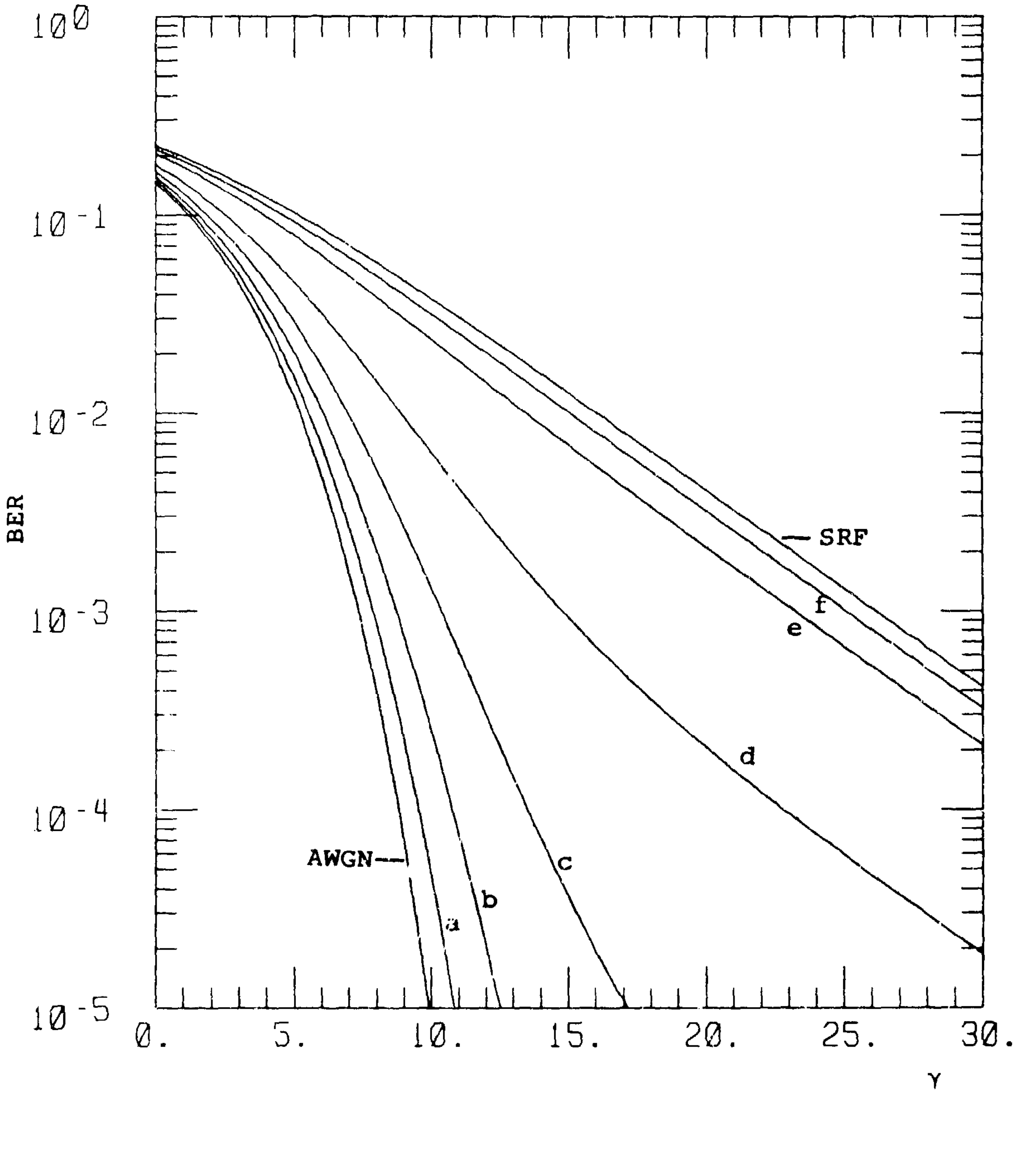

Figure I-2. BER for ΔPSK, α = 1.

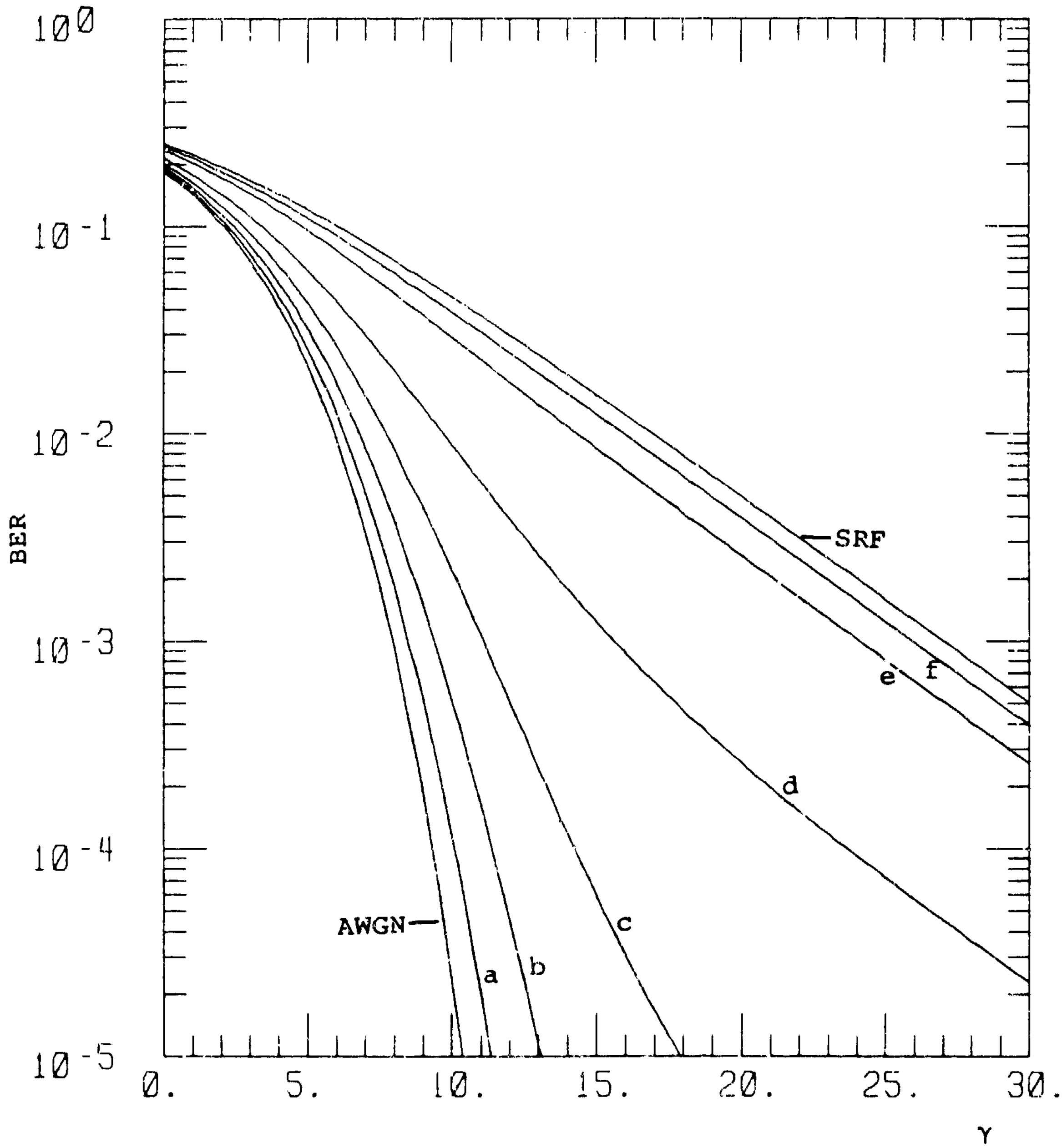

Figure I-3. BER for DBPSK, α = 1.

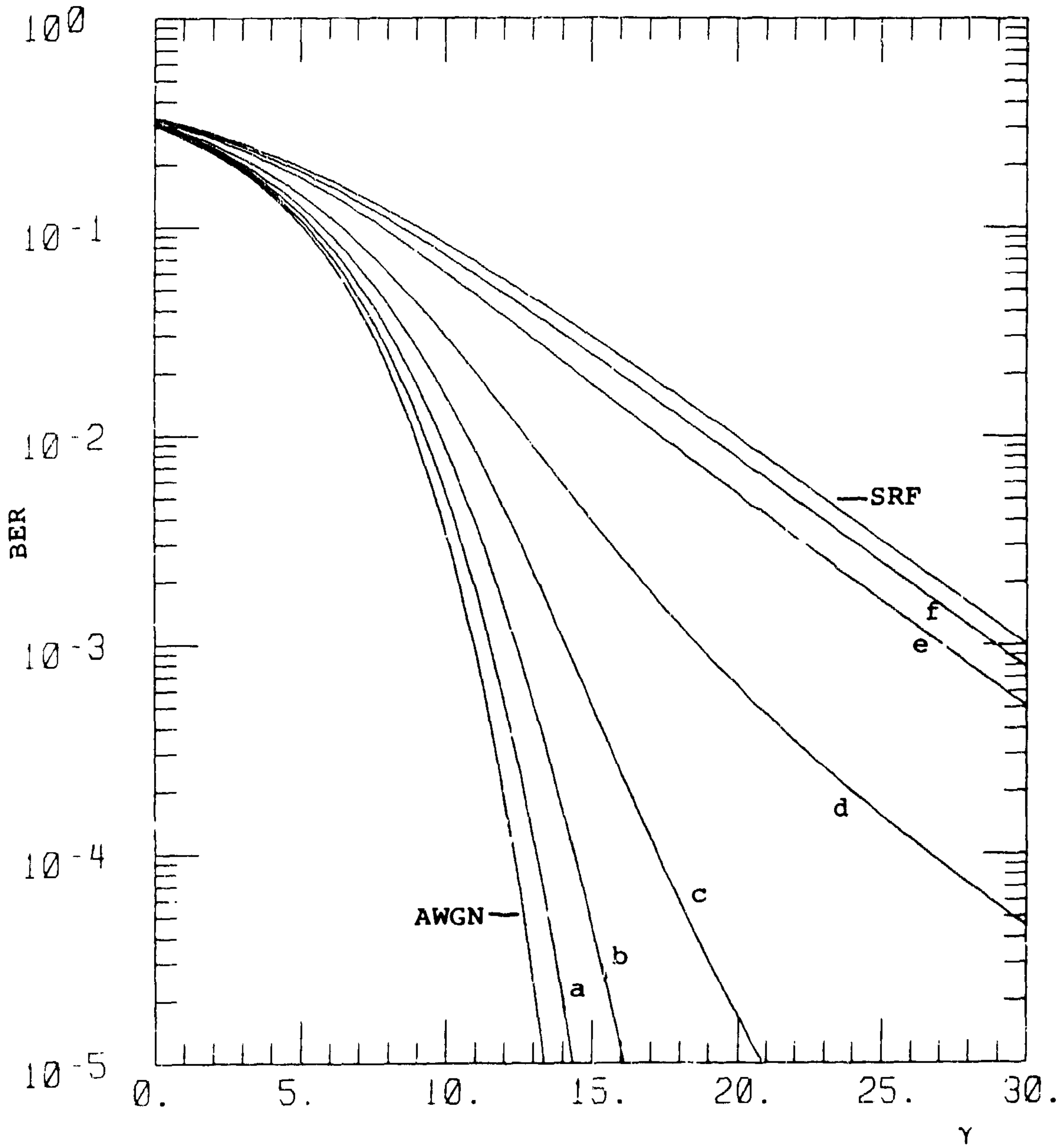

Figure I-4. BER for BFSK, $\alpha = 1$.

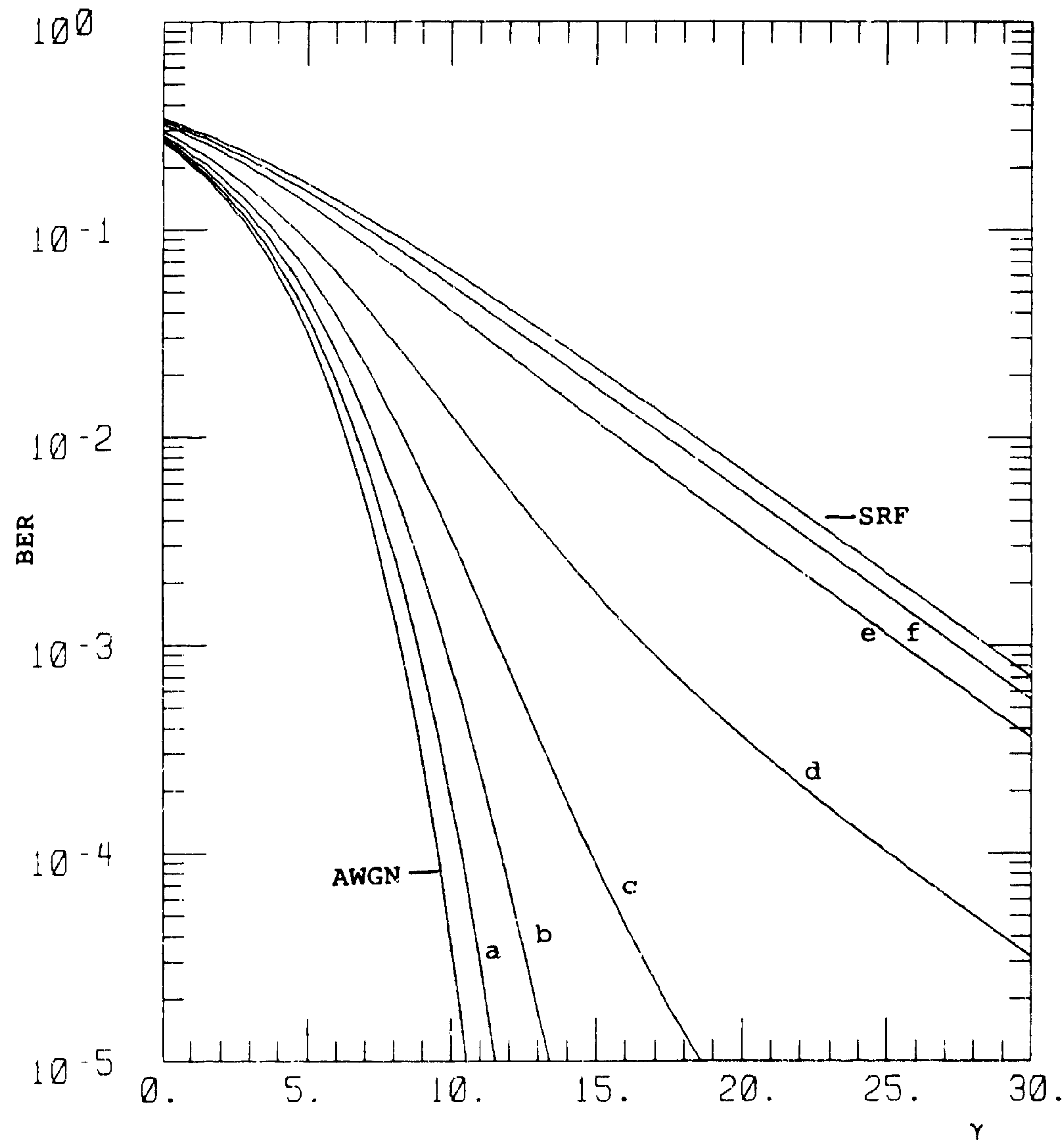

Figure I-5. BER for QFSK, α = 1.

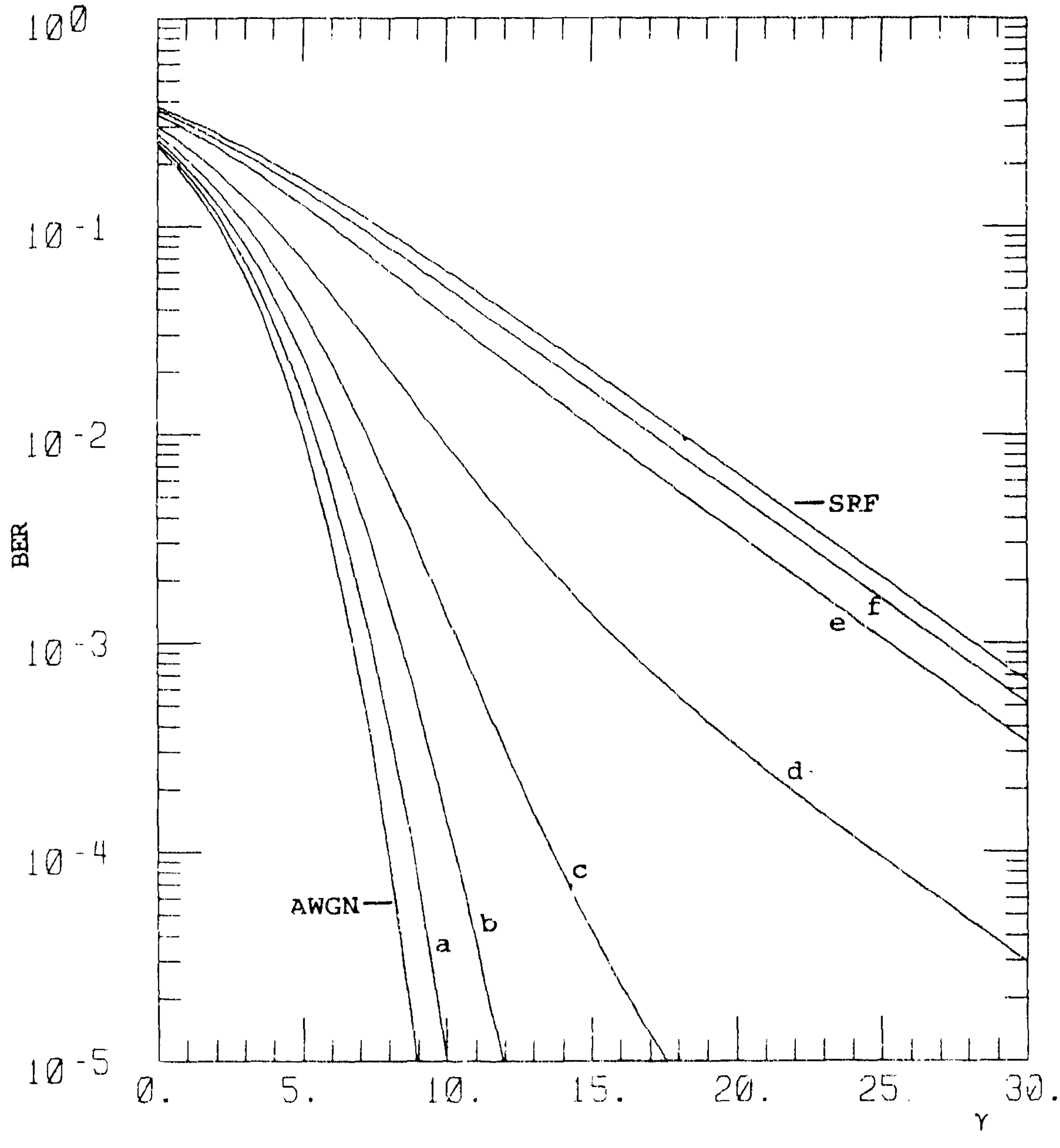

Figure I-6. BER for 8-ARYFSK, α = 1.

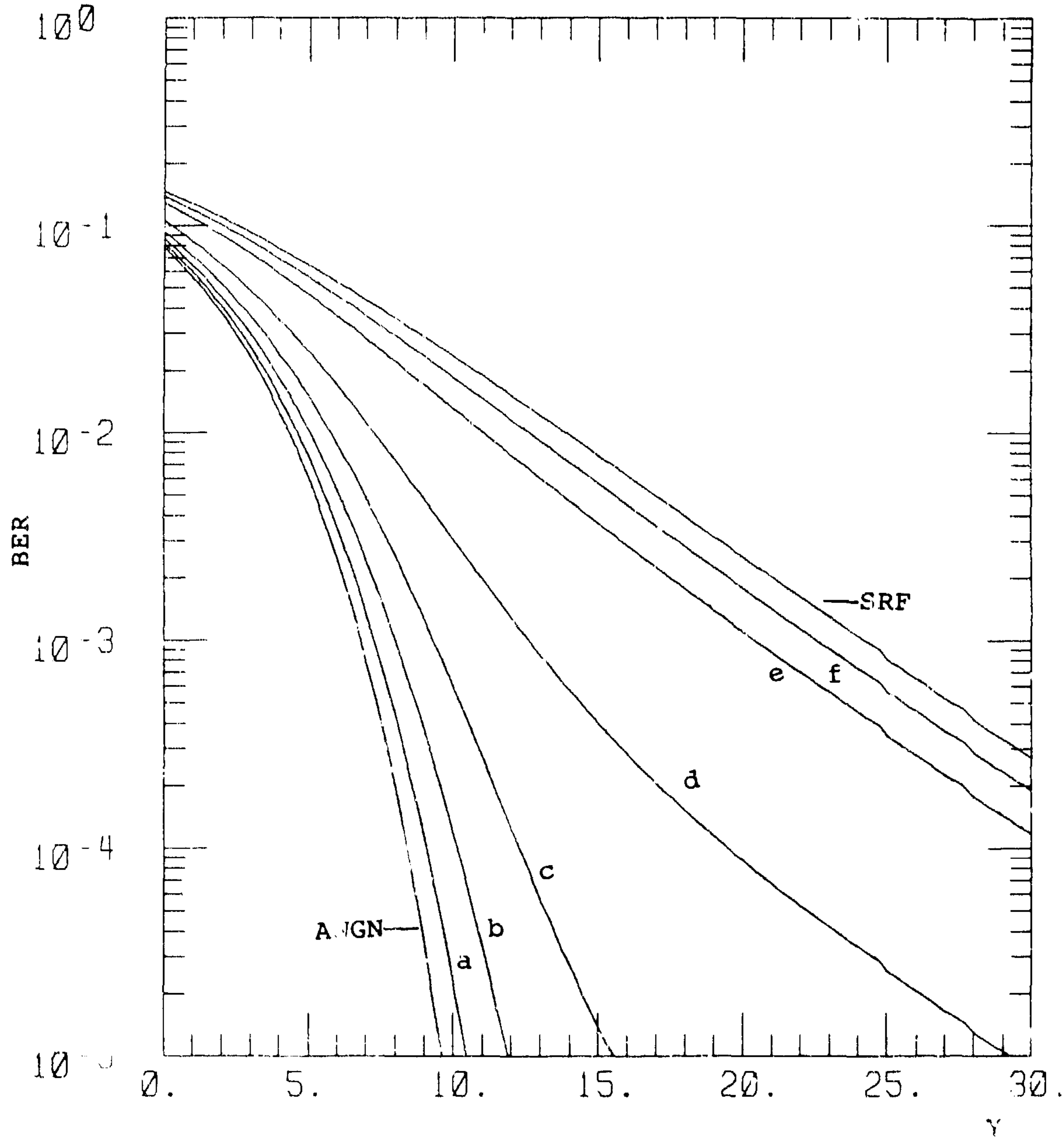

Figure I-7. BER for CPSK, $\alpha = 2$.

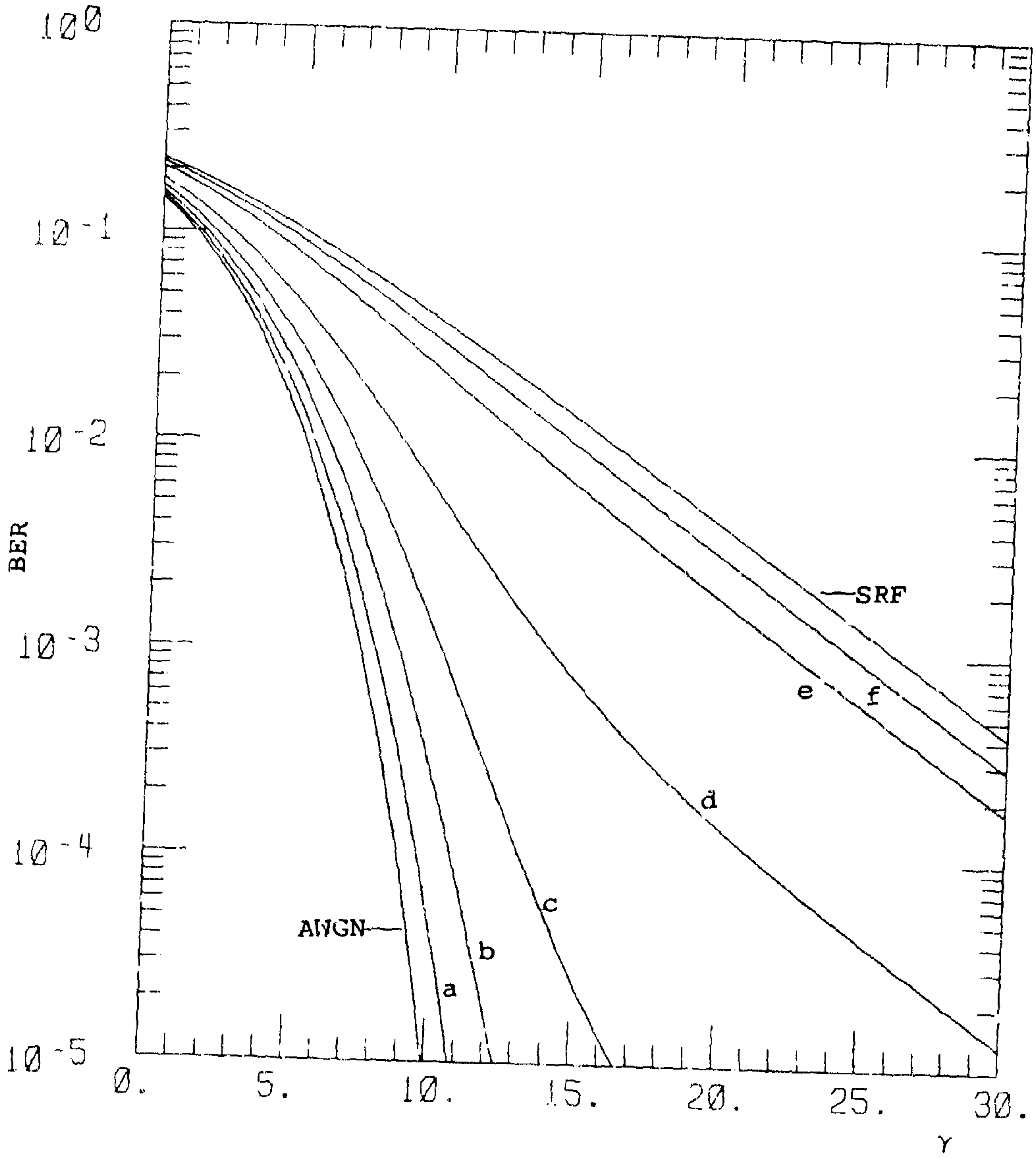

Figure I-8. BER for ΔPSK, $\alpha = 2$.

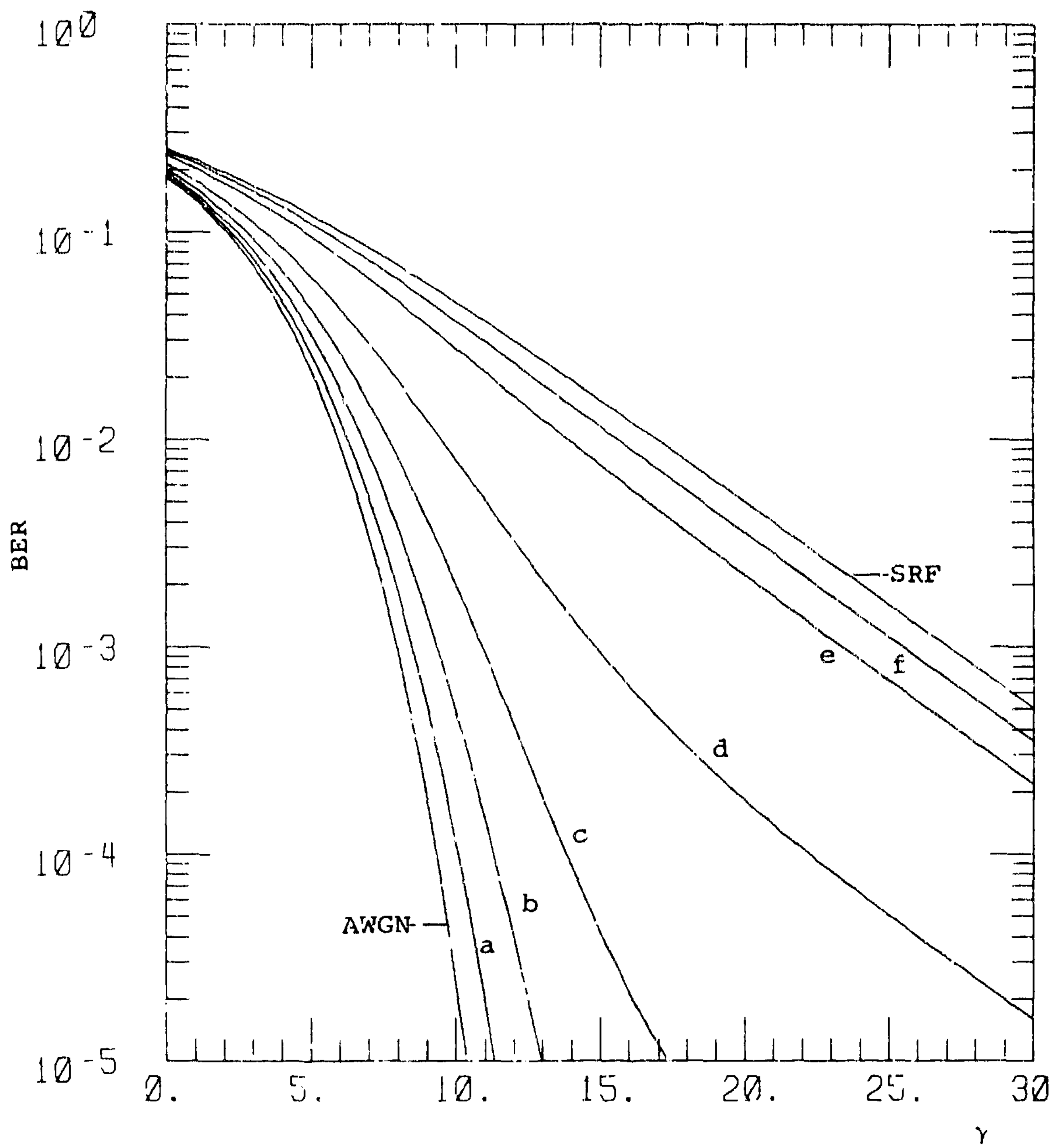

Figure I-9. BER for DBPSK, $\alpha = 2$.

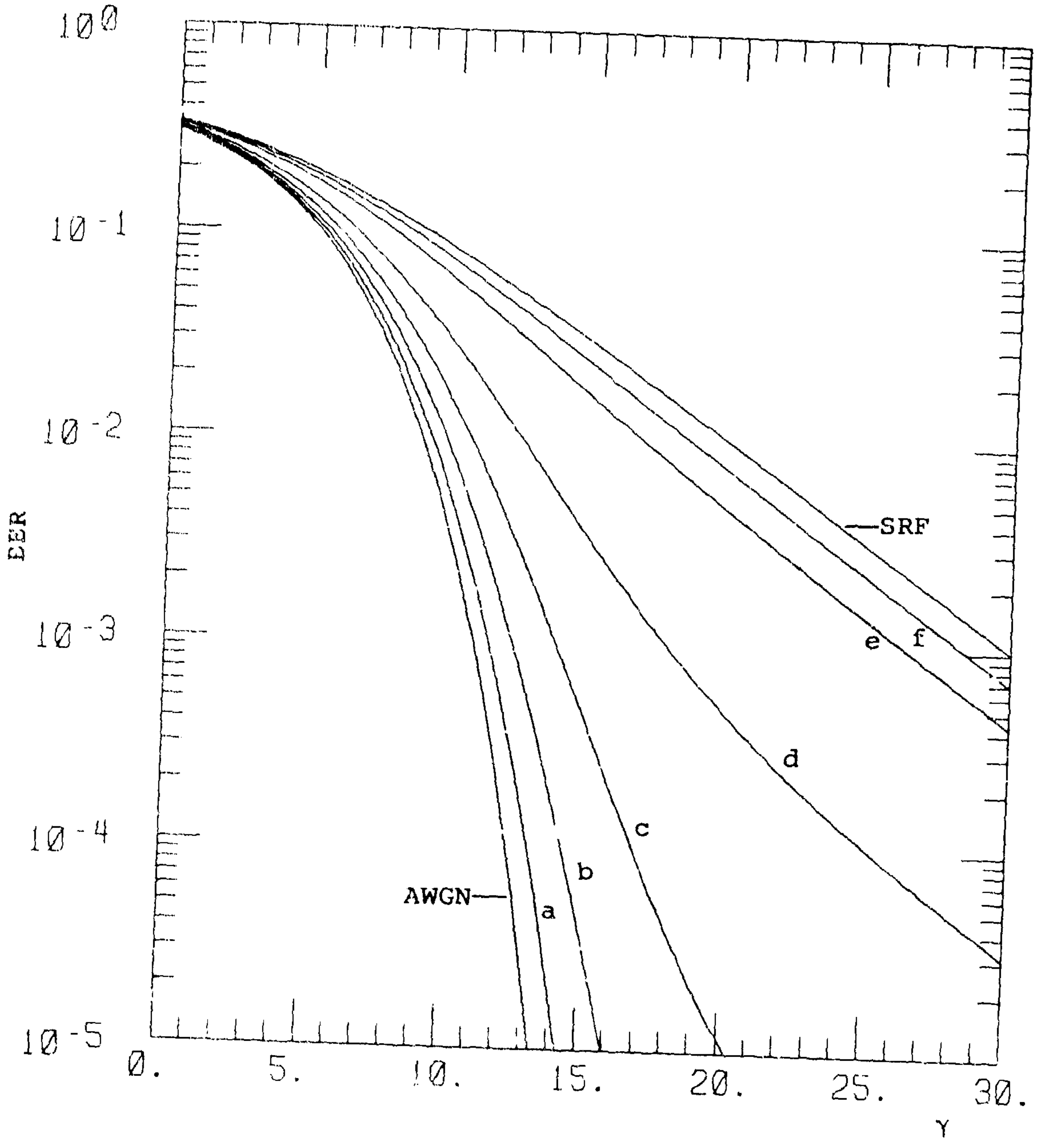

Figure I-10. BER for BFSK, α = 2.

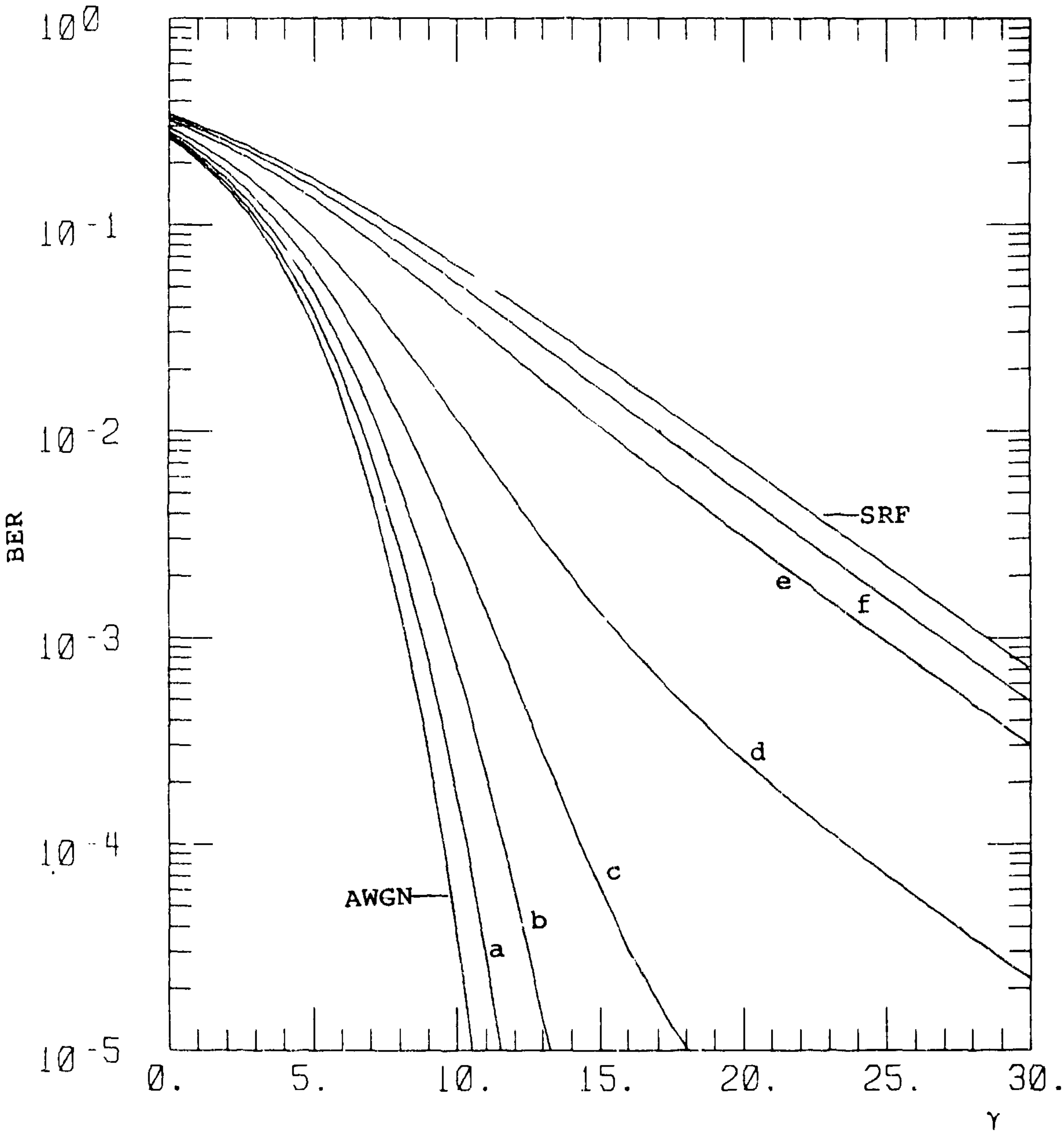

Figure I-11. BER for QFSK, $\alpha = 2$.

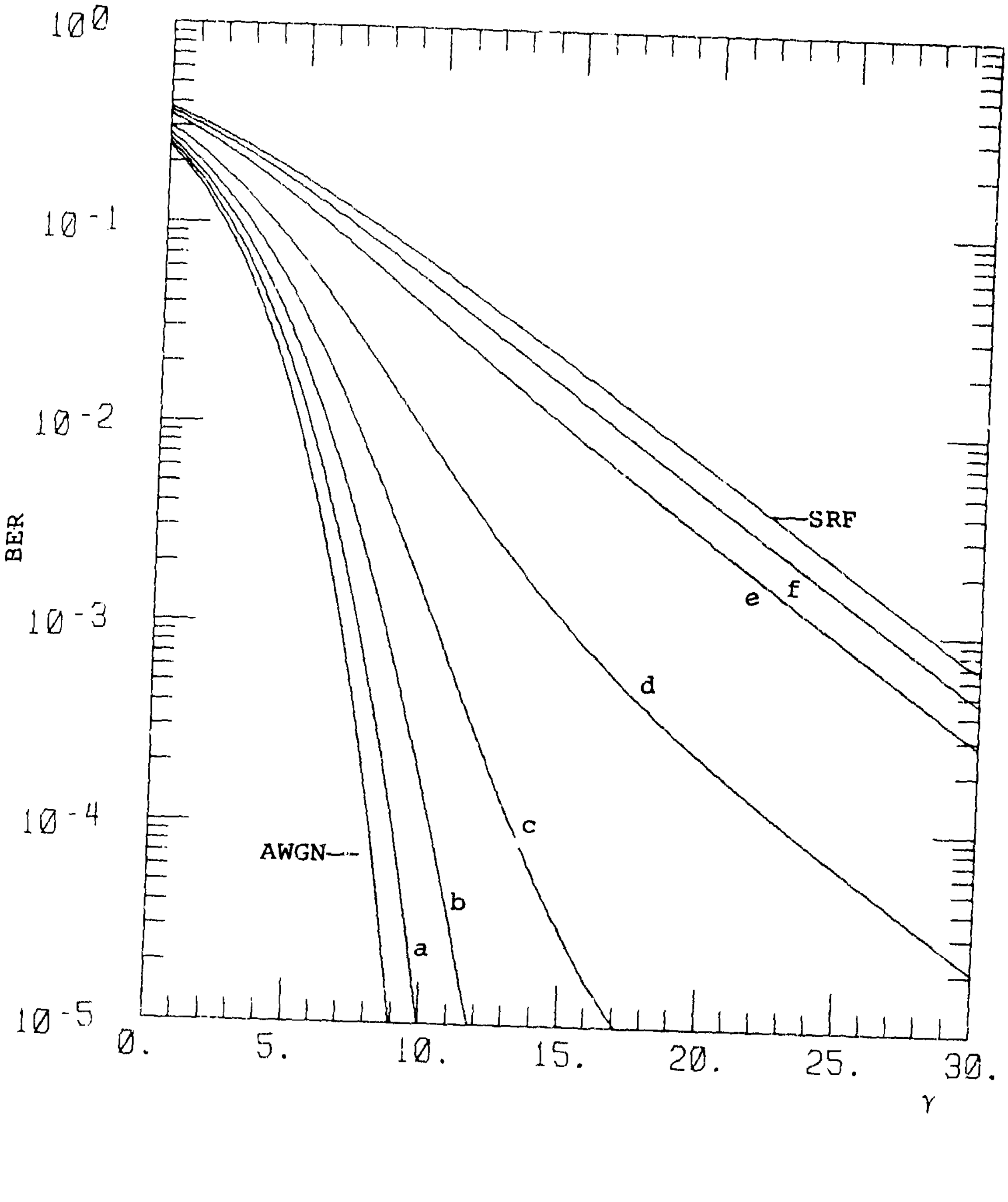

Figure I-12. BER for 8-ARYFSK, α = 2.

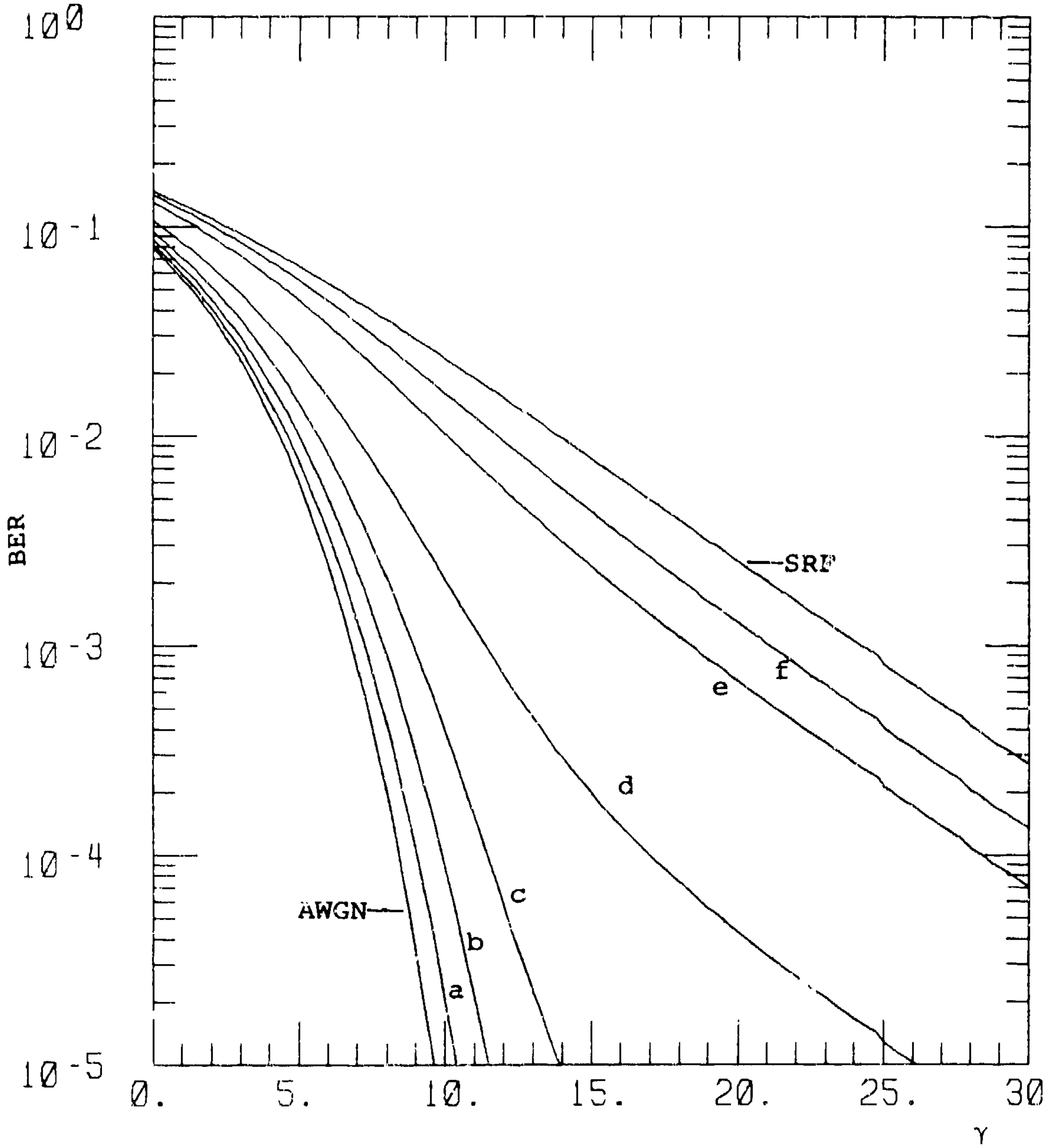

Figure I-13. BER for CPSK, $\alpha = 3$.

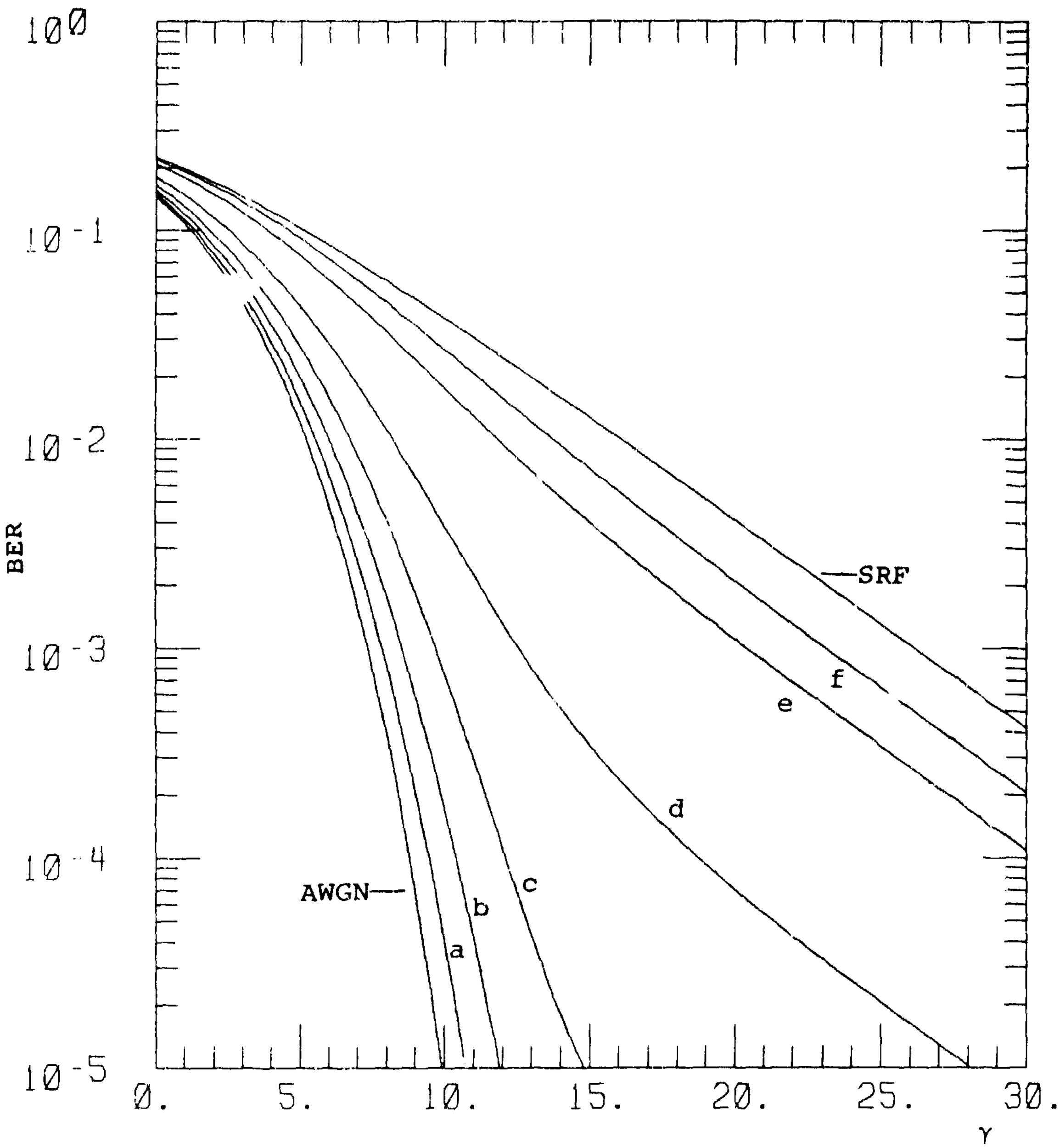

Figure I-14. BER for ΔPSK, α = 3.

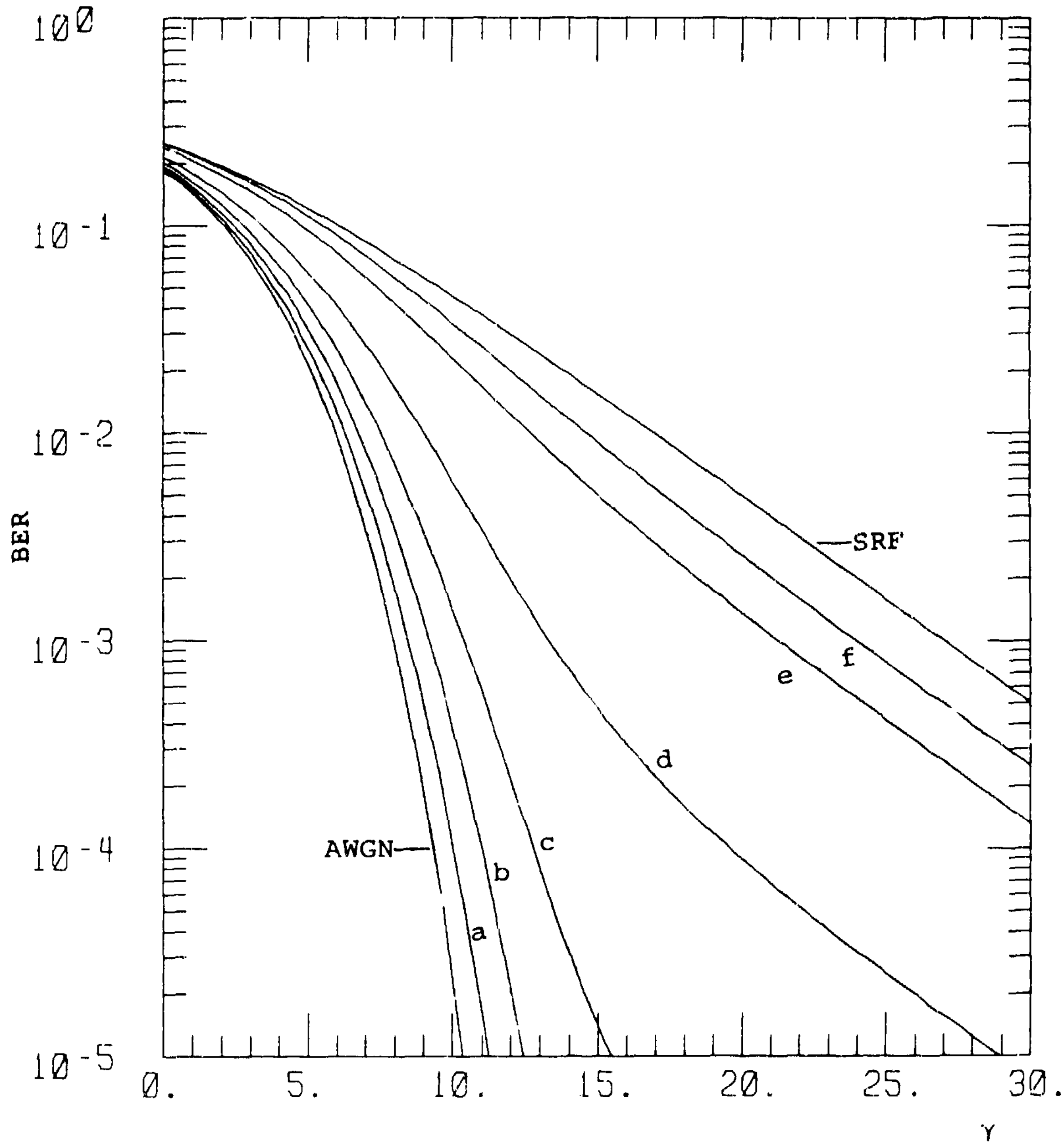

Figure I-15. BER for DBPSK, α = 3.

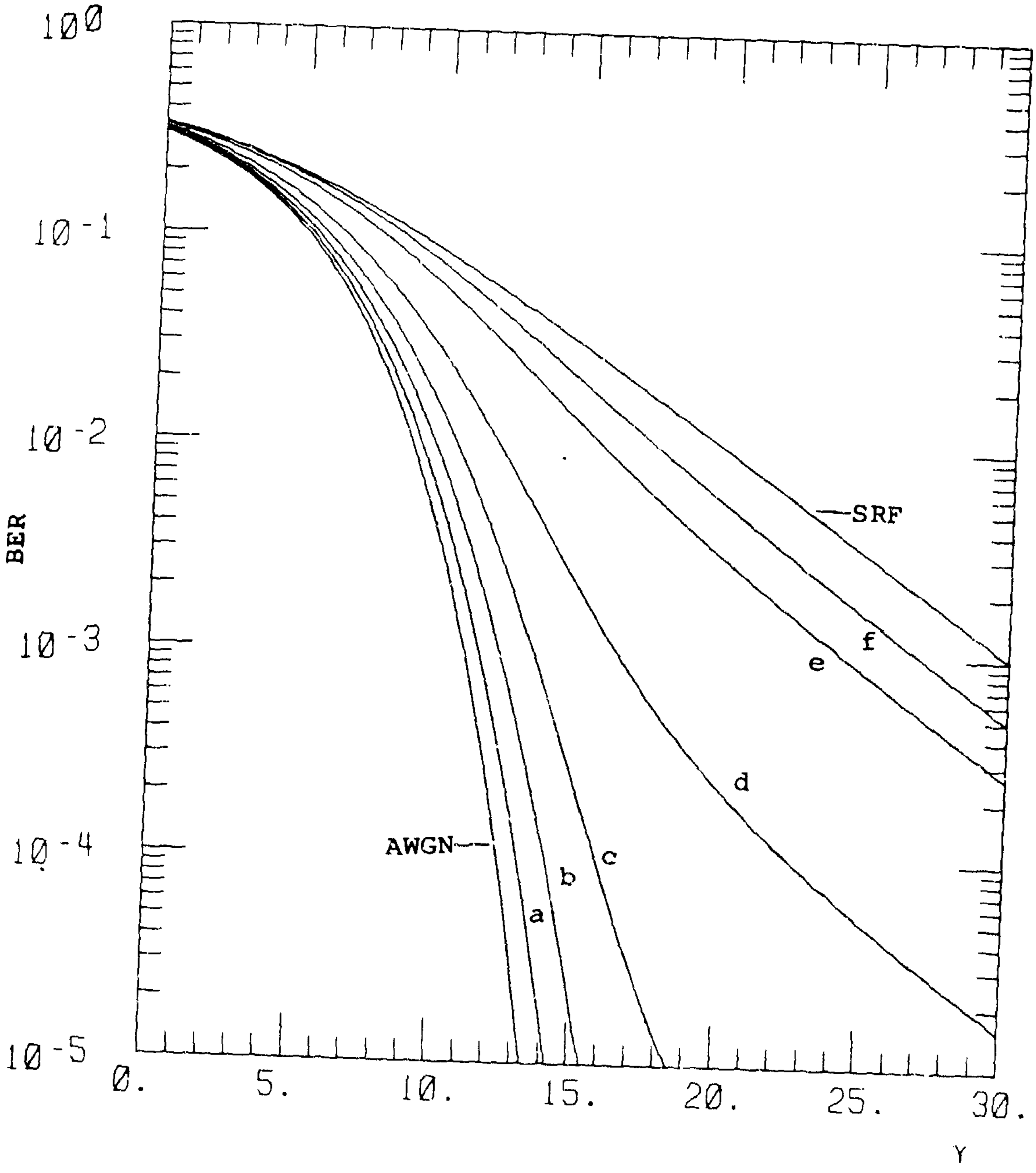

Figure I-16. BER for BFSK, α = 3.

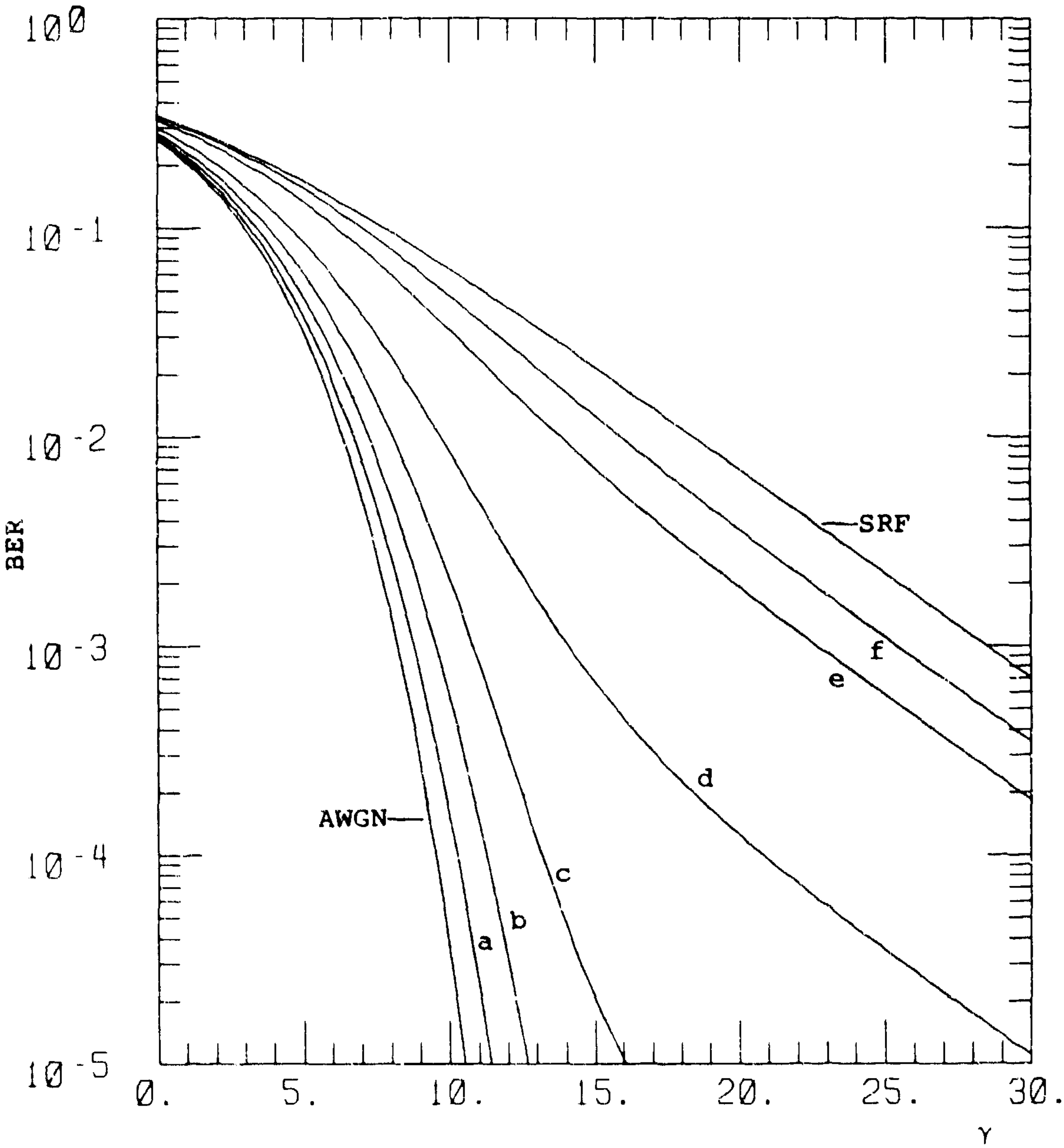

Figure I-17. BER for QFSK, $\alpha = 3$.

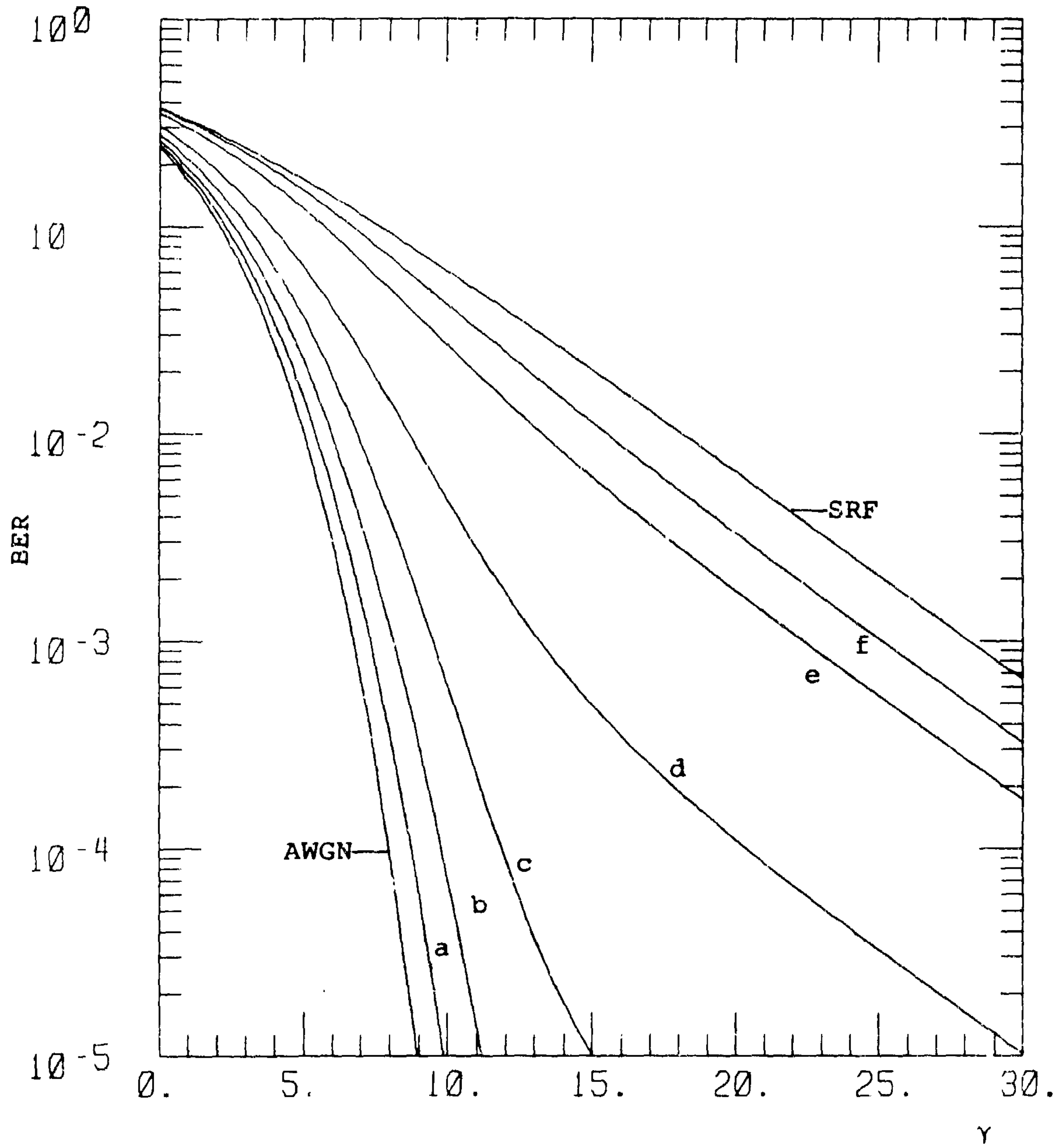

Figure I-18. BER for 8-ARYFSK, α = 3.

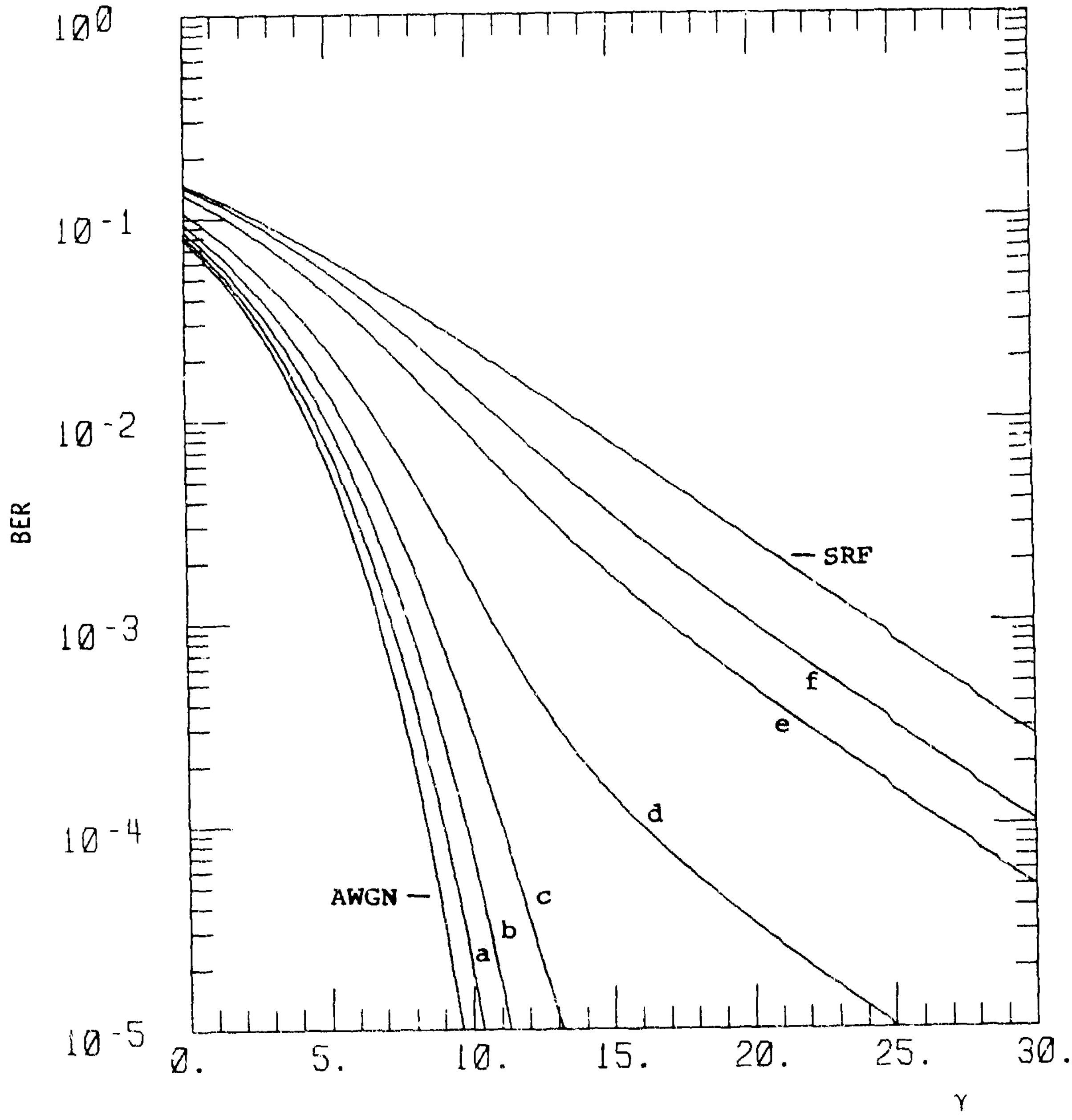

Figure I-19. BER for CPSK, α = 4.

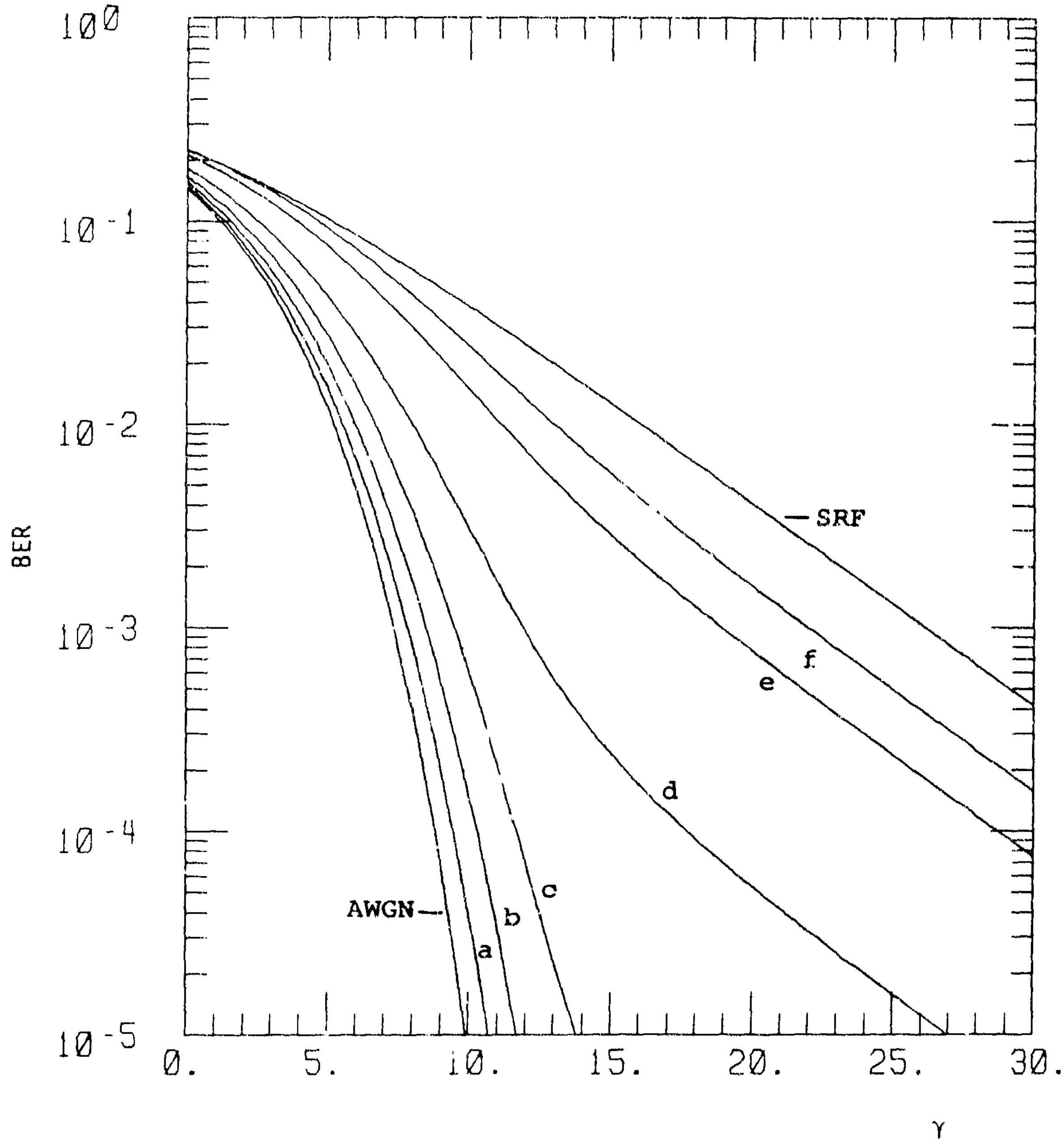

Figure I-20. BER for ΔPSK, α = 4.

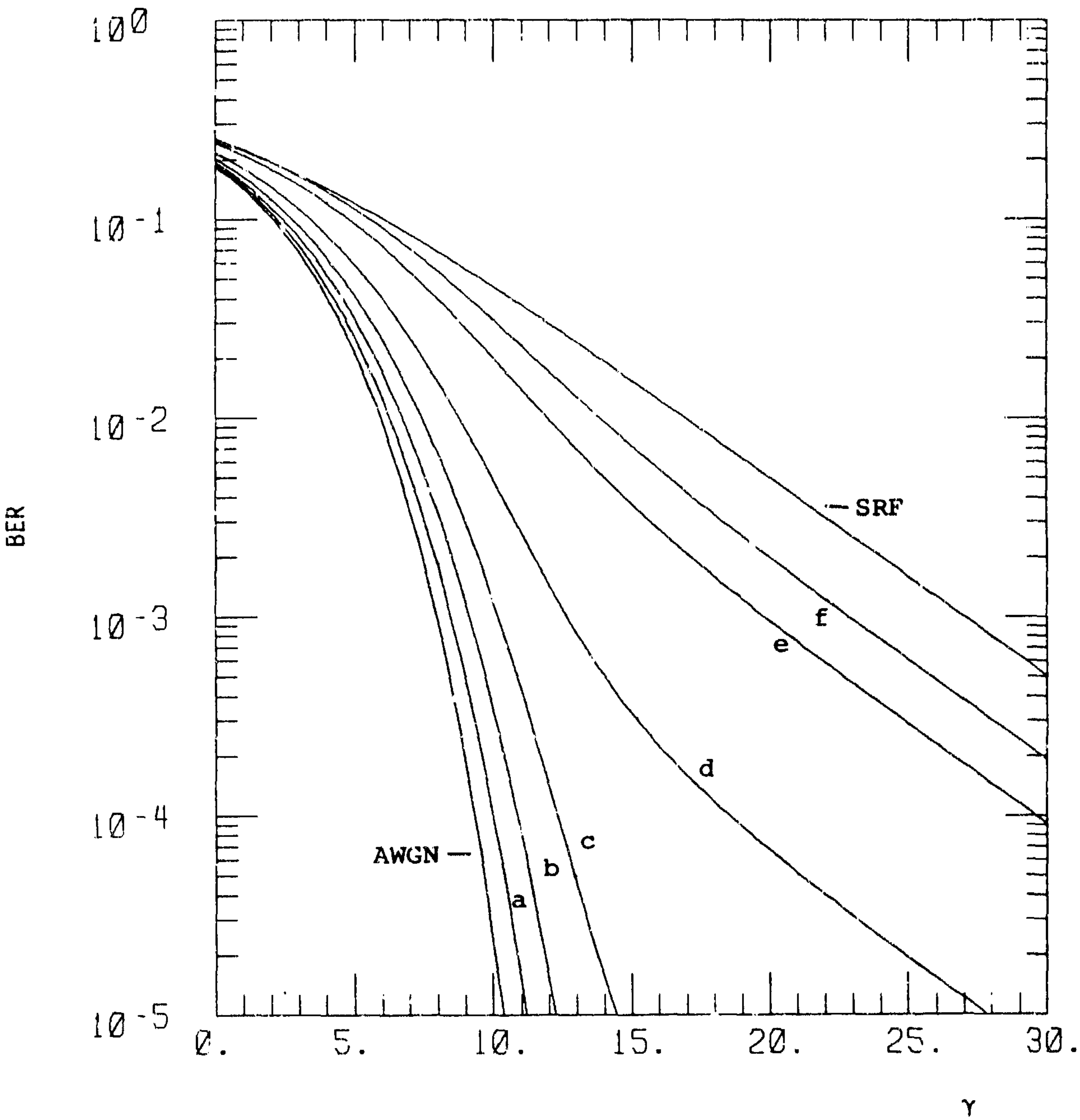

Figure I-21. BER for DBPSK, $\alpha = 4$.

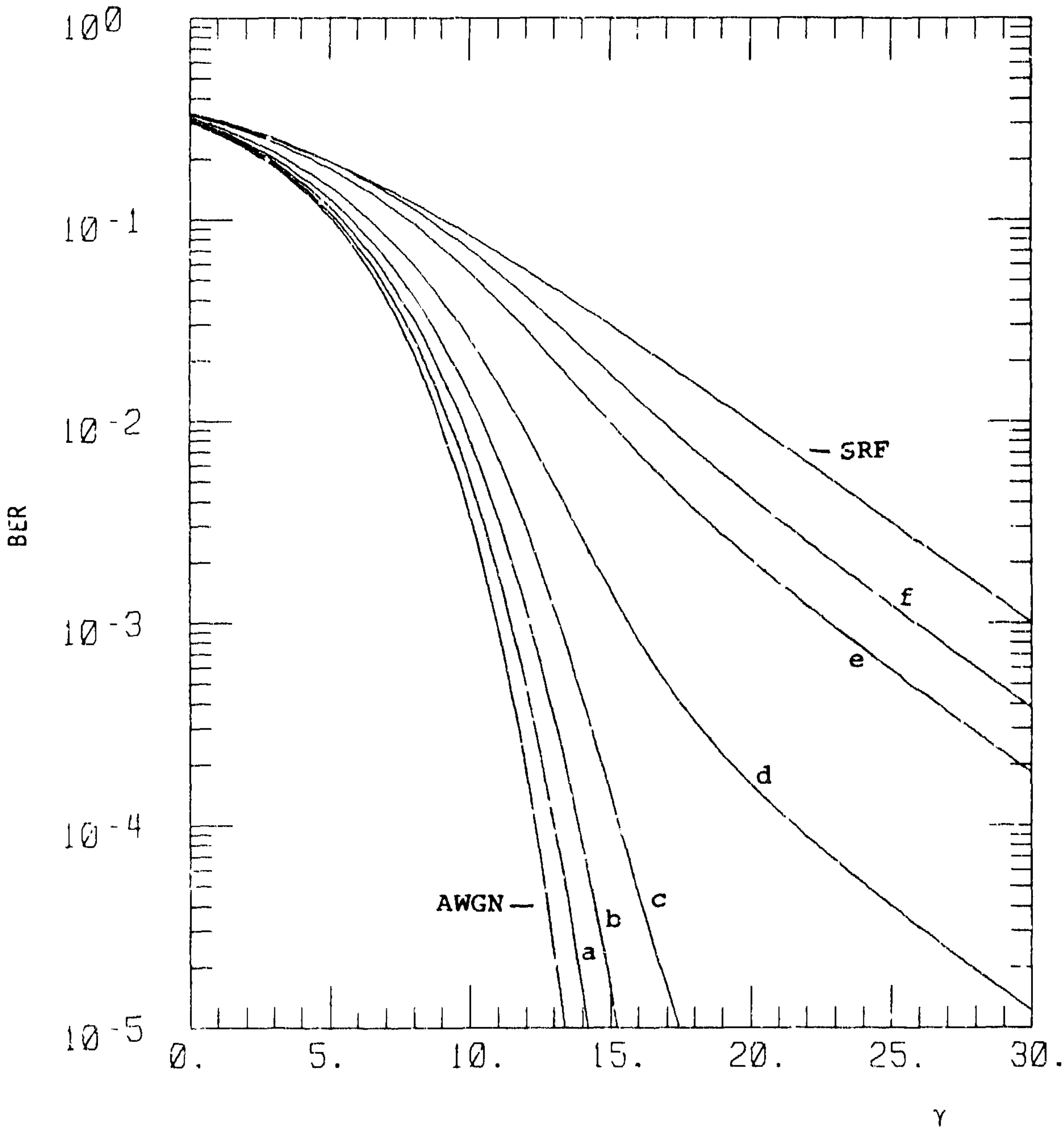

Figure I-22. BER for DFSK, $\alpha = 4$.

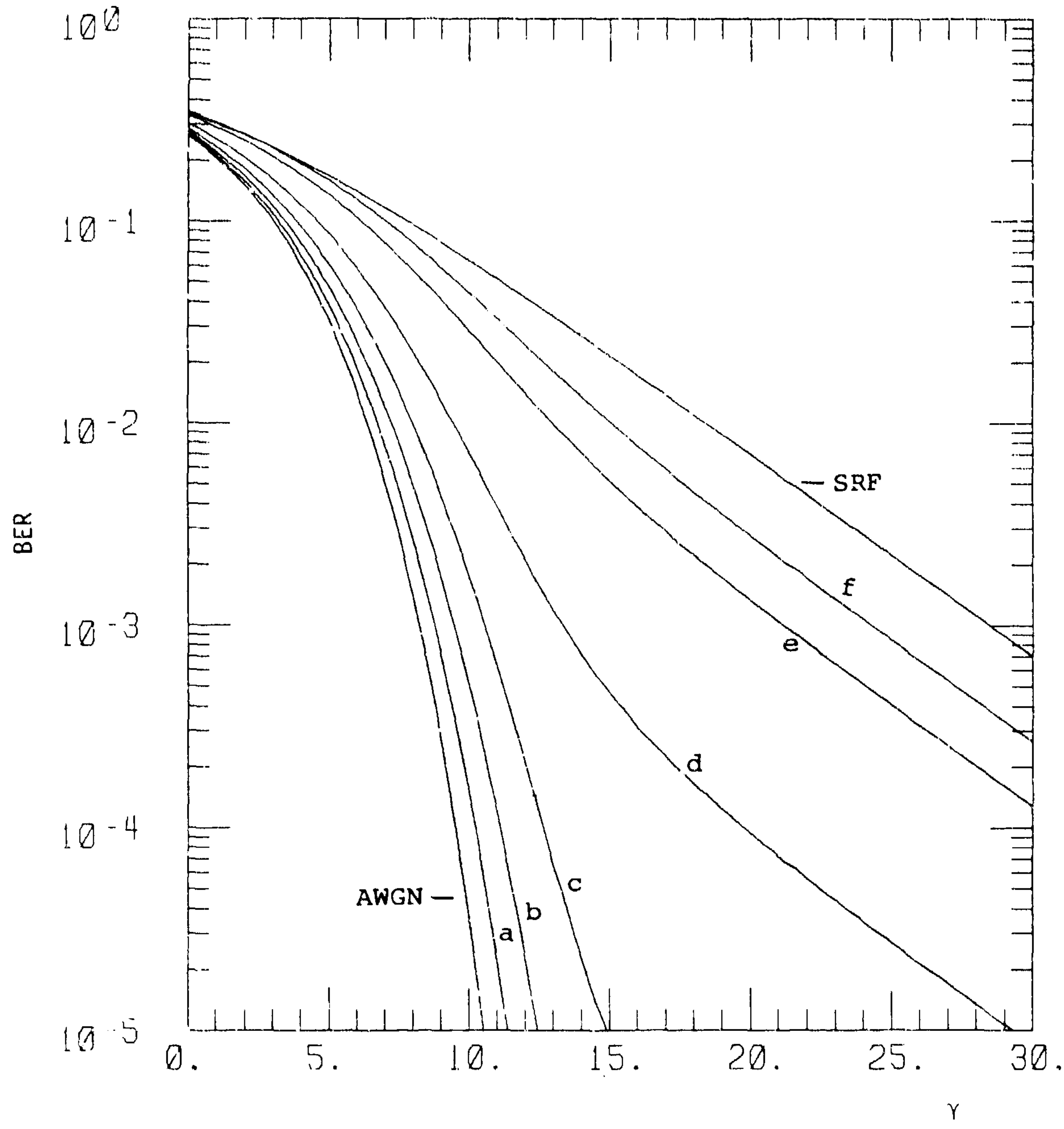

Figure I-23. BER for QFSK, $\alpha = 4$.

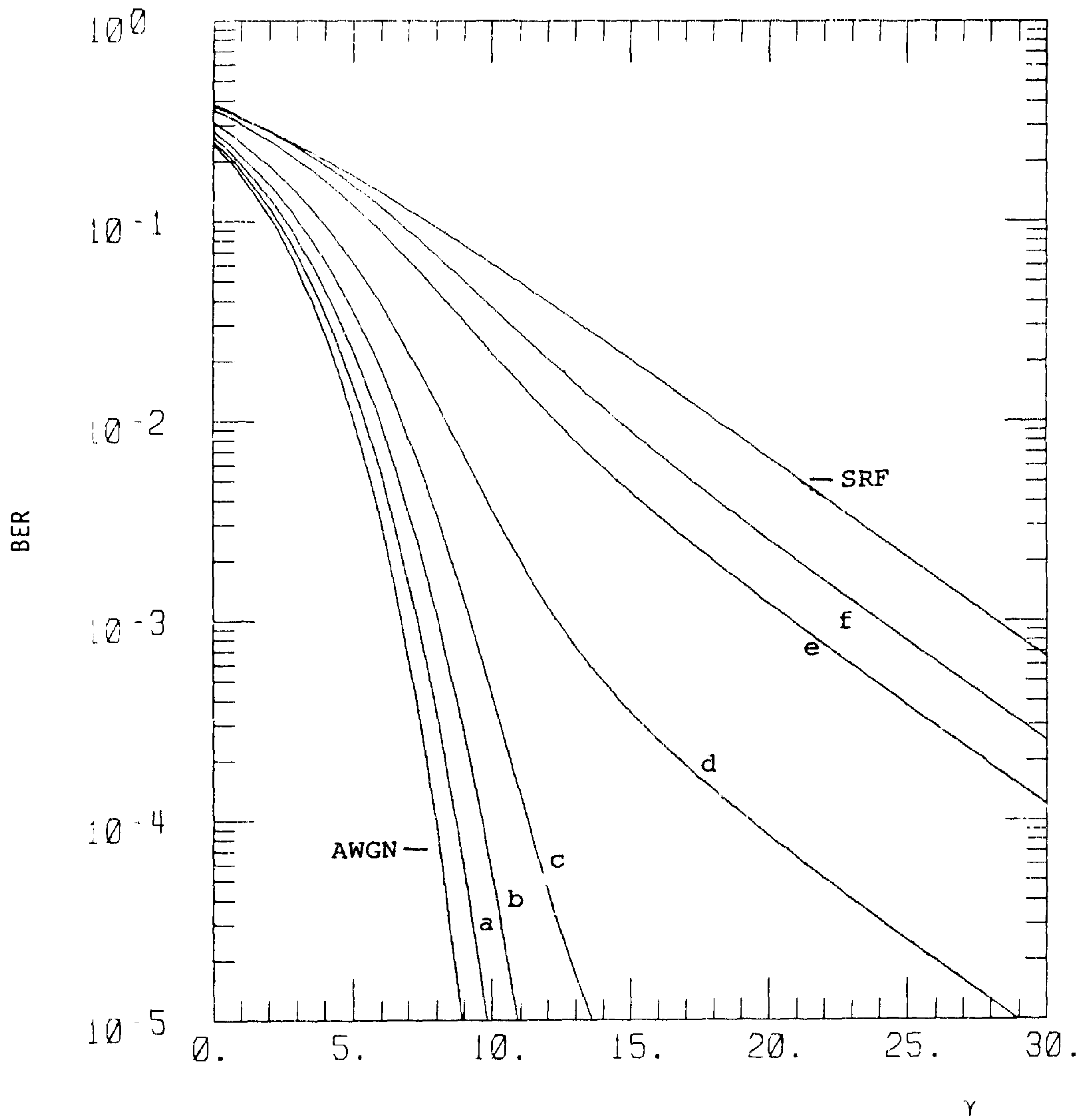

Figure I-24. BER for 8-ARYFSK, $\alpha = 4$.

APPENDIX J

CALCULATED BIT ERROR RATES FOR DBPSK COMPARED TO NAKAGAMI-M AND RICE FOR TWO POWER LAW PSD

This Appendix contains the calculated bit error rate for DBPSK compared to Nakagami-m (labeled as N) and Rice (labeled as R) for two power law PSD. Throughout, the calculated data is labeled C.

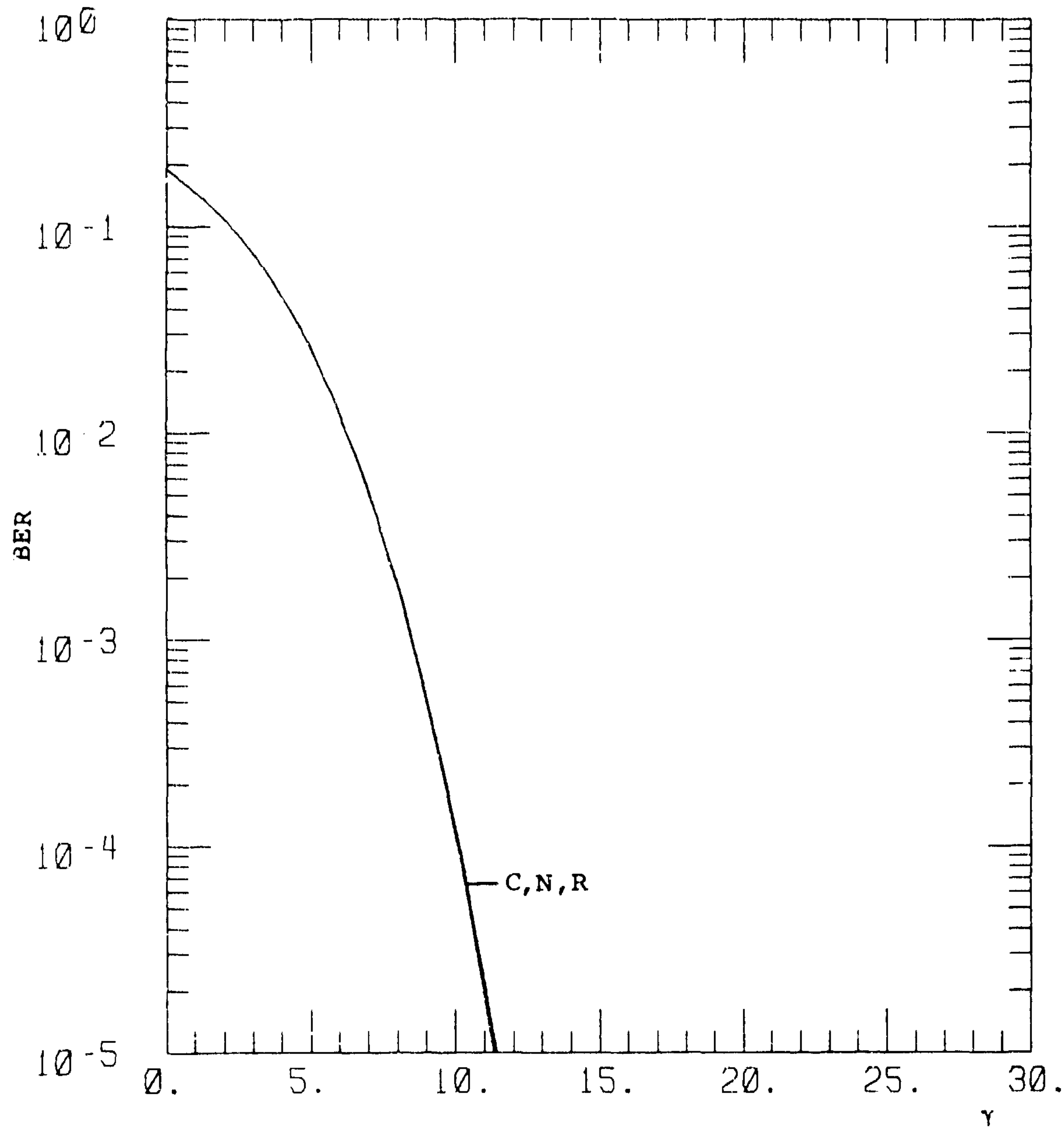

Figure J-1. BER for DBPSK
$\alpha = 1$, $\chi^2 = 0.01$, $S_4^2 = 0.040$.

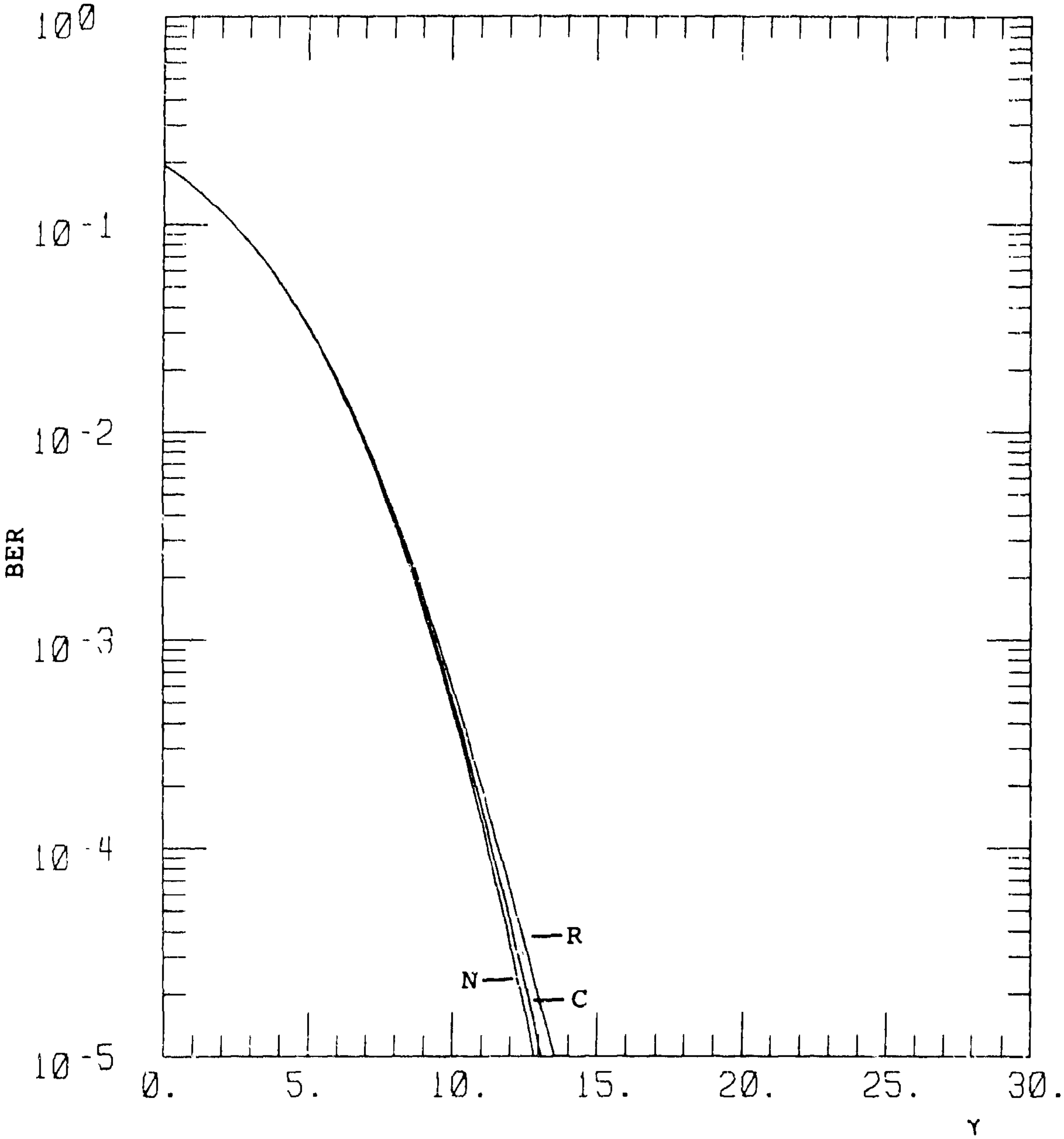

Figure J-2. BER for DBPSK
$\alpha = 1$, $\chi^2 = 0.025$, $S_4^{\ 2} = 0.097$.

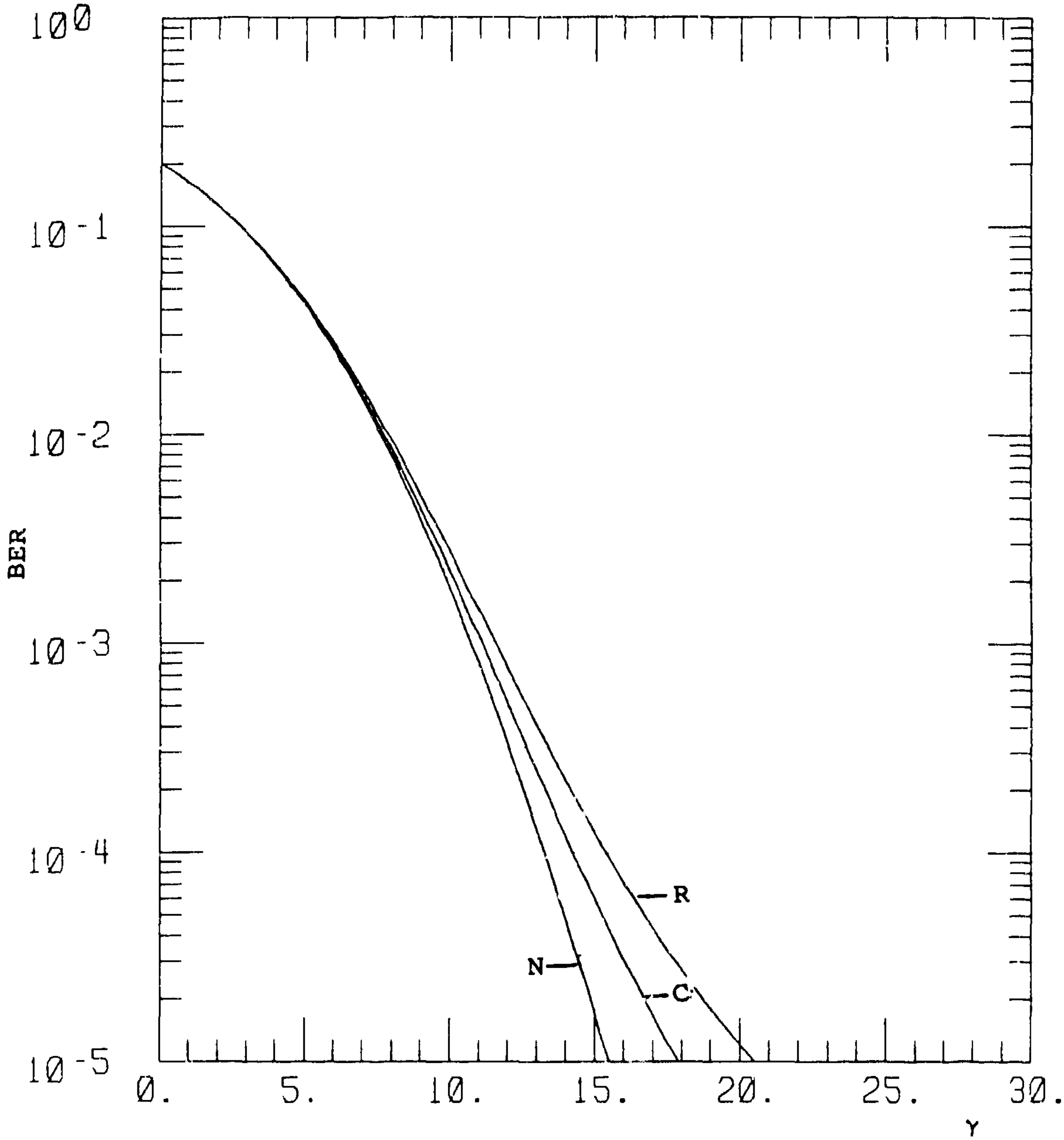

Figure J-3. BER for DBPSK
$\alpha = 1$, $\chi^2 = 0.05$, $S_4^{\ 2} = 0.188$.

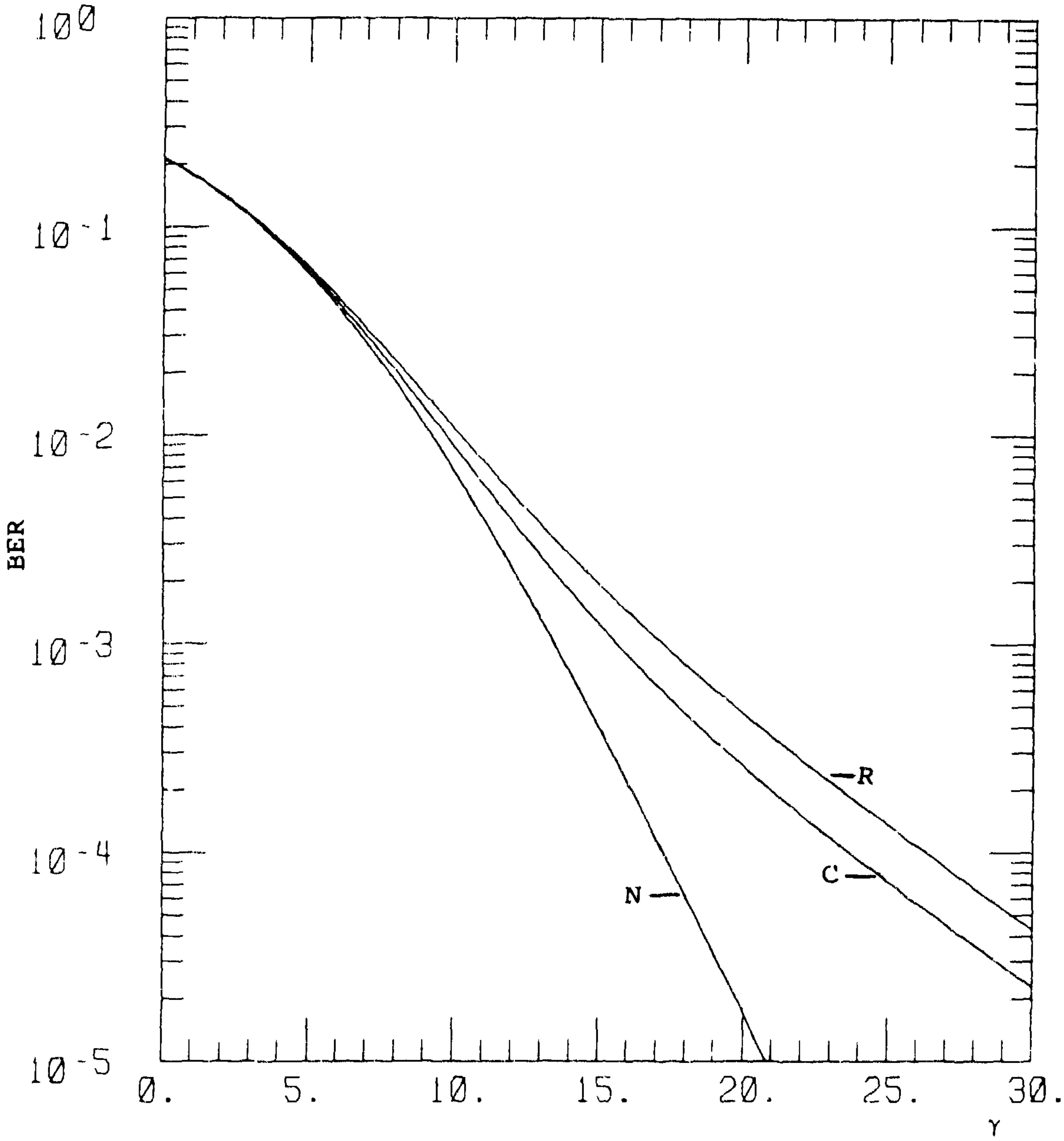

Figure J-4. BER for DBPSK
$\alpha = 1$, $\chi^2 = 0.1$, $S_4^{\ 2} = 0.347$.

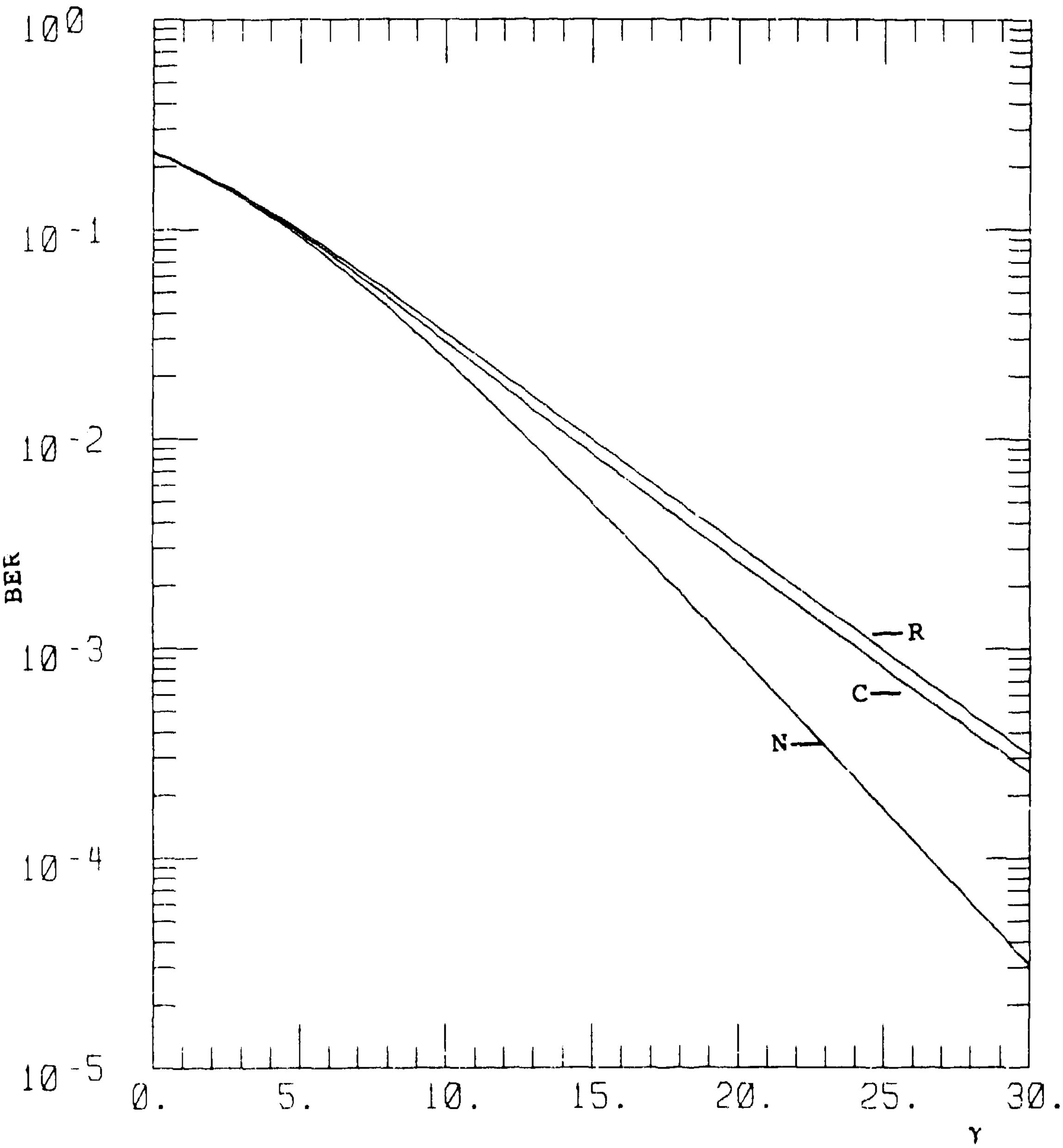

Figure J-5. BER for DBPSK
$\alpha = 1$, $\chi^2 = 0.25$, $S_4{}^2 = 0.672$.

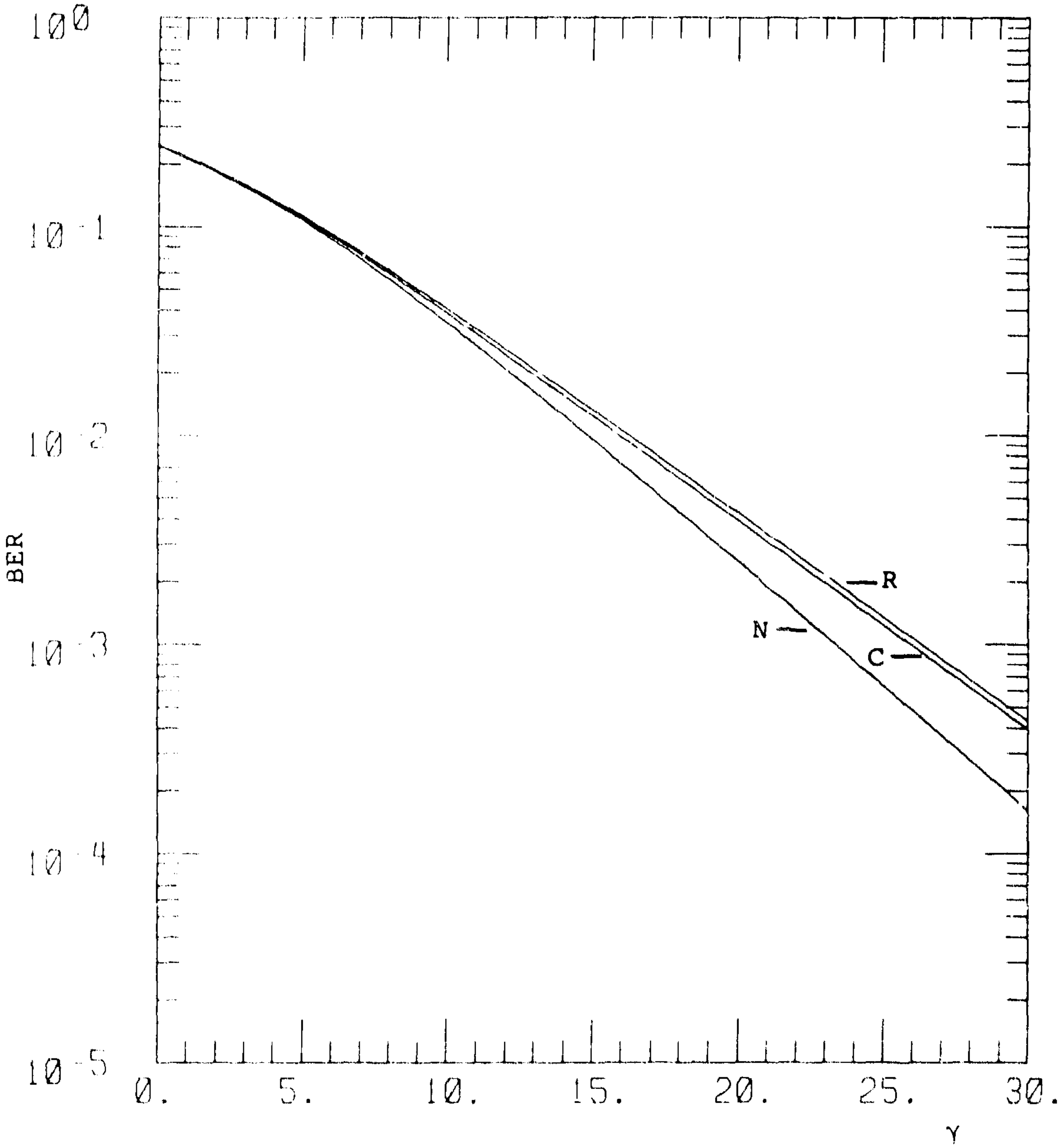

Figure J-6. BER for DBPSK
$\alpha = 1$, $\chi^2 = 0.4$, $S_4^2 = 0.837$.

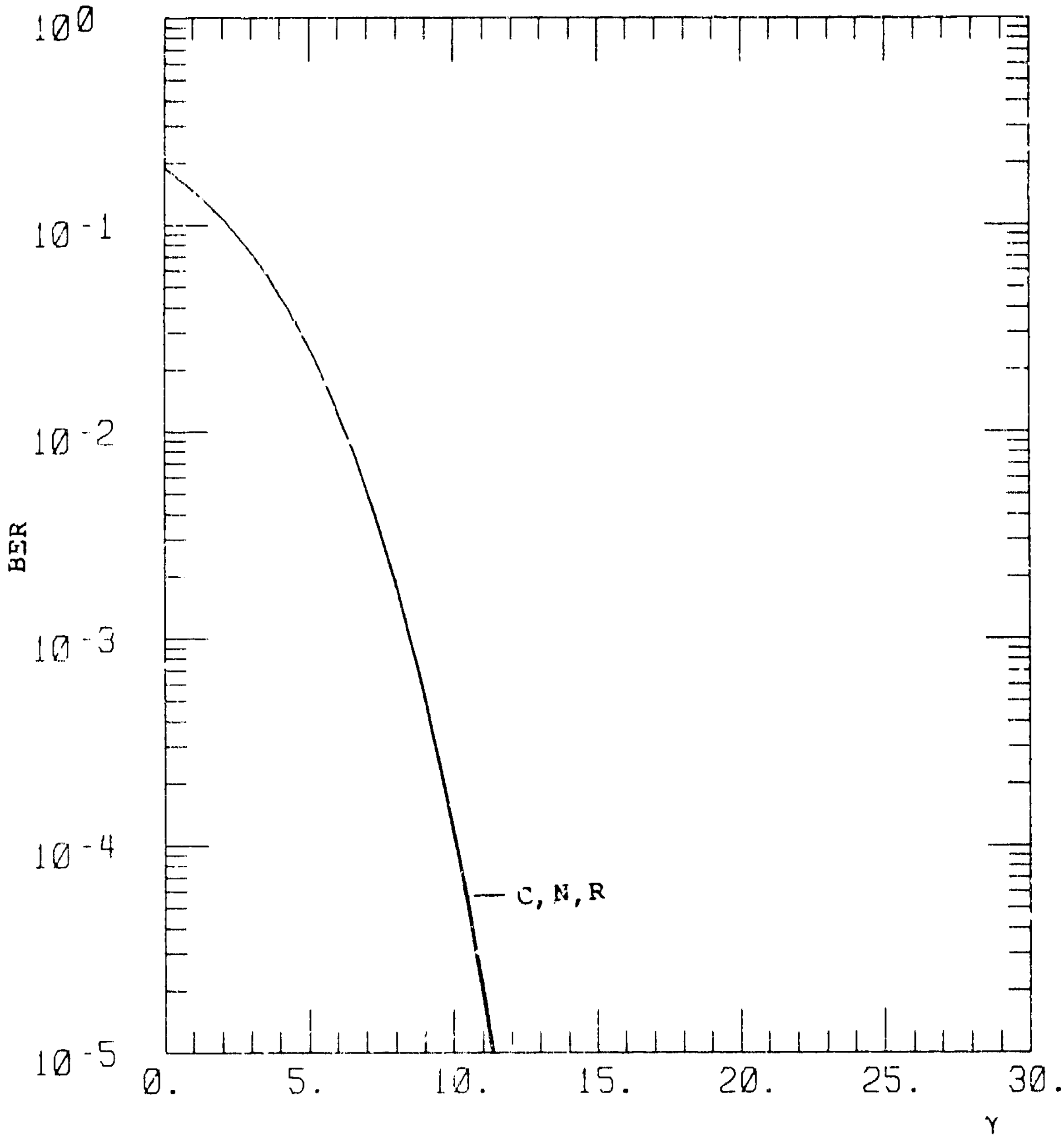

Figure J-7. BER for DBPSK
$\alpha = 2$, $\chi^2 = 0.01$, ${S_4}^2 = 0.039$.

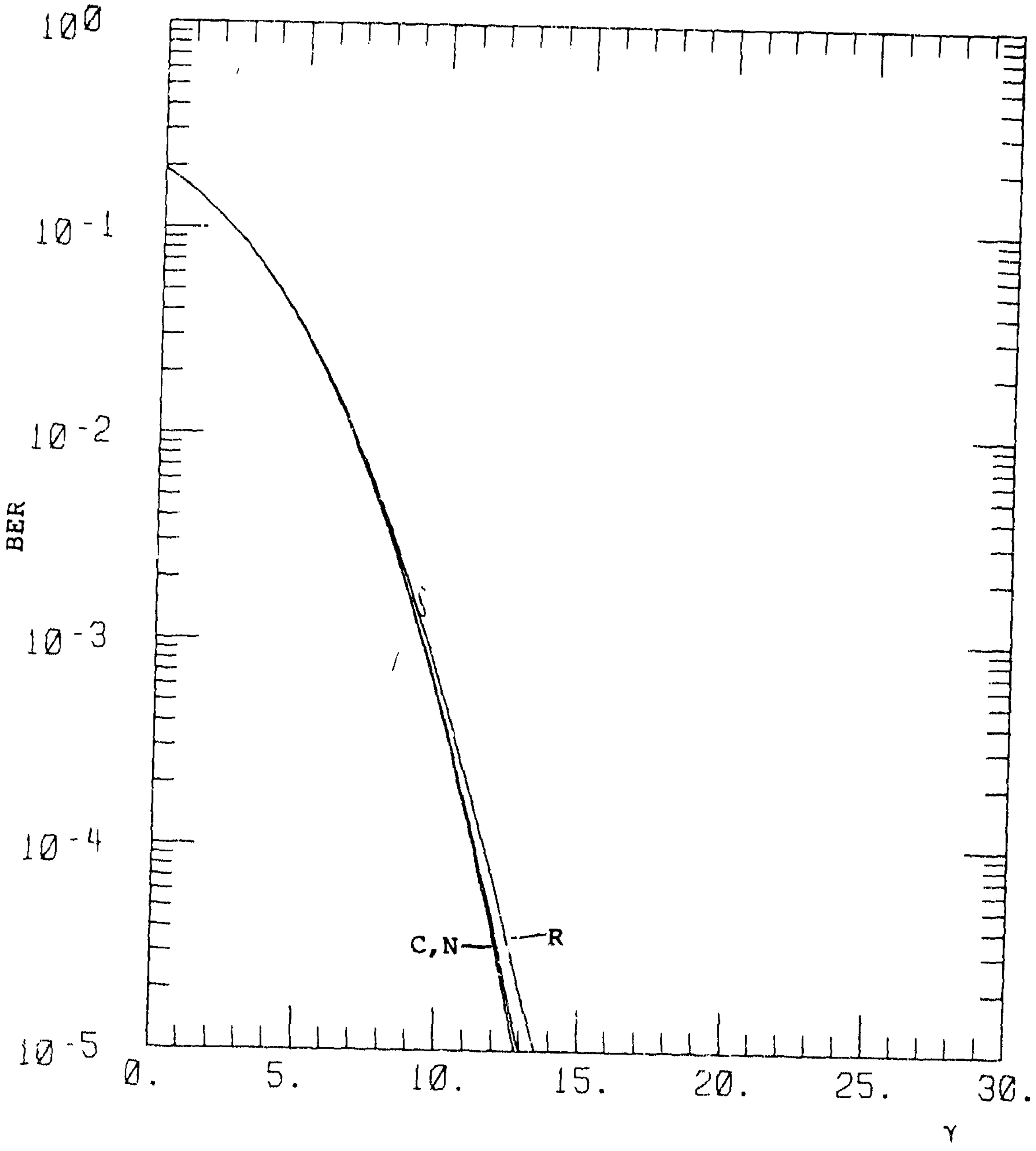

Figure J-8. BER for DBPSK
$\alpha = 2,\ \chi^2 = 0.025,\ S_4{}^2 = 0.097.$

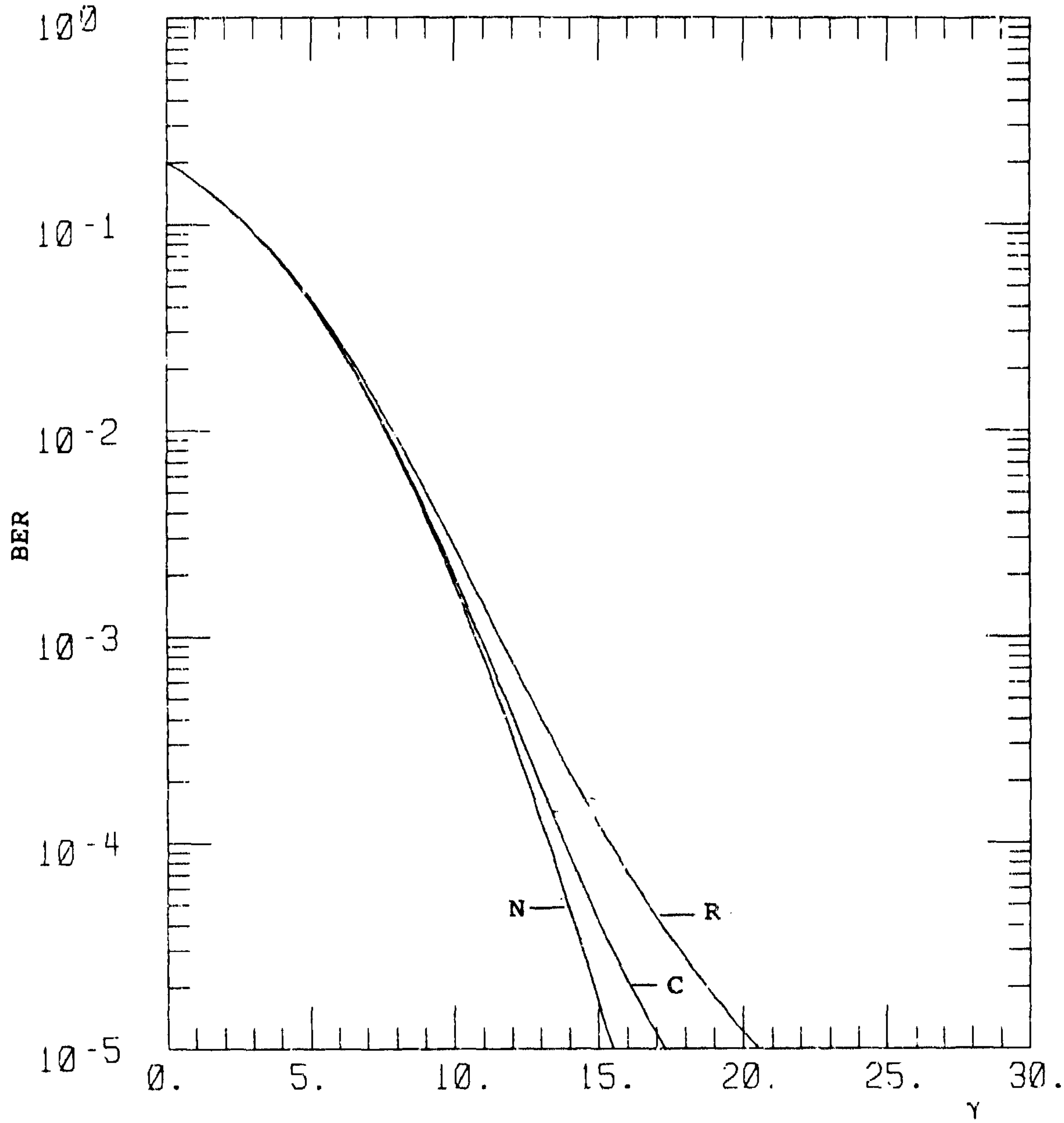

Figure J-9. BER for DBPSK
$\alpha = 2$, $\chi^2 = 0.05$, $S_4^2 = 0.188$.

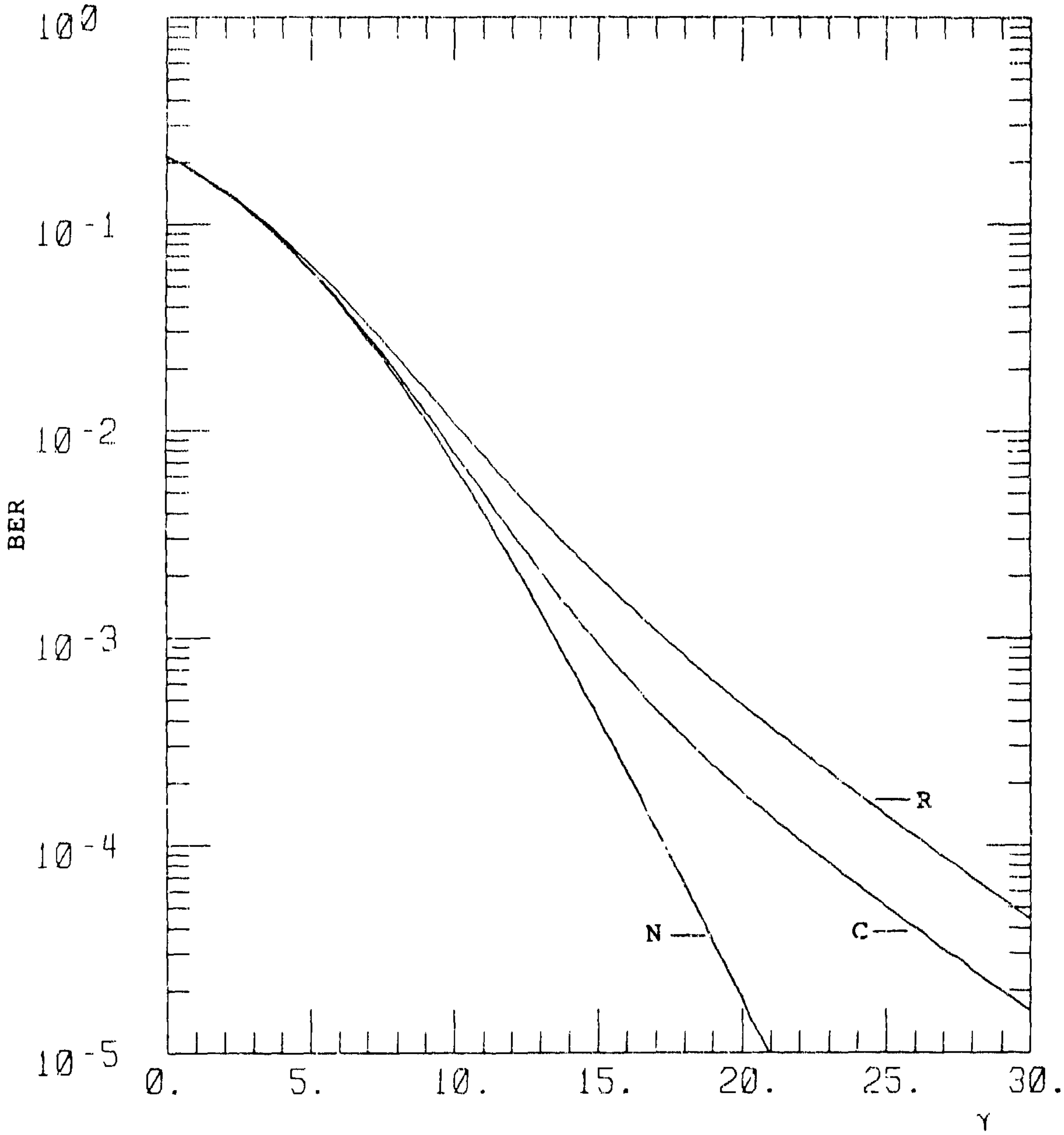

Figure J-10. BER for DBPSK
$\alpha = 2$, $\chi^2 = 0.1$, $S_4^2 = 0.350$.

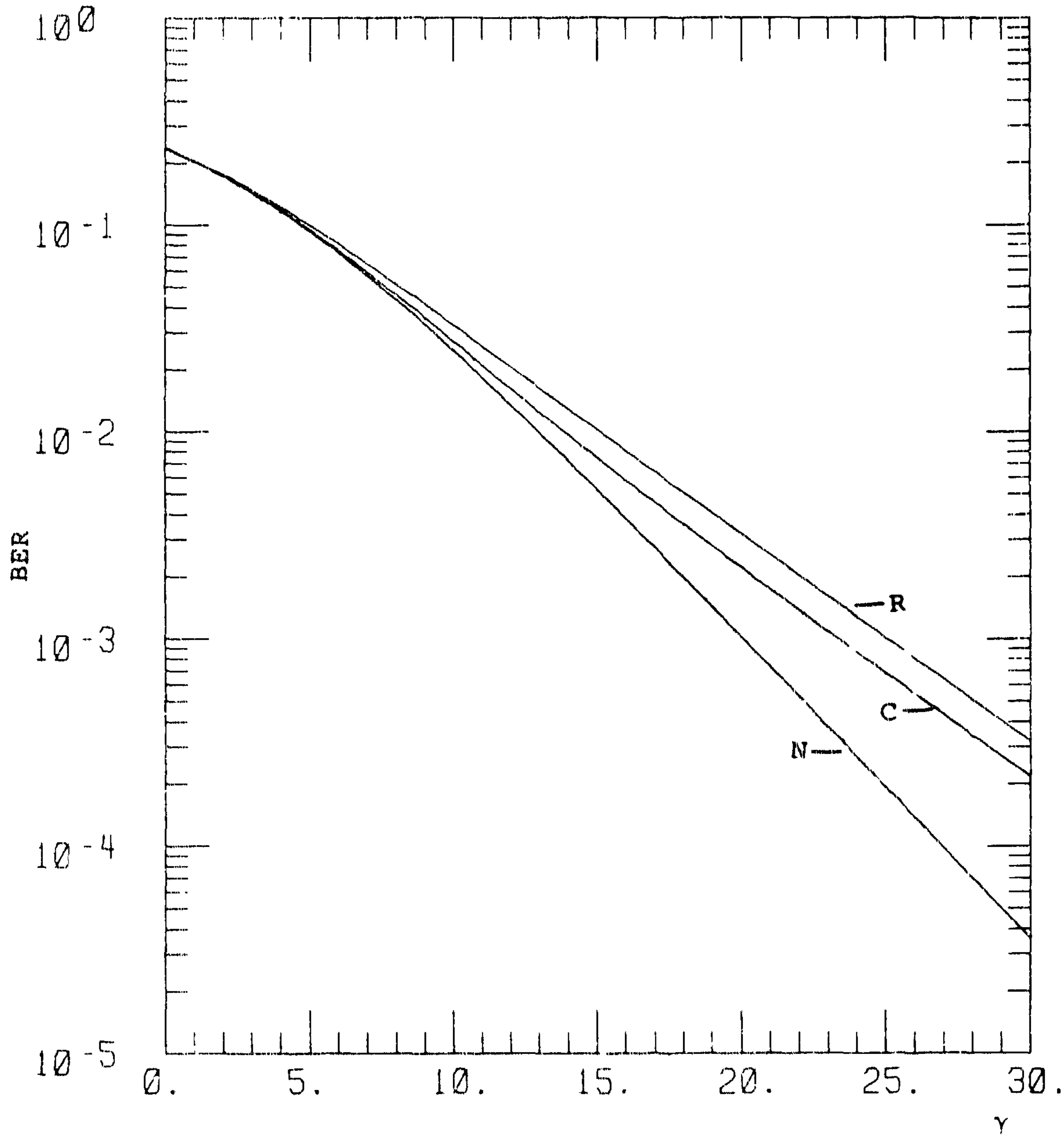

Figure J-11. BER for DBPSK
$\alpha = 2$, $\chi^2 = 0.25$, $S_4{}^2 = 0.684$.

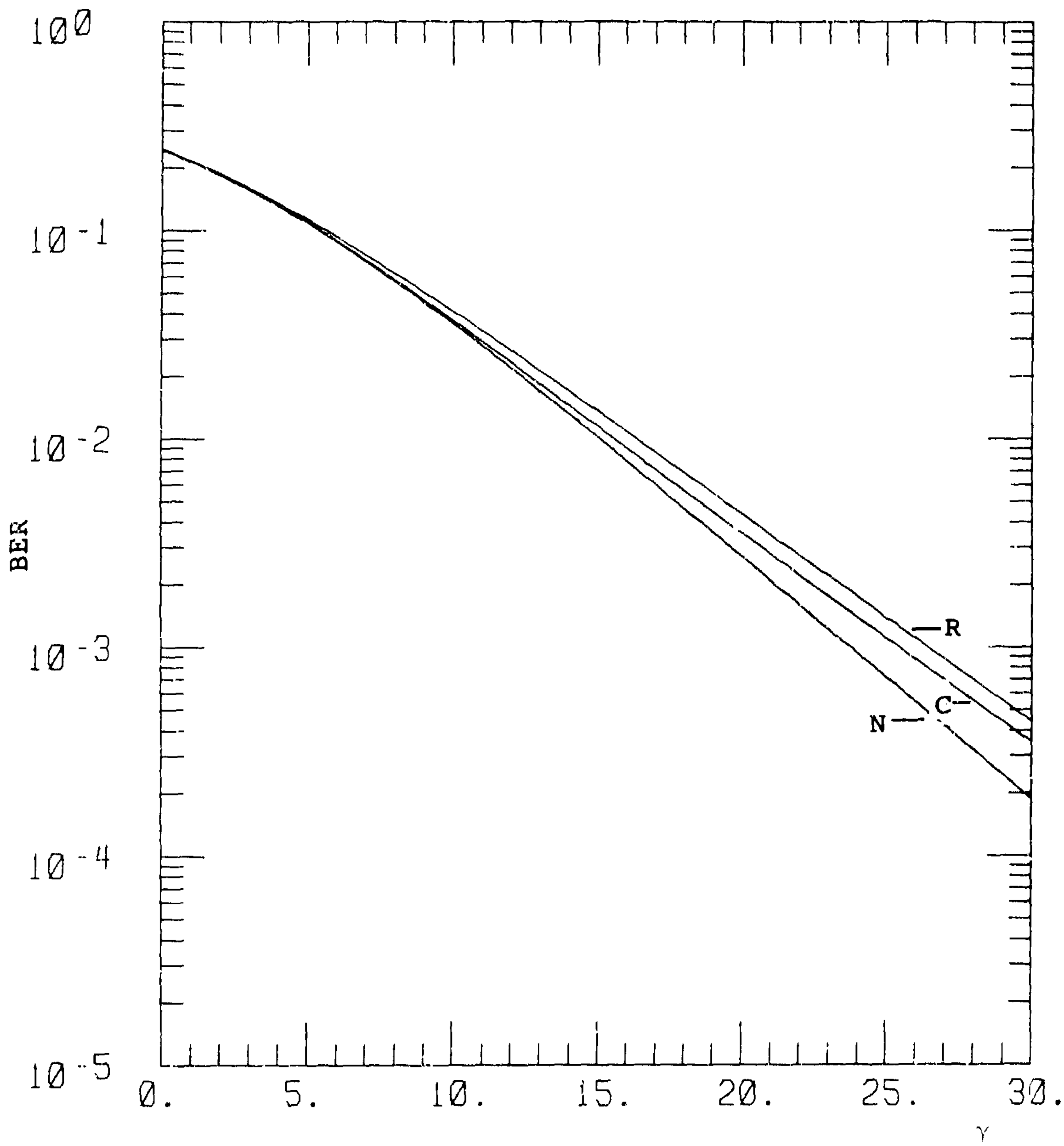

Figure J-12. BER for DBPSK
$\alpha = 2$, $\chi^2 = 0.4$, $S_4{}^2 = 0.854$.

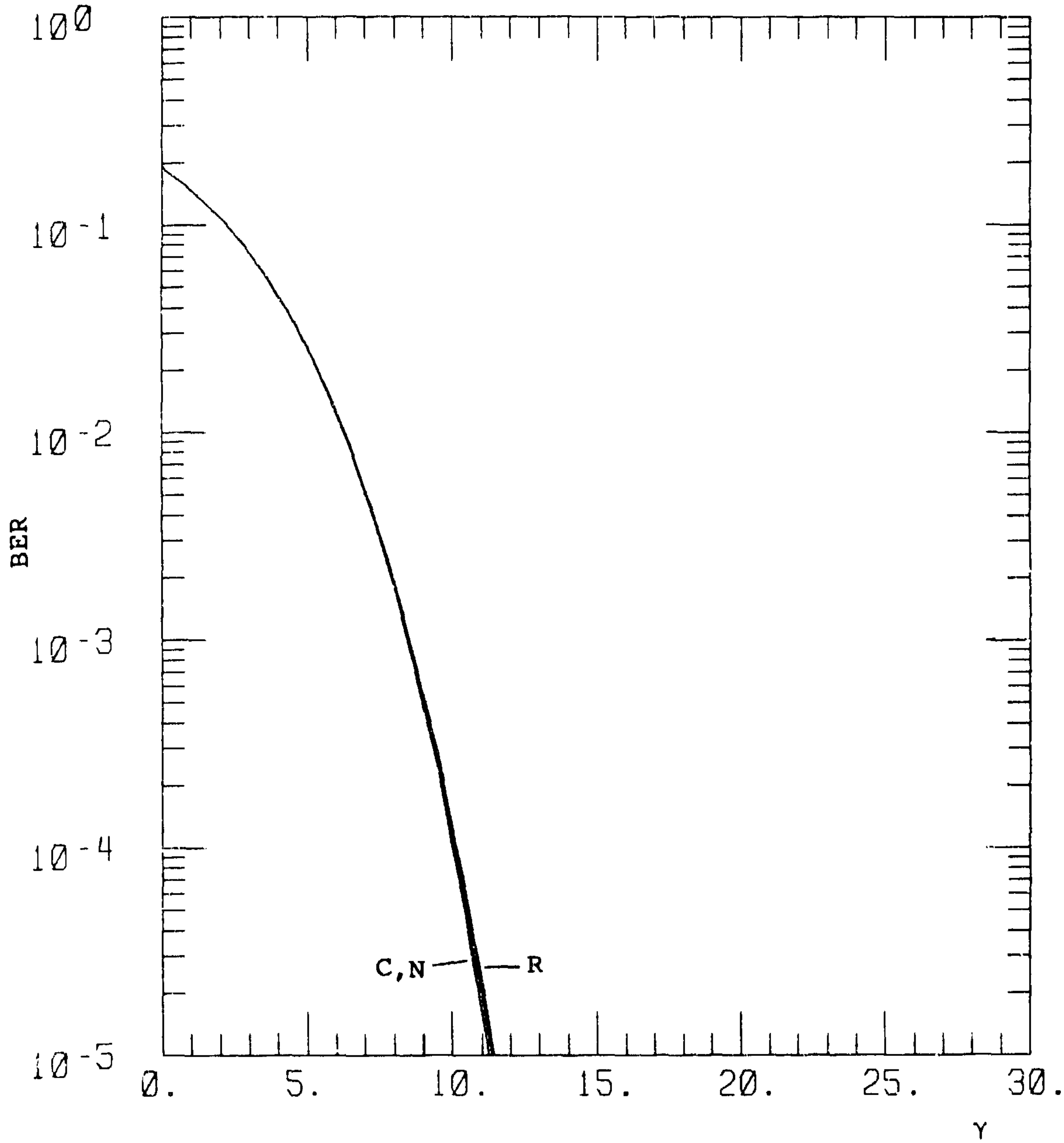

Figure J-13. BER for DBPSK
$\alpha = 3$, $\chi^2 = 0.01$, $S_4^{\ 2} = 0.040$.

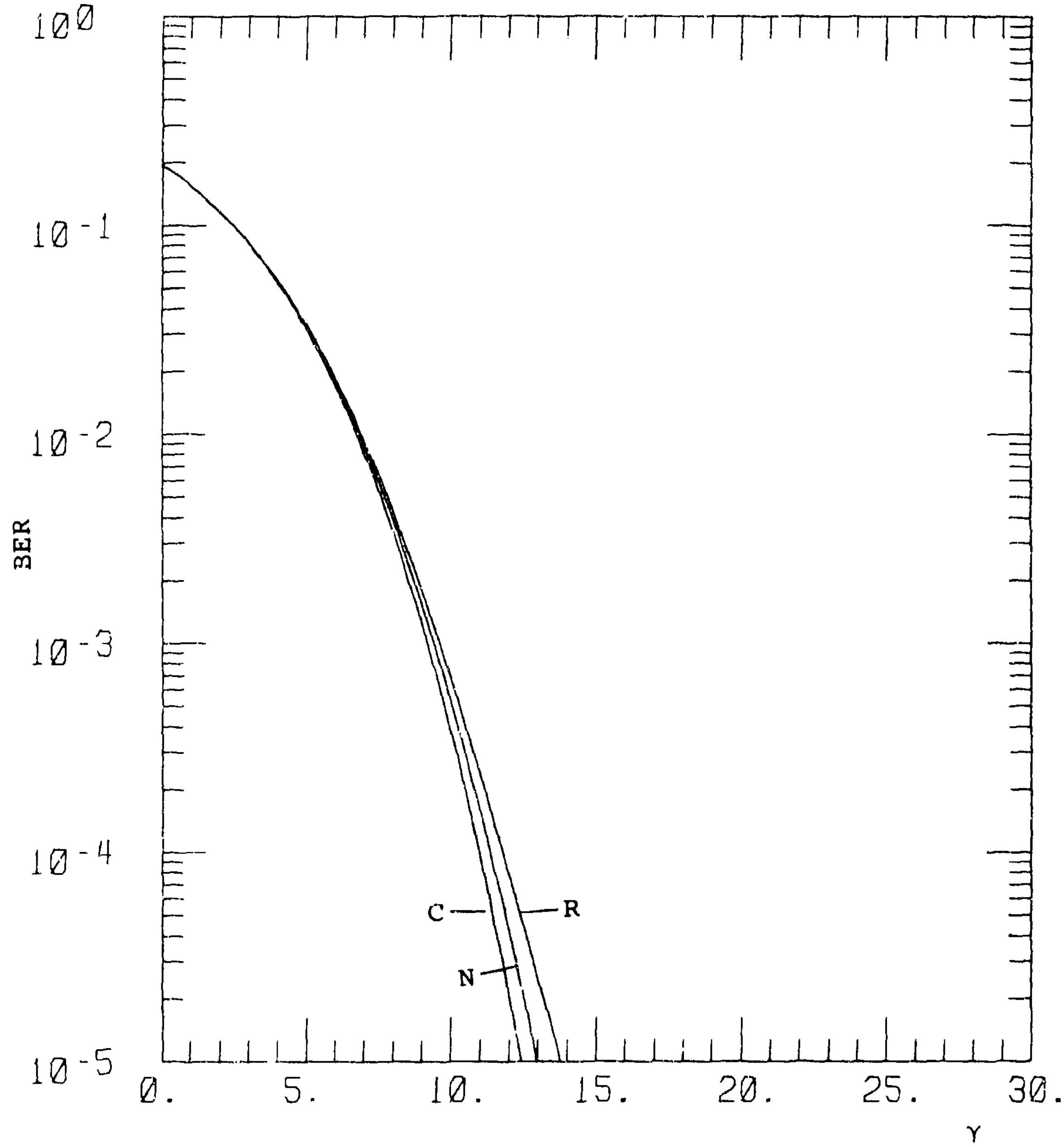

Figure J-14. BER for DBPSK
$\alpha = 3$, $\chi^2 = 0.025$, $S_4^{\,2} = 0.103$.

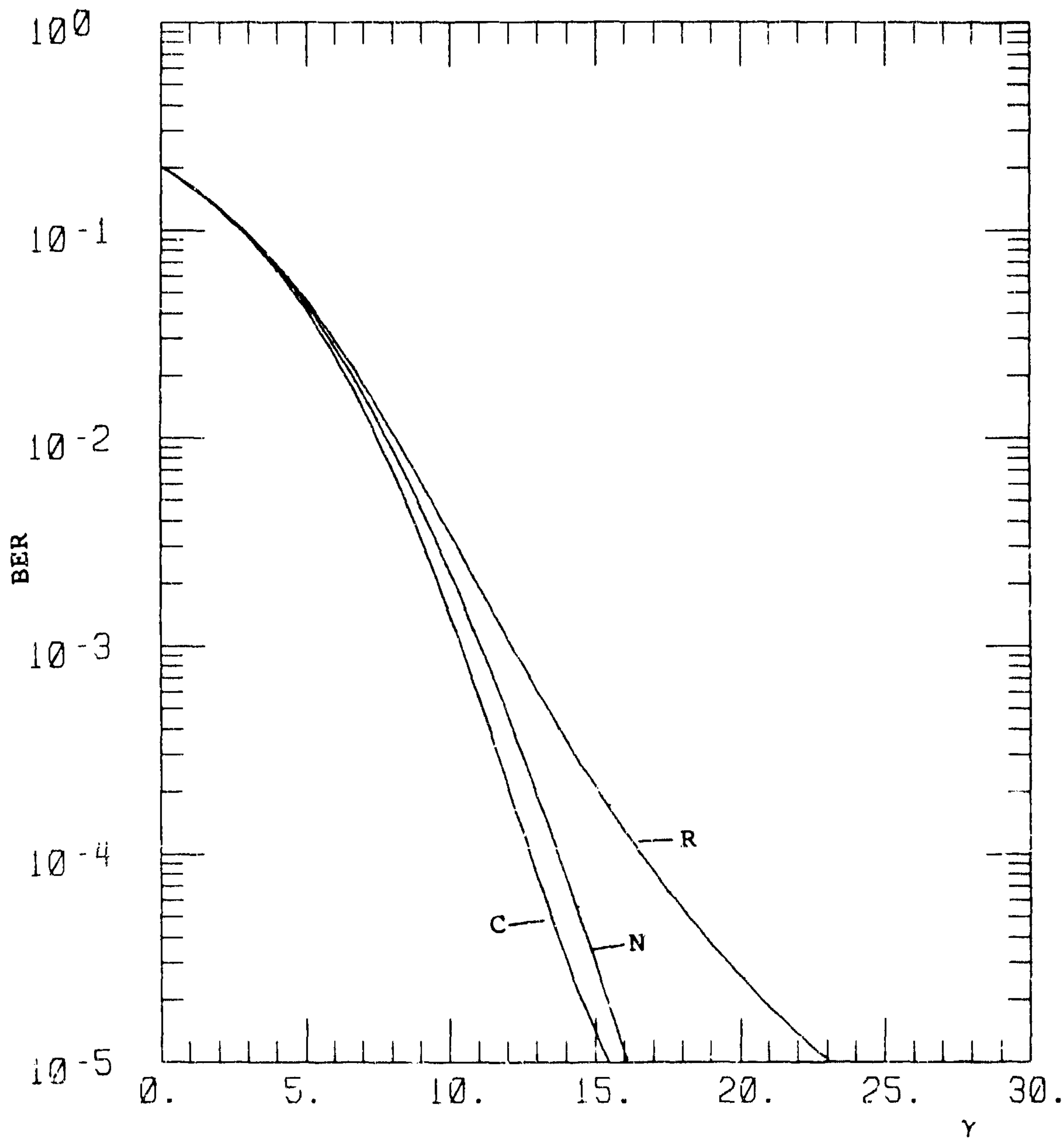

Figure J-15. BER for DBPSK
$\alpha = 3,\ \chi^2 = 0.05,\ S_4{}^2 = 0.208.$

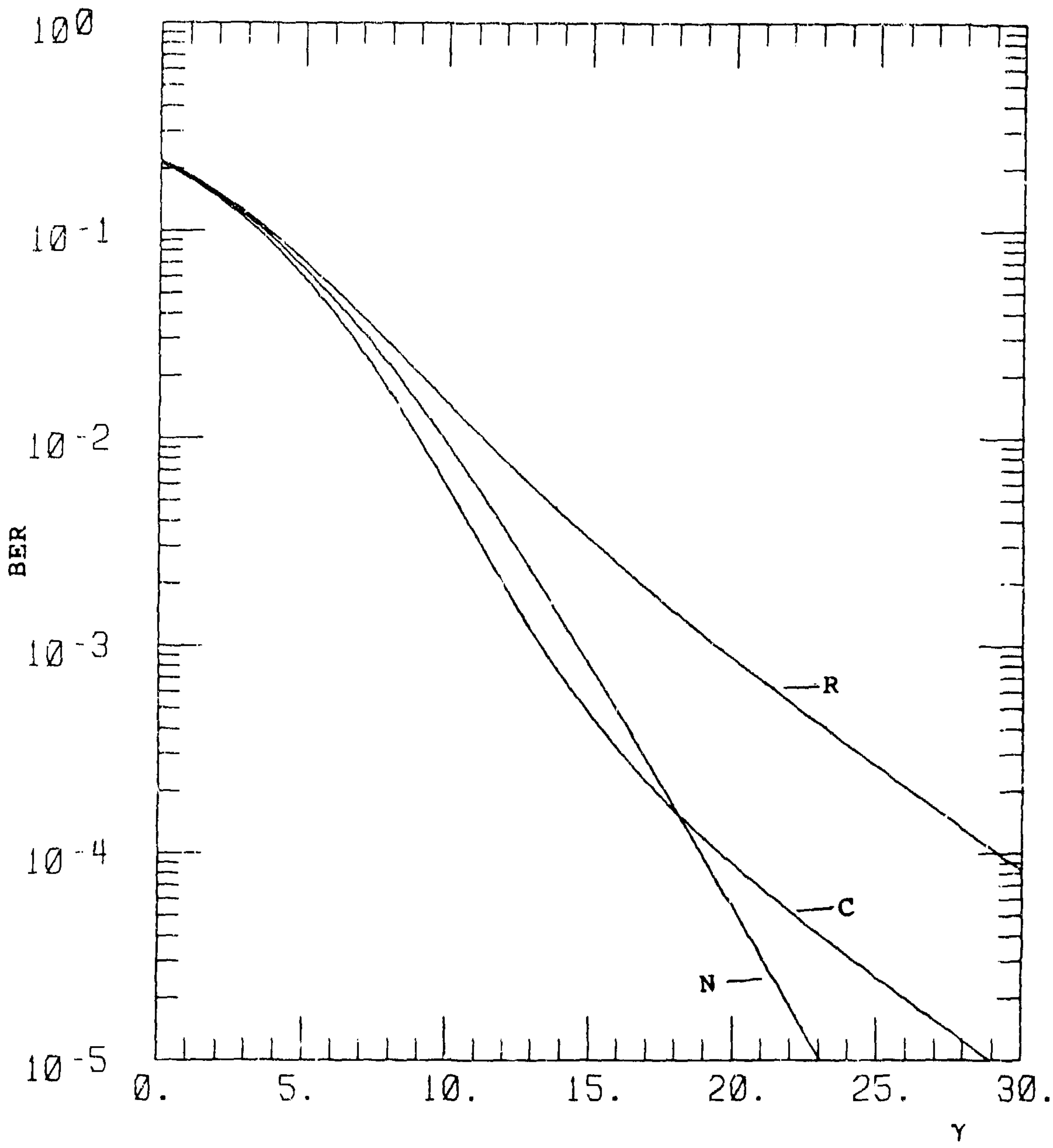

Figure J-16. BER for DBPSK
$\alpha = 3$, $\chi^2 = 0.1$, $S_4{}^2 = 0.409$.

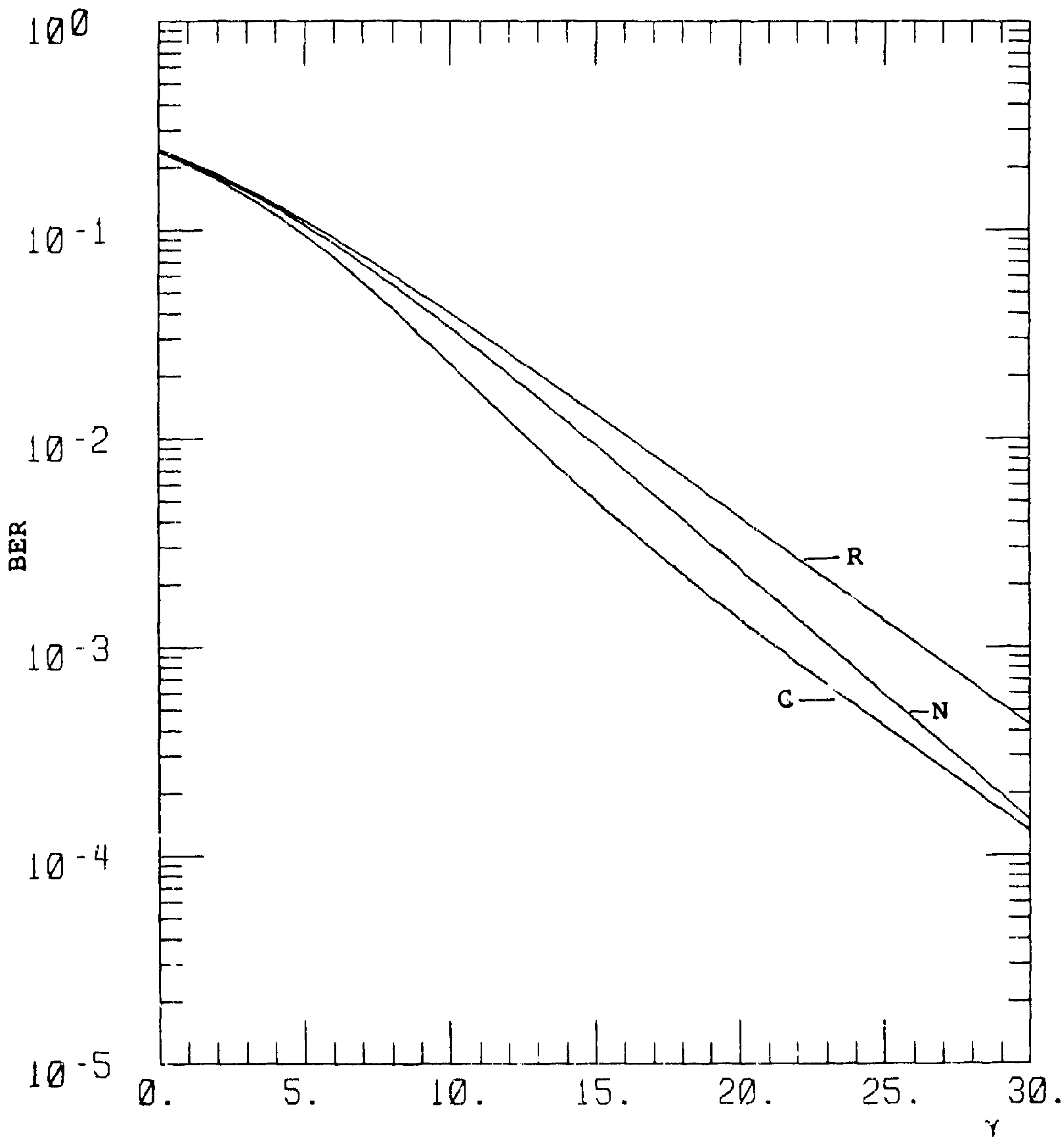

Figure J-17. BER for DBPSK
$\alpha = 3$, $\chi^2 = 0.25$, $S_4^{\ 2} = 0.827$.

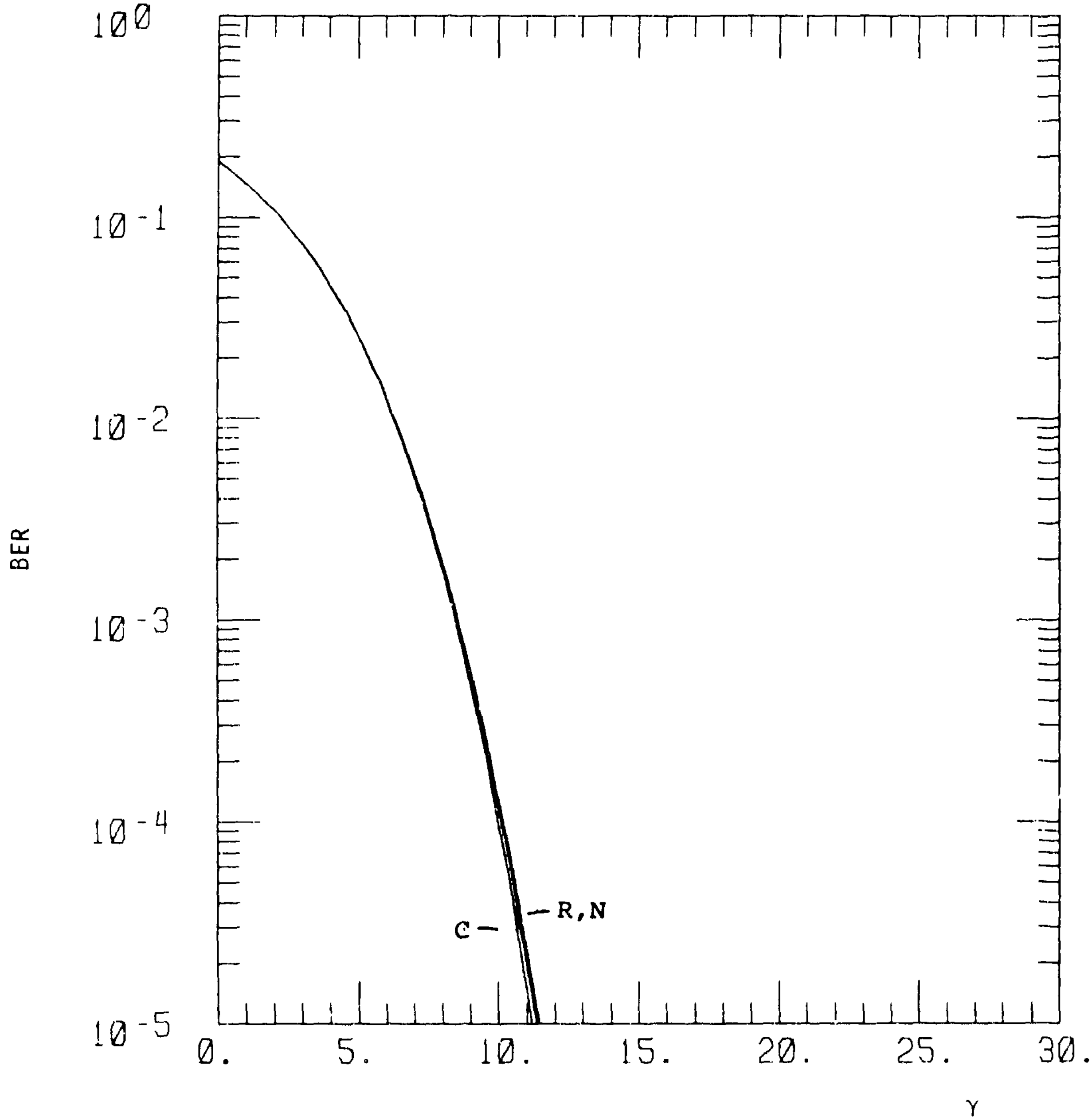

Figure J-18. BER for DBPSK
$\alpha = 4$, $\chi^2 = 0.01$, $S_4^{\,2} = 0.041$.

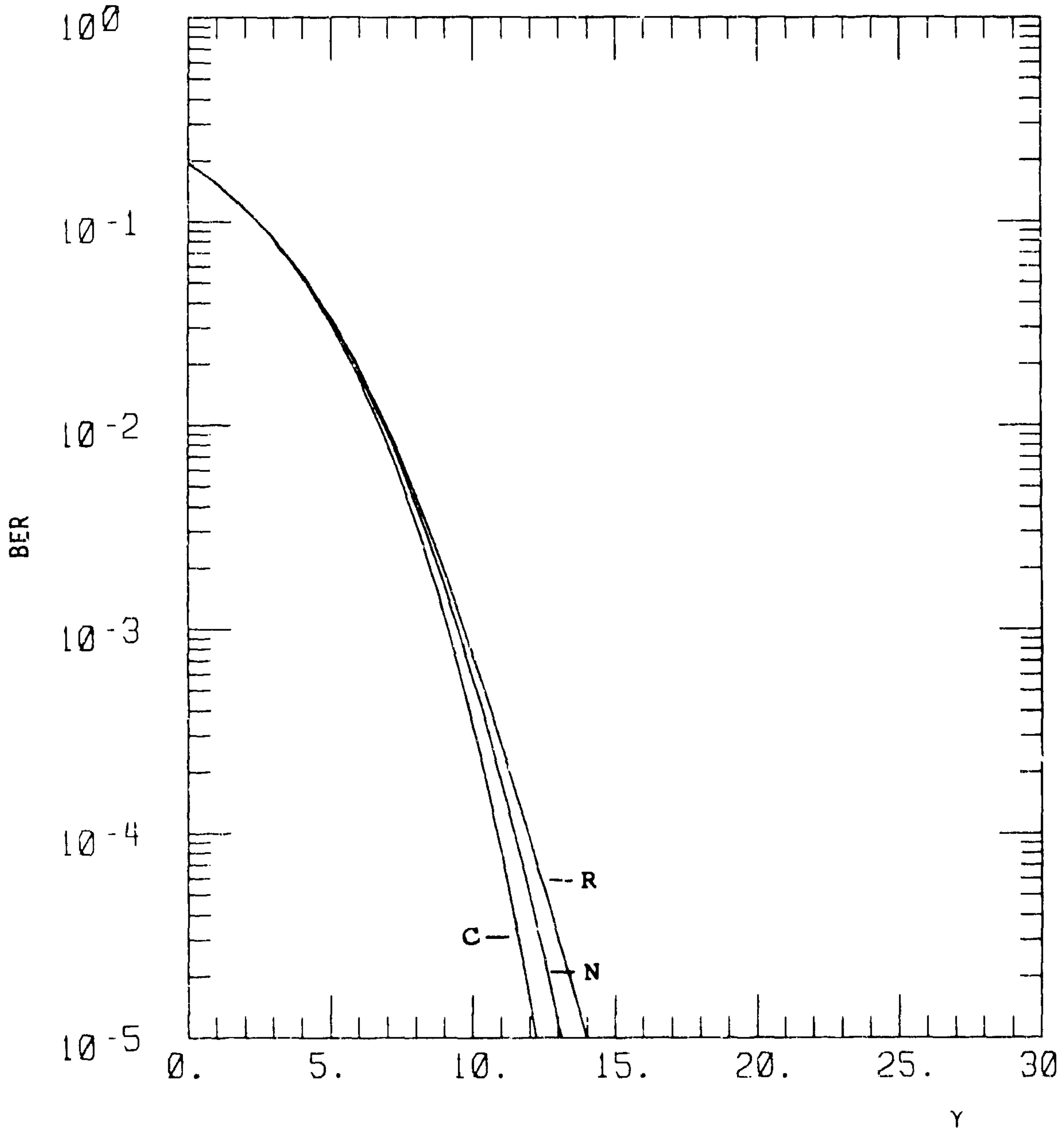

Figure J-19. BER for DBPSK
$\alpha = 4,\ \chi^2 = 0.025,\ S_4{}^2 = 0.107.$

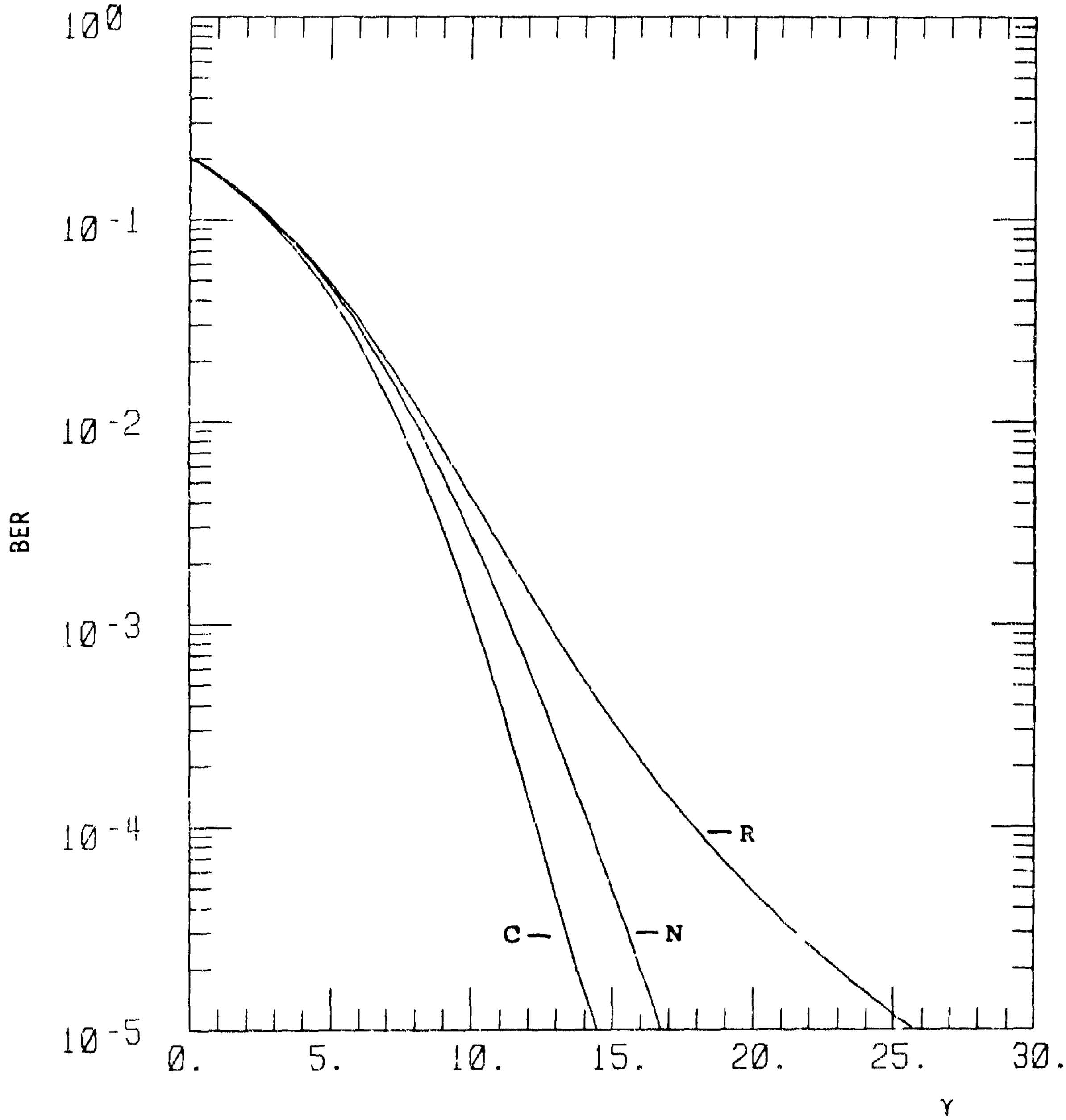

Figure J-20. BER for DBPSK
$\alpha = 4,\ \chi^2 = 0.05,\ S_4{}^2 = 0.227.$

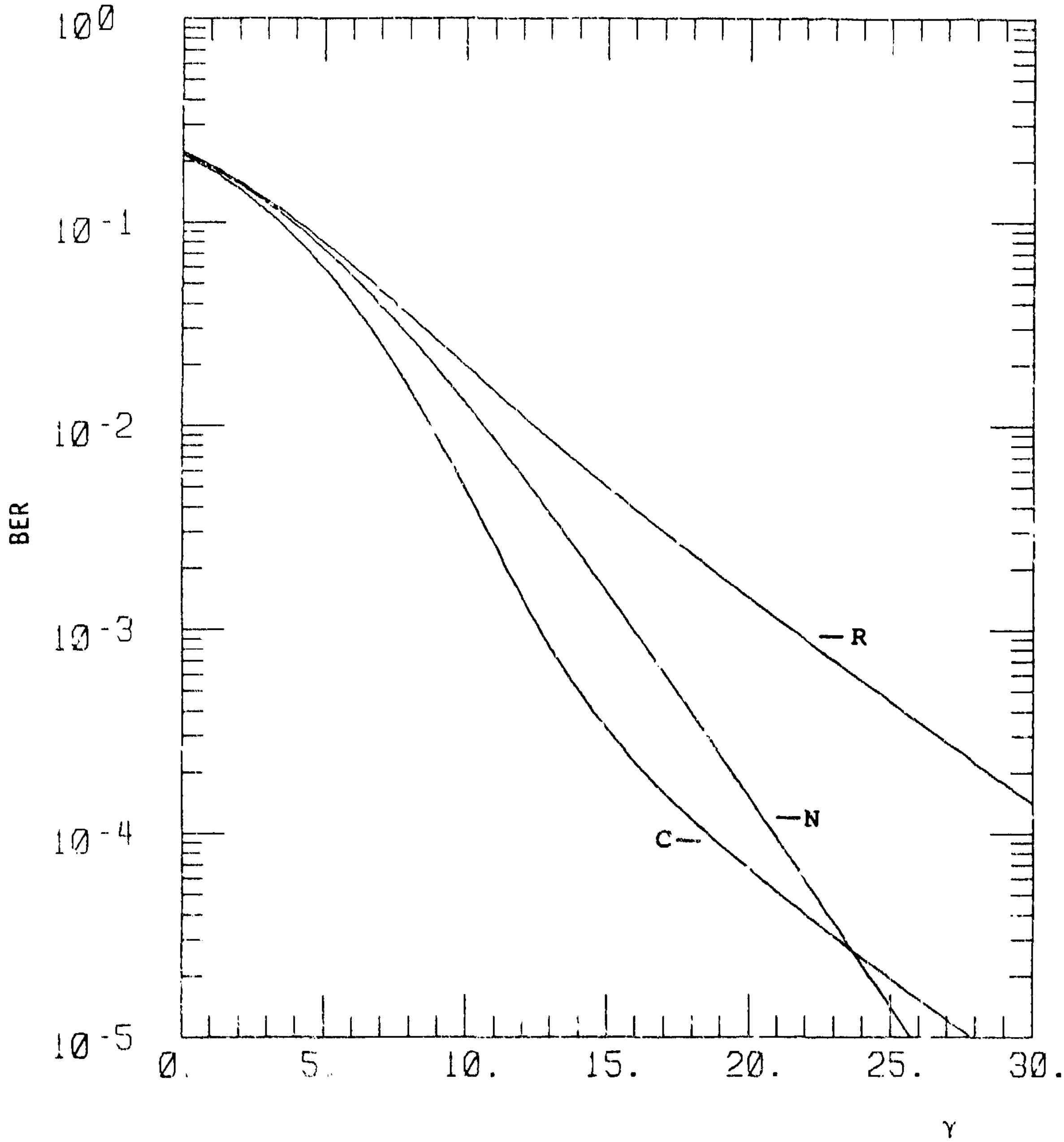

Figure J-21. BER for DBPSK
$\alpha = 4$, $\chi^2 = 0.1$, $S_4^{\;2} \simeq 0.479$.

DISTRIBUTION LIST

DNA-TR-89-150

DEPARTMENT OF DEFENSE

(US NUCLEAR COMMAND & CENTRAL SYST SUPPORT STAFF)
ATTN: SAB H SEQUINE

ASSISTANT TO THE SECRETARY OF DEFENSE ATOMIC ENERGY
ATTN: EXECUTIVE ASSISTANT

DEFENSE ADVANCED RSCH PROJ AGENCY
ATTN: DR MANSFIELD

DEFENSE COMMUNICATIONS AGENCY
ATTN: A320
ATTN: J DIETZ

DEFENSE COMMUNICATIONS ENGINEER CENTER
ATTN: CODE R410

DEFENSE INTELLIGENCE AGENCY
ATTN: DC-6
ATTN: DIR
ATTN: DT-1B
ATTN: RTS-2B
ATTN: VP-TPO

DEFENSE NUCLEAR AGENCY
ATTN: DFSP G ULLRICH
ATTN: NANF
ATTN: NASF
ATTN: OPNA
ATTN: PRPD R YOHO
YS ATTN: RAAE
ATTN: RAAE A MARDIGUIAN
ATTN: RAAE G ULLRICH
ATTN: RAAE K SCHWARTZ
ATTN: RAAE L SCHROCK
ATTN: RAAE M CRAWFORD
ATTN: RAAE P FLEMING
ATTN: RAAE S BERGGREN
ATTN: RAEE
4 CYS ATTN: TITL

DEFENSE NUCLEAR AGENCY
ATTN: TDNM
2 CYS ATTN: TDTT W SUMMA

DEFENSE TECHNICAL INFORMATION CENTER
2 CYS ATTN: DTIC/FDAB

JOINT DATA SYSTEM SUPPORT CTR
ATTN: C-312 R MASON

JOINT STRAT TGT PLANNING STAFF
ATTN: JK (ATTN: DNA REP)
ATTN: JKCS, STUKMILLER
ATTN: JLWT (THREAT ANALYSIS)
ATTN: JPEM
ATTN: JPSS

NATIONAL SECURITY AGENCY
ATTN: B432 C GOEDEKE

STRATEGIC DEFENSE INITIATIVE ORGANIZATION
ATTN: EN
ATTN: EN LTC C JOHNSON
ATTN: PTN C GIESE
ATTN: PTP LTC SEIBERLING
ATTN: TN

THE JOINT STAFF
ATTN: J6

DEPARTMENT OF THE ARMY

ARMY LOGISTICS MANAGEMENT CTR
ATTN: DLSIE

U S ARMY ATMOSPHERIC SCIENCES LAB
ATTN: DR F NILES
ATTN: SLCAS-AE-E

U S ARMY COMMUNICATIONS R&D COMMAND
ATTN: AMSEL-RD-ESA

U S ARMY FOREIGN SCIENCE & TECH CTR
ATTN: DRXST-SD

U S ARMY NUCLEAR & CHEMICAL AGENCY
ATTN: MONA-NU

U S ARMY NUCLEAR EFFECTS LABORATORY
ATTN: ATAA-PL
ATTN: ATAA-TDC
ATTN: ATRC-WCC

U S ARMY STRATEGIC DEFENSE CMD
ATTN: DASD-H-SA R BRADSHAW
ATTN: DASD-H-SA/R SMITH
ATTN: DASD-H-SAV

U S ARMY STRATEGIC DEFENSE COMMAND
ATTN: ATC-O W DAVIES

U S ARMY WHITE SANDS MISSILE RANGE
ATTN: STEWS-TE-N K CUMMINGS

USA SURVIVABILITY MANAGMENT OFFICE
ATTN: SLCSM-SE J BRAND

DEPARTMENT OF THE NAVY

COMMAND & CONTROL PROGRAMS
ATTN: OP 941

JOINT CRUISE MISSILES PROJECT OFC (PM-3)
ATTN: JCMG-707

NAVAL AIR SYSTEMS COMMAND
ATTN: PMA 271

NAVAL ELECTRONICS ENGRG ACTVY PACIFIC
ATTN: CODE 250 D OBRYHIM

NAVAL OCEAN SYSTEMS CENTER
ATTN: CODE 542, J FERGUSON

NAVAL RESEARCH LABORATORY
2 CYS ATTN: CODE 4100 H GURSKY
ATTN: CODE 4121.8 H HECKATHORN
ATTN: CODE 4183
ATTN: CODE 4700 S OSSAKOW
ATTN: CODE 4720 J DAVIS
ATTN: CODE 4750 P RODRIGUEZ
ATTN: CODE 4780 B RIPIN
ATTN: CODE 4780 DR P BERNHARDT
ATTN: CODE 4780 J HUBA

NAVAL SURFACE WARFARE CENTER
ATTN: CODE H-21

NAVAL TECHNICAL INTELLIGENCE CTR
ATTN: DA44

NAVAL UNDERWATER SYSTEMS CENTER
ATTN: CODE 3411, J KATAN

OFC OF THE DEPUTY CHIEF OF NAVAL OPS
ATTN: OP 654(STRAT EVAL & ANAL BR)
ATTN: OP 941D
ATTN: OP 981N

OFFICE OF NAVAL RESEARCH
ATTN: 1132SM/A TUCKER

SPACE & NAVAL WARFARE SYSTEMS CMD
ATTN: CODE 3101 T HUGHES
ATTN: PD 50TD
ATTN: PD50TD1 G BRUNHART
ATTN: PME 106-4 S KEARNEY
ATTN: PME-106 F W DIEDERICH

THEATER NUCLEAR WARFARE PROGRAM OFC
ATTN: PMS-42331F (D SMITH)

DEPARTMENT OF THE AIR FORCE

AIR FORCE CTR FOR STUDIES & ANALYSIS
ATTN: AFCSA/SAMI R GRIFFIN
ATTN: AFCSA/SASC

AIR FORCE ELECTRONIC WARFARE CENTER
ATTN: LT M MCNEELY

AIR FORCE SPACE SYSTEMS DIVISION
ATTN: YA
2 CYS ATTN: YN

AIR FORCE TECHNICAL APPLICATIONS CTR
ATTN: TN

AIR UNIVERSITY LIBRARY
ATTN: AUL-LSE

HQ AWS, DET 3 (CSTC/WE)
ATTN: WE

SECRETARY OF AF/AQQS
ATTN: AF/RDQI

STRATEGIC AIR COMMAND/XRFS
ATTN: XRFS

WEAPONS LABORATORY
ATTN: NTCA
ATTN: NTN
ATTN: SUL

DEPARTMENT OF ENERGY

EG&G, INC
ATTN: D WRIGHT

LAWRENCE LIVERMORE NATIONAL LAB
ATTN: L-31 R HAGER

LOS ALAMOS NATIONAL LABORATORY
ATTN: D SAPPENFIELD
ATTN: D SIMONS
ATTN: D WINSKE
ATTN: J WOLCOTT
ATTN: J ZINN
ATTN: R W WHITAKER
ATTN: T KUNKLE

SANDIA NATIONAL LABORATORIES
ATTN: D HARTLEY

SANDIA NATIONAL LABORATORIES
ATTN: A D THORNBROUGH
ATTN: CODE 9014 R BACKSTROM
ATTN: D DAHLGREN
ATTN: ORG 1231 T P WRIGHT
ATTN: ORG 9114 W D BROWN
ATTN: SPACE PROJECT DIV
ATTN: TECH LIB 3141

OTHER GOVERNMENT

CENTRAL INTELLIGENCE AGENCY
ATTN: OSWR/NED
ATTN: OSWR/SSD FOR L BERG

DEPARTMENT OF COMMERCE
ATTN: E MORRISON
ATTN: J HOFFMEYER
ATTN: W UTLAUT

U S DEPARTMENT OF STATE
ATTN: PM/TMP RM 7428

DEPARTMENT OF DEFENSE CONTRACTORS

AEROSPACE CORP
ATTN: A LIGHTY
ATTN: B P PURCELL
ATTN: C CREWS
ATTN: C RICE
ATTN: G LIGHT
ATTN: M ROLENZ

ANALYTICAL SYSTEMS ENGINEERING CORP
ATTN: SECURITY

ATLANTIC RESEARCH SERVICES CORP
ATTN: R MCMILLAN

ATMOSPHERIC AND ENVIRONMENTAL RESEARCH INC
ATTN: M KO

AUSTIN RESEARCH ASSOCIATES
ATTN: J THOMPSON

AUTOMETRIC INCORPORATED
ATTN: C LUCAS

BDM INTERNATIONAL INC
ATTN: L JACOBS

BERKELEY RSCH ASSOCIATES, INC
ATTN: C PRETTIE
ATTN: J WORKMAN
ATTN: S BRECHT

BOEING CO
ATTN: G HALL

CALIFORNIA RESEARCH & TECHNOLOGY, INC
ATTN: M ROSENBLATT

CHARLES STARK DRAPER LAB, INC
ATTN: A TETEWSKI

COMMUNICATIONS SATELLITE CORP
ATTN: G HYDE

CORNELL UNIVERSITY
ATTN: D FARLEY JR
ATTN: M KELLY

ELECTROSPACE SYSTEMS, INC
ATTN: P PHILLIPS

EOS TECHNOLOGIES, INC
ATTN: B GABBARD
ATTN: W LELEVIER

GENERAL RESEARCH CORP INC
ATTN: J EOLL

GEO CENTERS, INC
ATTN: E MARRAM

GRUMMAN AEROSPACE CORP
ATTN: J DIGLIO

GTE GOVERNMENT SYSTEMS CORPORATION
ATTN: W I THOMPSON, III

HARRIS CORPORATION
ATTN: E KNICK

HSS, INC
ATTN: D HANSEN

INSTITUTE FOR DEFENSE ANALYSES
ATTN: E BAUER
ATTN: H WOLFHARD

J S LEE ASSOCIATES INC
ATTN: DR J LEE

JAYCOR
ATTN: J SPERLING

JOHNS HOPKINS UNIVERSITY
ATTN: C MENG
ATTN: J D PHILLIPS
ATTN: R STOKES
ATTN: T EVANS

KAMAN SCIENCES CORP
ATTN: E CONRAD
ATTN: G DITTBERNER

KAMAN SCIENCES CORPORATION
ATTN: B GAMBILL
ATTN: DASIAC
ATTN: R RUTHERFORD

KAMAN SCIENCES CORPORATION
ATTN: DASIAC

LOCKHEED MISSILES & SPACE CO, INC
ATTN: J HENLEY
ATTN: J KUMER
ATTN: R SEARS

LOCKHEED MISSILES & SPACE CO, INC
ATTN: D KREJCI, Y001

LTV AEROSPACE & DEFENSE COMPANY
2 CYS ATTN: LIBRARY

M I T LINCOLN LAB
ATTN: D TOWLE
ATTN: I KUPIEC

MARTIN MARIETTA DENVER AEROSPACE
ATTN: H VON STRUVE III

MAXIM TECHNOLOGIES, INC
ATTN: B RIDGEWAY
ATTN: J SO

MCDONNELL DOUGLAS CORP
ATTN: T CRANOR

MCDONNELL DOUGLAS CORPORATION
ATTN: J GROSSMAN
ATTN: R HALPRIN

METATECH CORPORATION
ATTN: R SCHAEFER
ATTN: W RADASKY

METEOR COMMUNICATIONS CORP
ATTN: R LEADER

MISSION RESEARCH CORP
ATTN: J KENNEALY
ATTN: R ARMSTRONG
ATTN: R LARKIN
ATTN: S BELANGER
ATTN: W WHITE

MISSION RESEARCH CORP
ATTN: B R MILNER
ATTN: D ARCHER
ATTN: D KNEPP
ATTN: D LANDMAN
ATTN: F FAJEN
ATTN: F GUIGLIANO
ATTN: G MCCARTOR
ATTN: K COSNER
ATTN: M FIRESTONE
ATTN: R BIGONI
ATTN: R BOGUSCH
ATTN: R DANA

ATTN: R HENDRICK
ATTN: R KILB
ATTN: S GUTSCHE
ATTN: TECH INFO CENTER
ATTN: TECH LIBRARY

MITRE CORPORATION
ATTN: M R DRESP

MITRE CORPORATION
ATTN: J WHEELER
ATTN: M HORROCKS
ATTN: R C PESCI
ATTN: W FOSTER

NORTHWEST RESEARCH ASSOC, INC
ATTN: E FREMOUW

PACIFIC-SIERRA RESEARCH CORP
ATTN: E FIELD JR
ATTN: F THOMAS
ATTN: H BRODE

PHOTOMETRICS, INC
ATTN: I L KOFSKY

PHYSICAL RESEARCH INC
ATTN: W. SHIH

PHYSICAL RESEARCH INC
ATTN: H FITZ
ATTN: P LUNN

PHYSICAL RESEARCH, INC
ATTN: R DELIBERIS
ATTN: T STEPHENS

PHYSICAL PESEARCH, INC
ATTN: J DEVORE
ATTN: J THOMPSON
ATTN: W SCHLUETER

R & D ASSOCIATES
ATTN: C GREIFINGER
ATTN: F GILMORE
ATTN: G HOYT
2 CYS ATTN: L L DERAAD
ATTN: M GANTSWEG
2 CYS ATTN: M K GROVER

R & D ASSOCIATES
ATTN: J WALTON

RAND CORP
ATTN: C CRAIN
ATTN: E BEDROZIAN

RAND CORP
ATTN: B BENNETT

RJO ENTERPRISES/POET FAC
ATTN: A ALEXANDER
ATTN: W BURNS

S-CUBED
ATTN: C NEEDHAM
ATTN: T CARNEY

SCIENCE APPLICATIONS INTL CORP
ATTN: C SMITH
ATTN: D HAMLIN
ATTN: D SACHS
ATTN: E STRAKER
ATTN: L LINSON

SCIENCE APPLICATIONS INTL CORP
ATTN: J COCKAYNE

SCIENCE APPLICATIONS INTL CORP
ATTN: D TELAGE
ATTN: M CROSS

SRI INTERNATIONAL
ATTN: W CHESNUT
ATTN: W JAYE

STEWART RADIANCE LABORATORY
ATTN: R HUPPI

TELECOMMUNICATION SCIENCE ASSOCIATES
ATTN: R BUCKNER

TELEDYNE BROWN ENGINEERING
ATTN: J WOLFSBERGER, JR

TOYON RESEARCH CORP
ATTN: J ISE

TRW INC
ATTN: DR D GRYBOS
ATTN: R PLEBUCH/HARDNESS & SURV LAB
ATTN: H CULVER

TRW SPACE & DEFENSE SYSTEMS
ATTN: D M LAYTON

USER SYSTEMS, INC
ATTN: S W MCCANDLESS JR

UTAH STATE UNIVERSITY
ATTN: K BAKER, DIR ATMOS & SPACE SCI
ATTN: L JENSEN, ELEC ENG DEPT

VISIDYNE, INC
ATTN: J CARPENTER

FOREIGN

FOA 2
ATTN: B SJOHOLM

FOA 3
ATTN: T KARLSSON